THE TASMAN PROJECT OF SEAFLOOR MAGNETOTELLURIC EXPLORATION

by

IAN JAMES FERGUSON

A thesis submitted for the degree of Doctor of Philosophy

at the

Australian National University

January 1988

ABSTRACT

The Tasman Project of Seafloor Magnetotelluric Exploration was performed between December 1983 and April 1984 in order to investigate the electrical conductivity structure beneath the Tasman Seafloor and the Australian continental margin. Recordings were made at nine seafloor and nine land sites on a line extending from inland Australia to the Lord Howe Rise in the eastern Tasman Sea. Magnetic field recordings were made at all sites and horizontal electric field recordings at seven of the seafloor sites. In addition, oceanographic recordings were made at several of the seafloor sites, as an additional aim of the project was to provide physical oceanographic information on the Tasman Sea. Data return from the experiment was almost complete and the data quality high. All of the raw recordings have been converted into final magnetic field, horizontal electric field and oceanographic time series.

An analysis of the seafloor magnetotelluric (SFMT) data has been completed. The results indicate that geomagnetic induction in the Tasman Sea is a three-dimensional process dependent on the large-scale shape of the Tasman Sea. The seafloor impedances have a dominantly two-dimensional form with the B-pol impedance component (the component perpendicular to the trend of the Tasman Sea) being strongly attenuated near the Australian coastline. Evidence for the three-dimensionality includes large impedance skew-angles and consistent differences between impedances estimated using the SFMT and vertical gradient sounding (VGS) methods. The spatial consistency of these results supports the hypothesis of large-scale geomagnetic induction in the Tasman Sea. The induction arrows calculated for land and seafloor sites near the Australian coast exhibit significant components parallel to the coastline, providing further evidence for a three-dimensional process.

Evidence suggests that the most appropriate data to analyse using one-dimensional MT techniques are the E-pol impedances from three sites, TP3, TP4 and TP5, in the central Tasman Sea. Inversions were therefore performed on these data using delta-function and minimum-structure inversion algorithms. Delta function inversions were performed ~~to~~ in order to investigate the one-dimensionality of the data, the depth of resolution of the data, and the significance of differences between the conductivity models at the different sites. Minimum-structure inversions were performed in order to produce more physically-realistic conductivity profiles, and to examine which features in the profile are definitely required by the data. In addition to these inversions, the B-pol impedance terms from the seafloor sites were used with the MT anisotropy method to determine the minimum integrated crustal resistance of the Tasman Seafloor, 10^7 $\Omega.m^2$. The E-pol impedance terms were used to estimate the depth to the good conductor beneath each site with the MT asymptotic method.

The conductivity models obtained for sites TP3 and TP4 appear to define a reliable conductivity profile for the Tasman Sea. The Tasman Sea profile includes a high conducting layer occurring at a depth comparable to that for similar age lithosphere in the Pacific Ocean. The differences between the SFMT and VGS impedance estimates cause some ambiguity regarding the depth to the high conducting layer with the VGS and SFMT impedances estimates suggesting depths of 100 and 200 km respectively. Comparison of the conductivity models with other geophysical results suggests the correct depth lies between 120 and 150 km. At shallow depths the TP4 profile is more conductive than the TP3 profile. The higher conductance at TP4 cannot be explained by differences between the sediment layer at the two sites and is tentatively attributed to thermal effects associated with the source of an active seamount chain located near TP4.

The conductivity profile obtained for the third site, TP5, in the Central Tasman is probably only geophysically accurate at depths greater than 200 km. The deep structure at this site is more resistive than at sites TP4 and TP3 to the east, a result supported by the asymptotic-method results for sites near TP5. Confirmation of the conductivity results for the Tasman Sea will be provided by the application of three-dimensional MT modelling methods. In particular, thin-sheet modelling should indicate the accuracy of the assumptions made during the 1D analyses described in this thesis.

In addition to information on the sub-oceanic conductivity structure, the Tasman Project has provided valuable information in other areas. Induction arrows at the land and seafloor sites are currently being analysed for information on the electrical conductivity structure of the Australian continental margin. Physical oceanographic information on processes including tides, eddies, and internal waves has been obtained, and information is also available on geomagnetic source-fields in the Tasman Sea region.

TABLE OF CONTENTS

PART I

THE TASMAN PROJECT OF SEAFLOOR MAGNETOTELLURIC EXPLORATION

Chapter 1 Introduction to the Tasman Project of Seafloor Magnetotelluric Exploration

1.1 General Introduction

This thesis describes a large-scale geophysical investigation of the structure beneath the floor of the Tasman Sea using seafloor magnetotelluric exploration. Magnetotelluric (MT) sounding is an electromagnetic exploration technique which yields information on the electrical conductivity structure beneath the surface of the Earth or of the seafloor. The electrical conductivity structure is interpreted in terms of the geological and tectonic structure sounding the site. The MT method consists of measuring and interpreting fluctuations in both the Earth's magnetic field and the resulting electric currents induced in the Earth.

The Tasman Project of Seafloor Magnetotelluric Exploration (the "Tasman Project" or "TPSME") took place between December 1983 and April 1984. It comprised simultaneous geophysical recordings made at 18 sites situated on a 2400 km recording line extending from the eastern Tasman Sea across the Australian coastline and onto the Australian continent (Figure 1.1). The main objective of the Tasman Project was to investigate the structure beneath the Tasman Sea and additional aims were to study the structure of the Australian continental margin and to provide physical oceanographic information on the Tasman Sea.

The geophysical measurements made during the Tasman Project included recordings of the magnetic and electric (telluric) fields at nine sites on the Tasman Seafloor. These recordings formed the seafloor magnetotelluric (SFMT) data set. Additional magnetic field recordings were made at nine sites on the Australian continent in order to provide a comparison with the seafloor data, and to investigate the Australian continental margin. Seafloor oceanographic recordings of water velocity, pressure, vertical electric field and temperature were made at some of the Tasman Sea sites in order to assist the separation of oceanically induced signal from the MT data and also to produce information on the tides, eddies and other physical oceanographic phenomena of the Tasman Sea.

This thesis is divided into two sections. In section I, entitled "The Tasman Project of Seafloor Magnetotelluric Exploration" a detailed description is given of the experimental aspects of the Tasman Project. This description will include the aims of the project, the history of the project, the actual experiment, and details of the reduction of the seafloor recordings into final time series. The aim of this section is to provide a comprehensive description of the experiment within a single manuscript.

Section II of the thesis is entitled "The Analysis of Tasman Seafloor Magnetotelluric Data" and is based on the determination of the structure of the Tasman Seafloor using the recorded MT data. This section also describes the theory of MT and SFMT analysis and contains a review of previous determinations of seafloor conductivity structure. The

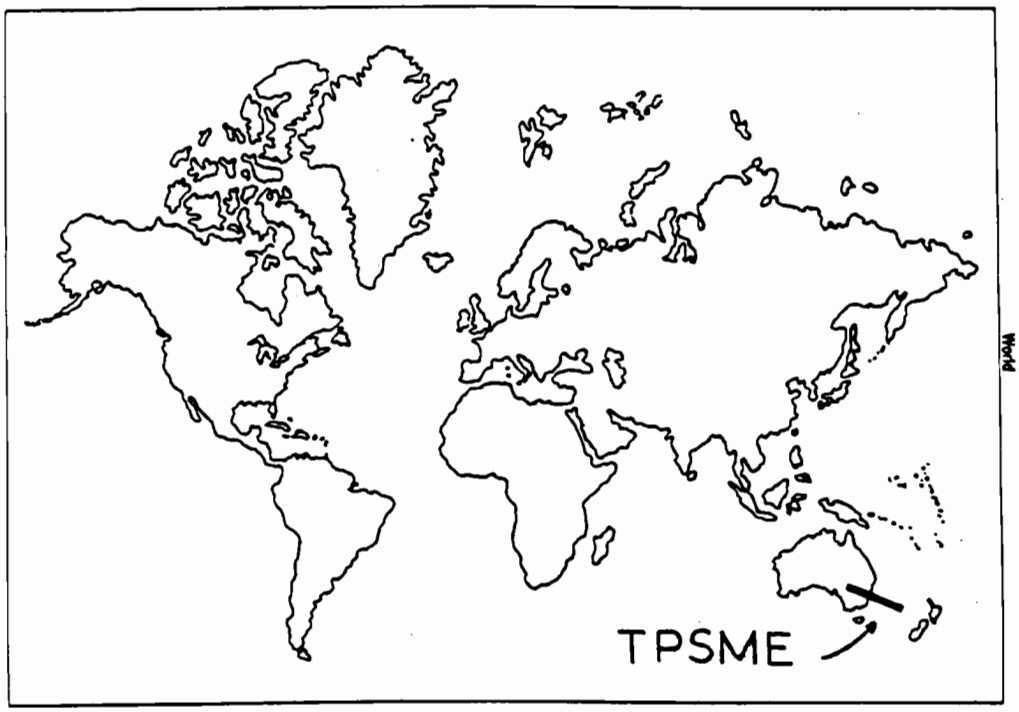

Figure 1.1 Map of the world showing the location of the Tasman Project of Magnetotelluric Exploration. The experiment involved geophysical recordings made along a 2400 km line extending from the eastern Tasman Sea across the Australian coast and onto the Australian continent.

Tasman Sea conductivity structure will be interpreted in terms of the existing geophysical and geological information on this region and compared with other seafloor conductivity results from around the world. The research described in this section, along with a significant contribution to the experiment and data reduction described in section A, forms the author's submission for his Ph.D. degree.

The remainder of chapter 1 includes a description of the aims of the Tasman Project within the broader framework of studies in the Earth Sciences. It also includes a more detailed introduction to the types of recordings made during the project and a description of the history and background to the experiment. Finally, the chapter lists the system of physical units, symbols and abbreviations used in this thesis.

1.2 Electromagnetic induction studies in the Earth and oceans

The Role of Geophysics

The aim of studies in the Earth Sciences is to increase our understanding of the Earth: its structure, its evolution and the physical processes occurring in, on and near it. It is hoped that the results from the Tasman Project will contribute to each of these areas. The electrical conductivity structure derived for the Tasman Sea will provide information on the geological structure beneath the Tasman Seafloor. Along with other geological and geophysical details this information will enable a better understanding of the tectonic evolution of the area. Finally, from the measurements made in the project, will come information on physical processes occurring on the Earth including the behaviour of electric currents induced in the Earth and the behaviour of various oceanographic processes such as tides, eddies and waves.

Direct observations of the Earth can be made only at a thin shell near the surface; our knowledge of its internal structure is derived from inferences based on the geology and geochemistry of crustal and rarer mantle rocks, and from geophysical observations of physical properties influenced by the material below the surface. Geophysicists have measured many physical quantities that interact with, or are generated from the interior of the Earth. These include observations of gravitational fields, seismic waves, heat flow, static magnetic fields and electromagnetic fields. From these observations geophysicists obtain information on density, elastic moduli, temperature, magnetization, and electric properties within the Earth. In turn this information is interpreted in terms of the geological structure. Often the use of more than one geophysical method can provide complementary information on the geological structure.

As the knowledge of the Earth increases so does the evidence for its heterogeneity. In addition to the directly observable diversity in crustal structure and the well-known layering of the interior of the Earth, geochemical and geophysical investigations provide evidence of lateral heterogeneity in the lower crust (eg. Finlayson et al. 1980), in the mantle (Davies 1984), and even at the core-mantle boundary (Morelli & Dziewonski 1987). In order to fully sample this heterogeneous Earth it is desirable to have closely spaced observations over the range of existing structures. In regions where geochemical and geological information is sparse geophysical investigation must be used.

The observed heterogeneity in the Earth results from a limited number of tectonic processes. For example much of the heterogeneity in the mantle is caused by processes including subduction, convection, thermal plumes and chemical depletion beneath continents and mid-ocean ridges. Adequate sampling of the heterogeneous structure enables the study of these processes; for example geochemical observations are used to study mantle convection (O'Nions et al. 1979) and seismic observations are used to study

subduction processes (Creager & Jordan 1986). Geophysical studies form an essential method for obtaining detailed and extensive information on the lower crust and mantle.

Geomagnetic Soundings

A number of different electromagnetic methods are used to investigate the Earth's electrical conductivity structure. The electrical conductivity of rocks is a very sensitive parameter and varies over many orders of magnitude. For example dry, cold granite may have a conductivity of 10^{-8} $S.m^{-1}$ (Duba et al. 1978) while molten basalt has a conductivity of order 10^{1} $S.m^{-1}$ (Waff & Weill 1975). These values should be contrasted with the conductivity of ocean water, 4 $S.m^{-1}$ (Larsen 1968), and of the atmosphere, of order 10^{-13} $S.m^{-1}$. As well as being a function of the mineralogy, the conductivity of a rock can depend upon the microstructure and arrangement of the composite grains, the water and volatile content of the rock, and the temperature, pressure and oxygen fugacity of the environment of the rock (Lastovickova 1983).

Because of the number of factors that influence rock conductivity, it is often difficult to interpret geophysical electrical conductivity results in terms of specific rock types or properties. The use of supplementary geophysical and geochemical information can however greatly improve the value of the conductivity results. For example, in the interpretation of regions of the high mantle electric conductivity, Oldenburg (1981) used predictions of the rock types, estimates of the relationship of partial melt to temperature and pressure, and laboratory measurements of mineral conductivities to infer the degree of partial melting necessary to produce observed conductivity profiles. Tarits (1986) provides an alternative explanation of the observed conductivity in terms of the presence of H_2O rich fluids.

Electrical conductivity measurements are of most value when they are used in a comparative manner. This procedure involves comparing the conductivity at a particular depth in the Earth with that at another depth, or comparing a conductivity profile from one location with that of another location. Changes between the conductivity values may then be interpreted in terms of changes in the factors controlling conductivity. For example, an increasing conductivity with depth may be interpreted in terms of increasing temperature and pressure while a conductivity anomaly in a particular geographical area could be interpreted in terms of a change of rock type.

Such a comparative approach is used in other areas of geophysical interpretation. Seismic results are often presented and compared in terms of velocity profiles (akin to conductivity profiles) rather than being interpreted in terms of specific rock types. In order to obtain the maximum information about the Earth it is beneficial to combine the results from different geophysical methods. The different methods may respond to different physical properties of the rocks and hence provide complementary data. Electrical conductivity results have a sensitivity to rock chemistry and water content that can provide

additional information to the physical rock properties derived from seismic results. Figure 1.2 illustrates two examples in which seismic and geoelectric results have been combined to provide maximum information on geological structure. Jones (1987) describes further examples in which MT results have greatly aided interpretation of seismic reflection results.

The electromagnetic methods used in the Tasman Project use the natural oscillations in the Earth's magnetic field as the source-field for probing the Earth's electrical conductivity structure. In particular the oscillations associated with magnetic storms and substorms have been used. These magnetic field oscillations are caused when surges in the solar wind interact with the Earth's magnetosphere and ionosphere causing electric currents to flow in these zones (Rokityansky 1982).

The external magnetic field oscillations reach the Earth's surface, essentially unattenuated by the poorly conducting atmosphere, and penetrate the surface. In the Earth the magnetic fields are gradually attenuated with increasing depth by opposing electric (telluric) currents that are able to flow in the electrically conducting rocks. This process of "geomagnetic induction" is primarily controlled by the electrical conductivity structure of the Earth. Within the period range considered in the Tasman Project (minutes to tens of hours) geomagnetic induction is a diffusive phenomenon. Longer period oscillations in the external magnetic field are able to penetrate deeper into the Earth than short period oscillations.

The magnetotelluric method involves measuring the horizontal magnetic field and the horizontal electric field oscillations at the Earth's surface. These data are used to determine the electrical conductivity below the recording site. The method makes use of the diffusive nature of the geomagnetic induction - by measuring the field oscillations at a range of periods, information is obtained on the conductivity structure over a range of depths. For the periods studied in the Tasman Project information will be obtained for a depth range of tens to hundreds of kilometres.

A second geomagnetic sounding method making use of the external inducing magnetic field variations is Geomagnetic Depth Sounding (GDS). This method basically involves interpreting the observed vertical magnetic-field oscillations. Unlike the horizontal magnetic-field components which are generally closely related to the external (inducing) magnetic-field oscillations, the vertical magnetic-field oscillations are largely internally induced. They are induced by interaction of the inducing magnetic-field with lateral variations in electrical conductivity. Vertical magnetic-field oscillations are usually very strong near coastlines, where a strong lateral conductivity contrast exists between the ocean and the land. Other electromagnetic sounding methods such as spatial gradient sounding and vertical gradient sounding (eg. Rokityansky 1982) may also be used to investigate the Earth's conductivity structure.

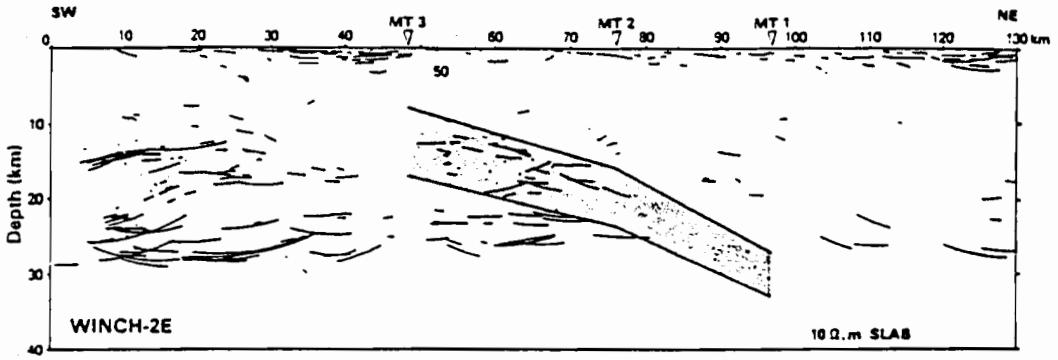

(a)

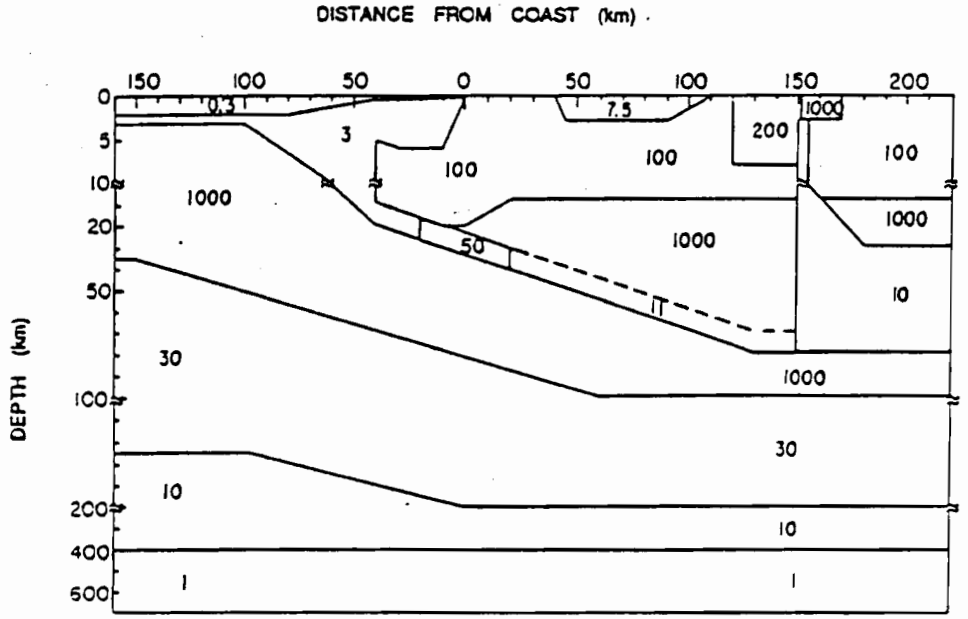

(b)

Figure 1.2 Examples of combined seismic and geoelectric geophysical results. (a) The Iapetus Suture of Britain and Ireland. The figure shows seismic reflections and a zone of high electrical conductivity (stippled) modelled from MT measurements made at the three sites indicated (Beamish & Smythe 1986). (b) Model of the subducting Juan de Fuca Plate at the western coast of North America, depths are in km and resistivity in Ω.m. The model has been constrained by seismic reflection data, for example the depth and dip of the subducting slab, and by various geomagnetic sounding results (Booker et al. 1987).

Marine Geomagnetic Soundings

The performance of geophysical surveys in the oceans is of great importance. The oceans occupy over 60% of the surface of the Earth and many of the processes influencing the oceanic crust and mantle such as seafoor spreading are different from continental processes. In order to understand the complimentary evolution of the oceans and continents it is essential to investigate the structure and tectonic processes of oceanic regions - marine geophysical studies, including geomagnetic sounding, can contribute greatly to such investigation.

Geomagnetic induction studies in the oceans have a number of particular applications. A main aim of such studies performed so far has been to determine one-dimensional (1D) electrical conductivity profiles of the oceanic lithosphere and mantle (Law 1983). Because oceanic crust is more laterally uniform than continental crust it should be easier to define characteristic profiles for the oceans than for the continents.

One of the particular aims of SFMT studies has been to examine the geoelectrical signature of the asthenosphere. The asthenosphere is interpreted to be the transitional zone between the rigid lithospheric plates at the surface of the Earth (comprising the crust plus uppermost mantle) and the underlying mantle. It is hypothesized to be a zone of reduced shear strength relative to the lithosphere and underlying mantle for motions with long time scales and is sometimes equated with a zone of reduced seismic S-wave velocity (the LVZ) and increased seismic attenuation (eg. Isacks et al. 1968). The asthenosphere was important in early plate tectonic theories as a thin zone of return flow beneath the lithosphere (Isacks et al. 1968, Jacoby 1970). Although it has since been shown that this return flow involves convection over the depth of the upper mantle or whole mantle (Schubert & Turcotte 1972) the concept of the asthenosphere forming a zone of decoupling between the lithosphere and underlying mantle still remains prevalent among geophysicists (Maxwell 1984, Muirhead 1985).

Explanations for the presence of the asthenosphere and seismic LVZ have included th presence at asthenospheric depths of small amounts of partial melting, the weakening of minerals by the presence of water and the presence of an aqueous phase in the rock (Elsasser 1971). Since all of these possibilities are likely to be associated with changes in the electrical conductivity of the rock, geoelectric measurements can be used to infer information on the nature and thickness of the asthenosphere (Oldenburg 1981, Tarits 1985). The geoelectric measurements can also be used to examine the predicted variation of lithospheric thickness with increasing age (Filloux 1981) and the electrical conductivity of other oceanic lithosphere and mantle structures such as subducting plates (Filloux 1982b, Yukutake et al. 1983).

Another important application of seafloor geomagnetic induction studies is the investigation of continental margins. Most previous geomagnetic investigations of continental margins have been land-based GDS studies (eg. Bennett & Lilley 1974) and

these results have been able to provide only broad constraints on the geoelectric structure. Seafloor geomagnetic induction studies near coasts, especially in conjunction with simultaneous land based observations, should permit the geoelectric structure of continental margins to be determined with much greater resolution. One question that such studies should resolve, is whether the electrical conductivity contrast between the oceanic crust/mantle and the continental crust/mantle contributes significantly to the geomagnetic coast effect, the enhancement of the vertical magnetic-field oscillations near coastlines (Parkinson & Jones 1979).

Large-scale seafloor geomagnetic studies may contribute to improving the interpretation of geomagnetic results by increasing the understanding of the current channelling phenomenon. Current channelling occurs when electric currents induced outside a study area are channelled by a good conductor into the study area, and "contaminate" the electric and magnetic fields associated with local geomagnetic induction. There is presently much debate on this subject (Jones 1983, Mosnier 1985), for example on what lateral scales current channelling may be important. Current channelling is difficult to study in land geomagnetic induction studies because the conductivities of the rocks cannot be measured directly. In contrast the ocean provides a relatively well defined conductivity structure; the ocean-water conductivity and the bathymetry are well known and the ocean conductance is significantly higher than that of the surrounding rocks. Large-scale oceanic geomagnetic induction studies, in association with land measurements, thus constitute an ideal method of studying current channelling.

Geomagnetic studies will also assist in understanding the gross flow of the oceanic electric currents induced by magnetic storms and other external source-fields, and in turn this knowledge will assist in the study of these external fields. A great deal of information on the external source-fields is derived from magnetic observatories or temporary magnetic arrays . Many of these observatories and arrays are located near coastlines and the magnetic field associated with currents flowing in the nearby ocean will be superimposed upon the measured external magnetic field. If a quantitative understanding of the electric current flow in the oceans can be obtained, it will be possible to evaluate the importance of the superimposed field and to subtract it from the measured magnetic field, in order to provide an improved estimate for the external field (Mareschal 1976).

A significant difference between marine and land geomagnetic induction studies is the presence of motionally induced signals in the marine electromagnetic fields. These fields are induced by the dynamo effect of conductive salt-water moving through the Earth's static magnetic field. Motionally induced signals exist over a broad period range; at periods of weeks to days the signals are induced by eddies and currents, at periods of days to hours the signals are induced by tides and internal waves and at periods of less than an hour the signals are induced by turbulence and other small scale motion (Filloux 1980a). Although these oceanically induced signals represent a source of noise on the geomagnetically induced signal, the use of remote-reference geomagnetic recordings permits the separation

two types of signal. Supplementary oceanographic recordings of the water motion may also facilitate this separation. After the separation the oceanically induced signal may be used to provide physical oceanographic information.

The measurement of water motion using seafloor electromagnetic recordings has a number of advantages over conventional measurements. It can be shown that for certain classes of motion, including relatively long wavelength features such as eddies and tides, the motionally induced seafloor horizontal electric-field can provide a measure of the barotropic flow, ie. the average flow over the water column (Chave &Filloux 1984, Sanford 1971). Using conventional instrumentation barotropic velocities must be obtained from recordings spanning the depth of the ocean. The seafloor horizontal magnetic field is also related to the barotropic velocity but in a more complex relationship involving the regional geoelectrical structure (Sanford 1971). Finally, the seafloor vertical electric field can be used to estimate the local, seafloor, east-west water motion. Variations in this component of the electric field are almost entirely of oceanographic origin (Chave & Filloux 1985, Sanford 1971).

A major difficulty of marine geophysics and particularly of seafloor recordings is the necessity for very specialized and reliable instruments. Land based MT surveys have been performed regularly since the 1950's (Kaufman & Keller 1981) however seafloor MT surveys have become routine only in the last decade (Law 1983). Although a number of institutions have developed seafloor magnetometers, only Dr Jean Filloux from Scripps Institution of Oceanography has constructed and regularly deployed instruments for measuring the seafloor telluric field.

1.3 Aims of the Tasman Project

This section lists the aims of the Tasman Project and notes the areas of study included in this thesis.

(1) The Tasman Project was conceived with the aim of investigating the electrical conductivity structure of the Earth beneath the Tasman Sea. This aim includes determining the basic 1D conductivity structure and examining this structure for any evidence of a highly conductive asthenospheric zone. The results from the Tasman Sea will be compared with those from the Pacific Ocean and the differences or similarities used to infer information on the processes such as seafloor spreading. This research forms the basis of section II of this thesis.

(2) A second aim of the Tasman Project is investigation of the geoelectric structure of the Australian continental margin and of specific tectonic features in the Tasman Sea such as the Tasmantid Seamount Chain and the Lord Howe Rise. In association with other geophysical and geological information these results will help define the structure and evolution of these tectonic features. This research is addressed in this thesis through the examination of MT results and some preliminary GDS results (induction arrows). The

work will be extended during the ANU Ph.D. Project of Mr R.L. Kellett.
(3) The Tasman Project results will be examined in order to provide information on current channelling effects and on the pattern of flow of electric currents induced in the ocean by geomagnetic storms and substorms. This study will be addressed briefly in this thesis.
(4) The Tasman Project data set is very well suited for studying the magnetic and electric fields associated with oceanic and ionospheric tides and the daily variation of the geomagnetic field. Such a study provides information on the ionosphere, the oceans and may also be used to provide information on the Earth's electrical conductivity structure. The analysis is being made as part of the ANU Ph.D. project of Mr N.L. Bindoff (Bindoff 1988).
(5) A final aim of the Tasman Project is to provide physical oceanographic information on the Tasman Sea. Oceanographic information will be obtained from the seafloor MT recordings and also from the other oceanographic recordings made during the recording period.

1.4 History and Background of the Tasman Project

The initial idea and planning of the Tasman Project were shared by Dr J.H. Filloux from the Scripps Institution of Oceanography, California and Dr F.E.M. Lilley from the Australian National University. During the 1970s and early 1980s Dr Filloux developed a set of SFMT instrumentation and by 1983 he had performed twelve array studies in the Pacific Ocean and one study in the Atlantic Ocean (eg. Filloux 1982a). In order to fully assess and understand the results of these studies it was important to obtain similar MT results from other oceans and lithospheric plates around the world. The Tasman Sea possesses an apparently simple lithospheric structure (eg. Weissel and Hayes 1977) and therefore provides a suitable location for such further SFMT study.

During the 1970s Dr Lilley performed several geomagnetic array studies in southeastern Australia (eg. Bennett and Lilley 1971, Tammemagi 1972). These continental array studies suggested that the southeastern Australian margin possesses a simple two-dimensional (2D) electrical conductivity structure. From other geophysical and tectonic information this coastline is believed to be a passive continental margin (Falvey & Mutter 1981). An MT experiment in the Tasman Sea provided an opportunity to extend the continental results and to make a close study of the continental margin itself.

The Tasman Project of Seafloor Magnetotelluric Exploration was planned and run under the auspices of the US Australia Science and Technology Agreement. In addition to scientists and staff from the Australian National University (ANU) and Scripps Institution of Oceanography (SIO) there were important contributions from other organisations, particularly the Royal Australian Navy and the Royal Australian Navy Research Laboratory (RANRL).

A vital requirement for any seafloor geophysics is a suitable ship. For the Tasman

Project the deployment and retrieval cruises were performed by HMAS *Cook*, an oceanographic vessel of the Royal Australian Navy. The provision of the services of the HMAS *Cook* and its crew formed part of the Australian Navy's contribution to civilian science. The HMAS *Cook* is a large oceanographic vessel (96 m, 2460 tonnes with a crew of around 135 officers and sailors) and this was an important factor in allowing a successful recovery of instruments in heavy seas.

Dr P.J. Mulhearn from RANRL in Sydney is a major collaborator in the oceanographic aspects of the Tasman Project. RANRL operated a recording current meter as part of the project and Dr Mulhearn co-ordinated various oceanographic measurements during the deployment and retrieval cruises. He has also collated and interpreted all of the available oceanographic information for the relevant region of the Tasman Sea during the recording period. This information, derived from sources including ship sets, satellite tracked buoys, infra-red satellite photographs, XBTs (expendable bathy-thermograph records) from naval ships in the region and AXBTs (air deployed XBTs) from RAAF aircraft, is important for comparison with oceanographic results from the deep sea instruments.

Data from two government magnetic observatories has been made available to the Tasman Project. The Canberra Magnetic Observatory, operated by the Australian Bureau of Mineral Resources, is situated on the Tasman Project recording line and the Observatory Section of the Bureau has kindly provided the relevant four months of magnetic data. An extension of the Tasman Project recording line passes close to the Eyrewell Magnetic Observatory, near Christchurch, New Zealand. The New Zealand Department of Science and Industrial Reasearch has kindly provided copies of observatory magnetograms for the four month recording period. The New Zealand data are important as they form a land reference for the eastern end of the seafloor magnetic recordings.

As part of the original Tasman Project, Dr A. White from Flinders University, operated a continental shelf magnetometer on the recording line near the Australian coast. This instrument returned only a small amount of useful data (due to sea-water permeating an underwater cable). Dr White has re-occupied this site and two other nearby shelf and slope sites in the "Continental Slope Experiment" from July to December 1986; the results from this experiment will be presented in later manuscripts.

During the recording period of the Tasman Project a number of other geomagnetic and oceanographic measurements were made in the Tasman Sea and surrounding areas. The data from these other experiments have not been used in analysing the main Tasman Project data however their existence should be noted as the data could be valuable in further research. Other geomagnetic recordings made during the recording period include magnetic-field recordings in Northern Tasmania (by Dr W. D. Parkinson from the University of Tasmania) and on the North Island of New Zealand (by Dr M. Ingham from the Victoria University of Wellington). During the Tasman Project, oceanographic recordings were made on the Australian continental shelf in the CSIRO Australian Coastal

Experiment (ACE) (Clarke & Thompson 1984).

A number of papers and abstracts describing analyses of data from the Tasman Project have already been published. An introduction to the project may be found in Filloux et al. (1985), a preliminary analysis of the MT data from a seafloor site in Ferguson et al. (1985) and a more detailed description and further analysis of the magnetic and electric data in Lilley et al. (1988). A number of oceanographic results have also been published; an analysis of the recorded pressure data may be found in Lilley et al. (1986b) and an analysis of the vertical electric-field data in Bindoff et al. (1986). The study of an oceanographic eddy which passed over the recording line during the Tasman Project is described in Mulhearn et al. (1986), Lilley et al. (1986a) and Mulhearn et al. (1988). This latter study has used horizontal electric-field, vertical electric-field, current-meter and surface oceanographic data.

1.5 Systems of Units and Notation used in Thesis

Throughout this thesis the SI system of units has been used wherever practicable. This procedure has involved using the fundamental MKSA units (metre, kilogram, second, ampere) or units derived from combinations of the fundamental units (for example the volt which equals 1 $A^{-1}.kg.m^2.s^{-3}$). In order to give numbers of convenient size the standard decimal multiples of these units have also been used (for example the kilometre or nanovolt). The main exception to the use of SI units is the use of units of hours and cycles per hour for specifying the period and frequency of geomagnetic variations. These units have been used because for the periods involved in the Tasman Project analysis they are much more familiar than units of seconds or kiloseconds.

Table 1.1 contains a list of units and symbols used in the thesis. A number of points should be noted in this table. In the description of magnetic quantities the magnetic induction, B, (also called the magnetic flux density) is measured in units of tesla whereas the magnetic field strength, H, is measured in units of $A.m^{-1}$. The two quantities are related by the magnetic permeability, μ, of the surrounding medium. Confusion arises in the use of these units because in the CGS electromagnetic system of units, for measurements in free space, μ equals unity and is dimensionless and the magnetic induction and magnetic field are identical. It is not clear whether magnetic field measurements of a particular kind measure H or B (Rokityansky 1982). This thesis follows the recommendations of IAGA (Rokityansky 1982) and expresses the magnetic "field" in terms of the magnetic induction.

Similarly in this thesis the electromagnetic impedance is defined as the ratio of the electric field to the magnetic induction. This means that the SI unit of impedance is $V.m^{-1}.T^{-1}$, which is dimensionally equivalent to the $m.s^{-1}$, the unit of velocity. The alternative definition of impedance, the ratio of the electric field strength to the magnetic field strength, is also used in thesis (but is designated by a different symbol) in order to

match the described electromagnetic theory with that in other publications.

Note from Table 1.1 that the conductivity of a medium may be expressed in units of $S.m^{-1}$ or by the equivalent resistivity in Ω.m. The conductivity is sometimes quoted in the literature in $mho.m^{-1}$; the mho is a unit name now replaced by the siemens, S.

Table 1.2 contains a list of other symbols used in this thesis and Table 1.3 contains a list a commonly used abbreviations and acronyms.

Table 1.1 Units and symbols of commonly used physical quantities.

Quantity and Symbol		SI Unit	MSVA†	Notes
Standard Quantities				
length	-	m	m	Also mm, km
time	t	s	s	Also hour (h)
frequency	f	s^{-1} (Hz)	s^{-1}	Also h^{-1}, cph
angular frequency	ω	$rad.s^{-1}$	$rad.s^{-1}$	
Electric Quantities				
electric charge	Q	C	A.s	C=coulomb
electric charge density	p	$C.m^{-3}$	$A.m^{-3}.s$	
electric current	I	A	A	
electric current density	J	$A.m^{-2}$	$A.m^{-2}$	
electric displacement	D	$C.m^{-2}$	$A.m^{-2}.s$	
electric field strength	E	$V.m^{-1}$	$V.m^{-1}$	V=volt
electric resistance	R	Ω	$A^{-1}.V$	Ω=ohm
electrical conductance	S	S	$A.V^{-1}$	S=siemens
electric resistivity	ρ	$\Omega.m$	$A^{-1}.V.m$	
electric conductivity	σ	$S.m^{-1}$	$A.V^{-1}.m^{-1}$	
electric permittivity	ε	$F.m^{-1}$	$A.V^{-1}.m^{-1}.s$	F=farad
absolute permitivity	ε_0	= 8.854×10^{-12} $F.m^{-1}$		
Magnetic Quantities				
magnetic field strength	H	$A.m^{-1}$	$A.m^{-1}$	
magnetic induction (field)	B	T	$V.m^{-2}.s$	Also nT, T=tesla
magnetic potential	Ω	A	A	
magnetic permeability	μ	$H.m^{-1}$	$A^{-1}.V.m^{-1}.s$	H=henry
absolute permeability	μ_0	= 1.25664×10^{-6} $H.m^{-1}$		
Electromagnetic Quantities				
impedance (this thesis)*	Z	$m.s^{-1}$	$m.s^{-1}$	Also $\mu V.m^{-1}.nT^{-1}$
impedance (alternative)	ζ	Ω	$A^{-1}.V$	
admittance (this thesis)*	A	$m^{-1}.s$	$m^{-1}.s$	
Weidelt's MT response	c	m	m	Also km

† Composite unit expressed in terms of units of metres (m), seconds (s), volts (V), amperes (A) and supplementary units radians (rad) and degrees Kelvin (K).

* In this thesis the impedance has been defined Z = E/B (see text).

Symbols written with a bold font in this thesis correspond to vector (or tensor) quantities. For example "**B**" is the magnetic induction vector.

Table 1.2 Other commonly used symbols in thesis

Symbol	Explanation
Magnetic field components	
F	Magnitude of magnetic field
D	Declination, angle between magnetic north and true north (positive for MN to east of TN)
General subscripts for electric and magnetic fields	
H,D,Z	Components to magnetic north, magnetic east and downwards
X,Y	Components to the geographic north and geographic east.
Statistical	
σ	Standard deviation†
σ^2	Variance
μ	Mean †
$F_X(\omega)$	Fourier transform of $f_X(t)$ (Transform defined with positive exponent)
S_{XY}	Crosspower between f_X and f_Y ($S_{XY} = \Sigma F_X F_Y^* / T$)
γ^2_{XY}	Ordinary squared coherence between components x and y ($\gamma^2 = S_{XY}S_{YX}/S_{XX}S_{YY}$)
$\gamma^2_{Z.XY}$	Multiple coherence between component z and components x and y
$\gamma^2_{ZX.Y}$	Partial coherence between components z and x with component y removed.
z, t, χ^2, F	Standardized normal, Student t, chi-squared and Fischer statistics.
λ	degrees of freedom
Vectorial	
∇, $\nabla.$,∇x ,∇^2	Gradient, Divergence, Curl and Laplacian.
Other	
T = Period	
δ = Sampling interval	

† Units or text will allow discrimination between repeated symbols such as standard deviation and conductivity, mean and permeability.

Table 1.3 Commonly used abbreviations in thesis.

Abbrev.	Explanation
Geomagnetic Induction Terms	
MT	Magnetotelluric
SFMT	Seafloor magnetotelluric
GDS	Geomagnetic depth sounding
VGS	Vertical gradient sounding
MVS	Magnetic variational sounding
E-POL	Electric polarization mode (of 2D induction)
B-POL	Magnetic polarization mode
1D, 2D, 3D	One, two, three-dimensional
AD, RR	Admittance, remote-reference formulations for MT impedance function.
Project Acronyms	
TPSME	Tasman Project of Seafloor Magnetotelluric Exploration
EMSLAB	Electromagnetic Sounding of the Lithosphere and Asthenosphere Beneath the Juan de Fuca Plate.
ACE	Australian Coastal Experiment
Instrument (or type of recording) in the Tasman Project	
MAG	Magnetometer
HEF	Horizontal Electric Field
VEF	Vertical electric field
PRESS	Pressure
TEMP	Temperature
Institutions	
ANU	Australian National University
RSES	Research School of Earth Sciences
SIO	Scripps Institution of Oceanography
RANRL	Royal Australian Navy Research Laboratory
General	
UT	Universal Time
LS	Least-squares Method
SNR	Signal to Noise Ratio (ratio of the signal power to the noise power).

For recording-site codes see Table 2.1 in chapter 2.

Chapter 2 Experimental Details and Field Work

This chapter will provide an outline of the experimental phase of the Tasman Project. It will detail the location of recording sites, the instruments deployed at each site and the recording details. A brief description will be given of the different instrument types and of the field work conducted in Australia and on the Tasman Sea.

2.1 Site Location and Recording Period

The reasons for siting the TPSME in the Tasman Sea were outlined in chapter 1. The position of the actual Tasman Project recording line (the line defined by sites GNS to TP3 in Figure 2.1) was chosen to facilitate the study of the conductivity structure of the Tasman Sea and of the Australian continental margin. The line was chosen so that it crossed the Tasman Sea and spanned a range of tectonic features including the Tasman Abyssal Plain, the Tasmantid Seamount Chain, the fossil Tasman Sea spreading ridge and the Lord Howe Rise. The line was secondly chosen to be perpendicular to the Australian coastline and to cross the coast where the coast possesses a 2D form and where previous geomagnetic studies have shown no evidence of complicating 3D electrical conductivity structure.

The recording line was finally chosen to pass through the Canberra Magnetic Observatory (CMO) so as to increase the number of available recording sites. An eastwards extension of this recording line passes close to the Eyrewell Magnetic Observatory (EYR) in New Zealand. The chosen line also lies close to the -44° parallel of geomagnetic latitude.

Recording sites at the eastern and western ends of the recording line are located to the north of the main (GNS-TP3) line. These more northerly site locations provide links with previous geomagnetic experiments. At site MYL, at the western end of the recording line, a magnetometer installed during a geomagnetic array study in the Cobar region (Lilley 1984) was re-activated during the Tasman Project. The two eastern-most sites on the recording line, TP1 and TP2, were chosen to lie north of the main line so that the sites were nearer to the location of a previous SFMT sounding off the North Island of New Zealand. This choice of sites also meant that the two sites were more strategically placed to study the electrical conductivity structure of the Lord Howe Rise.

The position and spacing of the individual recording sites of the Tasman Project were carefully chosen in order to maximize the value of the recorded data. A detailed map of the recording sites is given in Figure 2.1 and the geographical co-ordinates and site codes of each of the recording sites are listed in Table 2.1 . In order to adequately sample the Earth beneath the Tasman Sea, the recording sites were spaced across the width of the Tasman Sea. These sites span the range of plate ages for the oceanic lithosphere of the Tasman

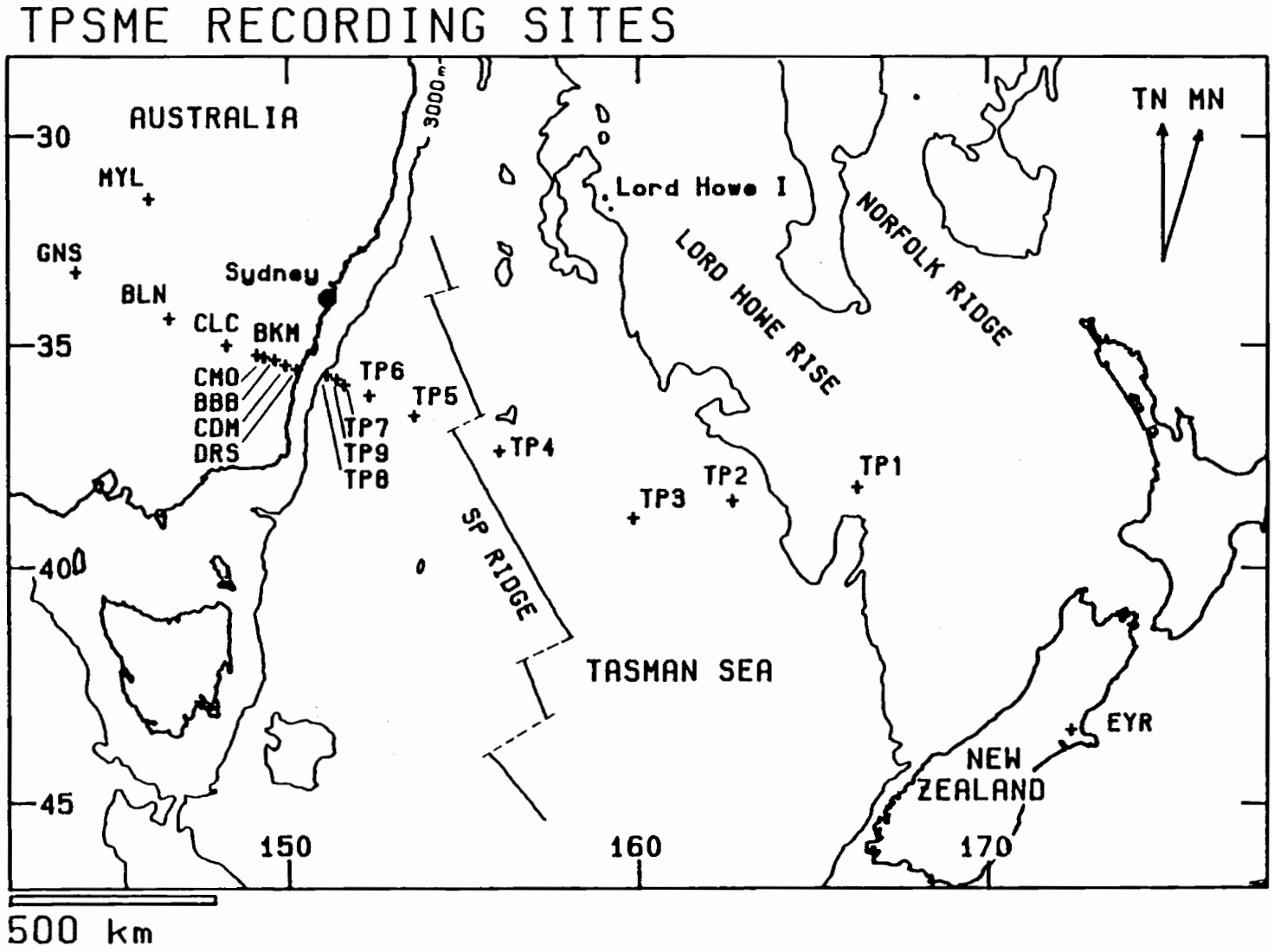

Figure 2.1 Tasman Sea Region. Full figure caption is on next page.

Caption for Figure 2.1: Map of the Tasman Sea Region showing the location of the Tasman Project recording sites. The 3000 m bathymetric contour shown on the map indicates the position of a number of important structures including:

1. The Tasman Abyssal Plain - the region of deep seafloor forming the western portion of the Tasman Sea. The ocean depth in this region is mainly between 4500 and 5000 m.
2. The Lord Howe Rise - a region of submerged continental crust. Near the top of the map the Lord Howe Basin separates the Dampier Ridge from the western margin of the Lord Howe Rise.

   Recording site TP1 lies in the Bellona Gap at the southern end of the Lord Howe Rise.
3. The Tasmantid Seamount Chain is a meridional chain of seamounts in the western Tasman Sea. The most southern seamount in the chain, the Gascoyne Seamount lies just north of recording site TP4. Lord Howe Island is the most southern member of a second meridional seamount chain.
4. The narrow, 2D, form of the Australian continental shelf where it is crossed by the recording line.

The map also shows the spreading ridge from which the Tasman Sea formed between 82 and 65 Ma.

Table 2.1: Location of TPSME Recording Sites

Code	Location	Co-ordinates				Depth (m)
		Geographical		Geomagnetic		
MYL	Cobar	31.533°S	146.133°E	-40.2°	222.2°	-
GNS	Ivanhoe	33.267	143.933	-42.2	220.1	-
BLN	Barellan	34.317	146.617	-42.9	223.3	-
CLC	Coolac	34.983	148.267	-43.3	225.3	-
BKM	Canberra	35.267	149.100	-43.5	226.3	-
CMO	Bungendore	35.317	149.367	-43.5	226.6	-
BBB	Braidwood	35.417	149.717	-43.5	227.0	-
CDM	Clyde Mtn	35.550	149.983	-43.6	227.4	-
DRS	Durras	35.667	150.283	-43.7	227.7	-
TP8	Tasman Sea	35.817	151.133	-43.7	228.7	4850
TP9		35.917	151.367	-43.8	229.0	4850
TP9a		35.907	151.383	-43.8	229.0	4850
TP7		36.000	151.600	-43.8	229.3	4840
TP6		36.233	152.250	-44.0	230.0	4836
TP5		36.717	153.583	-44.2	231.6	4660
TP4		37.550	155.967	-44.7	234.5	4460
TP3		38.900	159.833	-45.4	239.1	4980
TP2		38.500	162.633	-44.5	242.0	4800
TP1		38.217	166.183	-43.6	245.6	2550
EYR	Eyrewell	43.424	172.352	-47.5	253.9	-

Seafloor site positions are from HMAS *Cook* 's satellite navigation system. Position accuracy better than 0.5 km.

Geomagnetic co-ordinates are based on the 1980 IGRF with the North Magnetic Pole at 78.8° N, 70.9° W.

Seafloor: from approximately 65 Ma at site TP4 to 82 Ma at sites TP2 and TP8 (Weissel and Hayes 1977). Site TP3 (on lithosphere of 70 Ma age) was chosen to maximize the probability of sounding a site with the "normal" 1D electrical conductivity profile of the Tasman Sea. The site is located a maximum distance from major tectonic structures which could be associated with anomalous electrical conductivity structure.

In order to facilitate the investigation the electrical conductivity structure of the Australian continental margin and the geomagnetic coast effect, recording sites were spaced more closely near the Australian coastline. Both the land and the marine recording sites were arranged so that the spacing between the sites increased approximately exponentially with distance away from the coast. An additional benefit of the close spacing of near-coastal seafloor sites was that more sites were located in the (oceanic) East Australian Current. The East Australian Current (EAC) is a strong western boundary current of the Southwest Pacific Ocean and the Tasman Sea which flows along the western margin of the Tasman. The current is of great interest to physical oceanographers and has already formed the subject of a number of published oceanographic papers from the Tasman Project (Lilley et al. 1986a, Mulhearn et al. 1986).

While satisfying the requirements for investigating the Tasman Sea and the Australian continental margin the locations of the recording sites were chosen to investigate the electrical conductivity structure of specific tectonic features. Sites TP1 and TP2 were chosen to allow efficient study of the conductivity structure of the Lord Howe Rise and site TP4 was chosen to lie near both the fossil spreading ridge and the Tasmantid Seamount Chain which run meridionally through the Tasman Sea. (The tectonic evolution of the Tasman Sea Region is described in chapter 9.) On the land end of the recording line most of the sites lie on the predominantly Palaeozoic metasediments of the Lachlan Fold Belt. In order to allow comparison with these sites, the location of site GNS was chosen to be further west, in the Tertiary and Quaternary sediments of the Murray-Darling Basin.

On a local scale the recording site locations depended on instrumental and logistic constraints. The SIO seafloor instruments require deployment on flat seafloor and in a water depth of greater than 2000 m. These constraints meant that none of the seafloor instruments could be deployed on the Australian continental slope and that site TP1 was located in the deeper water of the Bellona Gap rather than on the crest of the Lord Howe Rise. Land recording sites were constrained to lie near serviceable roads, away from areas of magnetic, physical and other human disturbance such as highways, and in areas of reasonably soft soil.

Table 2.2 contains a list of the instruments operated at each of the recording sites. Seafloor magnetometers were deployed at all of the nine seafloor recording sites and horizontal electric field recorders at seven of these sites. The seafloor oceanographic instrumentation consisted of a pressure recorder deployed at site TP2, vertical electric field recorders deployed at sites TP5, TP6 and TP7 and a recording current meter deployed at

Table 2.2: Instruments operated during the TPSME

Instrument	Sites
ANU Gough-Reitzel magnetometer	MYL,GNS,BLN,CLC,BKM,BBB,CDM,DRS
SIO Seafloor magnetometer	TP8,TP9,TP7,TP6,TP5,TP4,TP3,TP2,TP1
SIO Horizontal electric field instrument	TP8,TP7,TP6,TP5,TP4,TP3,TP1
SIO Vertical electric field instrument	TP7†,TP6,TP5†
SIO Pressure instrument	TP2
Canberra Magnetic Observatory	CMO
Eyrewell Magnetic Observatory	EYR
RANRL Aanderra recording current meter	TP9a

† Instrument not recovered

site TP9a (located 34 km from site TP9). Gough-Reitzel recording magnetometers were deployed at each of the land sites.

The principal recording period of the Tasman Project extended from early December 1983 to late April 1984. This was the recording period of the seafloor instruments. The land magnetometers were installed well before this time in mid-1983 to allow relaxation of the instrument fibres, however only data from the principal recording period have been reduced for analysis. Data from the Canberra and Eyrewell Magnetic Observatories were obtained for the months of December 1983 to April 1984.

In order to avoid the cumbersome listing of year, month and day when specifying a particular time within the recording period, a simplified timing system has been adopted for analysis of the Tasman data. In this system, each day of the recording period is numbered consecutively; 1 December is day 0, 2 December is day 1 and so on through to 5 April which is day 126. (A table giving the conversion from day numbers to dates is given in appendix 1.) In this system each day number gives the number of elapsed days since the arbitrary start of the recording period at 0000 UT 01 December 1983. Unless it is otherwise specified, all times and day numbers quoted refer to Universal Time.

2.2 Instrument Details

This section will provide an outline of the instruments deployed in the Tasman Project. The outline will include a basic description of each type of instrument and a summary of the recording parameters, such as sensitivity and sampling rate, during the Tasman Project.

Scripps Seafloor Instruments

The Scripps Institution of Oceanography instruments used in the Tasman Project were developed and constructed by Dr J. Filloux and his technical team. The instruments share a number of common characteristics which will be described before the description of the individual instrument types.

The seafloor instruments are all contained in strong aluminium cylinders in order to withstand the 50 Mpa pressure at the deep seafloor. The size of the cylinders differs for the different kinds of instruments: the lengths of the magnetometers, horizontal electric field and pressure instruments are of order 2 m while the length of the vertical electric field instuments is of order 1 m. During the Tasman Project Dr Filloux deployed a trial pressure instrument which was encased in a glass sphere. Since the Tasman Project he has used this design for all of his new seafloor electric field and pressure instruments.

The seafloor instruments used in the Tasman Project are free-fall instruments which are deployed and retrieved without the use of cables. At deployment each instrument is attached by vacuum plates to a heavy tripod which acts as ballast, causing the instrument to be negatively buoyant in the sea water. (The vertical electrical field instruments are

attached to heavy chains instead of tripods.) The instruments are released over the side of the ship and sink to the seafloor where they stand vertically on their tripod. A horizontal plate attached near the top of each magnetometer and pressure instrument slows the descent of these instruments through the water. After the full recording period, a preset timing release detonates firing caps (squibs), which break the vacuum seal between the instrument cylinder and the tripod. The buoyant instrument cylinder then floats to the sea-surface for retrieval. Each instrument takes of order 2-3 h to complete the travel from the seafloor to the surface.

The resurfaced instruments are located using a directional antenna on the retrieval ship and CB radio signals transmitted by the instruments. Each instrument possesses two independent transmitter systems in case of the failure of one transmitter. Brightly coloured flags attached to the transmitter aerials on each instrument help its visual location. Figure 2.2 shows a photograph of an SIO seafloor instrument, a magnetometer, taken just before the instrument's deployment.

The transmission of radio signals by each instrument is required only after the instrument has resurfaced. In order to conserve power, signal transmission is started when a temperature sensor in each instrument detects a temperature of over 4 °C. Since this temperature corresponds to a depth in the ocean of approximately 2000 m instrument deployment is restricted to locations where the ocean is deeper than 2000 m.

The seafloor instruments are deployed on the flattest available seafloor. An internal photographic pendulum/compass assembly is used to record the tilt and horizontal azimuth of each instrument. The shadow-graph recorded by each assembly also indicates whether any significant change of orientation occurs during the recording period.

The seafloor instruments are powered by internal battery packs composed of dry cell batteries of the highest quality (bought directly from the manufacturer). Independent battery packs are used to power the recording system, the tripod release system and the radio transmitters.

The instruments record the data digitally on high quality audio cassette tapes. All of the instruments record data using the same basic method. The measured quantity (magnetic field, electric field or pressure) is converted into a voltage which is then converted by a linear voltage-controlled oscillator (VCO) into an oscillating signal with a frequency proportional to the input voltage. The oscillations are counted over a sampling interval and the resulting sum, corresponding to the measured quantity (averaged over the sampling interval) forms the data value. In order to conserve data storage, only the least significant byte of each data value is recorded. The more significant bytes of each data value are stored before every 64 data points along with timing and other information in a data "summary". Each set of 64 data points plus a summary is called a "record".

A description of the SIO deep seafloor magnetometers and horizontal electric field instruments will be published in 1988 in the book 'New Volumes in Geomagnetism and Geoelectricity' edited by J. Jacobs. Other descriptions of these instruments may be found

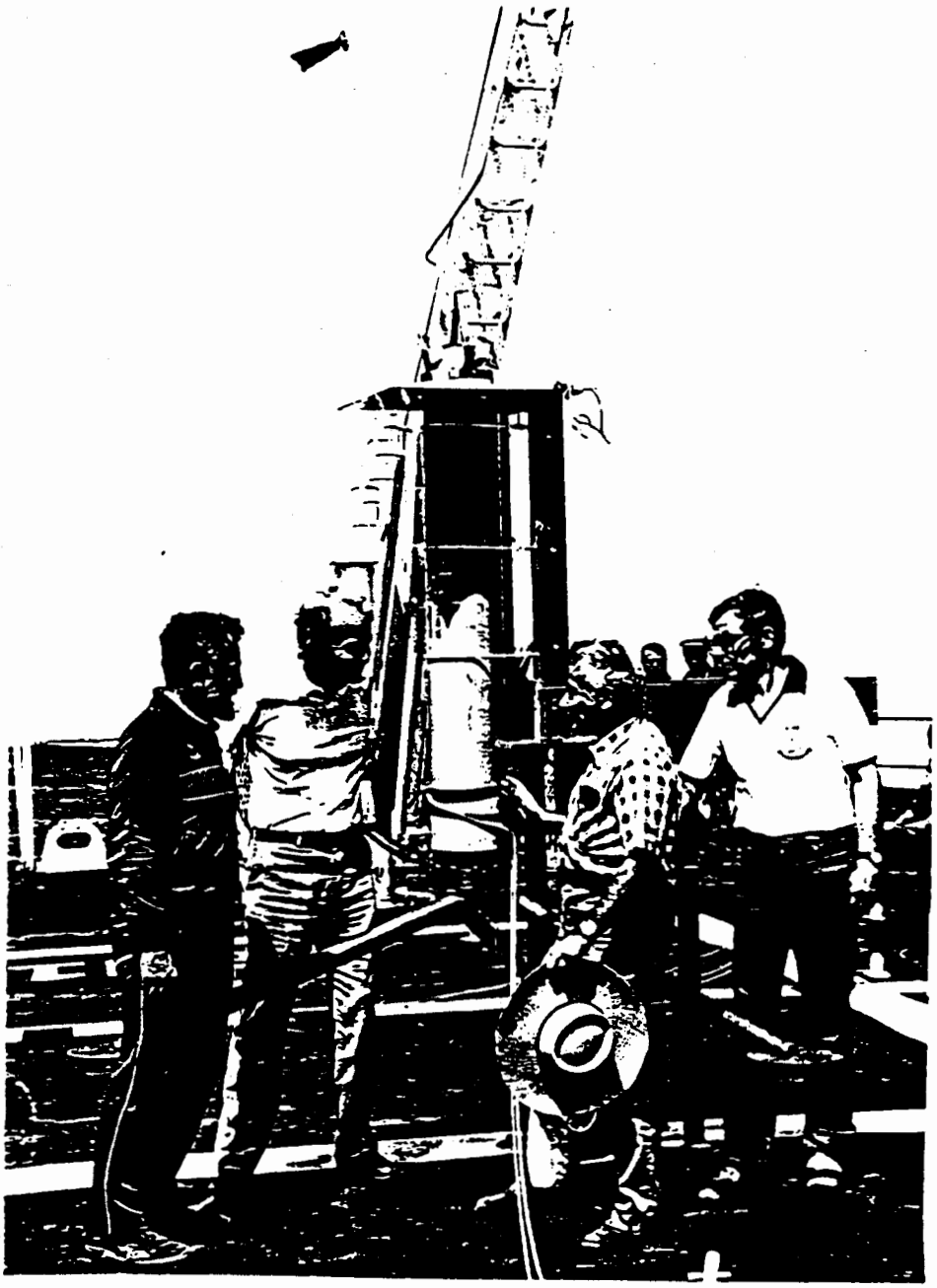

Figure 2.2 Photograph of an SIO seafloor magnetometer taken just before the magnetometer's deployment. Note the aluminium instrument cylinder, the ballast tripod attached to the base, the slow-down plate near the top of the cylinder and the transmitter antenna and flags. The magnetometer is being held by the special cradle on the quarterdeck of the *Cook*. Standing around the instrument are (l. to r.) Commander P. Cooke-Russell, captain of the *Cook* during the deployment cruise, and Drs F.E.M. Lilley, J.H. Filloux and P.J. Mulhearn.

in Filloux (1973, 1974, 1980a). The vertical electric field instruments are described in Chave & Filloux (1985) and Bindoff et al. (1986) and the pressure instruments in Filloux (1971, 1980d).

Seafloor Magnetometers

The SIO seafloor magnetometers used in the Tasman Project are based on suspended magnet sensors. The instruments use an optical system to detect the small movements of the three orthogonal magnets caused by the magnetic field variations. Electrical feedback systems null these movements and the nulling electric current thereby provides a direct measure of the magnetic field variations.

Each magnetometer contains an internal instrument cage which rotates within the instrument cylinder. At a preset time after deployment a small motor rotates this cage such that the two horizontal sensor magnets are aligned with magnetic north and magnetic east. If the instrument has been deployed on flat seafloor the third magnetic sensor is aligned vertically and the instruments measure variations of B_H, B_D and B_Z.

Each magnetometer component has a least count (digital recording increment) of approximately 1/6 nT however the actual instrument sensitivity is greater than this value. Instrument calibrations performed before and after the Tasman Project provided exact values for the least count of each component.

During the Tasman Project the magnetometers were set to a sampling rate of 32 data.h^{-1}. Each data record, consisting of 64 data points plus a summary, thus corresponds to two hours of recorded data. Each data point consists of the least significant byte of the B_H, B_D and B_Z data values while each summary contains the next two most significant bytes for each component plus timing information. This system provides a recording dynamic range of $2^{24} \times 1/6 = 3 \times 10^6$ nT, which is sufficiently large to record all of the geomagnetic variations that occurred during the Tasman Project.

Examination of the recorded time series reveals the presence of long period drift in the magnetic components. This drift occurs with time scales ranging from days to weeks and is caused by a number of processes. These include: relaxation of suspension fibres; settling of the instrument into the seafloor sediment; and long period drift in electronic components and battery voltages.

Horizontal Electric Field instruments

The SIO horizontal electric field (HEF) instruments are short-span recorders incorporating salt-bridge choppers to minimize electrode noise. The instruments measure the electric field over a span of 6 m.

Four 3 m plastic pipes arranged in a horizontal cross are attached to the top of each

instrument (Figure 2.3) and the electric field is sensed between the ends of opposite arms of the cross. Hollow electrically insulating tubing connects the open end of each arm of the cross with the chopper attached to the side of each instrument. The conducting sea water in these pipes (salt-bridges) thus forms part of the electrical circuit for the measured electric field variations. The chopper uses four Ag-AgCl electrodes to measure the electric field in the two horizontal directions and incorporates a switching mechanism to cancel electrode noise (see also chapter 5).

The chopper is connected to the inside of the instrument case through insulated electrical cables and special marine plugs. These cables provide power and timing information for the electromagnetically-driven chopper valve and connect the sensor electrodes with the signal processing and recording electronics.

A great deal of care is taken to minimize electrical noise on the HEF recordings. The aluminium instrument cases are annodized and enamelled and the iron tripods used to support the instruments are painted, in order to prevent chemically-induced electric fields caused by corrosion. All joints in the external piping and electrical system are tightly sealed and coated with electrically insulating jelly. In order to minimize electrode noise the electrodes are soaked for a number of days before deployment, in salt water from the Tasman Sea. Finally, in order to prevent biologically-induced electric noise caused by marine organisms (eg. shrimps) becoming trapped and decaying in the external pipes, the pipes are sealed as the instrument sinks through the biologically active upper regions of the ocean. (A dissolving "Life-saver" sweet provides an excellent time delay for the opening of the small clamps used to seal the pipes!)

During the Tasman Project the HEF instruments were set to a sampling rate of 64 data.h^{-1} (one record per hour) and each component has a least count of approximately 30 nV.m^{-1}. Each data value is stored as two bytes with the most significant byte being recorded only in the data summary. In the data summary the absolute voltage between each pair of electrodes is also recorded, providing an estimate of electrode noise and a record of the electrode drift with time.

Vertical Electric Field Instrument

The vertical electric field (VEF) instruments used in the Tasman Project measure the electric field between two electrodes spaced 160 m apart on a vertical wire. The upper electrode is suspended beneath a streamlined buoyant float which keeps the electrode line vertical. The lower electrode is attached to the instrument package which is weighted onto the seafloor by a heavy chain. At retrieval time this chain is released and the float and instrument package return to the sea surface. The VEF instruments use Ag-AgCl electrodes but as used in the Tasman Project do not have a chopping mechanism. The recorded signals therefore contain a superimposed long-period electrode drift.

During the Tasman Project the VEF instruments were set to sample at 128 data.h^{-1} (two

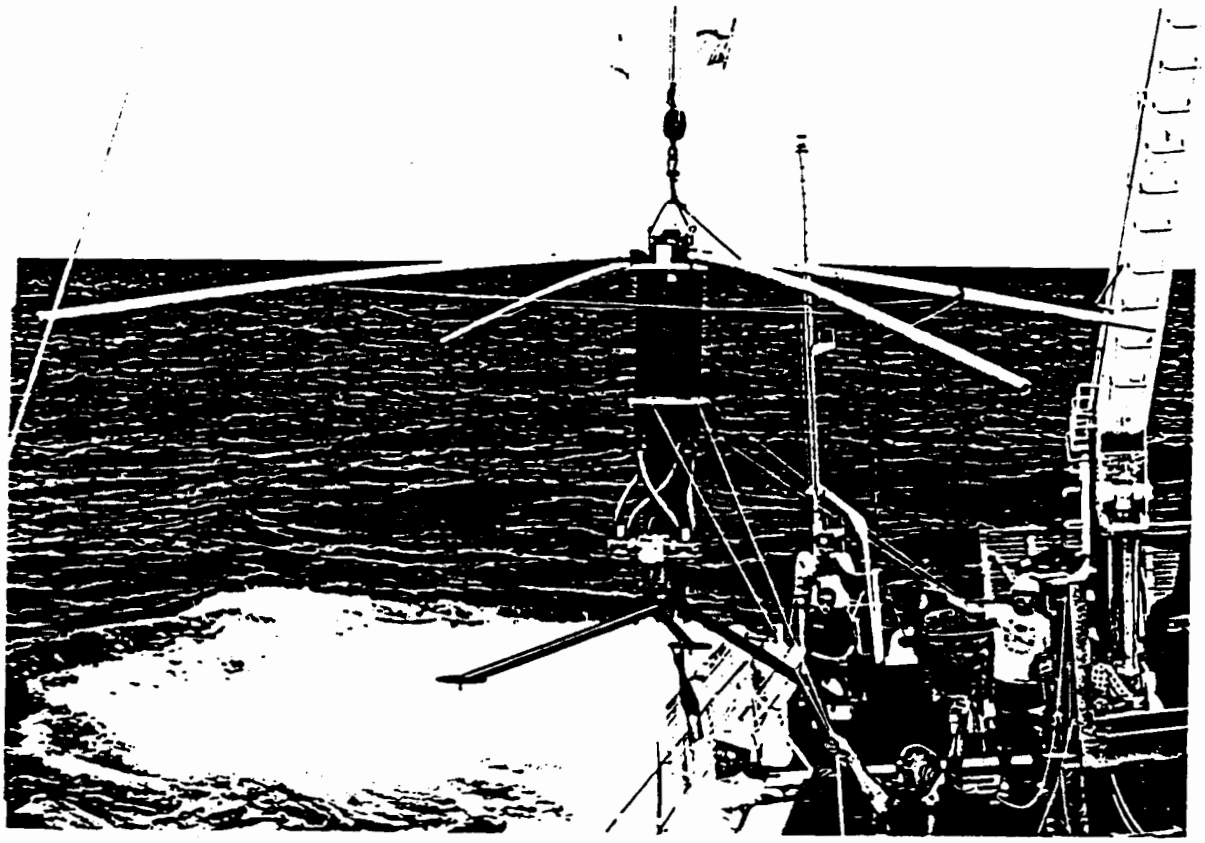

Figure 2.3 Photograph of an SIO horizontal electric field instrument. The electric field is measured between the arms of the salt-bridge at the top of the instrument. The chopper attached to the outside of the instrument cylinder is used to cancel out electrode noise (see chapter 5).

records per hour). Instrument calibrations indicated that the instruments have a least count of approximately 9.4 $nV.m^{-1}$ corresponding to an east-west water velocity of approximately 0.4 $mm.s^{-1}$. The VEF data summary, recorded every 30 min., stores the most significant byte of the vertical electric field measurements and also records variations in the ambient ocean temperature, measured by a temperature sensor inside the instrument. The least count of the recorded temperature data is 0.25×10^{-3} °C.

Pressure Instrument

The pressure instrument used in the Tasman Project uses a multi-turn Bourdon tube sensor to measure variations in the ambient pressure at the seafloor. The Bourdon tube, composed of specially treated alloy, is helical in shape. One end of this helix communicates with the outside of the instrument case through a flexible membrane while small angular rotations of the other end are sensed by an electro-optical feedback system and converted into the recorded values. The optical system uses a grid-type optical lever which permits the detection of very small angular rotations and thus the recording of very small pressure variations.

During the Tasman Project the pressure instrument had a least count equivalent to 0.390 mm head of sea water. The recorded data were of a similar format to that of the VEF data; the instrument recorded data at a sampling rate of 128 $data.h^{-1}$ and the most significant value of the data was recorded in a summary every 30 min. The pressure instrument also included a temperature sensor and recorded variations in the seafloor temperature every 30 min. with a least count of 0.25×10^{-3} °C.

RANRL Recording Current Meter

The recording current meter deployed during the Tasman Project was an Aanderaa current meter (Mulhearn et al. 1986). It was deployed at a height of 100 m above the seafloor in order to be located above the bottom boundary layer (where water currents are strongly affected by the seafloor). The instrument records the direction and speed of the water current at 15 min. intervals. It also records the absolute water temperature at the same sampling rate.

ANU Gough-Reitzel Magnetometers

The magnetometers used at the land sites in the Tasman Project were all Gough-Reitzel magnetometers from the set of ANU instruments. The performance characteristics of these instruments are described in Lilley et al. (1975). The magnetometer sensors consist of three orthogonal suspended magnets. An optical system records variations in the angular positions of these magnets on photographic film using a mirror system and a lamp flashed

at discrete intervals. The magnetometers record instantaneous, not averaged, measurements of the magnetic field.

During the Tasman Project the Gough-Reitzel magnetometers were installed so that they recorded magnetic variations in the magnetic north, magnetic east and vertical directions. On the films produced, the recorded data points form three traces corresponding to the magnetic field components. These recorded variations are later converted into magnetic variations using instrument calibrations. Time mark deflections are automatically added to the recorded traces at hourly and daily intervals.

The Gough-Reitzel instruments are encased in aluminium tubes of length 1.4 m and at deployment are buried vertically in the earth to minimize internal temperature fluctuations. An external heavy duty 6V wet cell is used to power the lamp in the optical system, to drive the film "camera" and to deflect the recorded traces during time marks. A smaller, internal, 9V dry cell is used to drive the timing electronics.

For the Tasman Project the sampling rate of the Gough-Reitzel instruments was set to 60 data.h^{-1}. Unlike the seafloor instruments the Gough-Reitzel data are recorded in analogue form. The sensitivity of the recorded data depends upon the relative strengths of the fibres on which the sensor magnets are suspended, the magnetic moments of the sensor magnets and on the strengths and positions of a number of supplementary compensating and "sensitivity magnets". During the Tasman Project the instruments were configured with sensitivities (magnetic change required to produce a 1 mm deflection of the recorded trace on the film) of approximately 20 $nT.mm^{-1}$ for B_H and 10 $nT.mm^{-1}$ for B_D and B_Z. With the 25 mm film-width between the sprocket holes these sensitivities give recordable dynamic ranges of about 500 nT for B_H and 250 nT for B_D and B_Z.

2.3 Field Work

Seafloor Instruments

The deployment and retrieval of the seafloor instruments in the Tasman Project were performed during cruises of HMAS *Cook*. The deployment cruise took place in late November - early December 1983 and occupied 14 days. The majority of this time was taken up by deployment of the SIO seafloor instruments. Much of the remaining time was spent taking oceanographic measurements, particularly Nansen casts, at sites between the Tasman Project sites (Mulhearn 1985). The RANRL recording current meter was also deployed during the cruise. Although one day of the cruise was lost during a brief period of heavy seas, the remainder of the cruise was in excellent weather and calm seas.

Prior to its deployment each seafloor instrument underwent a thorough preparation. This operation was performed by Dr Filloux and his technical team of H. Moeller, G. Pezzolli and T. Koch. The instrument preparation began in an oceanographic laboratory

on the *Cook* and included; checking instrument performance, accurately tuning the frequency of oscillators in the instrument clocks, and setting the tripod release (recovery) time. On board the deck of the *Cook* each instrument was inserted into its aluminium case, switched on, the end-plates placed on the cylinder and the instrument sealed.

The actual deployment took place from the quarterdeck at the aft end of the ship. Using a crane the instruments were lifted onto a special cradle on this deck. While held in a vertical position in this cradle the instruments underwent final preparation; attachment of the salt-water bridge and chopper onto each HEF instrument, attachment of the heavy tripod onto the base of each instrument, attachment of radio transmitter antenna and a check that the transmitters were functioning correctly. Using the ship's crane the instruments were then swung over the side of the ship, lowered gently into the water using a block and tackle, and released.

Each deployment site was carefully chosen to be an area of very flat seafloor. The *Cook* 's echo sounder was used to search for these locations and the final position of each site was recorded from the ship's satellite navigation system.

The recovery cruise for the SIO seafloor instruments took place in late March - early April 1984 and lasted 10 days. (The RANRL current meter was retrieved earlier, during a cruise by the CSIRO vessel R.V. *Sprightly* in March.) The main recovery cruise took place in bad weather and rough seas: the recovery of many instruments was made possible only by the size and hence stability of the *Cook*. The seafloor instruments were timed to come to the surface at a rate of one site per day (except for the first two days on which the instruments from sites TP8 to TP5 were retrieved). Because of the limited life of the batteries powering the radio transmitters in each instrument it was imperative that the *Cook* maintain its schedule and arrive at the necessary site close to the time of instrument resurfacing. Despite the rough seas this result was achieved.

After each instrument surfaced, it was located using first the radio signals it emitted and then its brightly coloured flags. The *Cook* was manoeuvred to lie on the upwind side of the instrument so that the instruments drifted towards the quarterdeck of the ship. If necessary a navy diver then swam out to the instrument and attached a shackle from the ship's crane. The instrument was lifted on board using the crane and onto the cradle on the quarterdeck. During the retrieval cruise an SIO portable laboratory (in a freight container) was mounted on the *Cook* 's quarterdeck. After the salt-bridge, chopper and slow-down plate were removed from each instrument it was carried to this laboratory where it underwent a timing check before being switched off.

The recovery rate of the seafloor instruments was excellent. Of the 21 Scripps seafloor instruments deployed 19 were successfully recovered. All of the deployed magnetometers, HEF and pressure instruments were successfully recovered, however two of the VEF instruments were not recovered. The VEF instrument at site TP5 was lost during the actual recovery, when rough seas caused the *Cook* to shear through the cable connecting the upper float, already on board, and the instrument package. The instrument package,

negatively buoyant without the float, sank to the seafloor. The VEF instrument at site TP7 was not sited at its recovery time and is believed to have failed to return to the sea surface after the failure of a battery pack.

Land Instruments

The land instruments were deployed some time before the main recording period, in July 1983, in order to allow the magnetometer fibres to relax into stable positions. The instrument at site MYL was actually deployed in 1982 for an earlier array project in the Cobar region. The instruments were deployed using 4-wheel drive vehicles from the ANU. Where possible instrument sites were chosen to lie several hundred metres from minor roads. Such site locations allow easy access while reducing cultural noise and interference.

Each instrument was buried in a vertical hole about 1.2 m deep. The holes were dug using a hand auger, crowbar and shovels and site locations were therefore chosen to be in areas of soft, dry soil. After instrument deployment, soil was piled over a bucket covering the top of each instrument. This soil increased the thermal insulation of the instruments and discouraged human and animal interference.

Immediately before and after the main recording period and once during the recording period routine service visits were made to each land instrument. During each of these visits the batteries powering the instruments were changed, the roll of recorded film replaced with a new roll, and the general performance of each instrument checked. The optics were also re-adjusted so that all of the magnetometer traces lay near the middle of the recorded film. This re-adjustment was made necessary by gradual drift of the magnetometer fibres. At each service visit a number of calibrations were performed on each instrument to allow the later determination of instrument sensitivities. The calibration involved deflecting each of the magnetometer traces using a small magnet of accurately known magnetic moment.

The land magnetometers all ran successfully throughout the main recording period with only minor data loss (see section 3.3) and no problems of interference by curious passers-by. The deployment of the land instruments was performed by Dr F.E.M. Lilley and Mr I.J. Ferguson from the ANU. Dr Lilley, Mr Ferguson and Mr N.L. Bindoff performed the service visits.

Chapter 3 Data Reduction

3.1 Introduction

In this chapter the reduction of the instrumental recordings from the Tasman Project into final geomagnetic and geoelectric time series will be described. For the seafloor data this reduction involves converting from digital recordings on audio cassette tapes into final time series, while for the land Gough-Reitzel magnetometer data it involves converting the analogue film traces into final time series. The chapter includes a description of the integration of the seafloor, land and magnetic observatory data into a unified Tasman Project data set.

The data reduction described in this chapter has all been performed at the ANU. The reduction of the data from the Aanderaa recording current meter was performed at RANRL in Sydney and is not described here. The chapter will concentrate on the reduction of the seafloor magnetotelluric data and the Gough-Reitzel land magnetic data but will include a brief summary of the reduction of the seafloor pressure and vertical electric field data.

This chapter is intended to provide only an outline of the data reduction; sufficient detail is included to account for the characteristics of the final time series and to provide an indication of the relevance of the data reduction to the overall Tasman Project. Details of the data reduction for each individual time series and descriptions of individual instrument characteristics are not included. A more detailed description of the data reduction is given in Ferguson (1986). The complete data reduction for the land and seafloor instruments is estimated to have taken two man-years and thus represents a significant component of the overall Tasman Project. The reduction has been performed using computing, digitizing and plotting facilities of the ANU Computer Services Centre and from the Research School of Earth Sciences (RSES), ANU.

The data recorded by both the seafloor and land instruments were of high quality. In order to reduce the data into final time series it was however necessary to make minor changes to the data such as removing drift from seafloor magnetic components or correcting occasional data bits lost during tape writing. Although this chapter concentrates on describing such changes it should be noted that the changes are minor and that the raw data form high quality time series which are very close to the final electromagnetic time series.

3.2 Reduction of Data from Seafloor Instruments.

The reduction of data from the SIO seafloor instruments occupied approximately one man-year and was performed mainly by I.J. Ferguson who reduced the magnetic and horizontal electric recordings. The reduction of the pressure data was performed by F.E.M. Lilley while the reduction of the vertical electric field data was performed by N.L. Bindoff. Most of the data reduction was done on a UNIVAC 1100/82 computer however a FACOM M160 was also used to read IBM binary-format data files.

Data Return

The SIO seafloor instruments operated extremely well during the Tasman Project with a high level of data return. The recovered instruments recorded 45 time series; 27 magnetic field components, 14 horizontal electric field components, 1 pressure recording, 1 vertical electric field recording and 2 temperature recordings. Of these 45 recordings 38 time series contained essentially complete and continuous data while only one time series contained no usable data.

The components with incomplete time series are as follows:

TP4 HEF - one component ends at Day 70 (caused by premature flattening of a battery pack.)

TP5 HEF - instrument stopped recording between Day 17 1800 h and Day 52 0400 h (cause unknown).

TP8 HEF - one component unrecorded (caused by failure of a battery pack).

TP9 MAG- a number of short data losses between the start of recording and Day 34 (caused by imperfections in data written to tape)

A summary of the data available for each component may be found in section 3.5 in Table 3.2. This table gives the start and end times of recording and other time series details. Minor data losses near the start of some time series due to a tape transcription problem and also due to rapid instrument drift are described below.

At sites TP1, TP3 and TP4 the horizontal orientation of the HEF instruments was not recorded successfully. As described below, approximate orientations for these instruments have been obtained by comparing the recorded data with the recorded data at site TP5.

The clock/timing systems of all of the instruments operated precisely during the recording period. The maximum timing error was for the HEF instrument at TP5 where at the end of the recording period the clock had lost 160 s. The timing losses or gains for all of the other instruments were considerably less than this value. For all the analyses of the

Tasman data performed to date, the periods considered are much longer than 160 s and no correction has been made to the timing. In order to provide a complete description of the Tasman Project data set a list of the observed timing losses and gains is provided in Table A2.1 in appendix 2.

All seafloor instruments were successfully deployed on very flat seafloor. No correction has been made for the very small tilt of each instrument.

Formation of Raw Time Series from Instrumental Recordings

The recordings were made by the seafloor instruments in binary format on audio-cassette tapes. These tapes were returned to Scripps Institution of Oceanography immediately after the retrieval cruise and read there using a specially designed data reader onto an IBM computer. In the data transcription, one file was formed for the recordings from each instrument and the original instrumental format was preserved. (The data were kept in binary format and each raw data record, ie. a set of 64 data points plus a summary, was written as one IBM record.) The data files were then copied to magnetic tape and a set of tapes posted to the ANU where the remaining data reduction has been performed.

At the ANU the data were read from the magnetic tapes using a FACOM computer which could directly read the IBM binary data. Additional effort was required to read occasional records of a longer or shorter length than the correct value; such records resulted from the omission of data bytes or the inclusion of spurious bytes during the recording or transcription of the data. For most of these incorrect length records it was possible to re-read the data (using the observed record length), locate and correct the spurious/missing bytes. All the data files contained a missing record approximately one day after the start of recording. These records were lost during the transcription of the cassette tapes onto the IBM computer. Since the missing records occur at the start of each time series the data have not been corrected.

On the FACOM computer the data files for each instrument were separated into individual files for each of the magnetic, HEF, VEF, pressure and temperature components. These new files were then transferred with the data in standard EBCDIC format to the ANU UNIVAC 1100/82 computer on which the rest of the data reduction was performed.

The first step in this data reduction comprised forming continuous time series. Each component was converted from its record format into a continuous series: this conversion procedure involved summing the most and least significant bytes for each data value, and progressively adding each record on to the end of the time series. During this process the timing information included in each data summary was checked and any missing data (such as for the TP5 HEF instrument) padded with a recognizable data value to produce a complete time series.

Removal of data spikes

All the time series contained occasional spikes. These spikes were produced when a single or number of data bits were incorrectly read or written during the initial data recording or later data transfer. The spikes tend to have magnitude 2^n ($\pm 2^m$) counts and the larger spikes are clearly distinguishable from geomagnetic activity.

A computer program was written which located these spikes in the data and allowed the user to interpolate a new value based on the surrounding data points. The only data spikes corrected were those that could clearly be distinguished from geomagnetic activity. Compared with the total number of data points the number of spikes requiring editing was very small. For the magnetic and HEF time series, a total of 5300 spikes were removed from approximately 4.8 million recorded data points (ie. < 0.1 %).

Removal of flat spots

Six of the magnetic field recordings contained small flat spots in which the data values tended to "stick" at a particular level. These flat spots are caused by an oscillator in the analog-to-digital circuitary locking at a harmonic frequency. The flat spots are characterized by a small range of data values in which the correct value is the replaced by the flat spot value. Outside this range is another small range of values for which the recorded data values are displaced from their true value, towards the flat-spot value (see Figure A2.1 in appendix 2 for an illustration of a flat spot).

A computer program was written to correct these flat spots. For each component the data were carefully examined in order to determine the range of data values replaced by the flat spot and the outer range of values in which data were drawn towards the flat spot. Correction of each flat spot involved "unstretching" the data in this outer range, and then interpolating across the flat spot using either a straight line or a parabola (depending on whether the data trace passed through the flat spot or peaked in it). The details of the corrected flat spots are listed in Table A2.2 in appendix 2.

Dedrifting the Data

The recorded magnetometer, pressure and VEF data all included long-period drift. In general such drift has an exponentially decreasing and/or a linear form and is caused by a number of processes including drift in electronic components, drift of the magnetometer fibres, changes in battery voltage and physical settling of the instruments in the seafloor sediment. A correction has been made to all the time series containing drift. The HEF instruments, with their system of signal chopping, eliminate (and record) the long-period

drift in the recorded signal.

Examination of the recorded magnetic data showed that some time series contained irregular long-period fluctuations with periods of order one week. This irregular signal is believed to be induced by the dynamo action of the water motion in an oceanographic eddy (Mulhearn et al. 1986, Lilley et al. 1986a). This assertion is supported by the observation that the largest irregular signal occurs in magnetic components from sites TP5-TP9 where such eddy effects are expected to be strongest. Since it was desired to retain these eddy signals in the data the long-period instrumental drift was removed using only a very basic scheme.

The dedrifting involved fitting to, and subtracting from, each time series a function of the form

$$d(t) = c_1 + c_2 t + c_3 \exp(-t / c_4) + c_5 \exp(-t / c_6) \qquad 3.1$$

For each time series the function was fitted, using basic graphical techniques, to 24 h running means of the data. The constant term, c_1, was chosen to give each time series a mean value of approximately zero. Table A2.3 in appendix 2 lists the parameters of the drift function for each time series.

For most of the magnetic time series the time scales, c_4 and c_6, of the exponential drift decay were found to be of order twenty days and five days respectively. Some components from sites near the coast contained an additional very rapid drift in the first one to two days of recording which was not able to be fitted by equation 3.1. This rapid drift may have been caused by instruments settling into seafloor sediment. Near the coast the sediment is deposited faster and is therefore likely to be softer than in the central Tasman Sea. For components containing this rapid drift the first few days of recording were deleted from the final time series.

The removal of the drift from the oceanographic VEF and pressure data is described in Bindoff et al. (1986) and Lilley et al. (1986) respectively. The VEF recordings contained a large drift component caused mainly by drift of the Ag-AgCl electrodes which made the contact with the ocean water. The drift was removed by least-squares fitting and subtraction of a function similar to that in equation 3.1. The pressure data contained only a very minor component of drift and for the analyses of the data performed to date, this drift has been removed by subtraction of a linear trend from the data.

Although the recordings from the HEF instruments contain no instrumental drift the recordings from sites near the Australian coast contained a large magnitude irregular signal induced by the oceanographic eddy (see Lilley et al. 1986a). This irregular signal was not subtracted from the time series.

Scaling the Data

The next stage of the data reduction involved scaling the time series from the recorded values (in counts) into physical units. This procedure involved multiplying each data value by a calibration factor determined from instrument calibrations performed before and after the recording period. The magnetic data were scaled into units of nanoteslas (nT), the electric data into units of nanovolts/metre ($nV.m^{-1}$) and the pressure variations into variations of the equivalent head of ocean water in millimetres.

Orientation of the HEF Instruments

The final stage of reduction of the HEF time series involved rotating the recorded time series into the magnetic north and magnetic east co-ordinate system. Before this operation could be performed it was necessary to calculate orientations for the HEF instruments at sites TP4, TP3 and TP1. Approximate orientations for these instruments were obtained by matching the recorded HEF fluctuations at the unoriented sites with those from the oriented TP5 instrument. This work was done in two stages of refinement.

Preliminary orientations for sites TP1, TP3 and TP4 were obtained using a number of short events of length of order 1 h. For each event the data from the unoriented sites was progressively rotated and compared with the oriented event at TP5 until the misfit between the two data sets was at a minimum. The misfit was taken as the sum of the squared difference between the two E_H time series plus the squared difference between the E_D time series. Instrument orientations determined from three to five events were averaged and the result adopted as the orientation.

More accurate orientations were subsequently determined using much longer events and a frequency-domain analysis. In this analysis, ten-day time series from the unoriented sites were progressively rotated and the coherences of the resulting time series with oriented E_H and E_D time series from TP5 used to define the correct instrument orientations. This method uses much more data than the earlier method and removes any bias caused by events that are particularly strong in either E_H or E_D.

Examination of the coherence results (Figure A2.2 in appendix 2) shows that the E_H and E_D components exhibit their maximum coherence between TP5 and the unoriented site at slightly different orientations. These differences increase with increasing period and can be shown to be caused by different degrees of linear polarization of the electric field at the two sites. The final orientation adopted for the unoriented sites was the average of the E_H and E_D results (and this value was also suggested at short periods where the E_H and E_D results were very similar). The final orientations for TP1, TP3 and TP4 are matched to

that at TP5 to within ±5°. It should be stressed however that these orientations are only relative to site TP5. Local electrical conductivity perturbations near either TP5 or the unoriented sites could bias the determined orientations away from the correct instrument orientations (see chapter 7).

After the determination of the approximate orientations of the HEF instruments at site TP1, TP3 and TP4, the HEF time series were rotated to magnetic north and magnetic east co-ordinates. For the TP8 and TP4 data (after Day 70) where there are recordings on only one component, the data cannot be rotated from their recorded orientation into north and east components. At TP8 the recorded component has an orientation of 349° (magnetic) while at TP4 the only recorded component after Day 70 has an orientation of approximately 206° (magnetic).

Patching the time series

At several places in the magnetic and HEF recordings short missing data segments interrupted otherwise continuous time series. Since most of the analyses to be performed on the data rely on using long time series, the missing segments were patched with corresponding data from an adjacent recording site. Although the inserted data are very similar to the missing data, time series containing more than 10% of patched data have generally been excluded from further analysis.

The process of patching each missing segment consisted of selecting the corresponding data from an adjacent site and adding a linear trend to the selected data such that it matched the missing segment at either end of the gap. Plotting of the time series confirmed that the patching was performed correctly.

Most of the missing segments resulted from wrong-length records in the raw data which contained too many missing bytes to enable accurate correction. The patched data segments are listed in Table A2.4 in appendix 2 and the presence of patched data in each component is noted in the summary of available data in Table 3.2. The main patching performed on the seafloor data involved patching a total of 58 h of missing data from the TP9 magnetic recordings. The missing data occurred in 10 separate segments between Day 16 and Day 34.

Instrumental noise on the seafloor data

Inspection of the HEF and magnetic time series reveals the presence of a high frequency noise in some recorded components. The absence of similar noise on other components strongly suggests that this noise is of instrumental origin. It should however be noted that high-frequency water motion such as turbulence may also induce noise in the electric and magnetic fields.

Table 3.1 gives a list of the components containing a significant level of instrumental noise and Figure 3.1 illustrates short time series for these components. Figure 3.1 also shows examples of magnetic and electric components which contain no apparent instrumental noise. Examination of the magnetic-field time series shows that at the highest frequencies the digital nature of the data introduces a background noise - the jump between adjacent count values is of the same order as the level of signal. For the HEF time series however, the level of one least count is much smaller than the signal level.

The features noted in the time series are confirmed by examination of the power spectra in Figure 3.2. The components containing significant levels of noise have increased power at frequencies above about 1 cph compared with components without noise. The noise spectra have slopes very close to 1/frequency, typical of a number of observations of electronic instrumental noise, for example the low-frequency noise on transistors. At the highest frequencies shown in the power spectra, the noise power is a factor of two to five greater than the signal power.

It can be shown that for instruments such as the SIO seafloor instruments which use counting techniques to obtain the digital form of the signal the variance introduced by digitizing is generally given by

$$\sigma^2 = \Delta^2 / 6 \qquad 3.2$$

where σ^2 is the variance and Δ is the least count (Irish & Levine 1977). The background power generated by the digitization is independent of frequency (i.e. has a "white" spectrum) and for the definition of power used here is given by

$$S_D = \sigma^2 \delta = \Delta^2 \delta / 6 \qquad 3.3$$

where δ is the sampling interval. For the SIO instruments, as set up for the Tasman Project, one can calculate the background power due to digitization of the signal to be 1.5×10^{-4} $nT^2.cph^{-1}$ for the magnetic components and 2.3×10^{-6} $(\mu V.m^{-1})^2.cph^{-1}$ for the HEF components. (See Filloux, 1974 for a detailed examination of the effects of signal chopping on the recorded HEF data.)

Figure 3.2 shows that for the magnetic components with no significant instrumental noise, at the highest frequencies the spectrum starts to approach the digitizing power level. At a frequency of 5 cph the signal and digitizing power levels are approximately equal. This result confirms the observations from the time series that the digitizing level becomes significant at the highest frequencies. In contrast, for the noise-free HEF components, even at the highest frequencies the signal level is still three orders of magnitude greater than the digitizing power level.

Table 3.1: Instrumental noise on seafloor components

Component	Typical Noise Level on time series
TP7 E_H	0.2 $\mu V.m^{-1}$
TP7 E_D	0.5 $\mu V.m^{-1}$
TP5 E_H and E_D	0.5 $\mu V.m^{-1}$
TP4 E_H and E_D	0.4 $\mu V.m^{-1}$
TP4 B_H	0.5 nT
TP2 B_Z	0.4 nT
TP3 B_Z	0.6 nT

Note that the values for noise are estimated from the time series without consideration of the noise frequency spectrum. The noise on the HEF components varies considerably with time; the above values are typical levels.

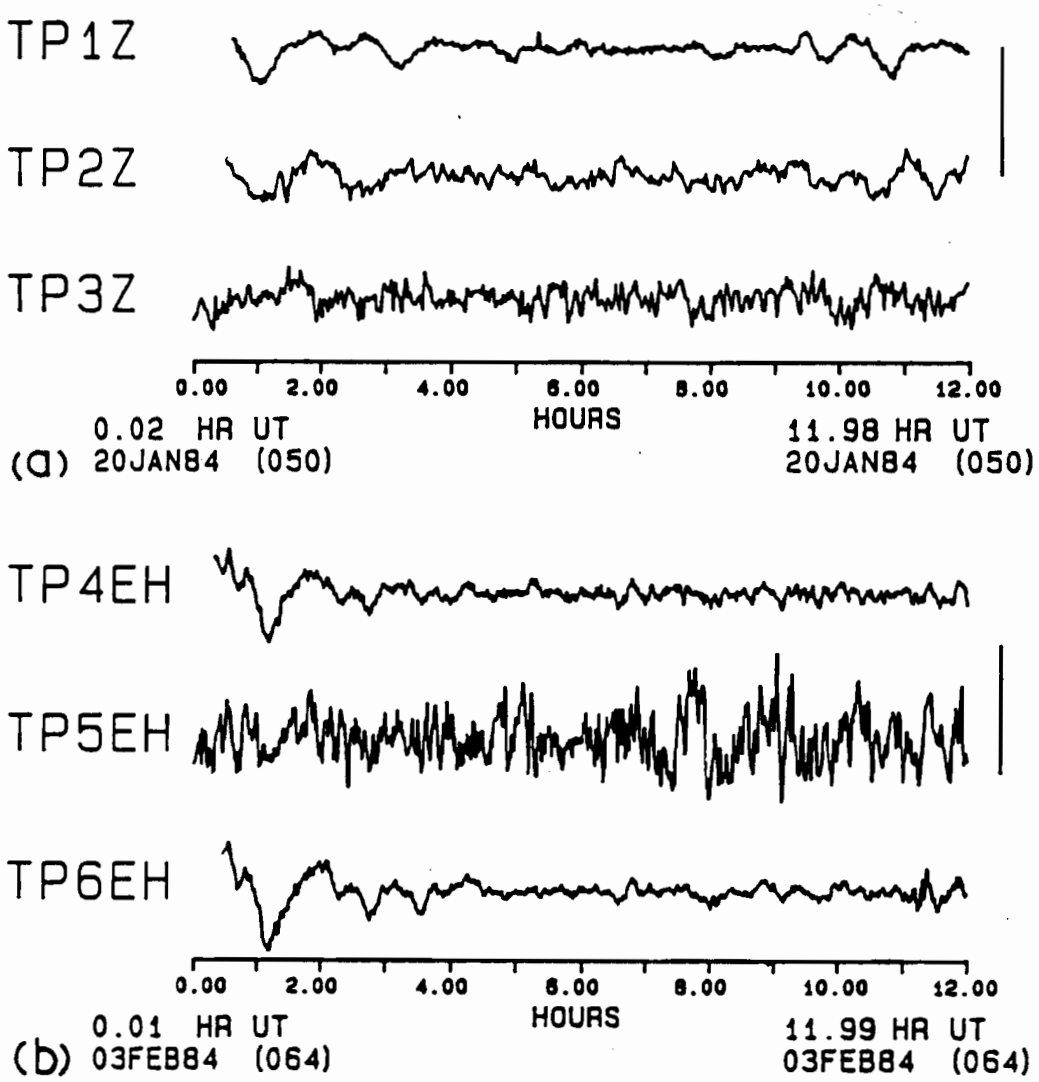

Figure 3.1 Examples of seafloor electric and magnetic time series containing instrumental noise. For these examples data have been high-pass filtered (with cut-off = 2.0 h) to remove longer period geomagnetic variations.

(a) Magnetic field data, scale bar = 5.0 nT, data density = 32 data.h^{-1}. TP2 B_Z and TP3 B_Z contain instrumental noise, TP1 B_Z is included for comparison. Note that one least count corresponds to 1/30 of the scale bar length and that the quiet TP1 B_Z component exhibits digitizing noise at this level. (Traces labelled Z refer to B_Z).

(b) HEF data, scale bar = 2.0 μV.m^{-1}, data density = 64 data.h^{-1} . TP5 E_H contains instrumental noise, TP4 E_H contains minor noise but becomes noisier in other parts of the record, TP6 E_H is included for comparison. One least count corresponds to 1/70 of the scale bar length.

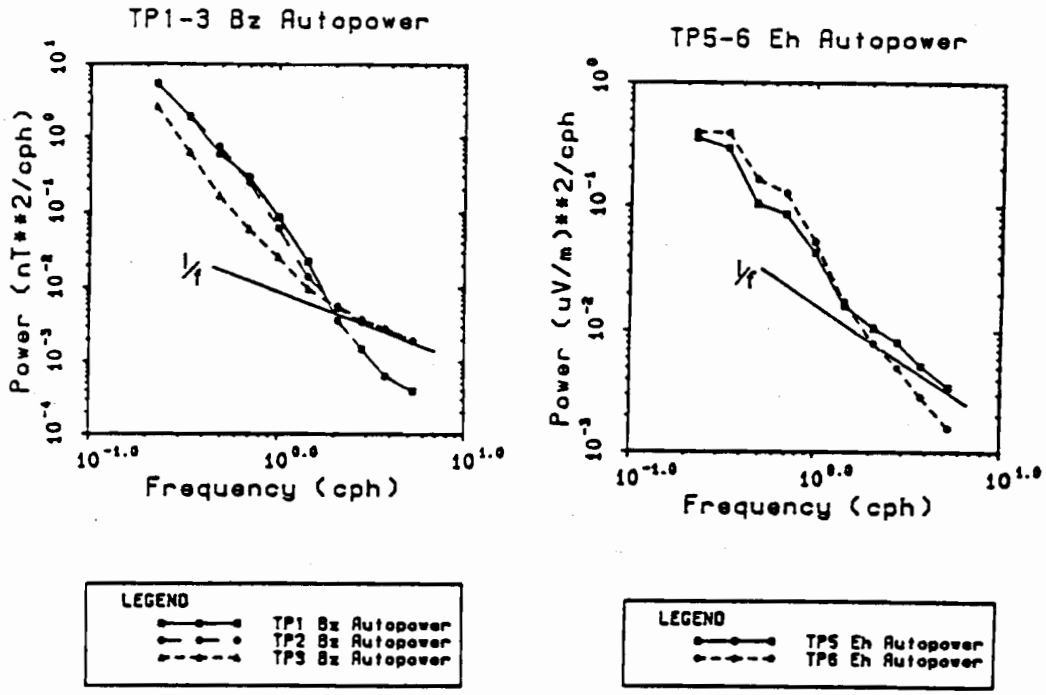

(a) (b)

Figure 3.2 Power spectra of components with and without significant instrumental noise. The spectra are calculated from 256 h time series, of density 32 data.h^{-1} (8192 points), commencing Day 84 00.00 h.

(a) Magnetic field components

(b) HEF components

Note that the components with significant noise, TP2 B_Z and TP3 B_Z and TP5 E_H, approach a (1/frequency) slope at high frequencies, where the noise levels become significant. The decrease in slope of the quiet TP1 B_Z component at high frequencies is interpreted as being caused by the presence of digitizing noise, which has a predicted power level of 1.5 x 10^{-4} nT^2.(cph)$^{-1}$. See chapter 6 for a discussion of the signal power-spectra.

3.3 Reduction of data from Gough-Reitzel magnetometers

The reduction of the recordings from the Gough-Reitzel magnetometers involved converting analogue traces on photographic film into digitized time series of magnetic-field variations. The digitization and reduction of the land data occupied approximately 0.75 man-years. It was performed largely by N.L. Bindoff and M.N. Sloane however F.E.M. Lilley, L.J. Ferguson and J. Cowley assisted in various aspects. The data reduction was performed using a digitizer, plotters and UNIVAC 1100/82 from the ANU Computer Services Centre.

Film Developing and Data Return

Before the levels of data return could be assessed (or were in fact guaranteed) the recorded films required photographic developing. This developing was performed using a commercial style microfilm developer at the ANU.

The data return from the Gough-Reitzel magnetometers was excellent with almost-complete time series available for all of the 24 recorded components. A list of the missing data in each component may be found in Table A2.4 in appendix 2; the time series containing longer segments of missing data (greater than 10 hours duration) are as follows:

BBB-all	Day 56 - 70	(caused by camera jam)
BKM-all	Day 0 - 18	(film not correctly aligned on camera sprockets)
BKM-B_H	Day 61 - 65	(B_H component occasionally off-scale)
BLN-all	Day 104 -114	(loss of three segments of about a day caused by film developing error)
MYL-all	Day 14 -16	(premature flattening of dry cell battery)
	Day 60 - 67	(premature flattening of dry cell battery) .

A number of shorter data losses were caused by the routine service visits to the instruments and B_H traces occasionally going off-scale during strong magnetic disturbances. The patching of the missing data is described below. The timing systems of the Gough-Reitzel instruments operated well during the Tasman Project recording period, with the maximum timing error between service visits being 113 s. Although no correction has been made for the timing drift, Table A2.1 in appendix 2 lists the observed timing gains and losses.

Digitizing the Analogue Film Data

The digitization of the Gough-Reitzel photographic films occupied most of the time required for the reduction of the land data. In order to permit the digitization of complete time series for each component the data were digitized at a level of resolution below the maximum level possible. For this "B-level" digitization, 12-hour segments of recorded data were projected onto a large digitizing table by an overhead projector, and digitized as a continuous record. This arrangement provides a magnification of the recorded film of approximately 2.8 times. The B-level digitization of the 24 Gough-Reitzel components required about 0.5 man-years.

A higher "A-level" digitizing resolution is permitted if the recorded film is projected onto the digitizing table at an increased magnification using a 35 mm slide projector. While this level is suitable for accurate digitization of individual geomagnetic events it is too time consuming to be suitable for digitizing long continuous time-series.

For B-level digitization the recorded traces have scale values on the digitizer table of approximately 7.0 $nT.mm^{-1}$ for B_H and 3.5 $nT.mm^{-1}$ for B_D and B_Z. The resolution and noise associated with digitization at these scales is discussed below. The time-scale on the original Gough-Reitzel films is 15 $mm.h^{-1}$ and after projection, the individual data points are spaced along the film in increments of 0.7 mm. During digitization each component is digitized as a continuous trace and the resulting data points (the positions of which depend upon the cursor speed) are interpolated to provide data at a density of 20 $data.h^{-1}$.

Calibration and Scaling of the Time Series

A number of calibrations were performed on the Gough-Reitzel instruments during the recording period. In these calibrations each magnetic trace is deflected by a magnet placed in a fixed position on the top of the instrument. Using appropriate formulae, the magnetic field produced at each sensor by the calibrating magnet can be accurately calculated, and with the measured trace deflections, used to calculate the scale value for each component.

In order to allow accurate determinations of the scale values at least 10 calibrations were performed on each magnetometer during the Tasman Project. When the results from early calibrations were examined it was evident that for some components the scale value was non-linear and varied with the position of the recorded trace across the film. The scale value variation across the film was itself smooth and linear. After this effect was noted calibrations were performed with the traces set in a wide range of positions across the film. Examination of the final set of calibration results allowed accurate definition for each component of both the average scale value and the linear variation of scale value across the film.

After digitization the 12-hour segments of magnetic field data were progressively

merged into a continuous time series and the data were then scaled into units of nanotesla using the determined scale values (including an allowance for the scale-value variation across the film). During this process a small correction was also made for an interaction that occurs between the magnetic fields of the B_H and B_Z sensor magnets (Lilley et al. 1975). Separate time series were formed for the three components recorded by each instrument. Finally where jumps occurred in the data, for example when traces were recentred during service visits, an increment was added to the later part of the time series so as to produce a continuous time series.

Each data point from the Gough-Reitzel magnetic data represents an approximately instantaneous measure of the magnetic field although the digitization process may result in a slight smoothing of the data. After digitization a timing value was stored with the value of each data point. This was necessary because, unlike the SIO data which always commenced at the start of a UT hour, the start of the Gough-Reitzel data after each service visit was at the start of an arbitrary minute.

Patching the Gough-Reitzel Data

The gaps in the Gough-Reitzel time series were patched using the same method as for the SIO time series. Because service visits were made to all the Gough-Reitzel magnetometers during the recording period, all components required some patching. The patched segments of data are listed in Table A2.4. For a number of the magnetometers the B_H trace entered the sprocket holes at the edge of the film during periods of strong magnetic disturbance. The small segments of data lost in the sprocket holes were interpolated during digitization.

Noise and Resolution of the Digitized Gough-Reitzel Data

The recorded Gough-Reitzel data do not appear to contain significant high-frequency instrumental noise. Most of the recorded components however contain a relatively small magnitude long-period drift caused by relaxation of the magnetometer fibres. This drift has not been subtracted from the data.

At sites CLC and BBB, located relatively near minor roads, passing motor vehicles have caused a number of minor spikes in the recorded data. At site BBB several jumps in the data were caused by the close passage of a bulldozer. These spikes and jumps were removed during digitization.

The level of accuracy with which the recorded Gough-Reitzel data can be digitized depended upon the clarity of the trace being digitized and upon the level of magnetic disturbance, but is typically of order ±0.5 mm (measured on the digitizing table). This

distance corresponds to an error of approximately ±3.5 nT in B_H, ±1.8 nT in B_D and B_Z, and 0.7 min. in the timing. The resolution of the digitizing table is 0.25 mm and therefore does not greatly increase the digitizing error.

The resolution of the digitized data may be examined using power spectra calculated from the time series. Figure 3.3 shows the power spectra calculated for site BBB and the adjacent magnetic observatory site, CMO, for the horizontal magnetic field components. For periods below 1 h the spectra are calculated from a time series of length 10 days, typical of the minimum time series length used for the Tasman Project data analyses.

The power spectra from BBB and CMO are almost identical for periods longer than 0.5 h. At shorter periods the BBB components show a decreased power level relative to CMO; at the highest resolved frequencies the BBB power is approximately 0.5 times that at CMO. These differences between the CMO and BBB power spectra are unlikely to be due to noise on the digital observatory data and the proximity of CMO and BBB (and examination of power spectra for other sites) suggests that the differences are not due to differences in geoelectrical structure between the CMO and BBB sites. The differences are therefore interpreted as being caused by a slight filtering of high frequencies during the hand-digitization of the Gough-Reitzel data. This result is confirmed by a comparison of the B_H time series from the CMO and BBB sites.

The power level of noise associated with digitizing can be calculated from the estimates of digitizing accuracy. Taking the digitizing errors given above as twice the standard deviation of the error distribution, and a typical initial digitizing sampling rate of 20 data.h^{-1}, one obtains power levels of 0.2 $nT^2.(cph)^{-1}$ for B_H and 0.04 $nT^2.(cph)^{-1}$ for B_D and B_Z using equation 3.2. Examination of Figure 3.3 shows these levels are slightly below the levels of signal at the highest frequencies available from the digitized data.

Figure 3.4 shows the phase of the crosspower between corresponding magnetic field components at BBB and CMO. Except for periods above 10 h, where error estimates are larger, the relative phase between CMO and BBB components corresponds to a time difference of less than 2 min. This time difference is shorter than the sampling interval of digitized Gough-Reitzel data. The power and phase results thus show that for analyses of time series of length 10 days or more, the digitized Gough-Reitzel data provide relatively accurate estimates of signal magnitude and timing. The results however do show some decrease in the accuracy of the hand-digitized data for periods less than 1 h.

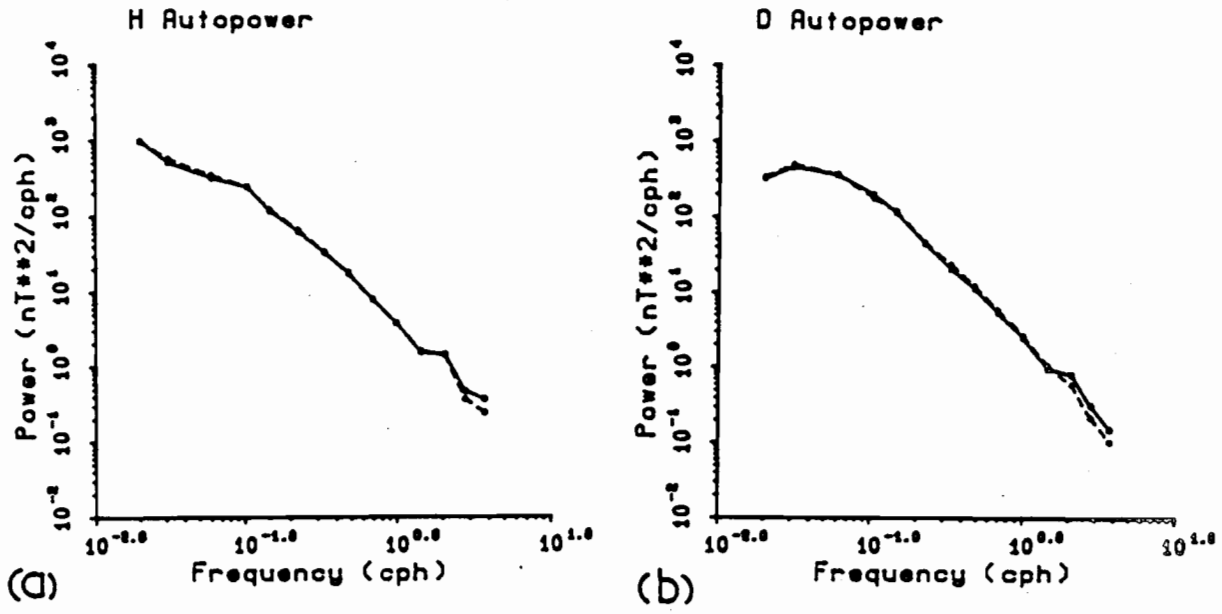

Figure 3.3 Comparison of power spectra at CMO (solid line) and BBB (dashed line). For frequencies greater than 1 cph the spectra are calculated using a 256 h time series of density 16 data.h^{-1}, for frequencies less than 1 cph the spectra are calculated using a 42.7 day time series of density 8 data.h^{-1}.

(a) B_H components

(b) B_D components

At frequencies less than 2 cph the spectra from the two sites are almost identical however at higher frequencies the BBB spectra contain reduced power. This result is interpreted as being caused by a slight filtering of the higher frequencies during the digitization of the BBB Gough-Reitzel data. The two recording sites are 34 km apart.

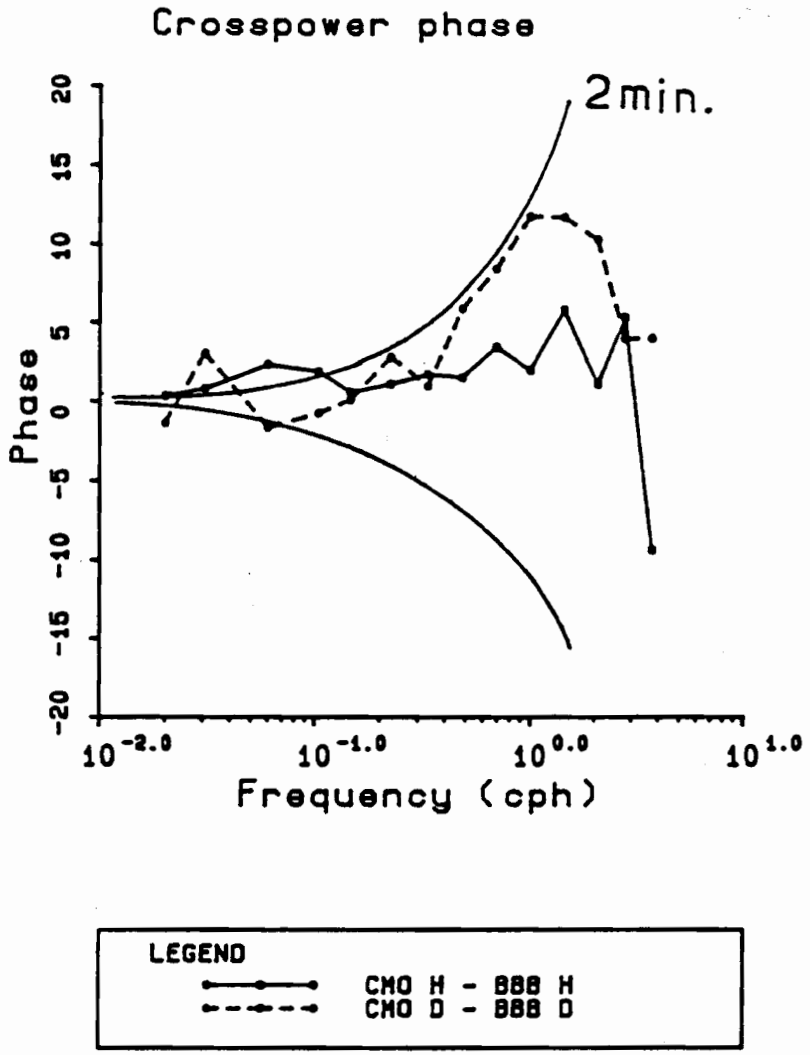

Figure 3.4 Crosspower phase (in degrees) between corresponding B_H and B_D components at CMO and BBB. The cross-powers are calculated from the same time series as the spectra in Figure 3.3. The smooth curves show the phase angle corresponding to a time difference of 2.0 minutes. The figure indicates that for calculations based on time series of length greater than 10 days, no consistent timing differences exist between the digitally recorded CMO data and the hand digitized Gough-Reitzel BBB data.

3.4 Magnetic Observatory Data

The magnetic data from the Canberra Magnetic Observatory were supplied on magnetic tape in standard IAGA format. This format includes the absolute values of the magnetic field components B_X, B_Y and B_Z at one-minute intervals. The data for each component are given to the nearest nanotesla.

The only data reduction required for the CMO data was to convert the data into a similar form as the seafloor and Gough-Reitzel data. This process involved rotating the horizontal components into B_H and B_D co-ordinates and subtracting a baseline from each of the components. The observatory data contain occasional missing data segments (Table A2.4). Shorter missing data segments were patched by linear interpolation while two longer segments of length greater than 24 h were patched with data from the adjacent BBB site. The patching from BBB involved duplicating every data value in order to increase the sampling density from that of the digitized Gough-Reitzel data.

The data from the Eyrewell Magnetic Observatory in New Zealand (site code EYR) were supplied in the form of photocopies of the observatory magnetograms. In order to produce digital time series these magnetograms were digitized using a process similar to that used for the Gough-Reitzel films. This digitization and the subsequent reduction of the EYR data were performed by R.L. Kellett and M.N. Sloane.

The scale value of the components on the Eyrewell magnetograms (5.5- 6.0 nT/mm) is of similar magnitude to the scales of the Gough-Reitzel data during B-level digitization. The accuracy of digitization of the Eyrewell data is therefore similar to that of the Gough-Reitzel data, described above. The time scale on the magnetograms is 20 $mm.h^{-1}$ and the digitized data were processed to give a sampling density of 32 $data.h^{-1}$.

3.5 Integration of Seafloor, Gough-Reitzel and Observatory Data Sets

After the completion of the data reduction the different data sets possessed a number of different sampling rates. The seafloor electric data had a density of 64 $data.h^{-1}$, the seafloor magnetic and EYR data a density of 32 $data.h^{-1}$, the Gough-Reitzel data had a density of 20 $data.h^{-1}$ and the CMO data a density of 60 $data.h^{-1}$. The different data sets were also in different formats, for example the digitized data points were all stored with timing values whereas the SIO data included only a starting timing value. In order to facilitate further analysis of the data, for example cross correlations between different data sets, it was necessary to produce a standardized data format and sampling rate.

There are a variety of possible forms for an integrated data format. Since this thesis is based upon the investigation of seafloor electrical conductivity and primarily involves the

seafloor magnetotelluric data, the data system adopted was based on the binary-valued sampling rates of the SIO seafloor instruments. In this system the density of the CMO data was reduced to 32 data.h^{-1} and the density of the Gough-Reitzel data to 16 data.h^{-1}. This system maintained the data as close as possible to the original density while allowing the different data sets to be easily averaged to a uniform density.

An interpolation procedure was used to reduce the density of the Gough-Reitzel data, and to produce a new time series with points evenly spaced from a single starting time at the start of a UT hour. In the interpolation procedure all original data points which fell inside the time interval corresponding to a new point, were averaged to provide the new data value. The averaging included a linear weighting based on the overlap between the time segment corresponding to each of the original data points and the time segment of the new data point. Because it is based on an averaging method the interpolation procedure will slightly reduce the amount of energy at the highest frequencies. However because the decrease in sampling rates is not large and the magnetic power spectra are steep (Figure 3.3) this effect will be almost negligible.

The oceanographic recordings were not incorporated into the integrated data set. However the pressure and VEF data are already in a very similar form to the other seafloor HEF and magnetic data (and have a binary-valued sampling rate of 128 data.h^{-1}) and so in the future could easily be added to the main data set.

Summary of Available Data

The final data set available from the Tasman Project includes 67 magnetic and horizontal electric field time series and in addition, one pressure, one vertical electric, one current meter and three temperature time series. Table 3.2 summarises important aspects of these time series: the start and end times of available data, the final data density, the estimated data resolution, whether the time series has been significantly patched and whether the time series contains significant instrumental noise.

Table 3.2: Details of Final Time Series

Site	Comp	Available Data Days/Decimal Hours	Density data.h^{-1}	Patching (see notes)	Noise
Seafloor HEF and magnetic components					
TP1	BH	D4 08.00-D121 14.00	32	-	-
	BD	D4 08.00-D121 14.00	32	-	-
	BZ	D4 08.00-D121 14.00	32	-	-
	EH	D4 03.00-D121 16.00	64	-	-
	ED	D4 03.00-D121 16.00	64	-	-
TP2	BH	D5 08.00-D120 14.00	32	-	-
	BD	D5 08.00-D120 14.00	32	-	-
	BZ	D5 08.00-D120 14.00	32	-	Yes
TP3	BH	D6 08.00-D119 14.00	32	-	-
	BD	D6 08.00-D119 14.00	32	-	-
	BZ	D6 08.00-D119 14.00	32	-	Yes
	EH	D6 07.00-D119 15.00	64	-	-
	ED	D6 07.00-D119 15.00	64	-	-
TP4	BH	D8 12.00-D118 14.00	32	-	-
	BD	D8 12.00-D118 14.00	32	-	-
	BZ	D8 12.00-D118 14.00	32	-	-
	EH	D8 08.00-D70 06.00 64	-	m	
	ED	D8 08.00-D70 06.00 64	-	m	
	E213°	D8 08.00-D118 15.00	64	-	Yes
TP5	BH	D12 00.00-D117 20.00	32	-	-
	BD	D12 00.00-D117 20.00	32	-	-
	BZ	D12 00.00-D117 20.00	32	-	-
TP5	EH	D9 05.00-D17 17.00 64	-	m	
		D52 03.00-D 117 21.00	64	m	Yes
	ED	D9 05.00-D17 17.00 64	-	m	
		D52 03.00-D 117 21.00	64	m	Yes
TP6	BH	D10 06.00-D 117 14.00	32	-	-
	BD	D10 06.00-D 117 14.00	32	-	-
	BZ	D10 06.00-D 117 14.00	32	-	-
	EH	D10 04.00-D 117 15.00	64	-	-
	ED	D10 04.00-D 117 15.00	64	-	-

Table 3.2 cont

Site	Comp	Available Data	Density	Patching	Noise
TP7	BH	D12 06.00-D116 18.00	32	-	-
	BD	D12 06.00-D116 18.00	32	-	-
	BZ	D12 06.00-D116 18.00	32	-	-
	EH	D12 03.00-D116 21.00	64	m	-
	ED	D12 03.00-D116 21.00	64	m	-
TP9	BH	D16 00.00-D116 16.00	32	mm	-
	BD	D16 00.00-D116 16.00	32	mm	-
	BZ	D16 00.00-D116 16.00	32	mm	-
TP8	BH	D14 00.00-D116 14.00	32	-	-
	BD	D14 00.00-D116 14.00	32	-	-
	BZ	D14 00.00-D116 14.00	32	-	-
	E349°	D11 03.00-D116 15.00	64	-	-
Land magnetic components					
DRS	BH	D0 00.50-D124 02.13	16	m	1
	BD	D0 00.50-D124 02.13	16	m	1
	BZ	D0 00.50-D124 02.13	16	m	1
CDM	BH	D0 00.38-D124 02.06	16	m,i	1
	BD	D0 00.38-D124 02.06	16	m	1
	BZ	D0 00.38-D124 02.06	16	m	1
BBB	BH	D0 00.63-D124 02.06	16	mm,i	1
	BD	D0 00.63-D124 02.06	16	mm	1
	BD	D0 00.63-D124 02.06	16	mm	1
BKM	BH	D19 00.00-D124 06.75	16	m,i	1
	BD	D19 00.00-D124 06.75	16	m	1
	BZ	D19 00.00-D124 06.75	16	m	1
CLC	BH	D0 01.25-D124 00.94	16	mm,i	1
	BD	D0 01.25-D124 00.94	16	mm	1
	BZ	D0 01.25-D124 00.94	16	mm	1
BLN	BH	D0 00.19-D124 00.94	16	mm,i	1
	BD	D0 00.19-D124 00.94	16	mm	1
	BZ	D0 00.19-D124 00.94	16	mm	1

Table 3.2 cont

Site	Comp	Available Data	Density	Patching	Noise
GNS	BH	D0 00.81-D124 00.94	16	m	l
	BD	D0 00.81-D124 00.94	16	m	l
	BZ	D0 00.81-D124 00.94	16	m	l
MYL	BH	D0 00.38-D112 10.88	16	mm	l
	BH	D0 00.38-D112 10.88	16	mm	l
	BH	D0 00.38-D112 10.88	16	mm	l
Observatory data					
CMO	BH	D0 00.00-D151 24.00	32	mm	-
	BD	D0 00.00-D151 24.00	32	mm	-
	BZ	D0 00.00-D151 24.00	32	mm	-
EYR	BH	D0 00.00-D124 24.00	16	-	-
	BD	D0 00.00-D124 24.00	16	-	-
	BZ	D0 00.00-D124 24.00	16	-	-
Oceanographic Recordings					
TP2	PRESS	D6 07.50-D120 16.50	128	-	l
	TEMP	D6 07.50-D120 16.50	0.5	-	l
TP6	VEF	D11 01.50-D117 16.50	128	-	-
	TEMP	D11 01.50-D117 16.50	0.5	-	l
TP9a	RCM	D12 07.25-D111 07.75	4.0	-	-
	TEMP	D12 07.25-D111 07.75	4.0	-	

Notes

1. Symbols used for patching

   m = minor patching, no patched segments exceed 5 h.

   mm = more significant patching, see Table A2.4 for details

   i = interpolation of component when in sprocket holes.

2. Symbols used for noise

   yes = instrumental noise present, see text

   l = long period drift has not been removed

3. Most seafloor components contain one or two hours of missing data in the first two days. This data was lost during tape transcription but could eventually be recovered.

4. For TP4 and TP8, where only one HEF component is available, the data cannot be rotated to E_H and E_D co-ordinates. The (magnetic) orientation of the available component is given in the table.

PART II

ANALYSIS OF TASMAN SEAFLOOR MAGNETOTELLURIC MEASUREMENTS

Chapter 4 Basic Physical and Mathematical Theory of Magnetotelluric Analysis

This chapter examines the physical and mathematical basis of MT sounding. The aim of the chapter is to provide the background theory which will be applied in the analysis of the Tasman data. The three sections in the chapter describe the general theory for the physical equations controlling geomagnetic induction and MT sounding, the mathematical methods used to estimate MT response functions and their errors, and the source-fields used for SFMT sounding.

Although some of the material presented in this chapter is derived from the scientific literature rather than being original research, the information presented is relevant to geomagnetic induction studies, and especially to the analysis and interpretation of the Tasman Project data. Section 4.1 describes the physical theory of geomagnetic induction, using SI units and a consistent notation scheme. Particular emphasis is placed upon aspects of the theory which are relevant to seafloor measurements. Section 4.2 examines the mathematical techniques applied in the analysis of recorded MT data. It describes the well-established techniques of time series analysis and newer remote-reference techniques important for the reduction of noise effects in seafloor data.

The study of the magnetospheric and ionospheric processes involved in the generation of magnetic source-fields is itself an enormous area of research and cannot be considered in detail in a thesis concentrating on solid-earth geomagnetic induction. Section 4.3 of this chapter is therefore restricted to a review of the phenomena involved in geomagnetic storm and substorm source-fields and an examination of how source-field characteristics may affect geomagnetic induction in the Tasman Sea region.

4.1 Theory of geomagnetic induction

In this section the physical equations controlling geomagnetic induction in a layered half-space are derived. The applications of the geomagnetic induction for MT sounding and for other geoelectric sounding methods are then considered. The extension of the theory for the case of a 2D conductivity structure will also be briefly considered.

4.1.1 Geomagnetic induction in a one-dimensional conductivity structure

Problem and Assumptions Involved

In this section the controlling equations for electromagnetic induction in a layered, conducting half-space will be derived. The problem to be solved is:

For a specified 1D conductivity structure, consisting of a layered, conducting half-space underlying an insulator, and a specified inducing

magnetic source-field located above the half-space, determine the electric and magnetic fields.

The analysis is aimed at deriving the equations contolling electromagnetic induction in the Earth's crust and mantle and therefore the following assumptions are made:

(1) The Earth can be modelled by a horizontal 1D conductivity structure consisting of a layered half-space beneath an insulator (the atmosphere).

(2) The inducing source-field is external to the conducting half-space (in the ionosphere and magnetosphere).

(3) The material in the half-space is stationary (ie. neglect induction by ocean movement).

(4) The magnetic permeability, μ, and electric permittivity, ε, in the half-space and the insulator are assumed to be isotropic, uniform, frequency-independent and equal to their absolute values, μ_0 and ε_0. The conductivity, σ, is isotropic (within each layer) and frequency-independent.

(6) The electromagnetic properties of the crust and mantle are such that at the periods studied, geomagnetic induction is diffusive and displacement currents may be neglected. Displacement currents are also negligible in the insulator.

The extension of the theory to SFMT sounding will involve determining the relationship of the electric and magnetic fields at the base of an uppermost conductive layer in the conducting half-space.

Figure 4.1 shows the co-ordinate system used in the analysis. The electromagnetic induction in the half-space is governed by Maxwell's equations 4.1-4.4 (in non-relativistic form), the constitutive equations 4.5-4.7 (for a stationary conductor) and standard electromagnetic boundary conditions 4.i-4.iii (Lorrain & Corson 1970). These equations are

$$\nabla \times \mathbf{E} = \frac{-\partial \mathbf{B}}{\partial t} \qquad 4.1$$

$$\nabla \times \mathbf{H} = \frac{\partial \mathbf{D}}{\partial t} + \mathbf{J} \qquad 4.2$$

$$\nabla \cdot \mathbf{B} = 0 \qquad 4.3$$

$$\nabla \cdot \mathbf{D} = p \qquad 4.4$$

$$\mathbf{D} = \varepsilon \mathbf{E} \qquad 4.5$$

$$\mathbf{B} = \mu \mathbf{H} \qquad 4.6$$

$$\mathbf{J} = \sigma \mathbf{E} \quad \text{(Ohm's Law for stationary conductor)} \qquad 4.7$$

Tangential **E** is continuous across the interface of two media 4.i

Tangential **H** is continuous across the interface of two media 4.ii

Normal **B** is continuous across the interface of two media 4.iii

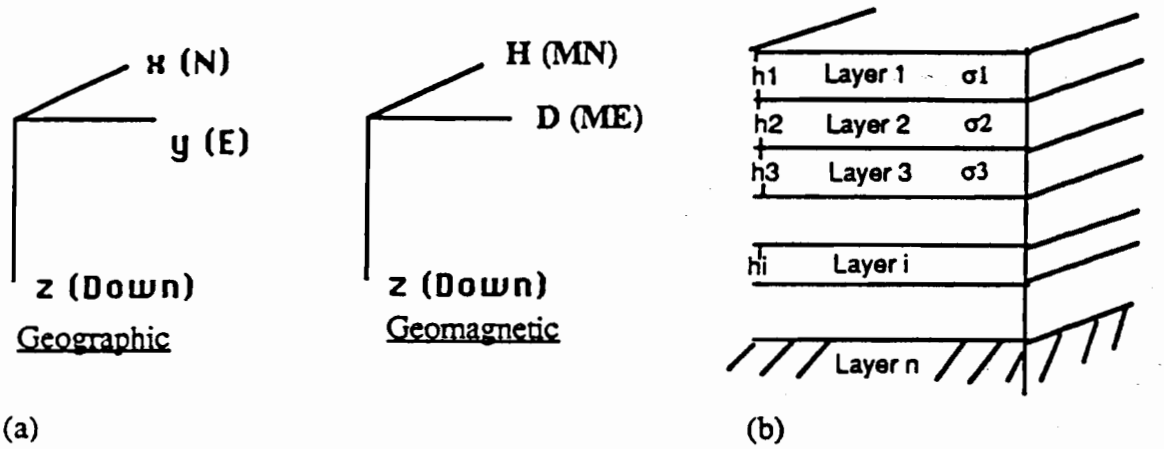

Figure 4.1 (a) Co-ordinate systems used in thesis and (b) 1D conductivity profile. The geographical co-ordinates are aligned with geographical north (N) and east (E) and the geomagnetic co-ordinates with magnetic north (MN) and magnetic east (ME). In the conductivity profile $\sigma = \sigma(z)$ for $z \geq 0$ and $\sigma = 0$ for $z < 0$. The profile is terminated by a half-space, layer *n*..

The quantities E, B, H, D, J, p are all functions of frequency and the bold print indicates the quantity is vectorial. The symbols and units for all quantities are given in Table 1.1 in chapter 1.

Derivation of (diffusive) induction equations

The geomagnetic induction process will be diffusive in nature if

$$\frac{\partial \mathbf{D}}{\partial t} \ll \mathbf{J} \qquad 4.8$$

meaning that displacement currents are neglible compared with the electric currents flowing in the Earth. Using a scale argument

$$\frac{\partial \mathbf{D}}{\partial t} = O\left(\frac{\mathbf{D}}{T}\right) = O\left(\frac{\varepsilon \mathbf{J}}{\sigma T}\right) \qquad 4.9$$

where T is the period of the oscillating electromagnetic fields. Comparing 4.8 and 4.9 indicates that displacement currents may be neglected for

$$T >> \frac{\varepsilon}{\sigma} \qquad 4.10$$

For the bulk of the Earth's crust and mantle the maximum electrical permittivity is

approximately $100\varepsilon_0$ and the minimum conductivity is approximately 10^{-7} S.m^{-1}. Substituting these extreme values into 4.10 indicates that geomagnetic induction will be diffusive for $T >> 10^{-3}$ s. For SFMT studies the minimum period considered is of order one minute and hence the geomagnetic induction involved will be of a diffusive nature.

Assuming the electromagnetic induction in this theoretical example is also diffusive, equation 4.2 reduces to

$$\nabla \times \mathbf{H} = \mathbf{J} \qquad 4.11$$

From this equation, equations 4.1-4.7, and standard vector identities the following equations are obtained for diffusive electromagnetic induction in a conductor;

$$\nabla \times (\nabla \times \mathbf{E}) = \frac{\nabla \mu}{\mu} \times (\nabla \times \mathbf{E}) - \mu \sigma \frac{\partial \mathbf{E}}{\partial t} \qquad 4.12$$

$$\nabla \varepsilon \cdot \mathbf{E} + \varepsilon \nabla \cdot \mathbf{E} = p \qquad 4.13$$

$$\nabla \times (\nabla \times \mathbf{H}) = \frac{\nabla \sigma}{\sigma} \times (\nabla \times \mathbf{H}) - \mu \sigma \frac{\partial \mathbf{H}}{\partial t} \qquad 4.14$$

$$\nabla \mu \cdot \mathbf{H} + \mu \nabla \cdot \mathbf{H} = 0 \qquad 4.15$$

Price (1950) shows that the volume charge distribution, p, can be taken as zero without loss of generality. Assuming that the magnetic permeability and electric permittivity are uniform equations 4.12-4.15 further reduce to

$$\nabla^2 \mathbf{E} = -\mu \sigma \frac{\partial \mathbf{E}}{\partial t} \qquad 4.16$$

$$\nabla \cdot \mathbf{E} = 0 \qquad 4.17$$

$$\nabla^2 \mathbf{H} = \frac{\nabla \sigma}{\sigma} \times (\nabla \times \mathbf{H}) - \mu \sigma \frac{\partial \mathbf{H}}{\partial t} \qquad 4.18$$

$$\nabla \cdot \mathbf{H} = 0 \qquad 4.19$$

The diffusive nature of the geomagnetic induction is indicated by equations 4.16 and 4.18, diffusion differential equations (Boyce & DiPrima 1969 p. 2). The diffusion equation may be compared with the wave equation which contains second derivatives with respect to time (and is important for seismology) and with Laplace's equation in which there is no derivative with respect to time (and is important for potential field geophysics such as gravity).

General solutions of induction equations

The general solutions for the electromagnetic induction equations 4.16-4.19 will now be obtained for electromagnetic induction in a layered (ie. 1D) half-space

$$\sigma = \sigma(z) \qquad z > 0$$
$$\sigma = 0 \qquad z < 0 \qquad 4.20$$

The analysis presented here proceeds in a similar manner to that of Price (1950, 1962). In the 1D conductor electric currents are constrained to flow parallel to the surface and thus $E_z = 0$. Examination of equation 4.16 suggests an exponential time dependence for **E**. Choosing a positive time dependence (see appendix 3) leads to solutions of the form

$$\mathbf{E} = Z(z)\, e^{i\omega t}\, \mathbf{F}(x,y) \qquad 4.21$$

where Z contributes only a scalar factor to **E**. Substitution of (4.21) into (4.16) and separation of variables gives

$$\frac{1}{\mathbf{F}}\left(\frac{\partial^2}{\partial x^2} + \frac{\partial^2}{\partial y^2}\right)\mathbf{F} = \frac{1}{Z}\left(\mu\sigma\frac{\partial Z}{\partial t} - \frac{\partial^2 Z}{\partial z^2}\right) = -\lambda^2 \qquad 4.22$$

where $-\lambda^2$ is a negative separation constant. The two equations

$$\left(\frac{\partial^2}{\partial x^2} + \frac{\partial^2}{\partial y^2}\right)\mathbf{F} = -\lambda^2\,\mathbf{F} \qquad 4.23$$

and

$$\frac{\partial^2 Z}{\partial z^2} = (\, i\omega\mu\sigma(z) + \lambda^2\,)\,Z \qquad 4.24$$

thus control electromagnetic induction in the 1D conductor.

Temporily setting aside the solution for Z which depends on the actual conductivity structure $\sigma(z)$, the solution for **F** will now be examined. Substitution of equation 4.21 into 4.17 gives

$$\frac{\partial Z}{\partial z}\,\mathbf{F}_z + Z\left(\frac{\partial F_x}{\partial x} + \frac{\partial F_y}{\partial y}\right) = 0 \qquad 4.25$$

This equation indicates that there are two classes of solutions for the electromagnetic induction. The first class corresponds to solutions of the form

$$F_z = 0 \quad \text{and} \quad \frac{\partial F_x}{\partial x} + \frac{\partial F_y}{\partial y} = 0 \qquad 4.26$$

and the second class will have the form

$$\frac{\partial Z}{\partial z}\,\mathbf{F}_z = Z\left(\frac{\partial F_x}{\partial x} + \frac{\partial F_y}{\partial y}\right) \qquad 4.27$$

It can be shown that the second class of solutions is associated with zero magnetic field above the conducting half-space (Price 1950) ie. the electric fields and currents associated with this class of solutions cannot be induced by an external source-field. This analysis will therefore consider solutions for **F** of only the first class. (Problems involving

geomagnetic induction by sources inside the conductor, such as ocean dynamos, must include the second class).

From equation 4.26 it follows that **F** will be of the form

$$\mathbf{F} = \left(\frac{\partial P}{\partial y} , \frac{-\partial P}{\partial x} , 0 \right) \qquad 4.28$$

where P is a scalar. Substitution in equation 4.23 yields

$$\left(\frac{\partial^2}{\partial x^2} + \frac{\partial^2}{\partial y^2} \right) P = -\lambda^2 P \qquad 4.29$$

for which solutions may be readily obtained. The solution for P and the value(s) for λ are related to the driving potential of the electromagnetic induction.

Using the solution for **F** the solution for **E** in the 1D conductor becomes

$$\mathbf{E} = Z\, e^{i\omega t} \left[\frac{\partial P}{\partial y}, \frac{-\partial P}{\partial x}, 0 \right] \qquad 4.30$$

From 4.1 and the exponential time dependence of **E**,

$$\mathbf{H} = \frac{-1}{i\omega\mu} \nabla \times \mathbf{E} \qquad 4.31$$

and substituting 4.30 into this equation and using 4.29 gives

$$\mathbf{H} = \frac{-1}{i\omega\mu} e^{i\omega t} \left[\frac{\partial Z}{\partial z} \frac{\partial P}{\partial x}, \frac{\partial Z}{\partial z} \frac{\partial P}{\partial y}, Z\, \lambda^2 P \right] \qquad 4.32$$

The MT impedance is defined as the ratio of the a horizontal electric field component to the orthogonal horizontal magnetic field component. In this section the two alternate forms of the impedance (Z and ζ) defined in chapter 1 will be used. The form involving the magnetic field strength is used so that the results included here match those of previous studies (eg. Price 1950). Thus

$$\zeta = \frac{E_X}{H_Y} = \frac{-E_Y}{H_X} \qquad 4.33$$

and from 4.31 and 4.32 the impedance is given by

$$\zeta = -i\omega\mu \frac{Z}{\left(\frac{\partial Z}{\partial z} \right)} \qquad 4.34$$

Equations 4.31, 4.32 and 4.34 form the general solutions for diffusive electromagnetic induction inside a layered half-space.

Solutions for electromagnetic induction in the insulator (atmosphere)

The solutions for the electromagnetic induction in the insulator overlying the half-space will now be obtained. In the insulator $\sigma = 0$ and from equation 4.7

$$\mathbf{J} = 0 \qquad 4.35$$

Thus

$$\nabla \times \mathbf{H} = \frac{\partial \mathbf{D}}{\partial t} \qquad 4.36$$

Now examining both sides of this equation, using a scaling method

$$\frac{\partial \mathbf{H}}{\partial t} = \frac{-\nabla \times \mathbf{E}}{\mu} \text{ and therefore } \mathbf{H} = O\left(\frac{T\,E}{\mu\,L}\right) \qquad 4.37$$

where L is a scale length related to the wavelength of the source-field. It follows that

$$\nabla \times \mathbf{H} = O\left(\frac{T\,E}{\mu\,L^2}\right) \qquad 4.38$$

and comparison with 4.9 indicates that

$$\nabla \times \mathbf{H} \sim 0 \qquad 4.39$$

for

$$T >> \sqrt{\varepsilon \mu}\ L \qquad 4.40$$

These results indicate that displacement currents may be neglected in the insulator if equation 4.40 is satisfied. Taking the maximum L as the diameter of the Earth, 4×10^7 m, and ε and μ equal to their absolute values gives $T >> 0.1$ s. At the periods used in SFMT sounding this criterion is satisfied and thus displacement currents may again be neglected in the atmosphere. This result means that equation 4.21 for **E** also applies in the insulator and **E** will be given by

$$\mathbf{E}^a = Z^a(z)\, e^{i\omega t}\, \mathbf{F}(x,y) \qquad 4.41$$

where the superscript "a" indicates a field in the insulator (atmosphere). From boundary condition 4.i it follows that **E** will have the same time dependence and horizontal vectorial form **F** in the insulator and in the conducting half-space.

Solutions of equation 4.29 which control **F** have the form

$$P = C_1 e^{+i\lambda \cdot r} + C_2 e^{-i\lambda \cdot r} \qquad 4.42$$

and

$$P = C_1 \sin(\lambda \cdot r) + C_2 \cos(\lambda \cdot r) \qquad 4.43$$

where $\lambda \cdot r = \lambda_x x + \lambda_y y$ and $\lambda_x^2 + \lambda_y^2 = |\lambda|^2$ and r is the horizontal position vector.

Solutions of the form 4.42 correspond to running waves in the source-field while solutions of the form 4.43 correspond to standing waves (Lilley 1975). Complicated waveforms can be expressed as integrals or sums over the wavenumber λ.

Through the continuity of F across the insulator / half-space interface the form of the source-field influences the geomagnetic induction. F (or P) and the wavenumber λ appear in the solution for E in the conductor and are thus involved in defining the electric and magnetic field components within the half-space. For example, from equation 4.32 it follows that a vertical component of the magnetic field will occur only for non-uniform source-fields ($\lambda \neq 0$).

The solutions for Z in the insulator will now be examined. Substituting $\sigma = 0$ into 4.24 the solution for Z becomes

$$Z^a = \alpha e^{-\lambda z} + \beta e^{+\lambda z} \qquad 4.44$$

and E is given by

$$\mathbf{E}^a = (\alpha e^{-\lambda z} + \beta e^{+\lambda z}) e^{i\omega t} \left[\frac{\partial P}{\partial y}, \frac{-\partial P}{\partial x}, 0\right] \qquad 4.45$$

Substituting equation 4.44 into the expression for H (equation 4.32) and simplifying leads to

$$\mathbf{H}^a = \frac{-1}{i\omega\mu} e^{i\omega t} \nabla \left(P \frac{\partial Z^i}{\partial z}\right) \qquad 4.46$$

ie.

$$\mathbf{H}^a = -\nabla \Omega \qquad 4.47$$

This form also follows directly from equation 4.39. The magnetic potential Ω may be expressed as a sum of parts due to the external (inducing) field and to the internal (induced field). Thus

$$\Omega = \frac{e^{i\omega t}}{i\omega\mu} P \frac{\partial Z^i}{\partial z} \qquad 4.48$$

$$= C_e e^{-\lambda z} + C_i e^{+\lambda z} \qquad 4.49$$

where

$$C_e = \frac{-\alpha\lambda e^{i\omega t}}{i\omega\mu} P \quad \text{and} \quad C_i = \frac{\beta\lambda e^{i\omega t}}{i\omega\mu} P \qquad 4.50$$

The potential $\Omega_e = C_e e^{-\lambda z}$ is the potential due to the external inducing field ($\rightarrow 0$ as $z \rightarrow \infty$) while $\Omega_i = C_i e^{+\lambda z}$ is the potential due to the induced, internal, currents ($\rightarrow 0$ as $z \rightarrow -\infty$).

The coefficient C_e (or alternatively α) is used to specify the source-field and is thus a given parameter for the theoretical geomagnetic induction problem. The value for C_i (or β) depends on the conductivity structure and is matched to C_e (α) through boundary conditions at the surface of the conductor.

Note that from equation 4.44 and equation 4.32 the ratio of internal to external horizontal magnetic field components is given by

$$S(\lambda) = \frac{H_h^i}{H_h^e} = \frac{-\beta}{\alpha} \qquad 4.51$$

while the ratio of internal to external vertical magnetic field components is the negative of this ratio

$$\frac{H_Z^i}{H_Z^e} = \frac{+\beta}{\alpha} \qquad 4.52$$

Solutions for induction in a uniform half-space

Analytical solutions for Z and thus for **E** and **H** exist for $\sigma(z) = c, cz^{-2}$ or $ce^{\gamma z}$ (where c and γ are constant) and for stacks of layers in which σ has one of these forms. Numerical solutions exist for more complex 1D electrical conductivity structures. The solutions for **E** and **H** in a half-space of uniform conductivity will be now be examined and then the solutions in a layered half-space.

For the uniform half-space

$\sigma = \sigma_0 \quad$ for $\quad z > 0$

and the solution to equation 4.24 becomes

$$Z = A e^{-\theta_0 z} + B e^{+\theta_0 z} \qquad 4.53$$

where

$$\theta_0 = \sqrt{\lambda^2 + i \omega \mu \sigma_0} \qquad 4.54$$

The solution for Z contains two arbitrary constants, A and B, the values of which are set by the boundary conditions at the top and the bottom of the layer. For electromagnetic induction in the uniform half-space $z > 0$ with the driving potential located in the region $z < 0$, the constant term B will equal zero, since the electromagnetic induction must decrease towards zero with increasing depth in the half-space. The constant term A is set by boundary conditions at the surface of the half-space such that the electromagnetic induction is matched to the external driving potential.

Therefore

$$Z = A e^{-\theta_0 z} \qquad 4.55$$

leading to

$$\mathbf{E} = A e^{-\theta_0 z} e^{i\omega t}\left[\frac{\partial P}{\partial y}, \frac{-\partial P}{\partial x}, 0\right] \qquad 4.56$$

$$\mathbf{H} = \frac{\theta}{i\omega\mu} A e^{-\theta_0 z} e^{i\omega t}\left[\frac{\partial P}{\partial x}, \frac{\partial P}{\partial y}, \frac{-\lambda^2}{\theta} P\right] \qquad 4.57$$

and

$$\zeta = \frac{i\omega\mu}{\theta_0} \qquad 4.58$$

Note that for zero wavenumber the impedance is given by

$$\zeta = \sqrt{\frac{i\omega\mu}{\sigma_0}} \qquad 4.59$$

The phase of the impedance is equal to the phase of **E** minus that of **B**. From appendix 3 and equation 4.59 (which is based on a positive time dependence) it follows that the phase lead of **E** relative to **B** is equal to $\pi/4$ radians or 45°.

From 4.56 and 4.57 it is evident that the attenuation of both the electric and magnetic fields with depth in the conductor is contolled by the factor $e^{-\theta_0 z}$. The depth at which the magnitudes of the fields are attenuated to 1/e their surface values is called the **skin depth** and is given (for zero wavenumber) by

$$\delta = \frac{1}{\mathrm{Re}(\theta_0)} = \sqrt{\frac{2}{\omega\mu\sigma_0}} \qquad 4.60$$

The skin depth is an important parameter in geomagnetic induction studies because it provides a rapid indication of the depth of resolution of the sounding method. Note that the factor $e^{-\theta_0 z}$ is a complex quantity, and there is thus a change in the phase of **E** and **H** with depth. At one skin-depth the phase of **E** and **H** relative to the corresponding surface fields is given by the phase of $\exp(-\delta\theta_o)$ ie. Im $(-\delta\theta_0)$ which equals -1 radian. The fields at one skin-depth lag behind the surface fields (see appendix 3).

The relationship of the internal magnetic and electric fields to the inducing magnetic field will now be examined. From boundary conditions 4.i and 4.ii it follows from 4.30 and 4.32 that both Z and $\partial Z / \partial z$ are continuous across the surface of the half-space. Taking the solutions for Z in the insulator and half-space, 4.44 and 4.53 (with B=0), give

$$\alpha + \beta = A \qquad 4.61$$

$$-\lambda\alpha + \lambda\beta = -\theta_0 A \qquad 4.62$$

Solving for β in terms of α gives

$$\beta = \alpha \left[\frac{\lambda - \theta_0}{\lambda + \theta_0} \right] \qquad 4.63$$

and for A

$$A = \alpha \left[\frac{2\lambda}{\lambda + \theta_0} \right] \qquad 4.64$$

Examination of equation 4.64 suggests that for uniform source-fields (with zero wavenumber) there can be no geomagnetic induction since A and hence E and H will be zero. This result is also physically realistic for the extreme case of perfectly uniform source-fields because the electric field at a particular depth will be identical at all horizontal points and there will be no electric potential to drive horizontal current flow. This situation is a well-known degeneracy in the 1D geomagnetic induction problem (eg. Price 1962). In practice source-fields will not be exactly uniform and the Earth will not be exactly 1D and current flow will occur. Price (1962) also argues that if the total field (induced plus inducing) has the property $\lambda = 0$ although $\lambda \neq 0$ for the separate induced and inducing fields then a determinate problem results.

One of the consequences of a uniform (or near-uniform) source-field is that from equation 4.63 α equals - β and from 4.51 the ratio of internal to external horizontal magnetic fields will equal one. Thus the horizontal magnetic field at the surface of the half-space is simply twice the inducing magnetic field. From 4.52 the ratio of internal to external vertical magnetic fields will equal minus one and there will be zero induced vertical magnetic field at the surface of the half-space. These results also apply for the case of a layered half-space treated next.

Solution for induction in a layered half-space

Analytical solutions for Z may be derived for a half-space consisting of a stack of layers, each of uniform conductivity. These solutions are recursive solutions in which the impedance at a particular depth is expressed in terms of the impedance of the underlying layer. The bottom layer in the stack is generally taken to be a half-space, for which the impedance is given by 4.58.

The solution for E in each layer will be given by 4.21, with continuity of tangential E causing F and the exponential time dependence to be continuous through the layers. Within each layer Z is given by

$$Z_n = A_n e^{-\theta_n z} + B_n e^{+\theta_n z} \qquad 4.65$$

with

$$\theta_n = \sqrt{\lambda^2 + i\omega\mu\sigma_n} \qquad 4.66$$

Note that z is now the depth within this particular layer only. The two constants for the solution of Z in each layer are set by boundary conditions which relate the induction in the particular layer to that in the overlying and underlaying layers. An additional boundary condition is required at the base of the lowest layer and at the top of the top layer. The passage of information through the boundary conditions at interfaces provides the physical mechanism for induction at depth to depend upon the source-field and for induction near the surface to depend on the conductivity structure at depth.

The recursive equations may be based upon the impedance (for example Patra & Mallick 1980) or, as derived here, on the parameter G defined by Schmucker (1970). G is defined for the i th layer as

$$G_i(z) = \frac{A_i e^{-\theta_i z} - B_i e^{+\theta_i z}}{A_i e^{-\theta_i z} + B_i e^{+\theta_i z}} = \frac{-\left(\frac{\partial Z_i}{\partial z}\right)}{Z_i \theta_i} \qquad 4.67$$

From continuity of tangential **E** and tangential **H** across boundaries it follows that across the boundary of the i th and $i+1$ th layers at z

$$G_i(z)\,\theta_i(z) = G_{i+1}(z)\,\theta_{i+1}(z) \qquad 4.68$$

Note that from 4.34 the impedance must also be continuous across horizontal boundaries.

With manipulation equation 4.67 can be written in the form

$$G_i(z) = \tanh\left(-\theta_i z + \frac{1}{2}\ln\left(\frac{A_i}{B_i}\right)\right) \qquad 4.69$$

For two depths z_1 and z_2 within the layer i the relationship between G at the two depths becomes

$$G_i(z_1) = \tanh\left\{\theta_i(z_2 - z_1) + \tanh^{-1}[G_i(z_2)]\right\}$$

$$= \frac{G_i(z_2) + \tanh[\theta_i(z_2 - z_1)]}{1 + \tanh[\theta_i(z_2 - z_1)]\,G_i(z_2)} \qquad 4.70$$

Letting z_1 and z_2 be the depths at the top and bottom of the ith layer (Figure 4.1) and h_i being the thickness of this layer, from 4.68 and 4.70

$$G_i = \frac{G_{i+1}\theta_{i+1} + \theta_i \tanh(\theta_i h_i)}{\theta_i + G_{i+1}\theta_{i+1}\tanh(\theta_i h_i)} \qquad 4.71$$

Note that where G is written without "(z)" it refers to the value at the top of the particular layer. Equation 4.71 relates G at the top of any layer in the half-space to G at the top of

the underlying layer. For depths within a layer equation G(z) is given by 4.70. For the bottom half-space (*n* th layer) $B_n = 0$ and from 4.67

$$G_n = 1 \qquad 4.72$$

Using equation 4.70 one may thus express G at the surface by the recursive formula

$$G_1 = \tanh \{ \theta_1 h_1 + \tanh^{-1} [\frac{\theta_2}{\theta_1} \tanh (\theta_2 h_2 + \tanh^{-1} .. $$

$$.. \frac{\theta_{n-1}}{\theta_{n-2}} \tanh (\theta_{n-1} h_{n-1} + \tanh^{-1} [\frac{\theta_n}{\theta_{n-1}}])...)]\} \qquad 4.73$$

From 4.34 and 4.67 the impedance at any depth can be calculated using

$$\zeta(z) = \frac{i \omega \mu}{\theta (z) G (z)} \qquad 4.74$$

The alternative recursive relationship to 4.73 in terms of the impedance is

$$Z = \frac{i \omega \mu}{\theta_1} \coth (\theta_1 h_1 + \coth^{-1} (\frac{\theta_1}{\theta_2} \coth (\theta_2 h_2 + ... \coth (\theta_{n-1} h_{n-1} + \coth^{-1} (\frac{\theta_{n-1}}{\theta_n}))...)))$$

(eg. Patra & Mallick 1980). The impedance thus depends upon the conductivity $\sigma(z)$, the wavenumber λ and the frequency ω. It should be noted that the impedance depends upon only the underlying conductivity structure and is independent of the conductivity in the overlying layers. This result is of great importance for seafloor MT measurements. It means that for a 1D conductivity structure one can use seafloor measurements of E and B to derive the impedance and hence underlying conductivity structure without any need to correct for the presence of the overlying ocean.

Final solutions for E and H in the conductor

The final solutions for E and H in the conductor will be defined in two steps, firstly the relationship of E and H at the surface to the inducing field will be defined and secondly the relationship of E and H at depth to the fields at the surface.

From continuity of tangential E and H and thus of Z and $\partial Z / \partial z$

$$\frac{Z^{i}_{z=0}}{\left(\frac{\partial Z^{i}}{\partial z}\right)_{z=0}} = \frac{Z_{z=0}}{\left(\frac{\partial Z}{\partial z}\right)_{z=0}}$$

and therefore

$$\frac{\alpha + \beta}{-\lambda\alpha + \lambda\beta} = \frac{-1}{G_1 \theta_1} \qquad 4.75$$

(from equations 4.44 and 4.67) The ratio of internal to external magnetic potential is found by solving for β giving

$$\beta = \alpha\left(\frac{\lambda - \theta_1 G_1}{\lambda + \theta_1 G_1}\right) \qquad 4.76$$

and the ratio of the internal to the external horizontal magnetic field components is given by $-\beta / \alpha$.

Given a specified inducing magnetic potential Ω_e (ie. specified α, P and λ) and a layered conductivity structure $\sigma(z)$ it is now possible to calculate G_1, θ_1 and thence caclulate the potential Ω_i due to the induced currents. The magnetic and electric fields in the insulator are given by 4.45 and 4.46 respectively. Since the horizontal magnetic field is continuous across the surface of the half-space, the field at the surface can be calculated from equation 4.46, the expression for the magnetic field in the insulating atmosphere. This field has contributions from both the external and internal sources. Using the surface impedance from equation 4.74 the surface electric field may be calculated. All that remains to fully solve the geomagnetic induction problem, is to calculate the magnetic and electric fields at depth in the conductor.

The values for **E** and **H** at depth will be derived from a recursive relationship giving the scalar function Z with depth. This allows **E** and **H** to be expressed as a ratio of their surface values. Using 4.67 the ratio of Z at two depths within one layer simplifies to

$$\frac{Z_i(z_2)}{Z_i(z_1)} = \cosh\left[\theta_i (z_2 - z_1)\right] - G_i \sinh\left[\theta_i (z_2 - z_1)\right] \qquad 4.77$$

Choosing z_1 to be the surface of layer i , z_2 to be the base, and using the condition of Z continuous across a horizontal boundary one obtains

$$\frac{Z_{i+1}}{Z_i} = \cosh(\theta_i h_i) - G_i \sinh(\theta_i h_i) \qquad 4.78$$

expressing the ratio of Z at the surface of a layer to Z at the surface of the overlying layer. (Note that in equation 4.78 Z written without "(z)" refers to the value at the surface of the particular layer.) One can then recursively find Z at the surface of any layer in terms of Z at the surface using

$$\frac{Z_n}{Z_1} = \frac{Z_n}{Z_{n-1}} \frac{Z_{n-1}}{Z_{n-2}} \cdots \qquad \cdots \frac{Z_2}{Z_1} \qquad 4.79$$

calculating each term on the right hand side using equation 4.78. Equation 4.77 may be used to calculate the ratio of Z (z) within any layer to its value at the surface of the layer. Now defining the surface values of **E** to be $\mathbf{E}_0$ and H to be $\mathbf{H}_0$ from 4.30 one obtains

$$\frac{\mathbf{E}(z)}{\mathbf{E}_0} = \frac{Z(z)}{Z_1} \qquad 4.80$$

and using 4.74 the horizontal magnetic field components $\mathbf{B}_h$ as a function of depth are given by

$$\frac{\mathbf{B}_H(z)}{\mathbf{B}_{H0}} = \frac{\theta(z)\, G(z)}{\theta_1\, G_1} \frac{Z(z)}{Z_1} \qquad 4.81$$

From equation 4.35 it can be seen that the vertical magnetic field component has the same dependence on Z as the horizontal electric field components and therefore

$$\frac{\mathbf{H}_Z(z)}{\mathbf{H}_{Z0}} = \frac{Z(z)}{Z_1} \qquad 4.82$$

Equations 4.80-82 give the value for all components of **E** and **H** within the conducting half-space. In association with the results for **E** and **H** at the surface and in the insulator, they complete the solutions of the problem of electromagnetic induction in a layered half-space with external source-field.

Physical Interpretation of Parameters

The physical meaning of some of the parameters involved in the electromagnetic induction will now be examined.

θ The parameter θ has dimensions of length^{-1} and each layer in the 1D conductivity structure has a particular value of θ. From equation 4.60 it may be seen that the inverse of the real part of θ_i is equal to, the skin-depth in a half-space with the same conductivity as layer i. The parameter θ is thus a measure of the attenuation scale within each layer.

G The parameter G is a dimensionless quantity which varies smoothly within each layer but is discontinuous between layers of different conductivity. G acts as a correction factor such that the product G(z)θ(z) in each layer is equivalent to the value of θ associated with a uniform half-space of the same conductivity as the layer. Within a uniform half-space G equals one. Comparison of the equations such as 4.58 and 4.74 or 4.63 and 4.76 illustrates how G acts as a correction factor.

λ The parameter λ is the wavenumber of the inducing magnetic field. For much of the

analyis in this thesis λ is assumed to be zero. The validity of this assumption may be examined by comparing the magnitude of λ^2 with that of $\omega\mu\sigma$ since λ^2 generally appears as a correction factor for this term, eg. in the definition of θ (equation 4.66).

For a 10 h period, typical observed apparent resistivities are of the order 10^1 to 10^2 Ω.m (eg. Filloux 1977, Tammemagi & Lilley 1971, Hermance & Pedersen 1980) and 10^3 Ω.m is therefore a realistic large estimate. An intentionally low estimate for $\omega\mu\sigma$ at this period is thus $\omega\mu\sigma = 2.19 \times 10^{-13}$ m^{-2} and in order that $\lambda^2 < 5$ % $\omega\mu\sigma$, the source-field must have a wavelength of greater than 6000 km. For mid-geomagnetic latitudes it is believed that source-fields have wavelengths of order 5000 km (eg. Chave et al. 1981) and therefore the assumption that λ equals zero, is probably justified at 10 h period.

The effect of finite source-field wavelength is examined more formally in Figure 4.2 In this figure the seafloor impedance is calculated above a moderately resistive conductivity profile for a varying source-field wavelength. The conductivity profile is based on an compilation of experimental conductivity results from seafloor studies. The figure shows source-field effects are strongest at long periods where $\omega\mu\sigma$ becomes small. However for periods shorter than 30 h and source-field wavelengths longer than 3000 km the wavenumber has only minor effect on the impedance. In section 4.3 source-field effects are assessed for the Tasman Project recording region.

Attenuation and penetration scale lengths for geomagnetic induction.

For a uniform half-space the attenuation of electric and magnetic fields with depth follows a simple exponentially decreasing form (equations 4.56 and 4.57) and the skin depth may be used to define a length scale over which geomagnetic induction is occurring. In a layered half-space the attenuation with depth will be a more complex function. As indicated by the differences between equations 4.81 and 4.82, the attenuation of the electric and magnetic fields will occur at different rates.

Figure 4.3 shows the attenuation for a 1D conductivity profile. The profile is intended to represent a typical oceanic profile and has been constructed from experimental determinations of conductivity. For depths of greater than 45 km the model is based on SFMT results for 32 my old lithosphere (Filloux 1980c) and for crustal depths the profile is a slightly modified form of results from controlled source soundings (Cox et al. 1986). The top layers of the model consist of an ocean of depth 5 km and conductivity 4.0 S.m^{-1} and 3 km of sediments of conductivity 1.0 S.m^{-1} (Larsen 1968).

The attenuation is a smooth function of depth for both E and H, and at a particular depth the attenuation is a smooth function of frequency. Examination of the results shows that the magnetic field is more strongly attenuated (in terms of amplitude and phase change)

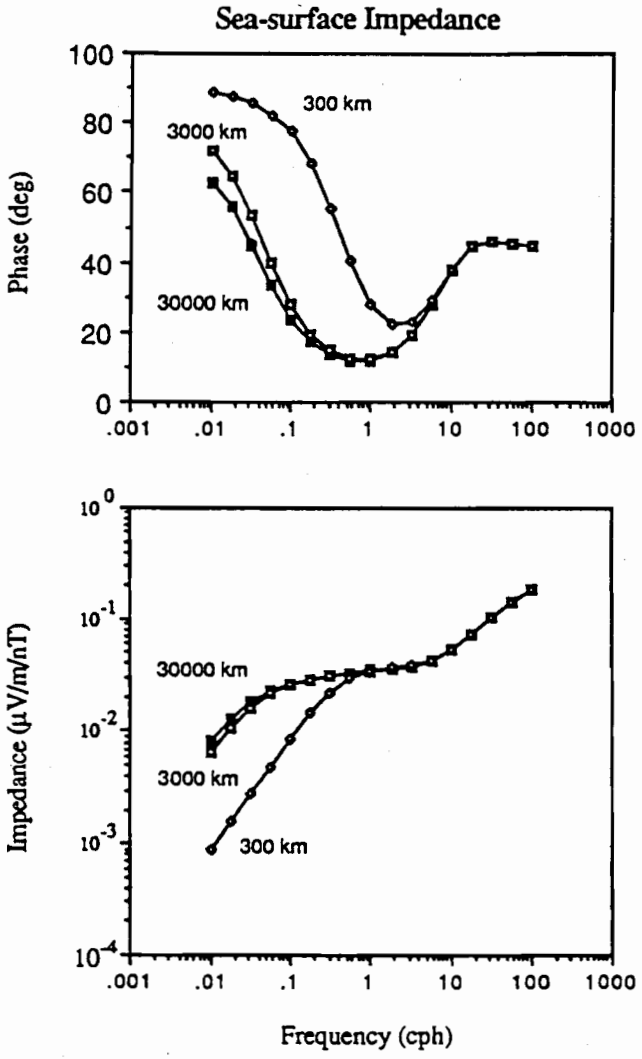

Figure 4.2 Examination of the influence of finite length source-fields on MT impedances. The sea-surface impedance was calculated over a synthetic 1D conductivity model (shown in Figure 4.3). The model includes relatively low values for the crustal conductivity which will tend to increase the influence of finite source-field wavelengths. For periods below 30 h and wavelengths above 3000 km the finite length of source-fields has a negligible effect on the sea-surface impedance.

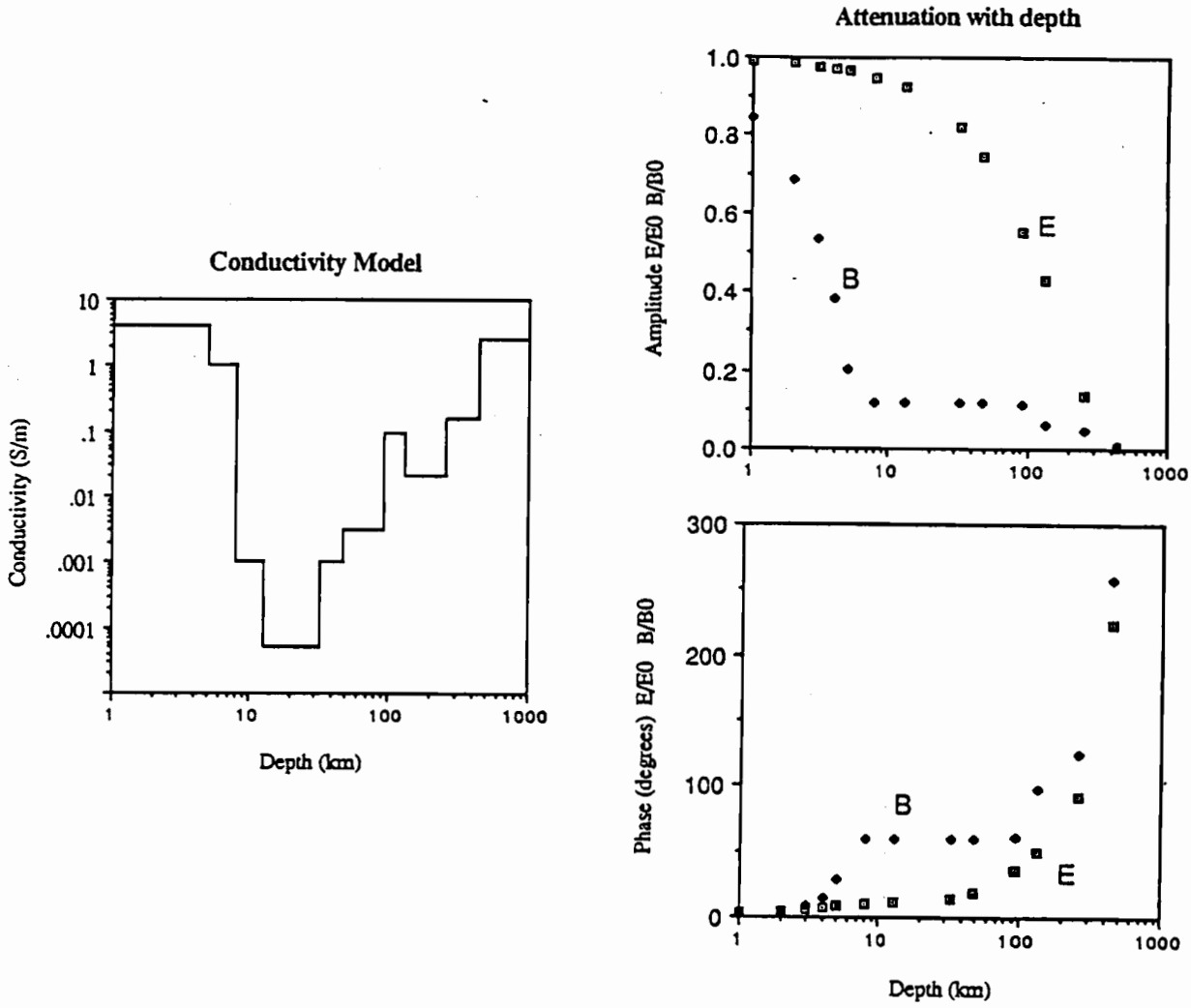

(a) (b)

Figure 4.3: Illustration of the attenuation of magnetic and electric fields for the conductivity profile shown in (a). The attenuation is plotted versus depth in the Earth (b) and versus frequency at the 5 km deep seafloor (c). The attenuation is calculated for a wavenumber of zero ie. a uniform source-field. Note that the attenuation is a smooth function of both depth and frequency despite the order-of-magnitude variations in the electrical conductivity profile. Figure 4.3c shows the attenuation which would occur at 5 km depth in a half-space of equivalent conductivity to the ocean. The presence of the resistive Earth beneath the ocean increases magnetic attenuation and decreases electric attenuation through the ocean.

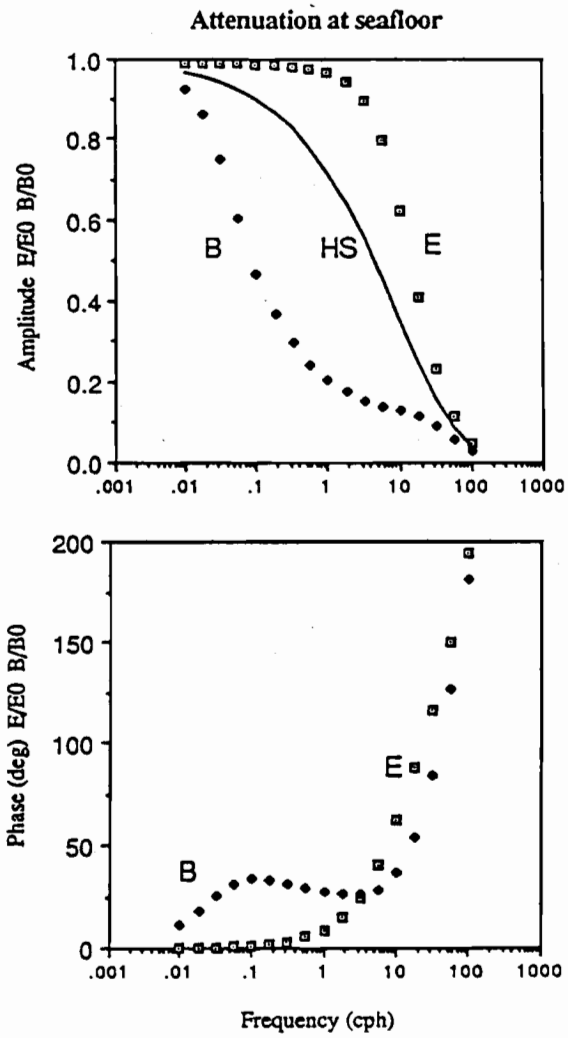
Attenuation at seafloor
Amplitude E/E0 B/B0
1.0
0.8
0.6
0.4
0.2
0.0
B
HS
E
.001
.01
.1
1
10
100
1000
Phase (deg) E/E0 B/B0
200
150
100
50
0
E
B
Frequency (cph)

Figure 4.3c

within the good conducting layers ($\sigma \geq 10^{-1}$ S.m^{-1}) but almost unattenuated through the resistive ($\sigma \leq 10^{-2}$ S.m^{-1}) layers. The electric field is preferentially attenuated in resistive layers. At the period of 1 h most of the attenuation of the magnetic field occurs in the ocean and at depths of greater than 100 km. The electric field shows little attenuation through the ocean and then a smooth attenuation with depth.

Note that for periods longer than 1 h the ocean may be reasonably approximated as a thin sheet ie. the horizontal electric field is invariant in the vertical direction . At these periods there is less than 5% amplitude attenuation or 10° phase change in the electric field through the ocean. This is an important result which will be used later in this thesis.

The presence of the resistive crust beneath the ocean tends to increase the magnetic attenuation and decrease the electric attenuation through the ocean compared with the attenuation when the ocean is underlain by a half-space of ocean conductivity. The resistive crust forces more of the telluric current to flow in the ocean. As the resistance of the crust increases, the magnetic field is attenuated more strongly while the electric field is attenuated less and the ocean more closely resembles a thin sheet.

Because of the different rates of attenuation of electric and magnetic fields with depth it is not possible to define a single skin depth for both the electric and magnetic fields. Although it is possible to define a skin depth based on either of the fields, the uneven attenuation rate with depth means such a definition does not provide an entirely satisfactory estimate for the depth scale of geomagnetic induction. Table 4.1 shows skin depths based on magnetic field values for the model of Figure 4.3.

Between the close frequencies of 0.1 cph and 0.178 cph the skin depth varies by 290 km, an effect resulting from the negligible magnetic attenuation in the crust and upper mantle. Despite the large differences in skin depths the attenuation will be very similar for the two frequencies. Within the poorly conducting part of the mantle the attenuation at 0.1 cph will be slightly less than 1/e and at 0.178 cph the attenuation will be sligthly larger than 1/e.

Alternative scale depths for geomagnetic induction in a layered half-space may be derived from two transformations of the MT impedance response function. The apparent resistivity is defined

$$\rho_a = \frac{|\zeta|^2}{\mu\,\omega} = \frac{\mu\,|Z|^2}{\omega} \qquad 4.83$$

The apparent conductivity σ_a is defined as the inverse of ρ_a. Substitution into 4.83, of the expression for the impedance over a uniform half-space with zero wavenumber (4.59), leads to

$$\rho_a = \frac{1}{\sigma_0}$$

Table 4.1 Skin Depth as a Function of Frequency

Frequency (cph)	Period (h)	Skin Depth (km)
0.0100	100.0	598.1
0.0178	56.2	544.9
0.0316	31.6	499.4
0.0562	17.8	459.6
0.100	10.0	296.7
0.178	5.62	6.94
0.316	3.16	4.74
0.562	1.78	4.33
1.00	1.00	4.08
1.78	0.562	3.92
3.16	0.316	3.80
5.62	0.178	3.72
10.0	0.100	3.64

The skin depths are calculated for the 1D conductivity profile shown in Figure 4.3 and are based on the depth at which the magnetic field amplitude is attenuated to 1/e of its surface value. For frequencies greater than 1.0 cph the skin depth is less than the depth of the ocean (5 km). Note the large change in skin depths between the close frequencies of 0.100 and 0.178. This effect is caused by the slow increase in magnetic field attenuation over the resistive parts of the conductivity structure.

ie. the apparent resistivity of a half-space is equal to the actual resistivity. For a layered half-space, using 4.74 one obtains

$$\rho_a = \frac{\omega \mu}{\left|\theta_1 G_1\right|^2} \qquad 4.84$$

For a layered half-space, at a particular frequency, the apparent resistivity represents the resistivity of a uniform half-space possessing the identical response. A measure of the depth of penetration of induction into a layered half-space may be obtained by substituting the apparent conductivity (from equation 4.84) into the equation for the skin depth in a uniform half-space (4.60). This substitution yields

$$\delta_a^i = \frac{\sqrt{2}}{\left|\theta_1 G_1\right|} \qquad 4.85$$

as a possible induction scale length in a layered conductor. Superscript i denotes the estimate as the first possible estimate.

A second common transformation of the MT impedance response function is into the parameter "c" defined by Weidelt (eg. Weidelt 1972),

$$c = \frac{\zeta}{i \mu \omega} = \frac{Z}{i \omega} \qquad 4.86$$

Substitution of equation 4.74 into 4.86 indicates that c for a layered half-space is given by

$$c = \frac{1}{\theta_1 G_1} \qquad 4.87$$

Schmucker (1973) suggests using

$$\delta_a^{ii} = \left|c\right| = \frac{1}{\left|\theta_1 G_1\right|} \qquad 4.88$$

as a measure of the depth of penetration of geomagnetic induction into the layered half-space - clearly this scale length only differs from that derived from the apparent resistivity by a factor $\sqrt{2}$. Other publications suggest using Re (c) as the scale length (eg. Larsen 1975) however as indicated by Schmucker & Jankowsky (1972) Re (c) gives the weighted mean depth of the current distribution. It is thus an inappropriate measure of the overall penetration depth of the geomagnetic induction.

4.1.2 Outline of two-dimensional geomagnetic induction theory

This thesis will contain only a brief outline of the extension of the geomagnetic induction theory to a 2D electrical conductivity structure. Although several basic results from 2D theory will be applied to the Tasman Project data, this thesis will contain only a minor amount of 2D interpretation.

The theory for 2D electrical conductivity structures is again based on Maxwell's equations, the constitutive equations and the standard electromagnetic boundary conditions given above. The case is considered where there is possible lateral variation in conductivity in the y-direction (Figure 4.4) ie. $\sigma = \sigma(y, z)$. The additional assumption of the source-field being uniform will be made here. With 2D structures separate solutions exist for the case of the magnetic field parallel to the strike of the conductivity structure , **B-polarization** (or B-pol) and for the case of the elecric field parallel to the strike of the structure, **E-polarization** (E-pol). The impedance component takes the symbol of the corresponding electric field direction. Note that the E-pol and B-pol cases are sometimes called the transverse electric (TE) and transverse magnetic (TM) modes respectively (Berdichevsky & Zhdanov 1984 p80, 83).

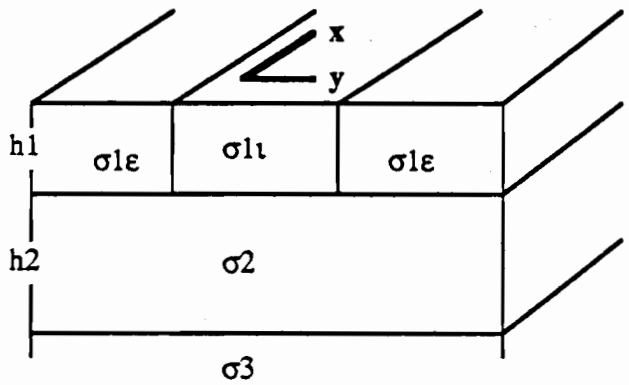

Figure 4.4 Two-dimensional conductivity model with $\sigma = \sigma(y, z)$. The model shown has a surface anomaly of conductivity $\sigma 1\iota$ in a surrounding layer of conductivity $\sigma 1\varepsilon$. It is underlain by a layer of conductivity $\sigma 2$ and a half-space of conductivity $\sigma 3$. Berdichevsky & Dmitriev (1977a,b) use this model, with $\sigma 3 = \infty$, for investigating the distortion of impedance curve caused by the surface anomaly.

Patra & Mallick (1980) show that geomagnetic induction in a 2D conductivity structure is again controlled by a diffusion equation

$$\frac{\partial^2 K}{\partial y^2} + \frac{\partial^2 K}{\partial z^2} - \lambda^2 K = 0 \qquad 4.89$$

where $\lambda^2 = i \omega \mu \sigma(y,z)$ as above. For the B-pol case B_X is obtained by replacing K in equation 4.89 and

$$\mathbf{B} = (B_X, 0, 0) \quad \mathbf{E} = (0, E_Y, E_Z) \quad H_X = H_X(y, z) \qquad 4.90$$

The electric field components are related to B_X by

$$\frac{\partial B_X}{\partial y} = -\mu \sigma(y,x) E_z \qquad \frac{\partial B_X}{\partial z} = -\mu \sigma(y,x) E_y \qquad 4.91$$

For the E-pol case E_X is obtained by replacing K in 4.89 and

$$\mathbf{B} = B(0, B_Y, B_Z) \quad \mathbf{E} = E(E_X, 0, 0) \quad E_X = E_X(y, z) \qquad 4.92$$

and the magnetic field components are related to E_X by

$$\frac{\partial E_X}{\partial y} = i \omega B_Z \qquad \frac{\partial E_X}{\partial z} = i \omega B_Y \qquad 4.93$$

In general solutions to 4.89 are difficult to obtain analytically and the equation is solved numerically by one of several methods (eg. Berdichevsky & Zhdanov 1984).

It is instructive to examine the physical basis of 2D electromagnetic induction. Berdichevsky & Dmitriev (1976a,b) and Berdichevsky & Zhdanov (1984) consider the geomagnetic induction associated with a surficial 2D anomaly and such a model will be briefly considered here. The model (Figure 4.4) consists of an inhomogeneous surface layer underlain by a resistive layer which is itself underlain by a highly conductive half-space. Some of the results from this model can be used to study the geomagnetic induction occuring at a 2D coastline however care must be taken because of the high integrated conductance of the ocean.

For the B-pol case electric current flow is across the anomalous surface layer and causes a build up of charge at its boundaries. Although the current associated with this charge build-up is negligible, the electrostatic field caused by the charges is significant and produces an anomalous electric field in the region of the boundaries (eg. Jones 1983). There is no anomaly in the magnetic field. The anomaly is termed a **galvanic anomaly** and is present at all inducing frequencies (Berdichevsky & Zhdanov 1984).

The strength of the galvanic anomaly will depend upon the factor τ where

$$\tau = \sqrt{\frac{\sigma_2}{h_1 h_2 \sigma_1^e}} \qquad 4.94$$

and h_1 and h_2 are thicknesses of the surface and resistive layers and σ_1 and σ_2 are their conductivities away from the anomaly (Berdichevsky & Dmitriev 1976a,b). At large values of τ the anomaly will be smaller, as compensation for the anomalous surface layer occurs in a more conductive intermediate layer and/or in a more shallow third layer. In the case of a coastline, the effect of the charge build-up is to drive the electric currents downwards (partially through the seafloor) as one moves from the ocean to the land (Figure 4.5). This effect is indicated by the presence of a vertical electric field component in equation 4.90.

For the E-pol case no excess charges build up on boundaries however an anomaly is created by an excess of electric current flowing through the conductive anomaly. The anomaly consists of an anomalous electric field E_X^A and an anomalous magnetic field B_Y^A and B_Z^A induced by the excess current. Such an anomaly is termed an **inductive-galvanic** type (Berdichevsky & Zhdanov 1984). The strength of the anomaly will decrease with decreasing frequency as more of the current flows in the highly conducting third layer. The anomalous magnetic field associated with an E-pol anomaly at a coastline constitutes the geomagnetic coast effect (Figure 4.6).

A significant difference between the B-pol and E-pol anomalies is that the B-pol anomaly depends upon a much more local conductivity structure. The galvanic B-pol anomaly depends only upon S1 (the integrated conductance of the upper layer) at the observation site while the inductive-galvanic E-pol anomaly depends on the mean value of S1 over a large vicinity of the observation site (Berdichevsky & Zhdanov 1984).

It may be shown (eg. Berdichevsky & Zhdanov 1984) that for measurement axes parallel and perpendicular to a 2D anomaly for both the E-pol and B-pol modes the horizontal electric field components (as a function of frequency) are linearly related to the orthogonal magnetic field components. Such a linear relationship is important because it means that the electric and magnetic fields will be related by a MT impedance function. For uniform source-fields the impedance function will depend only upon the electrical conductivity structure. Because of the differences between B-pol and E-pol solutions the impedance functions for the two orthogonal horizontal directions will generally differ in magnitude and phase.

Berdichevsky & Dmitriev (1976a,b) examine the impedance versus frequency response for the simple 2D structure of Figure 4.4. In their analysis the inhomogeneity is considered to be a small anomaly which distorts the normal (surrounding 1D) conductivity profile. For the normal profile the impedance curve may be asymptotically divided into two branches most easily seen after transformation of the response function into the equivalent apparent resistivity (Figure 4.7). The ascending branch, called the S1 line, is caused by the influence of the second, insulating, layer and is well defined by the formula

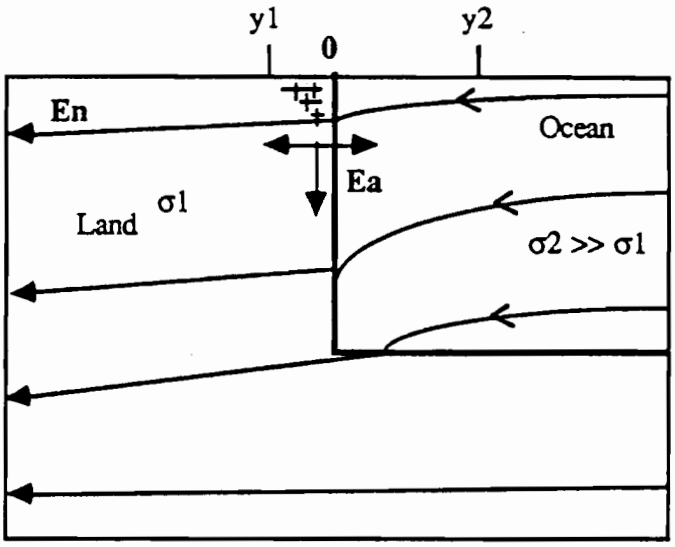

Figure 4.5 B-pol anomaly at a coastline. Electric charge builds up on the vertical boundary and produces an anomalous electric field Ea (including a vertical component). The electric currents are driven downwards and partially into the seafloor as they approach the coastline. Inside the anomalous region $y1 < y < y2$ a 1D interpretation of the impedance E_Y/B_X will not yield the correct conductivity of either the land or the ocean. The size of y2 will depend on the resistivity of the oceanic crust (see text).

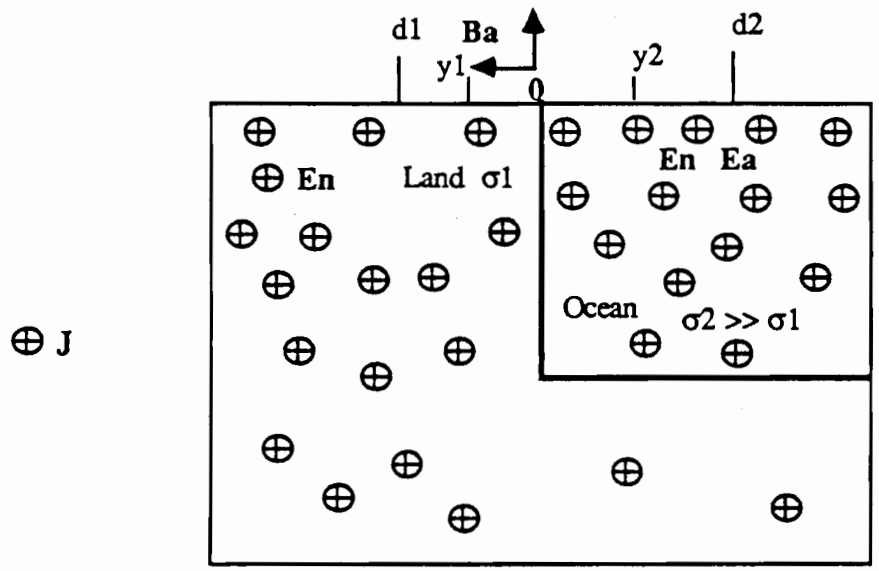

Figure 4.6 E-pol anomaly at a coastline: the geomagnetic coast effect. Excess electric currents flow in the conducting ocean relative to the more poorly conducting land. These currents induce an anomalous magnetic field near the coast. The anomalous magnetic field possesses both a vertical and horizontal component near the coast $y1<y<y2$ but the horizontal component decreases rapidly away from the coast leaving the vertical anomaly extending over a much larger distance $d1<y<d2$. Outside the range $y1<y<y2$ 1D inversion of the impedance E_X/B_Y will yield the correct conductivity over both the land and ocean. Note that the ocean attenuates the geomagnetic activity with depth more rapidly than the poorly conducting land.

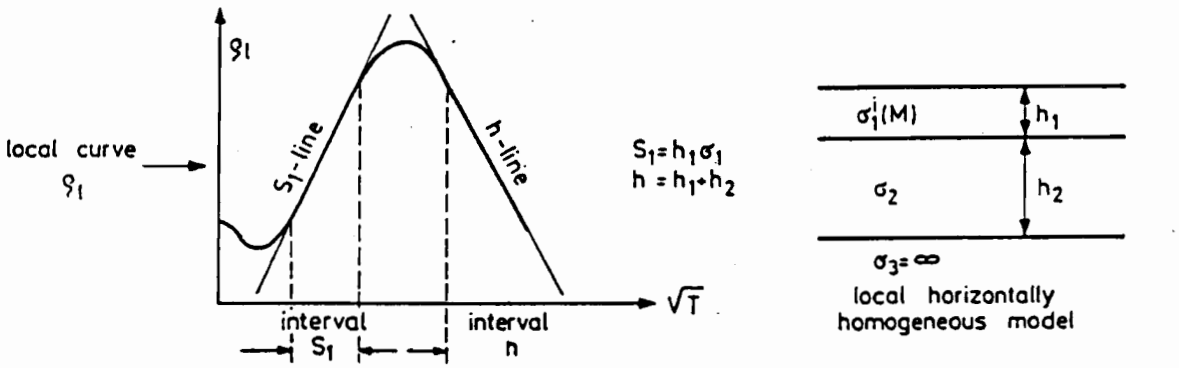

Figure 4.7: The apparent resistivity curve for a 1D conductivity model consisting of a surface conductor, an intermediate resistor and a deep conductor. The curve shows two main branches, an ascending "S-line" at short periods and a descending "h-line" at longer periods. The conductance of the surface layer and the depth to the lower conducting layer may be calculated from the slopes of the two branches (figure taken from Berdichevsky & Dmitriev 1976b).

$$Z(\omega) \cong \frac{1}{S_1} \qquad 4.95a$$

In terms of the apparent resistivity S is given by

$$S_1 \cong 357 \sqrt{\frac{T}{\rho_a}} \qquad 4.95b$$

(Jiracek 1984). The descending branch of the apparent resistivity curves, called the h-line, is caused by the influence of the conducting base, and is approximated by

$$Z(\omega) \cong -i\omega\mu h \qquad 4.96a$$

or

$$h \cong 357 \sqrt{T \rho_a} \qquad 4.96b$$

(Jiracek 1984) where h is the total depth to the conducting basement ($h_1 + h_2$). Many analyses of recorded MT data by USSR scientists are based on the asymptotic method of defining S1 and h from apparent resistivity curves (eg. Kovtun & Chicherina 1976). Modern asymptotic methods also allow for a finite conductivity for the underlying mantle layer (Trofimov 1973).

For the B-pol case the surface impedance at a point in the anomaly will give an impedance versus frequency curve with an undistorted value for S1 ie. the value for S1 for outside the anomaly. The h-line will however be distorted (called the S-effect) and the asymptotic approach will yield an incorrect estimate for the depth to the conducting base. For the E-pol case the surface impedance in the anomaly will include a distorted value for S1 ie. not the value for S1 outside the anomaly. The value determined for S1 will correspond to an averaged value for the conductivity of the upper layer with the width of averaging depending on the frequency. For the E-pol case the impedance will return the correct form of the h-line (Berdichevsky & Dmitriev 1976a,b).

Extending these results for the corresponding case of impedance measured at the ocean-surface near a coastline it is evident that the B-pol impedance will not lead to a correct estimate for either the conductance of the ocean or of the deep conductivity beneath the seafloor. The S-line will be biased towards the conductivity of the adjacent continent while the S-effect will severely distort the h-line. The magnitude of the factor τ will control the extent of the distortion and the horizontal extent of the anomaly from the coastline. The E-pol impedance near a coastline will return a distorted value for the S-line. The h-line however should be undistorted and its interpretation using asymptotic methods should lead to the correct depth to the conducting base or in an appropriate full inversion it should yield the correct deep electrical conductvity structure.

For SFMT measurements one considers frequencies with skin depths of order, or greater than, the depths of the oceans. At these frequencies for the B-pol case there will be transverse electric current flow at (and into) the seafloor and, at the seafloor, an anomalous electric field perpendicular to the coastline. This anomalous field will again cause B-pol impedances to be distorted from the impedances for the 1D oceanic structure. The E-pol seafloor impedances will be distorted for higher frequencies, corresponding to shallow depths, but will be appropriate for the true 1D structure at periods corresponding to the h-line.

The observed vertical magnetic field at 2D conductivity structures can be used to provide information on the conductivity. It may be shown (eg. Berdichevsky & Zhdanov 1984) that for a 2D conductivity anomaly and a uniform source-field, the induced vertical magnetic field (as a function of frequency) is linearly related to the magnetic field component perpendicular to the anomaly. The linear relationship, often expressed in terms of induction arrows, is dependent upon only the frequency and the 2D conductivity structure.

4.1.3 The magnetotelluric sounding method

The horizontal electric field measured at the Earth's surface is a direct measure of the electric currents induced by the fluctuations in the external magnetic field. The horizontal magnetic field measured at the surface contains a component of both the inducing fluctuations and a secondary magnetic field associated with the induced telluric currents. These results were derived above for the case of a theoretical 1D flat Earth but also apply for a heterogeneous, spherical Earth. The ratio of orthogonal horizontal magnetic and electric field fluctuations is called the MT impedance and as a function of frequency contains information for the electrical conductivity structure of a site. This principle forms the basis of MT sounding.

The theory for MT sounding was first descibed by Tikhonov (1950) and Cagniard (1953). These authors showed that at the surface of a layered medium the induced electric field (in the frequency domain) is proportional to the orthogonal component of the inducing magnetic field. These studies allowed the development of MT prospecting. Wait (1954) showed that the method required considerable uniformity of the inducing source-fields while Price (1962) developed the theory for induction by non-uniform source-fields in a layered medium. Other important steps in the development of the method included the extension of the MT method to a spherical Earth (Srivastava 1966) and the extension of the theory to 2D conductivity structures (d'Erceville & Kunetz 1962).

MT sounding involves three basic steps; measurement of temporal fluctuations of the magnetic and electric field components, reduction and analysis of these measurements to form a response function, and inversion of the response function to give the underlying conductivity structure. Useful results are generally obtained only in regions of 1D or 2D conductivity structures. MT measurements usually include measurement of the two horizontal and the two horizontal electric components (although only one set of orthogonal measurements is required in a region with a 1D conductivity structure). Studies frequently involve soundings at a number of sites, arranged in linear or 2D arrays, and often the soundings at the different sites are made simultaneously.

The MT Impedance Tensor

Electromagnetic response functions parameterize the response of the Earth to the inducing magnetic field and are generally chosen such that they are independent of the source-field. The simplest response function for MT studies is the MT impedance, the ratio (as a function of frequency) of a component of the electric field to the orthogonal component of the magnetic field. The presence of the magnetic field in the denominator of this ratio standardizes the results to be independent of the source-field magnitude. Alternative forms for the MT response function, such as the apparent resistivity, and

methods for calculating unbiased response functions from measured data are discussed in more detail below.

When a MT measurement includes two components of both the horizontal magnetic and electric fields the MT response can be expressed as a tensor. The MT impedance tensor, **Z**, is defined in vector notation

$$\mathbf{E} = \mathbf{Z}\,\mathbf{B} \qquad 4.97$$

For E and B expressed in terms of geomagnetic north and east co-ordinates (Figure 4.1) this vector equation becomes

$$E_X = Z_{XX}B_X + Z_{XY}B_Y \qquad 4.98a$$

$$E_Y = Z_{XY}B_X + Z_{YY}B_Y \qquad 4.98b$$

and

$$\mathbf{Z} = \begin{bmatrix} Z_{XX} & Z_{XY} \\ Z_{YX} & Z_{YY} \end{bmatrix} \qquad 4.99$$

As shown above for MT sounding over a 1D structure, $Z_{XY} = -Z_{YX}$, $Z_{XX} = -Z_{YY} = 0$ and **Z** will have the form

$$\mathbf{Z} = \begin{bmatrix} 0 & Z \\ -Z & 0 \end{bmatrix} \qquad 4.100$$

For MT soundings over a 2D conductivity structure **Z** will have a more complex form. Rotation of the co-ordinate system to axes parallel and perpendicular to the structure will however result in **Z** simplifying to the form

$$\mathbf{Z}(\theta_R) = \begin{bmatrix} 0 & Z_{12} \\ Z_{21} & 0 \end{bmatrix} \qquad 4.101$$

As described above for 2D conductivity structures the impedance magnitude $|Z_{12}|$ does not necessarily equal $|Z_{21}|$ and there are two estimates for the MT impedance; corresponding to electric field flow parallel and perpendicular to the strike of the conductivity structure. These two directions are called the principal axes; the major axis corresponds to the larger impedance and the minor axis to the smaller impedance value. For MT soundings over most 3D structures the impedance tensor will have a still more complex form and will not be able to be completely simplified by co-ordinate rotation.

The general rotational properties of impedance tensors are examined in appendix 4 and used in chapter 7 for analysis of Tasman Project impedances. A important parameter commonly used to estimate the degree of three-dimensionality of the conductivity structure tensor is the **skew** of the tensor. The skew is defined

$$S = \frac{|Z_{XX} + Z_{YY}|}{|Z_{XY} - Z_{YX}|} \qquad 4.102a$$

(Vozoff 1972) or in the slightly more general form

$$A = \frac{Z_{XX} + Z_{YY}}{Z_{XY} - Z_{YX}} \qquad 4.102b$$

(appendix 4). It is conveniently parameterized in terms of the **skew angle**

$$\theta_S = \tan^{-1} S \qquad 4.103$$

Although large angles of skew (say > 10°) indicate 3D conductivity structure, certain 3D structures with high degrees of symmetry may have low values of skew. It should also be noted that an incorrect orienation of the co-ordinate system for either the electric or magnetic data, or a near-surface distortion of the electric field may produce a significant (although frequency-independent) skew angle (Cox et al. 1980).

In many geological situations the near-surface conductivity structure will be much more heterogeneous than the deeper structure. Berdichevsky & Dmitriev (1976a) show that the distorting effect of surficial 3D inhomogeneities on impedance curves may be reduced by studying an effective impedance Z_{eff} instead of a single impedance component. Two different measures for Z_{eff} are

$$Z^{I}_{eff} = \sqrt{Z_{XX}Z_{YY} - Z_{XY}Z_{YX}} \qquad 4.104$$

$$Z^{II}_{eff} = \frac{Z_{XY} - Z_{YX}}{2} \qquad 4.105$$

The Forward and Inverse MT Problem in 1, 2 and 3 Dimensions

The "forward problem" in MT analysis consists of calculating the response function over a specified conductivity structure. For MT analysis the "inverse problem" involves directly calculating the conductivity structure from an observed response function. Because the observed response function is available only at discrete frequencies and over a limited frequency range, and is able to be defined to within only a particular certainty, the inverse problem includes calculating a range of conductivity structures which may fit the data.

The theory for the forward problem of MT induction in a 1D electrical conductivity structure is relatively straight-forward and has been presented by many authors, for example Price (1962), Schmucker (1970), Weaver (1970) and Kaufman & Keller (1981) and was described in section 4.1.1 above. Patra & Mallick (1980) show that the sphericity of the Earth may be neglected in 1D analyses for periods less than about five days.

Solutions for the 2D forward problem in MT analysis are generally obtained numerically. Analytical solutions exist for only the simplest models including two or three

layers or thin sheet irregularities in the top layer of 1D models. The 2D forward problem is generally solved using finite difference, finite element, integral equation, and electrical transmission line analogy numerical methods (Berdichevsky & Dmitriev 1976a, Jupp & Vozoff 1977). Numerical solutions for geomagnetic in 3D conductivity structures exist for certain simple structures. These structures include thin sheet irregularities in the top layer of one or 2D models (eg. Dawson & Weaver 1979) and 3D bodies embedded in 1D conductivity models (Wannamaker et al. 1984). Three-dimensional modelling is also performed using laboratory analogue models (Dosso & Nienaber 1986).

The inverse problem in MT analysis is very poorly constrained. It can however be shown (for the 1D case) that if perfect data are available at all frequencies the MT response function may be inverted to give a unique conductivity structure (Weidelt 1972, Johnson & Smylie 1971). Bailey (1970) presented similar results for the related problem invoving the ratio of internal to external magnetic fields. For real data which are band-limited and of limited resolution the solution of the MT inverse problem is very non-unique. In qualitative terms the ill-constrained nature of the problem arises because the surface MT response provides a very smoothed response to the conductivity structure. This effect is illustrated in Figure 4.8 which shows the smooth MT response for a very rough conductivity profile. Large variations in the conductivity structure do not produce very large variations in the response. Therefore for any observed response (with significant errors) there are many conductivity models capable of fitting the data.

Because numerous conductivity models may fit observed response functions inversion methods include further constraints to define the model which "best" fits the data in some sense. The constraints may be that the model has a layering observed from previous geophysical studies; that the conductivities fall within bounds predicted from laboratory measurements; or that the model be as smooth as possible. Many alternative schemes exist for 1D inversion of MT data - these are discussed in chapter 8. In addition several techniques exist for 2D inversion (eg. Jupp & Vozoff, 1977). Most 2D MT investigations however are still based on forward modelling methods. Because of the difficulty of the corresponding forward problem and problems of non-uniqueness, no methods for 3D inversion exist. Methods for determining conductivity profiles to fit observed 3D MT responses are very limited and 3D data are therefore generally interpreted using either an approximation to 2D responses or by analogue modelling.

A major question in many MT analyses is that of current channelling. The problem may be posed as, over what scale does the conductivity structure affect a local MT measurement ? For known conductivity structures it is possible to assess the effects of current channelling by simply including an appropriately large region into a forward model. In practice however one performs local MT soundings with little constraint on the regional or global conductivity distribution and it is difficult to directly assess the magnitude of current channelling. In his review of current channelling Jones (1983) advocates using "Occam's razor" and to invoke current channelling as an explanation of an observed

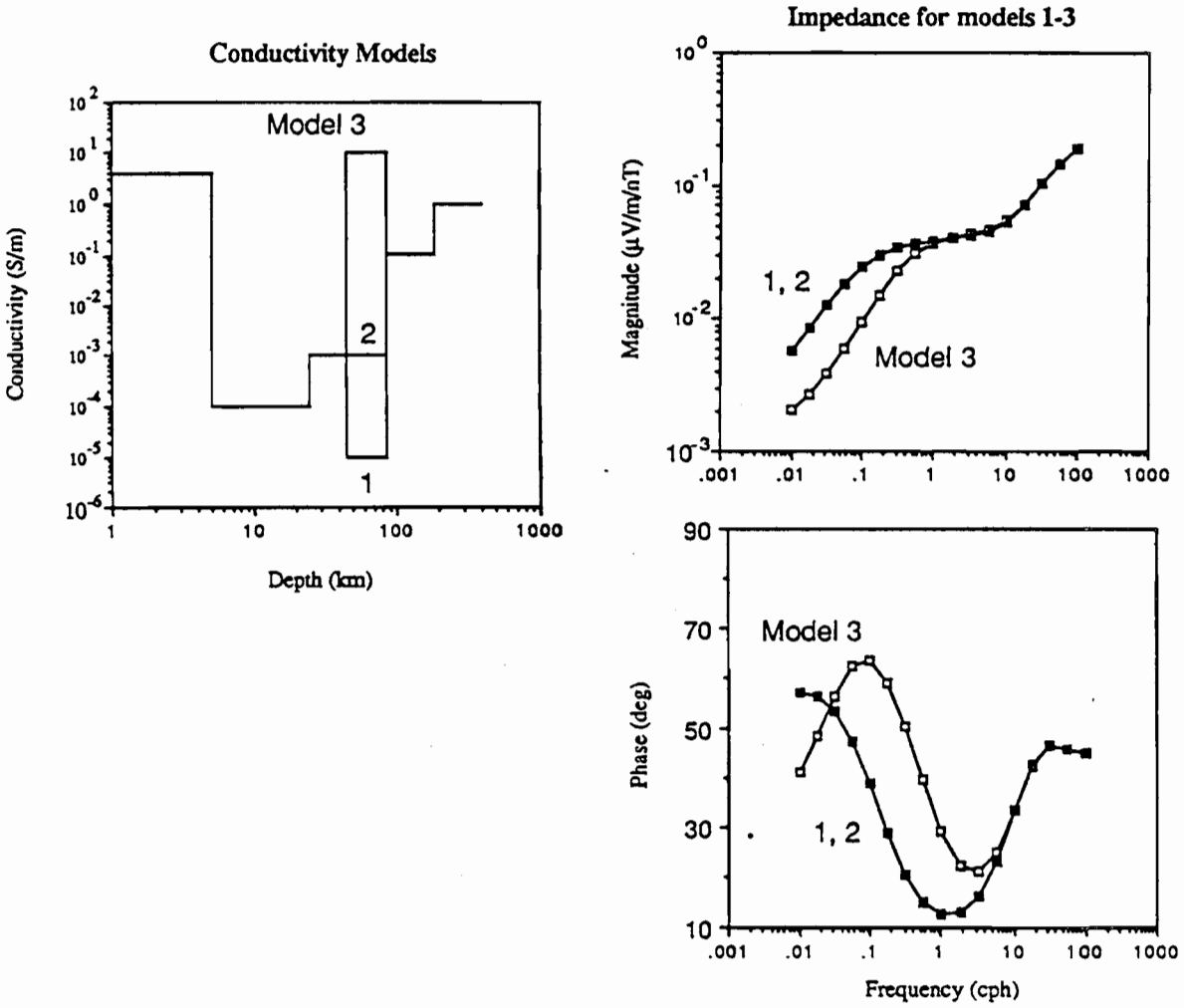

Figure 4.8: Examination of the sensitivity of the MT impedance to conductivity variations. The impedance is a smooth function of frequency despite order-of-magnitude changes in electrical conductivity between some adjacent layers. The impedance is relatively insensitive to resistive layers and exhibits no discernible differences for models 1 and 2, despite the existance of a 100 times difference in conductivity over a 40 km thick layer in the two models. Model 3 shows the impedance will respond to sufficiently conductive layers.

response only when local conductivity modelling fails to explain the data. Although perhaps a reasonable starting hypothesis, this approach must be treated with caution, for as indicated by Ranganayaki & Madden (1980) there are instances when apparently local responses (in their example, strictly 2D impedances) may be strongly affected by electric currents induced outside the local region.

4.1.4 Other geoelectric sounding methods

The vertical component of magnetic field fluctuations and the vertical and horizontal gradients of the horizontal components of the magnetic field are used in alternative geoelectric sounding methods. Magnetic variation sounding (MVS), spatial gradient sounding (SGS) and vertical gradient sounding (VGS) are basically 1D techniques. As for MT sounding however, MVS and VGS sounding can be applied to 2D conductivity structures. Geomagnetic depth sounding (GDS) is a method used for 2D conductivity structures.

Geomagnetic Depth Sounding

Fluctuations in the vertical component of the magnetic field at the surface of the Earth may arise from two sources. For uniform horizontal inducing-fields fluctuations in the vertical magnetic field are caused only by the interaction of the horizontal inducing field with lateral variations in the conductivity structure of the Earth. The strength of the vertical fluctuations depends upon the proximity, form and strength of the lateral conductivity contrasts. These principles form the basis of **geomagnetic depth sounding** (GDS). In this method measurements are made of the three components of the magnetic field and the observed patterns of vertical field fluctuations are used to map horizontal conductivity variations.

Note that in many publications the abbreviation GDS is generally used to refer to geomagnetic **deep** sounding (eg. Rokityansky 1982). The methods described under this title tend to be concerned with using spatial variations in the source-field to probe the 1D conductivity structure of the Earth (cf. using uniform source-fields to investigate 2D structure). In this thesis, GDS sounding mainly refers to the investigation of 2D structures while methods involving spatial variations of the source-field are grouped into magnetic variation sounding (MVS).

As stated above frequency-dependent induction arrows are used to represent the linear relationship between the vertical component of the magnetic field and the inducing horizontal components. The use of these arrows developed from early stereonet diagram representations by Parkinson (1959, 1962) and independently from the work of Wiese (1962). The arrows in use today are defined sligthly differently from both of these early arrows (Gregori & Lanzerotti 1980) and in this thesis are termed **induction arrows.**

For uniform source-fields the transfer functions a and b in

$$B_Z = a B_X + b B_Y \qquad 4.106$$

are frequency-dependent complex quantities depending only upon the conductivity structure. Induction arrows are formed for real and imaginary (quadrature) parts of the transfer function by plotting

$$C_r = - \mathrm{Re}(a)\,\mathbf{i} - \mathrm{Re}(b)\,\mathbf{j} \qquad 4.107$$

$$C_q = \pm \mathrm{Im}(a)\,\mathbf{i} \pm \mathrm{Im}(b)\,\mathbf{j} \qquad 4.108$$

where **i** and **j** are unit vectors to the geographical north and east respectively (Schmucker 1970). The signs chosen for the quadrature arrow depends on the time-dependence used in the analysis.

For a simple 2D structure consisting of a good conductor, such as an ocean, embedded in a poorly conducting half-space the real induction arrow will generally point to the good conductor at land sites, or away from the poor conductor at sea-surface sites (Jones 1986). The direction of the quadrature induction arrow is generally chosen such that at normal GDS frequencies (0.1 to 10 cph) it points towards the conductor with which it is associated (Lilley & Arora 1982, Chen & Fung 1985). For analyses is based on positive time-dependence this result is achieved by choosing the negative signs in 4.108 while for analyses based on a negative time-dependence the positive signs should be chosen (Lilley & Arora 1982).

Many geomagnetic array studies (eg. Bennett & Lilley 1974, Ingham et al. 1987) involve recordings of three components of the magnetic field and no electric field recordings. The results of such studies are often quantitatively interpreted using 2D modelling of the conductivity structure. In this execise the models are constructed so that they reproduce an observed response function, such as the ratio of the vertical magnetic field to the inducing horizontal magnetic-field component.

Magnetic Variation Sounding and Spatial Gradient Sounding

When the inducing magnetic field is not spatially uniform vertical magnetic-field fluctuations will be induced in the Earth, even where the there are no lateral conductivity anomalies. As for the MT response, the ratio of the vertical to the horizontal magnetic field depends upon the conductivity beneath the sounding site. In regions of non-uniform source-fields such as near the equator and in auroral regions, this relationship can be used to determine the conductivity structure. This method is called **magnetic variation sounding** (MVS).

There are two additional methods to MVS which make use of the spatial non-uniformity of the inducing field. **Spatial gradient sounding** (SGS) involves using the ratio of the vertical magnetic-field fluctuations to the spatial gradients of the horizontal magnetic-field fluctuations in order to define the impedance. An alternative method used to

derive the conductivity structure is based on the separation of the internal and external parts of the horizontal magnetic field. This method may be used when there is a sufficient density of recording sites beneath a non-uniform source-field. The method was used on a global scale in the earliest determinations of the electrical conductivity structure (eg. Lahiri & Price 1939) but may also be applied at a regional or continental scale (Porath et al. 1970).

The basic theory of MVS sounding may be derived from the 1D geomagnetic induction theory described above. From equation 4.32

$$\frac{H_Z}{H_X} = \frac{\lambda^2 Z\ P}{\frac{\partial Z}{\partial z}\ \frac{\partial P}{\partial x}} \qquad 4.109$$

and at the surface of a layered half-space

$$\frac{H_Z}{H_X} = \frac{-\lambda^2 P}{G_1 \theta_1 \frac{\partial P}{\partial x}} = \frac{\lambda^2 \zeta P}{i \omega \mu \frac{\partial P}{\partial x}} \qquad 4.110$$

Thus if the form of the source-field is known (ie. P and λ are specified) it is possible to determine the MT impedance from the ratio of the vertical to horizontal magnetic fields, and thus the 1D electrical conductivity structure. The basic equation for SGS sounding may also be derived from 4.32 as follows

$$\frac{H_z}{\frac{\partial H_x}{\partial x} + \frac{\partial H_y}{\partial y}} = \frac{Z\ \lambda^2 P}{\frac{\partial Z}{\partial z}\left(\frac{\partial^2 P}{\partial x^2} + \frac{\partial^2 P}{\partial y^2}\right)} = \frac{1}{G_1 \theta_1} = \frac{-\zeta}{i \omega \mu} \qquad 4.111$$

The ratio of the vertical magnetic field to the spatial gradients of the horizontal magnetic fields is thus simply related to the MT impedance ζ. Note that this method does not require any information on the wavenumber or on the form of the source-field.

Calculations based on the MVS and SGS have not been performed on the Tasman Sea data although the long magnetic east-west extent of the recordings may permit such investigations in the future. Results from MVS and SGS soundings (eg. Lilley et al. 1981, Volkomirskaya & Fonarev 1978) are however included in comparisons of Tasman Sea electrical conductivity profiles with those derived in other areas.

Vertical Gradient Sounding

A further method of geomagnetic sounding is called **vertical gradient sounding** (VGS). In this method the horizontal magnetic field is measured at points separated vertically, for example using seafloor and sea-surface measurements. The attenuation of the horizontal components between the two sounding sites is directly related to the

orthogonal, horizontal electric-current flow between the sites and thus the two magnetic field measurements may be simply related to the MT impedance. The VGS method has been used in the analysis of the Tasman data and the relevant equations are therefore now listed.

From equations 4.71 and 4.74 one may obtain

$$\zeta_1 = \frac{\zeta_2 + i\omega\mu \tanh(\theta_1 h_1)/\theta_1}{1 + \zeta_2 \theta_1 \tanh(\theta_1 h_1)/i\omega\mu} \qquad 4.112$$

relating the impedance at the top of the surface layer ζ_1, to that at the top of the underlying layer, ζ_2. For the analysis of the Tasman Project data ζ_1 and ζ_2 correspond to the sea-surface and seafloor impedance. Note that by re-arranging this equation it is possible to obtain

$$\zeta_2 = \frac{\zeta_1 - i\omega\mu \tanh(\theta_1 h_1)/\theta_1}{1 - \zeta_1 \tanh(\theta_1 h_1)/i\omega\mu} \qquad 4.113$$

which can be used to convert the sea-surface MT impedance, as obtained in floating ice measurements (Trofimov & Fonarev 1976), into the corresponding seafloor impedance.

Defining the ratio of the seafloor magnetic field to the sea-surface magnetic field

$$R_X = \left(\frac{H_{X1}}{H_{X2}}\right)^{-1} \qquad R_Y = \left(\frac{H_{Y1}}{H_{Y2}}\right)^{-1} \qquad 4.114$$

and using 4.77 and 4.113 the seafloor impedance can be expressed in terms of R

$$\zeta_2 = \frac{i\omega\mu}{\theta_1} \frac{(1 - R\cosh(\theta_1 h_1))}{R \sinh(\theta_1 h_1)} \qquad 4.115$$

This equation will be used to calculate alternative seafloor impedance estimates from the Tasman Project data.

An alternative VGS method involves using the seafloor electric field and the surface magnetic field. Defining the ratio

$$K_X = \frac{E_{X2}}{H_{Y1}} \qquad K_Y = \frac{-E_{Y2}}{H_{X1}} \qquad 4.116$$

the seafloor impedance impedance may be determined from

$$\zeta_2 = \frac{K\cosh(\theta_1 h_1)}{1 - K\theta_1 \sinh(\theta_1 h_1)/i\omega\mu} \qquad 4.117$$

It is very difficult to obtain three-component sea-surface magnetic field measurements. When applying the VGS method to oceanic measurements it is usual practice to replace the sea-surface magnetic field by that measured at a nearby land site (eg. Law & Greenhouse 1981, Poehls & Von Herzen 1976). This approach requires the source-fields to be

coherent between the land and ocean sites. For non-zero wavenumbers it is necesary to make a correction for the different electrical conductivity structure beneath the land and sea sites. From equation 4.76 giving the ratio of the internal to the external magnetic fields at the Earth's surface this correction is given by

$$\frac{H_{h\,2}}{H^R_{h\,1}} = \frac{H_{h\,2}}{H_{h\,1}} \left(\frac{\theta_1 G_1}{\theta_1 G_1 + \lambda} \right) \left(\frac{\theta_1^R G_1^R + \lambda}{\theta_1^R G_1^R} \right) \qquad 4.118$$

where superscript "R" refers to the remote land site. For uniform source-fields the wavenumber is zero and no correction is necessary.

Horizontal extent of impedance anisotropy

A final method of geomagnetic sounding used in the analysis of the Tasman Project data involves determining the resistivity of the ocean crust by examining the spatial extent of MT anisotropy from coastlines. This method will be applied in section 7.2 below.

Adjacent to a coastline a MT impedance will be strongly anisotropic with the B-pol impedance component affected by the presence of the coastine. As one moves away from the coastline the anisotropy decreases. It can be shown that the rate of decrease is related to the factor L (Cox 1980, Ranganayaki & Madden 1981, Chave & Cox 1983) where

$$L = \sqrt{\frac{\sigma_o d_o d_c}{\sigma_c}} \qquad 4.119$$

Thus L^2 is equal to the ratio of the integrated ocean conductivity to the integrated crustal resistivity. Note that L is simply the inverse of the parameter τ defined by Berdichevsky & Dmitriev (1976a) for indicating the strength of an anomaly at the edge of a 2D inhomogeneity. Since the integrated conductivity of the ocean is well known, measurements of the rate of decrease of anisotropy away from coastlines can be used to estimate the integrated resistivity of the ocean crust. Assuming some thickness for the oceanic lithosphere an estimate of the average resistivity may be obtained.

It should be noted that the distance scale for the anisotropy extent from a coastline represents an "adjustment distance" which indicates the typical horizontal region contributing to a SFMT measurement. As the resistivity of the ocean crust increases the influence of variations in the conductance of the ocean-sediment layer will extend over larger regions. Because of the S-effect, the impedance values obtained for deeper layers may also be biased by strong horizontal variations in the conductance of the uppermost conductive layers.

4.2 Estimation of Magnetotelluric Response Function

4.2.1 Alternative Forms of the Magnetotelluric Response Function

Several alternative forms of the MT response function have been introduced above. In this thesis the impedance Z (= E / B) is expressed in MVSA units of $V.m^{-1}.T^{-1}$ (ie. $m.s^{-1}$) or the more convenient $\mu V.m^{-1}.nT^{-1}$ (ie. $km.s^{-1}$) while the alternative impedance ζ (= E / H) is expressed in units of Ω or the more conveniently sized $m\Omega$ (Table 4.2).

The apparent resistivity has the same units as the actual resistivity ($\Omega.m = 1 / S.m^{-1}$) and the apparent resistivity / phase representation of the impedance thus provides a response function with readily interpreted physical significance. As found above for a uniform half-space the apparent resistivity is equal to the actual resistivity and is independent of frequency. Above a layered half-space the apparent resistivity will vary with frequency. At the shortest periods it will approach the resistivity of shallow layers while at the longest periods it will approach the resistivity of the deepest layers. In this way the apparent resistivity may be readily interpreted in terms of the actual conductivity structure.

It may be shown that the phase of the apparent resistivity is related to its magnitude through a dispersion relationship (eg. Parker 1983) and that the phase over a 1D electrical conductivity structure must always correspond to a lead of the electric field over the magnetic field of between 0 and 90°. In this thesis the phase of the apparent resistivity is defined as equal to the phase of the impedance ie.

$$\varphi(\rho_a) = \varphi(Z) = \mathrm{ATAN}\left(\frac{\mathrm{Im}(Z)}{\mathrm{Re}(Z)}\right) \qquad 4.120$$

(For a positive time-dependence the phase of Z is a lead and should lie between 0 and 90° while for a negative time-dependence the defined phase a lag and should lie between 0 and -90°.) A cursory examination of the phase may be sufficient to indicate the presence of 2D or 3D conductivity structure.

Another form of the MT response function, Weidelt's c term is defined in equation 4.86 and the meaning of the real part of c has also been introduced. The values of c at different frequencies may be directly interpreted in terms of the depth to an equivalent conductor. The real part of c gives the depth, z*, to the conductor while the imaginary part of c represents half the skin depth in the conductor (Schmucker & Jankowsky 1972). The skin depth may be converted into an equivalent conductivity or resistivity ρ^*, using equation 4.60.

The use of the representation z*, ρ^* to define an electrical conductivity profile is termed **direct inversion**. Such a procedure is to be contrasted with "true" inversion

Table 4.2: Relationships between MT response function magnitude.

Sym	Name	Units
Z_1	Impedance (E/B)	$\mu V.m^{-1}.nT^{-1} = mV.km^{-1}.nT^{-1} = km.s^{-1}$
Z_2	Impedance	$V.m^{-1}.T^{-1} = m.s^{-1}$
ζ_1	Impedance (E/H)	Ω
ζ_2	Impedance	$m\Omega$
c_1	Weidelt c response	m
c_2	Weidelt c response	km
ρ_a	Apparent resistivity	Ω.m

(a) Forms of the MT response function.

Z_2	ζ_1	ζ_2	c_1	c_2	ρ_a
$Z_1 10^3$	$Z_1\ 10^3\ \mu$	$Z_1\ 10^6\ \mu$	$Z_1\ 10^3 / 2\pi f$	$Z_1 / 2\pi f$	$Z_1^2\ 10^6\ \mu / 2\pi f$
	$Z_2\ \mu$	$Z_2\ 10^3\ \mu$	$Z_2 / 2\pi f$	$Z_2\ 10^{-3} / 2\pi f$	$Z_2^2\ \mu / 2\pi f$
		$\zeta_1\ 10^3$	$\zeta_1 / \mu\ 2\pi f$	$\zeta_1\ 10^{-3} / \mu\ 2\pi f$	$\zeta_1^2 / \mu\ 2\pi f$
			$\zeta_2\ 10^{-3} / \mu\ 2\pi f$	$\zeta_2\ 10^{-6} / \mu\ 2\pi f$	$\zeta_2^2\ 10^{-6} / \mu\ 2\pi f$
				$c_1\ 10^{-3}$	$c_1^2\ 2\pi f\ \mu$
	f in Hz				$c_2^2\ 2\pi f\ 10^6\ \mu$

(b) Frequency measured in cycles per second (Hz).

Z_2	ζ_1	ζ_2	c_1	c_2	ρ_a
$Z_1 10^3$	$Z_1\ 10^3\ \mu$	$Z_1\ 10^6\ \mu$	$Z_1\ 3.6\ 10^6 / 2\pi f$	$Z_1\ 3.6\ 10^3 / 2\pi f$	$Z_1^2\ 3.6\ 10^9\ \mu / 2\pi f$
	$Z_2\ \mu$	$Z_2\ 10^3\ \mu$	$Z_2\ 3.6\ 10^3 / 2\pi f$	$Z_2\ 3.6 / 2\pi f$	$Z_2^2\ 3.6\ 10^3\ \mu / 2\pi f$
		$\zeta_1\ 10^3$	$\zeta_1\ 3.6\ 10^3 / \mu\ 2\pi f$	$\zeta_1\ 3.6 / \mu\ 2\pi f$	$\zeta_1^2\ 3.6\ 10^3 / \mu\ 2\pi f$
			$\zeta_2\ 3.6 / \mu\ 2\pi f$	$\zeta_2\ 3.6\ 10^{-3} / \mu\ 2\pi f$	$\zeta_2^2\ 3.6\ 10^{-3} / \mu\ 2\pi f$
				$c_1\ 10^{-3}$	$c_1^2\ 2\pi f\ 10^{-3}\ \mu / 3.6$
	f in cph				$c_2^2\ 2\pi f\ 10^3\ \mu / 3.6$

(c) Frequency measured in cycles per hour.

The table gives the relationship between the **magnitude** (but not phase) of MT response functions (a) for frequency measured in Hz (b) and in cph (c). For example the magnitude of the apparent resistivity (in Ω) is given in terms of the magnitude of the impedance (in $\mu V.m^{-1}.nT^{-1}$) by the first row of column six. Thus for the frequency in Hz one obtains the familiar relationship

$$\rho_a = |Z_1|^2\ 10^6\ \mu / 2\pi f = |Z_1|^2 \times 0.2 / f\ .$$

methods which take into account the uncertainties in the data in the determination of the conductivity structure. The z*, ρ* direct inversion has several limitations. For example it will provide correct results only when the electrical conductivity increases monotonically with depth. Schmucker (1987) examines alternative direct inversion methods.

Table 4.2 lists the conversion factors between the magnitudes of all the different forms of the magnetotelluric response function. The phase of c is equal to the phase of the impedance minus 90°. The transformation between the various forms of the response function may be performed on the final response function estimates.

4.2.2 Estimation of the magnetotelluric response function

In this section the estimation of MT response functions from recorded electric and magnetic time series is considered. The estimation of the four-term impedance tensor and of the associated random errors is described. For real data the recorded time series are of a finite length and probably contain some component of noise. For much of this discussion both the signal and noise are assumed to be stationary; the noise is assumed to be random, Gaussian and uncorrelated between different time series and uncorrelated with the signal. There are many thorough treatments of the estimation of MT response functions in the scientific literature (eg. Patra & Mallick 1980). The description below concentrates on describing the theoretical basis of the methods applied to the Tasman Project MT data.

Spectral Analysis

The first step in the estimation of an MT impedance tensor involves conversion of the recorded time series into the frequency-domain. In the analysis of the Tasman Project data this procedure involved calculating the power spectral density functions for single components (autopowers) and appropriate pairs of components (crosspowers). The power spectral density function gives the average power over the length of the analysed time series as a function of frequency. Although methods exist for calculating MT impedances directly from the time domain data (eg. Kunetz 1972) such methods are more complex and are not discussed here.

Geomagnetic time series contain energy at a wide range of periods but for SFMT sounding only periods in the approximate range 5 min. to 50 h are used. At these periods the source fields comprise diurnal and tidal signals in narrow bands and broad-band signal induced by geomagnetic storms and substorms. The diurnal and tidal signals are approximately deterministic ie. periodic, and are excluded from this analysis of the Tasman data. The storm and substorm signal is however generally assumed to be stochastic or random (meaning that the signal at future times can be predicted from the signal at a previous time in only a statistical manner).

A stationary random process may be regarded as a process in which the time-averaged mean value and autocorrelation function (or alternatively the variance) do not vary significantly from one interval to the next. This is a practical rather than the formal definition of stationarity (Bendat & Piersol 1971). At mid-latitudes the geomagnetic storm and substorm fields tend to form periods of increased activity with length of a few hours to a few days separated by quieter periods of length a few days to a few weeks. For analysis periods of length 100 days the signal is approximately stationary with consecutive analysis intervals having similar mean and variance. For analysis periods of length 1 day however the signal may be strongly non-stationary with large differences occurring in the level of variance (ie. the level of geomagnetic disturbance) between consecutive days.

The concept of spectral analyis is different for stationary and non-stationary data. Early geomagnetic recordings were largely analogue in form and because of the time-consuming nature of hand digitization, most scientists digitized and analysed only a number of short, simple geomagnetic disturbances. Events such as bays (sub-storms) lasting 2-4 h were analysed with each event being regarded as a discrete geomagnetic event. Spectral analyis involved determining the total power present at each frequecy during the event. In this approach the data are treated as being non-stationary.

With modern instrumentation and the availability of long digital time-series it has become possible to analyse time series of length 100 days and longer. Over such time scales the signal is approximately stationary. The aim of the spectral analysis with stationary data is to define the average power level (per unit time) at each frequency. These values should be relatively constant over different time segments. The Tasman Project data were analysed using this "stationary" approach.

As longer time series of geomagnetic data are used in the Fourier analysis the power level of the stochastic signal approaches a constant level. The power associated with periodic signals however increases proportionally with the length of the event. A power spectrum derived from a long event will thus show a backgound power level due to the stochastic signal with emergent spectral lines caused by periodic sources such as the diurnal variation, ionospheric tidal lines and, in seafloor data, oceanic tidal lines. For Fourier analyses of discrete data of a finite length, side-band contamination may occur of spectral lines near strong diurnal or tidal lines.

Power spectra may be derived from time series directly using Fourier transformation or indirectly from correlation functions (Bendat & Piersol 1971). For the Tasman data the direct Fourier transformation approach was used, with the transformation being defined as the digital equivalent of

$$F(\omega) = \int_{-\infty}^{+\infty} f(t)\, e^{+i\omega t}\, dt \qquad 4.121$$

corresponding to an implied negative time dependence (see appendix 3). When dealing with stationary data, the transformation must involve integration over a truncated portion

(0, L) of the total time series. In the digital form of the transformation one obtains Fourier transform values at discrete spectral lines. If there are n equally spaced data points in (0, L) ie. $L = n\,\delta$ where δ is the sample interval one obtains Fourier transform estimates at

$$F(\omega_m) \text{ where } m = \frac{-(n/2)}{L}, \ \ldots, \frac{-2}{L}, \frac{-1}{L}, 0, \frac{1}{L}, \frac{2}{L}, \ldots, \frac{(n/2)}{L} \qquad 4.122$$

For input time series f(t) consisting of real data the Fourier transform is an even function and negative frequencies can generally be ignored except during inverse transformations.

The power spectral density function is defined

$$S_{FG}(\omega_i) = \frac{\sum_{m=1}^{p} F(\omega_m)\, G^{*}(\omega_m)}{p\,L} \qquad 4.123$$

where * indicates complex conjugation and the summation may be over the adjacent spectral lines within a band *i* or over a different data segments if the initial time series were subdivided before Fourier analysis. If F and G are identical components S will be an autopower and if they are different components S will be a crosspower. If f(t) is a magnetic field recording in nT and L is in seconds, the units of the Fourier transform $F(\omega)$ will be nT.s (or $nT.Hz^{-1}$) and the units of the autopower $S_{FF}(\omega)$ will be $nT^2.s$ or more appropriately $nT^2.Hz^{-1}$.

Note that there is some variation as to which index in the crosspower corresponds to the conjugated variable (see appendix 3). The definition of crosspower used in the above equation follows that of Schmucker (1970 p. 17 eq 3.5).

There are many published references describing the methods used for the digital Fourier transformation (eg. Kanasewich 1975, Bendat & Piersol 1971). Operations performed on time series before Fourier transformation include subtraction of the mean and/or a linear trend, and multiplication of the time series by a windowing function to reduce side-band effects from strong spectral lines. Other operations performed include filtering the data in order to exclude unwanted frequencies and to reduce aliasing, and filtering the time series to pre-whiten (or flatten) the frequency spectrum during the Fourier transformation. The actual transformation is generally performed using the computationally efficient Fast Fourier Transformation (FFT) technique (eg. Kanasewich 1975).

In the statistical approach to spectral analysis it follows that the each available time series is only one of an ensemble of possible time series generated by the random process (ie. a sample of all the possible storms, substorms etc.). In order to obtain the exact spectral representation of the process it would be necessary to transform all time series of this ensemble into the frequency-domain and average the results. With only one sample of the ensemble of time series available the frequency domain results can only be estimated with limited certainty. In fact it can be shown that the standard error of an autopower

estmate based on a single spectral line from an FFT is equal to the magnitude of the autopower itself (Bendat & Piersol 1971 p. 191). This result may be confimed by plotting individual spectral lines from a FFT analyis (see chapter 6) - the resulting spectrum is extremely erratic and it is sometimes difficult to discern the desired spectral characteristics.

The accuracy of spectral estimates may be increased by smoothing the raw spectrum. The smoothing is performed by averaging spectral estimates within broader frequency bands, by segmenting the original time series and averaging the spectral estimates from the different segments or by combining both techniques. Both of the smoothing techniques trade a decrease in the number of spectral estimates, ie. a decrease in resolution, against an increase in the accuracy of each estimate. The segmenting technique is perhaps superior for dealing with non-stationary data since it allows a weighting of the contribution of each segment (based upon the level of power in that segment) to the final spectral estimate. The segmenting method possesses the disadvantage of not returning spectral estimates at periods between the length of the total event and the length of the segment.

The Least-Squares Impedance Estimate

Estimation of the impedance tensor involves solving for Z in equations 4.2a & b now written

$$E_j = Z_{ji} B_i \quad j = x, y \quad i = x, y \qquad 4.126$$

The two equations j = x, y are independent, allowing the solutions for Z_{XX} and Z_{XY} to be obtained separately from Z_{YX} and Z_{YY}. An exact solution for each equation may be obtained from two exact independent estimates of (B_X, B_Y) and (E_X, E_Y). Observed data however contain noise (eg. the random noise arising from spectral analysis) and in general a large number of data values are used in the determination of the impedance. The derivation of the least-squares (LS) solution for Z from a large number of (B_X, B_Y) and (E_X, E_Y) values is now described.

Temporily choosing j = x we may write

$$E_{X\,k} = B_{i\,k} Z_{X\,i} + e_{X\,k} \qquad 4.127$$

where subscript k indicates the replication number (data set) and e is the error term resulting from random errors in E. The LS estimate for Z, Z^L is obtained by minimizing the squared magnitude of e with respect to Z. We thus minimize

$$\Sigma = \sum_{k=1}^{n} e_k e_k^* \qquad 4.128$$

$$= \sum_{k=1}^{n} (E_{X\,k} - B_{X\,k} Z_{X\,X} - B_{Y\,k} Z_{X\,Y})(E_{X\,k} - B_{X\,k} Z_{X\,X} - B_{Y\,k} Z_{X\,Y})^*$$

by solving

$$\frac{\partial \Sigma}{\partial Z_X^*} = 0 \text{ and } \frac{\partial \Sigma}{\partial Z_Y^*} = 0 \qquad 4.129$$

One obtains

$$\sum_{k=1}^{n} B_{X\,k}^*(E_k - Z_X B_{X\,k} - Z_Y B_{Y\,k}) = 0 \qquad 4.130$$

$$\sum_{k=1}^{n} B_{Y\,k}^*(E_k - Z_X B_{X\,k} - Z_Y B_{Y\,k}) = 0 \qquad 4.131$$

leading to

$$Z_{XX}^L = \frac{\sum E_X B_X^* \sum B_Y B_Y^* - \sum B_Y B_X^* \sum E_X B_Y^*}{\sum B_X B_X^* \sum B_Y B_Y^* - \sum B_X B_Y^* \sum B_Y B_X^*} \qquad 4.132$$

and a corresponding solution for Z_{XY}. Dividing numerator and denominator by event length L we may replace the sums by corresponding auto and crosspowers. Replacing E_X by E_Y one obtains the corresponding equations for Z_{YX} and Z_{YY}. The full set of solutions is

$$Z_{XX}^L = (S_{E_X B_X} S_{B_Y B_Y} - S_{E_X B_Y} S_{B_Y B_X})/D \qquad 4.133a$$

$$Z_{XY}^L = (S_{E_X B_Y} S_{B_X B_X} - S_{E_X B_X} S_{B_X B_Y})/D \qquad 4.133b$$

$$Z_{YX}^L = (S_{E_Y B_X} S_{B_Y B_Y} - S_{E_Y B_Y} S_{B_Y B_X})/D \qquad 4.133c$$

$$Z_{YY}^L = (S_{E_Y B_Y} S_{B_X B_X} - S_{E_Y B_X} S_{B_X B_Y})/D \qquad 4.133d$$

$$D = S_{B_X B_X} S_{B_Y B_Y} - S_{B_X B_Y} S_{B_X B_Y} \qquad 4.133e$$

The LS solution for the impedance will provide an unbiased estmate of the true impedance only if there is no noise present on the magnetic components and if there is no noise correlated with the signal. Errors on the electric field components will not introduce any bias into the impedance estimates.

The presence of noise on a time series generally produces an upwards bias in the autopower. For

$$F(\omega) = F_S(\omega) + F_N(\omega) \qquad 4.134$$

where S denotes signal and N denotes noise

$$S_{FF}(\omega) = S_{F_S F_S}(\omega) + S_{F_N F_N}(\omega) + 2\, S_{F_S F_N}(\omega) \qquad 4.135$$

ie. the total power equals the power of the signal component plus the power of the noise component plus an additional term associated with any noise correlated with the signal. Uncorrelated noise on magnetic components will bias the autopowers S_{BXBX} and S_{BYBY} upwards and from 4.133 the noise will thus bias the impedance terms downwards.

Another necessary condition for the LS method to provide an unbiased estimate of the impedance is that the error terms e_k possess a symmetrical distribution around zero. For errors with a Gaussian distribution the LS estimate provides an unbiased and efficient estimate of the true impedance (Bendat & Piersol 1971). Until the recent research of Egbert & Booker (1986) and Chave et al. (1987) few studies had examined the actual error distributions of MT data. Scientists either made an explicit assumption that errors formed a Gaussian distribution or often, making the assumption implicitly, simply applied Gaussian statistical methods. The results of Egbert & Booker (1986) suggest the assumption of Gaussian error distribution for MT data may not always be valid.

Determination of unbiased impedances

A number of methods have been developed to correct for the impedance bias caused by noise on magnetic field components. There are a variety of sources of such noise, for example, instrumental noise, cultural noise, noise resulting from hand-digitization, and in seafloor recordings, oceanically induced magnetic field signals. It is therefore important to be able to calculate unbiased impedances from data containing magnetic-field noise.

An alternative method for deriving the impedance is to use a LS formulation to derive the admittance A defined

$$\mathbf{B} = \mathbf{A}\,\mathbf{E} \qquad 4.136$$

in analogy with equation 4.97 for the impedance. The impedance tensor **Z** is equal to the inverse of the admittance tensor **A** but note that the individual terms of **A** are not simply the inverse of corresponding terms of **Z**. The solutions for the impedance derived from the LS estimate for the admittance are

$$Z^A_{XX} = (S_{B_Y E_Y} S_{E_X E_X} - S_{B_Y E_X} S_{E_X E_Y}) / D^A \qquad 4.137a$$

$$Z^A_{XY} = (S_{B_X E_X} S_{E_X E_Y} - S_{B_X E_Y} S_{E_X E_X}) / D^A \qquad 4.137b$$

$$Z^A_{YX} = (S_{B_Y E_Y} S_{E_Y E_X} - S_{B_Y E_X} S_{E_Y E_Y}) / D^A \qquad 4.137c$$

$$Z^A_{YY} = (S_{B_X E_X} S_{E_Y E_Y} - S_{B_X E_Y} S_{E_Y E_X}) / D^A \qquad 4.137d$$

$$D^A = S_{B_Y E_Y} S_{B_X E_X} - S_{B_Y E_X} S_{B_X E_Y} \qquad 4.137e$$

These impedance estimates contain no autopowers of magnetic field components and will

therefore be unbiased by random noise on the magnetic field components. However the estimates do contain autopowers of electric components and will be biased upwards by noise in the electric time series.

Seafloor electric field and magnetic field measurements both contain significant levels of oceanically induced noise. In a number of analyses of seafloor data Filloux (1980b, 1982a, 1982b etc.) has used the geometric mean of correponding impedance terms from standard LS impedance and admittance formulations in to estimate impedances with reduced bias. This method cancels the downwards bias of the LS impedances (caused by noise on magnetic field autopowers) with the upwards bias of the admittance-formulation impedances (caused by noise on the electric field autopowers). Such a method will produce unbiased estimates if the signal-to-noise ratio (SNR) is of the same magnitude for all components. If the noise on the electric field time series is however much larger than on the magnetic time series this method could actually increase the bias from that associated with a basic LS impedance estimate.

Sims et al. (1971) show there are six possible formulations that may be used to define the impedance (of which the LS and admittance formulations described above comprise two). All will be biased to some degree by noise on the magnetic and electric time series. Beamish (1986) and Gundel (1977) describe methods based on the observed coherences, for combining different impedance estimates in order to reduce bias. Goubou et al. (1978) define an impedance estimate in terms of crosspowers only but their tests showed this method produced relatively unstable results. Another method used to reduce bias is described by Kao & Rankin (1977). This is an iterative method which removes noise from the autopowers using the assumption that the crosspowers are noise free.

The method used to correct for noise in the Tasman Project data is the **remote reference method** described by Gamble et al. (1979a, 1979b). This method, examined in detail below, uses electric or magnetic data from a site remote from the main MT site in order to correct for noise. The method is capable of correcting for all noise except that which is coherent between the remote and main site. It is capable of correcting for noise which is correlated between the magnetic and electric time series at the MT site. The distance of the remote site from the MT site is limited by the requirement that the geomagnetic source-field is coherent between the two sites.

Several other methods are also used to estimate unbiased impedances. Singular value decomposition of spectral matrices containing all of the MT components recorded at a site enables the separation of signal from noise and hence the estimation of unbiased impedances (eg. Chave et al. 1980, Park & Chave 1984). Recently this approach has been extended to analyse the combined spectral matrix from an array of sites (Egbert & Booker 1985).

All of the methods described above, correct for bias caused by the presence of noise in an MT time series. The methods do not correct for the bias caused by any non-Gaussian distribution of noise. Recently published research by Chave et al. (1987) describes a

method for estimation of transfer functions (such as impedances) which takes into account the error distribution. This robust estimation procedure corrects for the presence of "outliers" in the error distribution which cause departures from a Gaussian distribution and can significantly bias least-squares impedance estimates. Egbert & Booker (1986) applied such robust estimation techniques to geomagnetic data and found significant differences between conventional and robust impedance estimates.

Robust estimation will not correct bias caused by correlated noise between the MT electric and magnetic time series. The most advanced method of impedance estimation should thus consist of a robustified form of the remote-reference method or an alternative multiple-site method.

4.2.3 The Remote Reference Method

In this section the remote reference method is examined in some detail. The derivation of the remote reference equations follows Gamble et al. (1979a). The remote-reference data will be denoted (R_X,R_Y) where R may be either the electric or magnetic field (frequency-dependent) Fourier transformat the remote site. Starting with equation 4.127 we multiply by R_X^* and R_Y^* to obtain

$$E_X R_X^* = Z_{XX}B_X R_X^* + Z_{XY}B_Y R_X^* + e_X R_X^* \qquad 4.138a$$

$$E_X R_Y^* = Z_{XX}B_X R_Y^* + Z_{XY}B_Y R_Y^* + e_X R_Y^* \qquad 4.138b$$

If we now sum over many values of E, B and R the last term in each of these equations will go to zero if the errors are uncorrelated with the noise and/or signal at the remote reference site. Note that the e may be associatedwith noise on either E or B. After summing and dividing by event length L, the sums may be replaced by corresponding crosspowers to give

$$S_{E_X R_X} = Z_{XX}S_{B_X R_X} + Z_{YX}S_{B_Y R_X} \qquad 4.139a$$

$$S_{E_X R_Y} = Z_{XX}S_{B_X R_Y} + Z_{XY}S_{B_Y R_Y} \qquad 4.139b$$

and we may now solve for Z_{XX} and Z_{XY}. A similar approach may be used to obtain Z_{YX} and Z_{YY} leading to the following remote reference equations.

$$Z_{XX}^R = (S_{E_X R_X} S_{B_Y R_Y} - S_{E_X R_Y} S_{B_Y R_X}) / D^R \qquad 4.140a$$

$$Z_{XY}^R = (S_{E_X R_Y} S_{B_X R_X} - S_{E_X R_X} S_{B_X R_Y}) / D^R \qquad 4.140b$$

$$Z_{YX}^R = (S_{E_Y R_X} S_{B_Y R_Y} - S_{E_Y R_X} S_{B_Y R_X}) / D^R \qquad 4.140c$$

$$Z^R_{YY} = (S_{E_Y R_Y} S_{B_X R_X} - S_{E_Y R_X} S_{B_X R_Y}) / D^R \qquad 4.140d$$

$$D^R = S_{B_X R_X} S_{B_Y R_Y} - S_{B_X R_Y} S_{B_Y R_X} \qquad 4.140e$$

Note that these impedance equations contain only crosspowers between remote and electric time series or remote and magnetic time series. The results will therefore be unbiased by any noise at the main MT site that is uncorrelated with noise and/or signal at the remote site. They will in fact be unbiased even when there is correlated noise between the electric and magnetic components at the main MT site.

The remote-reference impedance solution may be shown to be equivalent to the application of two LS solutions. The first LS solution determines the transfer function between the magnetic and remote time series (in analogous form to the MT LS solution between the electric and magnetic fields). This transfer function defines the proportion of the recorded magnetic field component which is coherent with the remote data ie. the signal component of the recorded magnetic field. The second LS solution determines the transfer function between the electric field and this signal portion of the magnetic field. The final remote-reference transfer function is therefore unbiased by (uncorrelated) noise on the either the magnetic field or electric field recordings.

The remote-reference site chosen for a MT site should be sufficiently distant such that there is no correlated noise between the two sites. Any correlated noise will cause a bias in the impedance estimate. The remote reference should however be sufficiently close to the MT site that the geomagnetic source-field is coherent between the sites. If the source-field is different at the two sites the magnitude of the magnetic signal at the MT site will be under-estimated and the impedance estimates may be biased. Although the source-field needs to be coherent between the two sites, the form of the remote reference need not be the same as that of the magnetic or electric field at the MT site. All that is required is that the remote reference is able to be related to the magnetic field at the MT site through a linear transfer function

$$\mathbf{B}(\omega) = \mathbf{N}(\omega)\, \mathbf{R}(\omega) \qquad 4.141$$

The impedance may thus be different between the remote and MT sites; either site could be a seafloor, sea-surface or continental site; the measurement axes may differ between the remote and MT site; and the remote reference may be either an electric or magnetic field recording.

It should be noted that it is the magnetic field (and not the electric field) on which the remote reference operates. One could alternatively formulate a remote-reference method based upon the admittance estimate in which the remote reference operates on the the electric field. If there is no correlated noise between the remote and MT sites both methoc will return the same impedance estimates.

At this point it is of value to summarise the LS, admittance and remote reference solutions for the impedance using the notation of Gamble et al. (1979a). This notation

uses the spectral matrix

$$[A\ B] = \begin{bmatrix} S_{A_X B_X} & S_{A_X B_Y} \\ S_{A_Y B_X} & S_{A_Y B_Y} \end{bmatrix} \qquad 4.142$$

Using this notation the LS, admittance and remote reference equations for the impedance can be simply written

$$Z^L = [E\,B]\,[B\,B]^{-1} \qquad 4.143$$

$$Z^A = [E\,E]\,[B\,E]^{-1} \qquad 4.144$$

$$Z^R = [E\,R]\,[B\,R]^{-1} \qquad 4.145$$

where, in each equation, Z has the form of the standard impedance tensor (equation 4.99). Note that the LS and admittance solutions are special cases of the remote reference solution in which R equals B and R equals E respectively.

An example of the use of the remote reference method will now be given to illustrate its effectiveness. Various aspects of the method will be discussed in more detail in chapter 7 while in section 4.2, below, the error analysis appropriate for the remote reference method is described.

The remote-reference method will be tested using a synthetic data set consisting of perfectly correlated time series related by specified transfer functions. Noise will be added to various time series, spectral analysis performed and then the impedances calculated using the LS, admittance and remote reference equations. The data set is generated from a pair of real B_H and B_D time series comprising a 1024 h time series from the CMO site. The sampling density is 8 data.h^{-1} giving 8192 points in the time series. These time series are renamed $B_X(t)$ and $B_Y(t)$ and are simply repeated to form the remote reference time series $R_X(t)$ and $R_Y(t)$. The electric-field time series are generated using

$$E_X(t) = 1.0\ B_X(t) + 3.0\ B_Y(t)$$

$$E_Y(t) = -2.0\ B_X(t) + 1.0\ B_Y(t)$$

corresponding to an arbitrary (frequency-independent) impedance

$$Z = \begin{bmatrix} 1+0\,i & 3+0\,i \\ -2+0\,i & 1+0\,i \end{bmatrix}$$

The noise is produced using a random number generator to form 8192 points with a specified standard deviation. The particular random number generator used produces a Gaussian white noise spectrum. For such a distribution with standard deviation σ and sampling density $1/\delta$ the power level generated is given by equation 3.3 ie.

$S_N = \sigma^2 \delta$

Because the signal time-series are generated from real data they possess a steep spectrum and the addition of the white noise produces a noise-to-signal ratio that increases rapidly with increasing frequency (Figure 4.9).

The remote-reference method was tested by adding various levels of noise to different combinations of the six time series. It was also tested by adding correlated noise between the MT magnetic and electric time series. In each of these cases the remote-reference impedance estimate gave an unbiased estimate of the correct impedance while the LS and admittance methods gave biased estimates. The addition of noise did however introduce random errors into the estimates (see section 4.2.4 below). The addition of correlated noise between the remote reference and MT components led, as expected, to biased remote reference impedance estimates.

Figure 4.10 shows an example in which uncorrelated noise was added to all six input time series. The signal and noise levels shown in Figure 4.9 give noise-to-signal ratios (of autopowers) ranging from order 10^{-2} to order one. Figure 4.10 shows the impedance estimated for component Z_{YX} using the three alternative sets of impedance equations. Although the LS and admittance impedance magnitudes are strongly biased the remote reference impedance magnitude shows only random errors.

4.2.4 Error Estimation in Magnetotelluric Analysis

In this section methods for estmating the influence of errors on MT parameters will be examined. The methods described, estimation of standard deviations and confidence limits etc., provide bounds on the variations of results caused by **random** errors. Random errors are caused by finite measurement accuracy, the limited accuracy of FFTs and by the presence of random noise (here assumed Gaussian) on the measured time series. Such errors may propagate to produce random errors in estimated power spectra, coherences and transfer functions. Confidence limits etc. do <u>not</u> allow for systematic errors, for example systematic measurement errors, or for bias of results, for example the bias of the LS impedance estimates. Such systematic errors produce **systematic** errors in power, coherence and transfer function estimates. A thorough treatment of error estimation may be found in Bendat & Piersol (1971 chapter 6).

Before describing error calculations it is convenient to give some definitions. The mean square error in the estimation of parameter Ω is defined

$$E[(\overline{\Omega} - \Omega)^2] = E[(\overline{\Omega} - E[\overline{\Omega}])^2] + E[(E[\overline{\Omega}] - \Omega)^2] \qquad 4.146$$

where E is the expectation operator and the overbar indicates an estmated quantity (Bendat & Piersol 1971). The first term on the r.h.s. of equation 4.146 gives the **variance** of Ω or the random part of the error (the squared deviation of each estimate from the mean

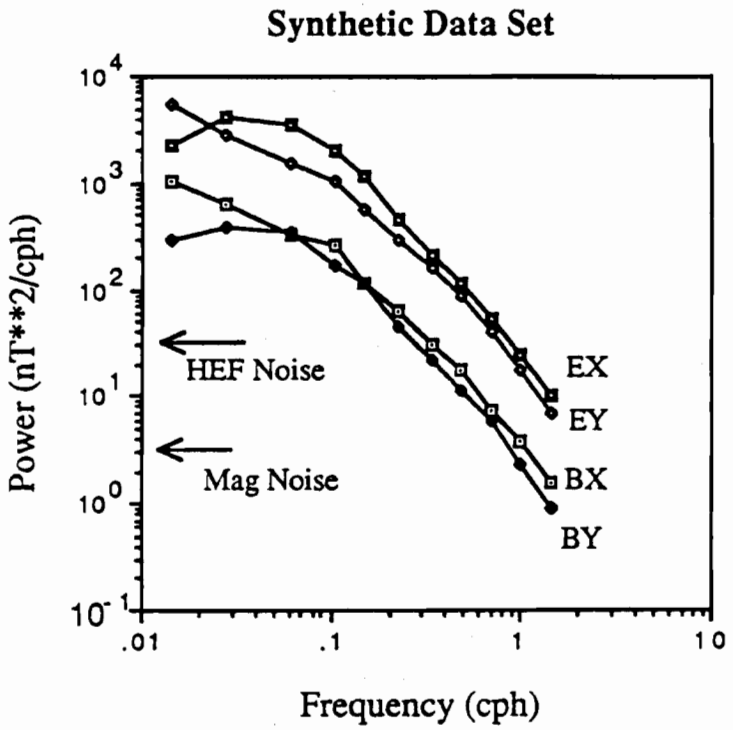

Figure 4.9: Power spectra of synthetic magnetic and electric field time-series used in trials of the remote reference procedure. The magnetic field data are derived from actual magnetic field recordings taken during the Tasman Project while the "electric field" data are related to the magnetic components through a time-domain "impedance tensor". Random noise was added to the synthetic electric and magnetic field time-series at the levels shown.

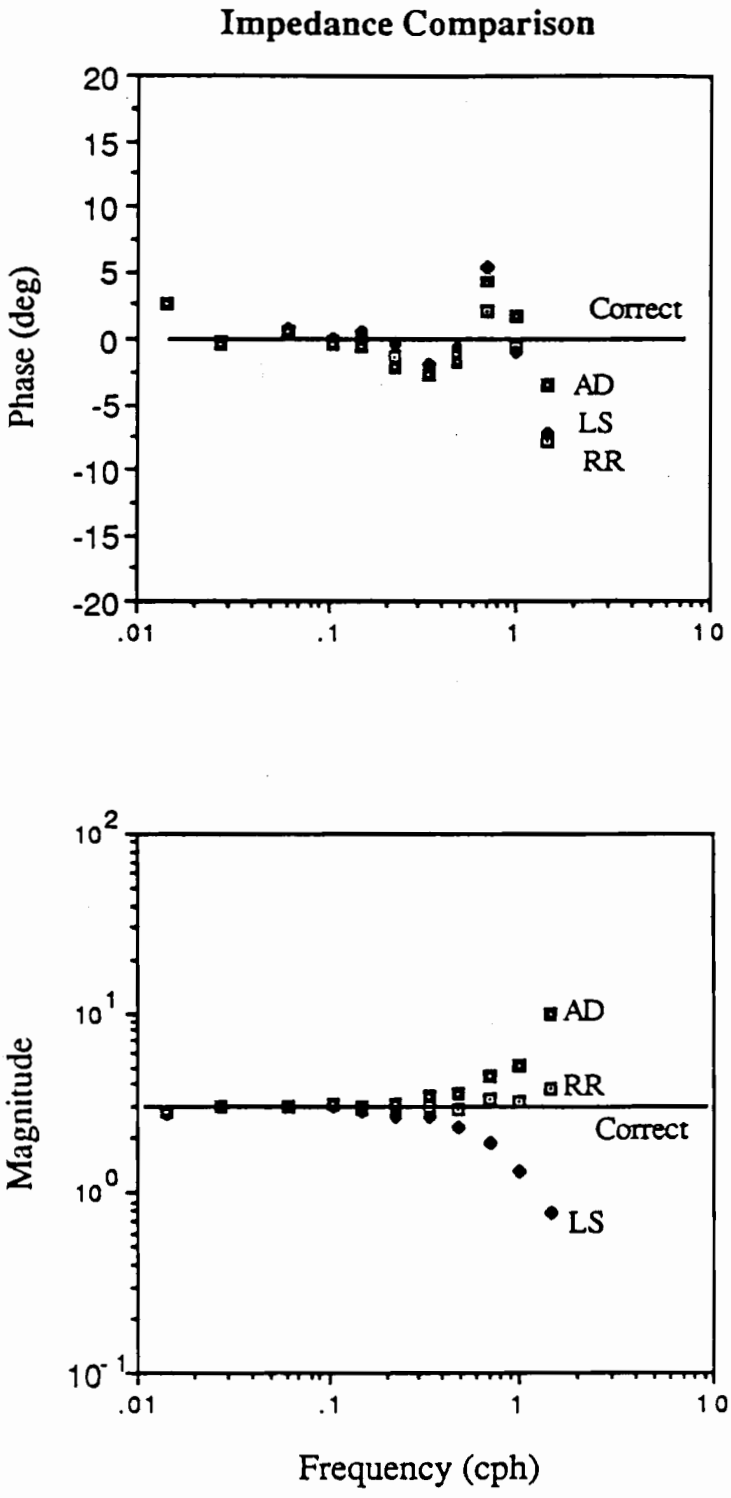

Figure 4.10: Comparison of remote reference impedance estimate (RR) with alternative least-squares (LS) and admittance formulation (AD) impedance estimates for noisy data. Noise was added to the synthetic data set at the level shown in Figure 4.9. The figure shows the three estimates for the Z12 impedance component (which has a true, frequency-independent value of 2.0 + 0.0 i). Although the noise produces significant bias in the magnitude of the LS and admittance estimates, the remote reference method shows only random errors.

estimate)

$$\mathrm{Var}[\bar{\Omega}] = \sigma^2[\bar{\Omega}] = E[\bar{\Omega}^2] - E^2[\bar{\Omega}] \qquad 4.147$$

The quantity σ is called the **standard error** or the **standard deviation.** The second term on the r.h.s. of 4.146 gives the square of the **bias error** (the squared deviation of the mean of the estmates from the true value). Dividing the standard error by the true value of the estimated quantity one obtains the **normalized standard error**

$$\varepsilon_r = \frac{\sigma[\Omega]}{\Omega} \qquad 4.148$$

also called the **coefficient of variation.**

Errors on Autopower Estimates

The statistical errors on power spectra result only from the statistical uncertanty associated with the FFT process. The presence of random noise on the time series introduces a bias, not a random error, into the power estimates.

Denoting the power estimate obtained from an individual spectral line (from a FFT) as S^n it can be shown (Bendat & Piersol, 1971) that

$$\varepsilon_r = \frac{\sigma[S^n]}{S^n} = \sqrt{\frac{2}{\lambda}} \qquad 4.149$$

where λ is the number of degrees of freedom. For a single spectral line $\lambda = 2$ and thus $\varepsilon_r = 1$ ie. the random variation of power estmates from individual spectral lines is of the same magnitude as the actual power value. It should be noted that ε_r is independent of the length of input time series - increasing the length of the time series will not decrease the magnitude of the random error.

Smoothing the power spectrum decreases the random error by increasing the number of input spectral lines used to define each result ie. by increasing the number of degrees of freedom of each estimate. For a frequency band of width B_f the number of input degrees of freedom is given by

$$\lambda = 2 B_f L \qquad 4.150$$

where L is once again the total length of the input time series. Note that the number of degrees of freedom is simply equal to two times the number of original spectral lines falling within the band. Averaging into bands of width B_f may be achieved by "frequency smoothing" into groups of $m = B_f L$ spectral lines, or "segment smoothing" by segmenting the original time series into m segments and averaging the value for each spectral line over

the m segments.

Substituting equation 4.150 into 4.149 one finds the standard error for the power estimate from a band of width B_f is given by

$$\varepsilon_r = \sqrt{\frac{1}{B_f L}} = \sqrt{\frac{1}{m}} \qquad 4.151$$

This equation indicates that for a specified frequency range increasing the total length of the input time series will result in a decrease in the standard error if smoothing is performed. The error decreases with the inverse of the square root of the event length.

It is convenient to express the uncertanty of the power estimates in terms of a confidence limit rather than the standard error. Bendat & Piersol (1971) show that the random errors on a smoothed power estimate have a χ^2 distribution with $\lambda = 2\, B_f L$. The $(1 - \alpha)$ confidence limit is then given by

$$\left[\frac{\lambda \bar{S}(\omega)}{\chi^2_{\lambda;\, \alpha/2}} \leq S(\omega) < \frac{\lambda \bar{S}(\omega)}{\chi^2_{\lambda;\, 1-\alpha/2}} \right] \qquad \lambda = 2\, B_f L \qquad 4.152$$

Note that when written without superscript "n", S refers to a band-averaged value. This equation will be used in chapter 6 to calculate confidence limits on power spectra derived from Tasman Project recordings.

When choosing a band-averaging system to determine a power spectrum, care should be taken that the frequency bands are sufficiently narrow to be able to represent all detail in the true spectrum. If bands are too wide a bias error may be introduced into the power estimates (Figure 4.11). For example, when analysing geomagnetic data containing deterministic diurnal and tidal lines it is necessary to define thin spectral bands around these frequencies so that the strong lines present do not bias the estimates of background power.

Time-domain averaging prior to spectral analysis will not alter the number of degrees of freedom associated with spectral bands. Although such averaging will change the effective number of input data points, the corresponding change in the number of output spectral lines simply involves omision of the highest frequency lines. For periods longer than the averaging interval, the number of input degrees of freedom will not be altered. If aliasing is significant, time-domain averaging may however cause biasing of spectral estimates.

Coherence Functions and Associated Error Estimates

The coherence function provides a measure of the degree of correlation of two time series as a function of frequency. The coherence between time series f(t) and g(t) is defined

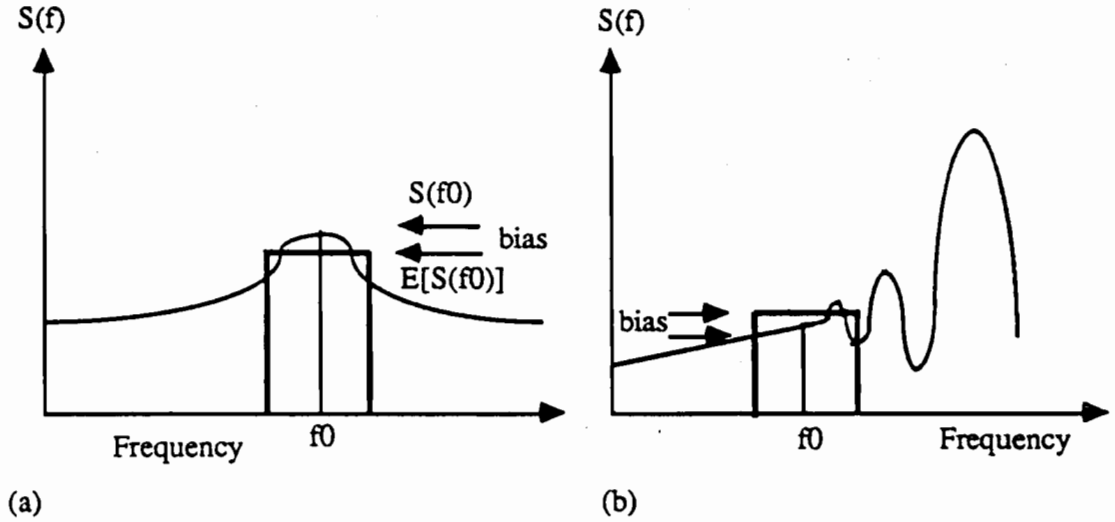

Figure 4.11: Illustration of bias error introduced by band averaging. In (a) the band is too broad to closely represent the spectrum at f0 and in (b) bias results from side-band effects associated with a strong spectral line near f0. The bias is equal to the difference between the true value of the power at frequency f0, ie. S(f0) and the estimate of the power derived from band averaging ie.E[S(f0)].

$$\bar{\gamma}^2_{FG}(\omega) = \frac{\left|\bar{S}_{FG}(\omega)\right|^2}{\bar{S}_{FF}(\omega)\,\bar{S}_{GG}(\omega)} \qquad 4.153$$

For time series which are perfectly correlated at a frequency ω_0, $\gamma^2(\omega_0) = 1.0$ and for time series which are uncorrelated at a particular frequency $\gamma^2(\omega_0) = 0.0$. Unless otherwise specified, in this thesis "coherence" refers to the squared quantity on the l.h.s of equation 4.153.

The coherence defined in equation 4.153 is the **ordinary coherence.** For multiple input systems (such as the impedance problem) it is commonly necessary to also use multiple and partial coherence estmates. The **multiple coherence** is used to provide a measure of how much signal in a time series is explained by (coherent with) the signal in more than one other time series. For the system

$$H_1(\omega)\,X_1(\omega) + H_2(\omega)\,X_2(\omega) + \ldots H_i(\omega)\,X_i(\omega) = Y(\omega) \qquad 4.154$$

the multiple coherence between the output $Y(\omega)$ and all of the inputs $X_i(\omega)$, $\gamma^2_{Y.X}(\omega)$, is given by

$$\gamma^2_{Y.X} = \frac{\sum H_i(\omega)\, S_{iY}(\omega)}{S_{YY}(\omega)} = 1 - \frac{S_{ZZ}(\omega)}{S_{YY}(\omega)} \qquad 4.155$$

where the estimation notation has been omitted from each coherence and power term and S_{ZZ} is the residual power in Y not explained by any of the inputs. Note that H_i should be an unbiased estimate of the transfer function. For the two input system of equation 4.98a the multiple coherence may be expressed in the form

$$\gamma^2_{E_X.B_XB_Y} = \frac{\gamma^2_{B_XE_X} + \gamma^2_{B_YE_Y} - 2\,\mathrm{Re}\left[\dfrac{S_{B_XB_Y} S_{B_YE_X} S_{E_XB_X}}{S_{B_XB_X} S_{B_YB_Y} S_{E_XE_X}}\right]}{1 - \gamma^2_{B_XB_Y}} \qquad 4.155b$$

where $\gamma^2_{BXBY}(\omega)$ etc. denote ordinary coherences as defined above. This form of the equation is convenient because it does not require the transfer functions to have been pre-calculated.

If two inputs X_i, X_j into equation 4.154 are themselves correlated to some degree then (unless H_j is zero and the X_j is not a true input) the ordinary coherence between X_i annd Y will not give a true indication of the degree of coherence of the two time series. For example if the transfer function H_j were zero the calculated coherence would still return a non-zero value. The **partial coherence** gives the corrected coherence between two time series after removal of the influence of a third time series from both time series being correlated. The partial coherence between input X_i and output Y after correction for the effects of input X_j is defined

$$\gamma^2_{iY.j}(\omega) = \frac{\left|S_{iY.j}(\omega)\right|^2}{S_{ii.j}(\omega)\, S_{YY.j}(\omega)} \qquad 4.156$$

where

$$S_{iY.j}(\omega) = S_{iY}(\omega)\left[1 - \frac{S_{ij}(\omega)\, S_{jY}(\omega)}{S_{jj}(\omega)\, S_{iY}(\omega)}\right] \qquad 4.157a$$

$$S_{ii.j}(\omega) = S_{ii}(\omega)\left[1 - \gamma^2_{ij}(\omega)\right] \qquad 4.157b$$

$$S_{YY.j}(\omega) = S_{YY}(\omega)\left[1 - \gamma^2_{Yj}(\omega)\right] \qquad 4.157c$$

Note that the presence of noise on a component used in an ordinary, multiple or partial coherence calculation will cause a reduction in the coherence value. Such a reduction cannot always be viewed as bias, since it is often the aim of the coherence calculation to determine the reduction in coherence caused by the presence of the noise.

Confidence limits on coherence functions have a complicated form. For coherence estimates in the range $0.35 \leq \gamma^2 < 0.95$ and with greater than 40 degrees of freedom (λ is defined as for the power estmates above) the $(1-\alpha)$ confidence limit is defined

$$\left[\tanh \{ w(\omega) - \frac{1}{\lambda - 2} - \sigma_w z_{\alpha/2} \} < \gamma_{FG}(\omega) \leq \tanh \{ w(\omega) - \frac{1}{\lambda - 2} + \sigma_w z_{\alpha/2} \} \right]$$

where

$$w(\omega) = \frac{1}{2} \ln \left[\frac{1 + \bar{\gamma}_{FG}(\omega)}{1 - \bar{\gamma}_{FG}(\omega)} \right] = \tanh^{-1} \left[\bar{\gamma}_{FG}(\omega) \right]$$

$$\sigma_w = \frac{1}{\lambda - 2} \qquad \lambda = 2 B_f L \qquad 4.158$$

and z_α is the 100α percentage point of the standardized normal distribution (Bendat & Piersol 1971). In most geomagnetic studies coherence functions are used in only a qualitative manner and small errors (say < 0.05) are not of great concern. For most of the range of cases where formula 4.154 is applicable the errors will be less than 0.05 (Figure 4.12) at the 95% confidence level.

A more important error for the coherence is the bias error resulting from the dependence of the coherence on the number of degrees of freedom λ. If the coherence between any two time series is calculated using power spectral values based on only two degrees of freedom it will always equal 1.0 (Bendat & Piersol 1971). As the number of degrees of freedom increases the coherence will decrease towards the true value. The test for zero true coherence compares a calculated coherence (at a particular value of λ) with the corresponding level of coherence which would be obtained between independent time series. If the calculated coherence exceeds the level of zero true coherence at some level of significance then the coherence may be considered significant.

The formula for the level of zero true significance, C, is given by Chave & Filloux (1985) as

$$C = 1 - (1 - \alpha)^{\frac{2}{\nu - 2}} \qquad 4.159$$

where α corresponds to the 100α % confidence level and ν is the number of degrees of freedom. For p input time series (p=1 for an ordinary coherence; p > 1 for a multiple

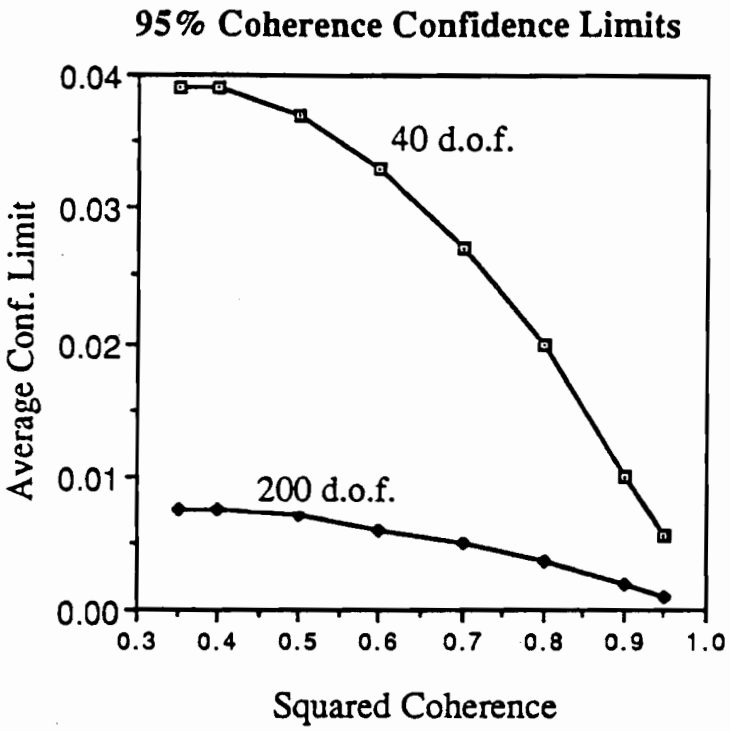

Figure 4.12: Magnitude of 95% level confidence limits on ordinary coherence estimates for 40 and 200 degrees of freedom (d.o.f.). For example for a squared coherence of 0.60 and 40 d.o.f the coherence lies in the range 0.60 ± 0.03. The confidence limits on coherence estimates are given by equation 4.158 and are assymmetric, with the upper confidence limit less than the lower limit. The confidence limit shown in the above figure is the mean of the magnitude of the upper and lower confidence limits.

coherence) and λ twice the number of input spectral estimates (as in 4.152)

$$\nu = \lambda - 2p + 2 \qquad 4.160$$

These formulae will be used in chapter 6 to evaluate confidence limits on coherences between Tasman Project recordings.

Error estimates on transfer functions

During the evaluation of transfer functions, random noise on input and output time series as well as statistical errors from FFTs will contribute to random errors in the resulting transfer functions. The derivation of equations for the random errors and thus confidence limits on multiple-input system transfer functions (such as the impedance) is described in Bendat & Piersol (1971). For the system of equation 4.155 the random error on transfer function H_i is given by

$$\left| \overline{H}_i(\omega) - H_i(\omega) \right|^2 \leq \overline{r}_i^{\,2}(\omega) \qquad 4.161$$

where

$$\overline{r}_i^{\,2}(\omega) = \frac{2q}{\lambda - 2q} \left(F_{n1,n2;\,\alpha} \right) \frac{\left[1 - \overline{\gamma^2_{y.x}}(\omega) \right]}{\left[1 - \overline{\gamma^2_{i.x}}(\omega) \right]} \frac{\overline{S}_Y(\omega)}{\overline{S}_i(\omega)} \qquad 4.162$$

q = the number of inputs

λ = number of degrees of freedom of each spectral estimate

$F_{n1,n2;\,\alpha}$ = 100α percentage point of an F distribution with $n1 = 2q$ and $n2 = \lambda - 2q$ degrees of freedom

$S_i(\omega)$, $S_Y(\omega)$ = estimates of autopowers for input i and output

$\gamma^2_{y.x}(\omega)$ = estimated multiple coherence between the output and all inputs

$\gamma^2_{i.x}(\omega)$ = estimated multiple coherence between input i and all other inputs

For a two input system such as an impedance determination (for the equation 4.98a $X1=B_X$, $X2=B_Y$, $Y=E_X$, $H1=Z_{XX}$, $H2=Z_{XY}$) the equation simplifies slightly with the multiple coherence $\gamma^2_{i.x}(\omega)$ becoming simply the ordinary coherence between the two inputs.

The transfer functions H (eg. the impedance terms) are usually complex numbers. Confidence limits on the real and imaginary, amplitude and phase components of H are given by

$$\left[\mathrm{Re}\left(\overline{H}_i(\omega) \right) - \overline{r}_i(\omega) \leq \mathrm{Re}\left(H_i(\omega) \right) \leq \mathrm{Re}\left(\overline{H}_i(\omega) \right) + \overline{r}_i(\omega) \right] \qquad 4.163a$$

$$[\ \mathrm{Im}(\overline{H}_i(\omega)) - \overline{r}_i(\omega) \le \mathrm{Im}(H_i(\omega)) \le \mathrm{Im}(\overline{H}_i(\omega)) + \overline{r}_i(\omega)\ ] \qquad 4.163b$$

$$\left[\ |\overline{H}_i(\omega)| - \overline{r}_i(\omega) \le |H_i(\omega)| \le |\overline{H}_i(\omega)| + \overline{r}_i(\omega)\ \right] \qquad 4.163c$$

$$\left[\ \overline{\varphi}_i(\omega) - \sin^{-1}\left(\frac{\overline{r}_i(\omega)}{|\overline{H}_i(\omega)|}\right) \le \varphi_i(\omega) \le \overline{\varphi}_i(\omega) + \sin^{-1}\left(\frac{\overline{r}_i(\omega)}{|\overline{H}_i(\omega)|}\right)\ \right] \qquad 4.163d$$

(Figure 4.13).

The bias error in transfer function estimates may result from non-linear or time varying transfer functions, bias in the autopower and crosspower estimates and noise on the inputs (Bendat & Piersol 1971). The last source was discussed in detail in section 4.2.3 above.

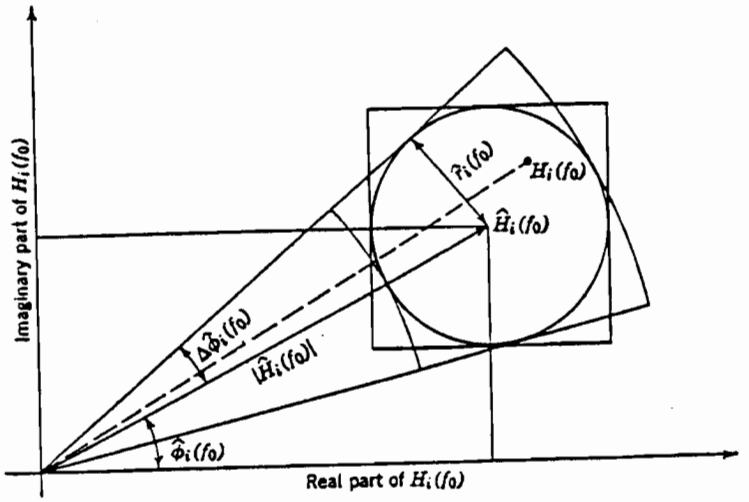

Figure 4.13: Illustration of the confidence limit on a transfer function. The confidence limit is equal for the real and imaginary components of the complex transfer function (from Bendat & Piersol 1971).

Error Analysis for Remote Reference Calculations

The full derivation for error estimates on remote reference impedances may be found in Gamble et al. (1979b). The variance on each remote reference term is given by

$$\mathrm{Var}\left[Z_{ij}^{R} \right] = \frac{\overline{|\eta_i|^2}\,\overline{|A_j|^2}}{N\,|D|^2} \qquad 4.164$$

where N is the ensemble of spectral lines (frequency averaging) or segments (segment averaging) used to estimate the impedance, the overbars now indicate averaging over the ensemble and

$$A_j^* = R_j^* \overline{B_k R_k^*} - R_k^* \overline{B_k R_j^*} \quad \text{and} \quad (j,k) = (x,y) \text{ or } (y,x) \qquad 4.165$$

$$D = \overline{B_X R_X^*}\,\overline{B_Y R_Y^*} - \overline{B_X R_Y^*}\,\overline{B_Y R_X^*} \qquad 4.166$$

For large N, η_i may be approximated by η_i^p given by

$$\eta_i^p = E_i - Z_{ij}^{R} B_j \qquad 4.167$$

with implied summation over index j. Dividing the denominator and numerator of 4.164 by L^4 one obtains

$$\mathrm{Var}\left[Z_{ij}^{R} \right] = \frac{\overline{|\eta_i^{p'}|^2}\,\overline{|A_j'|^2}}{N\,|D'|^2} \qquad 4.168$$

where

$$\overline{|\eta_i^{p'}|^2} = S_{E_iE_i} - 2\,\mathrm{Re}\left(Z_{iX}^{R} S_{B_X E_i} + Z_{iY}^{R} S_{B_Y E_i} - Z_{iX}^{R} Z_{iY}^{R} S_{B_X B_Y} \right) + |Z_{iX}^{R}|^2 S_{B_X B_X} + |Z_{iY}|^2 S_{B_Y B_Y} \qquad 4.169a$$

$$\overline{|A_j'|^2} = S_{R_jR_j} |S_{B_kR_k}|^2 - 2\,\mathrm{Re}\left(S_{R_jR_k} S_{B_kR_j} S_{R_kB_k} \right) + S_{R_kR_k} |S_{B_kR_j}|^2 \qquad 4.169b$$

and

$$|D'|^2 = \left| S_{B_XR_X} S_{B_YR_Y} - S_{B_XR_Y} S_{B_YR_X} \right|^2 \qquad 4.169c$$

The standard deviation is given, as above, by the square root of the variance.

Gamble et al. (1979b) provide the theory for relating the variance on an impedance to the variance on particular functions of the impedance such as the phase. They also provide

the following results. For the impedance component Z_μ where μ equals XX, XY, YX or YY

$$\mathrm{Var}[\mathrm{Re}(Z_\mu)] = \mathrm{Var}[\mathrm{Im}(Z_\mu)] = \frac{1}{2}\mathrm{Var}[Z_\mu] \qquad 4.170$$

$$\mathrm{Var}[\rho_{a\mu}] = 0.4\,T\,\rho_{a\mu}\,\mathrm{Var}[Z_\mu] \qquad 4.171$$

and

$$\mathrm{Var}[\varphi_\mu] = \frac{8\cos^4\varphi_\mu\,|Z_\mu|^2\,\mathrm{Var}[Z_\mu]}{|Z_\mu + Z_\mu^*|^4} \qquad 4.172a$$

which simplifies to

$$\mathrm{Var}[\varphi_\mu] = \frac{\mathrm{Var}[Z_\mu]}{2|Z_\mu|^2} \qquad 4.172b$$

An additional result applied to the Tasman data and derived using the theory provided by Gamble et al. (1979b) is

$$\mathrm{Var}[\mathrm{Re}(a\,Z_\mu)] = \mathrm{Var}[\mathrm{Im}(a\,Z_\mu)] = \frac{1}{2}a^2\,\mathrm{Var}[Z_\mu] \qquad 4.173a$$

and thus for C in m and Z in $\mu V.m^{-1}.nT^{-1}$ one obtains

$$\mathrm{Var}[\mathrm{Re}(C_\mu)] = \mathrm{Var}[\mathrm{Im}(C_\mu)] = \frac{1}{2}\left(\frac{1000}{\omega}\right)^2\mathrm{Var}[Z_\mu] \qquad 4.173b$$

Also note that

$$\mathrm{Var}[|Z|) = \frac{1}{2}\mathrm{Var}[Z] \qquad 4.174$$

A further result that can be derived from the remote reference method calculations is a separation of signal power from noise power for all input time series. These results are obtained as follows. If the noises on all components are uncorrelated with each other and with the signals, the matrix $[E^P E]$

$$[E^P E] = Z^R[BE] = [ER][BR]^{-1}[BE] \qquad 4.175$$

(using Gamble et al.'s notation) has the expectation value of the spectral density matrix $[E_S E_S]$ where subscript S denotes signal. Expansion of 4.175 confirms this result

$$[E^P E] = \begin{bmatrix} Z^R_{XX} S_{B_X E_X} + Z^R_{XY} S_{B_Y E_X} & Z^R_{XX} S_{B_X E_Y} + Z^R_{XY} S_{B_Y E_Y} \\ Z^R_{XY} S_{B_X E_X} + Z^R_{YY} S_{B_Y E_X} & Z^R_{YX} S_{B_X E_Y} + Z^R_{YY} S_{B_Y E_Y} \end{bmatrix} \qquad 4.176$$

Although Z^R is an unbiased estimate of the impedance, random errors in Z^R and in the crosspowers in 4.176 mean that $[E^P E]$ will not exactly equal $[E_S E_S]$. From symmetry it is

evident that the exact value of $[E_S\, E_S]$

$$[E_S\, E_S] = \begin{bmatrix} S_{E_{XS}E_{XS}} & S_{E_{XS}E_{YS}} \\ S_{E_{YS}E_{XS}} & S_{E_{YS}E_{YS}} \end{bmatrix} \qquad 4.177$$

must be Hermitean. The signal matrix is therefore estimated using the Hermitean part of $[E^P E]$ ie.

$$[E_S\, E_S]^P = \frac{1}{2}\left([E^P E] + [E^P E]^\dagger \right) \qquad 4.178$$

where the daggar denotes the Hermitean adjoint. Subtraction of the estimated signal powers from the total power provides an estimate of the noise powers.

In a similar manner the signal power on the magnetic field and remote reference are estimated from

$$[H_S\, H_S]^P = \frac{1}{2}\left([H^P H] + [H^P H]^\dagger \right) \text{ and } [H^P H] = [H R][E R]^{-1}[E H] \qquad 4.179a \text{ \& } b$$

$$[R_S\, R_S]^P = \frac{1}{2}\left([R^P R] + [R^P R]^\dagger \right) \text{ and } [R^P R] = [R E][H E]^{-1}[H R] \qquad 4.180a \text{ \& } b$$

Gamble et al. (1979b) indicate that the non-Hermitean parts of the matrix $[E^P E]$ provides an estimate of the degree of correlated noise present between time series. Tests using a synthetic data set revealed that this is true for correlated noise on pairs of components. When correlated noise is added to a third component however the magnitude of the non-Hermitean terms may in fact decrease.

An advantage of performing a signal / noise separation is that it is then possible to recalculate the multiple coherence between each electric field component and the signal portion of the two magnetic components. This coherence will provide a second measure (in addition to the signal / noise separation for the electric field data) of how well the electric fields are correlated to the source field at the MT site. The multiple coherence is re-calculated using equation 4.157 but with the original estimates of S_{BXBX}, S_{BYBY} and S_{BXBY} replaced by the signal portion of these powers obtained from 4.179.

Figure 4.14 illustrates the recalculation of multiple coherences for synthetic data and for real data. With synthetic data the method works well although noise on the remote reference components introduces random errors into the recalculated multiple coherence. With real data the method works only moderately well. Source-field differences between the remote and MT site and correlated noise may bias the estimates of the magnetic signal power and these estimates will also contain accumulated random errors. When applied to real data the re-calculated partial and multiple coherences occasionally fall outside the range of zero to one.

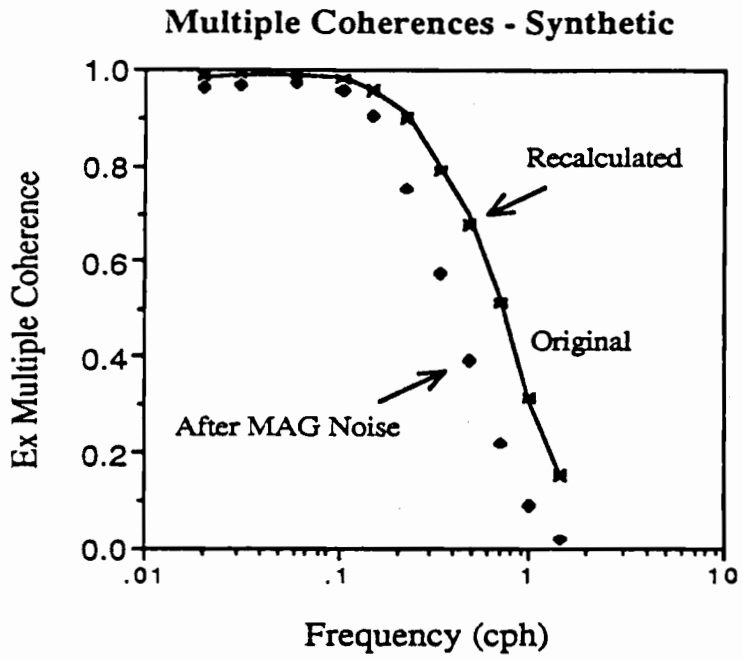

(a)

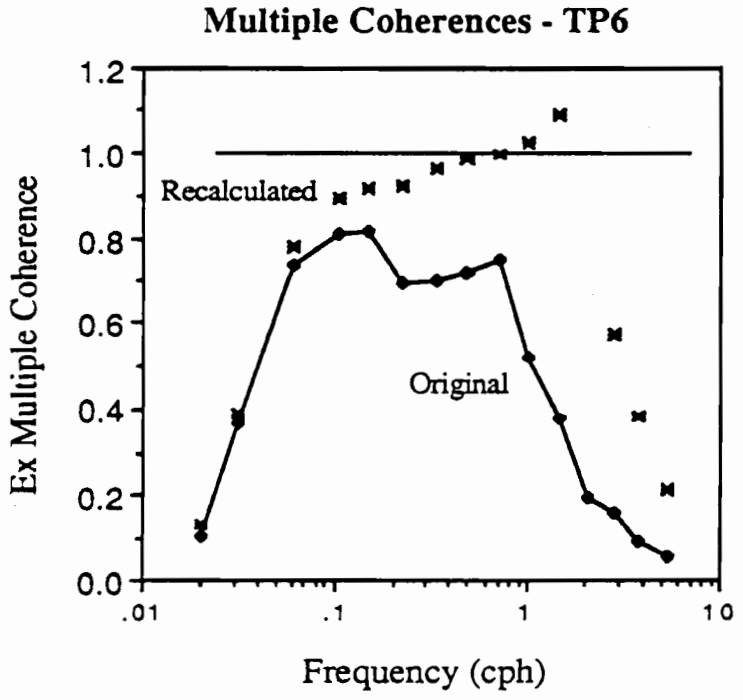

(b)

Figure 4.14: Recalculation of multiple coherences after signal/noise separation.
(a) Synthetic data; noise was added to the HEF components of a perfectly correlated data set to produce the original multiple coherences. Further noise was then added to magnetic components causing a decrease in the coherence. After the application of a signal / noise separation the multiple coherences were recalculated using the calculated signal portion only of the magnetic-field power. The recalculated coherences closely matched the original values.

(b) Real data; the multiple coherence recalculated for the E_X component at site TP6. The recalculated coherence values may be biased and fall outside the allowable range of [0,1].

4.3 Geomagnetic Storm and Substorm Source-Fields

This section will provide a review of magnetic storm and substorm source-fields and in particular examine an aspect of importance to geomagnetic induction studies: the spatial uniformity of the source-fields. Estimates will then be made for the scale of source-fields involved in the Tasman Project and for the possible effects of source-field non-uniformity on Tasman Sea geomagnetic induction. Because the subjects of the magnetosphere, ionosphere and magnetic source-fields comprise extensive areas of study in themselves, this thesis provides only a brief review (directly from the literature) of important aspects of these subjects.

Physical Features Involved in Storm and Substorm Generation

Before examining the dynamic behaviour of the electromagnetic fields during storms it is necessary to consider the different elements involved in the storm activity, viz. the Earth with its atmosphere, ionosphere and magnetosphere, the sun and the 'solar wind' generated by the sun.

The Earth itself is insulated from direct electric current flow from external regions by the insulating lower atmosphere. It does however influence the behaviour of electromagnetic fields in the ionosphere and magnetosphere, both through the interaction of the static magnetic field with these processes and also by providing a region of finite conductivity with which ionospheric processes couple. The actual distribution of electrical conductivity within the Earth does not influence the external, inducing patterns of electromagnetic activity (since the magnetic fields of induced telluric currents at ionospheric heights are small compared with the Earth's main field and locally induced fields).

The 'neutral' atmosphere extends from the surface of the Earth to a height of around 50 km and effectively insulates the Earth. At the Earth's surface the air has a conductivity of 10^{-13}-10^{-14} $S.m^{-1}$ however this value increases with altitude (Rokityansky 1982). Above the neutral atmosphere lies a region in which an appreciable fraction of air molecules are ionized, called the ionosphere (Parkinson 1983). The ionisation is caused by solar radiation of varying wavelengths; mainly 100 - 1,000 nm X-rays and 10,000-15,000 nm ultraviolet rays, and to a lesser extent cosmic radiation (Parkinson 1983, Egeland et al. 1973). The lower boundary of the ionosphere is around 50-65 km above the surface of the Earth. The upper boundary is not well defined; at around 1000 km the effect of heavy ions such as oxygen becomes less than that of lighter ions such as hydrogen and helium (Figure 4 15a) while at 1500 km the ion density is generally less than 1 % of the maximum (Parkinson 1983, Egeland et al. 1973).

The ionisization of the ions and electrons on the sunward side of the Earth increases the electrical conductivity of the ionosphere. The increased conductivity permits electric current flow and makes the region an important component in storm and substorm

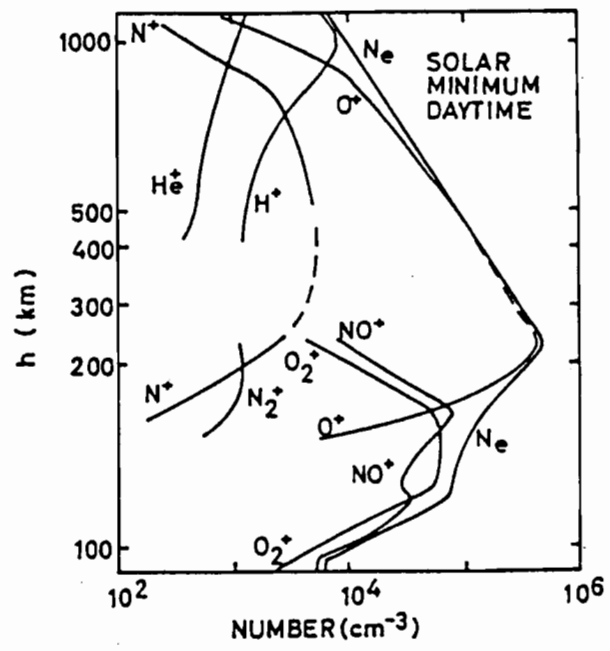

(a)

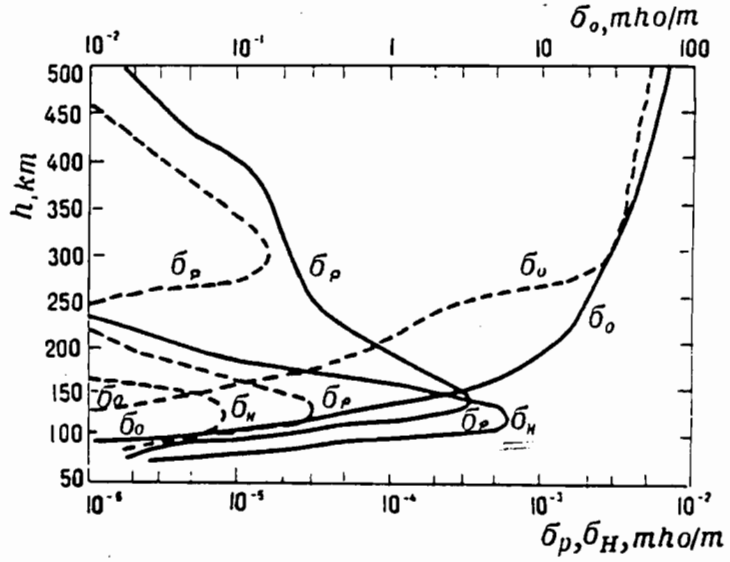

(b)

Figure 4.15: Composition and electrical conductivity of the ionosphere. (a) Density of different ions as a function of altitude (from Egeland et al. 1973). (b) Electrical conductivity of the ionosphere at mid-latitudes, solid curves are for noon and dashed curves are for midnight. Lateral electric current flow in the ionosphere is controlled by σ_H and σ_P (Hall and Pedersen conductivity respectively) and is concentrated around 110 km altitude. Field aligned currents are controlled by σ_0 (direct conductivity), and therefore have a much more conductive path (from Rokityansky 1982).

generation. In the ionosphere the presence of the geomagnetic field-lines and the relatively small density of the ionised particles results in the electrical conductivity being significantly anisotropic. Figure 4.15b shows the distribution of electrical conductivity with altitude. The high conducting region around 110 km is the location of much of the ionospheric electric current flow (Mareschal 1986).

The magnetosphere is defined as the region above the Earth's surface in which "physical processes are dominated by the geomagnetic field" (Egeland et al. 1973, p 103). The lower boundary of this region is around 120 km, below which the effect of particle collisions is greater than the influence of the geomagnetic field on the ions (Egeland et al. 1973). The upper boundary extends to approximately 11 R_E (Earth radii) on the sunward side of the Earth and to a much greater distance, at least to the lunar orbit ie. 60 R_E on the night side (Figure 4.16a). The upper region of the magnetosphere is composed mainly of protons and electrons while the lower region also contains heavier ions such as those of helium, oxygen, neon and nitrogen.

The final 'ingredient' for generating magnetic storms is the solar wind, a plasma mainly of electrons and protons continuously emitted from the sun. This plasma travels with a velocity of order 300-400 $km.s^{-1}$ (Rokityansky 1982, Volland 1984). The high electrical conductivity of the plasma "freezes" the magnetic flux lines permeating the plasma as it leaves the sun, and results in the solar wind carrying a frozen magnetic field. This field is called the interplanetary magnetic field, IMF (Figure 4.17). On arrival at the Earth the IMF is of a typical strength 3-5 nT and its field lines are aligned at approximately 45° to the Earth-Sun line (in the ecliptic plane) with a polarity which changes with a period of order one week. The solar wind is quite turbulent and the direction of the IMF often contains a substantial north-south component (Parkinson 1983). Changes in the intensity and velocity of the solar wind, and the polarity of the IMF influence the occurrence of magnetic storms and substorms (Volland 1984).

As the solar wind approaches the Earth it exerts a pressure which compresses the geomagnetic field on the sunward side of the Earth to 10-11 R_E. The region inside the boundary of the geomagnetic field comprises the magnetosphere and the boundary is called the magnetopause. The magnetosphere may be further compressed to radii of 6 R_E during magnetic disturbances (Volland 1984). During quiet geomagnetic periods only those geomagnetic field lines meeting the surface at geomagnetic latitudes of less than 72° close on the sunward side (Figure 4.16b). Field lines at higher latitudes and those on the night side of the Earth are swept into the magnetotail.

There exist several further structures in the magnetosphere which are of importance in substorm and storm generation. The first structure is the cleft which occurs between the geomagnetic field-lines closing on the sunward side of the Earth and those drawn into the magnetotail. The low magnetic field in this region allows some penetration of the solar wind. The second important structure is the neutral sheet occurring in the ecliptic plane in

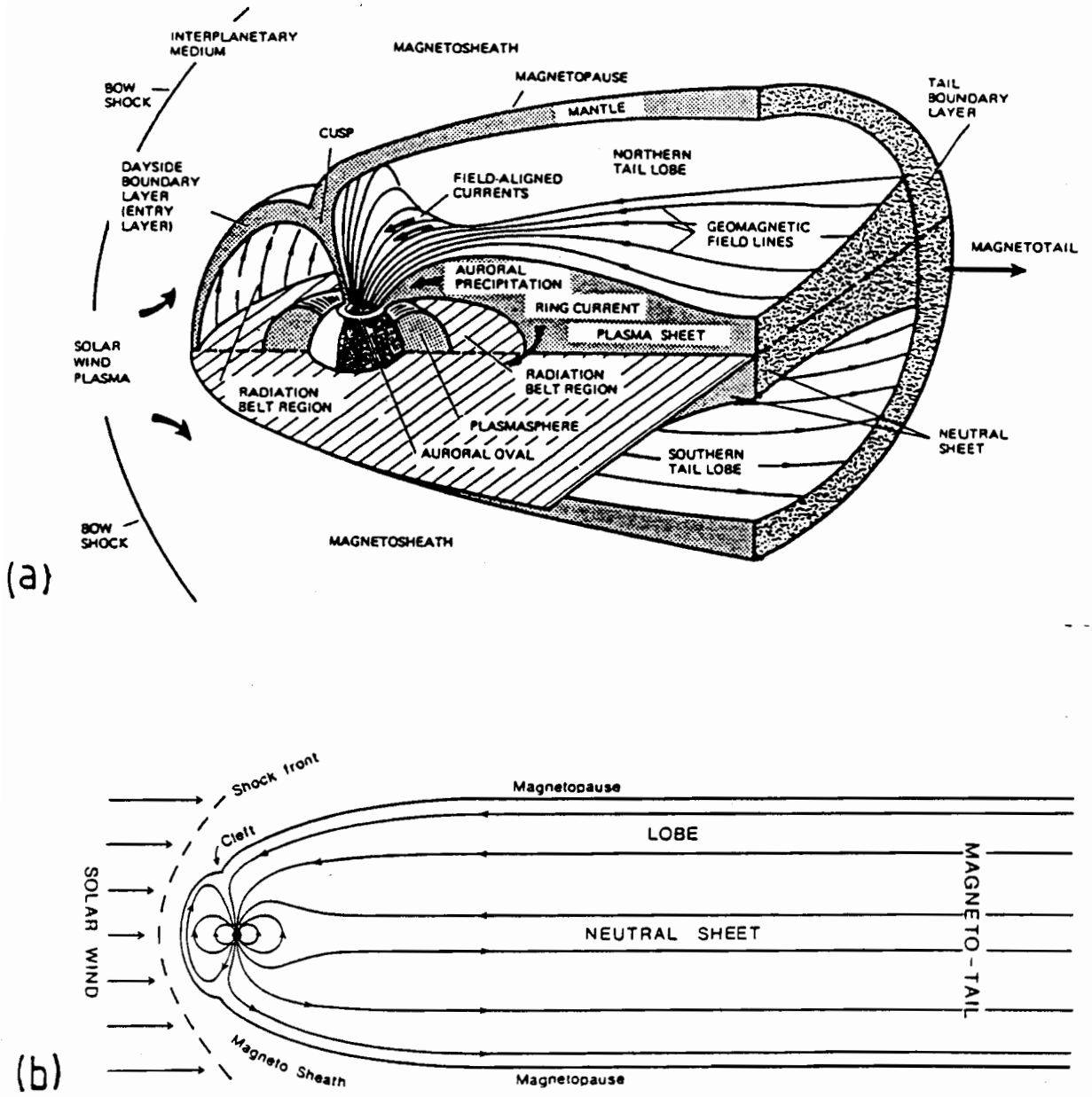

Figure 4.16: Structure of the magnetosphere. (a) Basic features (from Volland 1984). (b) Simplified view across the ecliptic plane showing magnetic field lines (Parkinson 1983). Most of the structural features of the magnetosphere are discussed in the text. The shock front is the position where the solar wind slows to sub-sonic velocity in the vicinity of the Earth.

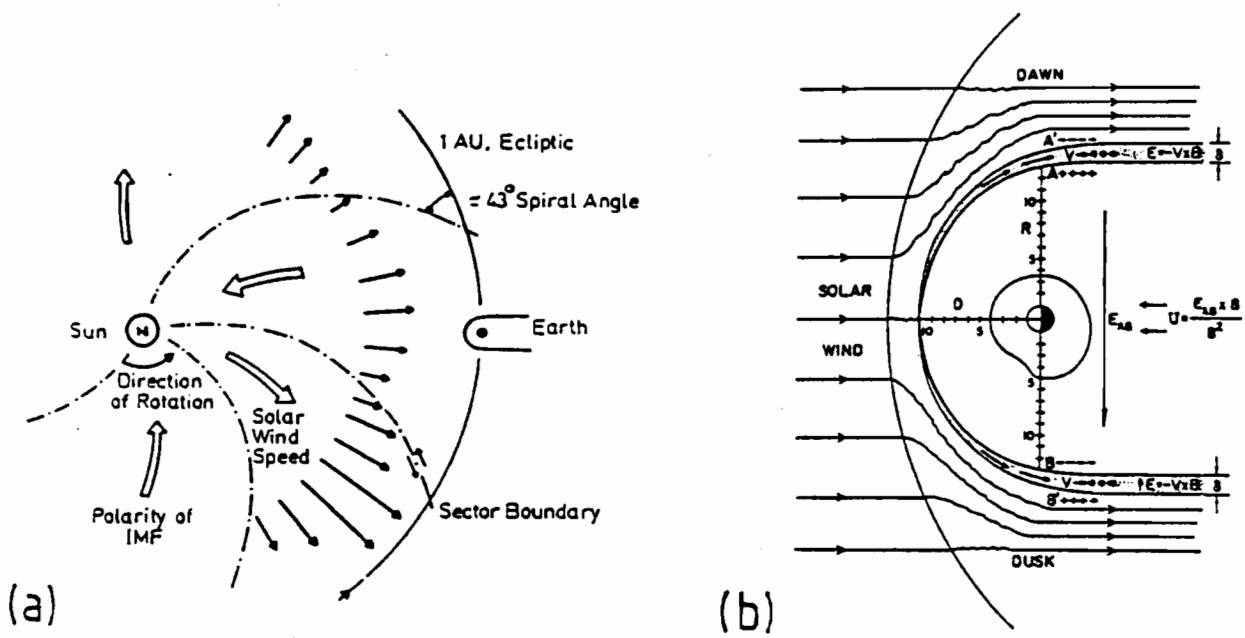

Figure 4.17: The solar wind and its interaction with the magnetosphere. (a) The solar wind is emitted from the sun and carries an interplanetary magnetic field IMF to the Earth. The small arrows show the strength and direction of the solar wind and the large arrows the direction and polarity of the IMF. (b) Equatorial view (from north) of the solar wind / magnetosphere interaction. The solar wind induces a westward electric field which drives magnetospheric convection (both figures from Volland 1984).

the magnetotail. The sheet lies between field lines directed away from the Earth and those directed to the Earth. Another important structure is the plasmapause, located at approximately 4 R_E, and separating the inner region of the magnetosphere (the plasmasphere) which rotates with the Earth and is relatively protected from the solar wind from the outer region of the magnetosphere which is strongly affected by the solar wind (Egeland 1973, Parkinson 1983). Finally, both inside and outside the plasmapause there exist energetic particles forming the Van Allen radiation belts.

Background Magnetospheric / Ionospheric Current Systems

There are a number of current systems which flow in the magnetosphere continuously or semi-continuously; storms and substorms can largely be described in terms of perturbations of these systems. Egeland et al. (1973) summarise the current systems as follows;

1. Magnetopause currents,
2. Neutral sheet currents,
3. The equatorial ring current,
4. Ionospheric auroral electrojet currents.

These four current systems are all interconnected and will now be discussed in more detail.

Magnetopause currents vary strongly with time but on average are directed from dawn to dusk (eastwards) on the day side of the Earth. The strong variation is caused by variations in the magnetic field just outside the magnetopause (Egeland et al. 1975). As highly conducting solar wind approaches the dipole field of the Earth, it too will have currents induced at its surface (Parkinson 1983). An eastwards current in the plasma, comprising an eastwards flow of protons and a westward flow of electrons, will cancel the dipole field in the cloud. This current will also increase the northwards field in the magnetosphere.

As the solar wind sweeps past the Earth the IMF it carries will induce an electric field aligned in the dawn to dusk direction across the ecliptic plain (Figure 6.17). This electric convection field is believed to be largely responsible for the stationary 'magnetospheric convection' or 'magnetospheric dynamo' system (Rokityansky 1982, Volland 1984) which produces the diurnal magnetic field variation at high geomagnetic latitudes (> 55°). In the neutral sheet, where the northwards component of the magnetic field is zero, the IMF-induced electric-field will cause a dawn to dusk (eastwards) current. Electrons will move towards dawn (westwards) and protons towards dusk. Because the highly conducting plasma 'freezes' magnetic-field flux lines, the neutral sheet current draws together magnetic field lines of opposite polarity in a process called 'field line reconnection' (Volland 1984). This process is important in models for the development of substorms.

The system of ionospheric currents in auroral regions involves the flow of current down geomagnetic field lines which connect the magnetopause to the ionosphere, and

closure of these field aligned currents through the ionosphere. Although their existence was proposed in the 1900's the existence of field-aligned (or Birkeland) currents was only confirmed by rocket observations in the 1960's. The field-aligned currents are an important source of geomagnetic variations at mid-geomagnetic latitudes (Kisabeth 1975) and are therefore important for geomagnetic induction studies.

There are two different configurations of currents (circuits) in the auroral ionosphere which superimpose to give the actual current flow. The first circuit involves a pair of current sheets occurring over the same longitude range with downgoing currents in a sheet slightly polewards of a sheet of upgoing current. The second circuit involves two current sheets at the same latitude but separated by 120° of longitude and centred on the line of midnight longitude (Parkinson 1983). The second circuit produces a diurnal variation in the auroral regions called the polar magnetic substorm as midnight sweeps diurnally over a point on the Earth's surface. The resulting ionospheric currents are characterised by a westward auroral electrojet (Hall) current in the local dawn hours and an eastwards current at local dusk. Inside the polar cap there is an almost homogeneous current flow and there may also be minor leakage to mid-latitudes (Rokityansky 1982). Figure 4.18 illustrates the observed surface magnetic field from a polar magnetic substorm.

The final current system is that of the equatorial ring current which is important in the theory of geomagnetic storms. The ring current can occur only at particular altitudes (3-10 R_E) where certain highly energetic particles (from the Van Allen belt) are trapped by closed geomagnetic field lines (Figure 4.19). As the trapped particles spiral between mirror points in the southern and northern hemisphere, close to the equatorial plane electrons are accelerated towards the morning meridian and protons towards night, thus creating a westward ring current (Volland 1984). The ring current is stronger on the night-side than the day-side indicating partial closure through descending field-lines and the auroral ionosphere (Volland 1984, Rokityansky 1982). According to Rokityansky (1982) the ring current is unlikely to produce magnetic field fluctuations of period less than about one hour.

Magnetospheric Substorms

The precise cause and dynamics of magnetospheric substorms are still much debated subjects and yet 'magnetospheric substorms are perhaps the most basic type of disturbances that occur throughout the magnetosphere' (Akasofu 1985). This thesis will contain only an elementary outline of proposed mechanisms for substorms. More detailed information may be found in Akasofu (1985), Volland (1984), Kisabeth (1975) and Kamide & Richmond (1986).

The magnetospheric substorm comprises what students of geomagnetic induction (especially at mid-latitudes) would simply refer to as a substorm. It is manifested in the surface magnetic field at lower latitudes as a 'bay' lasting one to several hours and forming

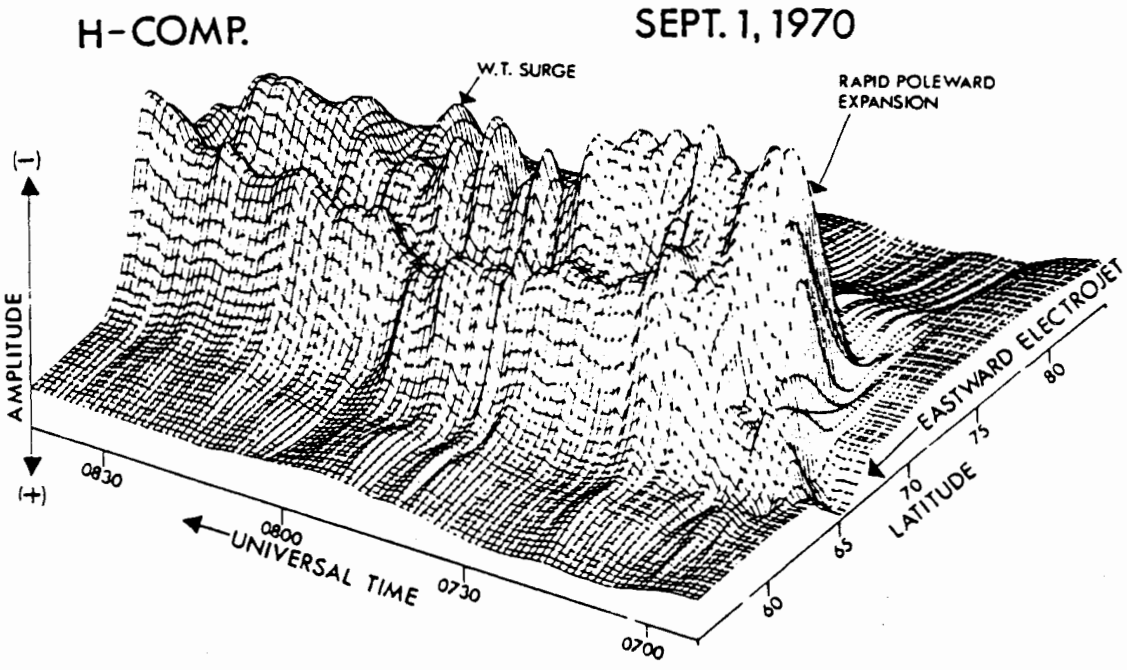

Figure 4.18: Perspective view of the development of a polar magnetic substorm (from Kisabeth 1975). Note the limited extent of the substorm B_H field into the mid-latitudes.

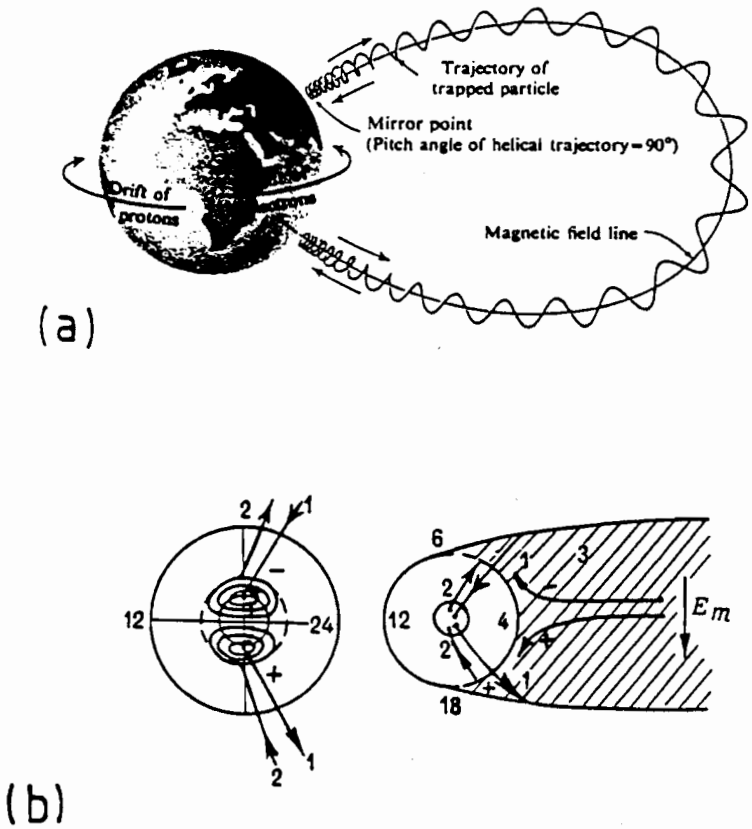

Figure 4.19: The equatorial ring current. (a) Charged particles trapped on geomagnetic field lines drift east (electrons) and west (positive ions) near the equatorial plane creating a westwards electric current (Volland 1984). (b) The ring current is asymmetric, with closure of the stronger night side current (4) though field aligned currents (2) and the auroral ionosphere. The figure also shows the field aligned currents between the auroral ionosphere and the magnetopause (1) (from Rokityansky 1982).

an increase in B_H over most of the night time hemisphere. It is likely that the irregular field fluctuations occurring during magnetic storms are also intense substorms (Parkinson 1983). Figure 4.20 illustrates a typical substorm, recorded during the Tasman Project. At higher latitudes a magnetospheric substorm is associated with other phenomena including polar magnetic substorms and an auroral substorms.

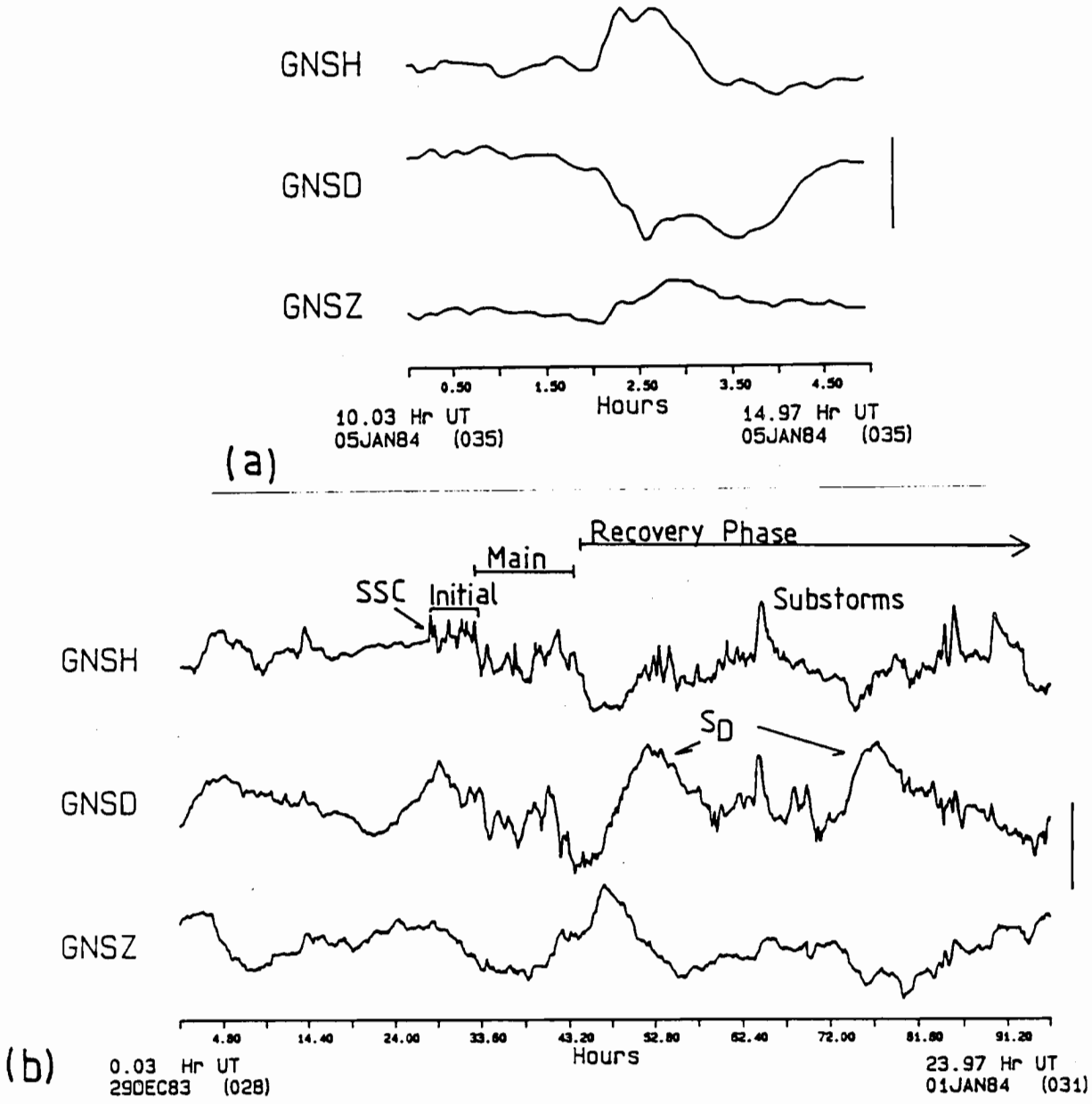

Figure 4.20: Magnetic substorm and magnetic storm recorded during the Tasman Project at site GNS.

(a) Substorm: the scale bar corresponds to 40 nT for B_H and B_D (labelled GNSH and GNSD respectively) and to 20 nT for B_Z (labelled GNSZ). Note the typical bay shape of the event and the significant B_D response.

(b) Storm: the scale bar corresponds to 80 nT for B_H and B_D and to 40 nT for B_Z. The storm shows a sudden commencement, initial and main phases but the recovery phase is partially masked by diurnal variation and shorter period field fluctuations. Note the enhancement of the diurnal variation in B_H and B_D (S_D) after the commencement of the storm.

The occurrence of substorms is closely related to the periods of southwards IMF. During these periods some of the geomagnetic field lines may link with IMF field lines, effectively opening the magnetosphere to the solar wind; this state is called the 'open magnetosphere' (Parkinson 1983, Volland 1984).

There are two main models relating the southwards IMF to substorm occurrence. In the first model the southwards IMF is proposed to cause an increase in the magnetic field in the magnetotail, enhancing field line reconnection and causing a meeting of field lines from either side of the neutral sheet (Figure 4.21). A region of magnetized plasma is free to be swept off by the solar wind leaving a shortened magnetotail of length 20-30 R_E (Volland 1984, Parkinson 1983). During contraction of the near-tail field, ions and electrons are heated and may precipitate into auroral regions creating the auroral activity which accompanies substorms. Energetic particles will enhance the ring current and cause an increase in the night-side ionospheric conductivity along the auroral oval resulting in an enhanced auroral (westward) current. Although this process of substorm generation is called 'explosive magnetic reconnection' Akasofu (1985) argues that it may be directly driven by the solar wind and the IMF, and need not involve the storage and sudden release of energy.

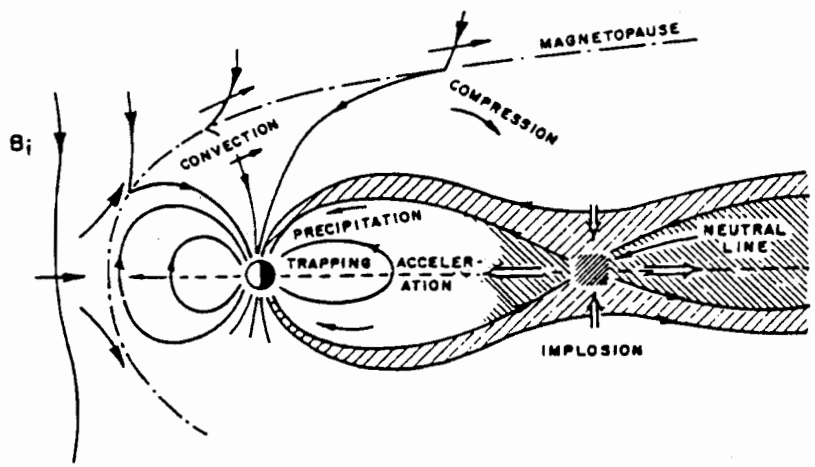

Figure 4.21: Illustration of the explosive magnetic reconnection model of magnetospheric substorm development (from Parkinson 1983).

The second mechanism proposed for substorm generation involves a thinning of the neutral sheet of the magnetotail and a diversion of the crosstail currents (Volland 1984). The process is again accompanied by the development of a current system involving field aligned currents and the night auroral electrojet and the streaming of plasma into the ring current. The completion of the circuit of the auroral currents is predominantly through field-aligned currents and the magnetosphere. An equivalent, purely ionospheric, current system can also explain the observed surface magnetic fields and was favoured in earlier models for substorms (eg. Silsbee & Vestine 1942). It is now thought that at most only a small fraction of current follows an ionospheric path (Parkinson 1983).

The substorm event as described above is called a DP1 event and produces substorm fields which extend to lower latitudes (Parkinson 1983, Egeland 1973). The background, current systems producing the polar magnetic substorms are called DP2 events. The current flow associated with these events is also enhanced during periods of southwards IMF but only very intense DP2 events produce magnetic fields at lower geomagnetic latitudes.

Magnetic Storms

Magnetic storms occur at the rate of several storms per month; eleven disturbances classified as principal magnetic storms occurred during the four-month Tasman Project recording period (BMR Observatory Reports). Parkinson (1983) classifies the features common to most storms as follows:

1. A sudden commencement (SSC) consisting of a sudden increase in B_H.
2. An initial phase lasting one or less hours during which B_H is increased above pre-storm values.
3. The main phase starting 2 to 10 hours after the SSC in which B_H decreases, by up to several hundred nanotesla. There is a corresponding numerical increase in the source-field B_Z component. Induced telluric currents increase B_H and decrease B_Z.
4. The recovery phase lasting several days during which B_H exponentially increases back to its pre-storm value.
5. Irregular fluctuations occurring in all three magnetic field components at a range of periods and lasting from the SSC until early in the recovery phase.

Figure 4.20 illustrates these features on a magnetic storm recorded during the Tasman Project.

The main phase of geomagnetic storms is caused by strengthening of the ring current, and is caused by a large injection of plasma from the magnetotail into the trapping regions in the inner magnetosphere (Parkinson 1983). The westward ring current causes the decrease in B_H at the Earth's surface. The recovery phase is related to a gradual decrease

in the ring current. Two levels of flow are proposed for the ring current, a level close to the Earth (<3 R_E) and one at greater distance. The fields of these currents are respectively called DR1 and DR2 and have different time constants of recovery after a storm (Parkinson 1983, Egeland 1973).

The prerequisite conditions and dynamics of the earlier stages of a storm are more complex. The SSC is caused by an increase in the solar wind and resulting compression of the sunward magnetopause. The magnetopause currents caused by the increased solar plasma produce the initial phase of the storm (denoted DCF). For the storm to develop, the IMF must possess a southwards component (Parkinson 1983). As mentioned above, the irregular shorter period variations which occur during storms (denoted DP = DP1 + DP2) are attributed to polar ionospheric currents (Egeland 1973).

Uniformity of Storm and Substorm Fields at Mid-Latitudes

From the point of view of geomagnetic induction studies the most important feature of geomagnetic activity is the form of the inducing magnetic field at the Earth's surface and in particular, for MT, GDS and VGS studies the uniformity, of this field. This aspect leads to the question of the relative contribution of each of the ionospheric / magnetospheric currents to the inducing magnetic field at the Earth's surface.

The magnetic field of substorms at mid-latitudes tends to be asymmetric around the the Earth. For example, the field of the DP1 component of substorms is reversed at mid-latitudes (cf. higher latitudes) in the morning sector but not in the evening sector (Parkinson 1983). During storms, magnetic fluctuations are related to both absolute time and to local time and therefore storms also contain globally asymmetric fluctuations (Egeland 1973). The SSC tends to occur within one minute all around the globe and is therefore approximately globally symmetric. In contrast the disturbance-daily variation, S_D, is related to the local time and therefore represents an asymmetry in the source-field.

At mid and low-latitudes the globally symmetrical part of the main phase of storms is related to the ring current (eg. Fukushima & Kamide 1973). The field produced at the Earth's surface will be in the B_H component and will be very uniform (from the definition of symmetry). Fukushima & Kamide (1973) examine the globally asymmetric field of storms and of substorms and attribute the asymmetry to eccentricity of the ring current, field-aligned currents and to polar ionospheric currents. For a point on the equator they estimate the relative contribution to asymmetry of the storm field of each of these currents to be respectively 23 nT, 44 nT and 26 nT. At the equator magnetic storm asymmetry is thus due predominantly to the asymmetric distribution of field-aligned currents.

In the mid-latitudes one would expect a relatively smaller contribution to source-field asymmetry from ring-current asymmetry and a higher contribution from polar ionospheric currents. During strong disturbances, when the centre of the auroral electrojet on the night

side of the Earth may be located at latitudes as low as 58° (Mareschal 1986) , the auroral ionospheric currents will contribute more strongly to source-field asymmetry at mid-latitudes.

Source-Field Uniformity in the Tasman Project

For the Tasman Project study, located at around 42° S (geomagnetic), it is possible to make some basic estimates of maximum source-field scale lengths. At periods less than one hour the source-field for B_H will be induced by auroral ionospheric currents and the field-aligned currents connecting the auroral currents with the magnetosphere. Since the Tasman Project is located approximately 2,000 km north of the southern auroral electrojet an estimate for the maximum north-south scale length is 2,000 km. Assuming longitudinal asymmetry of the source-field, a maximum east-west scale length is given by one third of the circumference of the Earth at 42° ie. 10,000 km.

For periods between one and several hours the average scale length for B_H will increase as the effects of the ring current become significant. The north-south scale length will increase because of the greater distance to the equatorial position of the ring current and the east-west scale length will increase with the increased longitudinal symmetry of the fields. At longer periods the B_H field will be dominated by the ring current. For these periods the maximum east-west scale length is taken as the Earth's circumference at 42° ie. 30,000 km.

Because the ring current and auroral electrojets are approximately zonal flows (except near the dawn and dusk meridians) it is be expected that field-aligned currents are the dominant source of B_D fields at shorter periods (Kisabeth & Rostoker 1971). At intermediate periods (say 6 - 24 h) the disturbed-daily variation field will also produce variations in the B_D component (eg. Egeland 1973). For periods shorter than about 24 h the maximum scale-lengths estimated for B_H should also be appropriate for B_D. At longer periods (longer than one day), where the B_H fields are associated almost entirely with the ring current, there will be no external source for B_D fluctuations.

How do these maximum source-field scale-lengths relate to spatial variations of individual magnetic-field components ? Examination of equations 4.42-43 and 4.32 indicates that the east-west variation in both B_H and B_D will depend on only the east-west scale-length. Similarly the north-south variation of B_H and B_D will depend on only the north-south scale length. Across the 42° S parallel of the Tasman Project recording line one would therefore predict spatial magnetic-field variations with scales less than the estimated maximum east-west source-field scale length ie.less than 10,000 km at short

periods and less than 30,000 km at long periods.

In chapter 6 typical scale lengths will be derived from coherence estimates for the recorded Tasman Project data. The results suggest typical scale lengths for B_H of 4000 km at short periods (< 10 h) and 18,000 km at long periods (16 h) and for B_D of 3000 km at short periods and 11,000 km at long periods. The observed B_H results are typically half the estimated maximum value but since the observed results represent an exponential scale distance (akin to skin depth) they are in quite good agreement with the maximum estimates. The observed B_D lengths are less than the corresponding B_H lengths. The cause is possibly that B_D fluctuations are more closely related to field-aligned currents (cf. auroral and ring currents) which have more non-uniform magnetic fields.

Finite length source-fields will cause observed MT impedances to depart from the corresponding values for uniform source-field and will also create source-field B_Z components (see section 4.1 eg. Equation 4.32). An estimation of the magnitude of these effects at 42° S may be made using the scale-lengths for the Tasman data. Taking an east-west scale distance of 4900 km (the average observed scale distance for B_H and B_D for periods 0.5 -16.7 h), assuming a north-south scale distance of 2000 km, and using these values as source-field wavelengths one obtains a combined wavenumber of

$$\lambda = \sqrt{\frac{1}{4.9^2} + \frac{1}{2.0^2}} \left(\frac{2\pi}{10^6}\right) = 3.4 \times 10^{-6} \text{ m}^{-1}$$

corresponding to a combined wavelength of 1850 km. From Figure 4.2 it can be seen a source-field wavelength of around 2000 km will give slightly different impedance values from an infinite wavelength source at periods longer than 10 h. For experimental data, such as from the Tasman Project, with accumulated uncertainties of the order of 5 % or greater at periods longer than 10 h (see chapter 7), it is unlikely that the effects of the finite wavelength could be resolved.

The wavenumber estimated above is based on many assumptions and is intended to be only an order of magnitude estimate. It is heavily biased towards the north-south scale length for which there are no supporting observations. The east-west scale length also represents an average over many magnetic events and is therefore likely to be shorter than the scale-length for any individual event. Finally, no formal attempt has been made to convert the exponential scales into exact wavenumbers. Even with these provisos, the conclusion that finite source-field effects will have at most a very small influence on the Tasman Project MT impedances is a firm result.

The finite length of the source-fields is however likely to have a much more significant effect on the vertical magnetic field fluctuations. From equation 4.110 it is possible to estimate the B_Z value associated with the finite length scales of the horizontal fields.

Temporarily assuming there is no spatial variation in the north-south direction and assuming a very simple form for the spatial variation of the source-field ie. letting C_2 equal zero in the solution for P (equation 4.43) one obtains the ratio

$$\left| P / \frac{\partial P}{\partial y} \right| = \frac{1}{\lambda_y} \tan (\lambda_y y)$$

This term varies with spatial position and becomes large where B_Y is small. (If the source-field were a segment of auroral current this effect would occur in the middle of the arc of current). Choosing a 'median' spatial position by letting the tan term equal unity and substituting into 4.110 gives

$$\left| \frac{B_Z}{B_Y} \right| \sim \frac{Z \lambda_Y}{\omega} \qquad 4.181$$

From Figure 4.2 a typical sea-surface impedance at 10 cph is 4×10^{-2} $\mu V.m^{-1}.nT^{-1}$ and at 0.1 cph is 3×10^{-2} $\mu V.m^{-1}.nT^{-1}$. Taking λ_Y as 2π / 4900 km, converting values into SI units and substituting into 4.181 gives the ratio of B_Z to B_Y to be 0.003 at 10 cph and 0.2 at 0.1 cph.

These results are again only order of magnitude estimates (based upon only east-west source-field variations and an unrealistically simple representation of the source field) but suggest that a significant B_Z will result from the non-uniformity of the source-field at frequencies of less than about 0.1cph (periods longer than 10 h). In chapter 6 it will be shown that source-field bias of induction arrows (indicating a significant source-field B_Z component) becomes significant at periods above about 4 h. This result agrees satisfactorily well with the predicted source-field bias. Mareschal (1981) performs a more sophisticated modelling of the relationship of the source-field B_Z component and the horizontal magnetic field components for geomagnetic latitudes higher than 52°.

Other Estimates of Mid-Latitude Source-Field Non-uniformity

Most geomagnetic studies performed at mid-latitudes simply assume that source-fields are reasonably uniform (at the array scale horizontal magnetic fields *look* uniform except in the presence of strong lateral discontinuities) and there have been only a limited number of quantitative estimates made of the spatial uniformity of mid-latitude geomagnetic source-fields. The problem is of course the large distances it is necessary to sample over in order to define the wavenumbers. The distribution of permanent magnetic observatories has a sufficiently broad scale but analyses of observatory data suffer aliasing problems from smaller scale locally-induced fields. Numerous investigations of source-field uniformity have however been performed at higher latitudes (eg. Bannister & Gough 1978) and at low

latitudes (eg. Oni & Agunloye 1974) where source-field scale lengths are shorter and moderately sized arrays may be used effectively.

An estimate of source-field wavenumbers at mid-latitudes was made by Chave et al. (1981) in a study performed at approximately 27° N (geographic). These authors estimated the source-field wavelength from observed MT and B_Z data to be approximately 5000 km. Although this length is longer than that estimated for the Tasman Project location, it is similar to the observed east-west scale-length for the Tasman data. Chave et al. (1981) also interpreted their data as suggesting that impedances were influenced by the east-west drift of north-south electric currents. Such a result could be explained by the east-west movement around the Earth of asymmetric substorm fields and connecting field-aligned currents. The Tasman Project data have not been investigated for evidence of source-field movement but it is suggested that this research be pursued in the future.

Conclusions

The magnetospheric / ionospheric sources of geomagnetic storm and substorms are complicated 3D current systems. Field-aligned currents contribute significantly to the magnetic field fluctuations measured at mid-latitudes on the Earth's surface and there are also contributions from the equatorial ring current and from polar ionospheric currents. Theory and observations suggest that source-field wavelengths in the mid-latitudes are of the order of thousands of kilometres. Such wavelengths will cause only slight corrections to MT impedances but will produce significant source-field bias of induction arrows at periods of order 10 h and longer. It is generally recognized that there remains much research to be performed in the areas of storm and substorm mechanisms and also in the effect of source-fields in geomagnetic induction studies.

Chapter 5 Previous Determinations of Seafloor Conductivity Structure

This chapter will review the previous determinations of seafloor electrical conductivity structure. Results on seafloor conductivity structure may be divided into two sections - determinations of deep conductivity structure for depths of tens to hundreds of kilometres, and determinations of shallower conductivity structure at crustal and sediment depths. This review concentrates mainly on the deeper conductivity results. The results presented in this section will be used to increase the understanding and interpretation of results from the Tasman Project.

Determinations of deep conductivity structure beneath the oceans are based upon natural source-field methods including SFMT soundings, MT soundings on ice-flows and oceanic islands, GDS and VGS (Law 1983). Artificial source-field methods provide insufficient power to sound to depths greater than approximately 30 km even when the inducing signal is applied directly onto the seafloor (Cox et al. 1986). The deep resolution of natural source-field methods is limited to around 600-800 km because of domination of the inducing signal at long periods by noise associated with mesoscale water motions. In the future, the performance of experiments with longer recording durations, the use of sophisticated noise-reduction techniques in data analysis (such as remote referencing or use of oceanographic information) and the location of experiments in oceanographically quiet areas may permit the determination of conductivity structure at greater depth.

The shallow resolution of the natural source-field results is limited by the shielding of the higher-frequency inducing signal by the conducting ocean-water. For MT type methods (based on inductive coupling between layers) resolution will be poor at depths shallower than 20-30 km. In many oceanic conductivity profiles this problem will be exacerbated by shielding of underlying resistive regions by a conductive sediment layer. The MT method will however return a reliable estimate for the integrated conductance of the upper part of the profile.

The determination of the conductivity at shallow depths ie. sediment, crustal and upper-most mantle depths has used varied methods. These methods include the estimation of integrated crustal resistivity using the observed extent of MT anisotropy from a coast-line (Chave & Cox 1983), the use of water velocity-fields with corresponding magnetic and/or electric field variations (Cox et al. 1980, Korotayev et al. 1984), control-source measurements (Cox et al. 1986) and direct resistivity measurements in DSDP holes (Von Herzen et al. 1983). The control-source methods have included horizontal electric dipole-dipole sounding (Cox et al. 1986), vertical bipole sounding (Edwards et al., 1981) and in future may include magnetic dipole-dipole soundings (Cheesman et al. 1987).

This chapter will provide a review of the instrumentation used in SFMT soundings, a review of determinations of deep seafloor conductivity structure and a brief review of oceanic crustal conductivity determinations.

5.1 Seafloor Magnetotelluric Instrumentation

A wide variety of instrumentation has been used in seafloor electrical conductivity studies (eg. Filloux 1973) however only SFMT instrumentation, as used in the Tasman Project, is reviewed here. SFMT recordings require seafloor magnetometers (often called ocean bottom magnetometers) and seafloor horizontal electric field recorders (alternatively called electrometers). Filloux (1987) and Mosnier (1984) give more general reviews of the instrumentation used in seafloor geoelectric studies.

The seafloor provides the most stable environment in the ocean for making MT recordings. Although successful MT recordings have been made on floating ice in the Arctic Ocean (eg. Trofimov 1979, Niblett et al. 1987) it has not been possible to develop artificial instrument platforms that are sufficiently stable to permit sea-surface recording of three component geomagnetic fluctuations (Alldredge & Fitz 1964). Because the magnetic fluctuations measured for MT studies, of order 1 - 100 nT, are so much smaller than the Earth's static magnetic field, of order 60,000 nT, extreme stability is necessary to prevent rocking of the magnetometer producing apparent magnetic field fluctuations. Filloux (1982a) in fact attributes very long-period fluctuations in the magnetic field data recorded near a spreading ridge, to tectonic tilting of the seafloor at the rate of 10^{-4} radians per month.

Compared with MT recording on continents and islands, seafloor recording possesses a number of distinct advantages and disadvantages. In summary, the disadvantages of recording on the seafloor are (Filloux 1973, Cox 1980):

D1. The need for extremely specialized instrumentation. Seafloor instruments must operate extremely reliably, under great ambient pressure and in a chemically corrosive environment. Complete electrical sealing of the electric field instruments is necessary.

D2. Oceanically induced signals (noise) in the seafloor electric and magnetic fields.

D3. The very small magnitude of the electric fields in the conducting ocean water.

D4. The expense of deployment and retrieval cruises for each experiment.

These disadvantages are balanced by the following advantages of SFMT recording:

A1. The stable environment of the seafloor provides very uniform temperature and salinity and is free from cultural noise and human interference to instrumentation.

A2. The ability to make to low electrical resistance contact with the sea water (balancing D3).

A3. The ability to use salt-bridge chopping to reduce the effects of electrode noise.

A4. The uniform electrical conductivity of the ocean water dominates small irregularities of conductivity in the oceanic crustal rocks and makes the seafloor electric field relatively homogeneous over large areas.

A5. Analysis of the seafloor electric and magnetic fields can provide oceanographic information (especially in conjunction with other oceanographic measurements) balancing D2.

A6. The desirability of making electrical conductivity soundings in largely unexplored regions of the Earth and investigating oceanic tectonic processes.
It is now generally accepted that it is possible to perform successful soundings, and that the extreme value of the conductivity results obtained, justifies the additional effort relative to land soundings (see reviews of Fonarev 1982 and Law 1983).

Seafloor Magnetometers

Magnetometers used in previous seafloor electrical conductivity soundings have made use of a number of different sensing methods. Instruments used to measure fluctuations in individual magnetic field components include suspended magnet magnetometers (eg. Filloux, 1973), fluxgate magnetometers (White 1979, Law & Greenhouse 1981), thin-film magnetometers (Poehls & Von Herzen 1976) and a SQUID magnetometer (Dinger et al. 1977). Proton precession magnetometers have also been used to measure variations in the total magnetic field (Filloux 1973). At present however only two types of magnetometers are in regular use in seafloor magnetic recordings; the suspended magnet instruments used by Filloux (1980a) and some Russian groups (eg. Korotayev et al. 1980) and fluxgate magnetometers, used by most other groups. Reviews of seafloor magnetometers may be found in Filloux (1973, 1980a), Mosnier (1982), Segawa (1986) and Filloux (1987).

Seafloor Horizontal Electric Field Instruments

The first use of seafloor horizontal electric field (HEF) measurements for investigating the electrical conductivity of the oceanic basement was in the mid-1960's (Cox et al. 1971). Measurements of oceanic electric fields have however been routinely used to determine water velocity since the 1950's, mainly using the GEK or geomagnetic electrokinetograph towed behind steaming ships (Von Arx 1950).

Because of electrode noise the early seafloor HEF measurements were made between the ends of a 1km long cable laid over the seafloor. The length of the cable increased the signal level, ie. the potential difference between the ends of the cable, relative to the electrode noise. The procedures involved in laying the cable on the seafloor so that it lay in the required direction were however time consuming and it was difficult to assess whether the cable lay in the desired configuration (Filloux 1987).

Without a major advance in electrode technology it will not be possible to construct short-cable seafloor electric field instruments with sufficient resolution for SFMT studies. With perfectly matched Ag-AgCl electrodes, seafloor electric field measurements using cables require a minimum electrode separation of 10 m, however "unavoidable electrode voltage mismatch" enforces the use of much larger separations (Filloux 1974). During the 1970's short-span instruments were developed by replacing the cables by salt-bridge pipes and using a chopping system to reject electrode bias and drift (Filloux 1974).

In the salt-bridge system the electric field is measured between the ends of hollow insulated pipes. These pipes are filled with the electrically-conducting ocean water which connects the open ends of the pipes to the sensing electrodes. The chopping system involves periodically reversing the two electrodes measuring the electric field in a given direction, so as to cancel out the electrode noise. This procedure may be achieved by periodic horizontal rotation of the electric field instrument (Sanford et al. 1978), however for seafloor instruments incorporating a salt-bridge, it is more efficient to simply switch the electrodes connected with opposite pipe ends. This method, illustrated schematically in Figure 5.1, was used by Dr Jean Filloux (1974) in his development of short-span seafloor HEF recorders. He has since developed seafloor VEF recorders based on the same principle.

A photograph of one of Dr Filloux' HEF instruments was shown in Figure 2.3. The electric field is measured in two orthogonal directions between the ends of the pipes forming the cross at the top of the instrument. These pipes are connected by insulated tubing to the chopper attached to the side of the instrument. In the chopper an electromagnetically driven valve system forms a double-pull double-throw switch which periodically reverses the salt water path between the electrodes and opposing salt-bridge arms.

The operation of the chopper may be outlined as follows. Denote the signal and electrode-noise in a particular horizontal direction as 's' and 'n' respectively and the measured potential difference as 'u'. In the first half of each sampling interval the measured potential difference between the pair of electrodes is

$$u_1 = s_1 + n_1 \qquad 5.1$$

The chopper then switches the electrodes attached to opposite salt-bridge pipes and for the second half of the sampling interval the potential difference

$$u_2 = - s_2 + n_2 \qquad 5.2$$

is recorded. Subtracting the results for each half of the interval gives

$$\frac{u_1 - u_2}{2} = \frac{s_1 + s_2}{2} + \frac{n_1 - n_2}{2} \equiv \frac{s_1 + s_2}{2} \qquad 5.3$$

ie. an estimate of the signal with the electrode bias removed. The measured potential difference is divided by the distance between the ends of the salt-bridge pipes to give the corresponding electric field. The approximation in equation 5.3 becomes an equality if any temporal variation in electrode bias is much slower than the sampling rate. Adding u_1 and u_2 provides an estimate of the electrode bias.

The short span HEF instruments developed by Dr Filloux are the only seafloor HEF instruments presently in regular use in SFMT soundings. Long-cable HEF instruments have however been operated successfully in previous SFMT experiments, for example by T. Daniel, in an experiment north of Hawaii (Chave et al. 1981). For the recordings of

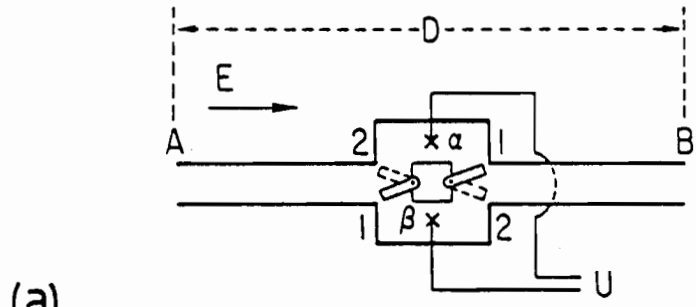

(a)

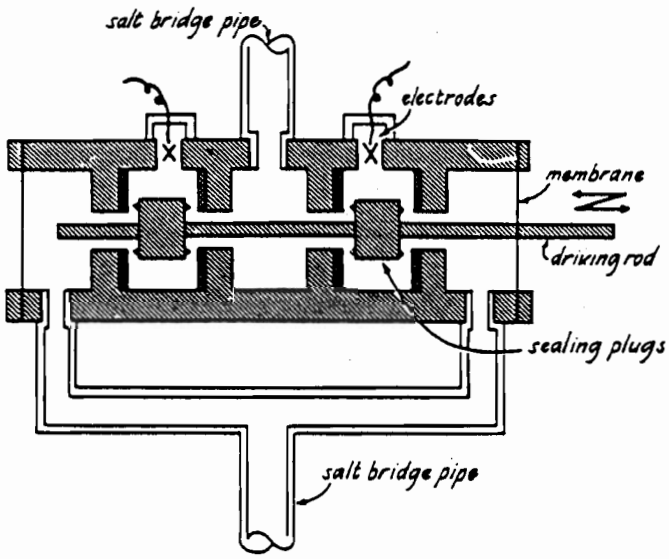

(b)

Figure 5.1: Schematic illustration of salt-bridge chopper (from Filloux 1973, 1980a).

(a) Electrode α is connected to the ocean at point A, and β at point B (where A and B are at the ends of the salt-bridge pipes). After switching, α is connected to point B, and β to point A, for the second half of the sampling interval.

(b) The double-pole double-throw 'water chopper' used to switch the electrodes every half-cycle.

high-frequency fluctuations in the seafloor horizontal electric-field required in some control-source methods, it is not possible to use a chopping technique and electric field recording is restricted to the use of long-cable electric field instruments (Webb et al. 1985). Although scientists now have more experience in deploying such instruments, and use acoustic transponders to accurately determine the cable location, it may still require more than five hours to deploy each instrument.

5.2 Results of Deep Conductivity Determinations

During the last two and a half decades approximately 30 geomagnetic induction experiments have been performed with the aim of determining the deep geoelectric structure beneath the ocean floor. This number includes soundings made on smaller oceanic islands such as Hawaii and Iceland, but does not include continental shelf experiments (eg White & Polatajko 1979, Law 1981) or experiments on larger islands such as Japan. The results from the experiments provide a significant data base with which to compare results from the Tasman Project. Such a comparison will greatly aid the geophysical interpretation of the Tasman Project results.

Although there have been a significant number of previous deep conductivity studies, the results have been obtained using a wide variety of methods, for example SFMT, floating ice MT, island MT, GDS and VGS sounding and the results have been obtained in diverse tectonic regimes including oceanic lithosphere, submerged continental lithosphere, spreading ridges and subduction zones. The number of studies based on similar methods in any particular tectonic regime is quite limited. In addition most of the deep conductivity determinations have been located in the Pacific and Arctic Oceans with the remaining few studies in the Atlantic Ocean. On a global scale the deep sub-oceanic conductivity structure has been poorly sampled and there is a strong need for many further studies to be performed.

Before reviewing the individual sounding results it is useful to perform an overview of all the experiments. Table 5.1 lists details of all of the major deep oceanic sounding experiments performed to date and Figure 5.2 shows the location of most of these experiments. The experiments may be broadly divided as follows

i. Geographic Location: Pacific Ocean - 15 seafloor experiments (plus experiments on Hawaiian Islands); Arctic Ocean - 8 floating ice experiments; Atlantic Ocean - 2 seafloor experiments (plus experiments on Iceland).

ii. Tectonic Regime: "Normal" undisturbed oceanic lithosphere - 8; Near spreading ridges - 4; Near subduction zones - 4; Submerged continental lithosphere - 4; Ocean islands - 3; Uncertain - 5

iii. Sounding Method: Seafloor MT Sounding - 15; Floating Ice MT Sounding - 8; Vertical Geomagnetic Sounding - 2; Other methods (including island soundings) - 5.

These classifications are all approximate since some experiments have used more than one

Table 5.1: Previous Sub-Oceanic Deep Conductivity Determinations.

Experiment Project Name	Year	Geographic Location	Tectonic Setting	Sounding Method	References
Pacific Ocean					
SF (seafloor)	1965	NE Pacific 33°N 127°W	Normal (+Seamounts)	SFMT	Cox et al. 1971 Filloux 1967
AGGY III	1976 Aug-Sep	NCentral Pacific 26°N 151°W	Normal	SFMT	Filloux 1977,1980b
AGGY I & II	1976	NCentral Pacific 27°N 150°W	Normal	SFMT	Chave et al. 1981
SF Revisited	1977 May-Jun	NE Pacific 31°N 128°W	Normal	SFMT	Filloux 1980b,1980c
JDF (Juan de Fuca Ridge)	1978 June	NE Pacific 47°N 129°W	Sp Ridge	VGS	Law & Greenhouse 1981
Hawaii	1978 Jun-Aug	NCentral Pacific 18°N 150°W	Normal-Island	SFMT	Tarits et al. 1986
Marianas (SEATAR)	1978 Sep-Dec	W Pacific 18°N 144-146°E	Subduction	SFMT	Filloux 1982b,1982c
PR 21° (ROSE)	1979 Jan-Apr	NE Pacific 21°N 108-110°W	Sp Ridge-Normal	SFMT	Filloux 1982a
PR 12° (ROSE)	1979 Feb	NE Pacific 12°N 102-103°W	Sp Ridge-Normal	SFMT	Filloux 1981,1982a
Murray	1979-80 Oct-Jan	NCentral Pacific 32°N 128°W	Normal	SFMT	
Japan	1981 Jul-Sep	NW Pacific 39°N 142-150°E	Subduction-Normal	SFMT	Filloux & Yukutake 1982 Yukutake et al. 1983
New Zealand	1982	SW Pacific	Subduction	SFMT	
Tasman	1983-84 Dec-Apr	Tasman Sea	Normal (+Seamounts) Sub Cont	SFMT	Ferguson et al. 1985 Lilley et al. 1988
EMSLAB	1985 Aug-Sep	NW Pacific 44-46°N, 125-131°W	Sp Ridge-Normal-Subduction	SFMT	Filloux et al 1988 Booker et al 1988
BEMPEX	1987	N Pacific	Normal	SFMT	Chave et al 1988 Luther et al 1987

Table 5.1 continued

Experiment Name	Year	Geographic Location	Tectonic Setting	Sounding Method	References
Arctic Ocean					
Gakkel Ridge	?	W Arctic ~82°N ~100°E	Uncertain	Ice MT	Trofimov & Fonarev1976 Fonarev 1982
Lomonosov Ridge	?	C Arctic ~84°N ~120°E	Sub Cont	Ice MT	Trofimov & Fonarev1982 Fonarev 1982
Podvodnikov Basin	?	C Arctic 82°N 140°E	Sub Cont	Ice MT Ice MVS	Trofimov 1973 Trofimov & Fonarev1976 Volkomirskaya & Fonarev 1976
East Siberian Sea	?	C Arctic	Sub Cont	Ice MT	Trofimov & Fonarev 1976 Fonarev 1982
Chukchi Plateau	?	E Arctic ~78°N 170°W	Uncertain	Ice MT	Trofimov & Fonarev1976 Fonarev 1982
Canadian Basin	1976-77	E Arctic 83-84°N 120-140°W	Uncertain normal (?)	Ice MT	Trovimov 1979 Fonarev 1982
Medeleiev Ridge	?	E Arctic	Uncertain	Ice MT	Fonarev 1982
Alpha Ridge (CESAR)	1983	E Arctic 85°N ~100°W	Deformed oceanic lith	Ice MT	Niblett et al. 1987
Atlantic Ocean					
Atlantic (MODE)	1973 Mar-May	NW Atlantic 27°N 70°W	Normal	SFMT VGS	Cox et al. 1980 Poehls & Von Herzen 1976
Islands					
Oahu, Hawaii	1969-71	N Central Pacific	Island Hot Spot	Island MT	Larsen 1975
Hawaii	?	N Central Pacific	Island Hot Spot	Island GDS	Klein & Larsen 1978
Iceland	1977,80	N Atlantic	Island Sp ridge	Island MT	Beblo et al. 1983

Notes 1. Under tectonic setting, "normal" means normal oceanic lithosphere; "seamounts", "sp ridge","island" and "subduction" mean proximity to a seamount chain, spreading ridge, ocean island or subduction zone; and "Sub Cont" means submerged continental lithosphere.

2. Under sounding method "SFMT" means seafloor magnetotelluric, "VGS" means vertical gradient sounding, "Ice MT" means MT on floating ice, "MVS" means magnetic variation sounding, "Island MT" means MT on an ocean island and "GDS" means geomagnetic depth sounding.

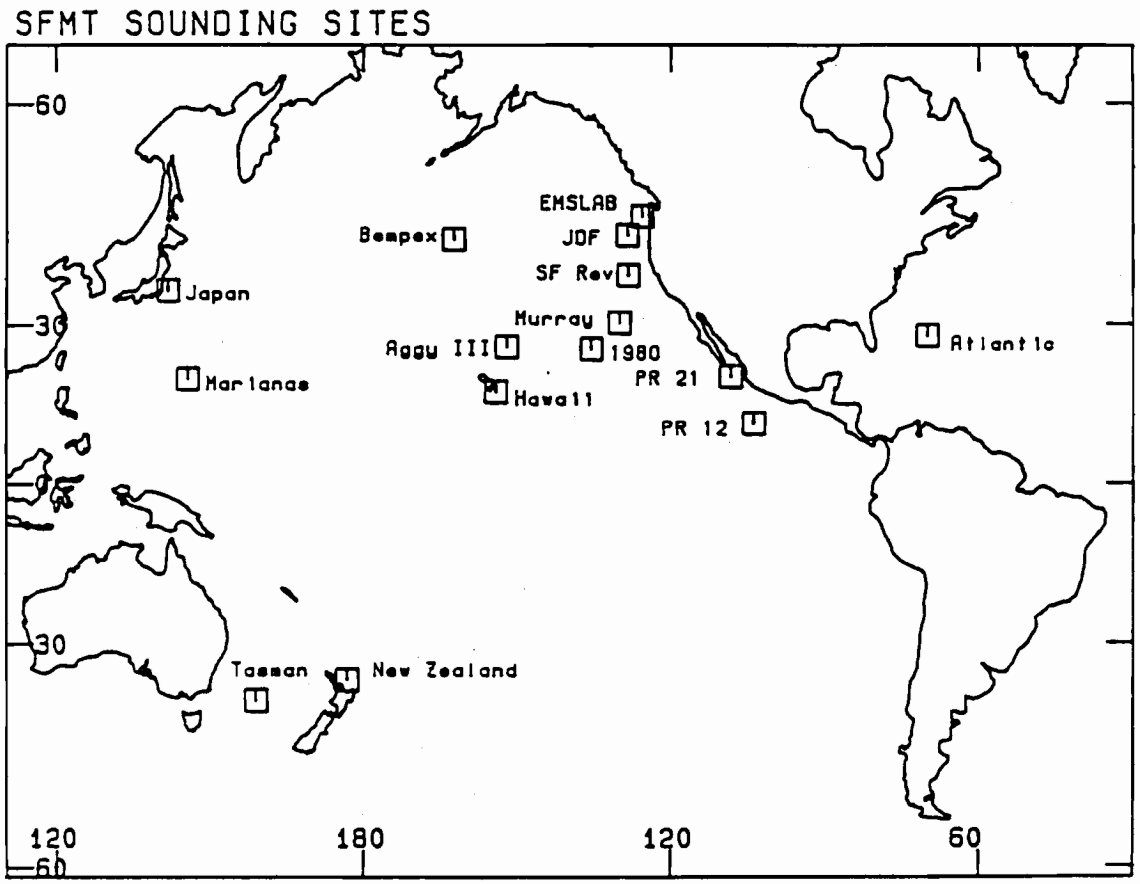

(a)

Figure 5.2: Maps showing location of previous deep seafloor conductivity determinations. The experiments and their locations are listed in Table 5.1.
(a) Pacific Ocean and adjacent regions. (b) (Over-page) Arctic Ocean (after Demenitskaya & Karasik 1969).

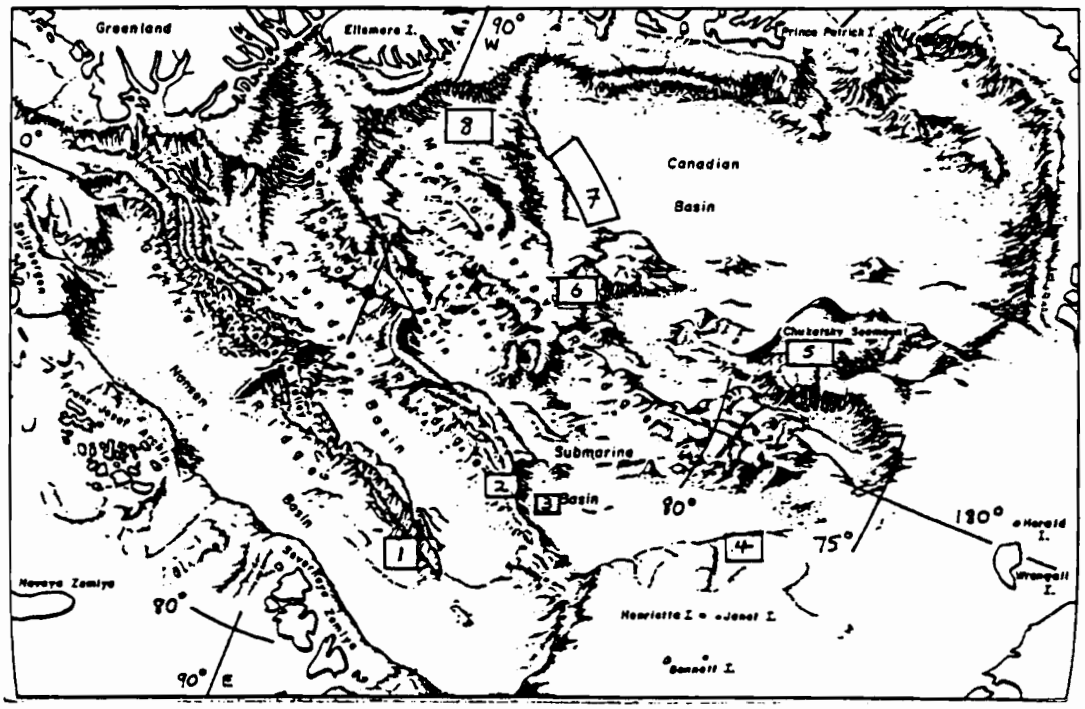

Site Locations

1 = Gakkel Ridge, 2 = Lomonosov Ridge, 3 = Podvodnikov Basin, 4 = East Siberian Sea
5 = Chukchi Plateau, 6 = Mendeleiev Ridge, 7 = Canadian Basin, 8 = Alpha Ridge

Figure 5.2b.

sounding method and some experiments span a range of tectonic structures.

The aim of all deep geoelectric soundings is to determine the electrical conductivity of the Earth as a function of depth and horizontal position. Since the electrical conductivity is a unique quantity it should in principle be possible to directly compare conductivity results derived from different experiments. In practice however, different analysis and inversion methods (see chapter 4 and 8) may produce differing conductivity models from a given set of recorded data. It is therefore necessary to take care in comparing results obtained using different methods, and in some cases it is more useful to compare MT response functions rather than the inverted models.

Soundings of "Normal" oceanic lithosphere.

There have been approximately ten deep conductivity soundings over normal oceanic lithosphere - lithosphere formed through a simple process of seafloor spreading and remaining tectonically undisturbed (Table 5.1). Such lithosphere is characterised by magnetic lineations from which the lithospheric age can be determined. Deep conductivity soundings near spreading centres and subduction zones represent soundings of very young and usually very old lithosphere respectively; the tectonic structure near these zones differs from that for simple oceanic lithosphere and may produce associated differences in the electrical conductivity structure. The passage of an oceanic plate over a hot spot may also alter the tectonic state and conductivity structure of the surrounding lithosphere.

Most of the conductivity soundings of normal oceanic lithosphere have been in the Pacific Ocean. The one deep sounding experiment in the Atlantic Ocean is also over undisturbed oceanic lithosphere (Cox et al. 1980) but of all the soundings in the Arctic Ocean only the sounding in the Canadian Basin is possibly of this tectonic regime (Fonarev 1982, Niblett et al. 1987).

Figure 5.3 shows the conductivity models from a number of soundings over oceanic lithosphere in the Pacific Ocean. The soundings are from lithosphere with a range of ages: 2.7, 30, 72 Ma and > 130 Ma respectively for the PR12, SF Revisited, AGGY III and Mariana forearc soundings (Filloux 1977, 1980c, 1981, 1982b). The two soundings from 'normal' lithosphere, SF Rev and AGGY III show a high conducting layer at intermediate depth (around 100 km) and a deeper rise in conductivity. The PR12 sounding (located 120 km from the spreading ridge) shows a more shallow HCL at 20 km, a second possible HCL near 100 km depth and then a deeper rise in conductivity. In the Mariana forearc profile the conductivity rises occur at the increased depths of 400 km and 800 km.

The results show an increasing depth to the HCL (or to the most shallow conductivity rise) with increasing lithospheric age, from 20 km at PR12 to (?)400 km at the Marianas. There is also an indication that the conductivity of the HCL (or the conductivity below the conductivity rise) decreases with increasing lithospheric age. The depth to the deep conductivity rise also increases with increasing lithospheric age, from 200 km at PR12 to

800 km at the Mariana forearc.

A possible contribution to the differences between the Pacific Ocean conductivity models may arise from the choice of the final impedance component from the observed impedance tensors. The PR12 and SF Revisited results are based on using Z_{eff}^1 (equation 4.104), the AGGY III results on Z_{eff}^2 (4.105), and the Mariana and Juan de Fuca (JDF) results on a single impedance component. Differences arising from these methods are however unlikely to explain the total variation between the conductivity models.

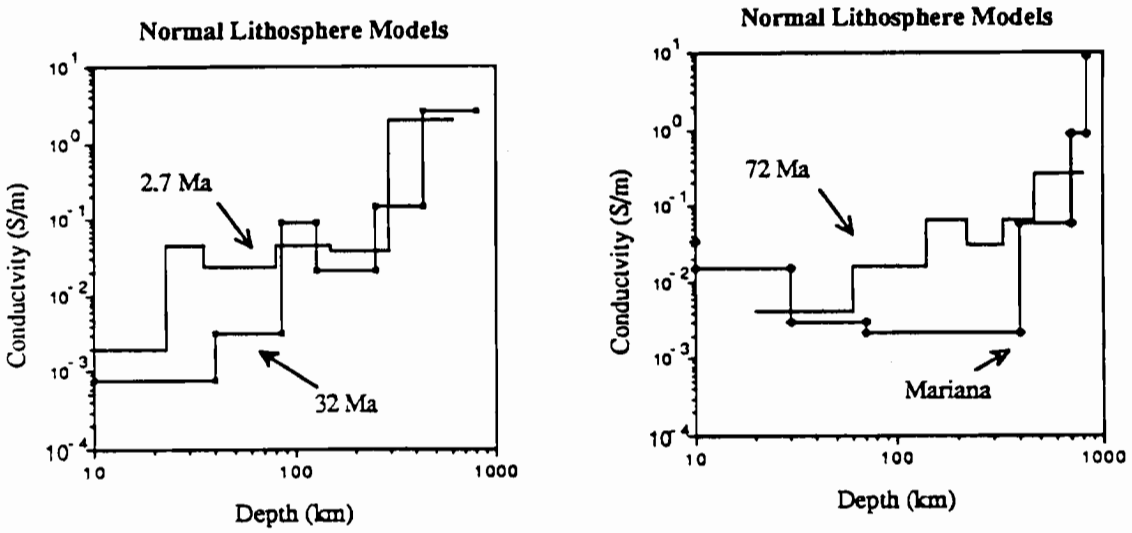

Figure 5.3: Conductivity models for normal oceanic lithosphere with a range of ages, from experiments and analyses by Filloux (1977, 1980c, 1981, 1982b). Profiles are shown for PR12: site 2B(2.7 Ma), SF Revisited (30 Ma), AGGY III (72 Ma) and the Mariana forearc (> 130 Ma) experiments. Note that the depth to the first conductivity rise (or HCL) increases with increasing lithospheric age from 20 km near the spreading ridge to ?400 km for the Mariana forearc. The depth to the deepest conductivity rise also increases with lithospheric age from 200 km near the spreading ridge to 800 km at the Mariana forearc.

A number of different inversions have been performed on a data set consisting of the MT responses from the SF Revisited and AGGY III sites, and a VGS data set from 1 Ma lithosphere near the Juan de Fuca spreading ridge (Law & Greenhouse 1981). For these sites, with lithospheric ages of 1, 30 and 72 Ma respectively , Oldenburg (1981) obtains depths to the conductive zone of 70, 120 & 180 km. Using a more rigorous statistical treatment, Oldenburg et al. (1984) confirm the existence of this trend but note that it is not as strong as earlier proposed. They obtain depths to the conductive zones of 40 km, 70 km and 80 km. Tarits (1986) obtains similar depths to these using a different inversion scheme.

The existence of a trend relating the conductivity structure to the lithospheric age is shown unequivocally by the MT response for each site (Figure 5.4). The responses show a clear increase in apparent resistivity with increasing lithospheric age (although there is no corresponding trend evident in the phase). The apparent resistivity response shows a consistent difference between the AGGY III and SF Revisited sites. However because the magnitude of the difference is small compared with the error-bar magnitude, the statistical treatment of Oldenburg et al. (1984) finds no statistical difference between the responses at the 95 % confidence. The discrepancy arises because the χ^2 statistical measure used by Oldenburg et al. (1984) strictly requires the misfit between the two responses to have a normal distribution.

The conductive zone beneath the Pacific Ocean sites is inferred to represent an electromagnetic response to the asthenosphere (Filloux 1980c, Oldenburg 1981, Tarits 1986). The increase in conductivity is attributed to partial melting and/or the presence of H_2O rich fluids. The geophysical significance of the conductive region will be discussed in more detail in chapter 9.

The conductivity structure observed in other parts of the Pacific Ocean is in good agreement with the results shown above. Figure 5.5 compares the conductivity model at AGGY III with a model obtained by Chave et al. (1981) from data recorded at a site approximately 300 km away on 50 Ma lithosphere. The two conductivity models are very similar; both show an HCL at around 200 km depth and a deep rise in conductivity at 400 to 500 km depth. Analysis of data collected to the southwest of Hawaii on 80 Ma lithosphere also shows similar results although at this site the conductivity begins to rise gradually at 300 km depth (Tarits et al. 1986, Filloux pers. comm. 1987).

Figure 5.5 also shows a conductivity model derived from MT soundings on Oahu (Larsen 1975) and GDS soundings on Hawaii (Klein & Larsen 1978). The model for Hawaii includes a smaller rise in conductivity at around 200 km and a deep HCL at 320 km. In the upper 300 km the conductivity in the Hawaiian model is of a very similar magnitude to that at AGGY I & III. The differences between the Hawaii results and the SFMT results may be associated with the tectonic location of Hawii at the active end of a hot spot chain (eg. Jarrard & Clague 1977). SFMT recordings by Filloux (pers comm.

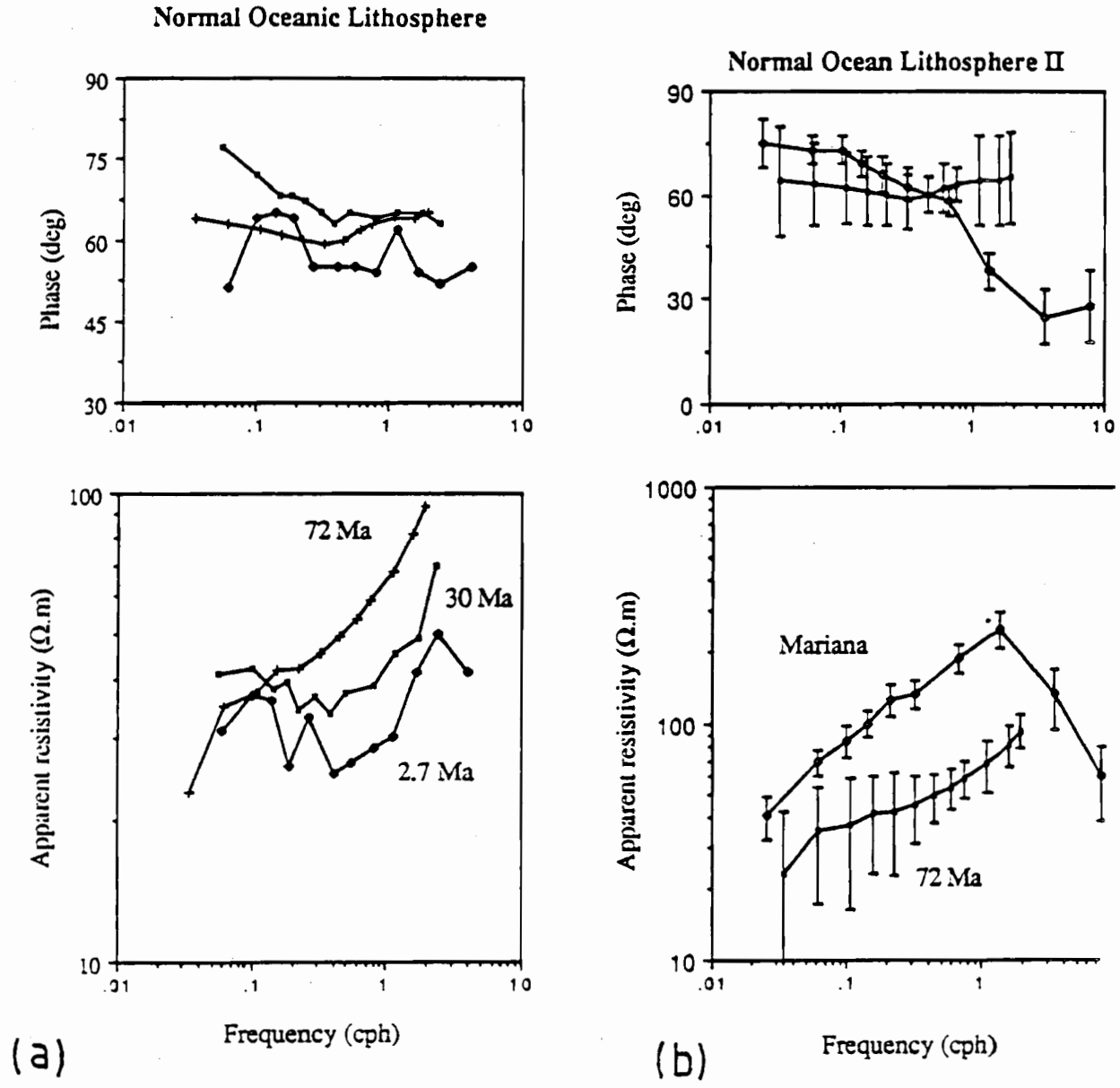

Figure 5.4: MT response for the sites shown in Figure 5.2. (a) The response for sites on 2.7, 30 and 72 Ma lithosphere. (b) The response on 72 Ma lithosphere and at Mariana forearc with 95 % confidence-limit error bars. The large error bars on the AGGY III data reflect the shorter recording period and finer band-averaging.

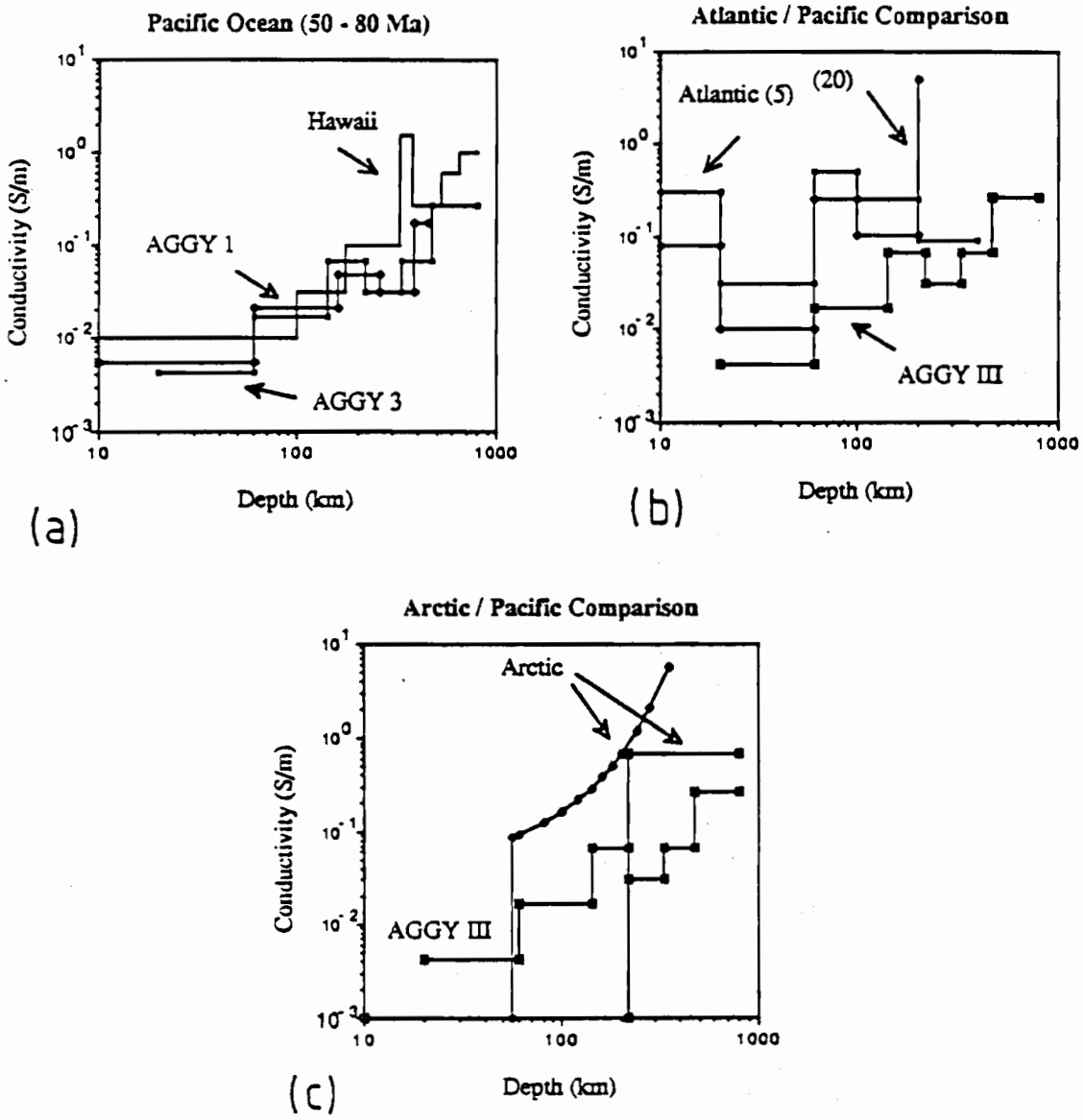

Figure 5.5: Conductivity models for sites on 'normal' oceanic lithosphere. In each panel the Pacific Ocean AGGY III model is used for comparison. (a) Models for Pacific Ocean sites near Hawaii: AGGY I denotes a model from 50 Ma lithosphere (near AGGY III); Hawaii denotes a model obtained using recordings on Hawaii and Oahu Islands, Hawaii. (b) Models from Atlantic Ocean: site 5 from 150 Ma and site 20 from 140 Ma lithosphere. (c) Results from Arctic Ocean: the two models represent two inversions of MT recordings from the Canadian Basin (lithospheric age between 125 and 79 Ma).

1987) to the south of Hawaii indicate anomalous conductivity structure, from which important information on the mechanism of the island formation may be gained. Final results from the BEMPEX experiment in the North Pacific (Luther et al. 1987) should provide additional conductivity profiles for Pacific Ocean 'normal' oceanic lithosphere.

The conductivity models derived for the Atlantic Ocean are more conductive than Pacific Ocean models in the upper 300 km (Figure 5.3). SFMT soundings on 140 - 150 Ma lithosphere between the Bahamas and Bermuda indicate conductivities which are 5 to 10 times more conductive than at AGGY III (Cox et al. 1980). The results show an HCL at 60 - 100 km depth, an HCL-depth associated with much younger lithosphere in the Pacific Ocean. VGS results from nearby 80 - 110 Ma lithosphere (Poehls & Von Herzen 1976) are in good agreement with the Atlantic SFMT results. These results from the Atlantic Ocean are based on recordings from relatively noisy seafloor magnetometers (Poehls & Von Herzen 1976) and require duplication before the higher conductivity observed in the Atlantic experiments is accepted as representative of the whole Atlantic Ocean.

Figure 5.5c compares conductivity models from the Arctic Ocean with that of AGGY III. The Arctic results are derived from floating-ice MT recordings in the Canadian Basin in the East Arctic Ocean (Figure 5.2). This region is considered to be of oceanic origin. The lithospheric age is somewhat uncertain but results from other parts of the Canadian Basin suggest an age of ocean crust formation of between 125 and 79 Ma (Sweeney 1985).

The layered model for the Arctic consists of an infinite resistor in the upper 220 km, underlain by a half-space of 0.7 $S.m^{-1}$. Such a simple model, derived using asymptotic techniques, should be considered an under-use of the valuable recorded data. Trials with asymptotic techniques have shown that the depth determined to the good conductor corresponds to the deep rise in conductivity rather than to a more shallow HCL (chapter 7). The 220 km depth observed for such a rise in the Arctic is much more shallow than the corresponding depths found for Pacific Ocean lithosphere of the same age (Figure 5.3).

The second model for the Arctic Ocean consists of an exponential increase in conductivity below an infinite resistor of thickness 55 km. The model gives a poor fit to the observed phase, indicating the exponential conductivity increase is too rapid (Trofimov 1979). The location of the start of the rise at 55 km is however valuable information. It suggests that no HCL occurs at depths more shallow than 55 km and that the first strong increase in conductivity occurs around 55 km depth. Such a depth is more shallow than expected for an HCL in lithosphere of age ~ 100 Ma, but is in accord with the relatively shallow depth observed for the deeper conductivity increase. Soundings in other regions of the eastern Arctic Ocean; MT soundings on the Chukchi Plateau and magnetic variation soundings on the Mendeleiev Ridge, indicate deep structure similar to that of the Canadian Basin (Trofimov 1979, Fonarev 1982) however these regions are however unlikely to represent undisturbed oceanic lithosphere (Trofimov & Fonarev 1976, Niblett et al. 1986).

In chapter 9 the Tasman Sea results will be compared with previously determined

conductivity profiles of normal oceanic lithosphere. The results will indicate whether the lithosphere beneath the Tasman Sea falls onto the trend defined by the Pacific Ocean, or whether it is anomalous.

Deep Conductivity Determinations in Other Oceanic Tectonic Settings

A number of deep seafloor conductivity soundings have been located near spreading ridges. Conductivity models from the SFMT experiments of Filloux (1981, 1982a) on the Pacific Rise at PR12 and PR 21, and the VGS measurements by Law & Greenhouse (1981) at JDF on the Juan de Fuca ridge are shown in Figure 5.6a. The models share a number of common features: a shallow HCL with its top at 20 to 40 km depth and a deep conductivity rise at 250 to 300 km, suggesting that these are characteristic features of the conductivity structure near spreading ridges. As well as possessing similar structure, the models show similar values for conductivity at each depth.

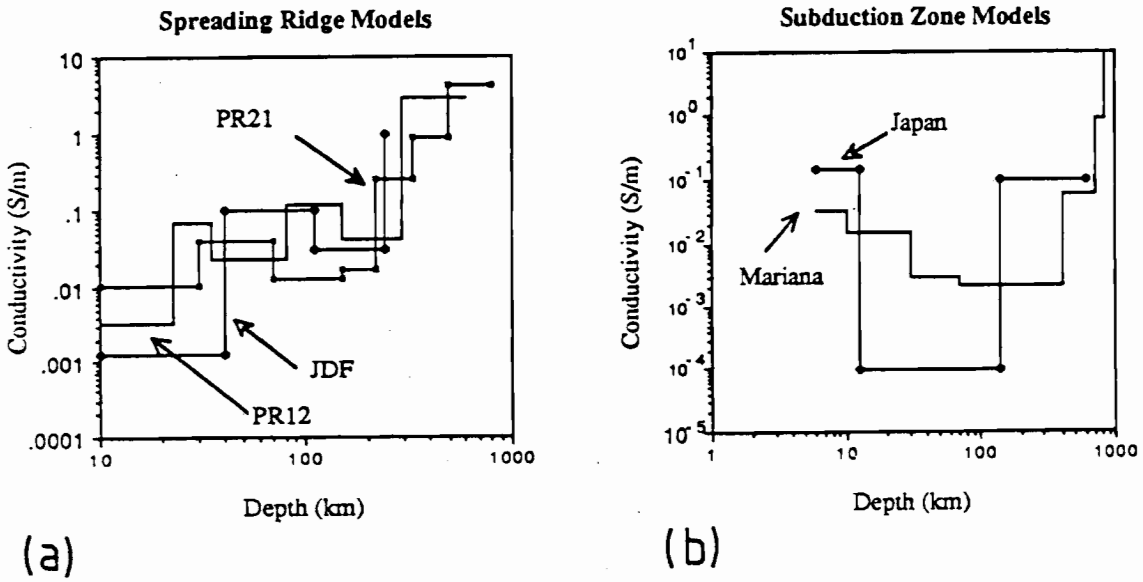

Figure 5.6: Conductivity models from near (a) spreading ridges and (b) subduction zones. The spreading ridge models come from the Pacific Rise region at site 2B at PR12; site 1A at PR21 (Filloux 1981, 1982a); and from the inversion of Oldenburg et al. (1984) of data from sites 1 and 2 near the Juan de Fuca Ridge (Law & Greenhouse 1981). The subduction zone models come from the Mariana forearc (Filloux 1982b) and from site S4 near Japan (Yukutake et al. 1983).

The models shown are derived from lithosphere of slightly different ages. For PR12, the model is for 2.7 Ma lithosphere (120 km from ridge), for PR21 it is for ~ 3 Ma lithosphere (~100 km from ridge) and for JDF it averages 1 Ma (30 km from ridge). It is interesting to contrast the results for these sites with results from Iceland where more dense traverses across the spreading ridge have been performed. Figure 5.7 shows the results of such a study by Beblo et al. (1983). The MT results show a definite HCL rising from a depth of around 20 km at the edge of the study, 50 - 100 km from the spreading centre, to around 10 km beneath the actual volcanic system. Given that there is some flexibility in MT inversions, the depths to the HCL observed in the seafloor studies are only slightly deeper than those observed beneath Iceland. The slight differences may be associated with the different tectonic setting of Iceland from normal spreading ridges.

Soundings of regions near spreading ridges have been performed in the international EMSLAB experiment (Booker et al. 1987) near the Juan de Fuca Ridge, and on the Gakkel Ridge in the Arctic Ocean (Trofimov & Fonarev 1976). No profiles from the region near the spreading ridge have yet been published by the EMSLAB Group. Although the Arctic Ocean MT soundings have not been fully inverted they indicate that the depth to the good conductor is greater than 300-400 km (Trofimov & Fonarev 1976). This value is deeper than observed at other ridges. The spreading on the Gakkel ridge is however slow, with a half-rate of 5 $mm.yr^{-1}$ (Srivastava 1985), and the deep structure beneath the ridge may therefore perhaps differ from ridges such as the Pacific Rise or Juan de Fuca with faster spreading rates.

Figure 5.6b shows conductivity profiles obtained from SFMT soundings near subduction zones: the Mariana subduction zone (Filloux 1982b) and the Japan subduction zone (Yukutake et al. 1983). The Mariana model is derived from recordings on the forearc, approximately 120 km west (on the continent side) of the trench while the Japanese model is from a location approximately 250 km east of the trench on the oceanic plate. Because of differences in the quality and quantity of recorded data, the Mariana data reveal more detail of the conductivity structure than the Japan data. The two models however show two important similarities. Both models include a region of high conductance in the upper part of the profile, ~ 700 S in the upper 60 km in the Mariana forearc model and ~1800 S in the upper 10 km of the Japan model. A diagnostic feature of high conductance at shallow levels, is a decrease in the phase response at short periods, to angles of less than 45°. A significant proportion of the conductance may be attributed to the build-up of conductive sediments on the older part of the plate and to the accumulation of such sediments in the forearc (eg. Filloux 1982b).

The second feature of both the Mariana and Japan conductivity models is the low conductance at intermediate depths (of around 100 km) compared with sites on younger lithosphere. This result supports the observed trend of the conductivity decreasing with increasing lithospheric age (Figure 5.3).

The conductivity structure of most subduction zones will be difficult to identify using

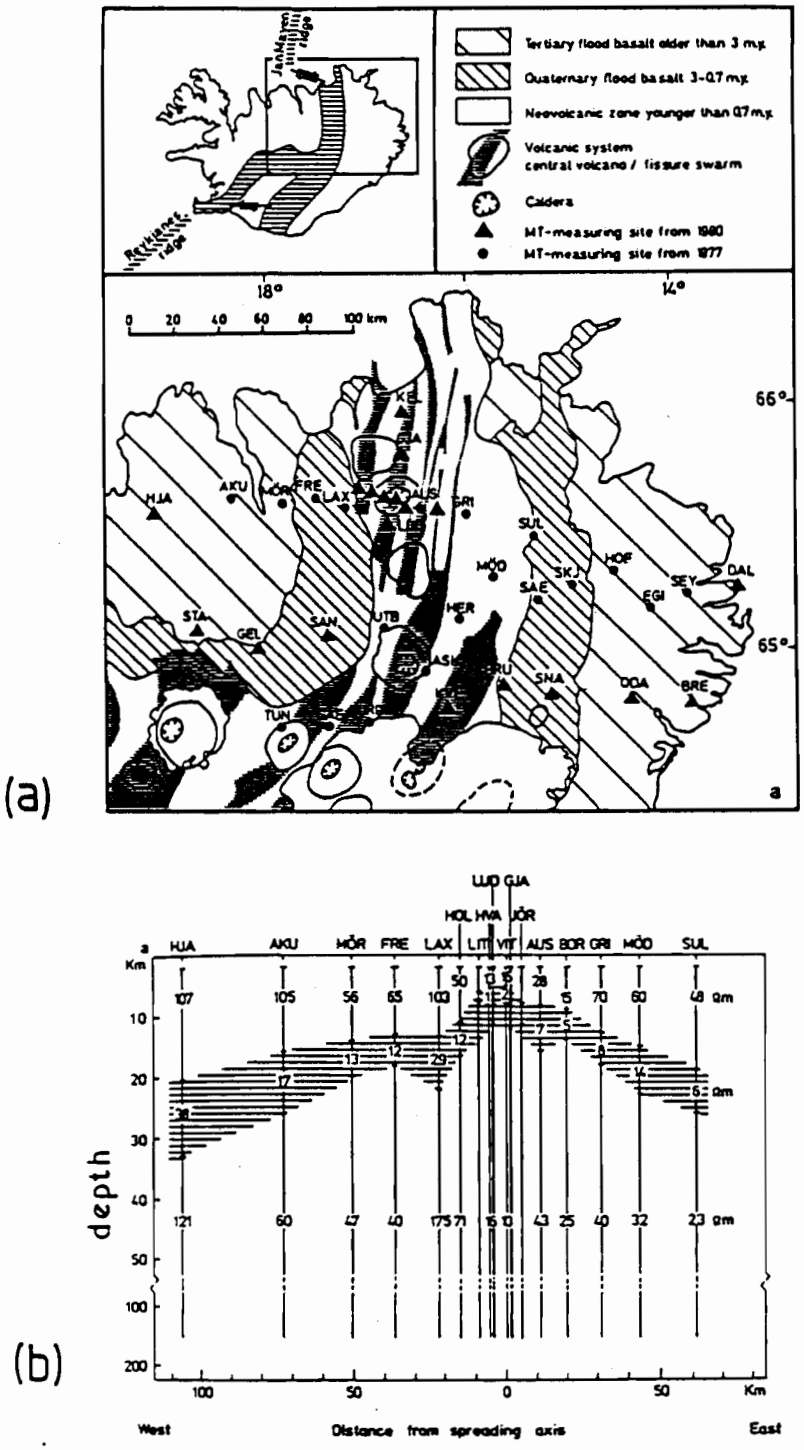

Figure 5.7: MT results from a traverse across the mid-Atlantic ridge in Iceland (from Beblo et al. 1983). (a) Map showing the location of MT recording sites. The conductivity profile shown in (b) is along the northern east-west line of sites. The profile shows a region of low resistivity (high conductivity) located at 10 to 20 km depth. The HCL rises to its most shallow depth beneath the active volcanic system.

1D SFMT soundings. The steeply dipping subducting slab is likely to cause strong departures from horizontal layering in the conductivity structure, and 1D analysis techniques will give only broad averages of the conductivity. For subduction zones with simple structure, a sufficiently dense array of seafloor instruments may allow a 2D analysis. Such an approach has been used in the analysis of the EMSLAB SFMT soundings which extended across the subduction zone beneath the western United States. This analysis has been complicated however by the presence of 3D effects. The SFMT recordings made near the subduction zone off New Zealand also show strong 3D effects (J.H. Filloux pers. comm. 1987).

Varied conductivity models have been reported for other oceanic tectonic settings. Results from submerged continental regions such as the Lomonosov Ridge in the Arctic Ocean show depths to the good conductor of greater than 300 km, values similar to those observed on continental shields and platforms (Fonarev 1982). In contrast, the more sophisticated 2D analysis of Niblett et al. (1987) determined a shallow depth, of 70-85 km, for the rise in conductivity beneath the Alpha Ridge in the Arctic Ocean. This depth is very shallow for the late Cretaceous age indicated for the lithosphere in this region and a possible cause is suggested to be a 'hot spot' source for the Alpha Ridge (Niblett et al. 1987).

In summary, previous determinations of sub-ocean conductivity profiles have shown that there is good consistency between profiles obtained in similar tectonic settings and that there are significant differences between the profiles from different tectonic settings. The Tasman Project recording sites are located on or near a range of tectonic settings including 'normal' oceanic lithosphere (eg. TP3, TP5), a fossil spreading-ridge and hot spot chain (TP4) and submerged continental lithosphere (TP1). Where possible the results from the Tasman Project will be compared with those from previous studies (see chapter 9). This comparison will help define the range of structures associated with these tectonic settings and will also aid the interpretation of the Tasman Project results.

5.3 Results of Shallow Conductivity Determinations

One-dimensional SFMT studies do not provide detailed information on sediment and crustal conductivity. The conductivity of these regions is however an important parameter in geomagnetic induction, especially in 2D or 3D conductivity structures, justifying a brief review of the results of shallow conductivity determinations.

Sediment Layer

The conductivity of seafloor sediments may be directly measured in the laboratory, determined from seafloor electromagnetic measurements or indirectly from measurements of sediment porosity. Estimates for average sediment conductivity average around 0.8-1.2

$S.m^{-1}$.

An example of laboratory measurement of sediment conductivity is given in Filloux (1967). He obtains an average conductivity for sediment cores taken from near the seafloor of 1.8 $S.m^{-1}$. The results indicated more variability in conductivity is associated with the different sediment types (with clays being more conductive than calcareous oozes) than is due to varying compaction over the top 7 m of the profile. Filloux (1967) estimates an average conductivity of 0.8 $S.m^{-1}$ for the whole sediment column, a value which accounts for the reduction of porosity with depth.

Electromagnetic measurements of sediment conductivity have been based both on using natural oceanically induced source-fields and on using control-source techniques. The oceanic source-field method is based on comparing either the electric and magnetic field associated with ocean currents, or the electric field and the measured velocity field (eg. Teramoto 1971, Cox et al. 1980, Korotayev et al. 1984). The methods resolve the integrated conductivity rather than the conductivity itself, however such results can be used with additional information on sediment thickness to give average sediment conductivity values. The accuracy of the oceanic source-field method depends upon a precise separation of oceanic and ionospherically induced signal, a precise definition of the water velocity field, and critically upon the validity of the assumption that the water velocity field is 2D and the conductivity structure is 1D (eg. Sanford 1971). These points have not always been fully considered in some of the electromagnetic determinations of sediment conductivity.

Although not all control-source methods provide estimates of sediment conductivity, the MOSES (modified magnetometric resistivity) method described by Edwards et al. (1981) does. In a MOSES study in Bute Inlet, British Columbia, Edwards et al. (1985) determined sediment conductivity to be 0.5 $S.m^{-1}$ and in a further study near the Juan de Fuca Ridge, sediment conductivities of 1.2 $S.m^{-1}$ were obtained (Nobes et al. 1986a).

Because the salt water in the sediment pore spaces is generally several orders of magnitude more conductive than the sediment matrix, the conductivity of the sediments depends strongly on the sediment porosity and permeability and less strongly on the actual sediment composition. From measurements of porosity (either direct measurement on cored samples or indirect estimates derived from seismic velocities) it is possible to derive the electrical conductivity. The electrical conductivity of the pore-water is temperature dependent and an accurate estimate of the sediment conductivity should therefore incorporate information on the sediment temperature such as from heat flow measurements (Nobes et al. 1986b).

Without temperature information, it is necessary to make simplifying assumptions about the temperature in order to obtain approximate sediment conductivities. Table 5.2 shows some estimates of sediment conductivity for the Tasman Sea made by Dr P.J. Mulhearn (pers. comm. 1987) using such assumptions. The average conductivity obtained for the Tasman Sea sediments is 0.9 $S.m^{-1}$ but this value will be a minimum

Table 5.2: Estimates for Tasman Sea sediment conductivity and thickness.

Site	Sediment Type	Porosity %	conductivity $S.m^{-1}$	Travel Time s	Av speed $m.s^{-1}$	Depth m
TP8	detrital silt and mud	44	0.74	0.5	1980	990
TP9	"	40	0.65	0.6	2080	1250
TP7	"	40	0.65	0.6	2080	1250
TP6	"	42	0.91	0.55	2000	1100
TP5	calcareous clay and mud (>30% clay)	48	0.84	0.4	1900	760
TP4	calcareous ooze	44	0.74	0.5	2000	1000
TP3	pelagic clay	64	1.26	0.23	1740	400
TP2	calcareous ooze	57	1.09	0.25	1760	440
TP1	pelagic clay	67	1.36	0.2	1700	340

Note: Results were calculated by P.J. Mulhearn. The sediment type and travel times are based on charts produced by the Ocean Sciences Institute, University of Sydney. The average porosity and seismic velocities for each sediment type were obtained from Hamilton (1976, 1985) and the electrical conductivity related to the porosity using Bullard & Parker (1971). The conductivity of the interstitial water is assumed to be the conductivity of sea-water at 1° C, salinity: 35 ‰, 4000 m depth.

estimate because the temperature of the interstitial water was assumed to be a constant 1° C. Table 5.2 also shows results for sediment thicknesses in the Tasman Sea, obtained by Dr Mulhearn from seismic observations and estimates of seismic velocity for different sediment types.

Crustal and Uppermost Mantle Layers

Estimates for crustal conductivities range from around 0.1 $S.m^{-1}$ in the upper part of the crust where the presence of water in cracks and pores is important, to of order 10^{-4} to 10^{-5} $S.m^{-1}$ at depth.

Conductivity estimates for the upper part of the crust have been obtained from direct down-hole resistivity measurements (eg. Von Herzen et al. 1983). The oceanic crust is divided into the several sub-layers, with increasing depth: layer 2A consisting of pillow

basalts, layer 2B consisting of basalt flows, layer 2C consisting of sheeted basalt dykes and layer 3 consisting of electrically resistive gabbros (Nobes et al. 1986a). Layers 2A and 2B contain fractured basalt and thus have sufficiently high porosity and permeability to be reasonably conductive. Down-hole resistivity measurements in this zone have given conductivities of 0.06 to 0.14 $S.m^{-1}$ for 6 Ma crust (Von Herzen et al. 1983, Becker et al. 1982). Results from young crust on the mid-Atlantic Rise (Hyndman & Salisbury 1984) and 108 Ma cretaceous crust (Salisbury et al. 1980) give conductivities of similar magnitude.

The transition from layer 2B to the more massive basalts of layer 2C occurs at a depth between about 500 and 1200 m (Nobes et al. 1986a) and is accompanied by a decrease in porosity and an increase in electrical resistivity. In down-hole resistivity studies in DSDP holes in young, 6 Ma, and 108 Ma lithosphere, a transition to conductivities of around 10^{-3} $S.m^{-1}$ in layer 2C has been measured (Salisbury et al. 1980, Becker et al. 1982, Hyndman & Salisbury 1984).

Control-source electromagnetic measurements on the sea-surface agree with the down-hole resistivity results and also provide information on deeper regions. The MOSES measurements near the Juan de Fuca Ridge indicate a basement conductivity of 0.12 $S.m^{-1}$ with a thickness of at least 1000 m, which is interpreted as being entirely within layers 2A and 2B. The electric field dipole-dipole control-source system does not provide any constraint on the conductance of sediment / fractured basalt layers but indicates a transition to much lower conductivities in the lower oceanic crust and uppermost mantle (Young & Cox 1981, Cox et al. 1986).

The study by Young & Cox (1981) on young oceanic lithosphere, 7km from the East Pacific Rise, indicated conductivities of about 4×10^{-3} $S.m^{-1}$ or less, extending from 2km depth to the upper mantle. The depth resolution of the method extends from about 1 to 20 km and the authors exclude the possibility of the presence of a zone of molten basalt more than about 200 m thick within this range. The control-source study of Cox et al. (1986) was located on 6 Ma lithosphere in the North Pacific and its results indicated that layers with considerable electrical resistance must exist below 5 km depth. In order to choose between non-unique inverted models the authors use assumed mantle compositions and laboratory measurements of conductivity to constrain the deeper parts of the conductivity profile. The resulting range of models include a most-resistive layer which ranges from a 6 km thick layer (at a depth of 5 to 11 km) with conductivity 10^{-6} $S.m^{-1}$, to a 24 km thick layer (at a depth of 5 to 29 km) with a conductivity of 10^{-5} $S.m^{-1}$.

Attempts have been made to measure crustal resistivity by measuring sub-audio (ELF) frequency signals which penetrate into a continent and propagate beneath an adjacent ocean. Experiments with both natural and artificial sources have been unsuccessful but suggest a lower limit for the conductivity of near-bottom rocks of 10^{-2} $S.m^{-1}$ (Cox 1980). These results are not likely to be as reliable as the seafloor control-source measurements. The relatively high conductivity of the seafloor sediments and upper crust will make accurate

measurement of the seafloor signals difficult.

The MT anisotropy method provides an estimate for crustal resistivity averaged over a large horizontal scale. From the observed anisotropy in the MT response at SF Revisited and AGGY III, Chave & Cox (1983) conclude that the MT adjustment distance L for the northeast Pacific Ocean is less than 700 km. This value suggests that the integrated resistivity of the crust is less than 3×10^7 $\Omega.m^2$ and for a 30 km thick resistive layer, the conductivity must be greater than 10^{-3} $S.m^{-1}$. These values are much less resistive than the control-source results of Cox et al. (1986). The discrepancy is suggested to be caused by the different measurement scales. A limited number of narrow conductive pathways from the seafloor to the mantle, for example at spreading ridges or transform faults, could reduce the resistivity determined by the MT anisotropy method without affecting the more localized control-source measurements (Chave & Cox 1983). The Tasman Project data should allow an accurate estimate of the adjustment distance of MT anisotropy in the Tasman Sea, and thus of the crustal resistivity.

Chapter 6 Time Series and Basic Parameters of the Tasman Project Data

The aims of this chapter are to present the time series recorded in the Tasman Project and the preliminary analysis and parameterization of the data. The chapter will include descriptions of the geomagnetic time series, power spectra of the various components, coherence functions between components and finally the induction arrows which parameterize the geomagnetic response to major lateral boundaries in conductivity structure. It will also include a description of the techniques used for time series analysis.

The main aim of this thesis is to investigate the electrical conductivity structure beneath the Tasman Sea and Australian continental margin and the most important results from this chapter will therefore be the induction arrows. A full description of the determination of the arrows and a qualitative interpretation of the arrows is included. Quantitative modelling of the results is deferred until the availability of further data from the Continental Shelf Experiment (see chapter 1) and is not included in this thesis.

It is important to examine preliminary stages of the data analysis, such as time series and power spectra, for two reasons. The first reason is that many of the final results derived from induction arrows (or MT impedances) are visible in more elementary representations of the data. The direct observation of these features will confirm that the results are independent of the analysis method, and may also indicate the appropriate analysis method to follow. For example, observation of strong anisotropy in the horizontal electric field time series can indicate two-dimensionality of the MT impedance, and therefore the need for determining full impedance tensor results.

The second reason for examining time series, power spectra, coherences etc. is that these results contain important information on the underlying physical processes on which induction arrows and impedances are based. They provide information on the form of the source-field (eg. the magnitude and frequency of geomagnetic disturbances), the spatial uniformity of the source-field across the recording line and on the presence and form of any noise in the data. Although induction arrows and impedance results are influenced by these effects the arrows and impedances may not provide direct information on them.

6.1 Time Series

The recording period of the Tasman Project produced 67 MT (magnetic and horizontal electric field component) time series each of approximately 120 days length. A large-scale plot of each of the full time series has been produced and closely examined to provide information on the data quality and geomagnetic effects. Although it is impractical to present the full set of complete time series in this thesis, careful examination of selected components and of selected portions of the time series, reveals many of the important features of the data. It is possible, for example, to observe many of the relationships between magnetic and electric field components which are quantified later in numerical

analyses.

Full-length time series for selected sites spanning the recording line are shown in Figure 6.1. The magnetic field recordings shown in Figure 6.1 exhibit the regular diurnal variation Sq and also a number of magnetic storms, for example near days 29, 60, 88 and 110. A list of the major magnetic disturbances recorded at Australian Geomagnetic Observatories during the Tasman Project recording period is given in Table 6.1. At the scale of Figure 6.1 the magnetic storms are most easily recognized by the disturbance-time increase in the daily variation ie. SD (Egeland et al. 1973). There is clear correlation of the magnetic disturbances between the different components and between the different sites. Figure 6.2 shows the daily K-index sums for the recording period and provides a quantitative measure of the level of geomagnetic disturbance. A correlation exists between high K-sums and periods of strong magnetic disturbance in the recorded Tasman Project data.

Note that between the periods of strong geomagnetic activity there is a background level of lower magnitude activity consisting of events such as a magnetic substorms. There are numerous days during the recording period with K-sums of between 10 and 20 (Figure 6.2). These periods, together with the periods of stronger magnetic disturbance, provide suitable signal for geomagnetic induction studies. During the recording period there were also a few very quiet days with K-sums of less 8.

The vertical magnetic field component exhibits the expected coast effect (Parkinson and Jones 1979) with enhanced activity at substorm and storm periods at sites near the coast. This effect will be examined in more detail in Figure 6.3 below. At diurnal periods the B_Z components in Figure 6.1 show a different pattern from the higher-frequency coast effect and increase in magnitude away from the Australian coastline. The daily variation of B_Z becomes larger towards the inland of the Australian continent and most strongly towards the eastern side of the Tasman Sea. This effect is discussed in Bennett & Lilley (1973) and will be treated in Bindoff (1988); the diurnal variations are excluded from the geomagnetic induction studies in this thesis.

The differences between magnetic field components at very long periods (of order weeks to months) such as the difference in slope between the CMO and GNS B_Z traces are caused by instrumental drift. No correction for drift in the land data has been made and the seafloor magnetic field components may also contain a residual drift signal induced by long-period oceanic effects.

Figure 6.1b shows the full-length time series for all of the electric field recordings. For the seafloor recording sites near the Australian coast, the electric field data are dominated by irregular long-period (days to weeks) variations. These signals are interpreted as oceanic in origin and resulting from the dynamo action of ocean water movement in the Earth's steady magnetic field. The long-period electric field signals can be closely related to satellite and oceanographic evidence of an oceanic warm-core ring

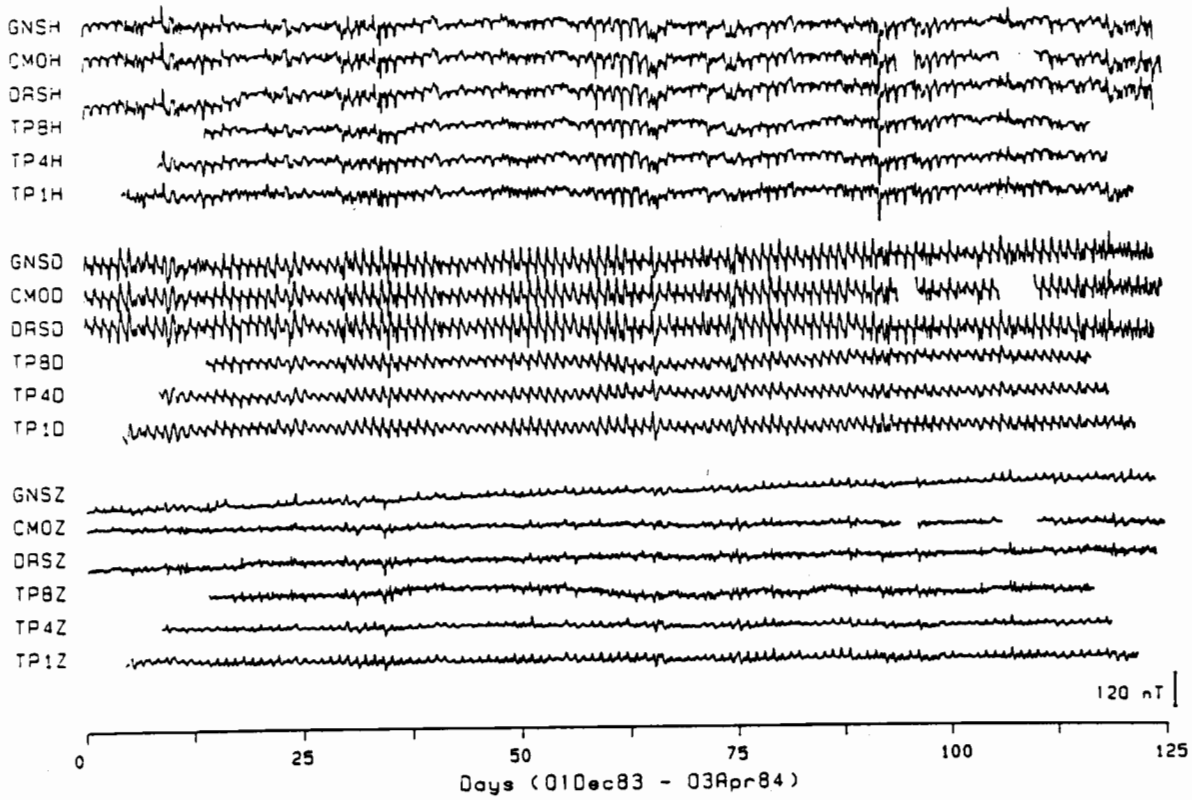

Figure 6.1: Full length time series for magnetic and horizontal electric components from sites spanning the Tasman Project recording line. The zero time mark is at 0000 h 1 December 1983 UT. The data plotted are hourly mean values; the bars at the right of the diagram indicate the vertical scale.

(a) Magnetic field time series for B_H, B_D and B_Z components.

(b) Horizontal electric field time series for E_H and E_D components. The traces labelled EU refer to components which have not been rotated to magnetic north and east (see chapter 3). Note the long-period irregular fluctuations in the horizontal electric field components from sites near the Australian coast. Also note the "beating" which is visible in the horizontal electric field data and more weakly developed in the magnetic field data.

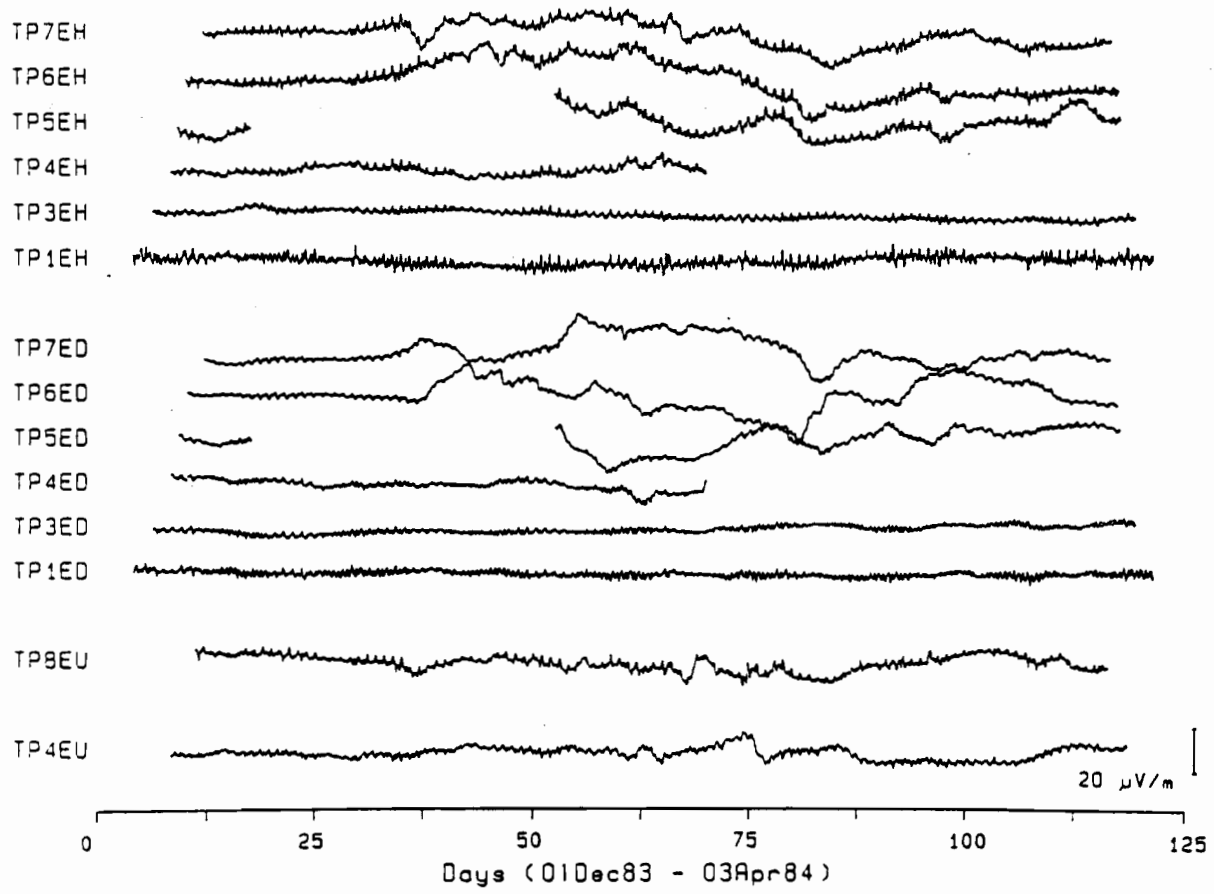
TP7EH
TP6EH
TP5EH
TP4EH
TP3EH
TP1EH
TP7ED
TP6ED
TP5ED
TP4ED
TP3ED
TP1ED
TP8EU
TP4EU
20 µV/m
0
25
50
75
100
125
Days (01Dec83 - 03Apr84)

Figure 6.1b

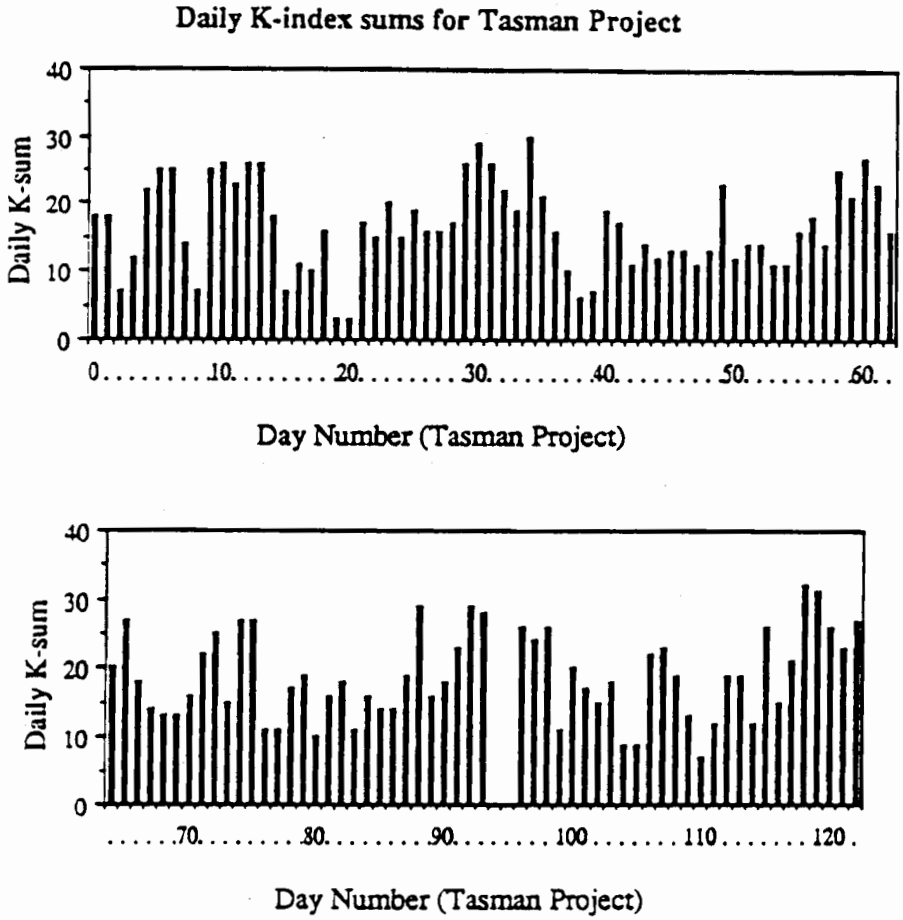

Figure 6.2: Daily K-index sums from Canberra Magnetic Observatory for the duration of the Tasman Project recording period. Data are taken from the monthly Geophysical Observatory Reports distributed by the Australian Bureau of Mineral Resources. Note the coincidence of periods of high K-sums with the geomagnetic disturbances visible in Figure 6.1, for example around days 29 and 94.

Table 6.1 Magnetic Activity During the Tasman Project Recording Period

Commencement Time			Disturbance
Tasman Day	UT Day	Time	
09	10DEC83	0312	Principal Magnetic Storm/ssc
29	30DEC83	0347	Principal Magnetic Storm/ssc
34	04JAN84	04--	Principal Magnetic Storm
64	03FEB84	1514	Principal Magnetic Storm/ssc
73	12FEB84	14--	Principal Magnetic Storm
81	20FEB84	1556	ssc (sudden commencement)
86	25FEB84	0312	sfe (solar flare event)
87	26FEB84	09--	Principal Magnetic Storm
91	01MAR84	11--	Principal Magnetic Storm
96	06MAR84	05--	Principal Magnetic Storm
116	26MAR84	1800	Principal Magnetic Storm
118	28MAR84	14--	Principal Magnetic Storm
122	01APR84	03--	Principal Magnetic Storm

Data are taken from Bureau of Mineral Resources Geophysical Observatory Reports for December, 1983 and January-April 1984. The listed disturbances were recorded at Canberra Magnetic Observatory, Gnangara Observatory (in Western Australia) and/or the Charters Tower Observatory (in Queensland).

crossing the recording line (Mulhearn et al. 1986, Lilley et al. 1986a). Such rings (or eddies) pinch off from the East Australian Current as it flows between 30° and 34° S (Godfrey et al. 1980). The magnitude of the long-period electric field signal associated with the warm-core ring is much larger than has been observed in previous seafloor electric field measurements (J.H. Filloux, pers comm.) reflecting the intense nature of the East Australian Current.

Electric field signals induced by tidal ocean movements produce the approximately 14 day modulation of the diurnal variation signal evident in Figure 6.1b. Examination of Figure 6.1a, particularly of the B_D components, indicates the presence of a similar, though

smaller, tidal modulation in the magnetic field data. Although the very long-period oceanic signals dominate the electric-field time series, a close examination of these data reveals the same high-frequency disturbances that are present in the magnetic field data. For example the electric field components in Figure 6.1b show the magnetic storm commencing on day 29. At site TP1, the most shallow seafloor site (being on the Lord Howe Rise), the electric field signals at diurnal, tidal and shorter periods are stronger than at the deeper seafloor sites.

Figure 6.3 shows a 24 h segment of the recorded time series (day 29 in Figure 6.1) at an enlarged scale. The segment includes a sudden magnetic storm commencement at 0347 UT and subsequent storm activity (see section 4.3 for details). Figure 6.3a shows the magnetic field data for sites spanning the land and sea parts of the recording line while Figure 6.3b shows the magnetic field data for the complete set of seafloor sites. The figure shows that there is reasonable coherence of the source-field over the recording line. Although the form of the field fluctuations varies between sites, for example between land and seafloor sites, each fluctuation is recorded at sites spanning the recording line. It will be shown below that most of the variation between sites is due to the induced response in the Earth, and that the inducing source-field is coherent over distance scales of thousands of kilometres.

At storm and substorm periods (less than 24 h) the vertical magnetic component B_Z is strongly enhanced at sites near the Australian coast. This coast effect is the geomagnetic response to the conductivity contrast between the ocean and the continent with a possible contribution from the corresponding conductivity contrast in the underlying crust and mantle. The coast effect decreases smoothly with increasing distance to sea, with the quietest B_Z components occurring at sites TP4 and TP3 in the central Tasman Sea. At sites TP2 and TP1 the level of activity in B_Z rises indicating a "coast effect" associated with the bathymetric contrast of the Lord Howe Rise with the deeper ocean to the west.

Close examination of the feature labelled I on Figure 6.3a suggests that the increased signal in B_Z near the Australian coast is correlated with fluctuations in the B_D magnetic field component . The feature shows that for fluctuations with periods of order 1 hr the B_Z component at sites near the coast correlates inversely with the B_D component ie. the magnetic field component approximately transverse to the coast. Such a correlation is expected for the coast effect which is an E-pol anomaly (see chapter 4). At shorter periods it is difficult to assess with which horizontal component B_Z correlates, since the B_D component itself is correlated with B_H near the coast (see below). However examination of the feature II, which at the inland site GNS occurs mainly in B_D not B_H, again suggests that the B_Z component is correlating inversely with the B_D component.

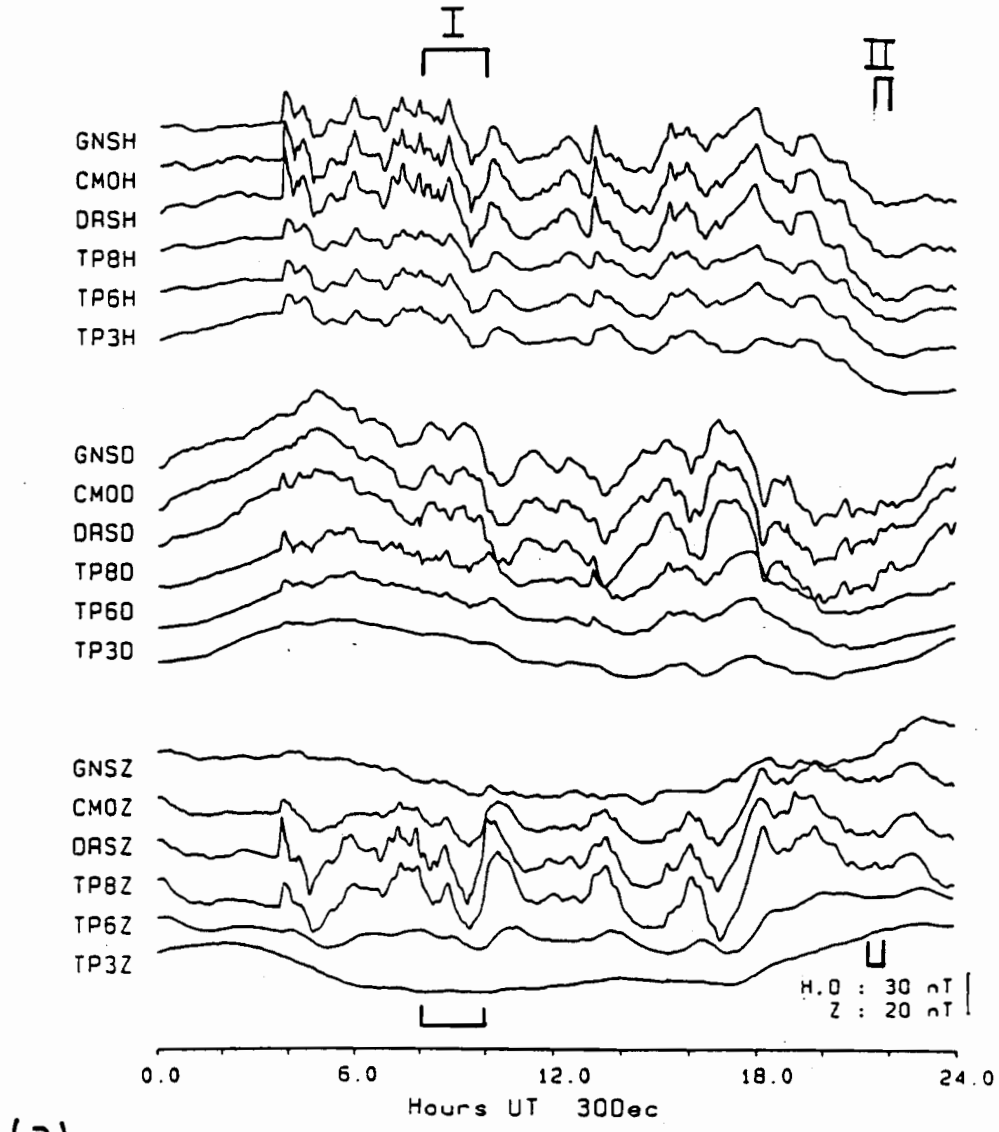

Figure 6.3: Examples of the time series for a single day, 30 December 1983 (which is Day 29 in Figure 1). The data are plotted at a density of 16 points per hour and the labelled segments are discussed in the text. Note the sudden commencement (SSC) of a storm at 0347 UT.

a. Magnetic field components from sites spanning the recording line.

b. Complete set of seafloor magnetic field data.

c. Horizontal electric field data.

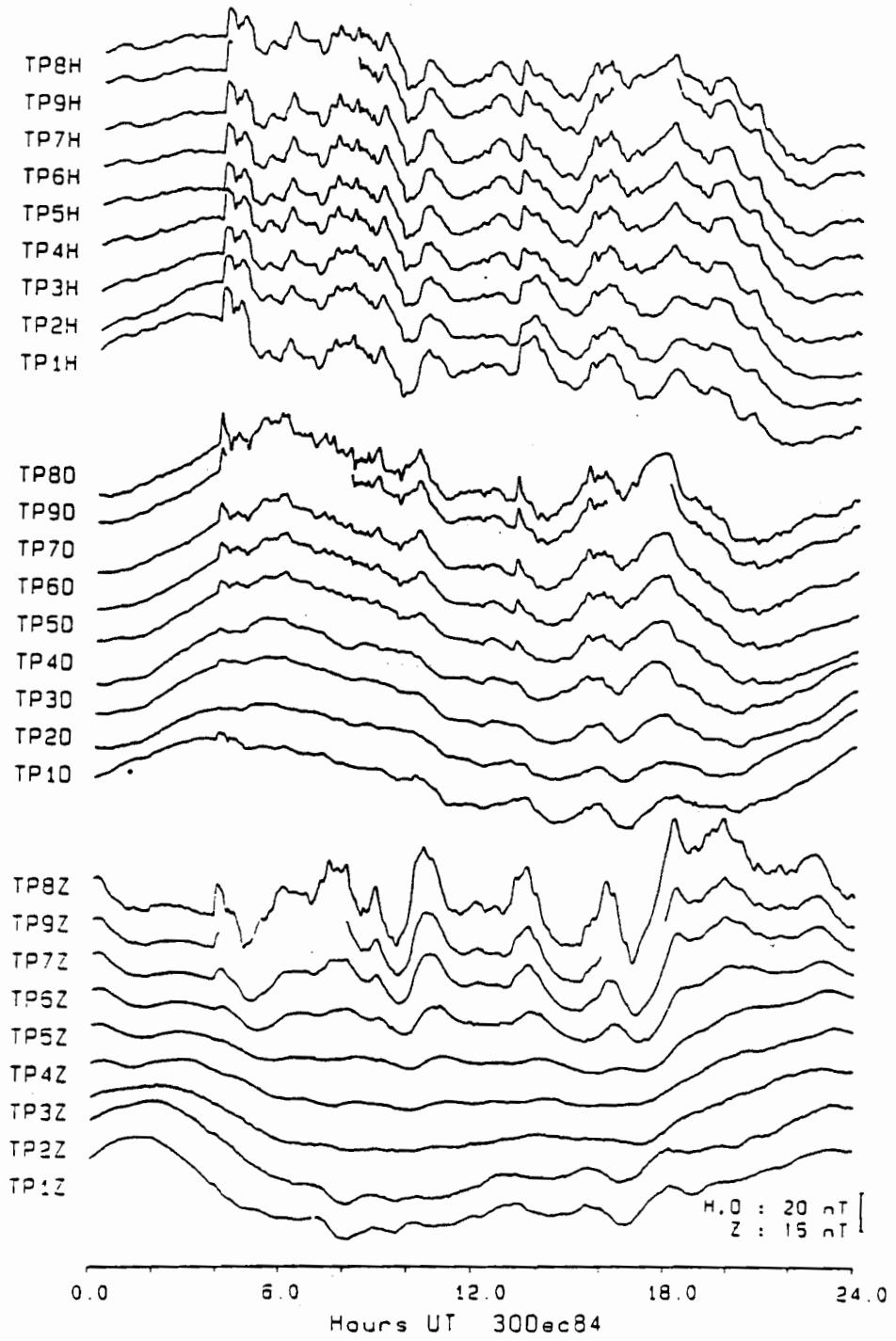
TP8H
TP9H
TP7H
TP6H
TP5H
TP4H
TP3H
TP2H
TP1H
TP80
TP90
TP70
TP60
TP50
TP40
TP30
TP20
TP10
TP8Z
TP9Z
TP7Z
TP6Z
TP5Z
TP4Z
TP3Z
TP2Z
TP1Z
H.0 : 20 nT
Z : 15 nT
0.0
6.0
12.0
18.0
24.0
Hours UT 30Dec84

Figure 6.3b

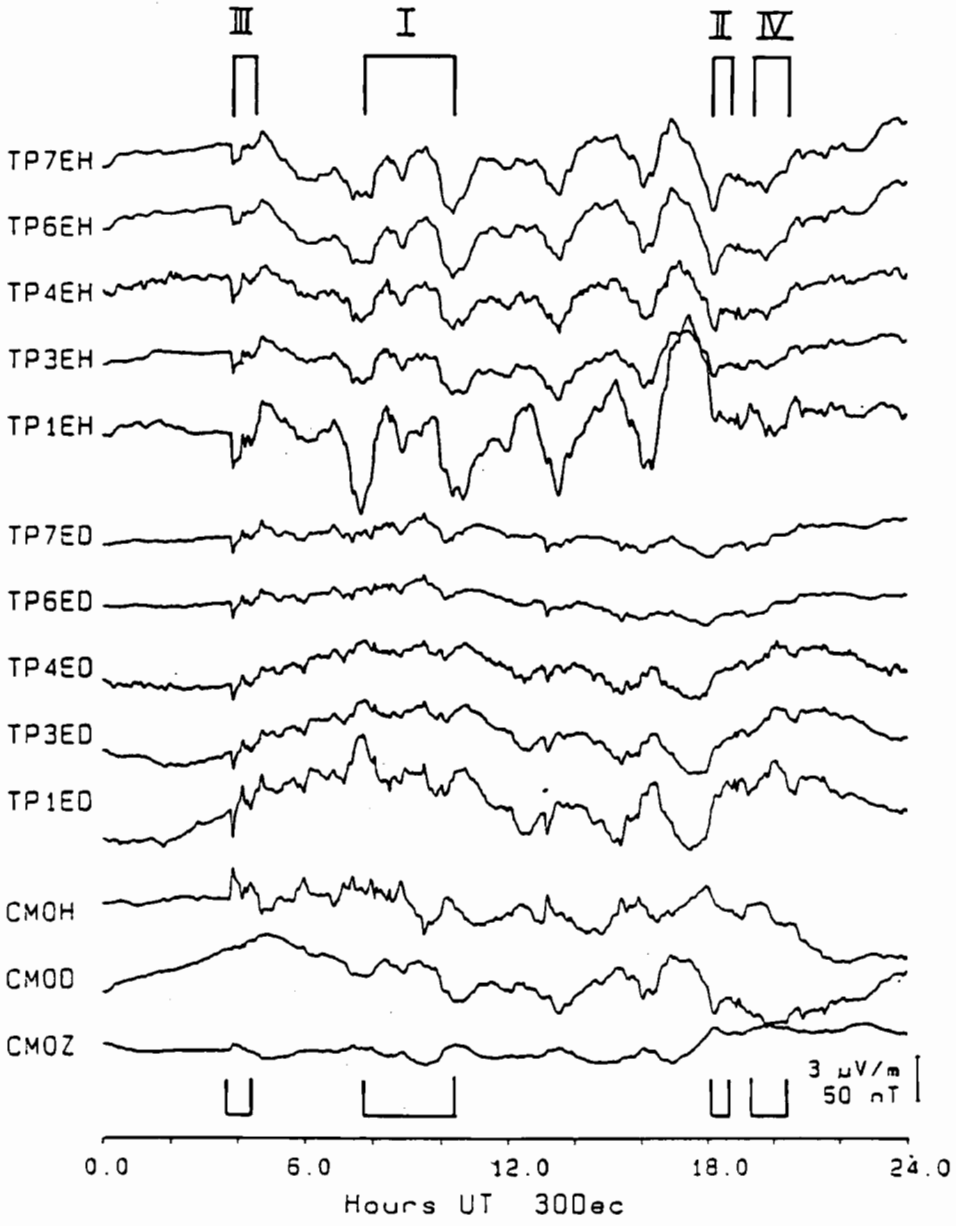
III
I
II
IV
TP7EH
TP6EH
TP4EH
TP3EH
TP1EH
TP7ED
TP6ED
TP4ED
TP3ED
TP1ED
CM0H
CM0D
CM0Z
3 μV/m
50 nT
0.0
6.0
12.0
18.0
24.0
Hours UT 30Dec

Figure 6.3c

The magnetic data show that the seafloor B_H and B_D components are attenuated relative to the land components. For example the B_D component at at site TP3 contains little energy at periods of less than 2 h, while the B_H component at the same site is clearly attenuated relative to the B_H component at land sites. The B_D component appears to be more strongly attenuated than the B_H component at all of the seafloor sites. The attenuation of the magnetic field fluctuations with depth in the ocean is caused by the shielding effect of the conducting ocean water and as predicted by the theory in section 4.1 this effect is strongest at the highest frequencies.

Close examination of Figure 6.3b indicates that the attenuation of the B_D component varies strongly with distance from the Australian coast with the attenuation increasing from site TP8 to site TP4. Spatial variations in attenuation will be caused by spatial variations in ocean depth and the underlying conductivity structure. The strong dependence of the B_D attenuation with distance from the Australian coast however suggests the influence of (E-pol) 2D effects associated with the Australian coastline. The much stronger attenuation of B_D than B_H at all seafloor sites also suggests that effects from the Australian coastline may extend large distances into the Tasman Sea. The form of B_H is moderately similar across the Tasman although sites near the coast contain a larger (less attenuated) high-frequency content than sites in the Central Tasman. This effect is probably due to the B-pol anomaly associated with the coastline.

Further examination of Figure 6.3a shows that for sites near the Australian coast the B_D component contains signal not present at inland and Central Tasman sites. This extra signal is correlated with the B_H time series. The phenomenon is illustrated particularly well by the geomagnetic storm sudden commencement . Away from the coast at GNS and TP3 the SSC is evident only in B_H , whilst near the coast, at DRS and TP8, the SSC has a significant B_D component. The effect appears to be extend further in the seawards direction. Seafloor site TP6, which is 190 km from the coast, still has a significant B_D component in the sudden commencement; however at CMO, only 90 km from the coast, the B_D component is not discernible. These observations provide a strong indication that the pattern of geomagnetic induction in the Tasman Sea contains a 3D influence.

Figure 6.3c shows the electric field components for the same time period as the magnetic fields in Figure 6.3a&b. The CMO magnetic data are included in the figure to permit direct comparison of the electric and magnetic field data. Perhaps the most noticeable feature of the figure is the relatively large size of the electric field fluctuations at site TP1. This observation is explained, at least in part, by the more shallow depth of the site. For a given sub-seafloor conductivity profile (and thus a given seafloor impedance)

the larger seafloor magnetic fields at a shallow site must be balanced by larger electric fields. For the remaining sites, Figure 6.3c shows the level of E_H disturbance decreases slightly in magnitude from that at TP7 and TP6, to that at TP4 and TP3. The E_D disturbances are relatively uniform but are slightly larger at TP3 and TP4 than at TP6 and TP7. This last effect may be partly due to a 'contamination' of the E_D data by the larger E_H fluctuations caused by a slightly incorrect instrument orientation (see chapter 3).

Examination of the time series (eg. the features I and II in Figure 6.3c) indicates that the activity in E_H correlates with the magnetic B_D component. Features III (the SSC) and IV show that E_D is correlating with B_H. The E_D/B_H ratio, ie. the impedance in the magnetic east direction, appears to be significantly smaller than E_H/B_D ratio, the impedance in the magnetic north direction, for all seafloor sites. This result suggests the final MT impedances will be significantly anisotropic. Inspection of the SSC in Figure 6.3c also shows that at higher frequencies (above about 1 cph) E_H is partially correlated with B_H. This observation supports the earlier evidence for a 3D influence in the geomagnetic induction.

Summary of Time Series Observations

The examination of the time series described above provides important preliminary information on the processes of geomagnetic induction in the Tasman Sea region. The following conclusions may be drawn:

1. Geomagnetic induction at all sites in the Tasman Sea is dominated by non-1D effects.
2. Spatial variations in field components tend to be gradual and large-scale rather than dominated by strong local effects. Most of the spatial variation appears to be related to the boundaries of the Tasman Sea.
2. There are strong 2D effects near the Tasman Sea boundaries as shown by the observed coast-effect at the Australian coastline and over the Lord Howe Rise.
3. Two-dimensional effects however extend large distances from the coastline, as shown by the unequal attenuation of B_H and B_D at sites in the central Tasman Sea.
4. The geomagnetic induction contains a 3D component, as shown by the correlation of B_H and B_D near the Australian coastline.

A full interpretation of these effects will be made later using induction arrows and MT impedances. Some preliminary results may however be drawn from the time series observations. From the observations it appears that electric current flow in the Tasman Sea is preferentially in the longitudinal, rather than the transverse, direction. Such current flow explains the uneven attenuation of B_H and B_D and the anisotropic impedance ratios.

The tendency for the spatial variation of field components to relate to the Tasman Sea boundaries suggests the anisotropic current flow is due to the large-scale shape of the Tasman Sea and not to locally-anisotropic conductivity structure at each site. At this stage it cannot be discriminated whether the anisotropic current flow is due to restriction of transverse current flow by the Australian coast and Lord Howe Rise, or to enhancement of longitudinal current flow by large-scale 3D induction effects or by current channelling effects.

The 3D effects observed near the Australian coastline are explained by a deviation of perpendicular electric currents by the Australian coastline into the longitudinal direction. The magnetic field associated with the deviated currents (approximately B_D) will therefore be partially correlated with the magnetic field (approximately B_H) which induced the originally transverse currents. The longitudinal electric field (approximately E_H) will also be partially correlated with this magnetic field component. It is not possible to tell from the time series observations whether such a deviation of currents is part of a 3D geomagnetic induction process, or a simpler current channelling phenomenon in which ohmically flowing currents are deviated along the path of least electrical resistance.

6.2 Spectral Analysis

This section describes the conversion the Tasman Project MT recordings into the frequency domain. The theoretical background to the methods used may be found in section 4.2 of chapter 4. In summary, the data were converted into the frequency domain using standard Fourier transformation of long time-series. Smoothed auto and crosspower estimates were obtained by averaging over relatively broad frequency-bands and omitting narrow frequency-bands around tidal and diurnal lines.

The first step in the data analysis involved choosing the sections of time series to be used in spectral analysis. To facilitate computation, the spectral analysis was based on time series of two different lengths. Longer period results ($T \geq 1$ h) were derived from analysis of segments of 42.7 days (2^{10} h) and short period results ($T < 1$ h) from segments of 10.7 days (2^8 h). Each long-period (LP) segment consists of 8192 (2^{13}) data points with a sampling rate of 8 data.h^{-1} while short-period (SP) segments comprised either 8192 data points at 32 data.h^{-1} or for analyses involving Gough-Reitzel data, 4096 data points at 16 data.h^{-1}. The required sampling rates were obtained by simple arithmetic averaging of the final Tasman Project time series (which also have sampling rates of 2^m data.h^{-1}).

In geomagnetic induction studies it is generally desirable to analyse simultaneous recordings from across the span of recording sites. Such an approach reduces the effect of non-stationarity on the results. For example, a transfer function between two different sites can be calculated directly from the auto and crosspower spectra without the need to standardize the power at each site to some third, overlapping, recording. Since

simultaneous data is available from nearly all Tasman Project sites (Table 3.2) it was decided to restrict analysis to periods where corresponding data are available for all (or at least most) sites.

Table 6.2 shows the segments chosen for analysis of the Tasman Project data and Table 6.3 shows the availability of data for each instrument. The two long period (LP) segments were chosen such that at least one segment had been recorded at every site. The five short period (SP) segments were chosen from periods of at least moderate geomagnetic disturbance. The recent study of Egbert & Booker (1986) has shown that during periods of strong geomagnetic disturbance the source-field is least uniform and may introduce noise into analyses which are based on assumptions of uniform source-fields . Their study was applied however, to magnetic field recordings made on land. For seafloor data, in which there is usually a larger level of other noise (oceanically induced) the choice of segments in geomagnetically active periods provides data with an improved SNR. The results of Egbert & Booker (1986) should nevertheless be considered in further analyses of the Tasman Project data.

Table 6.2 Data Segments used for MT Analyses

Event	Start	End		Length (h)
LP1	D20 0.0	D62	16.0	1024
LP2	D62 0.0	D104	16.0	1024
SP1	D26 0.0	D36	16.0	256
SP2	D57 0.0	D67	16.0	256
SP3	D84 0.0	D94	16.0	256
SP4	D95 0.0	D105	16.0	256

Table 6.3 Data available for selected MT analysis events

Instruments	Percentage Missing Data in Event					
	LP1	LP2	SP1	SP2	SP3	SP4
TP1 MAG	*	*	*	*	*	*
HEF	*	*	*	*	*	*
TP2 MAG	*	*	*	*	*	*
HEF	*	*	*	*	*	*
TP3 MAG	*	*	*	*	*	*
HEF	*	*	*	*	*	*
TP4 MAG	*	*	*	*	*	*
HEF	*	N	*	*	N	N
TP5 MAG	*	*	*	*	*	*
HEF	N	*	N	*	*	*
TP6 MAG	*	*	*	*	*	*
HEF	*	*	*	*	*	*
TP7 MAG	*	*	*	*	*	*
HEF	*	0.1	*	*	*	*
TP8 MAG	*	*	*	*	*	*
TP9 MAG	5.3	*	13.3	*	*	*
DRS MAG	0.3	0.4	*	*	*	*
CDM MAG	0.3	0.3	*	*	*	*
BBB MAG	14	17	*	N	*	*
CMO MAG	0.3	4.9	*	*	5.9	10.5
BKM MAG	0.3	0.3	*	*	*	*
CLC MAG	*	0.3	*	*	*	*
BLN MAG	*	0.3	*	*	*	7.5
GNS MAG	*	0.2	*	*	*	*
MYL MAG	6.2	12.9	*	N	*	*

Notes * = Event is complete

N = Greater than 50% of data is missing

Each of the selected segments was analysed as a complete time series without further segmentation. Before Fourier transformation a least-squares linear trend defined by

$$u(t) = c_0 + c_1 t \qquad 6.1$$

where for the time series $u_1, u_2 \ldots u_n$ with digitizing interval δ,

$$c_0 = \frac{2(2n+1)\sum_{i=1}^{n} u_i - 6\sum_{i=1}^{n} i u_i}{n(n-1)} \qquad 6.2a$$

and

$$c_1 = \frac{12\sum_{i=1}^{n} i u_i - 6(n+1)\sum_{i=1}^{n} u_i}{\delta n(n-1)(n+1)} \qquad 6.2b$$

(Bendat & Piersol 1971 p. 291) was removed from each time series. Removal of this least-squares trend produced data with a zero mean value.

After removal of the trend, a cosine taper was applied to both ends of the time series over 1/64 of the time series length. The taper is defined by the weighting function w_i which is multiplied with each data point. The weighting function is given by

$$\begin{aligned} w_i &= \frac{1}{2}\left(1 - \cos\left[\frac{\pi(i-0.5)}{p}\right]\right) && 0 \le i \le p \\ &= 1 && p < i < (n-p) \\ &= \frac{1}{2}\left(1 - \cos\left[\frac{\pi\{n-(i-0.5)\}}{p}\right]\right) && (n-p) \le i \le n \end{aligned} \qquad 6.3$$

where p is the number of data points to be tapered at each end of the time series. In order to correct for the reduction in variance caused by the application of the taper the time series were multiplied by a correction factor defined by

$$\kappa = \sqrt{\frac{n}{\sum_{i=1}^{n} w_i^2}} \qquad 6.4$$

No further filtering was applied to the time series prior to Fourier transformation. Examination of some trial spectral results indicated that the power spectra of both electric and magnetic time series were relatively steep, decreasing with increasing frequency. Errors arising from aliasing of higher frequencies will thus be negligible, obviating the need for high-frequency filtering. The removal of drift (during data reduction) and a linear trend from each time series reduced the requirement for low-frequency filtering. At both ends of the spectrum of available frequencies from the Fourier transformation spectral lines were omitted from the final band averaged estimates. Spectral lines outside the period

range ($0.1L$, $2T_N$) where T_N is the Nyquist period 2δ, were not used for further analysis.

The actual Fourier transformation was performed using an IMSL subroutine FFTRC which defines the digital Fourier transformation from a to X for k = 0, 1, ... n / 2 by

$$X(k+1) = \sum_{j=0}^{n-1} a(j+1)\, e^{2\pi j k / n} \qquad 6.4$$

Because each input time series consisted of 2^m data points it was not necessary to add zeros prior to Fourier transformation. The digital Fourier transform corresponds to an analytical form of the transform with a positive exponent and thus produces spectral data with an implied negative time-dependence (appendix 3).

Figure 6.4 shows the spectral lines from the Fourier transformation of a seafloor horizontal electric-field recording. The figure shows strong spectral lines at diurnal and semi-diurnal tidal periods emerging from a background level of Fourier transform values. Note that around the strong deterministic spectral lines there is side-band 'contamination' of adjacent spectral lines. Between the periodic spectral lines the Fourier Transform values are quite scattered, reflecting the large random errors in these data. After conversion to power values and smoothing these 'background' data form the basic auto and crosspowers used in the geomagnetic induction study.

The TP3 E_D component was chosen for illustration in Figure 6.4 because it contains strong geomagnetic and tidal components. Table 6.4 lists the major diurnal and tidal lines predicted in the data. The diurnal lines occur at the frequency 0.042 cph, where there is a strong spectral peak associated with the 24 h component of Sq, and the P1 and K1 tidal frequencies. A smaller peak at a slightly lower frequency possibly corresponds to the 01 and Q1 tidal frequencies. At the semi-diurnal frequency, 0.083 cph, there is a group of strong spectral lines associated with the S2 and K2 tidal lines and the 12 h harmonic of Sq. A larger peak at 0.085 cph is associated with the M2 tidal line and there is also a suggestion of a peak in the spectral lines associated with the N2 tidal frequency.

Power spectra were calculated using equation 4.123 with smoothing over spectral lines. Some further smoothing was also obtained when the power spectra from the different LP and SP segments were averaged to produce final spectra. The band-averaging scheme was chosen such that the final bands adequately represented the form of the frequency spectrum and such that narrow bands around the clusters of tidal and diurnal periods at 24, 12, 8 and 6 h could be omitted from further analysis. Figure 6.5 illustrates the band-averaging scheme used for the analysis of the Tasman Project data and Table 6.5 summarises these data.

The band-averaging scheme, chosen in an ad hoc manner, was designed such that each frequency band contained as many spectral lines as possible (particularly at high and low frequencies where noise levels are highest) and that the bands were approximately evenly distributed over the log frequency spectrum. Some adjustment of bandwidths was

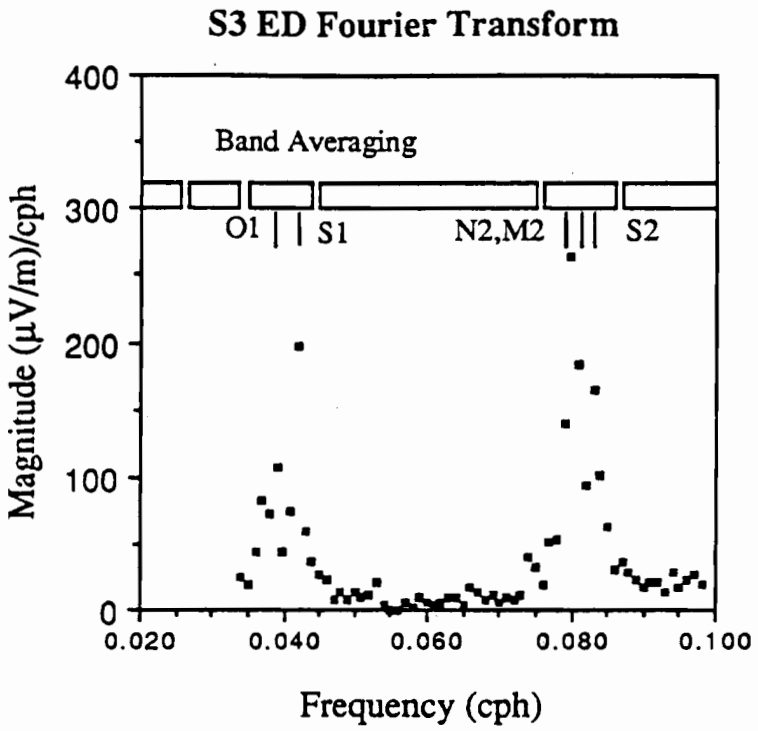

Figure 6.4: Magnitudes of the raw Fourier Transforms for the E_D component at site TP3. The time series analysed was an LP segment of 1024 h and 8192 data points. The figure shows spectral lines m = 35 to 100 (corresponding to frequencies f = (m/1024) cph). Also shown are the positions of the major diurnal and semi-diurnal deterministic signals, and the band-averaging system used to eliminate the deterministic signal.

Note that the bands around the tidal clusters are sufficiently wide to remove all spectral lines significantly affected by side-band contamination. For the TP3 E_D component , the ratio of the M2 magnitude to the background Fourier transform magnitude is relatively high and side-band contamination will be stronger than for other components.

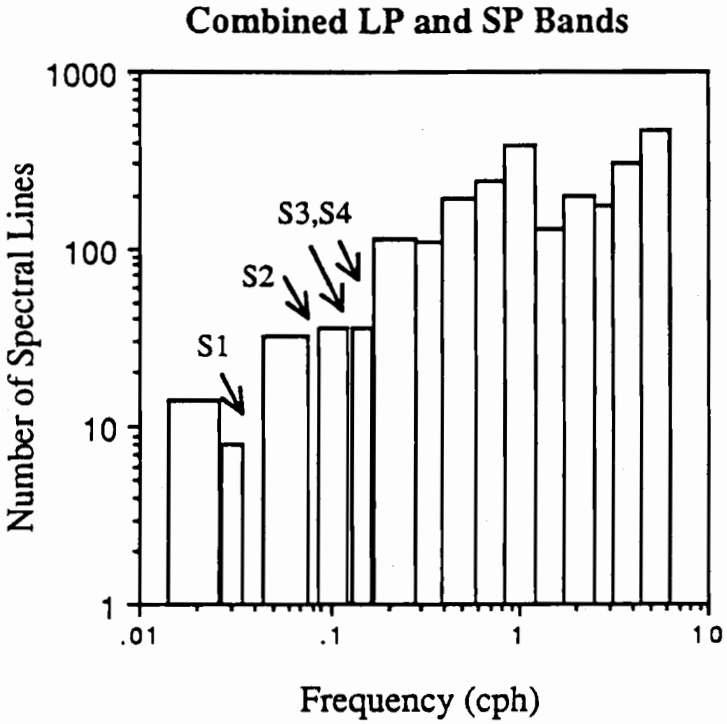

Figure 6.5: Band-averaging system used on the Tasman Project data and listed in Table 5.4. Results for frequencies equal to and less than 1 cph are derived from LP segments and results for higher frequencies from SP segments. Narrow bands around periods of 24, 12, 8 and 6 h (labelled respectively S1-S4) are omitted from further analysis.

Table 6.4 Major Periodic Signals in Geomagnetic Data

Constituent	Period (h)	Frequency (cph)*10^{-2}	Relative Magnitude	Spectral Line in 42.7 day analysis
1 Ionospheric				
S1	24.0	4.167	Variable	42.7
S2	12.0	8.333	"	85.3
S3	8.0	12.50	"	128.0
S4	6.0	16.67	"	170.7
2 Diurnal Ocean Tides				
Q1	26.868	3.722	0.136	38.1
O1	25.819	3.873	0.710	39.7
P1	24.066	4.155	0.330	42.5
K1	23.934	4.178	1.000	42.8
3 Semi-diurnal Ocean Tides				
N2	12.658	7.900	0.192	80.9
M2	12.421	8.051	1.000	82.4
S2	12.000	8.333	0.467	85.3
K2	11.967	8.356	0.127	85.6

The table is intended to provide an outline of the main deterministic signals present in geomagnetic data. Such signals include the geomagnetic daily variation Sq induced in the ionosphere and magnetosphere. This signal and its harmonics are included in Group 1 above. Oceanic geomagnetic and geoelectric recordings also contain deterministic signals induced by ocean tides. The largest tide of the diurnal and semi-diurnal bands (K1 and M2) and other tides with a magnitude of >10% of this tide are shown in Groups 2 & 3. Magnitudes are from the equilibrium tidal potential (Melchior 1983) while the relative magnitudes are with respect to either K1 or M2. Both land and ocean geomagnetic recordings contain additional signal at these tidal periods induced by ionospheric tides.

The table also gives the position of the tidal frequencies in terms of the spectral lines from the Fourier Transform of an LP segment. Groups of tides with close frequencies such as (S1,P1,K1) and (S2,K2) will not produce separate spectral lines.

Table 6.5: Band Averaging System used on Tasman Data.

Band	Period (h)	Frequency (cph)	Period Range (h)		Spectral Lines	No. Events	DOF	Notes
1	50.0	0.020	73.1	37.9	14	2	56	*
2	32.5	0.031	36.6	29.3	8	2	32	
3	25.3	0.040	28.4	22.8	10	2	40	S1 *
4	16.7	0.061	22.3	13.3	32	2	128	
5	12.3	0.081	13.1	11.6	11	2	44	S2 *
6	9.62	0.104	11.5	8.25	36	2	144	
7	8.00	0.125	8.19	7.82	7	2	28	S3 *
8	6.85	0.146	7.76	6.13	36	2	144	
9	6.01	0.166	6.10	5.92	6	2	24	S4 *
10	4.44	0.225	5.89	3.57	114	2	456	
11	3.00	0.333	3.56	2.59	108	2	432	
12	2.08	0.481	2.59	1.74	194	2	776	
13	1.44	0.694	1.74	1.23	241	2	964	
14	1.00	1.00	1.23	0.841	387	2	1548	
15	0.692	1.45	0.839	0.590	130	4	1040	
16	0.481	2.08	0.590	0.406	196	4	1568	
17	0.357	2.80	0.406	0.318	175	4	1400	
18	0.267	3.75	0.318	0.231	304	4	2432	
19	0.190	5.26	0.231	0.162	475	4	3800	

* These bands are generally not included in further analysis.

performed in order to maximize coherences at either end of the spectrum. For example, at the long period end of the spectrum a narrow band around 30 h was chosen instead of a broader band with more degrees of freedom but with much lower coherences between the components.

The narrow bands defined around the clusters of tidal and diurnal lines were designed to be sufficiently wide to reject both the spectral lines and the associated side-band contamination. Three spectral lines were omitted on either side of each major diurnal and tidal lines. Therefore the bands omitted comprised the frequency range between the diurnal tides Q1-K1, the semi-diurnal tides N2-S2, the spectral line at the frequency of S3 and S4, plus three spectral lines adjacent to each group.

It is possible to estimate a maximum value for the remaining side-band contamination remaining after omission of the three spectral lines surrounding the periodic signals. For finite-length segments each deterministic signal forms a truncated sine wave of the form

$$f(t) = A \sin(\omega_0 t) \qquad 0 < t \leq L$$

$$= 0 \qquad \text{elsewhere} \qquad 6.5$$

The Fourier transform of this function is given by

$$\left| F(\omega) \right| \sim \frac{A}{(\omega - \omega_0)} \left| \sin\left(\frac{(\omega - \omega_0) L}{2} \right) \right| \qquad 6.6$$

(where a symmetrical part of the transform around the frequency $-\omega_0$ is neglected). The amplitude $|F(\omega)|$ is plotted in Figure 6.6 for a sine wave with a period of 12 h and can be seen to contain a number of minima and maxima near the main peak. For the Fourier transform of discrete data the positioning of spectral lines $F(\omega_m)$ on the continuous transform $F(\omega)$ will depend on the number of wavelengths of the wave in L and the number of zeros added before transformation. In the worst case, the contamination of spectral lines adjacent to the true frequency, will fall off with the same rate as the envelope of the side-band maxima. This envelope, divided by the magnitude of the true spectral peak, is defined by

$$M(\omega) = \frac{2}{L(\omega - \omega_0)} \qquad 6.7$$

For the M2 tide in the TP3 E_D data and an LP analysis (as shown in Figure 6.4) the frequency of the periodic signal falls between spectral lines 85 and 86. Omitting these two lines and three adjacent lines on either side of the peak one finds the maximum remaining contamination, defined by equation 6.7, to be 7.4 %. The actual contamination will generally be less than this value since the spectral lines will not co-incide exactly with

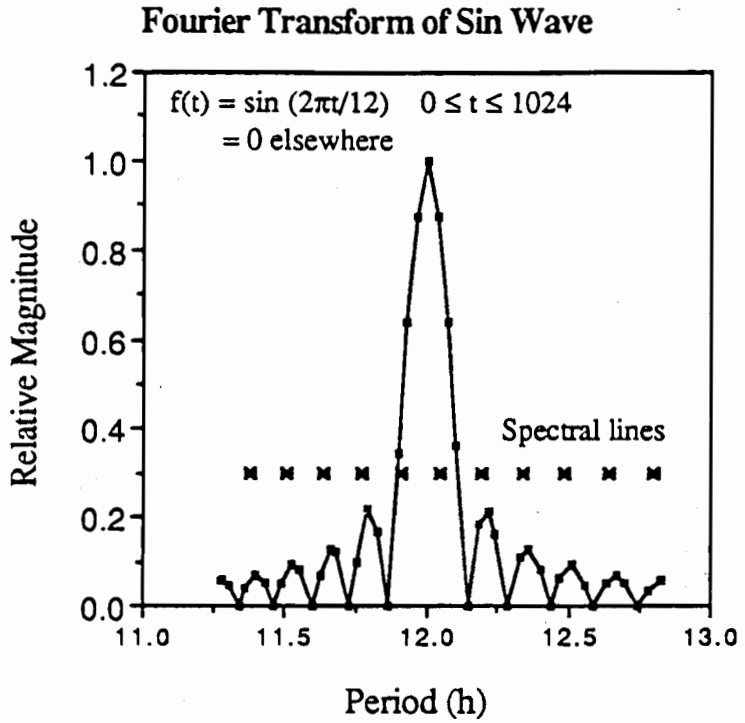

Figure 6.6: Side-band effects arising from the Fourier transformation of a periodic signal. The solid line shows the continuous Fourier Transform of a sin wave of period 12 h truncated to an LP (1024 h) segment. The asterisks show the position where the spectral lines from a discrete transform would occur.

side-band maxima. Application of a cosine taper to the time series before Fourier transformation will further reduce side-band contamination (eg. Bendat & Piersol 1971).

For E_D at site TP3 the amplitude of the M2 tidal line is A = 0.69 $\mu V.m^{-1}$ (N.L. Bindoff pers. comm., 1987) and the background power is approximately S_{EDED} = 0.5 $(\mu V.m^{-1})^2$ / cph. For an LP analysis the ratio of the spectral peak F_{det} to the background stochastic Fourier amplitude F_{stoch} will therefore be given by

$$\frac{F_{det}}{F_{stoch}} = \frac{\left(\frac{AL}{2}\right)}{\sqrt{S_{E_D E_D} L}} = \frac{355.3\ \mu V.m^{-1}.(cph)^{-1}}{22.6\ \mu V.m^{-1}.(cph)^{-1}} = 15.7$$

The maximum contamination of the first bands not omitted from analysis will thus be 0.07 x 15.7 = 1.05 ie. the contamination will be of a similar magnitude as the background signal. When the effects of; tapering, location of spectral lines away from side-band maxima, and averaging of the slightly contaminated spectral lines into broader bands, are considered it may be concluded that the contamination of the final spectral band averages

will be negligible. Because this example represents the maximum side-band contamination of the Tasman Project components, it is concluded that the adopted band-avaraging system adequately removes the deterministic signals from all recorded components in the Tasman data.

Figure 6.7 shows a typical autopower spectra from the Tasman data including the 95% confidence limits calculated from equation 4.152. The results are based on the analysis of two LP and four SP segments. The size of the error bars varies as the number of spectral lines included in each band-averaging changes. Except at the longest periods the error bars are very small. It is concluded that the band-averaging system provides an appropriate balance of resolution and accuracy; the structure in the spectrum is adequately represented and the errors are adequately small. It should however be noted that the steep nature of the geomagnetic power spectra will introduce minor bias in the band-averaged power estimates. The spectral value for each band will be weighted upwards, towards the higher power levels of the lower-frequency spectral-lines in each band.

Although not performed in this analysis of the Tasman Project data it is recommended that two further pre-Fourier transformation operations be performed on the time series in future analyses of the data. The first recommended operation is pre-whitening the spectra before Fourier transformation. This procedure would reduce possible bias caused by band averaging over steep spectra. The second recommended operation is removal of periodic tidal and diurnal lines before Fourier transformation. This procedure would allow narrower frequency bands to be notched out around the deterministic lines, without the risk of side-band contamination.

6.3 Power Spectra

In this section autopower spectra from the various Tasman Project recording sites are presented and discussed. Unless otherwise stated, the power spectra were derived from two LP and four SP segments and the error estimates are given in Table 6.6. Figure 6.8 shows autopower spectra for sites TP3 and GNS, typical mid-ocean and inland continental sites. At site GNS the power spectral density functions (power) for the two horizontal components of the magnetic field are very similar. The only significant difference between the two spectra occurs at frequencies greater than 1 cph, where the B_H component contains slightly more power than the B_D component. As will be shown below using induction arrow results, there is no evidence for any strong lateral conductivity boundaries near site GNS. The ratio of the B_H and B_D power at this site may therefore be assumed to be representative of the corresponding ratio of these components in the source-field (at a geomagnetic latitude of around -42° and during the time of the Tasman Project recordin period). The B_Z spectrum at GNS shows a reduced level of power compared

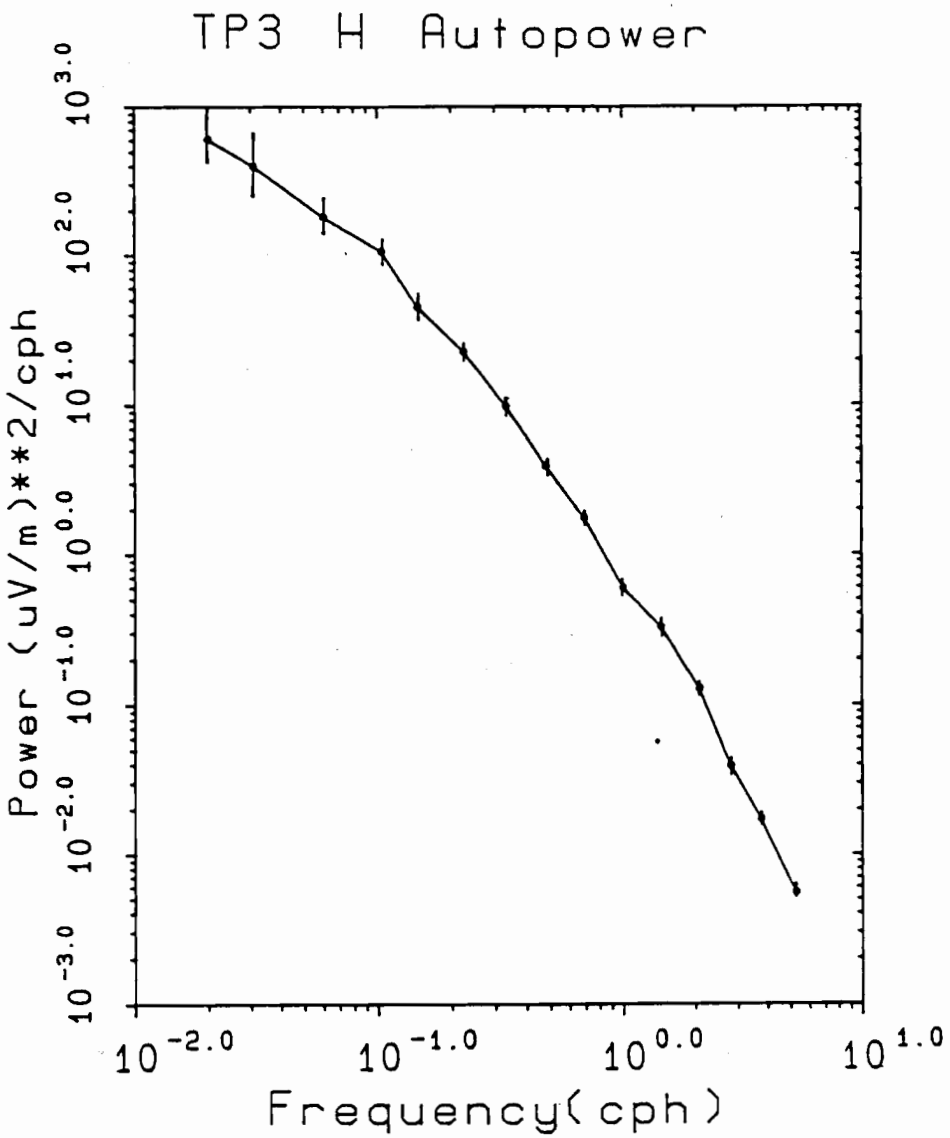

Figure 6.7: A typical autopower spectrum (for the TP3 B_H component) from the Tasman Project showing 95% confidence limits. The autopower was calculated using two LP and four SP segments. Note the steep form of the spectrum, a characteristic of all of the Tasman Project magnetic and horizontal electric field recordings. The confidence limits are listed in Table 6.6.

Table 6.6: 95% Confidence Limits on Power Spectral Estimates.
A. All Segments Included.

Band	Period	Lines/Segment	Segment	λ	$\lambda/\chi^2_{\lambda;0.975}$	$\lambda/\chi^2_{\lambda;0.025}$
1	49.95	14	2	56	0.71	1.50
2	32.51	8	2	32	0.65	1.75
3	16.65	32	2	128	0.79	1.30
4	9.615	36	2	144	0.80	1.28
5	6.849	36	2	144	0.80	1.28
6	4.443	114	2	456	0.88	1.14
7	2.999	108	2	432	0.88	1.15
8	2.079	194	2	776	0.91	1.11
9	1.442	241	2	964	0.92	1.10
10	1.000	387	2	1548	0.93	1.07
11	0.693	130	4	1040	0.92	1.09
12	0.481	196	4	1568	0.93	1.07
13	0.357	175	4	1400	0.93	1.08
14	0.267	304	4	2432	0.95	1.06
15	0.190	475	4	3800	0.96	1.05

Note that the confidence limits are defined by

$$\left[\frac{\lambda\,\bar{S}(\omega)}{\chi^2_{\lambda;\,\alpha/2}} \le S(\omega) < \frac{\lambda\,\bar{S}(\omega)}{\chi^2_{\lambda;\,1-\alpha/2}}\right]$$

where λ is the number of degrees of freedom, α is chosen to be 5% and the overbar signifies the estimated quantity. Table 6.6A gives confidence limits are for power spectra based on two LP segments and four SP segments. For cases in which some of the segments are excluded from the power estimates, the confidence limits are larger and are given in Table 6.6B.

Table 6.6B. Confidence Limits for Incomplete Data Sets

Band	Period	Lines/Seg	Segments	λ	$\lambda/\chi^2_{\lambda;0.975}$	$\lambda/\chi^2_{\lambda;0.025}$
1^	49.95	14	1	28	0.63	1.83
2	32.51	8	1	16	0.56	2.31
3	16.65	32	1	64	0.73	1.46
4	9.615	36	1	72	0.74	1.43
5	6.849	36	1	72	0.74	1.43
6	4.443	114	1	228	0.83	1.21
7	2.999	108	1	216	0.84	1.22
8	2.079	194	1	388	0.87	1.16
9	1.442	241	1	482	0.88	1.14
10	1.000	387	1	774	0.90	1.11
11	0.693	130	3	780	0.91	1.11
			2	520	0.89	1.13
12	0.481	196	3	1176	0.92	1.09
			2	784	0.91	1.11
13	0.357	175	3	1050	0.92	1.09
			2	700	0.90	1.11
14	0.267	304	3	1824	0.94	1.07
			2	1216	0.93	1.08
15	0.190	475	3	2850	0.95	1.05
			2	1900	0.94	1.07

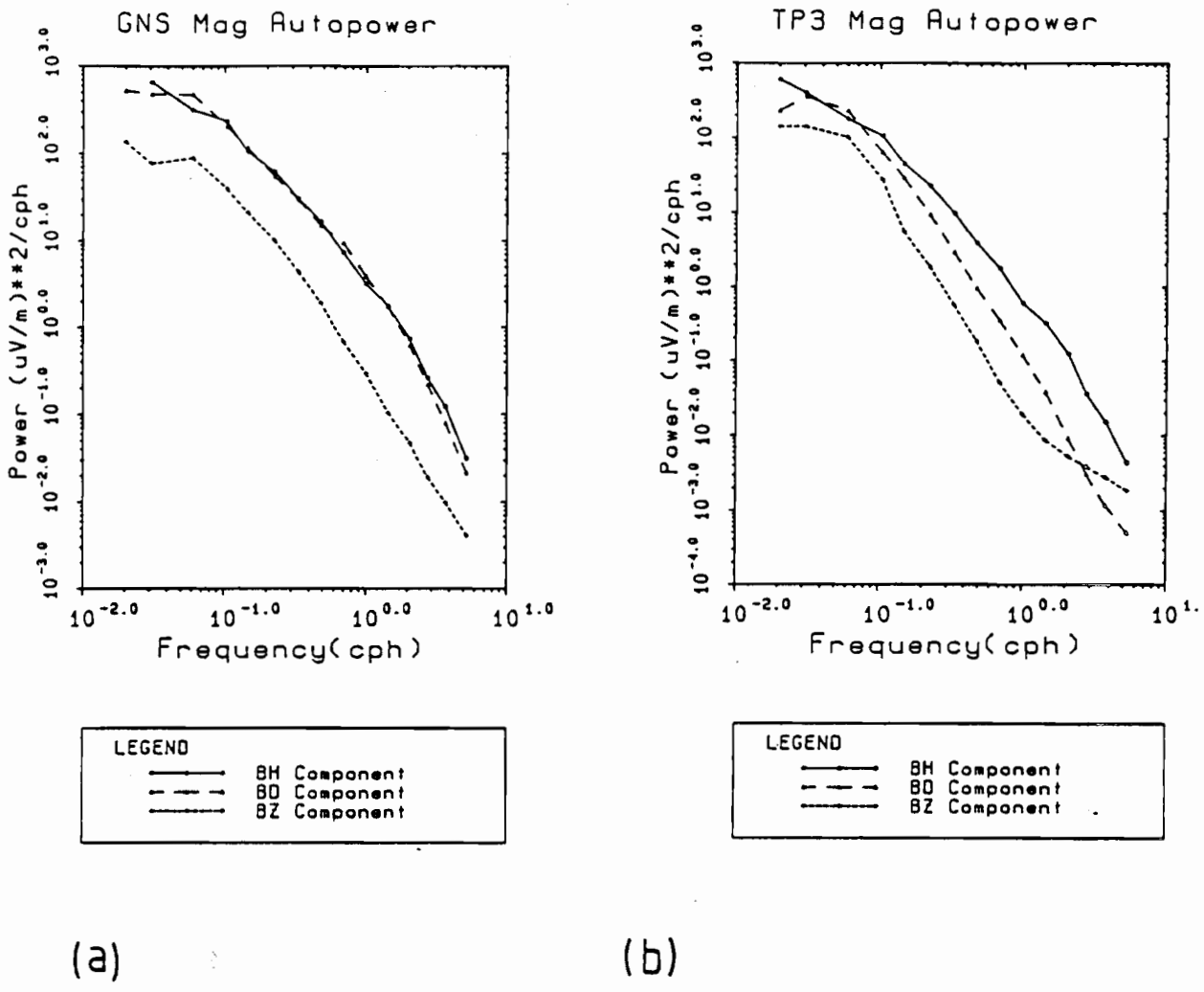

Figure 6.8: Autopower spectra for magnetic field components at an inland continental site, GNS, and mid-ocean site, TP3.

a. Autopowers at GNS.

b. Autopowers at TP3

c. Comparison of the horizontal magnetic field components at TP3 and GNS.

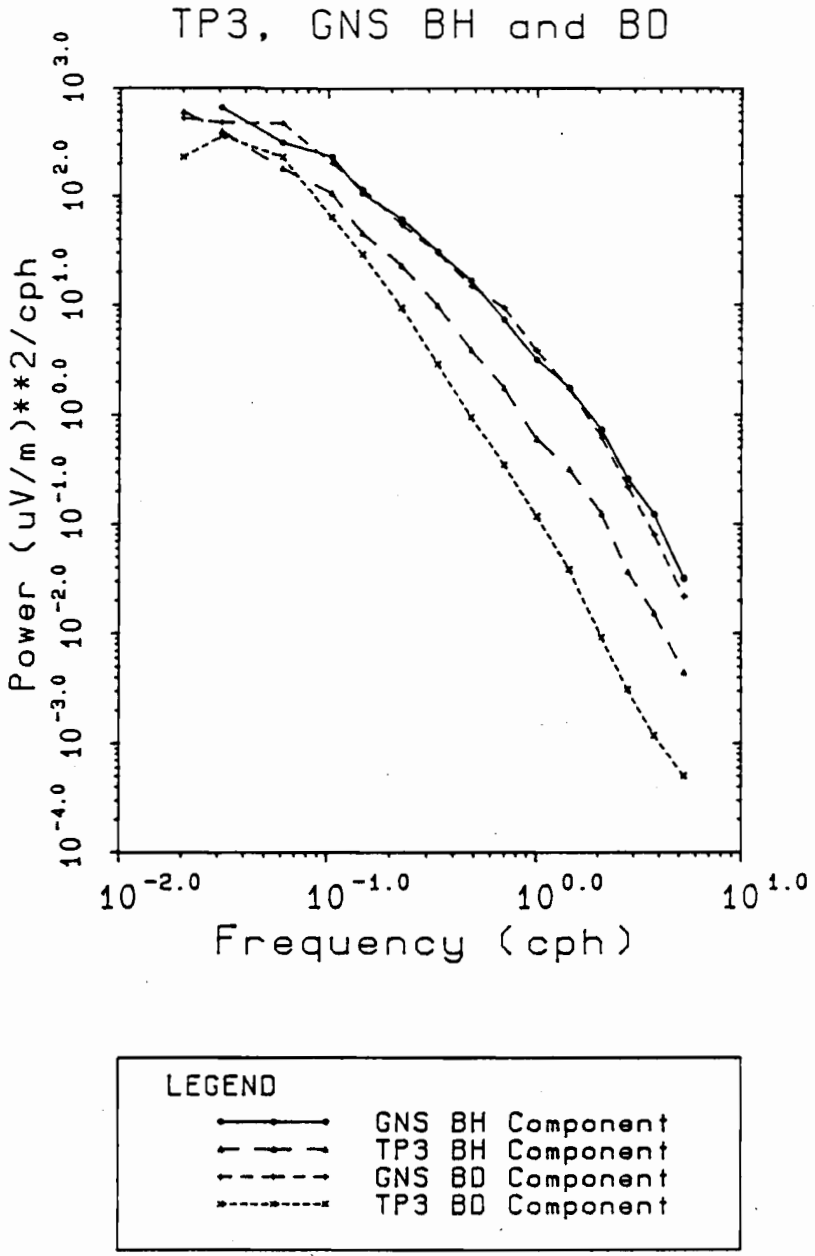
TP3, GNS BH and BD
Power (uV/m)**2/cph
$10^{3.0}$
$10^{2.0}$
$10^{1.0}$
$10^{0.0}$
$10^{-1.0}$
$10^{-2.0}$
$10^{-3.0}$
$10^{-4.0}$
$10^{-2.0}$
$10^{-1.0}$
$10^{0.0}$
$10^{1.0}$
Frequency (cph)
LEGEND
GNS BH Component
TP3 BH Component
GNS BD Component
TP3 BD Component

Figure 6.8c

with the horizontal components. Over the whole frequency range the value for the B_Z power is very close to 1/5 of the value for the B_H and B_D power.

At site TP3 the power spectra for B_H and B_D show significant differences, with the B_D component possessing lower levels of power. The difference between the components is greatest at the highest frequencies. At periods longer than 10 h the level of power is similar for both components but for the highest frequency band, 5.3 cph, the B_H power is approximately an order of magnitude larger than the B_D power. The difference in power between B_H and B_D at the seafloor site is due to the greater attenuation of the B_D component through the ocean. Since TP3 has a geomagnetic latitude which differs less than 4° from that of GNS (where results indicate equal levels of B_H and B_D in the source-field) it is unlikely that source-field differences contribute to the difference in power.

The power spectrum for B_Z at TP3 has a similar shape to the B_D spectrum. Over most of the frequency range the B_Z component has a factor of 5 less power than B_D; the change in slope of the B_Z spectrum at periods of less than 1 h is caused by instrumental noise (chapter 3). The similarity of the B_Z and B_D spectra suggests the two components are related by a transfer function which is approximately frequency-independent between 0.02 cph and 5.3 cph. It is not possible to determine from the power spectra alone, whether such a correlation of B_D and B_Z is caused by geomagnetic induction, correlation of source-field B_D and B_Z components, or correlated oceanic noise on B_D and B_Z.

Figure 6.8c compares the B_H and B_D power levels at GNS and TP3. The power spectra confirm the time series observations showing that the power is reduced at the seafloor site relative to the land site. This effect is greatest at the higher frequencies, as is expected for attenuation of seafloor horizontal magnetic fields by the conducting ocean-water.

Figure 6.9 shows the power spectra for a selection of sites spanning the continental section of the recording line. Table 6.7 lists the distance of the various sites from the Australian coast. As expected from the time series observations the power spectra for B_D and B_H are relatively uniform across the continental part of the recording line. For B_D, at frequencies higher than 1.0 cph, there is slightly more power at coastal sites than inland sites. This extra power can be explained by an increase in B_D associated with the E-pol coast effect and by the additional B_H-correlated signal noted in the B_D time series at coastal sites. The B_H spectra suggest that, over the whole frequency range, there is also a slightly higher level of power at the coastal sites DRS and CDM than at the inland sites BKM and

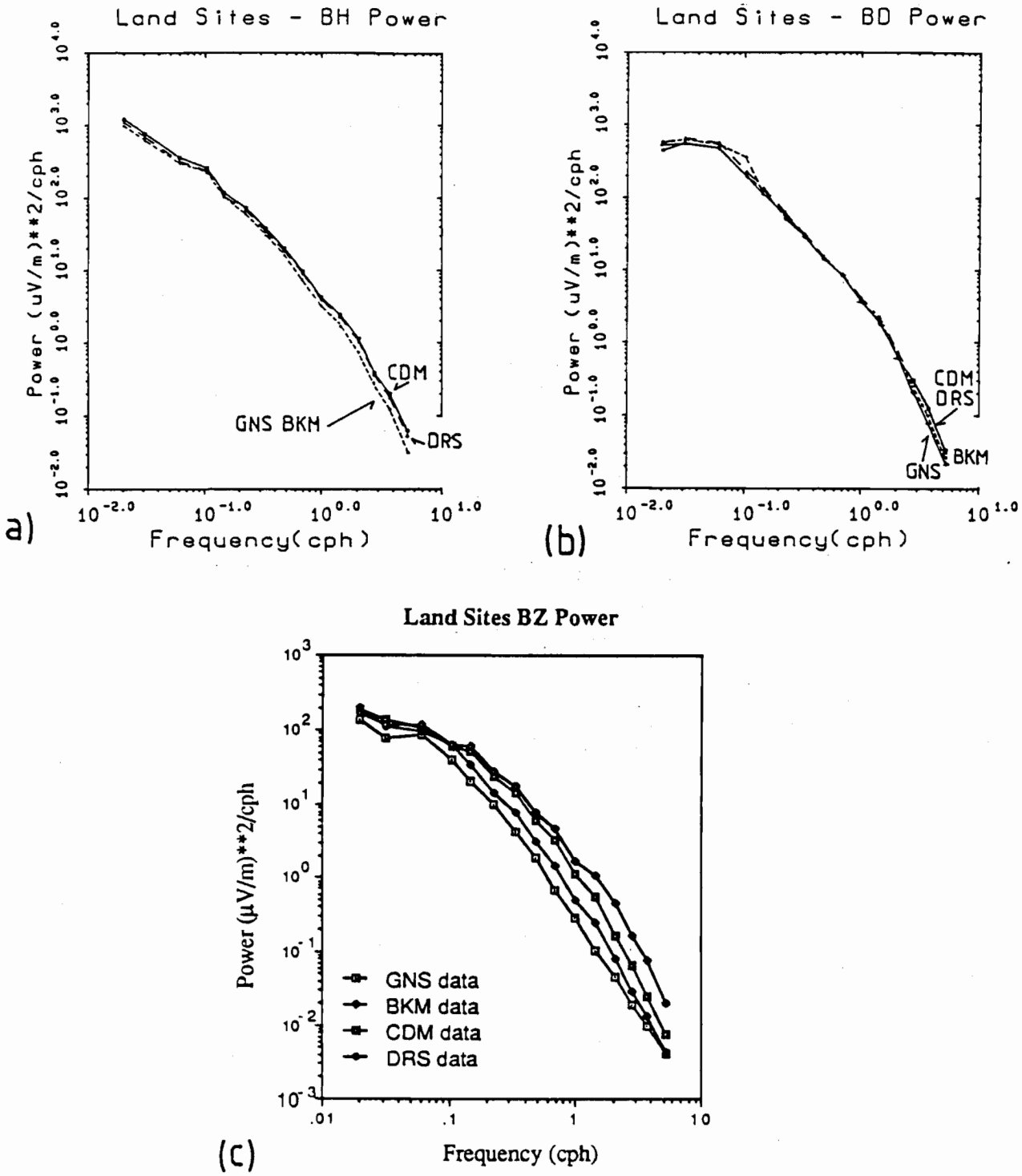

Figure 6.9: Autopower spectra for magnetic field components at sites spanning the continental section of the recording line. Site DRS is at the coastline and CDM, BKM and GNS are respectively 30, 116 and 640 km from DRS.

a. B_H component. (The traces for GNS and BKM overlie)

b. B_D component. (The traces for DRS and CDM overlie)

c. B_Z component.

Table 6.7: Inter-site Distances, Distances from Coast and Magnetic Declination.

Site	Distance (km) to					Declination
	DRS	Coast	CMO	L.H. Rise	EYR	(Degrees)
MYL	598	550	516			9.3
GNS	640	550	548			9.3
BLN	366		274			10.4
CLC	198		107			11.2
BKM	116		24.9			11.9
CMO	91.5		0.0		2160	12.0
BBB	58.3		33.5			12.2
CDM	30.0		61.5			12.3
DRS	0.0		91.5			12.4
TP8	78.5		169			13.2
TP9	102		192			13.4
TP7	124		215			13.5
TP6	188		279			14.0
TP5	318		410			15.0
TP4	548		640	-596		16.2
TP3	917		1009	-354	1160	17.7
TP2	1138	1130	1229	-109	981	18.3
TP1	1438	604	1530	+203	777	18.8

Notes

1. Distances are calculated between the site co-ordinates specified in Table 2.1 using spherical trigonometric relations.
2. The distance to the coast is to the nearest coastline. For sites GNS to TP3 the closest point on the coast is taken as DRS, for MYL and TP2 the closest coastal point is to the north of DRS, for GNS the closest coast is the southern Australian coast and for TP1 the closest coastline is that of New Zealand.
3. The distance to the Lord Howe Rise is the distance to the western 3000m contour of the Rise; negative distances correspond to sites to the west of this line.
4. Declinations are from Finlayson (1973) corrected for secular variation to 1984 values.

GNS. Such a result is not explained by 1D or 2D geomagnetic induction theory and it is therefore interpreted as either a 3D effect.

In contrast to the horizontal magnetic-field components, the power spectra for the B_Z components display significant changes across the recording line. There is a clear coast effect visible in the B_Z power spectra with increased levels of power near the coast. This effect diminishes with decreasing frequency and is barely resolved at frequencies smaller than 0.1 cph. The coast effect also diminishes at high frequencies where Figure 6.9 shows the power spectra from the different sites starting to converge.

The autopower spectra for the magnetic field components at a range of seafloor sites are shown in Figure 6.10. The B_H component is relatively uniform across the sites but shows a slight increase in attenuation at mid-ocean sites with increasing frequency. This result confirms a similar observation made from the time series. The B_D magnetic field component shows large differences in the level of power at the different seafloor sites. There is a strong increase in power with increasing proximity to the Australian coast which is interpreted as the E-pol anomaly in B_D. This strength of this effect increases with increasing frequency. As will be shown in chapter 7 there is also a significant contribution to the B_D power from oceanic noise particularly at sites near to the Australian coast.

The power spectra for the seafloor B_Z components are shown in Figure 6.10c. A clear coast effect is evident with the power level decreasing with distance from the Australian coast. A comparison of Figures 6.9 and 6.10 indicates that the power level in B_Z at site TP8 is very similar to that at DRS. Because site TP1 is located at a much shallower depth than the other seafloor sites, the power spectra of the TP1 magnetic field components have different characteristics from the other sites (eg. less attenuation of the horizontal magnetic field components) and these data were therefore excluded from Figure 6.10.

Figure 6.11 shows the power spectra for a range of the seafloor horizontal electric field components. The power spectra are based on only one LP and two SP segments and error bars are therefore larger than those shown in Figure 6.7. At all sites the spectra for the horizontal electrical field are less steep than those for the horizontal magnetic field components reflecting the increase in the impedance function with decreasing frequency.

The E_H power is relatively uniform across the Tasman Sea, however sites near the Australian coast exhibit slightly greater power than those in the Central Tasman. This effect is strongest at periods above 24 h, where the extra power near the coast is attributed to noise induced by meso-scale water motion. This signal was previously noted in the time series. The oceanically-induced signal appears to be strongest a small distance away

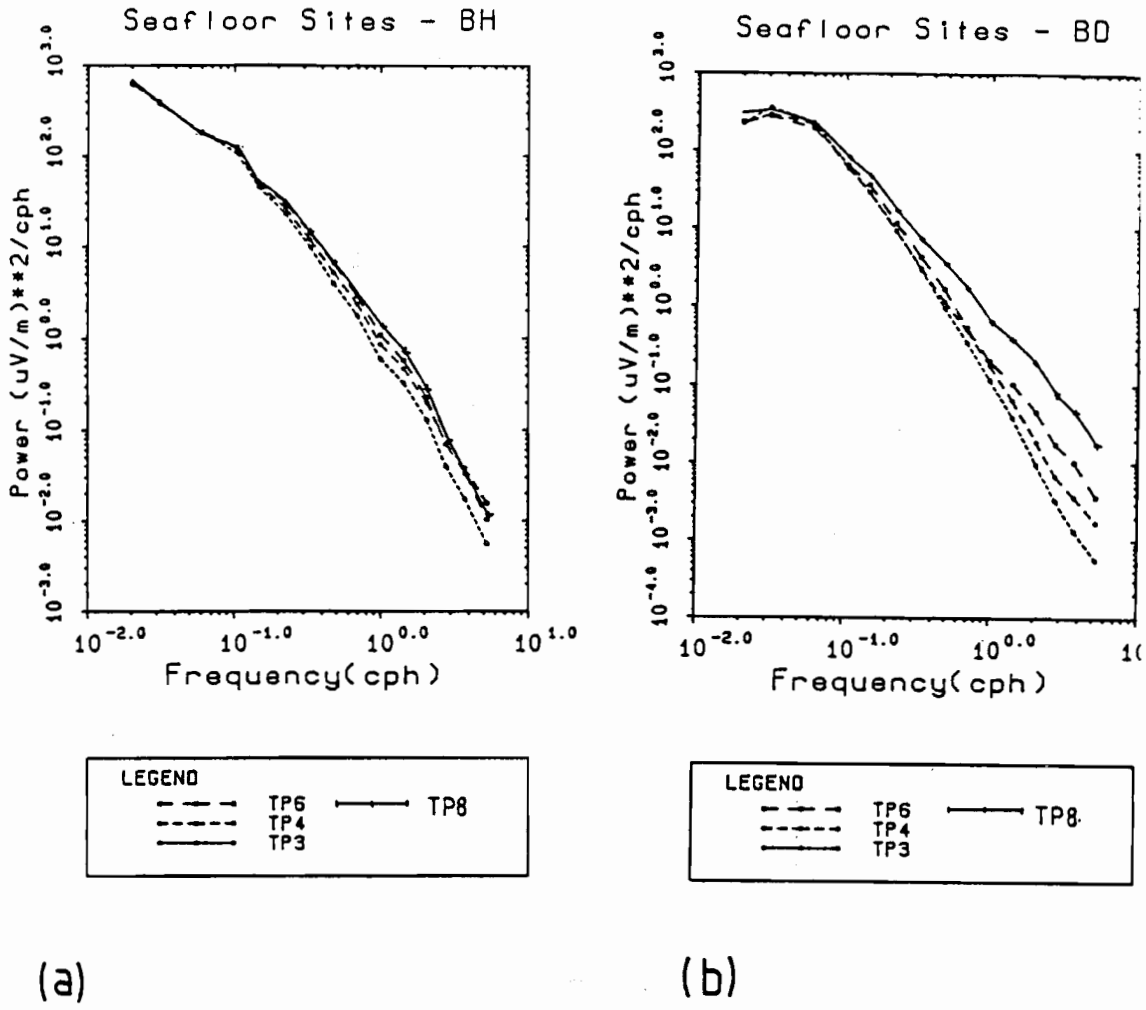

Figure 6.10: Autopower spectra for magnetic field components at sites from the seafloor section of the recording line. Sites TP8, TP6, TP4 and TP3 are respectively 78, 190, 550 and 920 km from the Australian coast.

a. B_H component, b. B_D component, c. B_Z component.

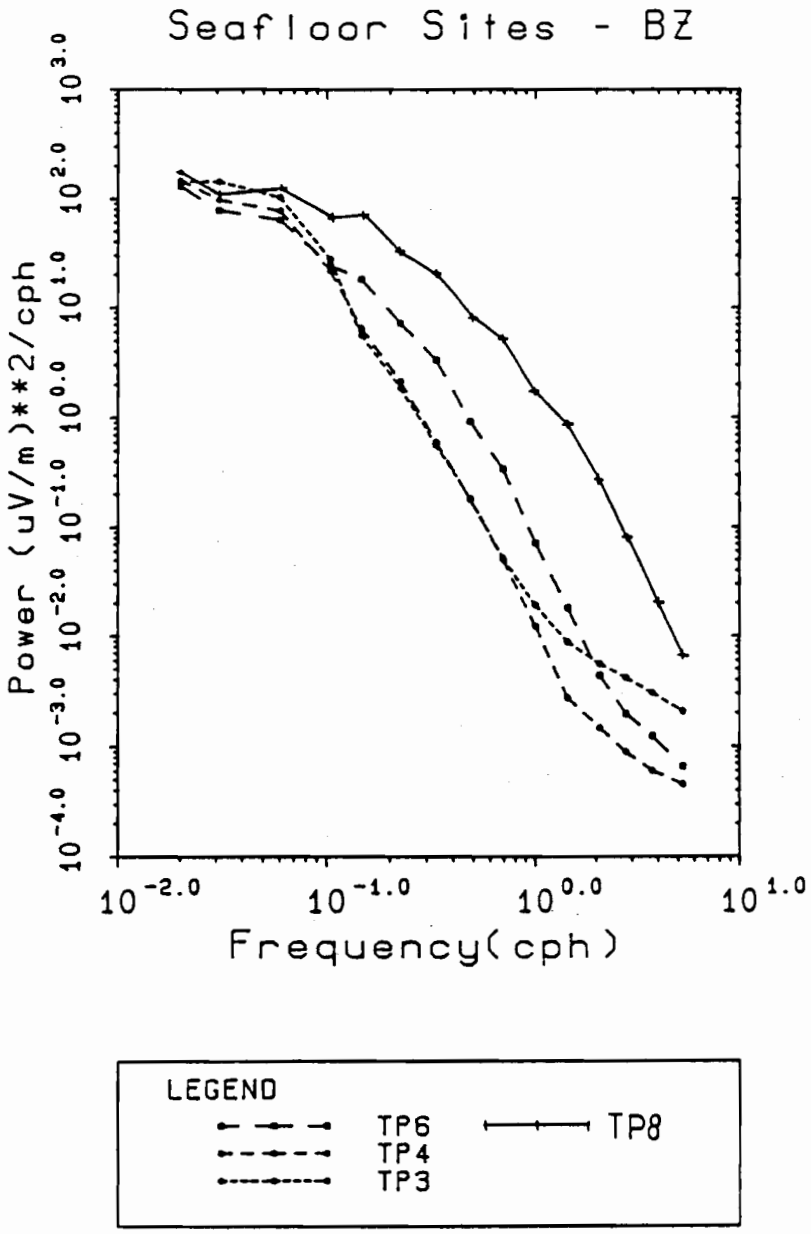
Seafloor Sites - BZ
Power (uV/m)**2/cph
$10^{3.0}$
$10^{2.0}$
$10^{1.0}$
$10^{0.0}$
$10^{-1.0}$
$10^{-2.0}$
$10^{-3.0}$
$10^{-4.0}$
$10^{-2.0}$
$10^{-1.0}$
$10^{0.0}$
$10^{1.0}$
Frequency(cph)
LEGEND
TP6
TP4
TP3
TP8

Figure 6.10c

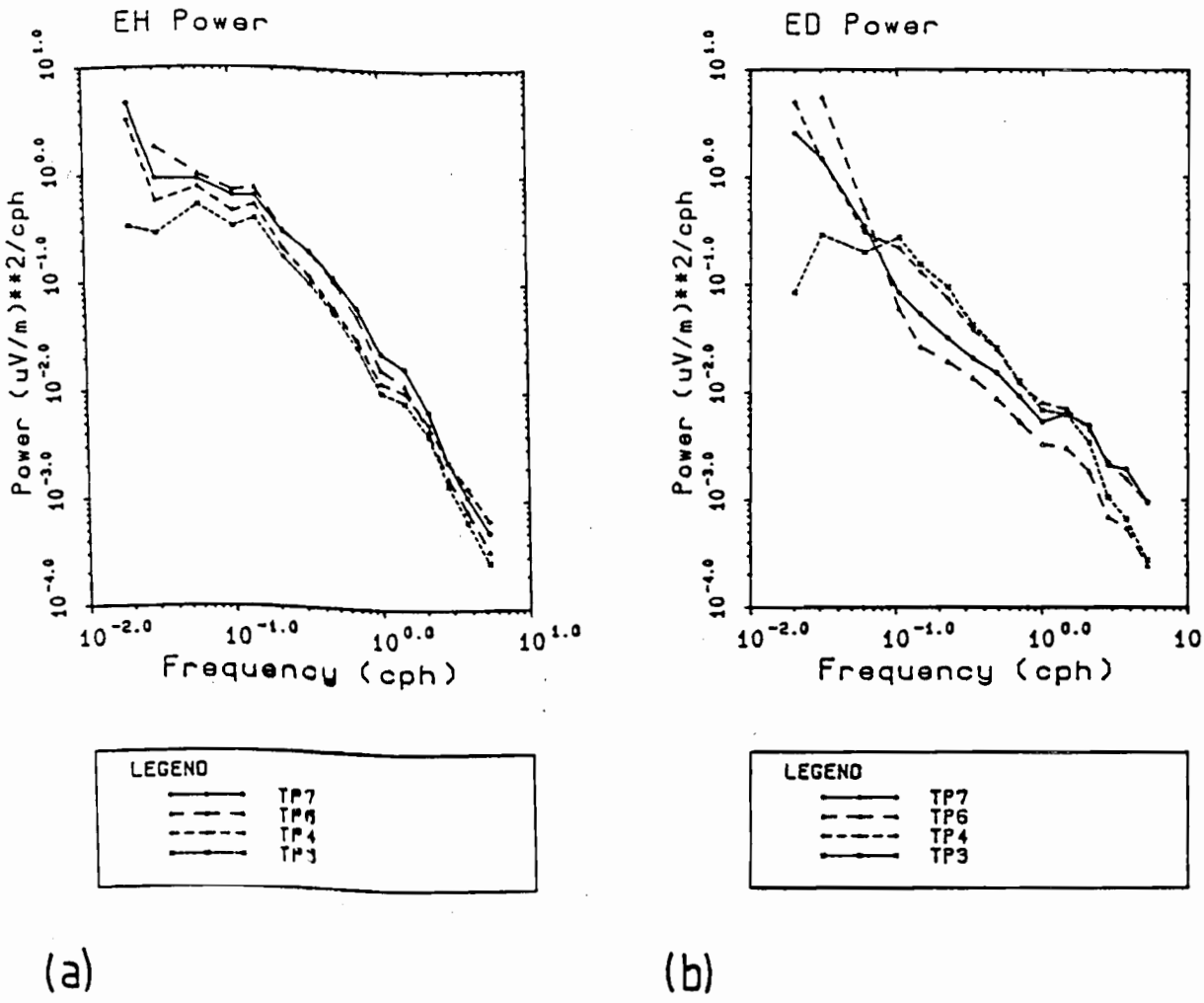

Figure 6.11: Autopower spectra for seafloor horizontal electric field components. Spectra are based on one LP and two SP segments only and random errors will therefore be larger than for magnetic power spectra.

a. E_H component, b. E_D component.

from the coast, at site TP6. The E_D power spectrum varies considerably between the Tasman seafloor sites. At low frequencies, sites near the Australian coast again contain more power than site TP3 in the Central Tasman while in the central part of frequency range, 0.1 -1.0 cph, the strongest E_D power is at sites TP3 and TP4. These results confirm earlier observations from the time series.

The inflection in all the HEF power spectra between the bands at 1 h and 0.69 h is a spurious feature caused by the change from results derived from long-period events to those derived from short-period events. Examination of the power in long-period bands derived from an SP segment or short-period bands from an LP segment reveals no corresponding change in slope. The relatively high values for the power at periods of less than 1 h, for the E_H and E_D components at sites TP4 and TP7 is attributed to instrumental noise (see chapter 3).

Examination of the autopower spectra for the various components has confirmed many of the observations of the geomagnetic phenomena made from the time series. In addition the power spectra have shown the frequency dependence of certain processes, such as the attenuation of the seafloor horizontal magnetic fields.

6.4 Coherence Functions

6.4.1 Ordinary Coherences Functions

Two main parameters control the level of coherence between time series. Firstly, the coherence between the two time series is controlled by the similarity of the physical process generating each time series. For example, the coherence between the B_H components measured at adjacent recording sites will be high if the source-field is very similar at the two sites, while the coherence between two components B_H and B_D from at a single site will be low if there is no relationship of the two components in the source-field. The second parameter affecting the coherence between two time series is the level of noise on each of the time series. An increase in the level of (uncorrelated) noise on either or both time series will cause a decrease in the coherence.

In this section the coherence between various sets of Tasman Project recordings are presented with the main aim of examining the uniformity of the geomagnetic source-field across the recording line. The results of this research are important because the remote reference and other multiple site techniques used in chapters 6 and 7, rely on a strong uniformity of source-field between the different sites. The coherences are also of interest because they provide a preliminary indication of the characteristics of the noise on each component.

Figure 6.12 shows the ordinary coherence for the B_H and B_D components between

CMO and selected sites on the continental section of the recording line. The coherences are calculated for pairs of sites separated by distances increasing from 34 km (CMO to BBB) to 107 km (CMO to CLC) to 548 km (CMO to GNS). The level of true zero coherence at the 95% confidence level is shown in Figure 6.12a and indicates that the coherence for all sites, and for all frequency bands, is resolved at this level of significance. The confidence limits on the coherence estimates themselves, are very small and have magnitudes of less than 0.02 for all coherences shown (see section 4.2). For all other coherences shown in this section the confidence limits are also very small and the coherence values exceed the level of true zero coherence.

The following features of the coherence functions between land magnetic field components are to be noted

1. For both B_H and B_D the coherence decreases strongly at short periods. The coherence between B_D components also decreases at long periods. The maximum coherence tends to occur in the period range 5-10 h.

2. The coherence between B_H components is higher than the B_D coherence between the same sites.

3. The coherence decreases with increasing inter-site distance.

Making the assumption that the noise level is approximately uniform at each of the (Gough-Reitzel) land sites, the third observation indicates an increasing non-uniformity of the source-field with increasing inter-site distance. The decrease in coherence at short periods however occurs at a similar rate at all inter-site distances and is therefore attributed mainly to a decrease in the SNR. This change is explained by the decreasing signal level at high frequencies (see Figure 6.7) and also an increase in noise associated with the hand-digitization of the Gough-Reitzel data. For the B_D components the decrease in coherence at long periods is also interpreted as being caused by a decrease in the SNR. Such a decrease will result from a decrease in the source-field B_D signal, associated with the absence of B_D-inducing source-field processes at longer periods.

Figure 6.13 shows the coherence between seafloor B_H and B_D recordings for inter-site distances ranging from 130 to 597 km. At periods longer than 1 h, the inter-site seafloor B_H coherences have a similar magnitude to land B_H coherences over the same inter-site distance. At shorter periods the seafloor B_H coherences are higher than the corresponding land values even though the seafloor data contains a significant component of oceanically induced noise. This result supports the hypothesis that the low short-period coherence values for land components are caused by hand-digitizing noise.

The seafloor B_D coherence functions are much more irregular than the B_H coherence functions. At both long and short periods the coherence between the seafloor B_D

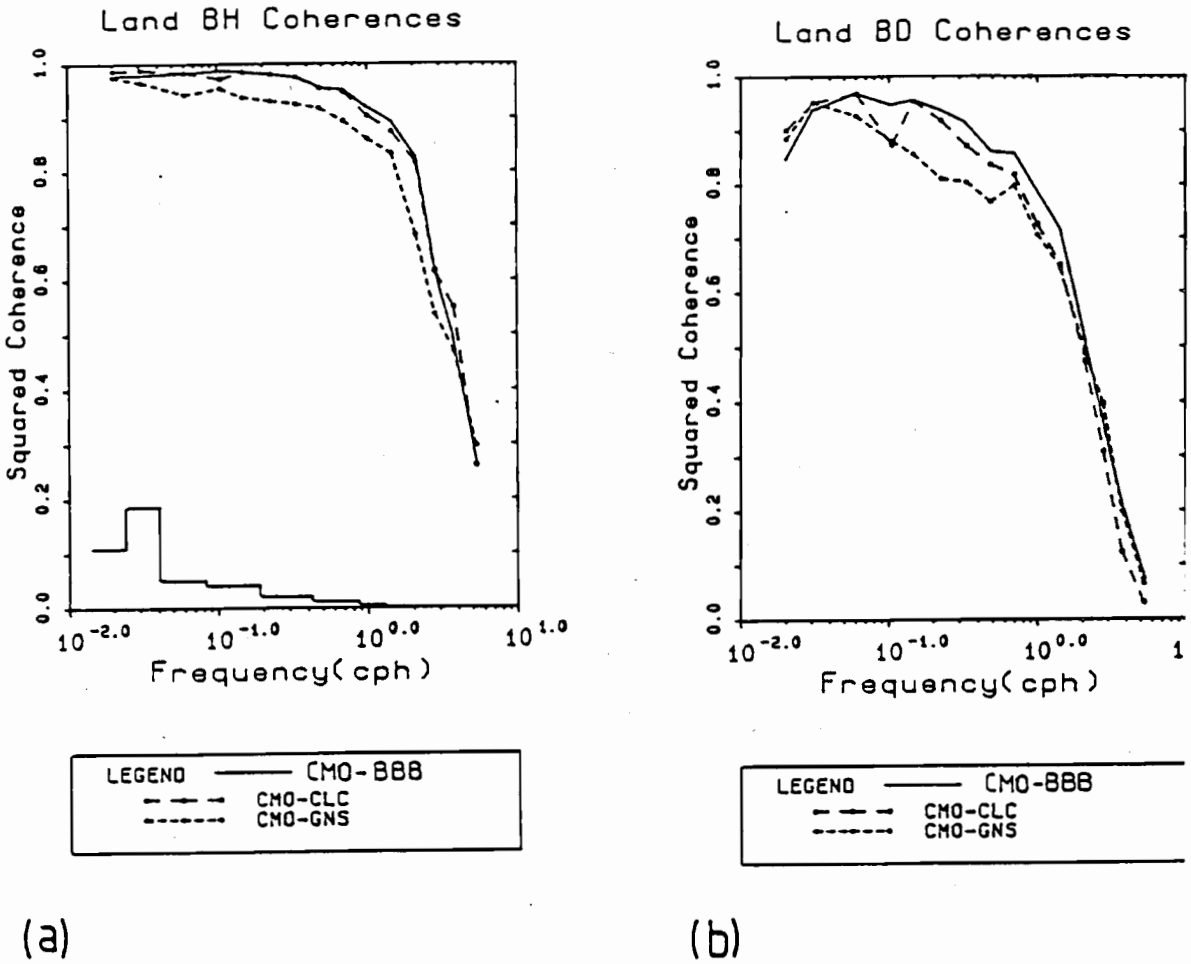

Figure 6.12: Ordinary coherence function between horizontal magnetic field components from land sites. Note that the distances of BBB, CLC and GNS from CMO are respectively 34, 107 and 550 km.

a. B_H component. Also shown is the level of zero true coherence.

b. B_D component.

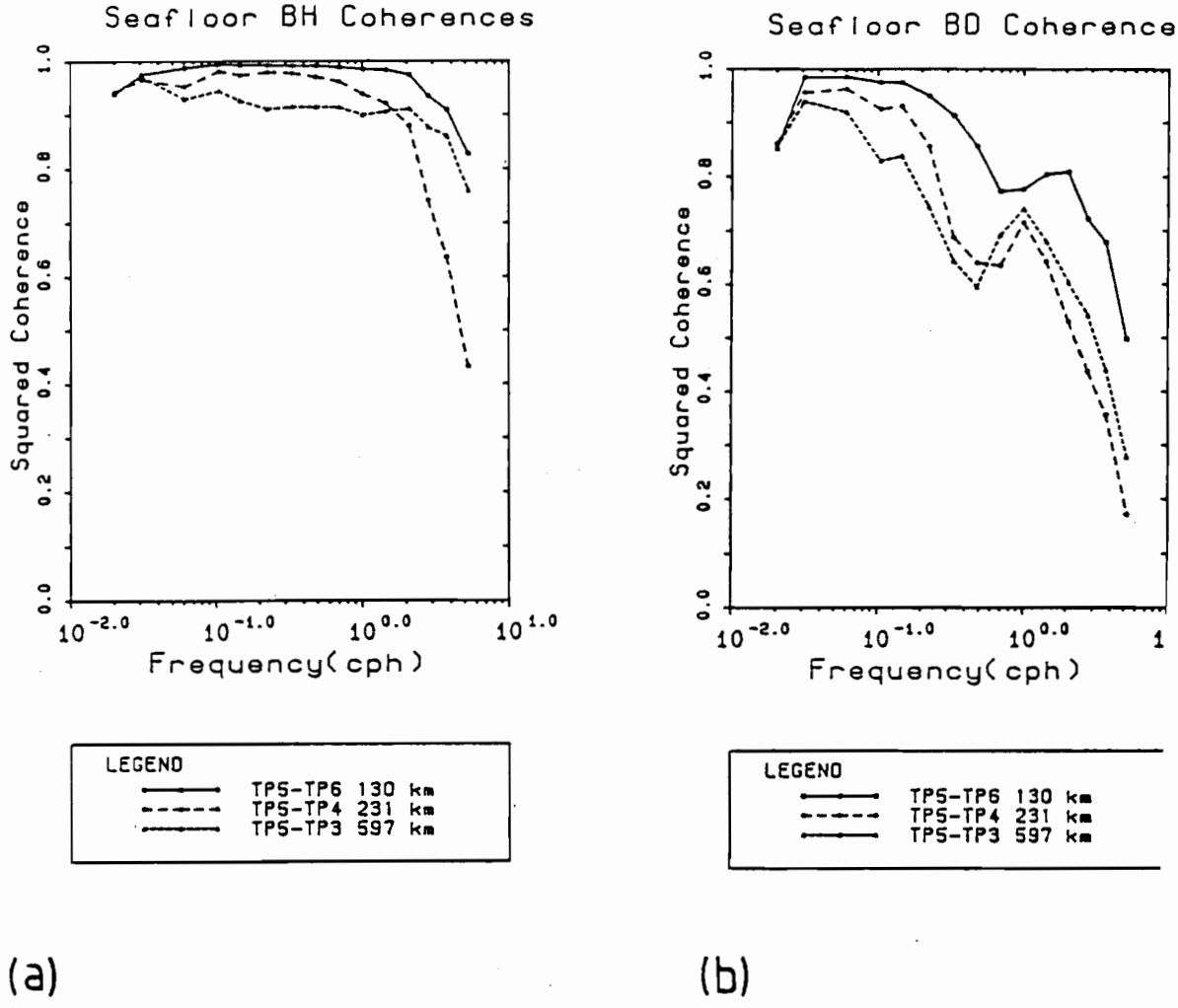

Figure 6.13: Ordinary coherence function between horizontal magnetic field components from seafloor sites. a. B_H component and b. B_D component.

components is similar or higher than the corresponding land values. However in the period range 1-2 h the seafloor B_D coherence functions have a pronounced minimum. Only part of this minimum may be explained by the transition from LP to SP results. The changes in slope around the minimum are defined individually by LP results and by SP results, and therefore the minimum requires further explanation. The most plausible explanation for the coherence minimum is that there is a decrease in the SNR in the B_D data in the period range 1-2 h.

For both the B_H and B_D components, in the highest frequency bands the TP3-TP5 coherence is higher than the TP4-TP5 coherence, despite corresponding to a much greater inter-site distance. This effect is probably due to a higher level of oceanic noise at TP4 than at TP3.

6.4.2 Multiple Coherence Functions

Examination of the time series (eg. Figure 6.3) showed that the B_D component at near-coastal seafloor and land sites contains additional signal correlating with B_H. This extra signal will cause a decrease in the ordinary coherence estimate between B_D at these and other sites. In order to accurately examine source-field uniformity over the coastal parts of the recording line it is therefore useful to consider the multiple coherence of various components with both B_H and B_D time series.

Figure 6.14 shows the multiple coherence of the B_H and B_D components from EYR in New Zealand with the two horizontal magnetic field components at CMO. Although the two sites are 2160 km apart, the multiple coherence for the whole frequency range is well above the level of zero true coherence at the 95% confidence level. Over much of the frequency range the B_H coherence exceeds 0.6 and the B_D coherence exceeds 0.35. These results suggest that the source-fields are reasonably coherent over a distance scale of 2000 km at frequencies between 0.03 and 5.0 cph. The B_H coherence tends to be higher than the B_D coherence by 0.1-0.2 units suggesting that the source-field is more uniform for B_H than B_D. Errors associated with the hand-digitization of the EYR data probably contribute to the rapid drop-off in the multiple coherence at frequencies higher than 1 cph.

Figure 6.15 shows the multiple coherence between the seafloor horizontal magnetic field components and the CMO horizontal magnetic field components. These coherences are higher than those between EYR and CMO reflecting the shorter inter-site distances (CMO to TP7 is 215 km, CMO to TP5 is 410 km and CMO to TP3 is 1009 km). The B_D multiple coherences are again lower than the corresponding B_H values and show a distinct

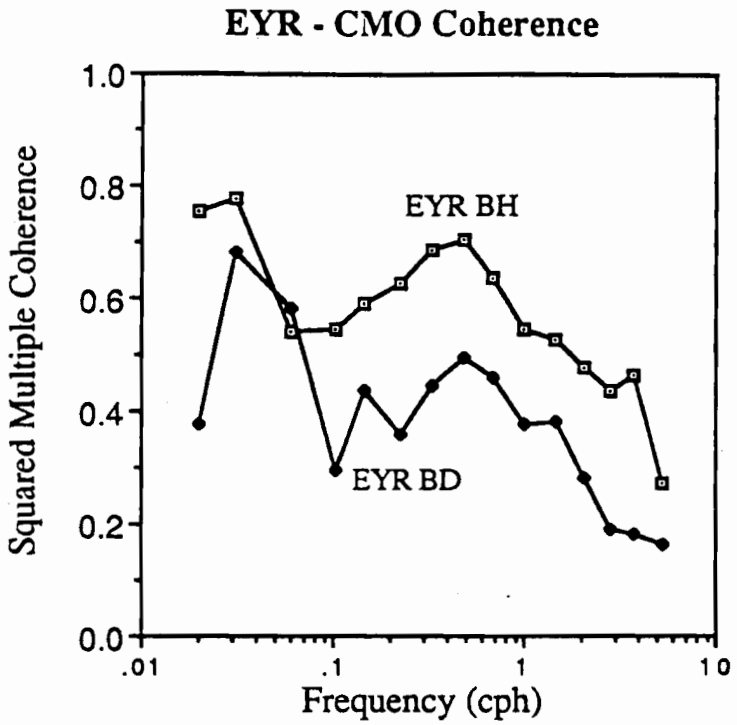

Figure 6.14: Multiple coherence of B_H and B_D from EYR with the horizontal magnetic field components at CMO. Note that both coherence functions are all well above the level of zero true coherence (at the 95 % confidence level).

minimum at a period of approximately 3 h. Since all of the time series involved in these multiple coherence calculations are taken from digital recordings the decline in coherence at high frequencies can no longer be attributed to digitization noise. The decrease is therefore interpreted as indicating either an increase in oceanic noise at high frequencies and/or a decrease in source-field uniformity at these frequencies. Chave & Filloux (1984) observe similar patterns of coherence between seafloor magnetic field components and data from the Tuscon observatory.

Figure 6.16 shows the multiple coherence between the seafloor horizontal electric field time series and the horizontal magnetic field at CMO. The multiple coherences are much lower than the corresponding multiple coherences of the seafloor magnetic fields. This result occurs because the oceanically induced noise is much stronger in the electric field than in the magnetic field. The effects of the oceanic noise are strongest at the long and short periods in the spectrum; the multiple coherence is a maximum between 3 and 5 h. The multiple coherence between the horizontal electric field at TP3 and the horizontal magnetic field components at CMO has a different form from the corresponding coherence for the other seafloor sites. This effect is probably explained by the lower oceanic

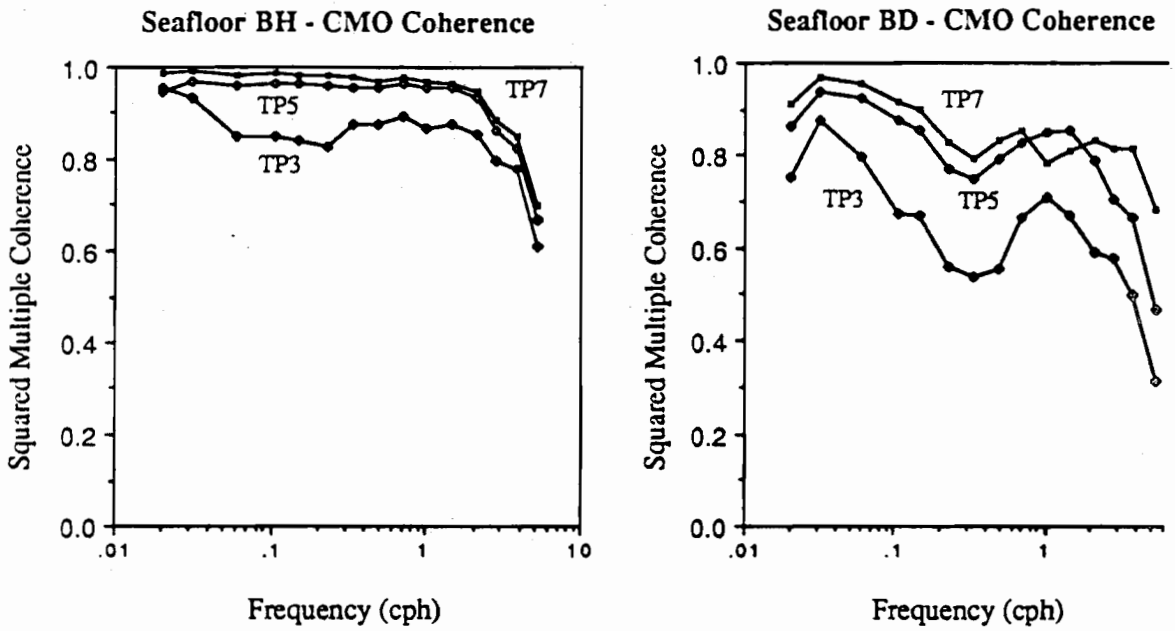

Figure 6.15: Multiple coherence of B_H and B_D from seafloor sites with horizontal magnetic field components at CMO.

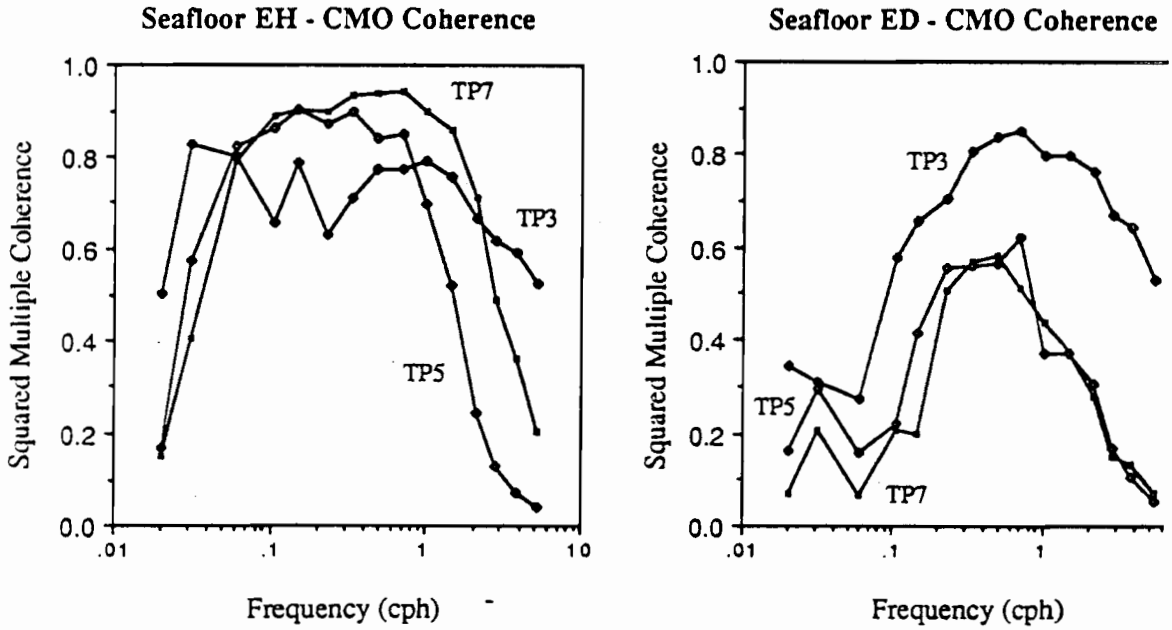

Figure 6.16: Multiple coherence of E_H and E_D from seafloor sites with horizontal magnetic field components at CMO.

noise levels at TP3.

Multiple coherences have been calculated between B_Z and B_H, B_D at each site. The results indicate that the strongest coherence occurs at sites where the coast effect is strong and the B_Z signal is largest. This multiple coherence estimate is used in the calculation of confidence limits for the induction arrows at each site. The discussion of the correlation of B_Z with other components is therefore deferred until section 6.5 in which induction arrows are presented.

6.4.3 Crosspower Analysis

The coherence results show that although the geomagnetic source-field is relatively uniform across the Tasman Project recording line, there is a decrease in coherence with increasing inter-site distance. This non-uniformity may be quantified by examining the variation in the B_H and B_D crosspower between different sites as a function of inter-site distance. A standardized form of the crosspower

$$A_i = S_{ii}^{CMO,X} \sqrt{\frac{S_{ii}^{CMO}}{S_{ii}^{X}}} \qquad 6.8$$

(where "i" is B_H or B_D and $S_{ii}^{CMO,X}$ is the crosspower in the component between CMO and site X) is used. This standardized crosspower corrects for the local variations in the B_H and B_D autopower, for example that caused the coast effect in B_D, and therefore provides a measure of the source-field coherence between two sites. It is proportional to the square root of the corresponding coherence term;

$$A_i = \sqrt{\gamma_{ii}^2}\ S_{ii}^{CMO} \qquad 6.9$$

The uniformity of the geomagnetic source-field will vary between different geomagnetic disturbances. For example intense geomagnetic storms have less uniform source-fields while substorms are believed to have relatively uniform fields (Egbert & Booker 1986). This analysis attempts to define an 'average' value for the source-field non-uniformity over a variety of geomagnetic events. The results are based on the same IP and SP events used in the analyses described above, and are thus derived from a selection of quiet periods and moderate geomagnetic disturbances.

Table 6.8 and Figure 6.17 show the observed and corrected crosspowers, for the period of 2.1 h, between CMO and six other sites comprising Australian and New Zealand land sites, and seafloor site TP3. The distance from CMO to these sites ranges from 34 km to 2160 km. After correction of the autopower variations at the different sites (with correction factors ranging from 1.0 to 3.6) the variation in crosspower with increasing

Table 6.8 Crosspower Dependence on Inter-site Distance

Site CMO to	Distance (km)	B_H Crosspower (nT^2/cph) Observed	Corrected	Cor Fac	B_D Crosspower (nT^2/cph) Observed	Corrected	Cor Fac
CMO	0	19.20	19.20	1.000	12.41	12.41	1.000
BBB	34	18.67	18.82	1.008	11.66	11.53	0.989
DRS	92	18.49	18.83	1.018	12.83	11.56	0.901
BLN	274	17.82	18.74	1.052	12.30	11.36	0.922
GNS	548	17.08	18.39	1.076	11.87	10.87	0.916
TP3	1009	7.895	17.51	2.217	2.289	8.26	3.610
EYR	2160	12.45	13.46	1.081	7.68	7.11	0.926

The table shows the magnitude of the B_H and B_D crosspower between CMO and other sites at the period of 2.1 h. The B_H crosspower is between B_H at CMO and B_H at the second site and the B_D crosspower is defined in a similar manner. The table shows the observed crosspowers and the correction used to standardize the crosspower for local variations in the autopower at each site. The corrected crosspower is a measure or inter-site coherence of the source-field.

inter-site distance is well approximated by an exponential function. The length-scales associated with the B_H and B_D exponential functions are adopted as the scales of the source-field uniformity. The use of exponential functions to fit the observed variations is motivated by the empirical observations rather than an assumed knowledge of source-field configuration. Their use however appears to be appropriate since one would expect source-field uniformity to decrease monotonically with increasing inter-site distance along a line of constant geomagnetic latitude (and for distances less than half the Earth's circumference).

The length-scales for the 2.1 h crosspower data are 6430 km for B_H and 3890 km for B_D. These scales have been derived from simple fits of exponential functions to the data. Due to the uneven distribution of inter-site distances the exponential curves are strongly biased towards the CMO-EYR crosspower value and the correlation coefficient is artificially high. The length scales are however intended to be used as guides only to source-field uniformity and for this purpose they are sufficiently well-determined.

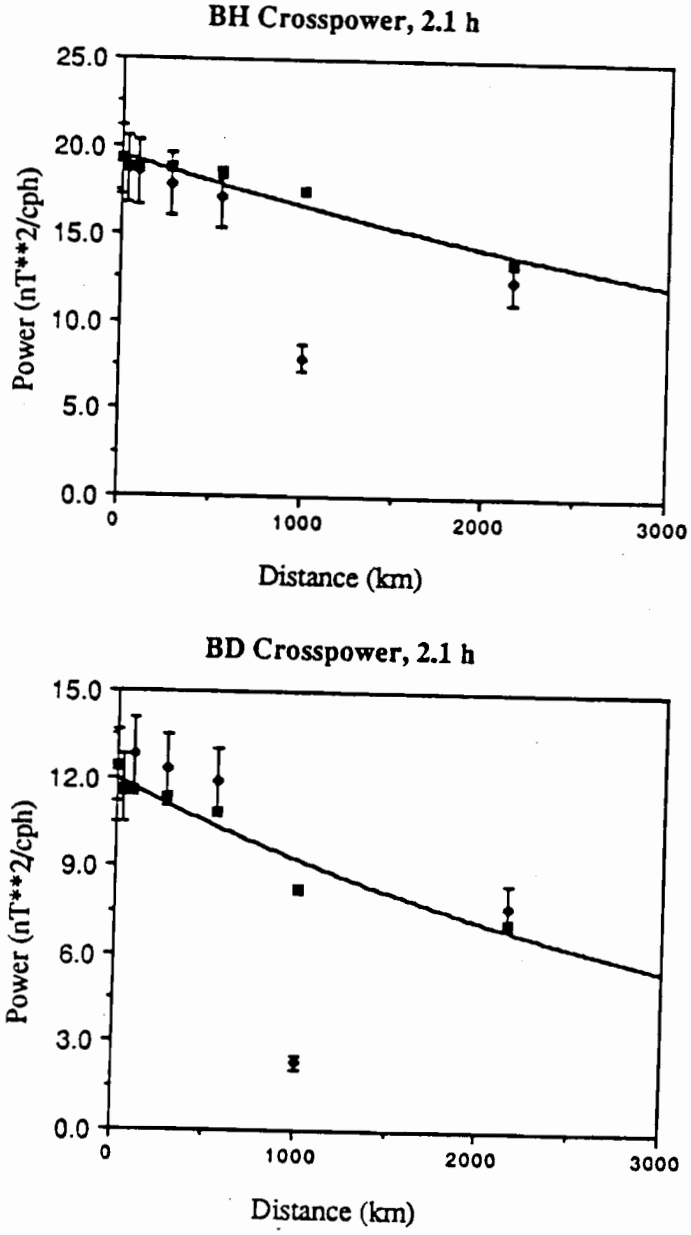

Figure 6.17: Diagrams showing variation in crosspower as a function of inter-site distance. The results are for the period band of 2.1 h and are tabulated in Table 6.8. The diamonds show the observed crosspower and the squares the standardized crosspowers, corrected for the local variations in the autopower. The error bars are 95 % confidence limits and the curves are the exponential functions which have fitted to the data. The exponential scale distance for B_H is 6430 km and for B_D is 3890 km.

Experimentation with fitting different exponential functions to the data suggests the length scale for B_H must lie in the range 5000-7000 km and the scale for B_D in the range 3000-4500 km.

Figure 6.18 shows the crosspower data for a range of periods, and the exponential curves fitted to these data. In most cases the fit to an exponential function is reasonable. For the short periods (1 h and less) both the B_H and B_D TP3-CMO crosspower deviate from the exponential function defined by the other sites. At these frequencies the autopower correction term is large and the misfit is probably caused by bias in this term. Table 6.9 lists the length-scales derived for B_H and B_D. The scale for B_D is generally shorter than for B_H and for both B_H and B_D the length-scale decreases with decreasing period. Over the available period range of 0.5 - 16.7 h the average B_H scale length is 5900 km and the average B_D scale length is 3900 km.

The length-scales may be used to quantify the effects of source-field non-uniformity on results derived from more than one site. An example occurs in chapter 7 in which the horizontal magnetic field recorded at CMO is used to derive VGS results for the seafloor sites. The crosspower functions between CMO and the seafloor horizontal magnetic field components, which are used in the VGS calculations, require correction for the crosspower decrease due to source-field non-uniformity. Since the source-field length-scales are derived from the same data segments as those used in the VGS analysis, a direct correction can be made from the results in Table 6.9, without need to account for non-stationarity. For example, for TP3 which is 1009 km from CMO, an average correction for the decrease in crosspower in B_D is given by $(e^{-1009/3900})^{-1} = 1.3$.

6.5 Induction Arrows

This section describes the determination and the form of the induction arrows at the Tasman Project recording sites. The induction arrows parameterize the variation in B_Z, and will therefore define lateral changes in conductivity structure along the recording line. The induction arrow results are presented for a range of frequencies and for all sites. Although the results are interpreted only in a qualitative manner here, they will be used in the future for 2D modelling of the electrical conductivity structure of the Australian continental margin.

Induction arrows presented in this thesis are calculated using a reference horizontal magnetic field (that at CMO) rather than the local horizontal magnetic field at each site. Such arrows are most similar in form to those from "traditional" land surveys and may be qualitatively interpreted in the same manner. The use of the seafloor horizontal magnetic-field in arrow calculations will produce arrows with substantial differences from the

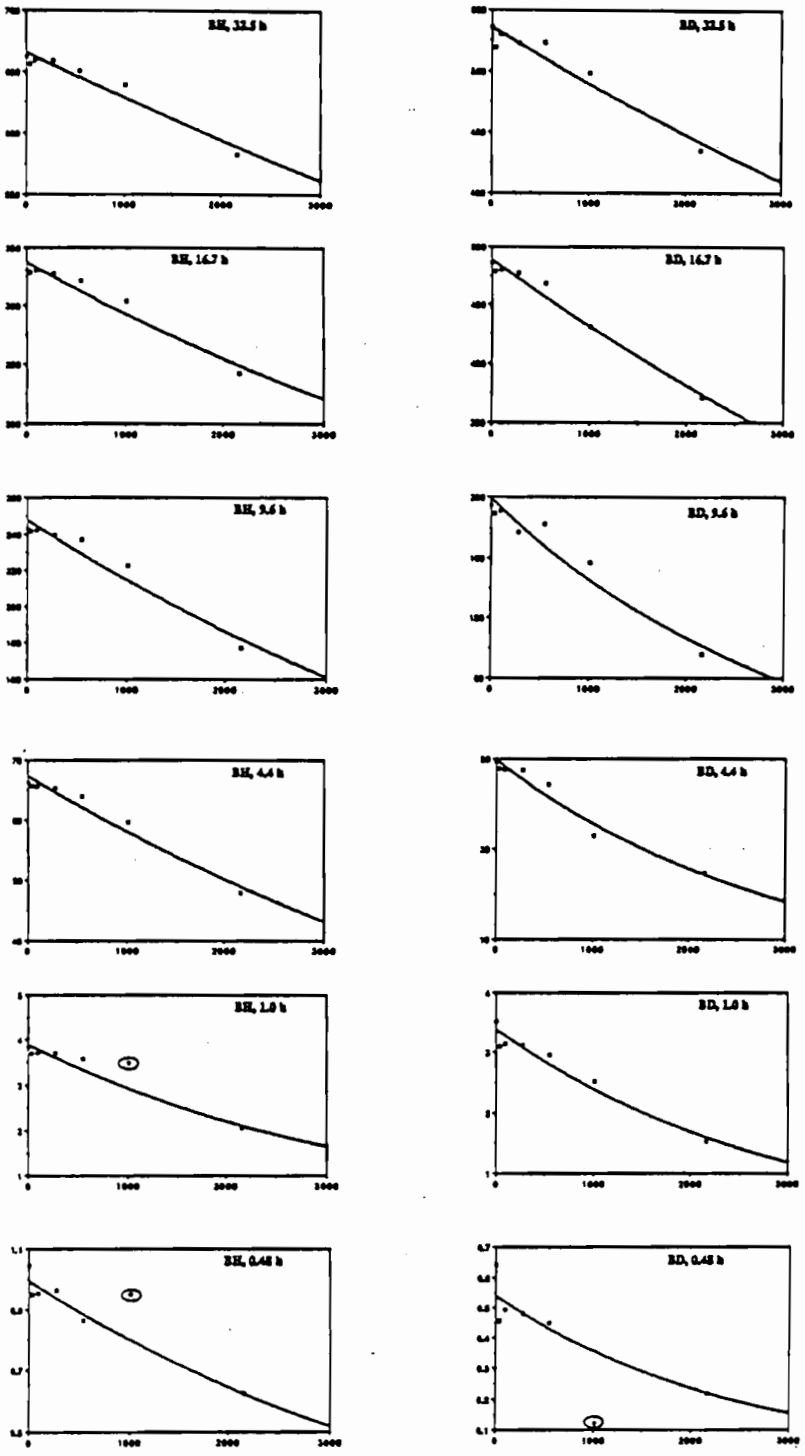

Figure 6.18: Inter-site coherence for different periods. Each panel shows the crosspower at different inter-site distances and the exponential curve fitted to the data. Circled points in the short period results correspond to crosspower values between CMO and TP3 which are excluded from the fitting of the curve. Table 6.9 lists the exponential scale distance for each of the periods.

Table 6.9: Distance scales for inter-site coherence.

Period (h)	B_H Length (km)	r	B_D Length	r
32.5	17600	.97	11120	.97
16.7	7070	.97	8030	.97
9.6	6980	.97	3180	.97
4.4	6760	.98	2990	.98
2.1	6430	.98	3890	.96
1.0	3760	.94	2850	.98
	3490	.99*		
0.48	5070	.91	1850	.72
	4600	.98*	2400	.95*

* Result derived after exclusion of TP3 datum.

The length scales, D, have been derived by fitting corrected crosspowers, A, against inter-site distance, d, with the function

$A = A \exp(-d / D)$

The table also gives the value of the correlation co-efficient, r. The length scales are intended to be used only as approximate estimates and have not been derived using the most formal statistical methods. The uneven spacing of data used in the curve fitting means that the derived length scale depends heavily on the magnitude of the crosspower at EYR and that the correlation coefficient is artificially high.

corresponding sea-surface arrows, because of the attenuation of the horizontal magnetic field through the ocean. Such seafloor arrows are difficult to interpret directly, since spatial variations in the arrows are caused by spatial variations in both the vertical and the horizontal magnetic fields.

Calculation of B_Z Transfer Functions and Induction Arrows

The transfer functions between the vertical component of magnetic field and the north and east components, a and b, were obtained by a least-squares fit to equation 4.106. In analogy with the least-squares MT impedance solution (4.133) the transfer functions were obtained using

$$a = (S_{B_Z B_H} S_{B_D B_D} - S_{B_Z B_D} S_{B_D B_H})/D \qquad 6.10a$$

$$b = (S_{B_Z B_D} S_{B_H B_H} - S_{B_Z B_H} S_{B_H B_D})/D \qquad 6.10b$$

$$D = S_{B_H B_H} S_{B_D B_D} - S_{B_H B_D} S_{B_D B_H} \qquad 6.10c$$

The calculations were based on the band-averaging system and data segments described in sections 6.2 and 6.3. In general B_H and B_D are the horizontal magnetic field components from site CMO, and B_Z is from the site of interest. Confidence limits for both a and b (which are usually not equal) were obtained using equation 4.162.

The transfer functions have been converted into induction arrows using 4.107 and 4.108 and also resolved into components parallel and perpendicular to the Australian coastline. The negative time dependence of spectral terms (see appendix 3) means that the quadrature arrows (which are not reversed) should point towards a good electrical conductor (Lilley & Arora 1982, Table 1). In the calculation of the induction arrows a correction for the local declination (Table 6.7) was made at each site. The resolution into longitudinal (parallel) and transverse (perpendicular) components of the transfer function assumed the trend of the coast is 25° (east of true north). This value is close to being perpendicular to the recording line orientation of 113° and is derived from measurements of the trend of the coast and the continental shelf over varying north-south distance scales.

The calculation of the random error distribution on the induction arrows and resolved transfer function components is more complex than calculation of the quantities themselves. It is common practice to represent the errors on induction arrows by circular regions with radii related to the total unexplained power in B_Z (Schmucker 1970). However in general the magnitude of the confidence limit is different for the two transfer functions a and b and information is lost by using a circular error estimate.

It is assumed here that the error distribution for each transfer function is Gaussian and thus given by

$$p(i) = (\sigma_i \sqrt{2\pi})^{-1} \exp\left[\frac{(i-\mu_i)^2}{2\sigma_i^2}\right] \qquad 6.11$$

where variable i corresponds to either transfer function a or b, σ_i is the standard deviation of the corresponding error distribution and μ_i is the actual transfer function estimate. If the assumption is made that the errors are independent in the directions corresponding to a and b (ie. magnetic north and east in the current analysis) the combined error distribution becomes

$$p(a, b) = p(a)\, p(b) = (\sigma_a \sigma_b 2\pi)^{-1} \exp\left[\frac{-1}{2}\left(\frac{(a-\mu_a)^2}{\sigma_a^2} + \frac{(b-\mu_b)^2}{\sigma_b^2}\right)\right] \quad 6.12$$

which indicates that lines of constant probability (eg. confidence limits) are ellipses.

Elliptical error distributions are used in this thesis with the semi-major and semi-minor axes of the ellipse given by the magnitude of the confidence limit on the a and b transfer functions (Figure 6.19). The errors on the real and imaginary (quadrature) components of the transfer function are assumed to be equal. The error on a geographical component of the induction arrow is taken to be the radius of the error ellipse in that vectorial direction. The true 2D error distribution on (a,b) is unknown but will depend on various factors including the distribution of random noise in the different directions. The elliptical error distribution forms an approximation to the true distribution (Figure 6.19).

General Form of Induction Arrows

The results for the induction arrows at each Tasman Project site and for the components of the transfer functions parallel and perpendicular to the Tasman Sea are tabulated in appendix 5. These results will now be presented in graphical form and described. The confidence limits will be omitted from most induction arrow plots to improve clarity however Figure 6.20 shows examples of the 95% confidence limits. At most sites the magnitude of the errors decreases approximately monotonically with decreasing period; the error ellipses at 9.6 h are typical of the random error magnitudes in longer period bands while those at 1.0 h are typical of the errors for shorter period bands.

The 95% confidence limit is a relatively large random error estimate (for example compared with the standard deviation ie. the 67% confidence limit). This result is illustrated by the error ellipses for the period of 9.6 h. The consistency of the real arrows between adjacent land sites suggests the arrows are quite well resolved in contrast with the error ellipses which suggest relatively poor resolution. The error ellipses on the arrows at the 1.0 h period are very small. This result indicates random errors are small, however th arrows may also contain small bias errors which are not allowed for in the calculation of t

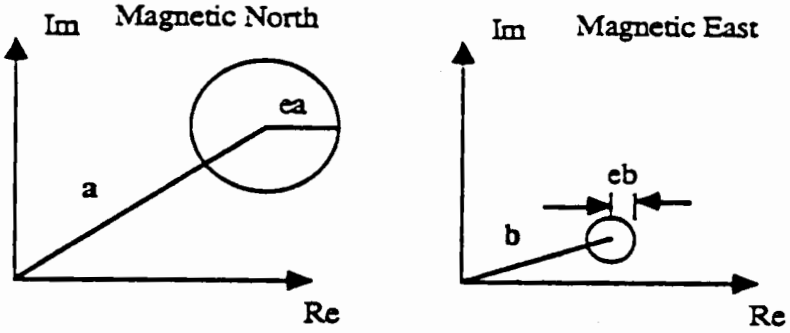

A. Transfer Functions a and b

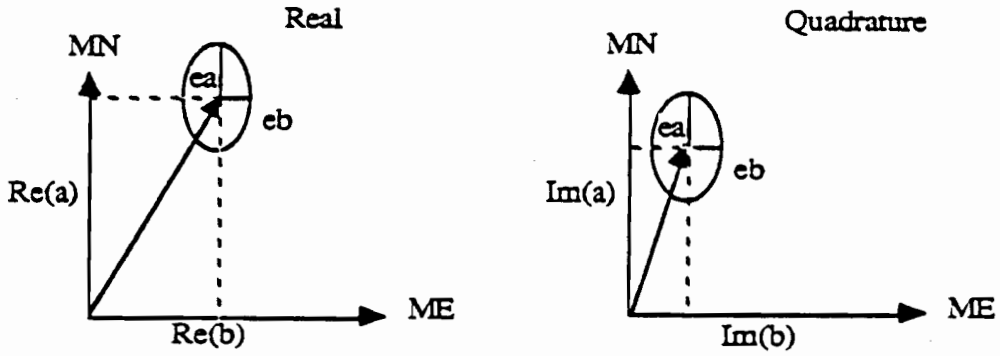

B. Induction Arrows with real and quadrature parts.

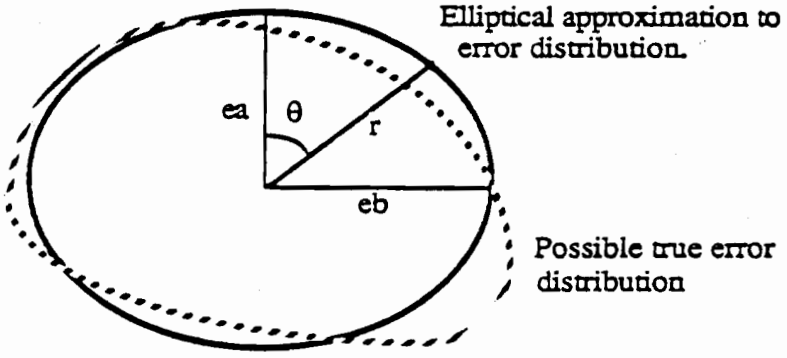

C. Errors on arbitrary components of transfer functions

Figure 6.19: A,B Schematic illustration of induction arrow representation. C.The error distribution is assumed to be an ellipse with semi-major and semi-minor axes corresponding to the error estimates, e_a and e_b, in the magnetic north and east directions.

The error, r, in any other direction, θ, is given by

$$r = \frac{e_a e_b}{\sqrt{e_a^2 \sin^2\theta + e_b^2 \cos^2\theta}}$$

The elliptical error distribution may only be an approximation to the true distribution.

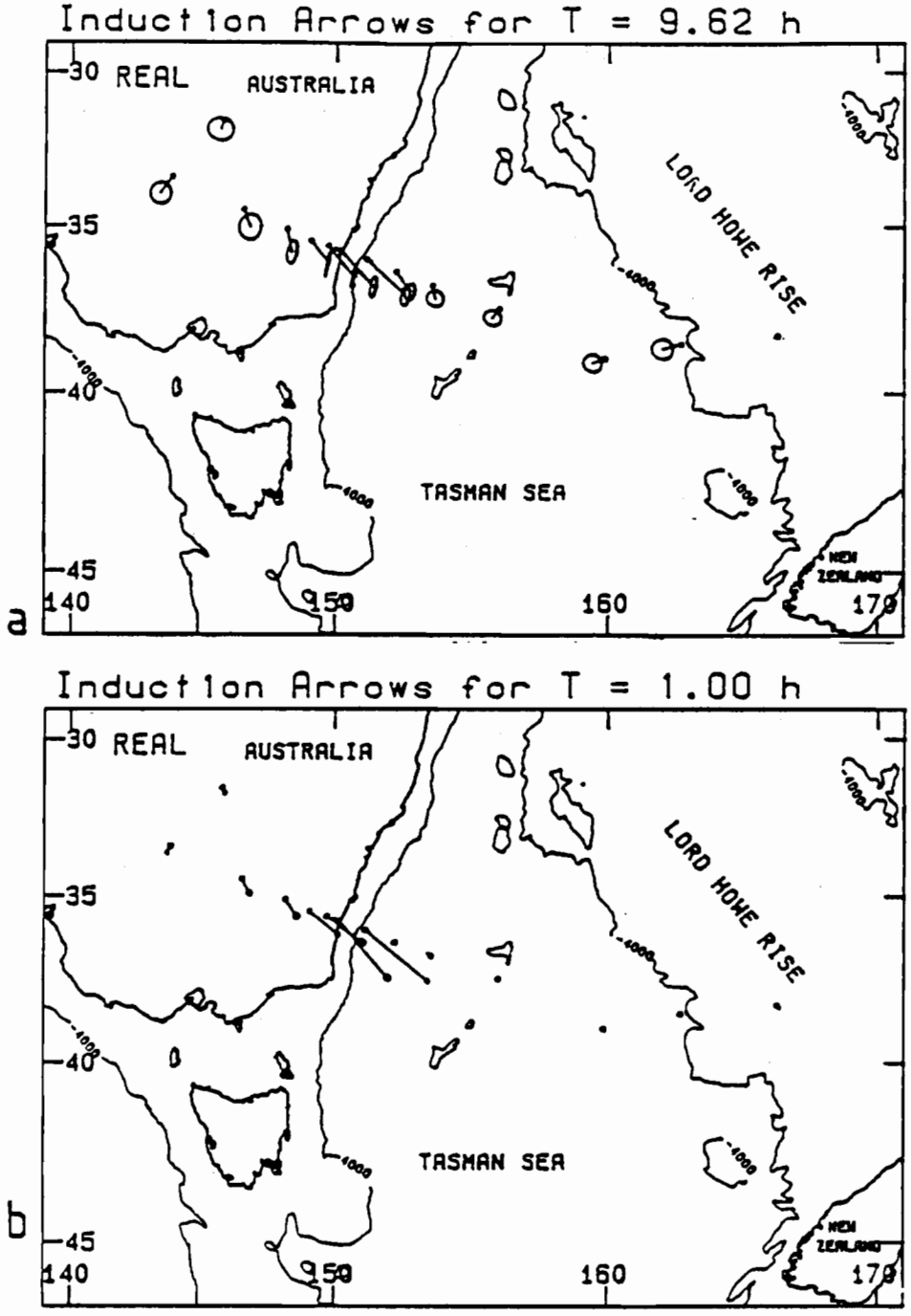

Figure 6.20: Examples of 95% confidence limit ellipses on real induction arrows. Note that the random errors are assumed to be equally distributed between real and quadrature components. The arrows for some of the sites near the Australian coast have been omitted for clarity.

(a) Arrows at 9.6 h period; confidence limits are typical of those for longer period bands.

(b) Arrows at 1.0 h period; confidence limits are very small, typical of those for the shorter period bands.

confidence limits.

Figure 6.21 shows the real and quadrature induction arrows for sites extending across the recording line and for periods between 1.0 h and 16.7 h. Figure 6.22 shows the arrows for sites near the Australian coastline (sites CLC-TP5) plotted at a larger scale. The three most important features of the induction arrows are; a strong coast effect at the Australian coastline, a weaker "coast effect" over the Lord Howe Rise, and at longer periods strong southwards components of the real arrows and westward components of the imaginary arrows. The first two features parameterize relationships observed between the field components in the time series (section 6.1).

The full lateral extent of the coast effect can be best seen in Figure 6.21. At periods between 1.0 and 9.6 hours the real component of the induction arrows shows an increasing component as the Australian coast is approached. This effect is visible at all land sites except site GNS where the southward trend of the arrow is explained by the proximity of the site to the deep ocean south of the continent (Table 6.7). The distance the coast effect extends into the Tasman Sea is shorter than the corresponding distance across the continent and decreases strongly with decreasing period. Figure 6.22 shows the coast effect in more detail. The real component of the induction arrows shows a systematic coast effect, with the maximum amplitude occurring between sites DRS and TP8 and at periods between 1.0 and 4.4 h. The oceanward extent of the coast effect falls off rapidly at periods less than 4.4 h, with progressively fewer recording sites showing a discernible coast effect at shorter period bands. The landward extent of the coast effect falls off much more slowly. Although the arrows at the long period bands are dominated by source-field bias effects (described below) the sites still show an increasing eastwards component with proximity to the coast.

Figure 6.22 shows the quadrature induction arrows also exhibit a systematic pattern near the Australian coastline. For the shorter period bands ($T \leq 1.0$ h) the quadrature induction arrows point systematically westwards with maximum amplitude near the coast. For intermediate period bands ($2.1 \leq T \leq 9.6$h) the eastward component of land quadrature arrows is very small and there is an eastwards reversal in the seafloor arrows at sites near the coast. The reversal of the quadrature arrows near the coast is visible in the 16.7 h results and indicates that even at this period the induction arrows are responding to the conductivity anomaly at the coastline.

The coast effect over the Lord Howe Rise is most clearly defined for the period bands between 4.4 and 9.6 h for which the induction arrows have a significant component perpendicular to the trend of the Lord Howe Rise. At the 9.6 h period the coast effect of the Lord Howe Rise extends at least 350 km to site TP3 and possibly as far as TP4. The coast effect over the Lord Howe Rise is much smaller than that of the Australian continent particularly at short periods. This result is explained by the submerged nature of the Rise. At short periods a significant proportion of the induced electric currents will flow over the top of the Rise and not contribute to an anomaly.

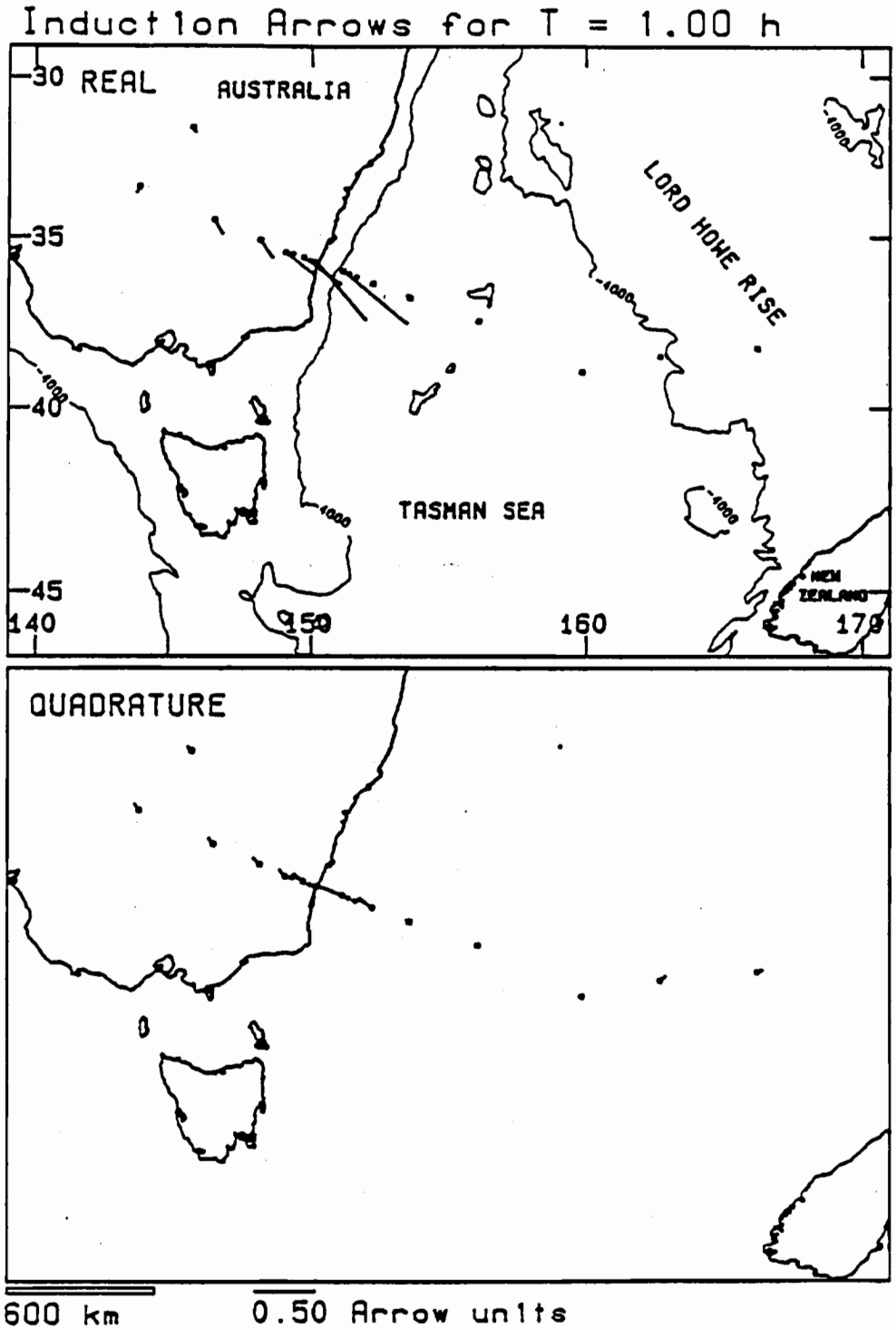

Figure 6.21: Real and quadrature induction arrows at sites spanning the recording line for periods between 1.0 to 16.7 h. The arrows at some sites near the Australian coast have been omitted for clarity. The arrows are determined using the horizontal magnetic field from CMO and the local vertical magnetic field.

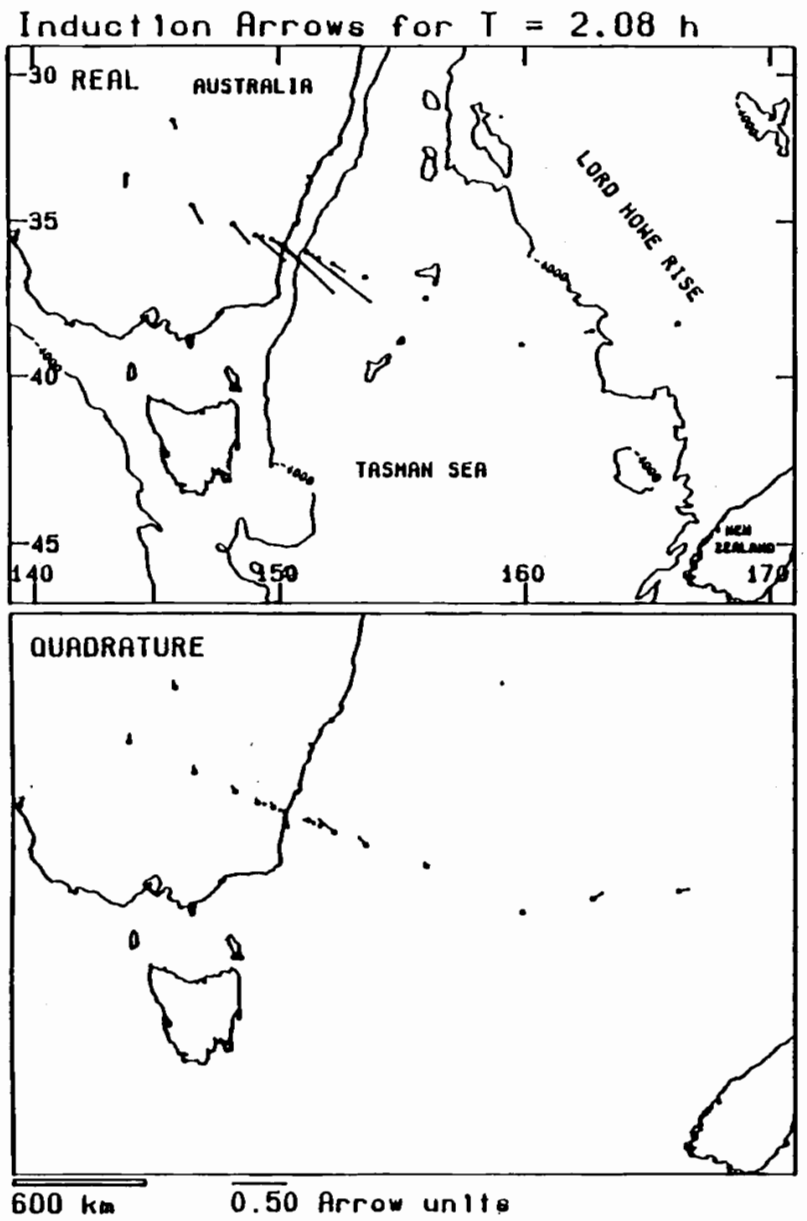
Induction Arrows for T = 2.08 h
30 REAL
AUSTRALIA
LORD HOWE RISE
35
40
TASMAN SEA
45
140
150
160
170
NEW ZEALAND
QUADRATURE
600 km
0.50 Arrow units

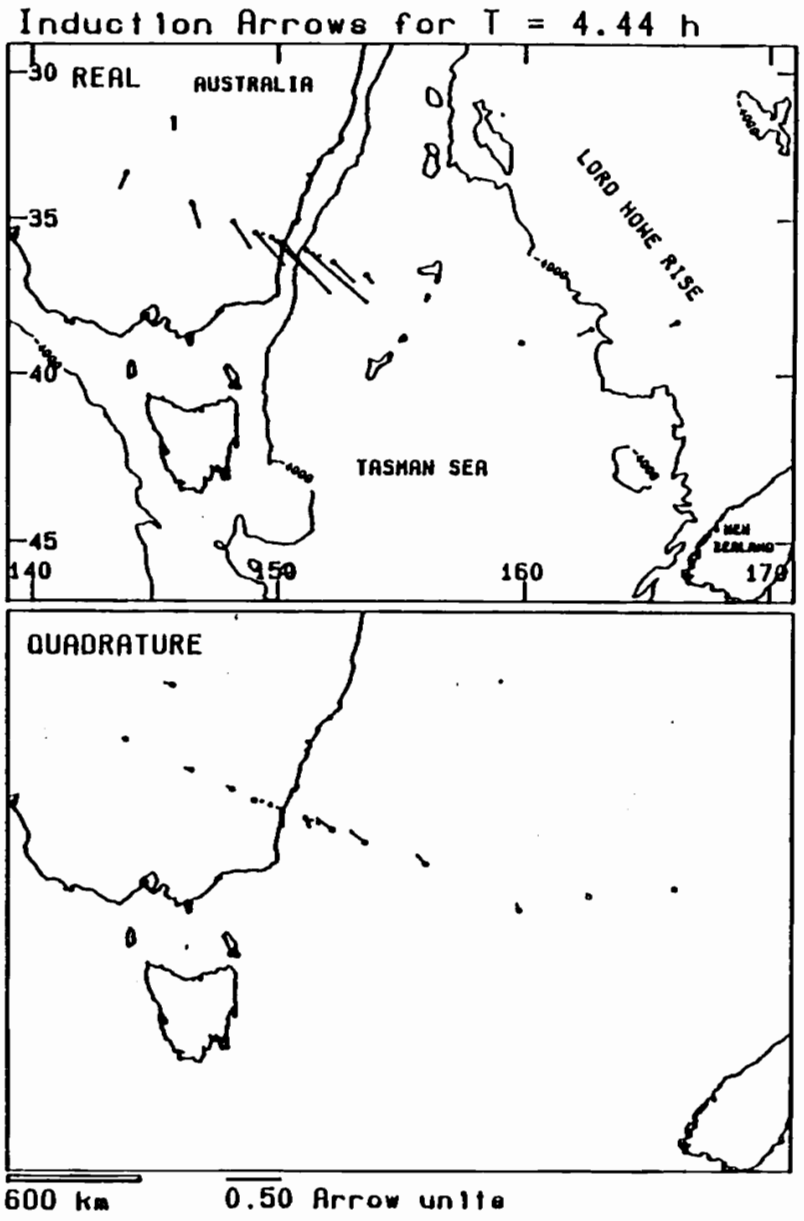
Induction Arrows for T = 4.44 h
30 REAL
AUSTRALIA
LORD HOWE RISE
35
40
TASMAN SEA
45
140
150
160
170
NEW ZEALAND
QUADRATURE
600 km
0.50 Arrow units

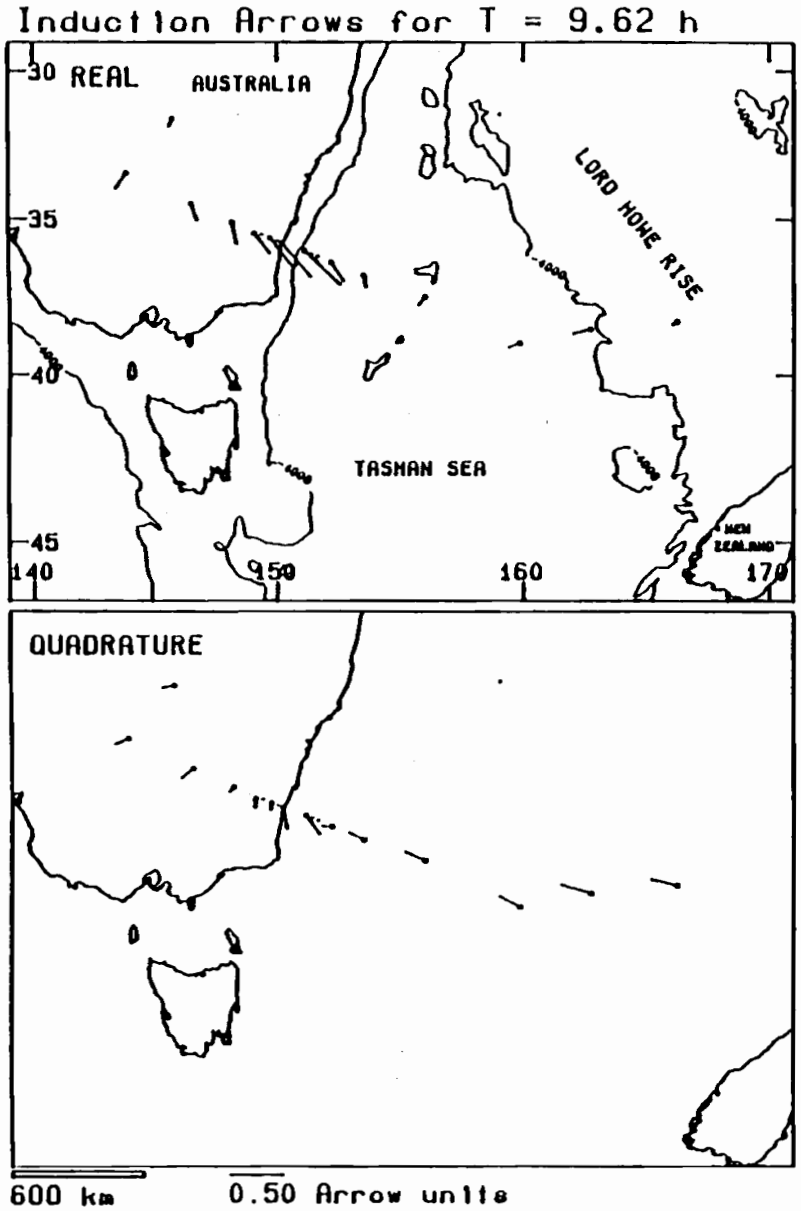
Induction Arrows for T = 9.62 h
30
REAL
AUSTRALIA
LORD HOWE RISE
35
40
TASMAN SEA
45
140
150
160
170
NEW ZEALAND
QUADRATURE
600 km
0.50 Arrow units

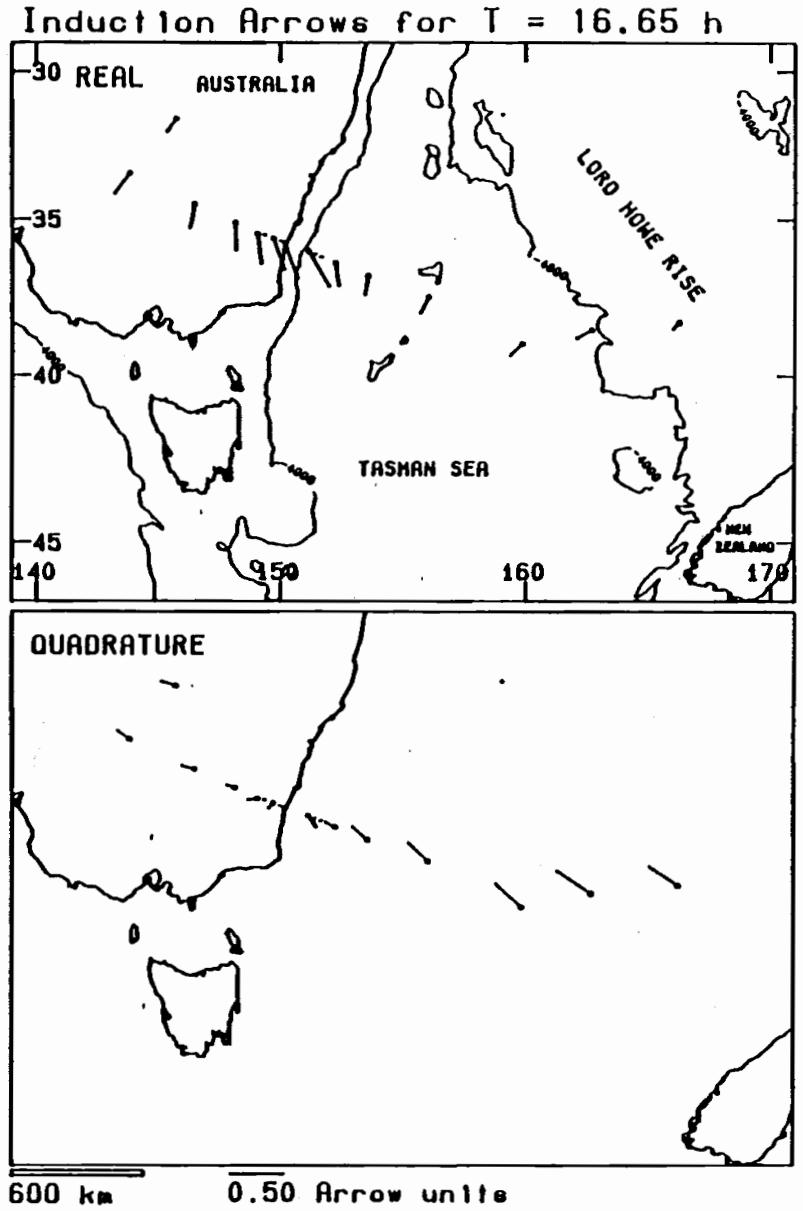
Induction Arrows for T = 16.65 h
30
REAL
AUSTRALIA
LORD HOWE RISE
35
40
TASMAN SEA
45
140
150
160
170
NEW ZEALAND
QUADRATURE
600 km
0.50 Arrow units

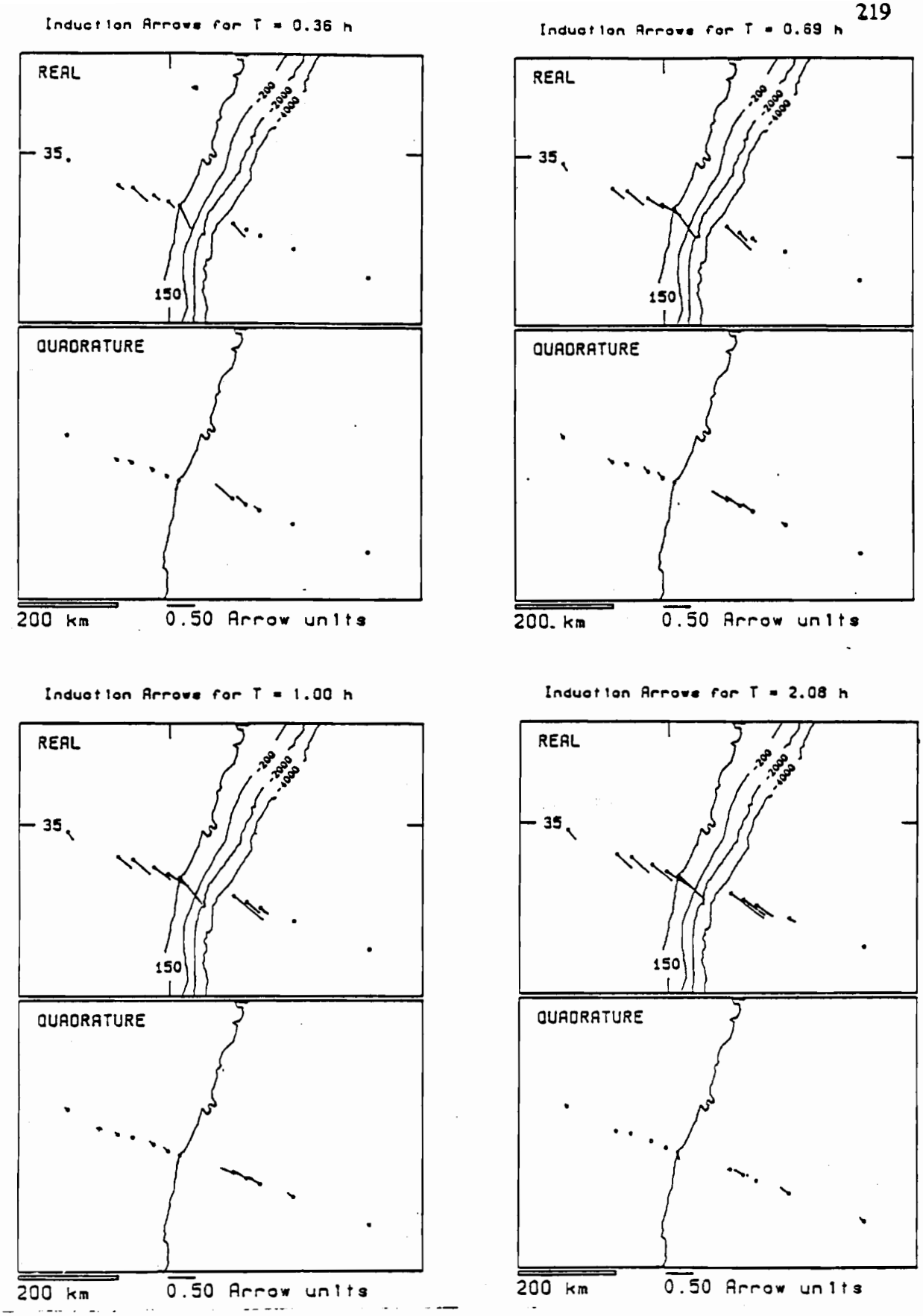

Figure 6.22: Real and quadrature arrows at sites near the Australian coastline for periods between 0.4 and 16.7 h. The arrows are determined using the horizontal magnetic field from CMO and the local vertical magnetic field.

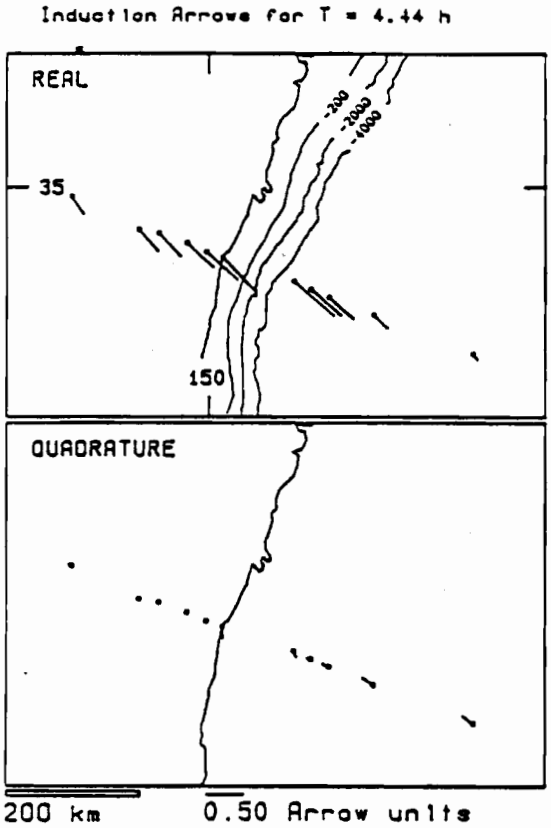
Induction Arrows for T = 4.44 h
REAL
35
150
-200
-2000
-4000
QUADRATURE
200 km
0.50 Arrow units

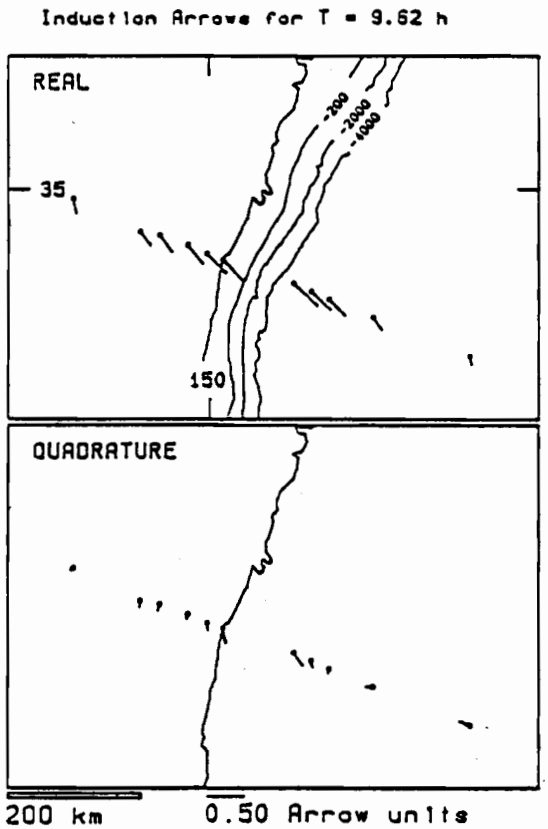
Induction Arrows for T = 9.62 h
REAL
35
150
-200
-2000
-4000
QUADRATURE
200 km
0.50 Arrow units

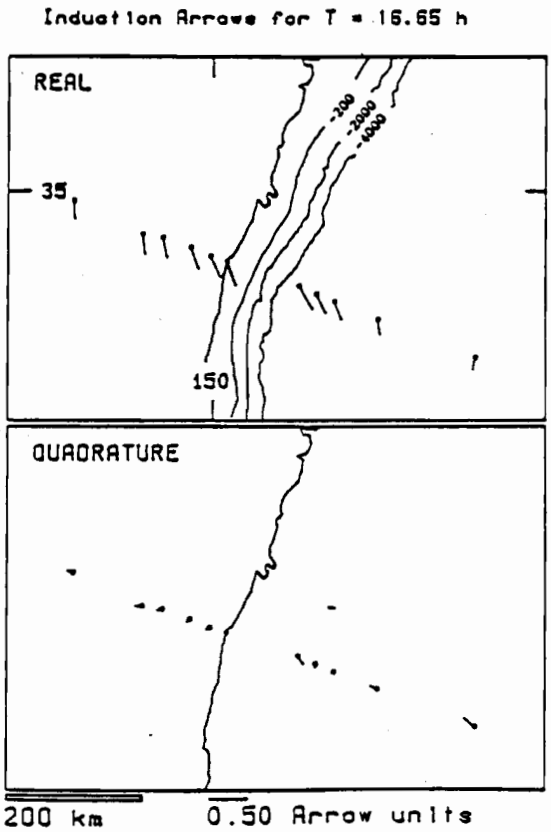
Induction Arrows for T = 16.65 h
REAL
35
150
-200
-2000
-4000
QUADRATURE
200 km
0.50 Arrow units

A decrease in the magnitude of the induction arrows at sites distant from CMO will result from the source-field variations between CMO and distant sites. Such source-field variations will reduce the crosspower between B_H and B_D at CMO and B_Z at the distant site and thus cause a reduction in the magnitude of the induction arrow. From the crosspower analysis described above, the reduction in induction arrow magnitude for site TP1 (1530 km from CMO) is estimated to be less than 50%. This effect is therefore too small to cause the observed decrease in the coast effect over the Lord Howe Rise at shorter periods.

The "coast effect" seen in the induction arrows at the Australian coast and at the Lord Howe Rise was also noted earlier in the time series and power spectra. It is attributed to the E-pol magnetic field anomaly associated with the lateral electrical conductivity boundary of these features. The vertical magnetic field fluctuations are caused by a greater density of electric current flow in the Tasman Sea relative to the Australian continent and Lord Howe Rise. The B_Z component is correlated with the magnetic field component normal to the conductivity boundaries ($\sim B_D$) and the induction arrows are as a result aligned perpendicular to these boundaries.

Modelling shows that the real component of surface induction-arrows will generally point towards regions of increased electrical conductivity. In the ocean, for periods less than about 5 h (where most of the telluric current flow occurs in the ocean) and periods longer than 0.5 h (below which the ocean ceases to behave as a thin sheet) the induced vertical magnetic field will be similar at the seafloor and at the sea-surface. In this period range seafloor induction arrows calculated using surface horizontal magnetic field values will therefore behave in the same manner as sea-surface arrows. From Figure 6.21 it is evident that the real component of Tasman Project induction arrows behave in the expected manner, pointing away from the more poorly conducting Australian continent and Lord Howe Rise.

The strong southward component of all real arrows and westward component of all quadrature arrows at periods longer than 4.4 h is interpreted as source-field bias. Bias will be caused by the existence of a B_Z component in the source field which may be correlated with the B_H and/or B_D components. Unless a separation of internal and external magnetic fields is performed in a geomagnetic induction study, induction arrow results from the study will be biased towards this source-field relationship. This effect is discussed in section 4.3. The longer-period Tasman Project induction arrows are interpreted as indicating a strong source-field correlation of B_Z with B_H (in-phase) and of B_Z with B_D (quadrature-phase).

At an exactly 2D electrical conductivity boundary there should be no component of either the real or the quadrature induction arrow parallel to the boundary. The induction arrows at the Australian coastline however have significant longitudinal components suggesting 3D influences in the conductivity structure. This result has already been noted

from time series observations and is therefore not a result of an incorrect analysis method. The longitudinal induction arrow components are discussed in more detail below.

An important implication of Figures 6.21 and 6.22 is the absence of any other strong conductivity anomalies than those associated with the Australian coast and the Lord Howe Rise. The response of all of the observed arrows appears to be related to only these features (and to source-field bias). The induction arrow data set is therefore ideal for studying the conductivity structure of the Australian continental margin.

Transverse Component of Induction Arrows

The transverse component of the induction arrows across the Australian coastline will ultimately be used for quantitative 2D modelling of the continental margin. This work will be performed by R.L. Kellett and therefore presented in a later thesis. Several profiles of the data are however presented here and compared qualitatively with model calculations and compilations of previous observations in published papers.

Figure 6.23 presents the real and quadrature parts of the transverse component of the induction arrow, for a range of periods, and for sites extending across the recording line. Before interpreting the results it is instructive to assess their accuracy. A preliminary examination of the real components, particularly those at shorter periods, shows that the value at CMO is anomalously high compared with the values at the surrounding sites. The quadrature value at CMO also tends to lie away from the smooth trend defined by the quadrature results at surrounding sites. For periods longer than 0.7 h the anomaly in the CMO results is relatively minor, not exceeding the magnitude of the 95% confidence limit error bars. The anomalous effects are however significant at shorter periods and because the induction arrows at these short periods may ultimately be used for numerical modelling the problem requires further consideration.

It is possible to discount the horizontal magnetic field values from site CMO, used in the arrow calculations as the source of bias. Induction arrows for sites DRS - CMO, re-calculated using the horizontal magnetic field results from site BBB show very similar results. The anomalous transfer function values at CMO are therefore attributed to the B_Z magnetic field component used in the calculations. The source for the bias must be either an anomalously large B_Z component (correlated with B_D) at CMO or anomalously low values of B_Z at surrounding sites. Although an anomalously large B_Z at CMO could be caused by either a local electrical conductivity structure or instrumental / calibration problems, the lack of any further evidence for a local electrical conductivity anomaly and the observatory standard of the data, make such possibilities unlikely. It is more probable that the bias is caused by an under-estimation of B_Z at the other land recording sites caused by the hand-digitization of Gough-Reitzel data at these sites (also see chapter 3).

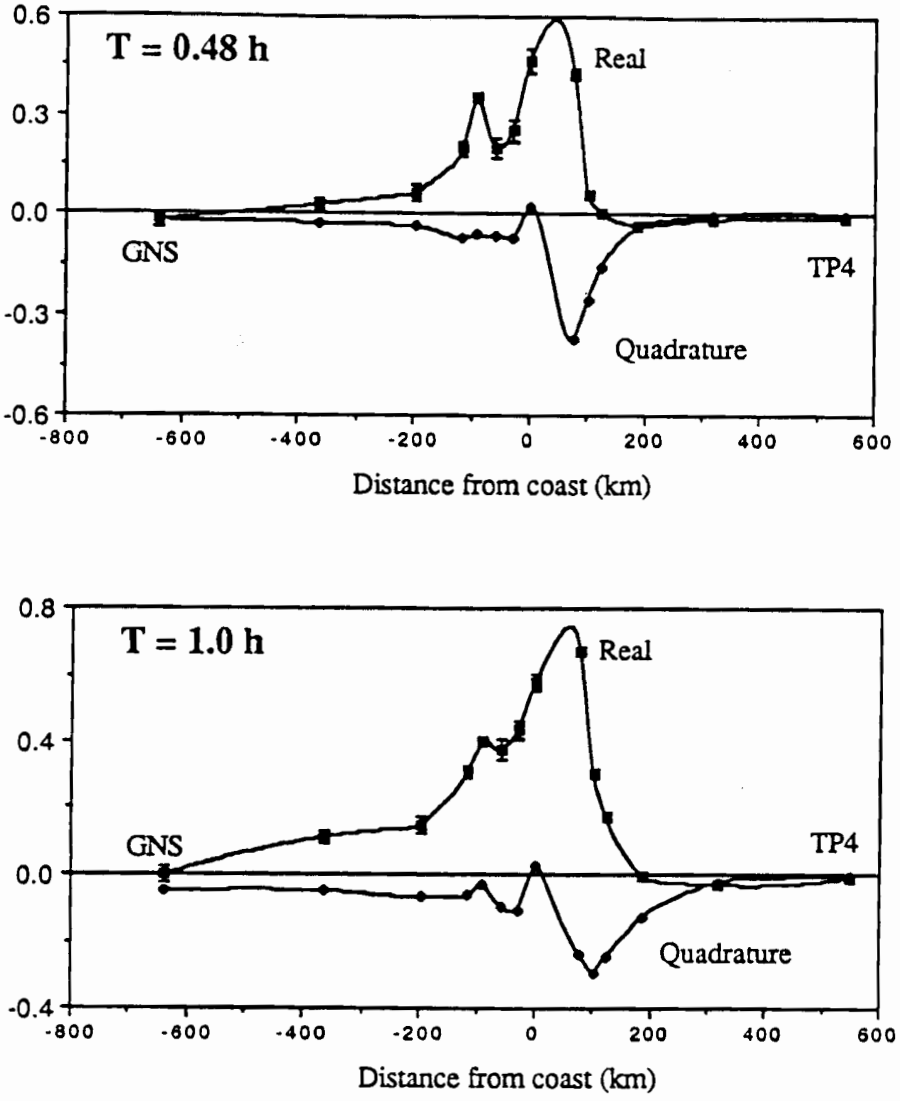

Figure 6.23: Profiles showing transverse component of induction arrows as a function of distance from the coast. The vertical axis on all figures corresponds to induction arrow units, with positive values corresponding to a seaward orientation, and the horizontal axis gives the distance from the Australian coastline, with positive values corresponding to the seaward side of the coast. The error bars are 95% confidence limits and are assumed to be equal for real and quadrature components. The interpolated line through the data points is included only to provide clarity and does not have any intended physical significance. On the profiles for the shorter period results, the continental side of the profile includes an anomalous point approximately 100 km from the coast. This point corresponds to the datum at site CMO and is probably caused by a reduction in the induction arrow length at the adjacent Gough-Reitzel sites.

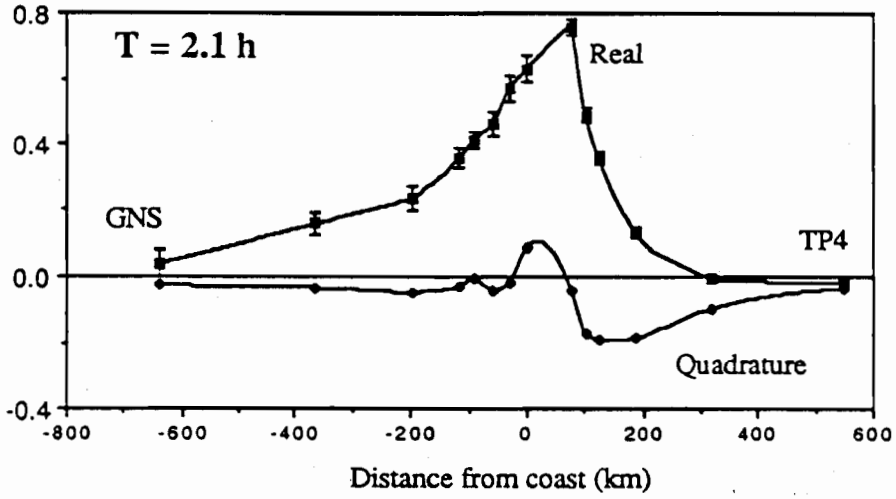
T = 2.1 h
Real
GNS
TP4
Quadrature
0.8
0.4
0.0
-0.4
-800
-600
-400
-200
0
200
400
600
Distance from coast (km)

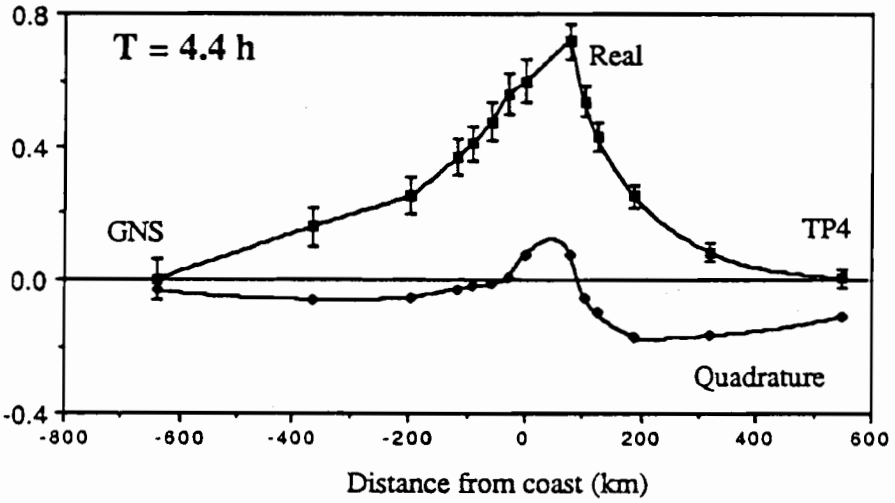
T = 4.4 h
Real
GNS
TP4
Quadrature
0.8
0.4
0.0
-0.4
-800
-600
-400
-200
0
200
400
600
Distance from coast (km)

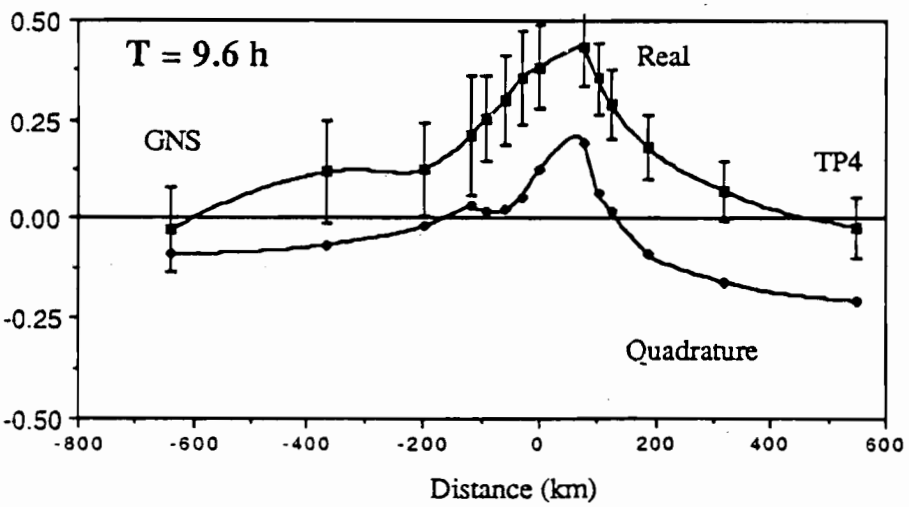
T = 9.6 h
Real
GNS
TP4
Quadrature
0.50
0.25
0.00
-0.25
-0.50
-800
-600
-400
-200
0
200
400
600
Distance (km)

A second check for bias in the transfer functions can be made by comparing the results from the Tasman Project with those from previous studies. Bennett & Lilley (1971) calculate transfer function results for a profile extending from Moruya on the southeast coast of Australia to Griffith, approximately 410 km inland. Sites BWD, SVY and GRF from the earlier study lie close to BBB, BKM and BLN of the present study and in Table 6.10 the transfer function results from the two studies are compared. Although the Tasman Project arrows are calculated relative to a reference horizontal magnetic field while the earlier study uses the local field, at a period of 1 h there is little variation in the horizontal magnetic field across the inland part of the recording line (Figure 6.9) and the

Table 6.10 Comparison of induction arrows from different studies.

Study	Site	Period (min)	|a|	|b|
1969	BWD	60	0.32	-0.48
TPSME	BBB	60	0.16	-0.35
1969	SVY	60	0.30	-0.34
TPSME	BKM	60	0.15	-0.28
1969	GRF	60	0.22	-0.06
TPSME	BLN	60	0.11	-0.09
1969	MRY	80	0.56	-0.61
Array	MRY	80	0.49	-0.55

The table shows comparisons between the real parts of transfer functions a and b. Comparisons are between the 1969-70 Tasman 'traverse' and the 1983-84 TPSME and between the 1969-70 traverse and the 1971 southeast Australian array experiment. The data from the 1969-70 traverse were digitally recorded whereas the TPSME and southeast Australia array data were recorded in analogue form and have been hand-digitized. The data from the earlier experiments are taken from Bennett & Lilley (1971) and Bennett (1972). The array results are an average of the Bennett's power spectra and Fourier spectra methods (Bennett 1972, p 76).

two sets of results can therefore be directly compared. Except for GRF where the east component of the transfer function is small, the transfer functions determined in the earlier study are significantly larger than those from the Tasman Project.

The majority of the difference between the Tasman Project and earlier results is attributed to a reduction in signal in the hand-digitized Gough-Reitzel data. The earlier Tasman traverse used digital, biased proton-precession magnetometers. A comparison of results from the 1969-70 traverse with the later 1971 Gough-Reitzel instrument array study (Bennett 1972) also finds the transfer function results based on hand-digitized Gough-Reitzel data have smaller magnitude than the transfer functions derived from the digital recordings. A component of the difference between the 1969-70 traverse and the other results may also be due to the earlier results being based on analyses exclusively from magnetically disturbed periods. As discussed in Bennett (1972) a strong southwards bias of the arrows may be due to source-field non-uniformity, which tends to be strongest when short events are analysed.

The availability of digitally recorded data from the Continental Shelf Experiment combined with the CMO data, should allow a numerical assessment to be made of the bias in the induction arrows. A correction for the bias should be performed before quantitative modelling of the coast effect using data at periods below 40 min. For this thesis the examination of further coast effect results will be mainly restricted to periods longer than 0.7 h where bias effects may be neglected.

Examination of the transverse real component in Figure 6.23 shows that as the period increases the "coast-effect profile" becomes progressively more broad and also more symmetric. The peak of the profile also appears to move oceanwards at longer periods. At 0.5 h the real components at TP8 and DRS are approximately equal suggesting a maximum coast effect mid-way between these sites; however, at longer periods site TP8 has a significantly larger real component than DRS suggesting that the peak of the coast effect lies closer to TP8. Such a movement of the maximum of the coast effect is explained by the gradually deepening ocean. At shorter periods electric current flow tends to be in much more shallow water and therefore at short periods the coast effect is significantly influenced by the electrical conductivity contrast at the Australian coast. At longer periods a greater amount of current flows in deeper water and the coast effect is dominated by the electrical conductivity contrast between the deep ocean and the edge of the Australian continental shelf. There is also the possibility of deep conductivity variations occurring to the east of the coastline.

It is of interest to note a deflection in the coast effect profile occurring at all frequencies approximately 200 km inland from the coast. The slope of the profile defined by sites GNS, BLN and CLC tends to be flatter than that defined by sites BKM to DRS. Although further analysis is necessary to confirm and accurately define this feature, it is possible that it is related to a deep electrical conductivity contrast, either beneath the Australian continental margin or closer to this part of the profile. The absence of a

corresponding effect on the ocean portion of the profile, the similar position of the deflection at all frequencies, and the co-incidence of the position of the deflection with western edge of the Eastern Australian Highlands suggest the feature could relate to a conductivity contrast at depth.

The shape of the observed transverse real component of the B_Z transfer function may be qualitatively compared with 2D finite-difference model calculations by Fischer & Weaver (1986). Figure 6.24 shows the theoretical coast effect for the case of a 1600 S ocean with two possible configurations for the deep electrical conductivity structure. For the distance scaling of 1 unit equalling 300 km, the responses correspond to results at 1.0 h period. The real induction arrow response is similar for both the model results and is similar to the observed Tasman Sea response at 1.0 h. The profiles have an asymmetric form with a decay extending over approximately 600 km on the land side of the profile and 100 to 200 km on the ocean side. Because of the similarity of the model profiles, and the available density of the recording sites, it is not possible to discern whether the Tasman Sea conductivity profile lies closer to model 2 or model 3. The results from the Continental Slope Experiment, located between the DRS and TP8 sites, will increase the data density in the region where the induction arrows change rapidly, and will be invaluable in modelling the coast effect.

Examination of further models presented in Fischer & Weaver (1986) shows that as the conductance of the ocean decreases, the shape of the coast effect anomaly in the real component becomes more symmetric, as the decay of the coast effect on the ocean side spreads over an increasingly large distance. The same effect is observed with increasing periods in the Tasman Project data (Figure 6.23). The processes of decreasing the ocean conductance and increasing the period both correspond to decreasing the number of skin-depths making up the ocean thickness.

The profile for the model quadrature induction arrow component shows more 'structure' than for the real component. It has a "bipolar" form with positive and negative peaks on either side of the coastline. The quadrature profile varies significantly between conductivity models 2 and 3. This sensitivity makes the quadrature component useful for resolving the conductivity structure. Unfortunately the quadrature coast-effect anomaly is of a smaller magnitude than the real anomaly (Figures 6.23 and 6.24) and therefore has larger relative errors.

The quadrature component of the Tasman Project induction arrow has approximately the form of that for model 3. At the period of 1 h it shows opposite peaks at DRS and at TP9. The observed peak at TP9 lies further seaward than the peak for model 3, probably indicating the effect of the continental shelf. At longer periods the observed Tasman Sea anomaly becomes more symmetric, an effect also noted in the model quadrature results for oceans of reduced conductance. The Tasman Sea quadrature response lies much closer to the model 3 profile than the model 2 profile, suggesting the contribution of deep

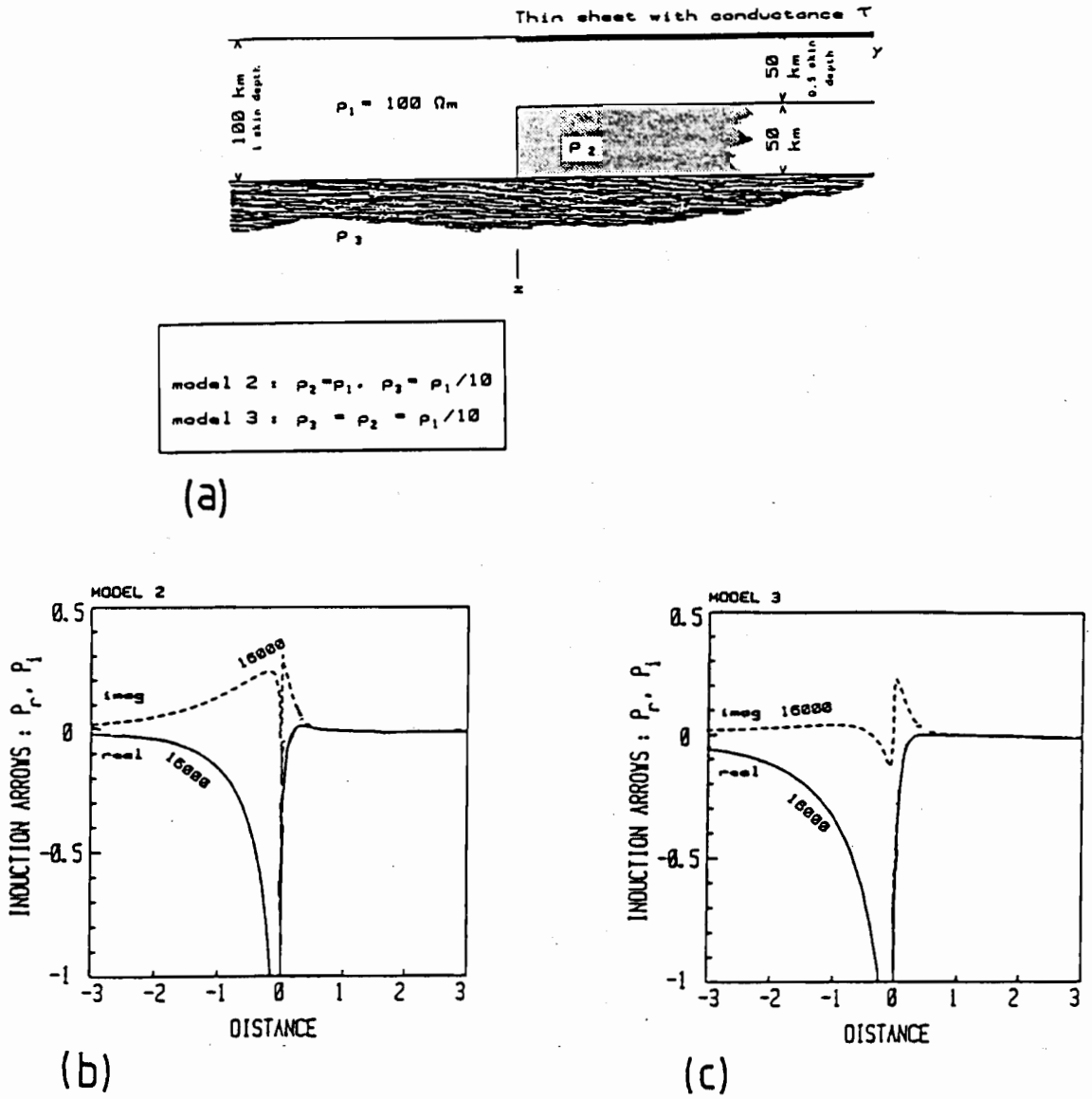

Figure 6.24: The coast effect for theoretical conductivity models (from Fischer & Weaver 1986).

(a) The conductivity models used in the calculations. Model 3 includes a deep conductivity rise beneath the continental margin.

(b and c) Real (solid line) and quadrature (dashed line) components of the induction arrow for model 2 and 3.

For the period of 1.0 h the distance scale on the figures is one unit equals 300 km. Note that the vertical axis scale used in these results has the opposite sign to that in the previous figure. The induction arrow components shown in this figure are from surface induction arrows calculated using the local horizontal magnetic field values. Spatial variations in the horizontal magnetic field component near the coastline will cause the coast effect anomaly to vary slightly from that defined using arrows based on a reference horizontal magnetic field.

conductivity contrasts to the Tasman Sea response.

Previous modelling of the electrical conductivity structure of the Australian continental margin by Bennett (1972) and Bennett & Lilley (1974) suggests the presence of deep conductivity contrasts at the continental margin. Their results, also based on modelling of the coast effect, show a zone of increased conductivity at shallow depths beneath the Tasman Sea (Figure 6.25). The top of this conductive zone lies between 0 and 50 km beneath the seafloor and its western edge is displaced 10 to 50 km east of the coastline. The use of the Tasman Project data in conjunction with data from the Continental Slope Experiment should refine this model.

The results from the 1969-70 Tasman traverse (Bennett & Lilley 1971) have been compared with profiles from other parts of the world (Figure 6.26). The results for southeast Australia are similar to those from other non-shield continental areas such as western Canada. The induction arrows from the continental shields are larger than those from more mobile tectonic environments indicating a consistent difference in the electrical conductivity structure. Although smaller than the previously determined southeast Australian arrows, the results from the Tasman Project fall within the scatter of results for the mobile tectonic environments. Compilations of quadrature induction arrow results have unfortunately not been published. Since the quadrature component can be used successfully in 2D modelling studies (eg. Ogawa et al. 1986) compilations of quadrature results could also be used to discriminate between the different tectonic structures of continental margins.

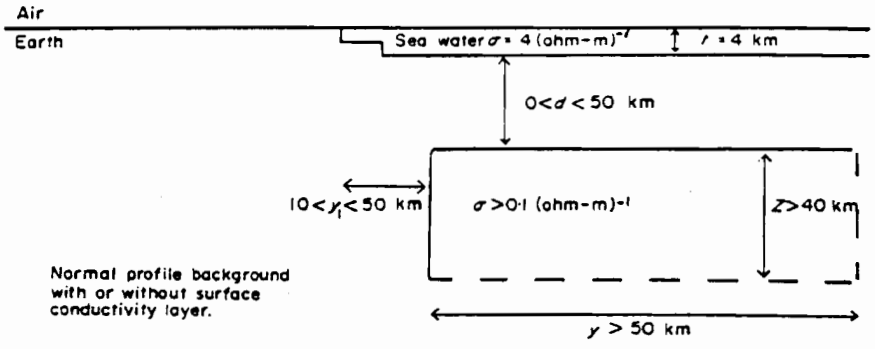

Figure 6.25: Electrical conductivity model for the western Tasman Sea and southeast Australia (from Bennett & Lilley 1974).

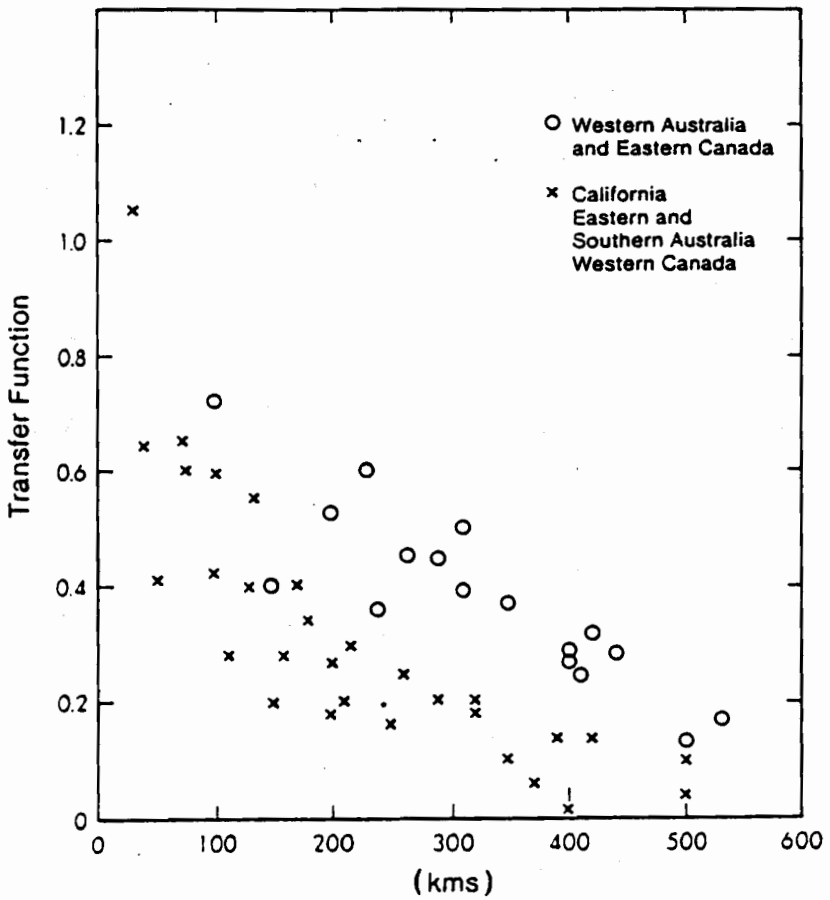

Figure 6.26: Compilation of coast effect results (from Parkinson & Jones 1979). The diagram shows the magnitude of the real component of the induction arrow as a function of distance from the continental slope. Tasman Project induction arrow results plot in the field defined by the crosses.

The frequency-dependence of the coast effect may be used to provide information on the conductivity structure (Parkinson & Jones 1979, Kellett et al. 1988). Figure 6.27 shows the amplitude of the real induction arrows at DRS and TP8 as a function of period. At both sites the maximum amplitude of the coast effect occurs around a period of 2 h, a relatively long period compared with many other coastal sites (Parkinson & Jones 1979). (The result for DRS is not attributable to the induction arrow bias noted above.) Coast-effect maxima at periods longer than 40 min. are interpreted by Rokityansky (1975) as indicating a significant deep contribution to the electrical conductivity contrast, which adds support to the hypothesis that such a contrast exists beneath the southeast Australian continental margin. Results from the Tasman Project (Figure 6.27b and c) also show an increase in the period of the maximum coast effect with distance from the coast. Such distance-dependence undoubtedly explains some of the scatter in the period of coast-effect maxima noted in compilations such as Parkinson & Jones (1979).

Figure 6.28 shows the real and quadrature transverse transfer function components across the Lord Howe Rise. The coast effect profile over the Rise is much smoother and smaller in magnitude than the profile over the Australian coastline. The peak in the coast effect appears to occur slightly to the east of site TP2, although with the wide site spacing at this end of the recording line, the peak is poorly defined. It is difficult to draw any definite interpretations on the electrical conductivity structure of the Lord Howe Rise from the coast effect profiles. Because of the low magnitude and poor definition of the coast effect, quantitative 2D numerical modelling is also likely to be inconclusive.

Longitudinal Transfer Function Component

The interpretations of the coast effect in terms of conductivity structure assume the response is that of a 2D conductivity structure. The presence of a longitudinal component of the induction arrows indicates this assumption is not strictly correct for the Tasman Sea. The implications of these departures of the data from two-dimensionality are discussed below.

Figure 6.29 shows profiles for the longitudinal component of the B_Z transfer function. Both the real and quadrature profiles show systematic changes across the recording line and resolve a strong southwards component of the induction arrow near the Australian coastline. This southwards component extends some distance into the Tasman Sea indicating that the strong southward trend of the induction arrows at DRS (the coastal site in Figures 6.21 and 6.22) is not an isolated anomaly caused by the local electrical conductivity structure. The distance-extent of the longitudinal anomaly increases with increasing period.

The DRS site exhibits the maximum negative peak of all the sites; however site TP8 also shows significant negative values in the real component suggesting the maximum

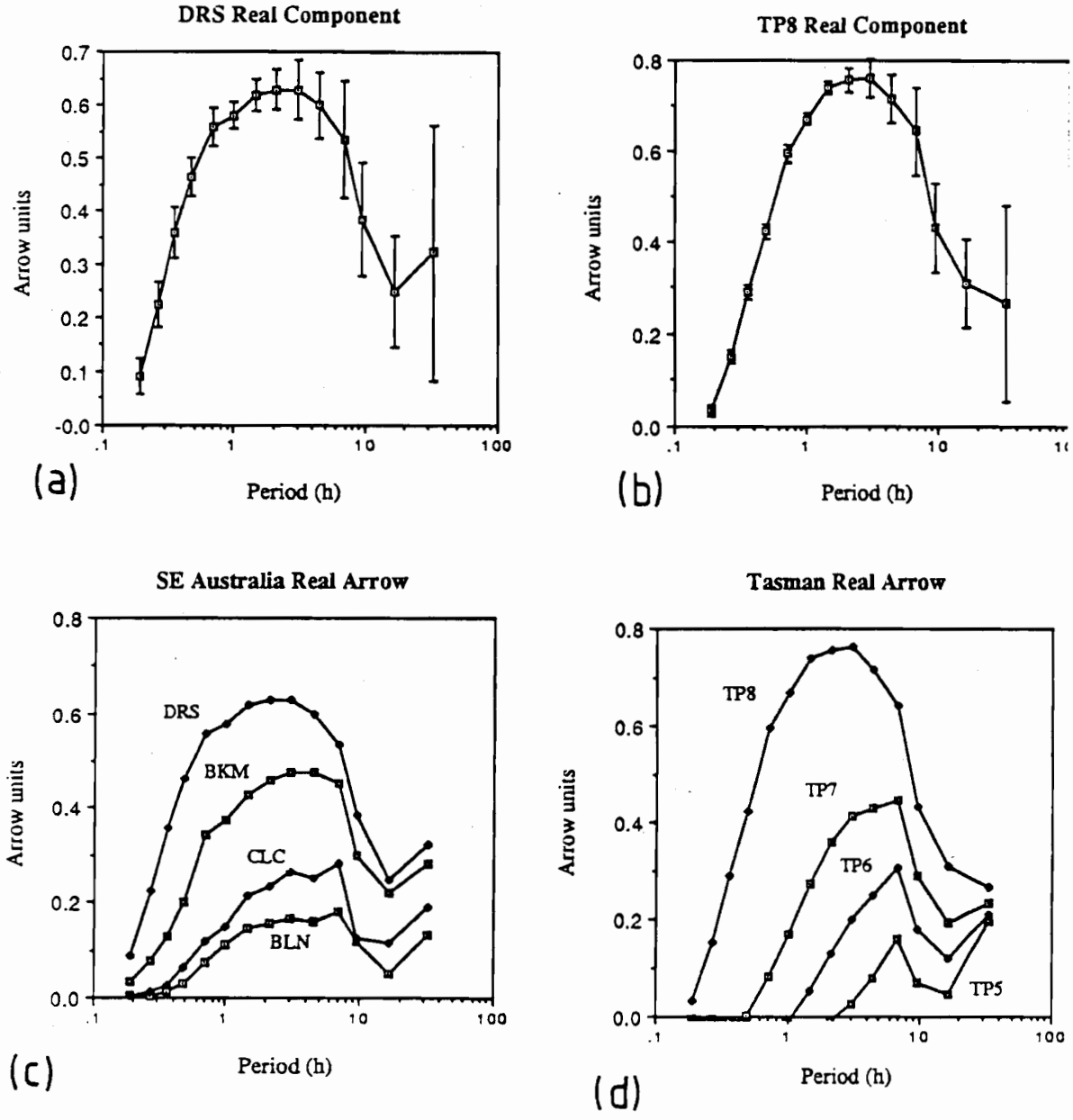

Figure 6.27: Coast effect as a function of period. The diagrams all show the magnitude of the real part of the (tranvserse component of the) induction arrow as a function of period. (a and b). The results for DRS and TP8 showing the 95 % confidence limits. (c and d). Compilations of results for land and marine parts of the Tasman Project recording line. Note the increase in the period of the maximum coast effect with distance from the coast.

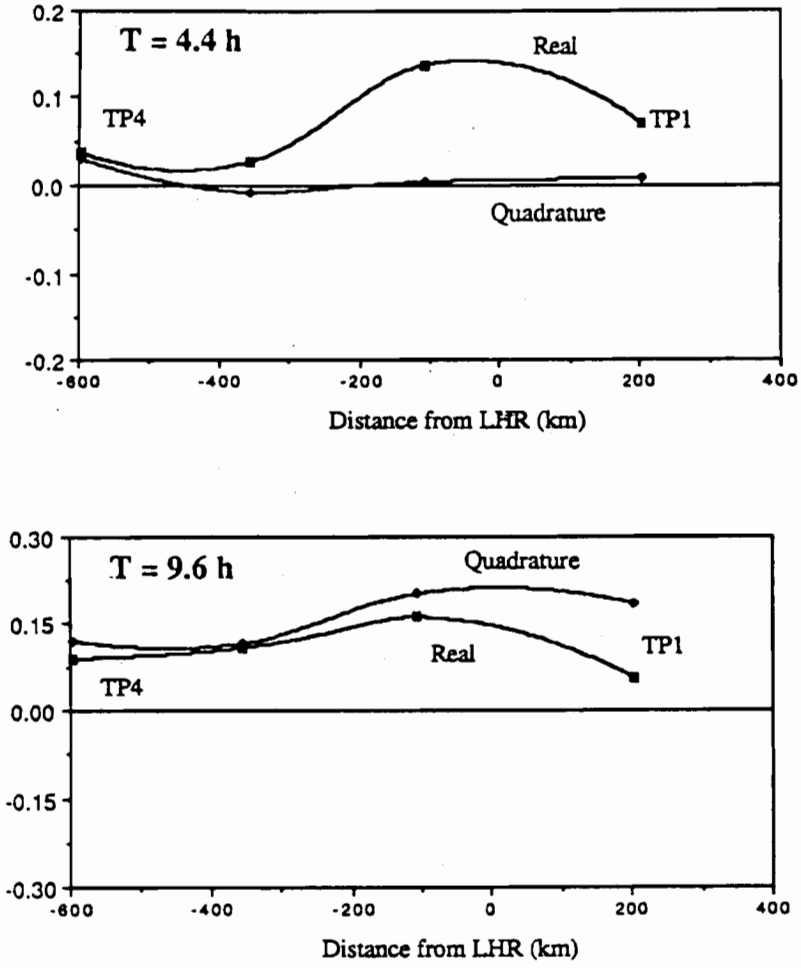

Figure 6.28: Profiles showing transverse component of induction arrows as a function of distance from the Lord Howe Rise. The figure has been arranged such that the coast effect has the same orientation as in Figure 6.23. The vertical axis on all figures corresponds to induction arrow units (with positive values corresponding to a westward orientation) and the horizontal axis gives the distance from the western 3000m contour of the Lord Howe Rise (with positive values corresponding to the eastward side of the contour). Error bars are larger than those shown for the corresponding periods in Figure 6.23. In order to define the transverse induction arrow components the trend of the Lord Howe Rise is taken as 30° west of True North.

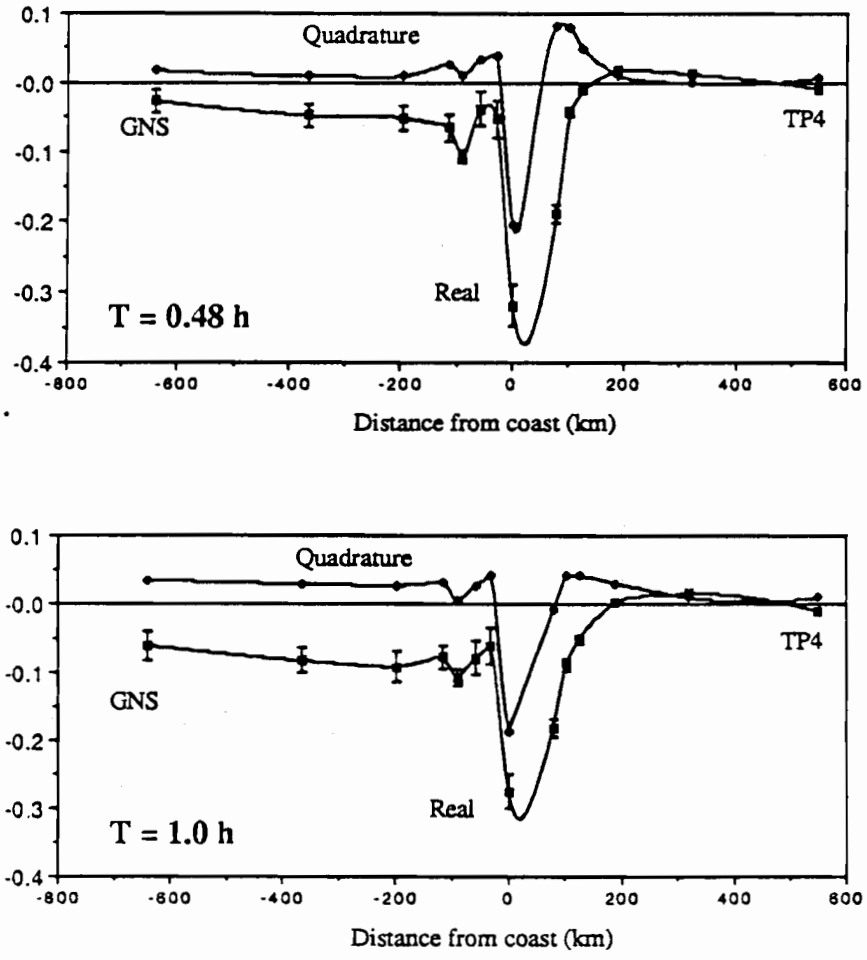

Figure 6.29: Profiles showing longitudinal component of induction arrows as a function of the distance from the coast. The positive direction on the vertical axis corresponds to an approximately northward pointing induction arrow. Other details are as for Figure 6.23.

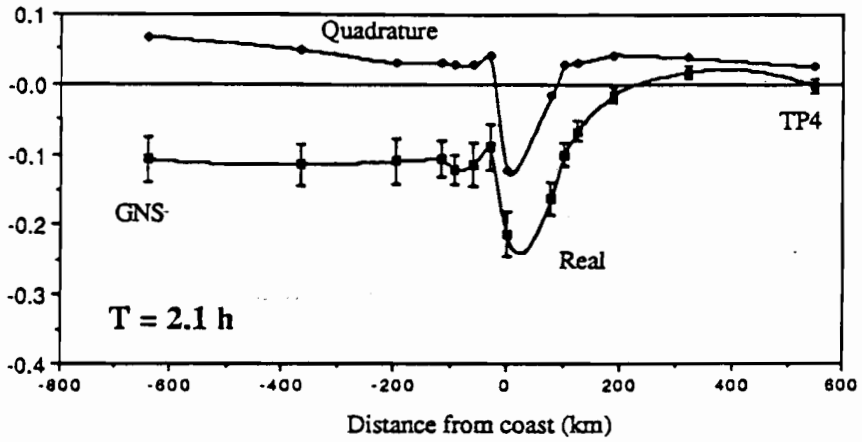
0.1
-0.0
-0.1
-0.2
-0.3
-0.4
Quadrature
TP4
GNS
Real
T = 2.1 h
-800
-600
-400
-200
0
200
400
600
Distance from coast (km)

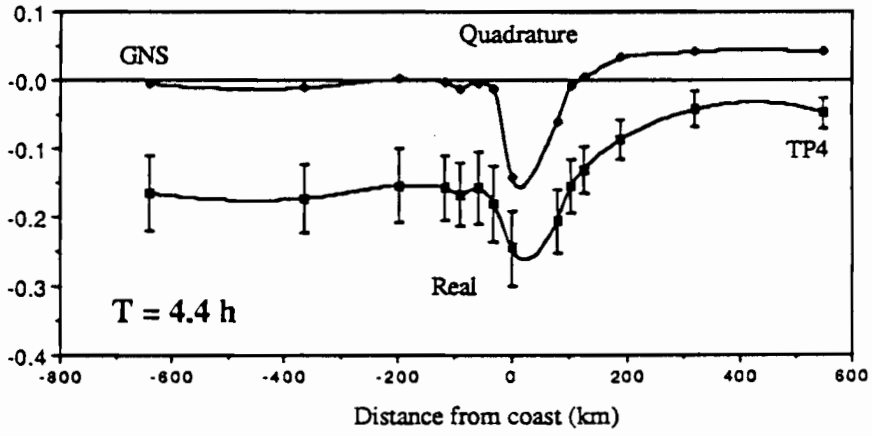
0.1
-0.0
-0.1
-0.2
-0.3
-0.4
GNS
Quadrature
TP4
Real
T = 4.4 h
-800
-600
-400
-200
0
200
400
600
Distance from coast (km)

longitudinal 'coast effect' occurs slightly off-shore from DRS. Across the inland portion of the recording line the real component is relatively constant, with a resolved southerly longitudinal component. This feature is unlikely to be due to numerical bias during the induction arrow calculations since such effects should also bias the seafloor results. If the feature is due to source-field bias its absence from the seafloor data is explained by the stronger attenuation of non-uniform (cf. uniform) source-field components through the ocean. The only well-resolved features on the (longitudinal transfer-function) quadrature profiles are the southward induction arrow component at DRS and, at short periods, a northward component at sites near the coast.

Figure 6.30 compares the longitudinal and transverse transfer function components for the period of 1 h. The longitudinal component of the transfer function at the coast is significant compared with the transverse component. At both DRS and TP8 the longitudinal real component is greater than 25% of the magnitude of the transverse component and at the DRS site the longitudinal quadrature component is in fact larger than the transverse quadrature component. This result implies the anomaly in the longitudinal component is not simply due to the choice of a slightly incorrect coastline-trend during the resolution of the transverse and quadrature components. Also the different form of the longitudinal and transverse profiles, as illustrated by the continental section of the real induction arrow profile, suggests the longitudinal 'coast effect' is a resolved anomaly. The similarity of the longitudinal and transverse quadrature components (Figure 6.30) however suggests that the smaller longitudinal quadrature-component may not be well resolved at sites other than DRS.

The observed extent of the longitudinal coast effect into the Tasman Sea suggests the anomaly is caused by regional, rather than local, three-dimensionality in the electrical conductivity structure. It is attributed to the deviation of transverse electric currents into the longitudinal direction by the Australian coastline (a phenomenon suggested by earlier time series observations). The vertical magnetic field associated with the deviated electric-current stream will be correlated with the longitudinal (horizontal) magnetic field component which induced the currents. This correlation will in turn cause a longitudinal component in the induction arrow.

The profiles shown in Figure 6.30 suggest that a zone of deviated currents occurs in a zone of finite width adjacent to the coastline. At higher frequencies this zone is narrow and longitudinal transfer function components occur only within 200 km of the coastline. At longer periods the zone is wider and longitudinal transfer function components extend further seawards. The 3D behaviour is attributed to the limited southern extent of the Australian continent rather than a local conductivity anomaly near DRS. This hypothesis is supported by the observation of 3D effects as far out into the Tasman as site TP5, 300 km from the coastline. The observation of similar 3D effects near the Lord Howe Rise also support the hypothesis.

The presence of significant longitudinal components of induction arrows has been

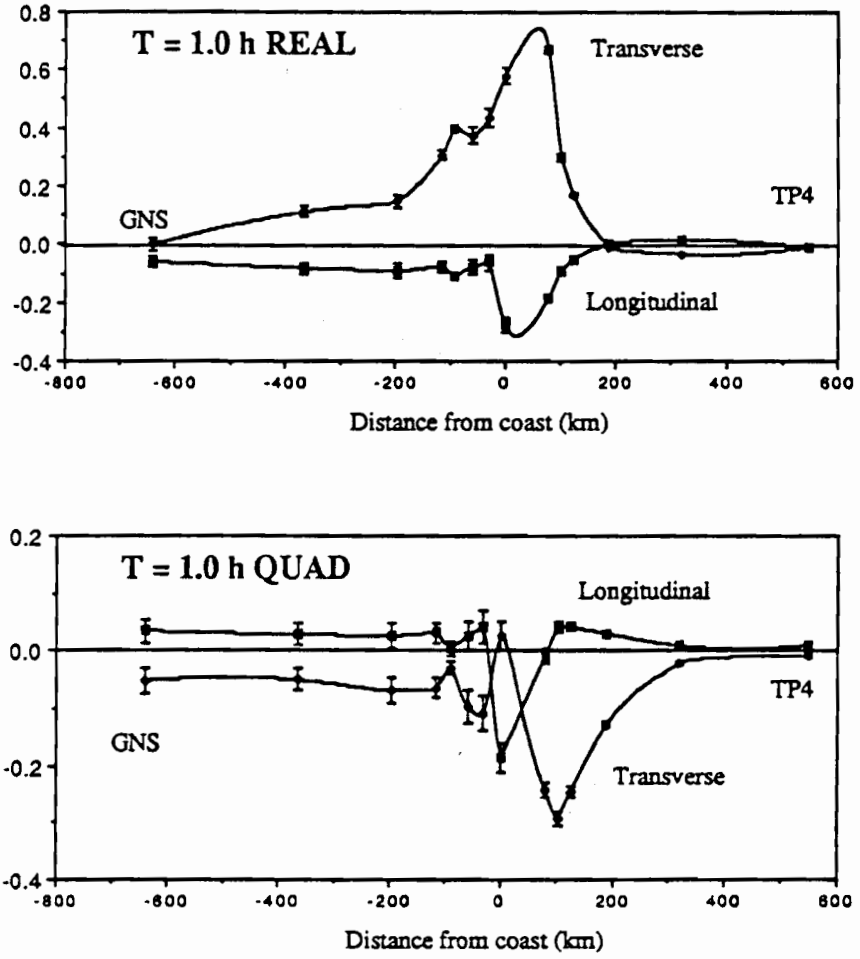

Figure 6.30: Comparison of transverse and longitudinal components of the induction arrow for 1.0 h period. The two panels compare the real and the quadrature induction arrow results.

observed in other geomagnetic induction studies and in analogue modelling studies. Examples from field studies include a large northward arrow component observed on the coast of the Japan Sea (Ogawa et al. 1986) and a significant southward arrow component at the NWR site approximately 160 km north of the Tasman Project recording line (Bennett 1972). In an analogue experiment Dr W.D. Parkinson used a spherical model of the Earth, an 'induction terrella', to examine the magnitude and direction of induction arrows (Parkinson & Jones 1979). The model arrow determined for eastern Australia possesses a strong southwards orientation.

Horizontal Magnetic Field Transfer Functions

Information on geomagnetic induction in the Tasman Sea is provided by the transfer functions between the horizontal components of the magnetic field at the different sites and the horizontal magnetic field at a reference site (CMO). Such transfer functions are derived from a least-squares fit to the equation

$$B_i = u_{iH} B_H^{CMO} + u_{iD} B_D^{CMO} \qquad 6.13$$

where B_i is the horizontal component at the second site and 'i' corresponds to either magnetic north or east. Note the similarity of this equation with the basic MT impedance equation. The horizontal magnetic-field transfer functions have been determined and plotted for all the Tasman Project sites; however only the important results are included in this thesis.

For the seafloor sites, the horizontal transfer functions u_{HH} and u_{DD} parameterize the attenuation of the horizontal magnetic field fluctuations through the ocean. (It is assumed that the reference B_H and B_D fields at CMO are closely correlated with the B_H and B_D source-field components.) The attenuation of the horizontal magnetic fields through the ocean is related to the electric current density in the ocean and to the underlying conductivity structure (see chapter 4). The transfer function u_{HH} is observed to vary systematically for the different Tasman Sea sites indicating variations in either the electric current density and/or the conductivity structure. It will be shown in chapter 7 (using B-pol impedances) that the spatial variation in u_{HH} is due to the attenuation of transverse Tasman Sea electric currents by the Australian continent and the Lord Howe Rise.

The transfer function u_{DD} is much smaller than u_{HH} confirming the anisotropic electric current flow in the Tasman Sea noted earlier. The u_{DD} transfer function is more spatially uniform than u_{HH} but still shows some variation (particularly in the phase) between the seafloor sites. E-pol impedances show that this variation is also largely attributable to 2D effects from the conductivity boundaries at the margins of the Tasman Sea. The

attenuation of the longitudinal magnetic field component ($\sim u_{DD}$) at sites TP3, TP4 and TP5 will be used in a VGS analysis in chapter 7 (based on equation 4.115) to estimate seafloor impedances.

The horizontal transfer function u_{DH} quantifies the amount of B_H signal present in the recorded B_D component. Time series and power spectra show this effect is significant at DRS. Horizontal transfer function results and autopower estimates for B_H and B_D indicate that proportion of the B_D signal at DRS which is correlated with the B_H source-field component, at a period of 0.3 h, is approximately 30%. This value decreases to 21% at a 1.0 h and to approximately 10 % at 4.4 h. These results confirm the earlier observations showing that a considerable proportion of the B_D signal at DRS may be associated with deviated electric current flow in the Tasman Sea.

The u_{DH} transfer function for the seafloor sites shows that for periods less than 4.4 h there is significant contamination of the recorded B_D component for sites extending from the Australian coastline to TP5; the magnitude of the u_{DH} transfer function is largest at site TP8 and decreases with distance to sea. The proportion of B_H-induced signal in the B_D component is larger at the seafloor sites than at DRS. For sites TP8 - TP5, at a period of 1.0 h, more than 50% of the observed seafloor B_D component is correlated with CMO B_H. At higher frequencies the relative proportion of B_H signal to B_D signal increases even further.

The limited distance the B_H contamination in the B_D signal extends inland (and also the limited inland extent of the longitudinal component of the induction arrows compared with the transverse component) suggests the deviated electric currents flow in a relatively narrow zone along the coastline.

Local Induction Arrows.

Induction arrows calculated using the local horizontal magnetic fields will show spatial variations reflecting the spatial variations in both the vertical and horizontal components of the magnetic field. With seafloor arrows the variations in the horizontal field may be sufficiently large that the local induction arrows bear little resemblance to the corresponding surface arrows or arrows calculated using a reference horizontal magnetic field. For example at Tasman Project sites TP7-TP9, at periods less than 1 h, the phase change of the B_D component through the ocean is greater than 90° and therefore the real component of tl local induction arrow is reversed such that it points towards the Australian coastline.

Figure 6.31 shows local induction arrows for the period range 0.6 to 4.4 h. As is

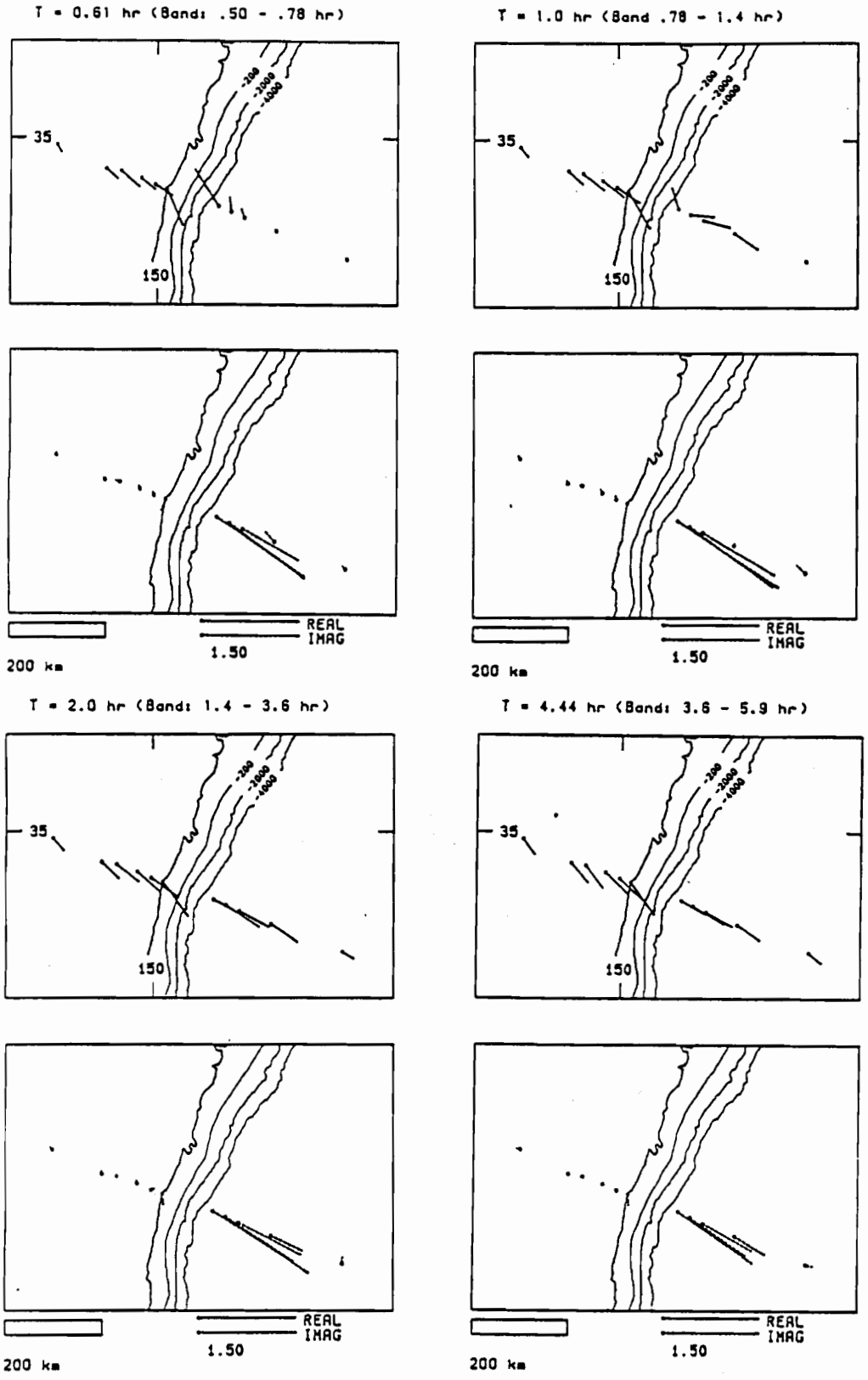

Figure 6.31: Induction arrows calculated using local horizontal magnetic field components. The arrows should be compared with those in Figure 6.22 which are calculated using a reference horizontal magnetic field. The rotation of the seafloor arrows at short periods is explained in the text.

be expected from the uniformity of the horizontal magnetic field between the land sites, the land arrows resemble closely the arrows calculated using CMO as the reference horizontal magnetic-field (Figure 6.21). The local seafloor arrows are however considerably different from the arrows presented above, with the major differences being the much greater magnitude (real and quadrature combined) of the local-arrows and the increased quadrature component. These differences are due to the attenuation and phase change of the horizontal magnetic-field with depth in the ocean (see Figure 4.3 for an illustration). The effect of the seafloor B_D phase is illustrated by the reversal in the east-west component of the real induction arrow in Figure 6.31. The reversal occurs at shorter periods and at sites closer to the coast, reflecting the spatial changes in the u_{DD} transfer function (in which the phase difference between the seafloor field and surface field increases with both decreasing period and increasing proximity to the coast).

The contamination of the seafloor B_D magnetic field by B_H signal introduces further complexity into the local induction arrows. This effect causes the northward component of the arrows at shorter periods (Figure 6.31). The form of the local arrows can however be closely predicted by combining information from the reference horizontal magnetic-field arrows and horizontal magnetic-field transfer functions.

Because of the dependence of the local seafloor induction arrows on the horizontal magnetic field and therefore on such parameters as the ocean depth there is little information to be gained by comparing the Tasman seafloor arrows with those determined in other studies (eg. Yukutake et al. 1983, Filloux et al. 1987). The arrows from these other studies are relatively large as is to be expected for seafloor arrows. The arrows from the EMSLAB experiment (Filloux et al. 1987) have smaller quadrature components (relative to the real component) than the Tasman Sea arrows reflecting the more shallow depth of the seafloor in the region of the EMSLAB experiment (2400 to 2600m).

6.6 Interpretation of the coast effect

The main contribution to the coast effect is accepted to be the enhanced flow of electric currents in the ocean relative to the more resistive continent (eg. Parkinson & Jones 1979). There is however debate on whether there is also a contribution from the deep conductivity structure (eg. Fischer & Weaver 1986) or from the large-scale deviation of electric current flow in the oceans (eg. Le Moeul & Menvielle 1982). There are various locations in the world where the coast effect is associated with deviated, or channelled, current. A classic example occurs at the coast of Cook Strait between the North and South Islands of New Zealand (Boteler et al. 1987, Ingham 1985). The flow of electric current through Cook Strait is in the opposite direction to that which would be associated with local induction. In other locations eg. Japan, California and southeast Australia both local induction and channelling have been proposed as explaining to the coast effect (eg. Menvielle et al.

1982).

It is possible that both channelled and local induction contribute to the observed coast effect at the southeast Australian coast-line. Reviews of conductivity results (see chapter 9) show consistent differences between typical oceanic and continental conductivity structures. Forward modelling shows that at a lateral transition between such structures (at a continental margin) local geomagnetic induction will produce a contribution to the coast effect, particularly at longer periods. There is also, however, strong evidence for current channelling in the Tasman Sea.

Direct evidence for the existence of large-scale deviation of electric currents in the Tasman Sea includes the B_H contamination of the recorded B_D signal at sites near the coast, and the existence of a longitudinal component in the induction arrows. Although these effects do not directly influence the transverse component of the coast effect they confirm the existence of a 3D form for electric current flow. In addition to the deviation of electric currents by the East Australian coast, this pattern may include a deviation of north-south flowing currents around the southern coastline of Australian and into the Tasman Sea. The presence of such additional currents flowing through the Tasman Sea would influence the coast effect.

Further evidence for the existence of channelling along the east coast of Australia comes from the analogue model study of Dosso (1985). In this study of the Tasmania and Bass Strait region, channelling of north-south electric currents around the east and west coasts of Tasmania was observed and also deflection of currents around the southeast coast of the Australian mainland. Such currents could flow along the western margin of the Tasman Sea through the area of study of the Tasman Project. Results from geomagnetic induction studies in Tasmania (Hermanto 1987) and from the analogue study also indicate current channelling occurs through Bass Strait.

As long as any channelled electric current is of a smaller magnitude than the locally induced current, the interpretations of the Tasman Sea coast effect made in this thesis should be valid. These interpretations have been based mainly upon the spatial form, rather than the exact magnitude, of the coast effect. Current channelling could however significantly alter the strength and frequency-response of the coast effect and therebye bias conductivity models determined during quantitative modelling. Opposing interpretations of the coast effect of southeast Australia have already been made by Bennett & Lilley (1974) in terms of local induction and by Menvielle et al. (1982) in terms of deviated currents. (The interpretation of Menvielle et al. however considered the coast effect at the 1.0 h period only, and therefore has not been shown to explain all of the information available on the coast effect.)

It is necessary to address the question of what approach should be taken to further the modelling of the observed Tasman Sea coast effect. The quantitative modelling of the additional coast effect information available from the Tasman Project and Continental Shelf

Experiment should perhaps proceed using both modelling approaches. Conventional 2D modelling (eg. as in Fischer & Weaver 1986) should be performed to determine whether local induction can produce all the observed features of the transverse component of the coast effect, and 3D thin-sheet modelling could be performed to determine the extent to which current channelling effects can also explain the observed (in this case, transverse and longitudinal) coast effect. The degree to which either approach fails to fit the data may provide information on the relative magnitude of the local induction and current channelling processes.

6.7 Summary of Basic Data Analysis

A number of important results have been obtained from the time series, power spectral, coherence function and induction arrow studies performed above. The results have provided important information particularly on the quality of the recorded data and on physical processes of geomagnetic induction in the Tasman Sea Region.

Data Quality, Statistical Treatment and Source Fields

From the time series and coherence results it is evident that the data recorded in the Tasman Project is of a high standard. The magnetic and electric field recordings are well-correlated between different instrument types and over distances of order 2000 km. Despite the high data quality there occur the inevitable limits of accuracy and sources of external and instrumental noise. The power spectra results show that instrumental noise occurs on some seafloor components and the hand-digitized Gough-Reitzel data loses accuracy at high frequencies. In most instances these effects are negligible at periods longer than one hour. The power spectra and coherence functions show the seafloor electric field data contain significant proportions of oceanographic noise both at long and short periods.

The long time-series available from the Tasman Project allow the estimation of autopowers and crosspowers with relatively small random errors. Because of bias errors the autopowers and crosspowers need to be used with care. Any time series noise will bia autopowers upwards and therefore bias the results of least-squares transfer function determinations. For the calculations performed in this chapter, the inputs are generally the horizontal magnetic fields from CMO, and any bias due to noise on these time series will b similar for all results. A second source of bias on some of the calculated results is due to an under-estimation of the crosspower between hand-digitized Gough-Reitzel components and other components.

In this thesis most of the analyses assume that the magnetic source-field is uniform across the whole recording line. From the coherence results there is certainly evidence fo reasonable uniformity with significant coherence existing between CMO and EYR over a

distance of 2000 km. An examination of the variation in crosspower across the recording line was used to quantify source-field variation and revealed typical scale lengths for B_H of 5900 km and for B_D of 3900 km.

Two-dimensional Features

From the raw time series it is evident that the geomagnetic induction in the Tasman Sea is influenced by 2D and 3D conductivity structure. This result is confirmed by examination of power spectra, induction arrows and horizontal magnetic field transfer functions. It is to be noted that 2D effects, for example anisotropic attenuation of the horizontal magnetic field through the ocean, extend all of the way across the Tasman Sea.

Induction arrow results at the Australian coastline reveal a strong coast effect. Comparison of the arrow profiles with theoretical arrow profiles suggests a contribution from a deep conductivity contrast. The maximum coast effect is slightly off-shore from the Australian coast; reflecting the position of the edge of the continental shelf and possibly an eastward component for the deep conductivity contrast. These results confirm earlier modelling by Bennett (1972) for the structure of the continental margin. The time series and induction arrow results also indicate a weak "coast effect" over the Lord Howe Rise.

Three-dimensional Effects

At a 2D conductivity structure there should be no correlation between B_Z and the longitudinal magnetic field or between the seafloor transverse and longitudinal magnetic fields. At such a boundary transverse electric currents will simply be deviated downwards into the more conductive mantle. The time series, coherences, induction arrows and horizontal magnetic field transfer functions from the Tasman Project however all indicate that there is a 3D component to the behaviour of the electric and magnetic fields at the Australian coastline.

Although the 3D effects contain limited direct information on the Earth's conductivity structure, it is necessary that they be understood before the application of 2D modelling to the Australian continental margin or the application of 1D or 2D MT techniques to the Tasman SFMT data. The 3D effects in the Tasman Sea are attributed to the large-scale shape of the ocean boundaries.

Chapter 7 Seafloor Magnetotelluric Impedances

This section will describe the calculation and interpretation of the seafloor MT impedances for the Tasman Sea. Impedances will be calculated using least-squares and remote-reference methods. Features of the impedance tensor, such as anisotropy and axis orientation, will be interpreted in terms of geomagnetic induction patterns in the Tasman Sea. They will be used to examine whether geomagnetic induction is 1D, 2D or 3D or if it can be approximated as 1D or 2D. In order to assess the magnitude of current channelling through the Tasman Sea, the MT impedance will also be estimated using the VGS method. Finally the results of the remote-reference calculations will be used to provide information on noise in the recorded data.

7.1 Preliminary Impedance Estimates

Initial impedance estimates were obtained for seafloor sites using the least-squares methods. The auto and crosspowers derived from the time series segments described in section 6.2 were fitted to the standard LS impedance and admittance formulations (equations 4.133 and 4.137). For sites TP5 and TP4 portions of the electric field time series were not available (see Table 6.3) and therefore the results for these sites are based on slightly fewer time series segments than at other sites. The 95 % confidence limit was calculated for each impedance estimate using equation 4.163.

Figure 7.1 shows examples of the impedance for sites TP6 and TP3. These sites are illustrated since they provide examples of sites with high and low levels of oceanographic noise. The impedance component shown is the component parallel to the approximately north-south trend of the Tasman Sea ie. the E-pol impedance. The impedance magnitudes determined using the LS and admittance formulations show large systematic differences, particularly at shorter periods. The two estimates for each phase value are however relatively similar. The differences between the LS and admittance results are attributed to bias caused by oceanically induced noise in the recorded electric and magnetic fields. The differences are much larger at TP6 than at TP3 which indicates that noise levels are higher at site TP6. This result is confirmed by the much lower partial coherence between the electric and magnetic fields at TP6 (Figure 7.1).

At long periods ($T > 10$ h) the oceanic noise is attributed to motional induction by oceanographic eddies. The signal of these eddies is noted in the time series and coherence functions described in chapter 6 and affects the horizontal electric field components much more than the magnetic field components. At shorter periods the oceanically induced noise is associated with short-period ocean-water movement such as internal waves and turbulence. Since the relative effects of the short period noise on the electric and magnetic field are not known, it is not possible to discern whether the short period bias in the impedances is due to upwards bias of admittance results by electric field noise or

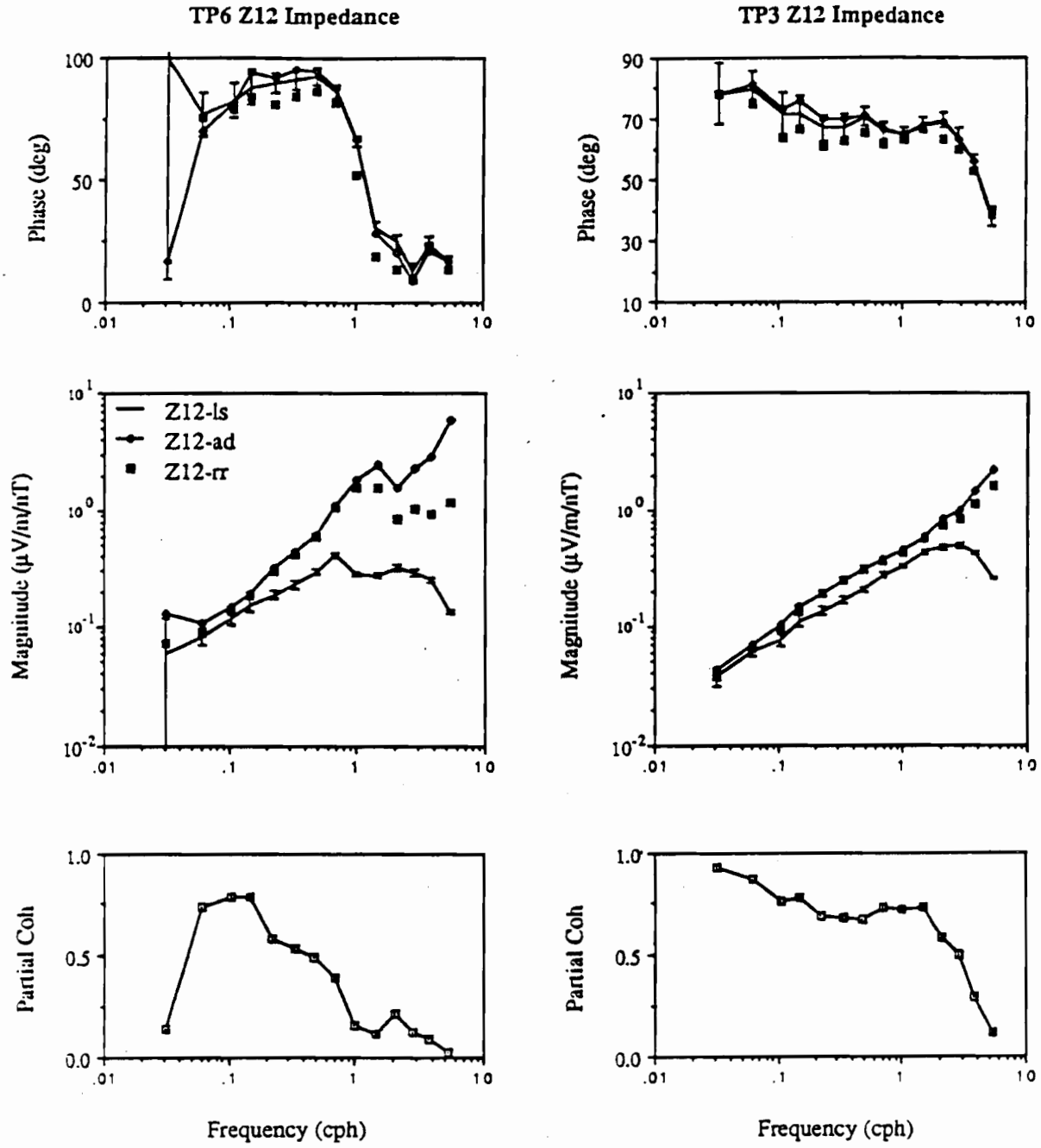

Figure 7.1: MT impedance at sites TP6 and TP3. The figure shows the E-pol (Z_{12}) impedance term estimated using the least-squares (ls), admittance formulation (ad) and remote-reference (rr) methods. The phase refers to the lead of E relative to B and the partial coherence is between the horizontal electric field component in the E-pol direction and the orthogonal magnetic field component.

downward bias of LS results by magnetic field noise. Remote-reference results suggest that both sources of noise contribute to the bias.

Examination of impedance results from other sites and of the different impedance tensor components shows consistent differences between LS and admittance results. It is concluded that it is necessary to use a noise reduction technique in order to obtain unbiased impedance estimates. In this thesis the remote-reference method (Gamble et al. 1979) is used.

The remote-reference results for the E-pol impedance at sites TP6 and TP3, calculated using equation 4.140 with CMO as the remote reference, are shown in Figure 7.1. The remote-reference impedance magnitudes lie between the upward-biased admittance magnitudes and the downward-biased LS magnitudes. For the longest period results at site TP6, the remote-reference estimates are similar to the LS estimates confirming the main source of bias is the oceanic noise in the horizontal electric field data. In the period range 10 h to 1h, the remote-reference results are closest to the admittance results suggesting the major source of bias at these periods is noise in the magnetic field. Finally, at the shortest periods there is contribution to the bias from both the horizontal electric and magnetic fields.

Choice of Remote Reference Site

The choice of the most appropriate remote reference to be used for each SFMT site will now be considered in more detail. As discussed in the chapter 4 an ideal remote reference site is a site which possesses coherent source-field signal but no coherent noise with the MT site. The remote-reference site should be as close as possible to the MT site without decreasing to a separation over which coherent noise occurs. Since little is known about the distance-scales of coherent noise in the Tasman Sea it is necessary to make an empirical investigation into the most appropriate remote-reference sites.

Figure 7.2 shows the remote-reference E-pol impedance for site TP5 when CMO, TP4 MAG and TP2 MAG are used as the remote reference. Consistent differences occur between the impedance magnitudes based on CMO as the remote reference and those based on TP4 or TP2 MAG. Smaller, but systematic, differences also occur in the phase results. The differences between the impedance magnitudes when TP4 and TP2 are used as the remote reference are much smaller than the differences between the results for CMO and those for either seafloor site.

The two possible causes for the differences between the remote-reference results are source-field variations and coherent noise. Consideration of the distances between site TP5 and the remote-reference sites TP4, TP2 and CMO (231 km, 410 km and 821 km respectively) suggests the differences are not attributable to source-field variations. For these distances it would be expected the TP4 and CMO remote reference results to be the most similar and the TP2 result to show the most bias. The effect of source-field

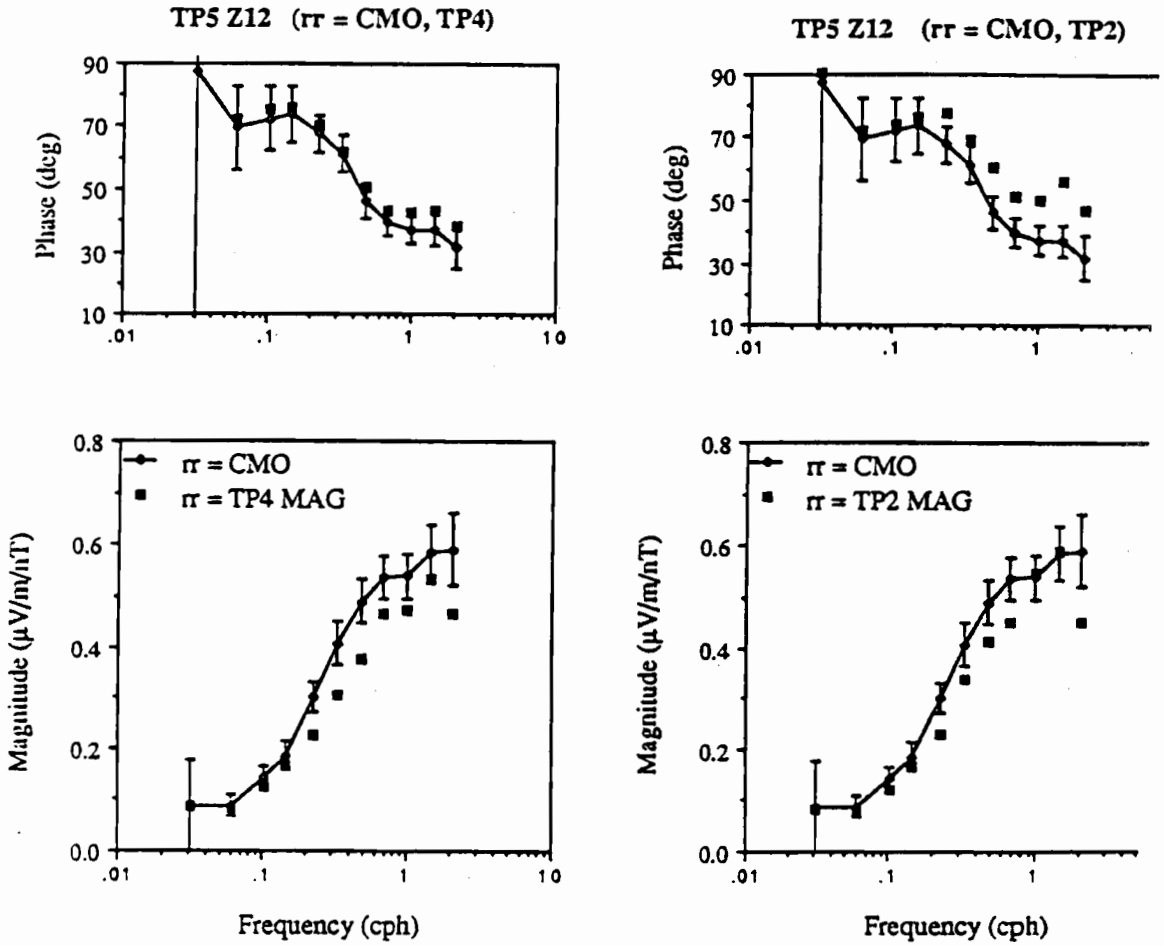

Figure 7.2: Remote-reference MT impedance at site TP5 calculated using the following remote references: the CMO horizontal magnetic field (continuous line), the TP4 horizontal magnetic field (squares on left panels), and the TP2 horizontal magnetic field (squares on right panels). The impedance is plotted in linear form, rather than the conventional logarithmic form, in order to highlight the differences between the different sets of results. The error bars are the 95% confidence limits for the LS impedance estimate at TP5 and will be similar to the remote-reference error estimates.

variations on remote-reference impedances is further investigated in Figure 7.3. This figure shows impedances calculated for site TP7 using both CMO and EYR as the remote-reference. These sites are respectively 215 km and 1949 km from site TP7 and therefore the EYR results should show much stronger source-field effects than the CMO results. The impedance estimates are however very similar for the two different remote references and become significant only at periods less than 0.7 h. These results show that the impedance differences noted in Figure 7.2 are not explained by source-field differences. It is therefore concluded that the differences must be due to coherent noise.

The similarity of the magnitudes of the TP5 impedance when either TP4 or TP2 MAG is used as the remote reference and similar observations at other MT sites, indicates that the coherent noise is present between the seafloor horizontal magnetic field components. Furthermore the persistence of the remote-reference impedance bias when the SFMT / remote reference site separation is as large as 820 km (the distance between TP5 and TP2) indicates that the coherent noise persists over distances in the Tasman Sea of order 1000 km. Similar coherent noise is also present between horizontal electric field components. The coherent noise at the seafloor sites will be investigated in greater detail and quantified in section 7.5.

An important implication of the coherent noise is that it is necessary to use a land site as the remote-reference site in order to obtain unbiased impedances. For SFMT sites TP7, TP6, TP5, TP4 and TP3, site CMO will be used as the remote reference. As discussed in chapter 6 the accuracy of the digital magnetic observatory data from CMO appears to be higher than the hand-digitized Gough-Reitzel data. Site TP1 lies significantly closer to the EYR site than to CMO (Table 6.9) and therefore the EYR recordings will be used as the remote reference for SFMT calculations at TP1.

Unrotated Remote-Reference Impedances

An initial set of remote-reference impedances was calculated with the horizontal electric and magnetic fields oriented in the geomagnetic co-ordinate system. It should remembered that the orientation of the HEF instruments at sites TP1, TP3 and TP4 was not recorded during the actual experiment and that the electric field recordings at these sites have been aligned, using statistical methods, to lie parallel to those at TP5 (see chapter 3). The MT impedance function determined for site TP4 is tabulated in Table 7.1 and illustrated in Figure 7.4. The Z_{HD} term (north electric field, east magnetic field) has the largest magnitude of the four impedance tensor elements and is approximately four times larger than the other three terms. This result immediately indicates that the impedance at site TP4 is not 1D. For a 1D impedance tensor the two off-diagonal impedance terms (Z_{HD} and Z_{DH}) should have equal magnitude and the two diagonal terms (Z_{HH} and Z_{DD}) should be zero.

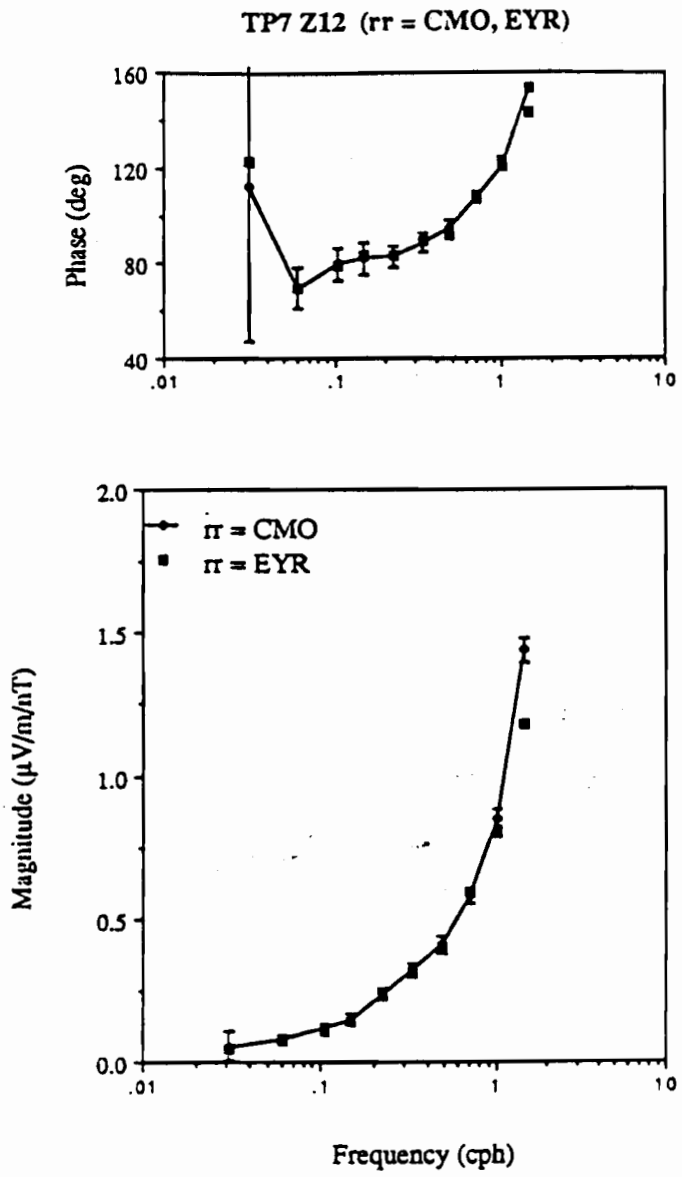

Figure 7.3: Remote-reference MT impedance at site TP7 calculated using the horizontal magnetic field from CMO and from EYR as the remote reference. Note the similarity of the results despite the different distance of the two remote-reference sites from the SFMT site. The extreme phase value at short periods is caused by 2D effects and is discussed in section 7.2.

Table 7.1a: TP4 impedance tensor elements, magnitudes and skew angle.

Period (h)	Frequency (cph)	$\|Z_{HH}\|$	$\|Z_{HD}\|$	$\|Z_{DH}\|$ ($\mu V.m^{-1}.nT^{-1}$)	$\|Z_{DD}\|$	θ_s (deg)
32.508	0.031	.0109	.0349	.0252	.0231	-13.7
16.650	0.060	.0045	.0632	.0279	.0132	-8.6
9.615	0.104	.0102	.0806	.0266	.0261	-16.9
6.849	0.146	.0248	.1153	.0322	.0314	-19.2
4.443	0.225	.0373	.1415	.0396	.0258	-18.8
2.999	0.333	.0478	.1779	.0379	.0389	-21.0
2.079	0.481	.0401	.2029	.0545	.0484	-19.0
1.442	0.693	.0487	.2630	.0592	.0526	-17.5
1.000	1.000	.0554	.2848	.0734	.0474	-16.1
.693	1.443	.0669	.3750	.0859	.0662	-16.0
.481	2.079	.0813	.4187	.0962	.0921	-18.0
.357	2.801	.1161	.5229	.0933	.1096	-20.2
.267	3.745	.1366	.5647	.1021	.0796	-16.8
.190	5.263	.1853	.7101	.1131	.1165	-19.4

The impedance was calculated using CMO as the remote reference.

Table 7.1b: Unrotated TP4 impedance, multiple and partial coherence, and 95% confidence limits

Period (h)	Multiple H	Multiple D	and	Partial Coherences HH	HD	DH	DD	Relative Confidence Limits HH	HD	DH	DD
32.508	.738	.261		.133	.646	.155	.145	2.498	.796	2.899	3.229
16.650	.813	.480		.019	.759	.364	.113	3.111	.236	.519	1.184
9.615	.836	.749		.120	.784	.496	.385	1.109	.197	.363	.519
6.849	.907	.790		.270	.845	.519	.452	.639	.165	.365	.450
4.443	.797	.748		.325	.708	.540	.194	.292	.127	.182	.463
2.999	.791	.724		.477	.745	.583	.285	.218	.118	.180	.355
2.079	.801	.751		.335	.781	.664	.273	.209	.082	.111	.247
1.442	.771	.715		.370	.749	.652	.186	.174	.075	.099	.264
1.000	.711	.660		.333	.708	.572	.091	.139	.070	.090	.360
.693	.592	.568		.267	.578	.478	.060	.131	.073	.091	.366
.481	.556	.578		.291	.520	.498	.066	.136	.088	.103	.362
.357	.356	.280		.158	.339	.164	.053	.151	.106	.195	.524
.267	.212	.263		.121	.193	.174	.019	.108	.086	.150	.635
.190	.059	.139		.034	.045	.075	.031	.075	.060	.138	.417

The headers H, D, HD etc. denote the axis / axes involved in the terms. Thus "H" heads the multiple coherence of E_H (with B_H and B_D), "D" heads the multiple coherence of E_D (with B_H and B_D) and "HD" heads both the partial coherence between E_H and B_D (with B_H removed) and the relative confidence limit on the Z_{HD} coherence.

The coherences shown in the table are all squared coherence terms; the multiple coherence is defined by equation 4.155 and the partial coherence by equation 4.156. The relative confidence limit is the ratio of the 95 % confidence limit to the magnitude of the impedance term. The error on the phase of the impedance is given by the inverse sine of this value (equation 4.163).

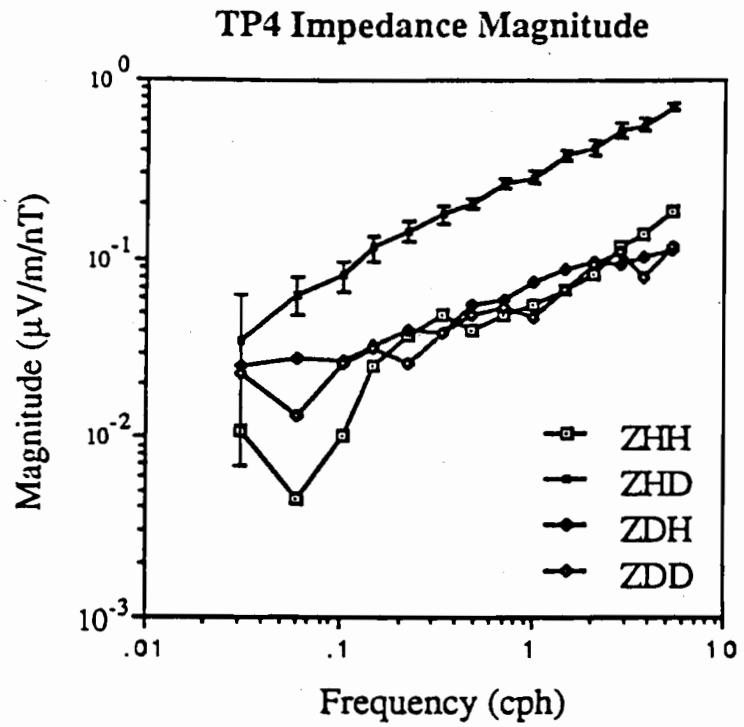

Figure 7.4: Magnitude of MT impedance tensor elements at site TP4. The impedance is calculated with the horizontal electric and magnetic fields in the geomagnetic co-ordinate system and with CMO as the remote-reference site. Note that the tensor is not of 1D form and has a Z_{HD} off-diagonal element which ~ 4 times larger than the magnitude of the other elements.

Table 7.1 also lists measures of the random error associated with the impedance tensor elements at site TP4. The best resolution (highest partial coherence and smallest relative confidence limits) occurs for the off-diagonal impedance terms and towards the middle of the available period range (T ~ 1 h). The multiple coherence for E_H is higher than for E_D. In future calculations the impedance values for the longest and the shortest spectral bands will be omitted because of the low resolution of the results. Long period bands will be omitted if the relative confidence limit (the ratio of the 95% confidence limit to the magnitude of the impedance term) exceeds about 0.6. Examination of results also show that erratic results may occur at the shortest periods even though the confidence limits are small. Short period bands are therefore omitted if the partial coherence corresponding to

impedance terms used in a calculation falls below about 0.05. For the short period results many spectral estimates are used in each band and the erratic results are therefore probably due to bias errors rather than random errors.

Table 7.1 lists the skew angle for the impedance at site TP4. The skew angle is significantly non-zero, with values exceeding 15° over most of the frequency range. This result indicates the impedance is more complex in form than that associated with a 2D conductivity structure. The skew angle is relatively independent of frequency suggesting that it is not caused by three-dimensionality of the electrical conductivity structure beneath the recording site.

The impedance at the other SFMT sites has a similar form to that at TP4, with a dominant Z_{HD} term and a Z_{DH} term of comparable magnitude to the diagonal impedance tensor elements. The anisotropy between the two off-diagonal impedance terms was originally noted in the raw time series (section 6.1) confirming that it is not a spurious feature caused by the analysis method.

Dimensionality of Tasman Sea Impedance

Given an impedance tensor which does not possess a simple 1D form, it is instructive to resolve the tensor into the form

$$Z = \begin{bmatrix} A+C & 1+B \\ -1+B & A-C \end{bmatrix} D \qquad 7.1$$

The terms A, B and C are called distortion elements and provide information on the dimensionality of the impedance response. A full description of the use and derivation of the distortion elements is given in appendix 4. For a 1D conductivity structure all of the distortion elements are zero. For 2D and 3D conductivity structures the distortion elements may be non-zero. In order to assess their significance the elements should be compared with unity.

For a 2D structure the B distortion element is related to the degree of anisotropy and the ratio of B/C is related to the angle between the present co-ordinate system and the principal axes. In general A should be zero for 2D structures since it is directly related to the skew angle (equation 4.102b). The skew angle gives the angle between the apparent principal axis co-ordinate system defined the magnetic field, and that defined by the electric field, and is in general non-zero for 3D conductivity structures. With 2D conductivity structures a non-zero value for A will occur only if there is an error in the orientation of the electric or magnetic field co-ordinate systems, or if a local near-surface heterogeneity causes a local deviation of electric current flow (eg. Cox et al. 1980). In this case both A and the ratio of B/C should be real and independent of frequency. For a 3D conductivity structure A, B and C will in general be complex and frequency-dependent.

Table 7.2 tabulates the distortion terms A, B and C calculated for site TP4 and Figure

7.5 shows the terms plotted on the complex plane. Each of the distortion elements is relatively independent of frequency and lies relatively close to the real axis. For TP4, A has a value of approximately (-0.3 + 0.0 i) corresponding to a skew angle of approximately 17°. The large magnitude of the B distortion element (0.6 - 0.05 i) reflects the strong anisotropy in the MT impedance while the non-zero imaginary component suggests a significant 2D or 3D component in the electrical conductivity structure. The C distortion element is close to (0.0 + 0.0i) indicating the principal axes lie close to the geomagnetic co-ordinate system. From the distortion elements it is possible to calculate the angles (α and β) by which the electric and magnetic field co-ordinate systems must be rotated to be aligned with the principal axes (see appendix 4). These angles were determined for each frequency band at TP4 and are listed in Table 7.2.

Table 7.2: Distortion elements of the TP4 impedance tensor

Period (h)	A		B		C		α (deg)	β (deg)
32.508	-.241	-.108	.161	.046	.527	-.116	-44.1	-30.4
16.650	-.150	.106	.388	.024	.052	-.099	-7.7	.7
9.615	-.298	-.153	.520	-.157	.171	.007	-16.8	.1
6.849	-.341	-.142	.567	-.048	.079	-.069	-13.9	5.3
4.443	-.338	-.083	.563	-.017	-.062	-.015	-6.3	12.5
2.999	-.378	-.131	.650	-.041	-.050	.016	-8.3	12.7
2.079	-.344	-.038	.586	-.105	.034	-.006	-11.2	7.9
1.442	-.315	-.045	.648	-.120	.012	.004	-9.2	8.3
1.000	-.288	-.025	.602	-.113	-.025	.023	-6.7	9.4
.693	-.286	.050	.637	-.099	-.005	-.017	-7.9	8.1
.481	-.322	.112	.647	-.139	.010	-.036	-9.8	8.3
.357	-.368	.034	.716	-.117	-.008	.029	-9.6	10.6
.267	-.298	.124	.694	.002	-.089	.008	-4.7	12.1
.190	-.352	-.007	.726	-.019	-.089	.099	-6.0	13.3

The table shows the real and imaginary parts of the distortion elements A, B and C and the angles α and β by which the electric and magnetic co-ordinate systems must be rotated clockwise to be in alignment with the principal axes.

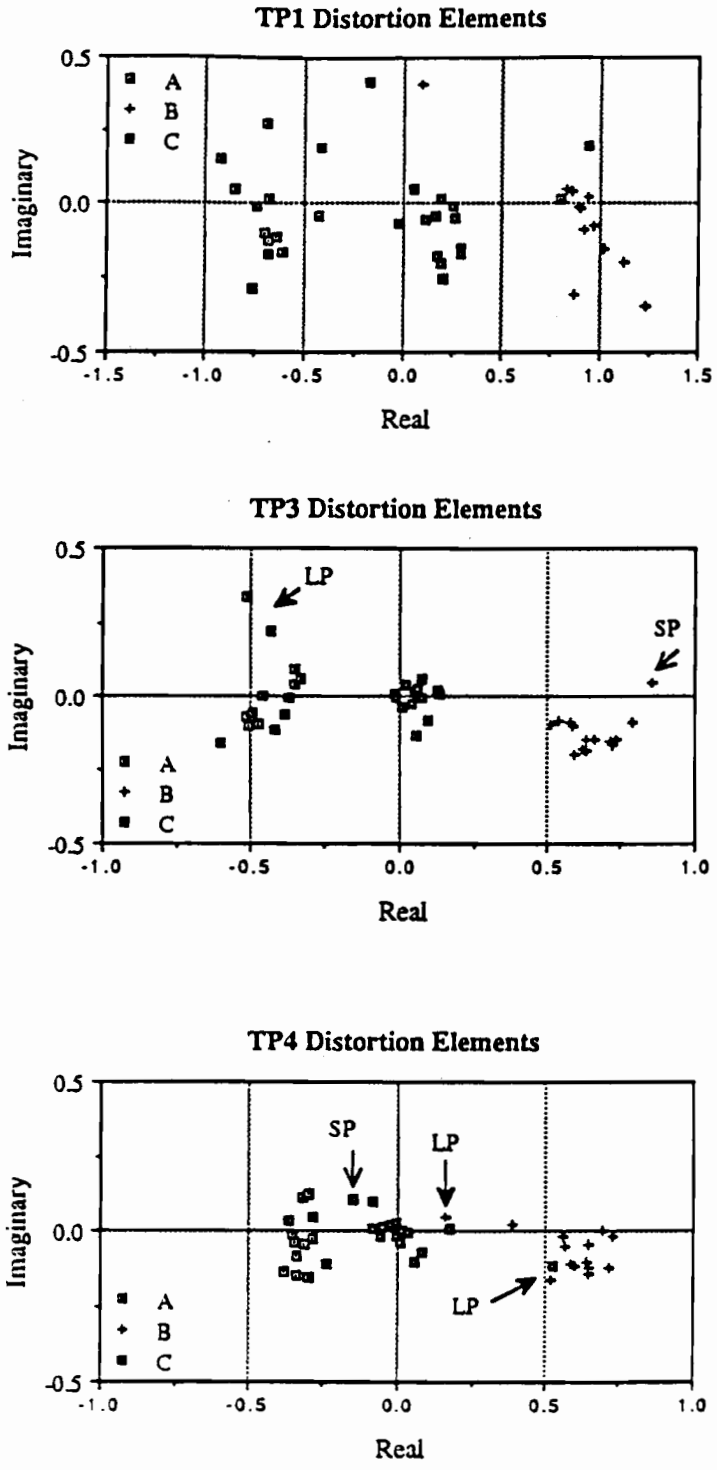

Figure 7.5: Distortion elements for SFMT sites. The calculation of the terms is described in appendix 4. No formal error estimates are shown however an estimate of the errors is given by the 'jitter' between the points. The erratic points lying outside the main field of results for each element will be removed after deletion of long period (LP) and short period (SP) results using confidence limit and partial coherence criteria. The distortion elements at all sites form relatively tightly-defined clusters which lie close to the real axis.

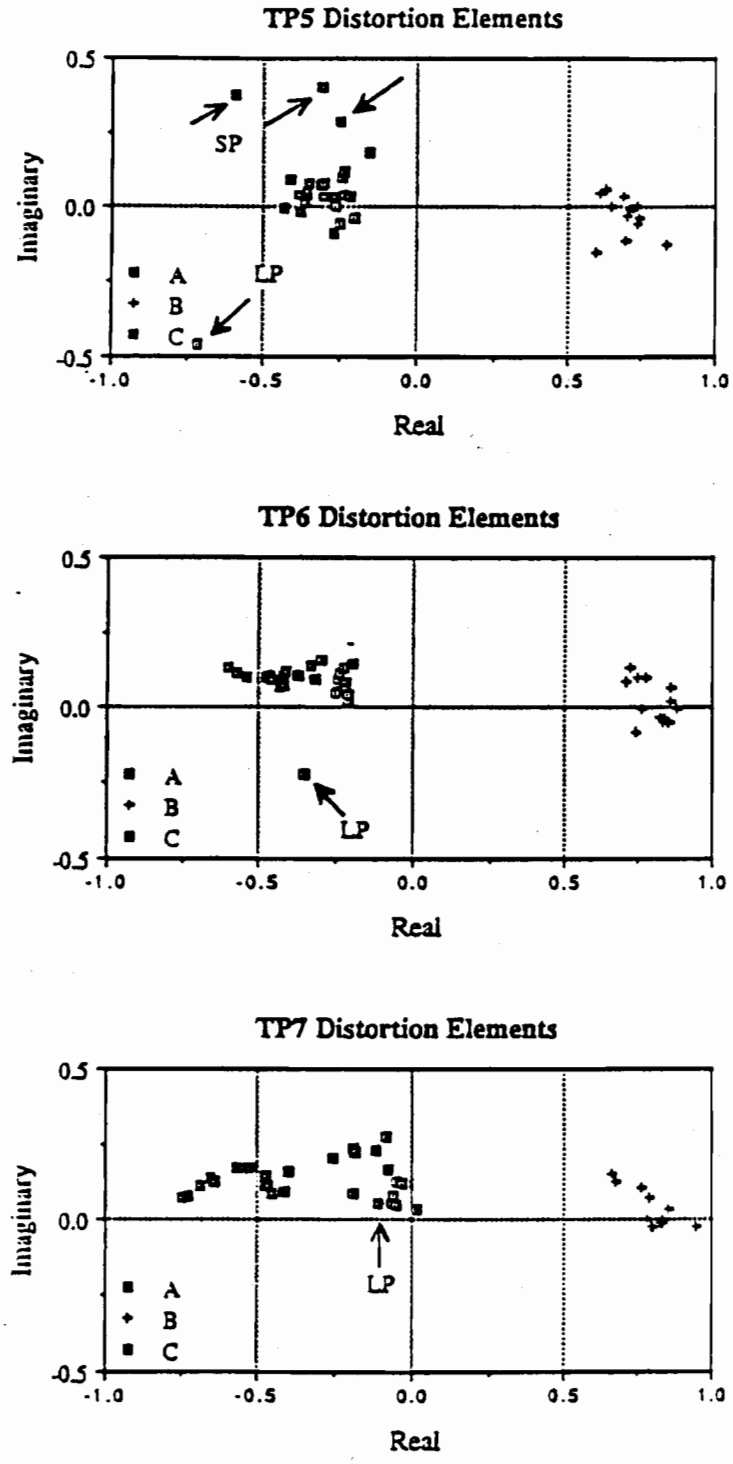

Figure 7.5 cont.

The dimensionality of the impedance response in the Tasman Sea is best determined by considering the data from all of the SFMT sites. Figure 7.5 illustrates the distortion elements for these sites and shows the form of the impedance tensor is spatially uniform. For all sites the values of B exceed 0.5 indicating strong anisotropy. At all sites the distortion elements are quite clustered and lie relatively close to the real axis. Small departures from this situation are discussed below.

Figure 7.6 illustrates the principal axis orientation, the anisotropy and the skew angle for the 2 h period, as a function of geographical position. (The values chosen for the axis orientation and skew are discussed in more detail below.) Except for the impedance magnitude (which increases with frequency as shown in Figure 7.4) the results are similar at other periods. The principal axis orientation is uniform across the Tasman Sea, with the major impedance axis aligned parallel to the trend of the Tasman. The major principal axis will be called the E-pol impedance and the minor impedance axis (which lies perpendicular to the trend of the Tasman Sea) will be called the B-pol impedance.

Examination of Figure 7.6 shows the anisotropy varies uniformly across the Tasman Sea with the SFMT sites nearest the coastline exhibiting the strongest anisotropy. This result is confirmed by the distortion elements, for which the value of B is maximum at sites TP7 and TP6. The skew angle also behaves in a systematic manner with geographical position. It increases systematically with distance from the Australian coastline; in the distortion elements this is reflected by a monotonic increase in the value of A from site TP7 to site TP1.

These results indicate that the form of the impedance is controlled by the large-scale shape of the Tasman Sea. The impedance varies smoothly over distance-scales of hundreds of kilometres suggesting that local three-dimensionality in the conductivity structure around the recording sites is minimal. Unless it were similar at all of the sites local three-dimensionality would introduce scatter into the observed impedance axes and would also probably cause a much stronger frequency-dependence of the distortion elements than that observed (Figure 7.6). The dominant feature of the impedances is the strong anisotropy. Its systematic variation across the Tasman Sea suggests the anisotropy is largely due to the attenuation of transverse electric currents by the conductivity boundaries at the edge of the sea.

The systematic variation in the skew angle across the Tasman Sea indicates that it too, is related to large-scale features rather than to deviation of electric current flow by local heterogeneities near each site. The observed increase to maximum skew values over the Lord Howe Rise suggests that the skew may be due to large-scale deviation of electric current flow by this feature. The sign of the skew angle is consistent with a deviation of north-flowing electric currents towards the west. Both the 2D and 3D features of the impedance are thus related to the morphology (the shape and bathymetry) of the Tasman Sea. The large conductivity contrast between the sea-water and the surrounding rocks (cf. the conductivity changes in the rocks) suggests this result is reasonable. A more

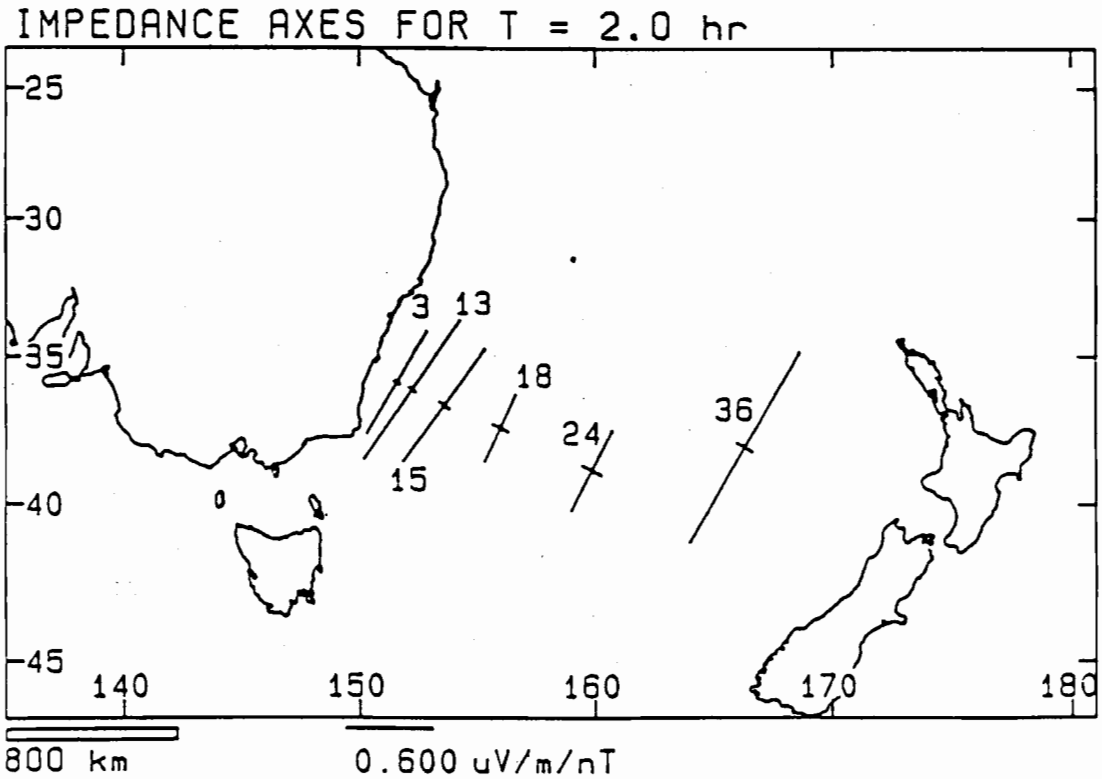

Figure 7.6: Diagram showing MT impedance; axis orientation, anisotropy and skew angle for the period of 2 h. The crosses show the major (E-pol) and minor (B-pol) impedance axes at the scale indicated at the bottom of the figure. The cross is centred on the site location; from west-to-east, TP7, 6, 5, 4, 3, and 1. The number at each site is the skew angle in degrees.

unexpected aspect of the results is the considerable distance the 2D and 3D effects extend into the Tasman Sea.

The SFMT impedances (and the induction arrow results in chapter 6) do not provide any evidence to suggest that the electrical conductivity structure beneath each seafloor site is more complicated than 1D. The MT analysis will therefore proceed with the assumption that the local conductivity structure at each site is 1D. The next stage in the MT analysis involves determining how the observed 3D impedances are related to the underlying 1D conductivity structure. A full solution to this question requires the application of a 3D modelling technique.

Since most of the spatial variation of the impedance tensor in the Tasman Sea is attributed to the shape of the Tasman Sea a suitable method of analysis would be thin-sheet modelling (eg. Vasseur & Weidelt 1977). In such modelling, the ocean is represented as an (electromagnetic) thin sheet and spatial variations in the conductance of the thin sheet model the shape and bathymetry of the ocean. The thin-sheet modelling would not be used directly to determine the conductivity structure beneath the seafloor but rather to determine how the 2D and 3D effects change the 'local' impedance values (ie. the impedance corresponding to the underlying 1D conductivity structure). Such modelling, of a region approximately 3000 by 3000 km centred on the Tasman Sea, should explain to first order the observed impedance anisotropy and skew. An alternative to thin-sheet modelling of the Tasman Sea region would be analogue modelling (eg. Dosso et al. 1985). Such modelling could again be used to study electromagnetic induction in a 3D structure in which the heterogeneity is confined to the upper layer.

Time constraints have limited the SFMT analysis in this thesis to a preliminary determination of the sub-oceanic conductivity structure. Because thin-sheet (or analogue) modelling procedures were not readily available at the time of the research, it was necessary to proceed without a formal model of the observed 3D impedances. The use of simplifying assumptions regarding the observed 3D impedances however makes it possible to obtain information on the deep conductivity structure. The final conductivity information must be interpreted with caution though, and assessed for spurious features caused by these simplifying assumptions (see chapter 8). There is considerable justification for obtaining as much information as possible from simple modelling and inversion techniques before moving on to more complicated modelling such as thin-sheet modelling. For example, if a 1D conductivity profile can be determined using simple inversion techniques, it may be used as the sub-oceanic conductivity structure required in thin-sheet modelling.

The distortion elements at each of the recording sites have a form similar to that associated with a static distortion of the electric field (ie. a frequency-independent rotation of the electric field data). This result suggests it would be a reasonable procedure to treat the data using the same method as for the case of a static distortion ie. to rotate the electric and magnetic fields to the principal axes (by the angles α and β) and thus remove the skew. Such a procedure will reduce the dimensionality of the problem to give a 2D impedance

tensor . It is acknowledged however that the 3D impedance terms at the seafloor sites cannot simply be due to static distortion since (as will be shown below) a large-scale deviation of currents flowing in the ocean will also have a significant magnetic field response. It therefore must be assumed that the procedure of deskewing the impedance tensor, produces E-pol and B-pol impedances which are appropriate for a 2D approximation to the Tasman Sea conductivity structure. This assumption should be verified in the future using 3D modelling.

A final question concerning the impedances which needs to be addressed is the accuracy of the method used to orient the horizontal electric field at site TP4, TP3 and TP1. Because the skew is different between TP5 and the unoriented sites, the method used for the orientation determination will have given slightly incorrect results. The method, which maximizes the similarity between the electric field data at each site, will have chosen an orientation partially biased away from the correct orientation and towards an orientation in which the skew at the unoriented sites is the same as at TP5. Because the skew at TP1, TP3 and TP4 is greater than at TP5, its magnitude will be under-estimated in the new orientations.

Examination of the relative magnitude of impedance tensor elements and autopowers suggests that the misorientation and under-estimation of the skew will be small. (This conclusion is based on observing that the portion of the electric field time series associated with the skew terms in the impedance is relatively small.) The observation that the skew angle increases monotonically across the Tasman Sea is a firm result since the correct skew at the eastern sites can only be greater than the determined values.

7.2 Two-dimensional Impedance Estimates

The next step taken in the data analysis involves rotating the electric and magnetic field co-ordinate systems into alignment with the principle axes and redetermining the impedances. The final rotation angles for site TP4 were defined using the arithmetic average of the values for α and β for the spectral bands between 9.6 h and 0.27 h ie. those bands with acceptable levels of random errors. The electric and magnetic co-ordinate systems were rotated by the resulting angles, -9.5° for α and +8.7° for β. It is not necessary to rotate the remote-reference data to the new co-ordinate system since the remote-reference components need only to be related to the two SFMT magnetic field components through a frequency-dependent transfer function (see chapter 4).

The principal-axis MT impedance for TP4 and associated parameters are listed in Table 7.3 and are illustrated in Figure 7.7. After rotation of the data the direction parallel to the Tasman Sea is denoted by the subscript "1" and the perpendicular direction by the subscript "2". The principal-axis impedances show the anisotropy between the E-pol and

Table 7.3a: TP4 principal-axis impedance tensor, magnitude and phase.

Period (h)	Frequency (cph)	$\|Z_{11}\|$	$\|Z_{12}\|$	$\|Z_{21}\|$	$\|Z_{22}\|$	$Ph(Z_{12})$	$Ph(Z_{21})$
			($\mu V.m^{-1}.nT^{-1}$)			(deg)	
32.508	0.031	.0221	.0421	.0351	.0352	98.1	58.6
16.650	0.060	.0073	.0759	.0232	.0045	69.5	79.2
9.615	0.104	.0077	.0956	.0262	.0180	66.3	44.3
6.849	0.146	.0067	.1474	.0380	.0159	59.1	45.4
4.443	0.225	.0233	.2156	.0425	.0155	46.9	42.4
2.999	0.333	.0153	.2466	.0477	.0182	46.8	38.2
2.079	0.481	.0053	.2606	.0626	.0164	50.8	34.5
1.442	0.693	.0037	.3120	.0668	.0184	49.1	32.2
1.000	1.000	.0051	.3527	.0811	.0169	47.5	36.1
.693	1.443	.0089	.4363	.0936	.0266	47.6	33.8
.481	2.079	.0220	.4870	.1064	.0300	40.6	31.5
.357	2.801	.0193	.5936	.1082	.0192	42.0	27.5
.267	3.745	.0442	.6420	.1174	.0609	29.7	38.3
.190	5.263	.0594	.7702	.1352	.0764	17.7	28.1

Table 7.3b: TP4 principal-axis impedance, coherences and confidence limits

Period	Multiple	and	Partial Coherences				Relative Confidence Limits			
(h)	1	2	11	12	21	22	11	12	21	22
32.508	.673	.223	.262	.526	.180	.082	1.564	.878	1.935	2.059
16.650	.807	.430	.073	.730	.409	.054	1.940	.213	.571	3.406
9.615	.842	.714	.172	.776	.608	.120	1.396	.176	.332	.759
6.849	.903	.771	.127	.835	.654	.070	2.359	.139	.269	.831
4.443	.784	.783	.048	.695	.693	.026	.458	.089	.141	.696
2.999	.775	.774	.085	.744	.736	.083	.684	.090	.123	.683
2.079	.794	.769	.010	.779	.752	.013	1.573	.066	.088	.690
1.442	.768	.726	.010	.758	.711	.014	2.257	.064	.087	.756
1.000	.724	.639	.009	.722	.639	.007	1.373	.056	.078	1.054
.693	.741	.674	.031	.732	.667	.006	1.012	.067	.090	1.018
.481	.584	.547	.059	.561	.535	.005	.457	.072	.096	1.183
.357	.408	.243	.011	.394	.241	.011	.774	.087	.165	3.204
.267	.237	.240	.027	.231	.239	.001	.273	.071	.123	.893
.190	.069	.127	.004	.066	.116	.015	.205	.052	.115	.671

Table 7.3c: TP4 principal-axis impedance tensor, residual distortion elements

Period (h)	A		B		C		α (deg)	β (deg)
32.508	-.037	.307	.103	-.355	.642	-.381	-35.2	-32.9
16.650	.074	.081	.535	.061	.052	-.006	-0.6	-4.8
9.615	-.057	-.146	.585	-.130	.155	.064	-8.3	-4.9
6.849	-.104	-.034	.595	-.078	.067	-.028	-6.3	-0.4
4.443	-.124	.024	.671	-.022	-.020	.085	-2.5	4.5
2.999	-.094	-.023	.678	-.041	-.003	.061	-2.4	2.9
2.079	-.032	-.015	.621	-.088	.055	.039	-3.2	-1.3
1.442	.012	-.048	.655	-.085	.007	.050	0.3	-0.4
1.000	.047	-.015	.630	-.060	-.024	.017	2.5	-0.2
0.693	.062	.021	.652	-.069	-.036	.002	3.4	-0.2
0.481	.057	.066	.644	-.046	-.016	-.004	2.3	-1.0
0.357	-.015	-.003	.697	-.066	-.012	.051	0.3	1.2
0.267	.036	.088	.692	.039	-.102	.008	5.2	3.1
0.190	-.089	-.030	.704	.046	-.008	.118	-2.5	2.6

The headings 1, 2, 12 etc. in Table 7.3a and 7.3b denote the axis / axes involved in the terms in a similar manner to Table 7.1. "1" denotes the major (E-pol) impedance axis which is longitudinal to the Tasman Sea and "2" denotes the minor (B-pol) impedance axis.

B-pol terms is significantly frequency-dependent and also that the phases of the E-pol and B-pol impedances are different. These observations indicate that the anisotropy is due to an inductive effect rather than a static distortion effect (see appendix 4).

Figure 7.8 shows the residual distortion elements for TP4 calculated after rotation to the principal axes. The frequency-dependence and imaginary component of the B element reflect the properties of the MT anisotropy noted above. Although the real parts of the A and C elements have been minimized by the rotation to the principal axes, the terms still possess small imaginary components. These terms indicate the departure of the data from a 'static distortion' form. The effect of the A and C elements is seen in the diagonal impedances in Figure 7.7 where for much of the resolved frequency range Z_{11} is a factor of only 2-4 smaller than the B-pol impedance.

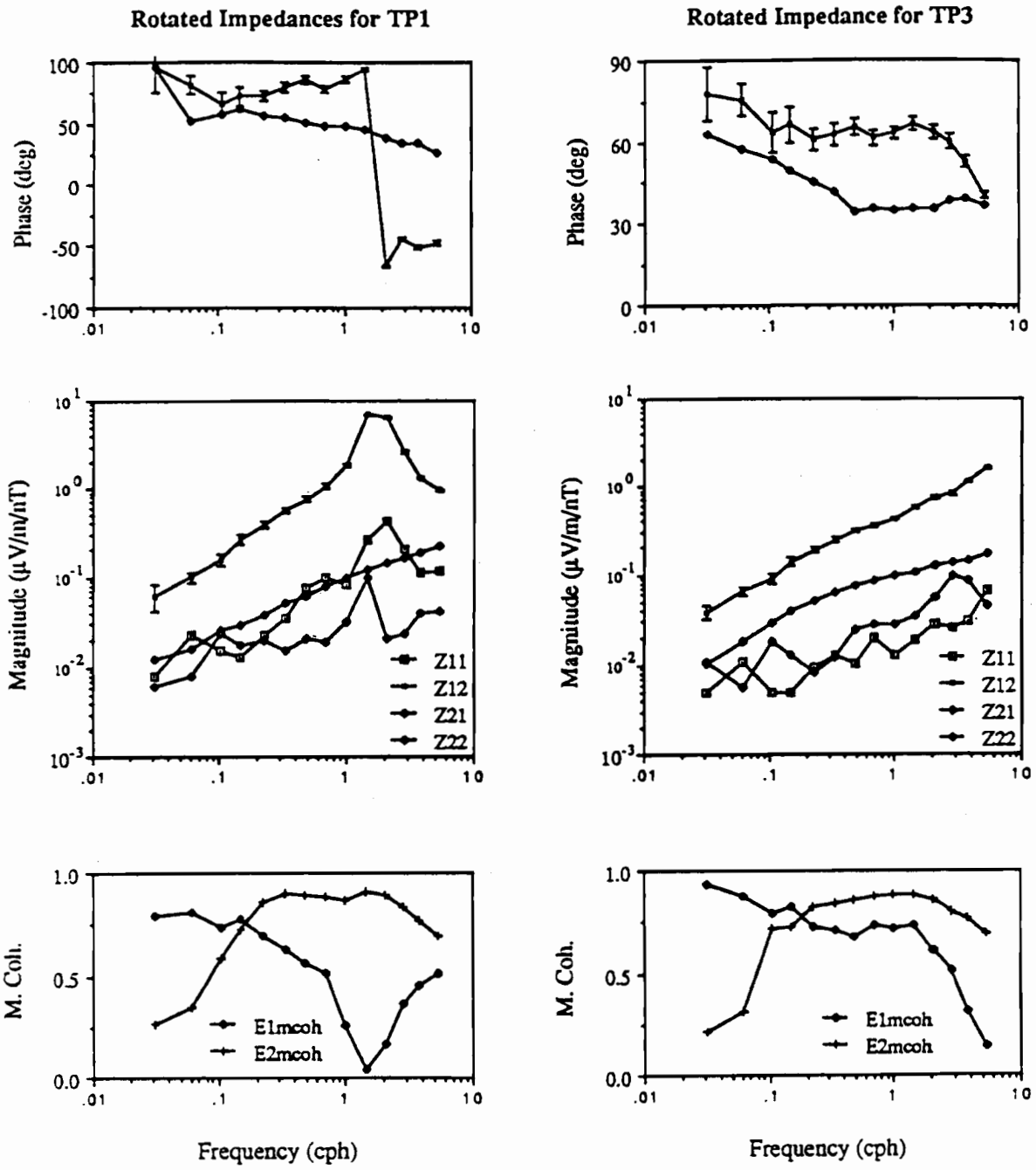

Figure 7.7: Principal-axis impedance tensor components at the SFMT sites. In the principal axis co-ordinate system the direction parallel to the Tasman Sea is denoted by "1" and the perpendicular direction by "2" (eg. Z_{12} is the E-pol impedance term). The diagram shows the magnitude of all four impedance tensor components and the phase of the Z_{12} and Z_{21} terms. Also shown is the multiple coherence of each electric field component (E_1 and E_2) with both horizontal magnetic field components.

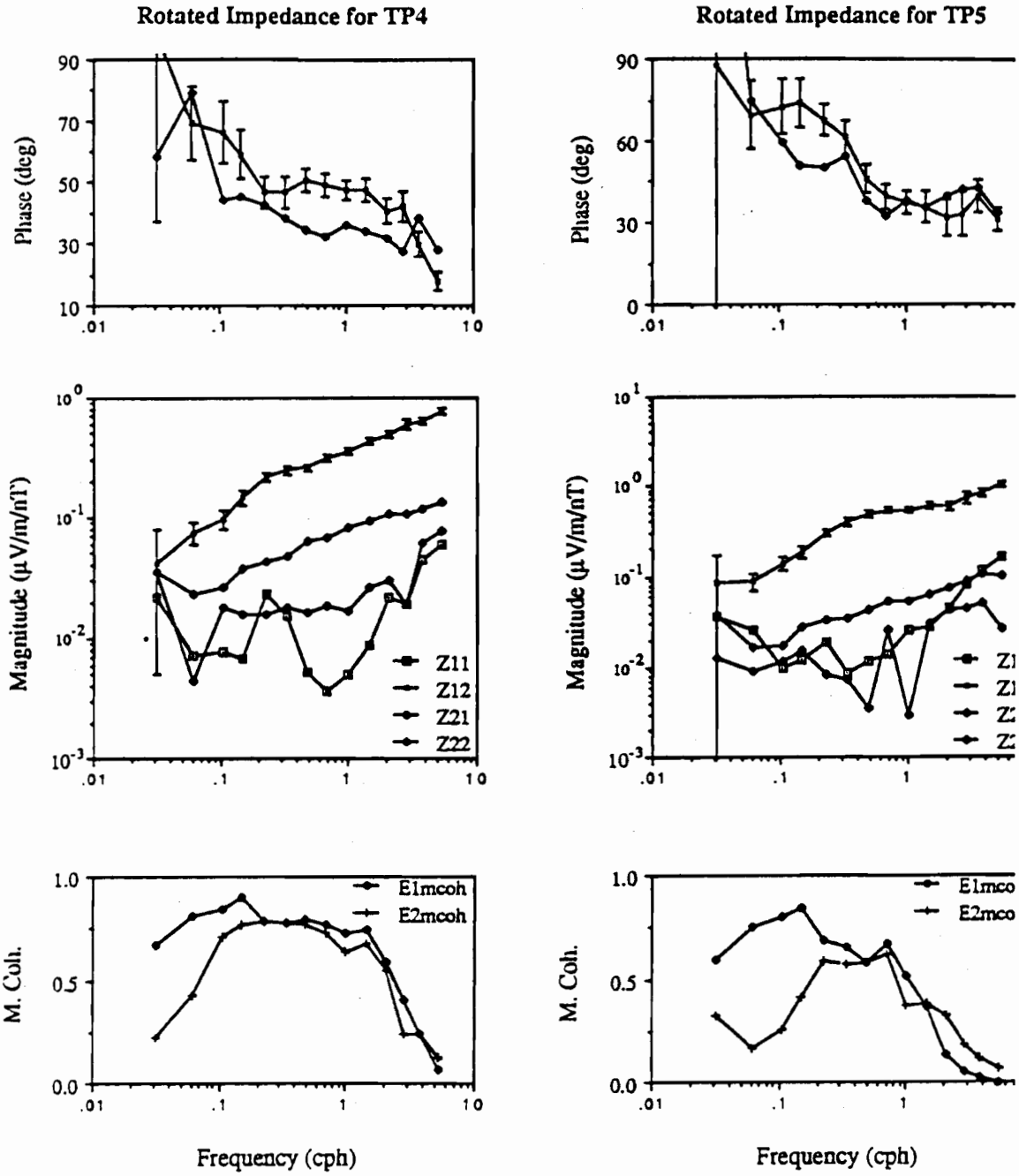

Figure 7.7 cont.

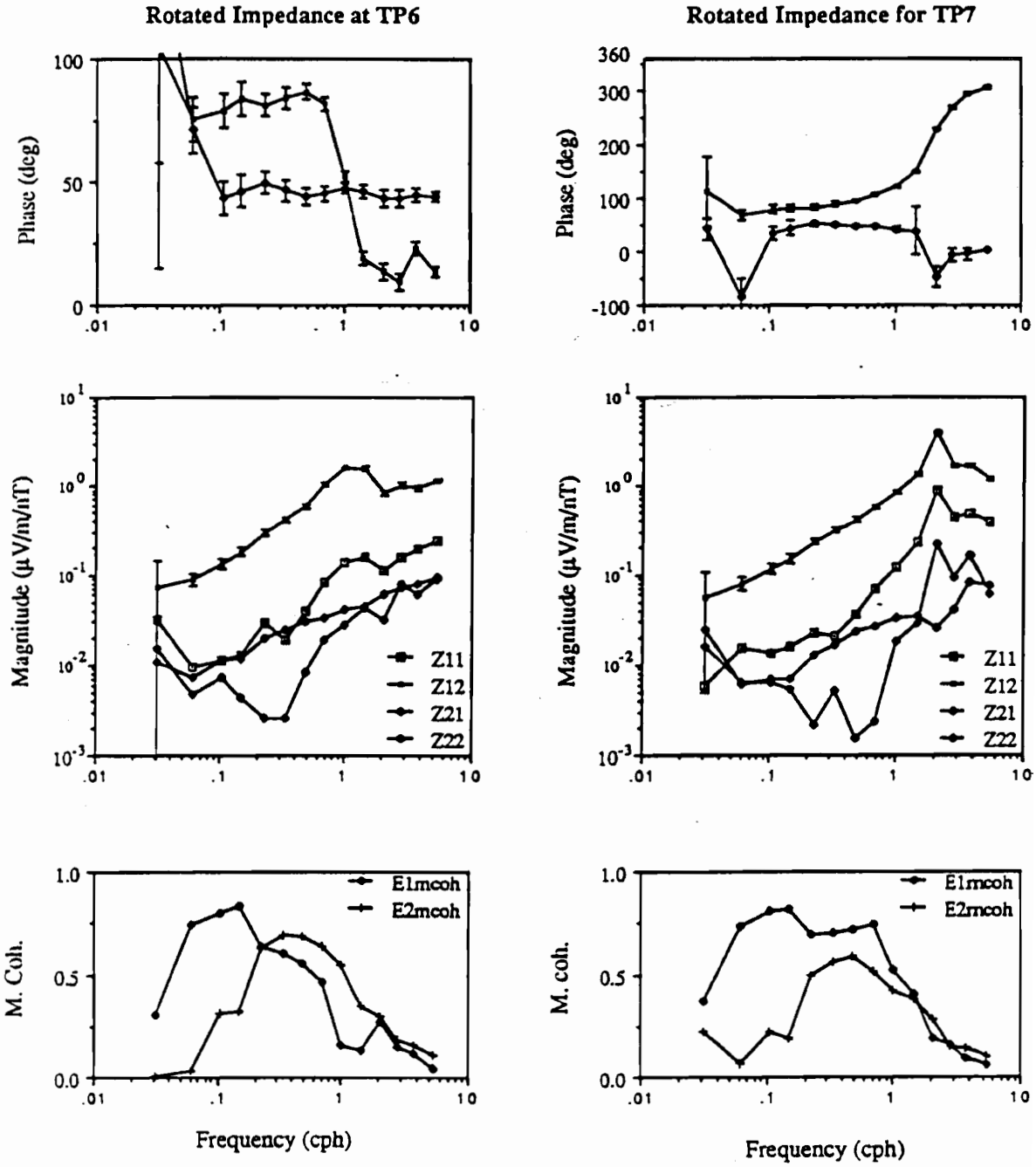

Figure 7.7 cont.

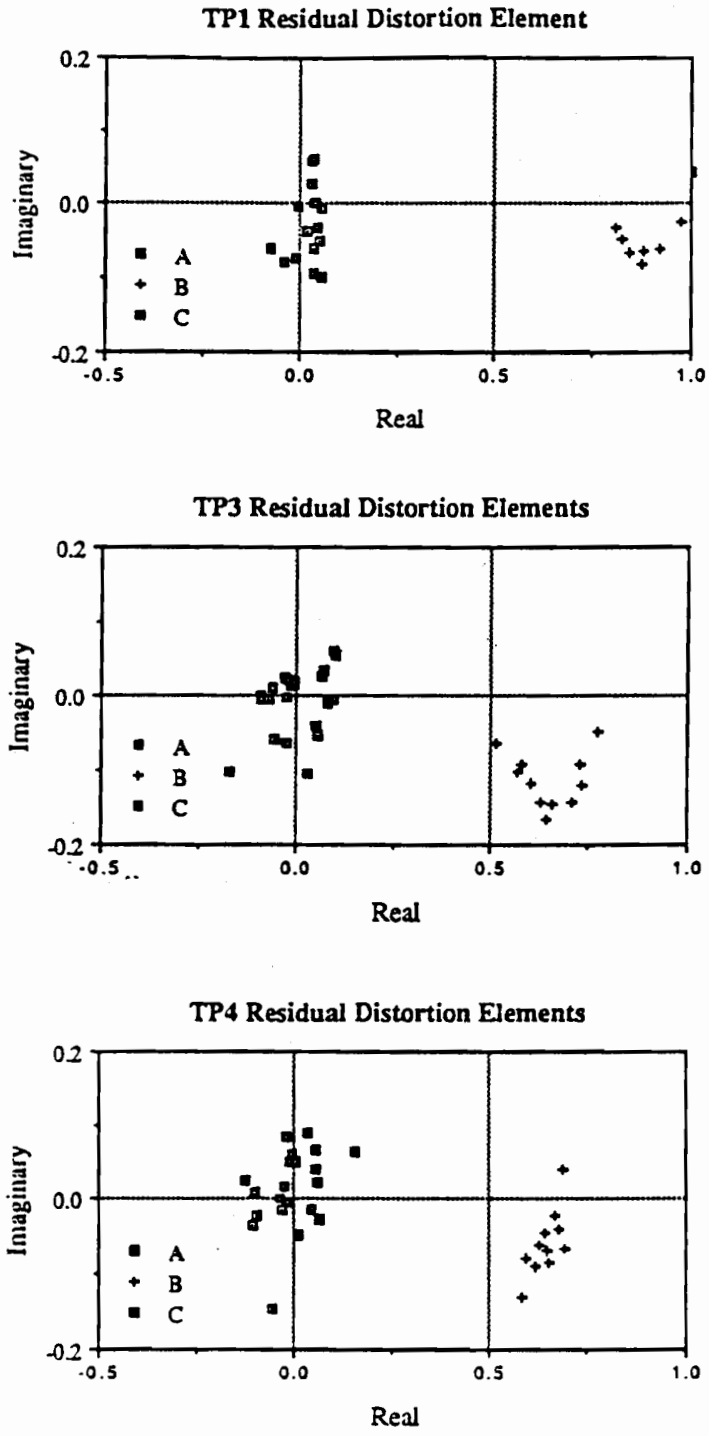

Figure 7.8: Residual distortion elements for each SFMT site, after rotation of the electric and magnetic field data to the principal axes. The diagram does not include the erratic short period and long period results omitted from the principal axis determinations. Note the relatively large values of A and C at sites TP7, TP6 and TP1.

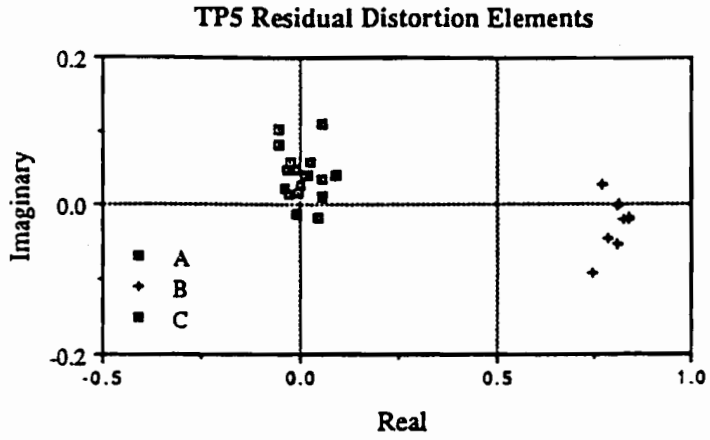

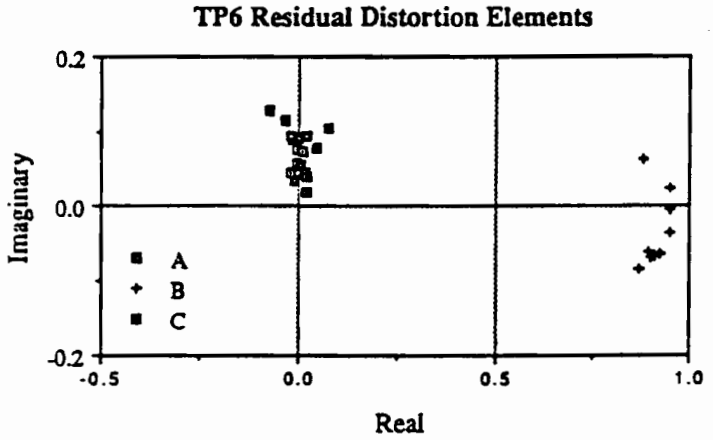

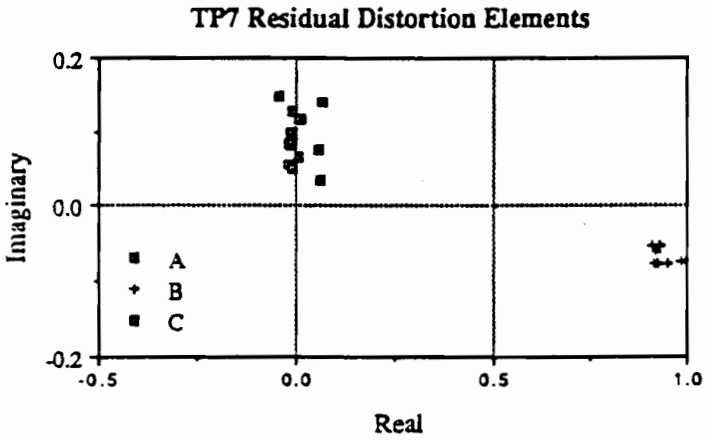

Figure 7.8 cont.

Table 7.4 lists the rotation angles determined for the other SFMT sites. As for site TP4, the angles are relatively independent of frequency although some irregular variation occurs at the longest and shortest period bands. Average rotation angles were obtained for each site by arithmetic averaging over the bands in the central part of the frequency range (Table 7.4). Bands at either end of the resolved spectrum were omitted using criteria based on relative errors and partial coherences, and for several bands where the distortion elements for the band were inconsistent with the cluster of angles defined by the remaining bands.

Table 7.4. Rotation angles to principal axes for SFMT sites, angles α and β.

Period	TP7		TP6		TP5		TP3		TP1	
	α	β	α	β	α	β	α	β	α	β
(h)					(deg)					
32.508	*-1.4*	*9.5*	*11.2*	*31.5*	*.1*	*39.5*	*-18.6*	*10.7*	*-20.6*	*22.1*
16.650	*14.9*	*20.3*	*8.8*	*20.4*	*-.9*	*14.4*	*-12.6*	*11.8*	*-18.9*	*17.1*
9.615	13.8	12.9	5.2	17.3	1.7	19.0	-22.4	9.1	*-23.2*	*15.4*
6.849	11.8	14.9	6.3	18.2	3.4	20.5	-18.6	8.6	-22.4	9.5
4.443	13.8	14.9	6.7	20.7	5.9	21.3	-15.5	10.9	-22.7	11.6
2.999	13.0	16.9	6.8	21.0	8.7	22.8	-14.2	13.0	-24.5	10.4
2.079	14.0	17.5	6.4	20.5	5.7	20.7	-18.4	7.1	-25.9	7.1
1.442	14.2	16.2	6.8	19.1	8.1	20.0	-14.5	8.4	-26.4	8.9
1.000	15.1	18.2	7.8	20.4	6.8	19.3	-12.8	8.3	-25.6	11.0
.693	*14.7*	*19.5*	7.8	20.5	6.9	20.3	-12.6	7.8	-22.5	13.1
.481	*15.9*	*23.3*	8.8	22.3	7.6	21.5	-11.3	8.2	-24.2	16.3
.357	*15.3*	*26.7*	*11.4*	*24.2*	*10.3*	*24.1*	-9.4	10.3	*-25.9*	*17.8*
.267	*18.3*	*29.5*	*10.9*	*28.0*	*5.6*	*25.8*	-8.5	10.0	*3.6*	*26.8*
.190	*16.0*	*31.3*	*10.8*	*28.9*	*-8.2*	*25.3*	*-15.2*	*9.9*	*-40.9*	*-6.5*
Mean	**13.7**	**16.3**	**6.9**	**20.0**	**6.1**	**20.6**	**-14.4**	**9.3**	**-24.6**	**11.0**

Results in italics are excluded from the final mean values. Exclusion is on the basis of random errors and the where individual distortion elements fall outside the cluster of results defined by the other frequency bands (eg. the 0.190 h result for site TP3). The angles for site TP4 are given in Table 7.2.

The rotated SFMT horizontal magnetic and electric field data sets were used (with CMO and EYR as remote references) to calculate remote-reference impedance functions. The full set of impedance functions and associated parameters are tabulated in appendix 6 and illustrated in Figure 7.7. The impedances initially appear to be quite complex in form, especially at sites TP7, TP6 and TP1, with phase angles lying outside the normal 1D range of 0-90° and with B-pol impedance elements smaller than the diagonal impedance elements. It will however be shown that most of the complexity is due to simple 2D effects.

The residual distortion elements for all sites are shown in Figure 7.8. The dominant feature of the rotated impedance at each of the sites is the strong anisotropy. The value of the distortion element B at all sites is greater than 0.5 and from equation A6.8 it therefore follows that the ratio of the major to the minor impedance is always greater than 3.0. This result is confirmed by examination of the major and minor impedance axes in Figure 7.7. The strength of the anisotropy varies between the different sites; it is strongest at sites TP7, TP6 and TP1, where the average value of B is larger than 0.9, and smallest at sites TP3 and TP4 where the value of B is around 0.6. At all sites B is frequency-dependent and contains a significant imaginary component, confirming the presence of 2D induction effects.

The residual distortion elements A and C are definitely non-zero for sites TP7, TP6 and TP1 and may have small non-zero imaginary components at the other SFMT sites. These terms indicate a departure from the 'static distortion' form of the impedances and indicate the influence of 3D induction effects (appendix 4). The existence of A and C elements with the same sign, as observed at TP7, TP6 and TP1, corresponds to a significant Z_{11} impedance term. At sites TP7, TP6 and TP1 the anisotropy is also large, causing the magnitude of the Z_{21} impedance element is to be less than that of Z_{11} (Figure 7.7).

Because the preliminary impedances at the seafloor sites exhibit significant skew, ambiguity arises as to the correct geographical orientation of the principal axes. Two possible orientations are; α degrees from the electric field co-ordinate system and β degrees from the magnetic field co-ordinate system. In this thesis the principal axes are assumed to lie in the orientation given by the magnetic field data. There are two reasons for this choice. Firstly it is probable that the electric field is distorted more from its 2D form than is the magnetic field (a statement supported by the similarity of the distortion elements to those due to static distortion). Secondly the orientation of the electric field instruments at sites TP1, TP3 and TP4 was not recorded directly and there is therefore less certainty regarding the electric-field co-ordinate system at these sites.

The axes based on the magnetic field differ from those defined by the electric field by less than 35° (Table 7.4) and should therefore be close to the true orientation. In the futu 3D modelling should be used to determine the exact principal axis orientation. Table 7.5 lists the geographical orientation of the principal axes at each site. The orientation varies

Table 7.5: Rotation angles to principal axes, skew and geographic orientation.

Site	Mean skew angle (deg)	Major axis orientation (clockwise from TN)
TP7	-2.6	29.8
TP6	-13.1	34.0
TP5	-14.5	35.6
TP4	-18.2	24.9
TP3	-23.7	27.0
TP1	-35.6	29.8

The skew angle is given by α-β where α and β are calculated according to the theory in appendix 4. The geographical orientation of the major principal axis is given by angle β plus the local magnetic declination. The orientation is defined using the horizontal magnetic field rather than the horizontal electric field.

by less than 11° across the Tasman, providing additional support for this choice of axes.

B-polarization Impedance Results

In this section the B-pol impedance component in the Tasman Sea is examined. From model studies it has been found that the effect of a 2D electrical conductivity structure such as a coastline extends further to sea, and is stronger for the B-pol mode than for the E-pol mode (eg. Fischer & Weaver 1986). For the E-pol mode both the electric and magnetic fields are continuous across the conductivity boundary whereas for the B-pol mode the electric field and the impedance are discontinuous at the boundary. The B-pol impedance terms will thus have strongly perturbed values near a coastline.

Figure 7.9 shows the minor impedance axis plotted as a function of distance from the Australian coastline for the period of 2.1 h. Corresponding results are observed at other frequencies. Over the distance range of 100 to 1000 km from the coast (defined by sites TP7 to TP3) the impedance magnitude and phase both vary smoothly. As predicted by the model results the impedance tends towards extreme values close to the coast. The impedance magnitude in Figure 7.9 is well fitted by an exponential function with a

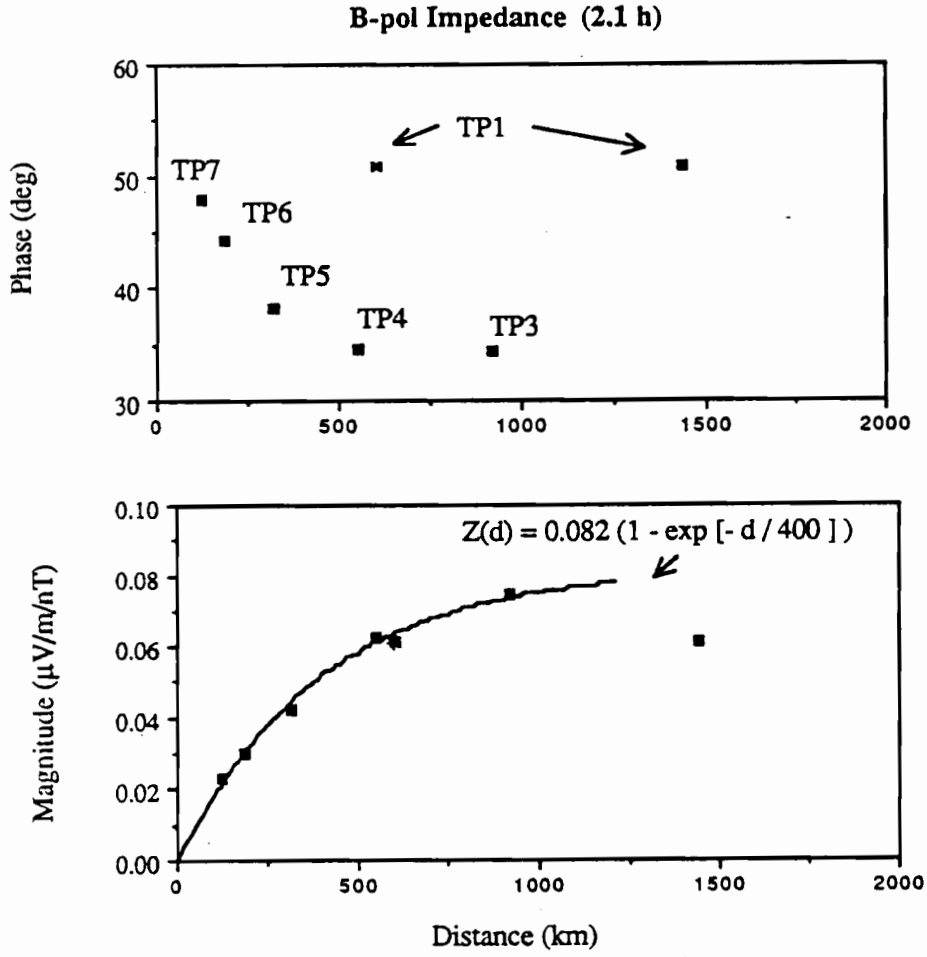

Figure 7.9: B-pol impedances in the Tasman Sea as a function of distance from the coast. The squares indicate points plotted at the distance of the sites from the southeast coast of Australia and the star indicates the TP1 result plotted at at the distance from the west coast of New Zealand. The impedance magnitudes from sites TP7 to TP3 fall on the exponential curve shown. The results are for the period of 2 h.

scale-length of 400 km ie.

$$Z(d) = 0.082 \, (1 - \exp [- d / 400]) \qquad 7.2$$

where Z is the B-pol impedance in μV/m/nT and d is the distance in kilometres from the Australian coastline. The direct dependence of the impedance on the distance from the coastline confirms that the MT anisotropy in the Tasman Sea is caused (at least in part) by the 2D electrical conductivity contrast at the Australian margin.

Figure 7.9 shows that significant 2D effects in the B-pol impedance extend at least 1000 km into the Tasman Sea. Equation 7.2 indicates that at this distance, the B-pol impedance is still 8% less than its correct value. Because the adjustment scale of the 2D anomaly is so large, the effects of the electrical conductivity contrast at the eastern margins of the Tasman Sea, ie. the Lord Howe Rise and New Zealand, must also contribute to the B-pol anomaly. Figure 7.10 illustrates model results which show that for narrow oceans, in which B-pol effects from opposite sides of the ocean overlap, the B-pol anomaly at each coastline still has an exponential-type spatial form. The B-pol impedance for site TP1 does not lie on the anomaly curve defined by the other SFMT sites, either when it is plotted at the distance from the Australian coast or from the New Zealand coast. This result shows the influence of the Lord Howe Rise on the B-pol impedance at site TP1. The strong anisotropy noted at the site (eg. Figure 7.8) also suggests that the B-pol impedance is affected by the lateral conductivity contrasts of the Lord Howe Rise.

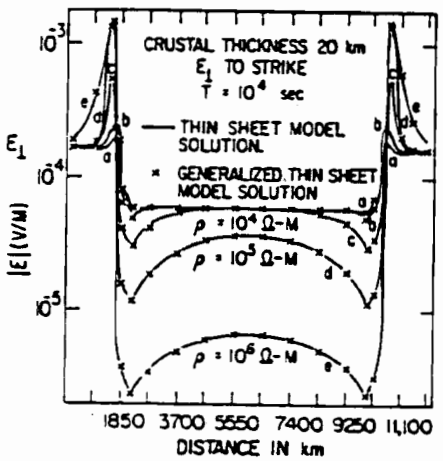

Figure 7.10: Diagram showing the overlapping 2D B-pol anomaly from two parallel coastlines (from Ranganayaki & Madden 1980). If the adjustment scale is large compared with the width of the ocean the perpendicular electric field does not reach its 1D value in the centre of the ocean. If the exponential distance-scale of the electric field variation at the coastline is used to estimate lithospheric resistance an under-estimate will result.

The 400 km exponential adjustment-scale for the B-pol anomaly means that none of the Tasman Project SFMT sites will be free of 2D B-pol effects. Site TP3, which is the farthest SFMT site from the Australian coast (917 km) is only 350 km from the Lord Howe Rise and is therefore likely to be influenced by a 2D B-pol effect from this feature. As long as the sub-oceanic electrical conductivity structure is similar for the different parts of the Tasman Sea the adjustment distance from the Lord Howe Rise anomaly should also be 400 km. The bathymetric contrast at the Lord Howe Rise is however smaller than at the Australian coastline and is therefore the strength of the 2D anomaly is also likely to be smaller.

As described in chapter 4, the distance B-pol effects extend from a 2D coastline is related to the ratio of the integrated conductivity of the ocean to the integrated resistivity of the oceanic crust. The Tasman Sea adjustment distance therefore allows an estimate to be made of the crustal resistivity beneath the Tasman Sea. These calculations were initially performed in co-operation with Dr F.E.M. Lilley.

Substituting the observed adjustment scale of 400 km and an estimated integrated conductivity for the ocean of 3.3 $S.m^{-1}$ x 5 x 10^3 m = 1.65 x 10^4 S into equation 4.119 an estimate for the integrated resistivity of 10^7 $\Omega.m^2$ is obtained for the lithosphere beneath the Tasman Sea. In chapter 8 it is found that the depth to a conductivity increase beneath the Tasman Sea is of order 100 km. Using this value, an estimate of 10^2 Ω.m is obtained for the resistivity of the Tasman Sea lithosphere.

The estimate of 10^7 $\Omega.m^2$ is a minimum estimate for the integrated resistivity for the following reasons. Firstly the possibility of a contribution to the B-pol anomaly from the eastern margins of the Tasman Sea means the adjustment-distance estimate of 400 km is a minimum estimate for a single-coastline adjustment-distance (Figure 7.10) . Secondly 3D effects are likely to reduce the observed scale distance from its 2D value. The B-pol anomaly is caused by a charge build-up on the conductivity boundary (chapter 4). Results in chapter 6 however show that electric currents flowing transverse to the Australian continent may be deviated into the north-south direction and thus cause the charge build-up to be less than for a 2D conductivity structure.

Ranganayaki & Madden (1980) show that the exponential scale-distance should be applied to the horizontal electric field perpendicular to a conductivity boundary rather than the B-pol impedance. Preliminary model calculations however suggest that the use of an adjustment-distance defined by the B-pol impedance will introduce less errors into the resistivity derivations than the differences between a realistic conductivity profile and the simple three-layer conductivity model assumed in the calculations.

E-polarization Impedance Results

Theoretical model studies of 2D anomalies at coastlines have tended to present results for the sea-surface rather than the deep seafloor (eg. Fischer & Weaver 1986). In order to

examine seafloor impedances a 2D modelling program was used to calculate the seafloor electric and magnetic fields at a typical continental margin. This research used a 2D finite-difference modelling program kindly provided by Prof. J. Weaver. At the Austral National University, R. L. Kellett set the program up to run on a VAX 1180 computer a has closely checked its performance. Because this thesis includes only a small amount o 2D modelling, details of the computations included here are limited to the parameters of each run. For further details regarding the calculation method see Brewitt-Taylor & Weaver (1976) and Weaver & Brewitt-Taylor (1978).

Figure 7.11 shows the simple conductivity model used in the modelling. The mod is intended to represent the conductivity structure of a typical coastline and no attempt ha been made to fit the Tasman Sea data. It includes an ocean of 4 km depth overlying 1 k of sediments which in turn overlie a relatively resistive conductivity profile. On the continental side of the model the upper 5 km layer is moderately resistive and the deeper layers are identical to those beneath the ocean. The model extends 2000 km to either sid of the coastline. The source-field used for the E-pol calculations induces a perpendicular magnetic field which has a unit total amplitude (induced plus inducing) at a point remote from the coastline.

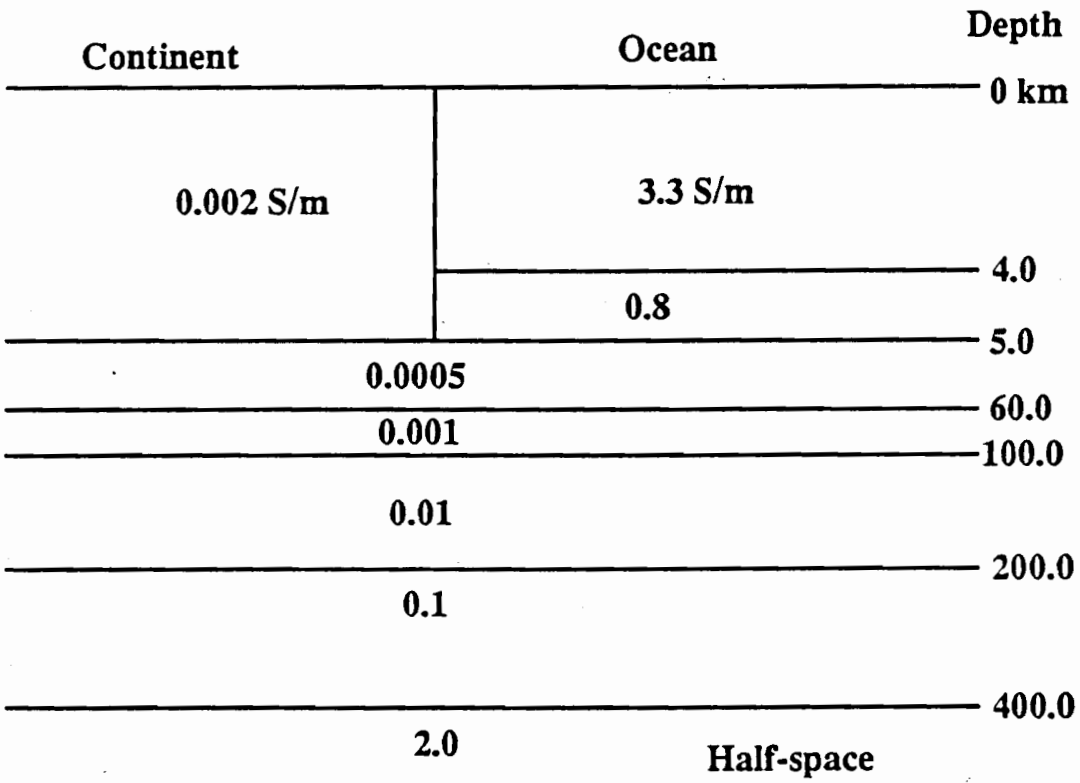

Figure 7.11: The theoretical 2D conductivity model of a continental margin used to investigate seafloor electric and magnetic fields. The simple model includes a 4 km ocean underlain by 1 km of sediments. It extends laterally for 2000 km on either side of the coastline.

The seafloor electric and magnetic fields were evaluated at four periods: 16.7 h, 2.0 h, 0.5 h and 0.25h. Figure 7.12 compares the seafloor perpendicular magnetic field (the component used in the E-pol impedance) from the 2D model with those observed in the Tasman Sea. The observed results are for sites 80, 120, 180 and 550 km from the Australian coast and the model results are for the (similar) distances from the model coast of 60, 100, 150, and 600 km. Although no attempt has been made to match the model and the observed data, there is sufficient similarity between the two sets of results to suggest that most of the spatial variation in the seafloor magnetic field is explained by 2D effects.

For both model and Tasman Sea results, at sites within 100 km of the coast, at shorter periods the phase increases steeply to values greater than 200°. The most extreme phases occur at a small distance away from the coast; at TP7 in the Tasman data and 100 km from the coast in the model data. Beyond 150 km from the coast (or TP6) the phase increases to a maximum at a period of about 2 h before decreasing to less than 45°. At larger distance from the coast the phase changes more slowly with frequency and shows more moderate maxima and minima than coastal sites. The phase values at 600 km from the coast in the 2D model are close to the 1D results.

The model and Tasman Seafloor perpendicular magnetic field magnitude also agree well. Close to the coast the attenuation is less than at other sites; the TP8 and 60 km sites have the largest magnetic field magnitude. At large distances from the coast (TP4 or 600 km) the magnitude forms a monotonically decreasing function of frequency, close to the 1D solution. Around 100 -150 km from the coast there is a region of increased attenuation at periods of around 1 h. Both the Tasman Sea and model results show that in this region, the attenuation exceeds that occurring further from the coast.

The model E-pol 2D effects are thus able to explain most features of the seafloor perpendicular magnetic field (including the extreme phase values noted at sites TP8-TP6). The spatial variations in the (parallel) electric field are smoother than those in the magnetic field and the model results correctly predict the form of the electric field variation. Some of the observed differences between the model and Tasman Sea electric and magnetic fields may be reduced by refinement of the conductivity model. For example, it may be possible to readjust the model so it could more closely fit the very large phase values noted near the Australian coast (Figure 7.12).

The 2D model results may be used to assess at which sites in the Tasman Sea the E-pol impedance may be treated as 1D. Since these results are based on an estimate for the conductivity structure of a typical continental margin (cf. the actual Australian continental margin) they should be assessed in the future using conductivity models for the Australian margin. Figure 7.13 compares the 2D E-pol impedances with the 1D seafloor impedance. At 1000 km from the model conductivity boundary the E-pol impedance is very close to the 1D impedance. At 300 km from the conductivity boundary, the phase of the E-pol impedance is within 5° of the 1D phase and the E-pol impedance magnitude is within 2% of the 1D value. These differences show that for sites 300 km from a coastline, the E-pol

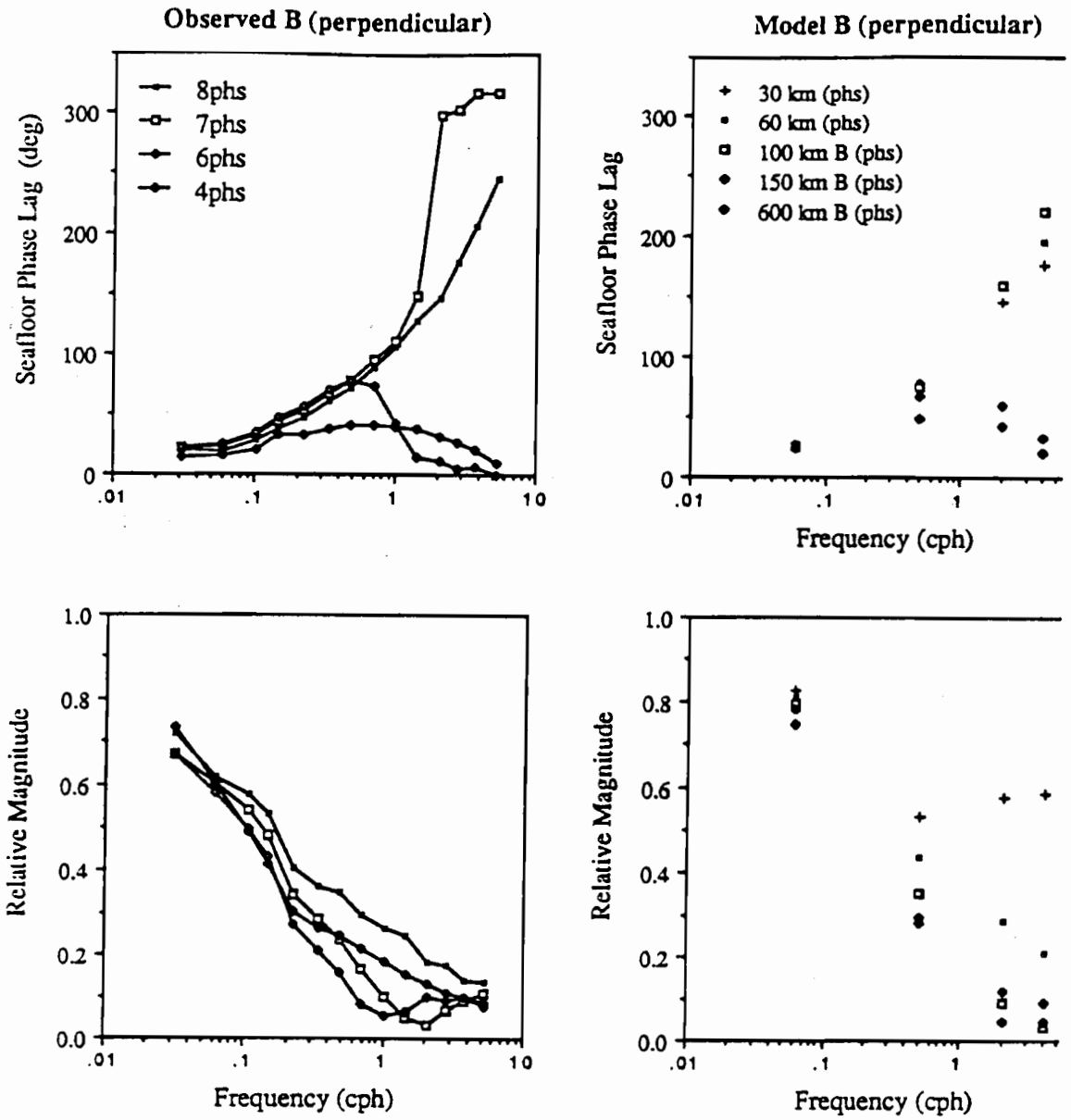

7.12: Observed and model results for the horizontal magnetic field perpendicular to a coastline. Both sets of results give the seafloor (perpendicular) magnetic field relative to a unit surface magnetic field at a point distant from the coastline. The same symbol has been used in both observed and model results to represent the response at a particular distance from the coastline. The observed results are based on the B_D magnetic field component which is approximately 10° from the exact trend of the Australian coastline. Note that although no attempt has been made to exactly match the model and observed results, the model (Figure 7.11) reproduces much of the observed variation in the observed results.

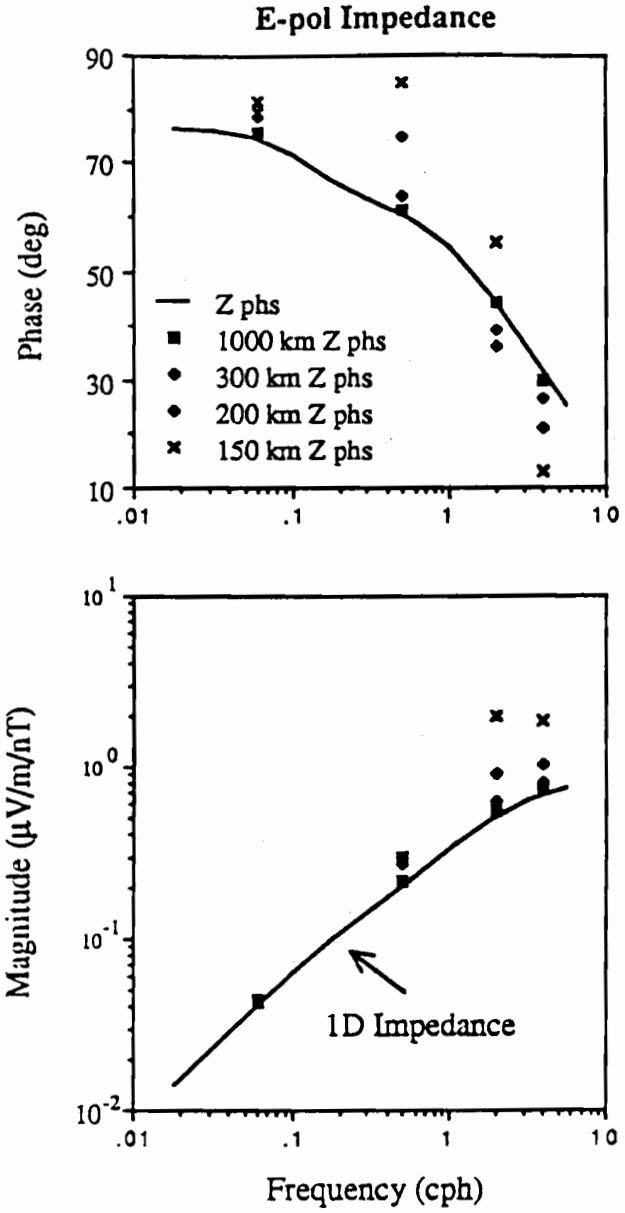

Figure 7.13: Variation from 1D MT response caused by 2D E-pol effects. The solid lin shows the 1D response for the oceanic end of the conductivity model in Figure 7.11 anc the symbols show the 2D response at different distances from the model coastline. At distances of less than 300 km from the coastline, the E-pol impedance is significantly different from the 1D impedance. The longest period result (at 17 h) lies close to the h-line of the corresponding sea-surface apparent resistivity and is relatively unaffected b the E-pol anomaly.

impedance contains a small but significant 2D influence. At distances less than 300 km from the coastline the E-pol impedance phase and magnitude exhibit stronger 2D effects.

The results of this study suggest that of the Tasman Project sites, only TP4 which lies 550 km from the Australian coast can be confidently regarded as having no 2D effects in the E-pol impedance. The 2D model results suggest that site TP5, which is 318 km from the Australian coast, will have E-pol impedances which are approximately 1D but may contain a 2D perturbation of order 10 %. Site TP3 which lies 350 km from the Lord Howe Rise may exhibit some 2D effects but these should be relatively weak (< 5 %) since the Lord Howe Rise creates a smaller lateral conductivity contrast than the Australian continent (as shown by the induction arrow results). Sites TP8, TP7, TP6 and TP1 will have strong 2D effects in the E-pol impedances.

Some of these strong 2D effects are visible in Figure 7.7. The extreme phase values of the E-pol (Z_{12}) impedance at sites TP1, TP6 and TP7 are attributable to extreme seafloor magnetic-field phase values noted above for the theoretical model. Similarly the peak in the E-pol response at sites TP1, TP6 and TP7, at the frequency of 2 cph, is explained by increased magnetic field attenuation at this frequency. This effect was noted above in the theoretical model for sites 100 to 150 km from the coastline.

As discussed in chapter 4, the h-line branch of the apparent resistivity curves should not be affected by E-pol 2D effects and can therefore be used to define the depth to a good conductor. Figure 7.14 illustrates the seafloor and sea-surface apparent resistivity response for a 1D profile comprising the oceanic part of Figure 7.11. The seafloor and sea-surface responses have different period ranges for the h-line, with the h-line for seafloor data extending to shorter periods than for sea-surface data because of the reduced effect of the surface conductance. When considering the effects of 2D distortion, the period range of the h-line should strictly be defined using the sea-surface apparent resistivity. Examination of Figure 7.13 however suggests that for sites more than 30 km from a coastline, the apparent resistivity (and hence the value determined for h) may be reasonably well-estimated at shorter periods than those of the sea-surface h-line. At the period of 2 h the impedance magnitude will be defined to within 50 % of its correct value and from 4.96b the value for h will also be defined with this accuracy.

Table 7.6 lists the values of the depth to the good conductor determined using the asymptotic method and the apparent resistivity values for the model profile (Figure 7.14). The h-lines return a value for h of around 400 km which corresponds to the depth at which the conductivity in the model increases from 0.1 to 2.0 $S.m^{-1}$. This depth is well-estimated at periods longer than 5.6 h in the seafloor data and periods longer than 18 h in the sea-surface data. These results suggest that the depth to the good-conductor, h, may be well estimated from seafloor E-pol data at periods longer than 6 - 10 h. The Tasman SFMT impedances contain well resolved E-pol impedance magnitudes in this range and can therefore be used to estimate h for the Tasman Sea.

Figure 7.15 shows the E-pol apparent resistivities for the Tasman Project data. All of

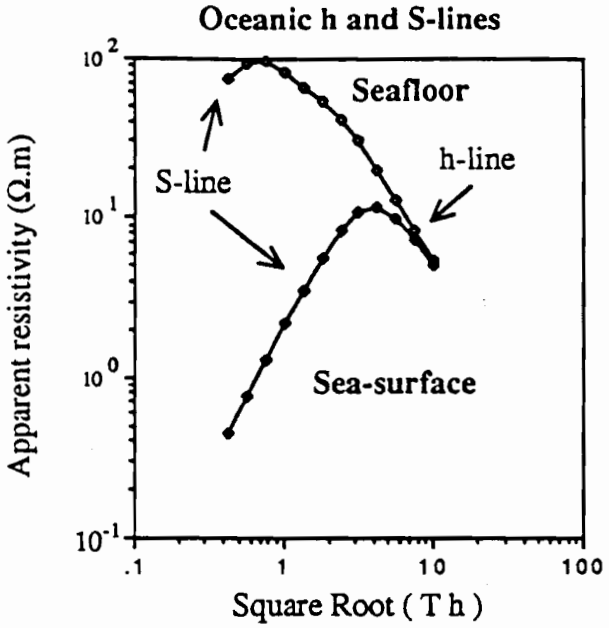

Figure 7.14: S-line and h-line for the oceanic profile shown in Figure 7.11. The h-line in the seafloor data occurs at a much shorter period (~0.6 h) than in the sea-surface data (~1 h).

Table 7.6: Use of h-line asymptotic method with synthetic oceanic data.

Period (h)	h (km) Seafloor	Surface
100.000	497.115	479.099
56.234	461.622	430.773
31.623	431.955	376.123
17.783	403.426	305.384
10.000	369.801	-
5.623	326.105	-
3.162	-	-

The table shows estimates made for the depth to the good conductor from the h-line from the seafloor and sea-surface apparent resistivity. The apparent resistivity curves are shown in Figure 7.14 and correspond to the oceanic part of the conductivity structure shown in Figure 7.11. The ~ 400 km depth determined for h corresponds to a conductivity increase from 0.1 to 2.0 $S.m^{-1}$ in the original conductivity profile.

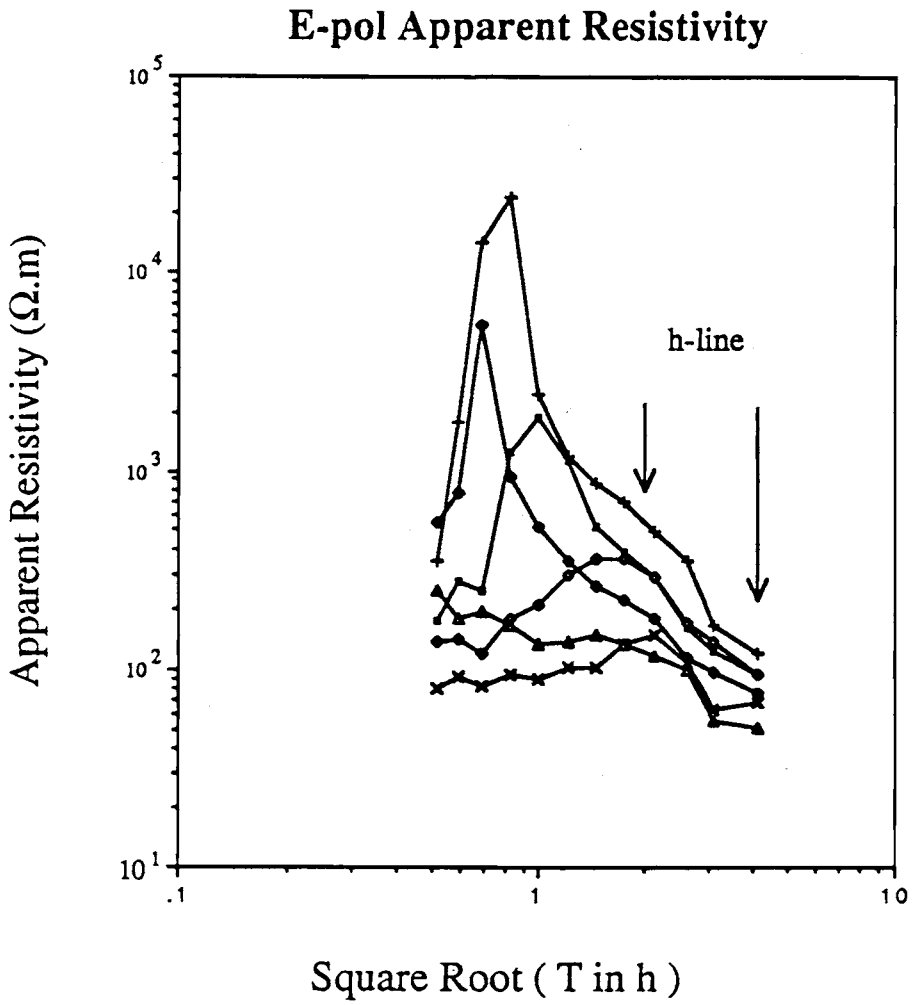

Figure 7.15: Apparent resistivity curves for the E-pol impedance at each of the Tasman Project sites. The symbols represent the following sites: + = TP1, filled diamond = TP7, filled square = TP6, Δ = TP3, open diamond = TP5 and x = TP4. At periods longer than 4 h each of the sites exhibits a well-defined h-line. Note that the extreme apparent resistivity values at short periods for sites TP7, TP6 and TP1 are due to 2D effects in the S-line part of the apparent resistivity curves.

the sites show a reasonably well-defined h-line over the period range between 4.4 and 16.7 h. At 32.5 hours (not shown on Figure 7.18) results are more erratic as error bars become large compared with the magnitude of the apparent resistivity. Table 7.7 lists the values derived for h using the asymptotic method for the period range of 4.4 to 32.5 h and average values of h for each site. As suggested by the reasonably smooth h-lines, the values for h do not vary greatly with frequency. The interpretation of the results for h is made in chapter 9 after 1D inversions have been performed on data from the central Tasman Sea sites. At this time it is noted that the depth to the good conductor varies significantly between the different seafloor sites. It is most shallow at sites TP3 and TP4 in the middle of the Tasman Sea. The good conductor becomes deeper at sites nearer the Australian continent and beneath the Lord Howe Rise at site TP1.

Thin-sheet or other 3D modelling should eventually be used to assess the validity of the E-pol impedance term derived for the Tasman Sea. Because of the strong anisotropy in the Tasman Sea it is likely the estimate is reasonable. Since the Z_{HD} term dominates the other raw impedance tensor elements the processes of rotation and deskewing the tensor change this term by only a small amount. The processes are therefore unlikely to introduce large errors into the term.

Table 7.7: Use of h-line asymptotic method with Tasman Project data.

Period	Depth to Conductor, h (km)					
(h)	TP1	TP3	TP4	TP5	TP6	TP7
32.5	1152 ± 399	712 ± 123	787 ± 691	1640 ± 1765	1352 ± 1702	1046 ± 951
16.7	957 ± 127	624 ± 63	726 ± 155	844 ± 185	843 ± 133	761 ± 122
9.6	856 ± 132	497 ± 63	528 ± 93	782 ± 135	741 ± 89	654 ± 80
6.8	1049 ± 129	557 ± 62	584 ± 81	726 ± 114	715 ± 83	597 ± 74
4.4	999 ± 70	485 ± 34	548 ± 49	770 ± 77	770 ± 58	604 ± 46
Av.	**983**	**548**	**582**	**787**	**768**	**644**

The average value of h for each site (shown in bold) is an arithmetic mean of the individual estimates weighted in inverse proportion to their error. The errors are 95 % confidence limits on the E-pol impedances.

Summarising the results for the E-pol and B-pol Tasman Sea impedances, it is concluded that at all sites significant 2D effects are likely to occur in the B-pol impedances while at sites TP6, TP7 and TP1 strong 2D effects are also likely in the E-pol impedances. The E-pol impedance at site TP4 should be a close estimate of the 1D impedance corresponding to the underlying conductivity structure, and the E-pol impedances at sites TP3 and TP5 should be relatively close to the 1D results. The 2D effects in the E-pol impedances do not affect the h-line part of the apparent resistivity curves and thus it is possible to use the h-lines to estimate the depth to the good conductor beneath the seafloor sites.

7.3 Three-dimensional Magnetotelluric Response

Skew

From the examination of time series, coherences and induction arrows in chapter 6 it is established that near the Australian coast transverse electric currents are deviated to flow parallel to to the coast. This process will create a significant Z_{11} impedance term, as currents initially induced by B_1 end up flowing in the E_1 direction, and a significant skew angle will result. The hypothesis that the much larger skew angles near the Lord Howe Rise are due to similar deflection of currents by this feature will now be examined.

If the observed skew is attributed to distortion of the electric current flow (as in the case of static distortion) then the skew angle indicates the angular deflection of the currents. At TP1 the skew angle is 36° and at TP3 it is 24° (Table 7.5) and as stated above, the sign of the skew angle is consistent with an anticlockwise deflection of north-south flowing currents. Consideration of the geometry of the Lord Howe Rise suggests that it could cause such a deflection. The Lord Howe Rise would however produce a clockwise deflection of east-west flowing currents which would contribute to a negative skew angle. Because of the impedance anisotropy, this contribution to the skew angle will however be much smaller than that from the north-south currents.

The observed skew angles at sites TP1 and TP2 are less than the angle between the trend of the Lord Howe Rise and the principal impedance axes (defined by the horizontal magnetic field) ie. ~ 60°. It is therefore concluded that the electric current flow is only partly deflected by the Lord Howe Rise. Because the electric current flow in the ocean occurs in a thin-sheet manner it is envisaged that partially deflected currents flow along and up the flank of the Rise. The decrease of the skew angle to the west suggests that the degree of deflection of currents decreases with distance from the Rise.

It is possible to make a semi-quantitative interpretation of the observed skew angle near the Lord Howe Rise. In this (non-physical) interpretation the electric current system is modelled as two layers, an upper layer in which currents are undeflected by the Rise and

a lower layer in which currents are totally deflected to flow parallel to the Rise. The method (which takes into account the impedance anisotropy) determines what relative thickness of the two layers gives the observed skew angle. It is found for site TP1 that about 70 % of the electric current flow is deflected by the Lord Howe Rise. For site TP3, which is approximately 350 km from the Lord Howe Rise the proportion of deflected currents is reduced to around 55 %.

Although this interpretation of the electric current flow is based on a non-physical representation, it should still give a reasonable estimate for the relationship between the bathymetry and the observed skew angles. The results suggest the observed skew angles are plausibly explained by the form of the Lord Howe Rise. An 'equivalent 70 % current deflection' at site TP1 seems very realistic when it is considered that the decrease in ocean depth at the Lord Howe Rise, from around 4500 m to 1500 m, is also of order 70 %. The result for TP3 is also realistic when the large distance-extent of ocean B-pol type anomalies (which would cause the current deflection) is considered.

Theoretical Estimates for Three-dimensionality

A number of studies have examined the MT response of electrical conductivity models which are dominantly 2D but contain some 3D perturbation (eg. Weidelt 1977, Ting & Hohmann 1981). Jones (1983) describes a theoretical model study by D. McKirdy of a finite-length strait between two continents (Figure 7.16). In this study, 3D effects were examined as the length-to-breadth ratio of the strait, τ, was varied. For the B-pol mode (electric field perpendicular to the strait), 3D effects persist at a point mid-way along the strait for values of τ as large as 12. For the E-pol mode the electric and magnetic fields reach 2D values at τ equal to 6. Although this study is not directly applicable to the Tasman Sea, which is much wider than a strait , the results do show the dependence of 3D effects on the linear extent of the 2D structure, and also that the distance extent of 3D effects is longer for the (approximately) B-pol mode.

Jones (1983) defines a "3D current channelling number", based on the ratio l / δ_h where l is the distance-extent of the 2D structure and δ_h is the skin-depth in the host medium. He indicates that when $l / \delta_h >> 1$, a 2D interpretation of the data should give approximately the correct conductivity structure. This measure accounts for the dependence on α noted in McKirdy's results but does not differentiate between the E-pol and B-pol modes.

For the Tasman Sea the extent of the 2D structure is estimated to be of order 1100 km, the distance from the Tasman Project line to the 2000 m contour to the south of Tasmania.

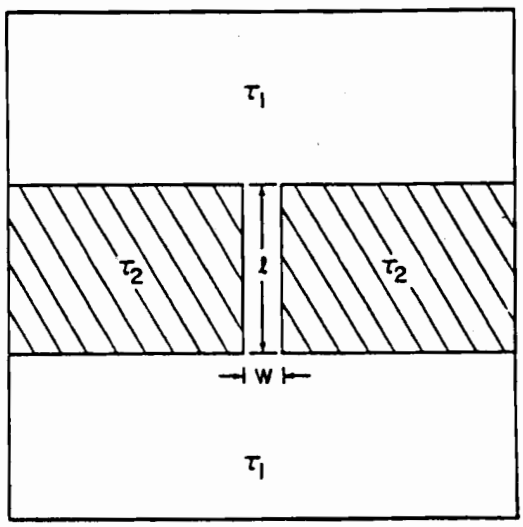

Figure 7.16: Conductivity model used by D. McKirdy to investigate 3D effects in electric and magnetic field data. The resistivity of the continents (striped regions) is set to be 30 times that of the oceans and the strait width is set to 1/3 of the skin depth in the underlying medium.

At higher frequencies where current channelling through Bass Strait becomes significant (Dosso et al. 1985) a more appropriate distance for sites in the western Tasman Sea may be the distance from the recording line to Bass Strait ie. 400 km. The depth scale is estimated using equation 4.85 and ranges from 570 km at 17 h to 45 km at 1.0 h. These depths are derived from the MT response of oceanic part of the theoretical conductivity model shown in Figure 7.11 (since this model reproduces the observed distance-extent of the 2D effects well). The data lead to ratios of l / δ_h for the Tasman Sea ranging of ~2 at the longer periods to >10 at shorter periods.

These numbers suggest that 3D effects in the Tasman Sea should be restricted to the longer periods (greater than ~ 10 h). Evidence from induction arrows and SFMT impedances shows that this conclusion is incorrect. Large-scale 3D effects, such as the skew, persist to short periods as do longitudinal induction arrow components at sites near the Australian coast. The discrepancy between the theoretical and observed results probably stems from the neglect of the electrical resistance (cf. the conductance) in defining the current channelling number. As shown by 2D modelling the extent and strength of B-pol (or galvanic) anomalies depend strongly on the integrated crustal resistivity. It is therefore probable that 3D effects, especially those involving the build-up of electric charge, will also depend upon the integrated resistance.

7.4 Vertical Gradient Sounding Impedance Estimates

Evidence from the SFMT impedances suggests that the 3D effects in the electric and magnetic fields in the Tasman Sea are due to large-scale 3D geomagnetic induction. The evidence for 3D induction includes the large-scale variation in the skew angle across the Tasman Sea and the small departures of the distortion elements from a 2D form. The large adjustment distance determined from the B-pol impedances also suggests 3D induction must occur since much of the Tasman Seafloor lies within 1000 km (ie. the distance B-pol effects extend) of non-parallel conductivity boundaries at the Australian continent and the Lord Howe Rise. Further information on 3D effects may be obtained from estimates of the seafloor impedance obtained using the vertical gradient sounding method.

It has been shown that E-pol effects should be small at sites TP3, TP4 and TP5 in the Tasman Sea. Any differences between the SFMT and VGS estimates of the E-pol impedance at these sites must therefore be due to 3D effects. Such differences would indicate that the seafloor electromagnetic fields do not possess the correct 1D relationship with the sea-surface fields at the site, and could be used to provide information on the 3D process.

For the VGS analysis, site CMO was chosen to represent the surface magnetic field. The VGS calculations are made assuming a uniform source-field and therefore no correction is required for the different conductivity profile at CMO and the seafloor site (see equation 4.118). Preliminary calculations suggest this assumption is reasonable at the source-field uniformity derived for the Tasman Project data determined in chapter 6. However the assumption should be verified in the future using final conductivity profiles for the Tasman Sea.

In the VGS calculation for each seafloor site, the horizontal magnetic field time-series from CMO was rotated to the same angle (relative to magnetic north) as the principal axes at the seafloor site. Power spectra were determined using all the available time series segments (Table 6.2), and then the transfer function R_2, between B_2 at CMO and B_2 at the seafloor site, determined using the standard least-squares method. The transfer function

R_2 is converted into the corresponding Z_{12} (E-pol) impedance with equation 4.115 and using the ocean depth given in Table 2.1, and an ocean electrical conductivity of 3.3 $S.m^{-1}$.

Figure 7.17 compares the E-pol impedance determined for sites TP3, TP4 and TP5 using the VGS and SFMT methods. Systematic differences are observed between the VGS and SFMT impedance estimate at each of the sites. At all three sites the VGS impedance magnitude is less than the SFMT impedance magnitude, by a factor which decreases from approximately 3 at the lowest frequency bands to approximately 1 at the highest frequency bands. Despite these differences each VGS magnitude versus frequency function has a very similar form to the corresponding SFMT magnitude function. For example, at site TP4, both curves show an identical deflection at the frequency of 0.15 cph. The differences between the VGS and SFMT phase estimates are less uniform. Although the VGS and SFMT phase estimates agree well in the frequency range 0.15 to 10 cph, at higher and lower frequencies, the VGS phase estimates are significantly smaller than the SFMT phase estimates. The differences between the VGS and SFMT results become larger towards the eastern sites.

The VGS estimates will be influenced by source-field differences between site CMO and the seafloor sites. The decrease of B_D crosspower as a function of increasing inter-site distance (chapter 6) will produce a corresponding decrease in the R_2 transfer function which will in turn affect the VGS impedance estimate. From the estimates of the source-field B_D scale-length made in chapter 6 it is possible to make a simple correction to R_2 to correct for the source-field non-uniformity. The source-field study and the VGS study are both based on the same time series segments and any errors introduced by using B_D results to correct B_2 data will be small.

Table 7.8 lists the source-field correction factors determined for the R_2 transfer function. The correction factors increase the value of R_2 by between 5% (for the longest period bands at TP5) and 90% (for the shortest period bands at TP3). Corrected VGS impedance estimates are shown in Figure 7.17; the correction for source-field non-uniformity reduces the VGS impedance magnitude and slightly increases the phase. The difference between the SFMT and corrected VGS impedance magnitude is similar at all sites and very close to a frequency-independent factor of two. The uniformity of this result increases confidence regarding the validity of the source-field correction.

The correction does not however greatly improve the differences between the VGS and SFMT phase estimates. It is improbable that 3D effects cause the differences between the phase estimates when the two magnitude estimates are so closely related and also when the VGS and SFMT phase functions have such a similar form at intermediate frequencies. Contributions to the phase differences may come from source-field phase variations and/or from numerical bias during the transfer function determination. It is possible that there are

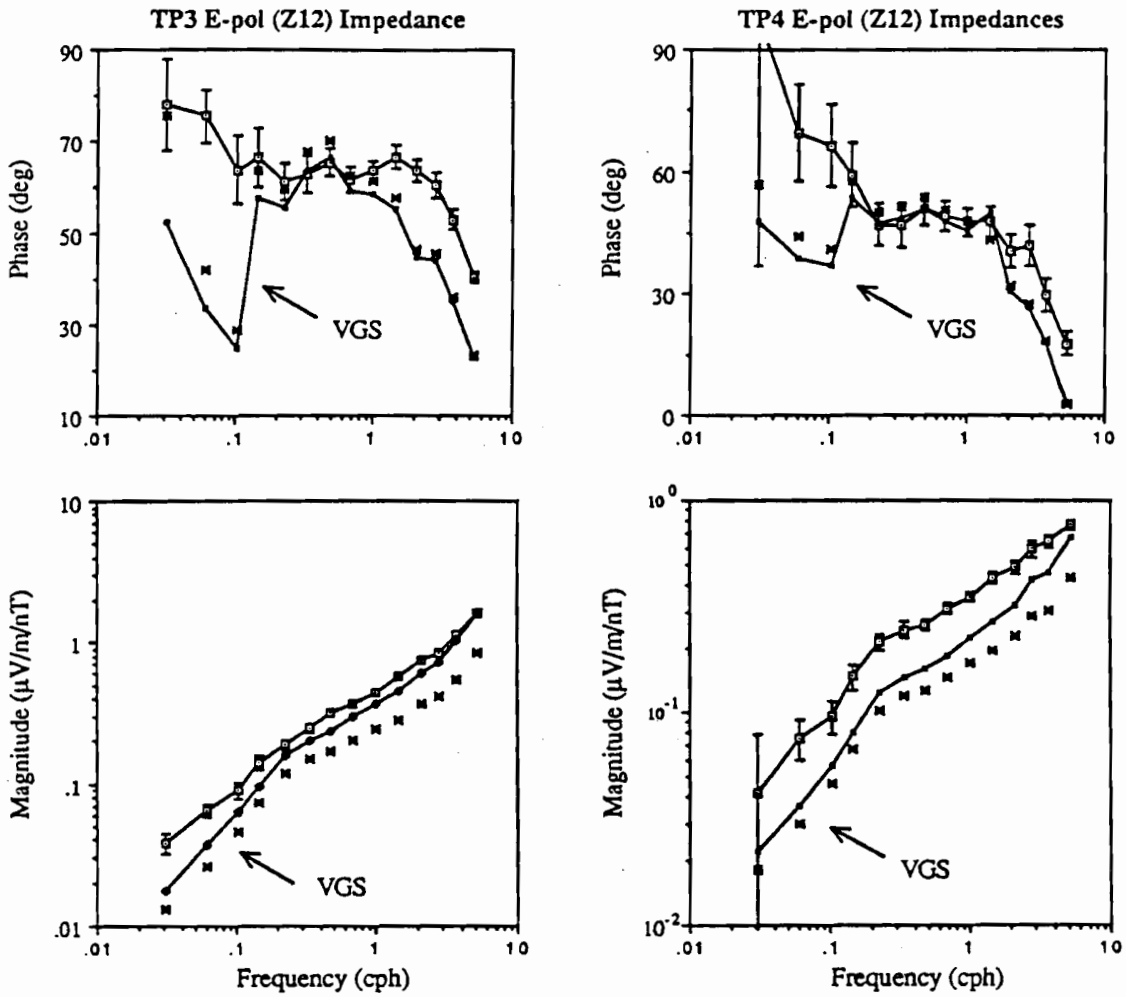

Figure 7.17: VGS estimates for the E-pol impedance at sites TP3, TP4 and TP5. For each site the raw VGS estimate is shown by the filled diamonds and the SFMT estimate by the open squares. The error estimates on the SFMT impedances are 95 % confidence limits. The stars show VGS estimates which have been corrected for the effect of source-field variations between the seafloor site and CMO (which is used as the estimate of the surface field).

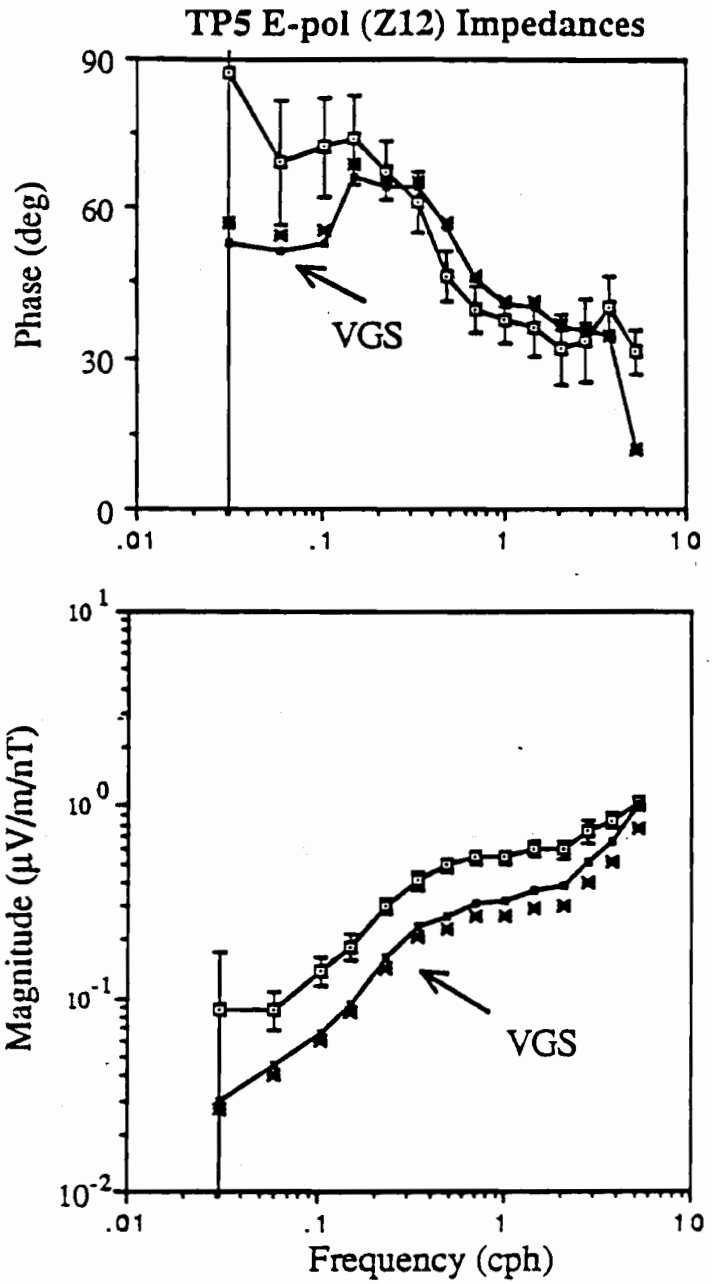

Figure 7.17 cont.

Table 7.8: Source-field correction factors for B_D transfer functions.

Period (h)	Scale Length (km)	Correction for CMO to site TP5	TP4	TP3
32.51	8000	.950	.923	.882
16.65	6500	.939	.906	.856
9.62	5400	.927	.888	.830
6.85	4900	.920	.876	.814
4.44	4300	.909	.862	.791
3.00	3800	.898	.845	.767
2.08	3400	.886	.828	.743
1.44	3000	.872	.808	.714
1.00	2700	.859	.789	.688
0.69	2350	.840	.761	.651
0.48	2100	.823	.737	.618
0.36	1900	.806	.714	.588
0.27	1700	.786	.686	.552
0.19	1600	.774	.670	.532

The source-field scale length for each period is derived from a fit to the source-field results obtained in chapter 6 ie.

$\ln(\text{scale}) = 7.883 + 0.319 \ln(\text{period})$

where the scale-length is in kilometres and the period is in hours. The logarithmic scales used in this function are appropriate for the large errors associated with source-field data however since a correction factor rather than absolute datum is being determined in this analysis, the exact form of the interpolation scheme is not too critical.

The correction factor for the transfer function between B_D at CMO and B_D at the seafloor site is given by

$D = \exp(-d / \text{scale})$

where d is the distance in kilometres from CMO to the seafloor site and 'scale' is the source- field scale length at a particular period. The transfer function should be divided by this correction factor. (Note that the correction factor for the longitudinal component of the horizontal magnetic field, B_2, will be similar to the factor for B_D.)

consistent source-field phase differences between the different sites which could effect th crosspower and thus R_2. This possibility is supported by the observation that the phase differences become larger with increasing inter-site distance. It is recommended that the source-field be examined for such effects. The possibility of numerical bias in the phase estimates is supported by the observation that the largest difference between the SFMT a VGS phase values occur at long and short periods where the SNR is lowest.

The final estimate for the VGS E-pol impedance shows the VGS impedance magnitude is close to 0.5 times the SFMT impedance. This result raises the possibility th the difference is caused by the use of an incorrect scale-value for one set of data during th data reduction. The most likely error would be the use of an HEF scale value which is t large by a factor of two. Careful checking fails to reveal such an error, and therefore the difference between the VGS and SFMT impedance magnitudes must be accepted as a correct result.

Current channelling from outside the Tasman Sea

It has been stated that any difference between the VGS and SFMT estimates is due to 3D induction effects. The effects of non-zero wavenumbers and moving source-fields (a discussed by Chave et al. 1981) vary too strongly with frequency to explain the almost frequency-independent VGS / SFMT differences. One further possible cause for the differences is the channelling through the Tasman Sea, of electric currents from a source outside the Tasman Sea region (of geomagnetic induction). Such currents are envisaged t flow in a simple ohmic manner in the ocean layer. The currents could be induced by non-uniform source-field components and flow in large circuits similar to those of the electric currents induced by the daily variation (eg. Bullard & Parker 1970). In order to influence the VGS and SFMT estimates in the Tasman Sea, the channelled electric currents must have a large component in-phase with the locally induced currents. The possibility that channelled currents cause the difference between the VGS and SFMT impedance estimates will now be examined.

Denoting the observed SFMT impedance by Z_O, the local 1D electric and magnetic fields by E_L and B_L, and the electric and magnetic fields associated with any channelled currents as E_C and B_C one has

$$Z_O = \frac{E_L + E_C}{B_L + B_C} \qquad 7.3$$

It is the aim of the geomagnetic sounding technique to determine the local impedance

$$Z_L = \frac{B_L}{E_L} \qquad 7.4$$

but observations will be biased towards the effective impedance of the channelled current

$$Z_C = \frac{E_C}{B_C} \qquad 7.5$$

If channelling is occurring in the ocean, the observed transfer function between the CMO horizontal magnetic field B_L^S (equivalent to the surface-field without the presence of channelling) and the seafloor horizontal magnetic field will also be altered to give

$$R_O = \frac{B_C + B_L}{B_L^S} \qquad 7.6$$

From equations 7.3-6 and 4.115, the standard 1D VGS form, one may obtain

$$Z_L = \frac{- C_1 Z_C + C_1 Z_O + (Z_C / R_O)}{C_2 Z_C - C_2 Z_O + (1 / R_O)} \qquad 7.7$$

where

$$C_1 = \text{COSH}(\theta_1 h_1) \quad C_2 = \frac{\theta_1}{i\omega} \text{SINH}(\theta_1 h_1) \qquad 7.8$$

Parameters C1 and C2 can be evaluated for a specified wavenumber, frequency and ocean depth / conductivity. Equation 7.7 shows that if the 'impedance' of the channelled current is known then from the VGS and SFMT observations it is possible to calculate the true local impedance.

A problem with this formulation is the necessity of relating E and B of the channelled currents, which formally requires knowledge of the underlying conductivity structure. If sea-surface magnetic field measurements were available above a seafloor site one could adopt a simpler procedure, and use a thin-sheet approximation to relate E to the vertical change in B through the ocean. Nevertheless it is possible to make a preliminary estimate for Z_C using the Biot-Savart law and assuming that the only significant electric current flow occurs in the ocean. This approach assumes that the ocean is underlain by an infinite resistor and therefore that no image currents induced beneath the seafloor by the channelled current.

For a uniform current density J_C in a sheet of infinite width and thickness h the magnetic field at the surface is calculated using the Biot-Savart relationship to be

$$B_C = \frac{J_C \mu h}{2} = \frac{\sigma E_C \mu h}{2} \qquad 7.9$$

For a northward current, an ocean conductivity of 3.3 $S.m^{-1}$ and an ocean depth of 5 km one obtains

$$Z_C = \frac{E_C}{B_C} = - 0.0946 \ \mu V.m^{-1}.nT^{-1}$$

The negative sign arises since at the seafloor, a northward electric current in the ocean causes a westward magnetic field. More advanced models incorporating a finite width for

the Tasman Sea change the Z_C values at TP3, TP4 and TP5 by less than 0.5 %.

Table 7.9 lists the corrected impedance function Z_L obtained for site TP4 by substituting the value for Z_C into equation 7.7 (assuming a uniform source-field). A quick examination of the results reveals that the impedances do not represent meaningful 1D solutions, for example the phase does not lie between 0 and 90°. The results indicate that current channelling cannot explain the difference between the VGS and SFMT impedances. Examination of the relative sizes of the VGS and SFMT impedances reveals that with magnitudes of Z_C less than about 0.2 to 0.3 $\mu V.m^{-1}.nT^{-1}$ (cf. the 0.09 $\mu V.m^{-1}.nT^{-1}$ for channelled currents) it is not possible to explain both the VGS and SFMT differences and return a plausible value for the local impedance.

The approximations made in the use of the Biot-Savart method to estimate Z_C are unlikely to have produced a strong under-estimate of Z_C. The main assumption, regarding the absence of image currents, would have caused the estimate of Z_C to be an over-estimate since any image currents at depth would increase the seafloor horizontal magnetic field and decrease the value of Z_C. Electric currents channelled in ohmic manner from outside the region of geomagnetic induction have 'effective impedances' which are too small to explain the differences between the VGS and SFMT estimates. It is concluded that there is negligible channelling of in-phase currents through the Tasman Sea from outside the region of geomagnetic induction.

The differences between the VGS and SFMT estimates are therefore confidently interpreted as being due to 3D induction effects. From the above calculations it can be seen that the most probable form of these effects is an increase the electric field in the ocean relative to the electric field which would occur in a 1D conductivity structure. It is emphasized that this is part of the geomagnetic induction process and not just a simple enhancement of ohmic current flow (such as channelled currents).

Three-dimensional Models

It is possible to make a preliminary investigation of possible 3D induction effects using 2D modelling. Figure 7.18 shows the VGS E-pol impedance estimated for site TP4 using an ocean conductivity of 1.8 $S.m^{-1}$. The VGS impedance magnitude is very close to that of the SFMT impedance. Although the ocean conductivity of 1.8 $S.m^{-1}$ is physically unreasonable, the result leads to speculation that the difference between the VGS and SFMT impedances could be caused by a B-pol type anomaly reducing the 'effective' ocean conductivity. A source for such a B-pol anomaly is the decrease in the ocean depth to the north of the Tasman Project recording line (Figure 2.1). Two conductivity structures were evaluated using the 2D modelling program in order to examine whether B-pol effects could

Table 7.9: Correction of TP4 E-pol impedances for current channelling.

Period (h) (h)	Magnitude Z_L (μV.m-1.nT-1)	Phase Z_L (deg)
32.5	.01766	-73.1
16.7	.02302	-107.8
9.6	.02669	-91.8
6.8	.00732	-144.1
4.4	.00542	-191.8
3.0	.00540	-209.5
2.1	.00341	-186.5
1.4	.00712	-154.3
1.0	.00620	-128.2
0.69	.01571	-124.5
0.48	.02216	-109.8
0.36	.03455	-107.7
0.27	.03419	-107.9
0.19	.05682	-97.2

The table gives the values for Z_L (the local impedance) at site TP4 determined with equation 7.7 and assuming a uniform source-field and a 5.0 km thick ocean of conductivity 3.3 $S.m^{-1}$. The method used to obtain Z_L assumes the observed differences between the SFMT and VGS impedance estimates are due to the presence of channelled current with an effective impedance of $Z_C = -0.0946\ \mu V.m^{-1}.nT^{-1}$. The resulting values for Z_L are not plausible 1D impedances indicating the channelled current hypothesis is incorrect.

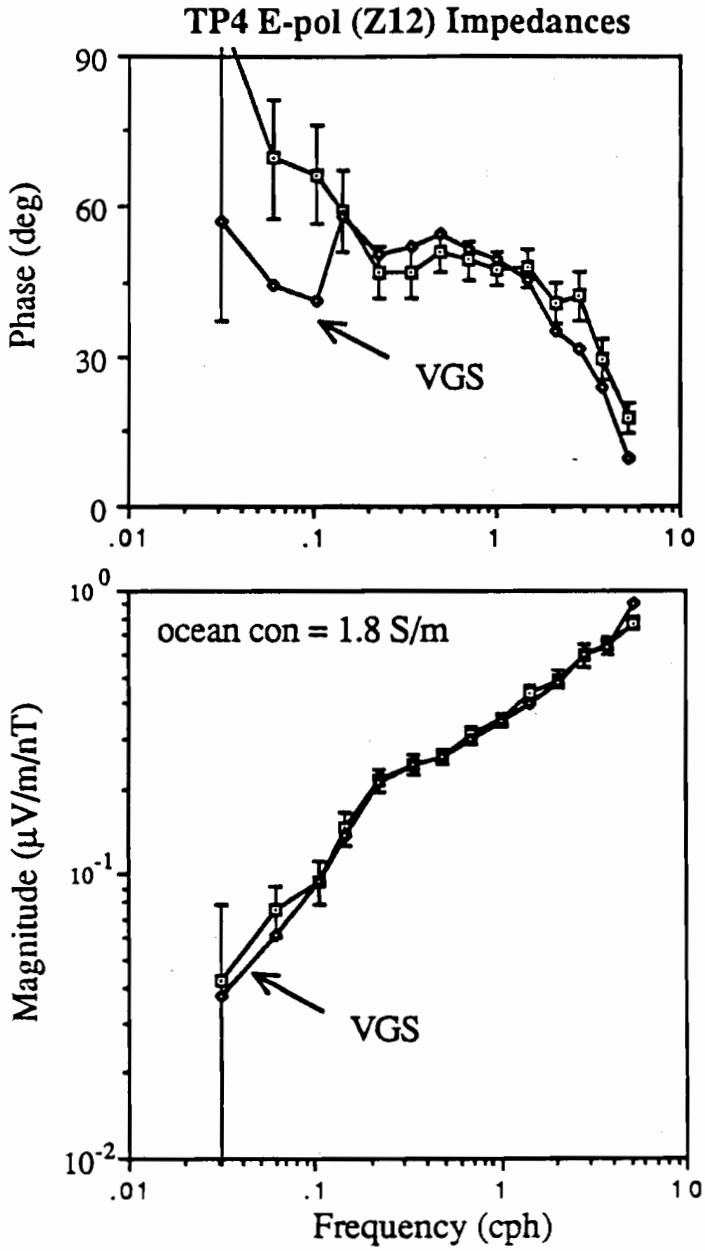

Figure 7.18: Recalculated VGS E-pol impedance at site TP4. For these VGS calculations the conductivity of the ocean was set to 1.8 $S.m^{-1}$ (a physically unrealistic value for the conductivity). The resulting agreement between the VGS and SFMT impedance estimates is however excellent.

in fact explain the difference between the VGS and SFMT impedance magnitudes.

The first conductivity structure is the model continental margin shown in Figure 7.11 and the second structure is a modified form of the first structure in which the coastline has been replaced by a halving of the ocean depth. Results from the 2D modelling show that neither structure produces a significant difference between the VGS and SFMT B-pol impedances. Figure 7.19a shows the VGS and SFMT impedance estimates determined at a range of distances from the model coastline in the first conductivity structure and Table 7.10 lists the results. At distances greater than 10 km from the boundary the SFMT and VGS estimates are in close agreement in both phase and amplitude, with phase differences not exceeding 10° and amplitude differences 10%. This agreement between VGS and SFMT estimates occurs even when the SFMT impedances are significantly distorted from the true 1D result. The addition of a 20 km thick resistive layer (of 5×10^{-6} $S.m^{-1}$) between 30 and 50 km depth does not cause any divergence of the SFMT and VGS estimates and similar results were also obtained at periods of 1 h and 17 h.

It is therefore concluded that for realistic conductivity models it is not possible for B-pol effects to create a factor of two difference between VGS and SFMT estimates. (While it is a negative result in this analysis, the agreement of the VGS and SFMT impedance estimates in strongly 2D models shows the value of VGS measurements. The results indicate accurate seafloor B-pol impedances may be obtained in seafloor experiments based only on magnetic field recordings.)

The E-pol results from the model in Figure 7.11 were examined to see if E-pol effects could cause differences between VGS and SFMT estimates. Figure 7.19b shows a plot of VGS and SFMT impedances against distance from the coast. Significant differences exist between the VGS and SFMT impedance estimates. These differences are relatively independent of frequency (Table 7.10), are dominantly in the impedance magnitude (cf. the phase), and vary only slowly with spatial position. E-pol type effects therefore have the required properties to explain the differences between the VGS and SFMT estimates at the Tasman Project sites.

As stated above it is unlikely that strictly 2D E-pol effects extend from the Australian coastline to sites TP5, TP4 and TP3, and therefore it is unlikely that such effects explain the SFMT / VGS impedance difference. The model results show that a SFMT / VGS impedance ratio of two is obtained only within 50 km of the coastline and that at these locations strong 2D effects are revealed by extreme values of the impedance phase. No such anomalous phase values are observed at sites TP3, TP4 and TP5. It is improbable that any alternative conductivity models for the Australian coastline could cause the strong differences between the VGS and SFMT impedances without producing other detectable 2D effects. The observed SFMT / VGS impedance differences in the Tasman Sea are therefore interpreted as being caused by 3D induction effects which possess a strong E-pol nature.

It is hypothesised that the source for such effects is the constriction of electric current

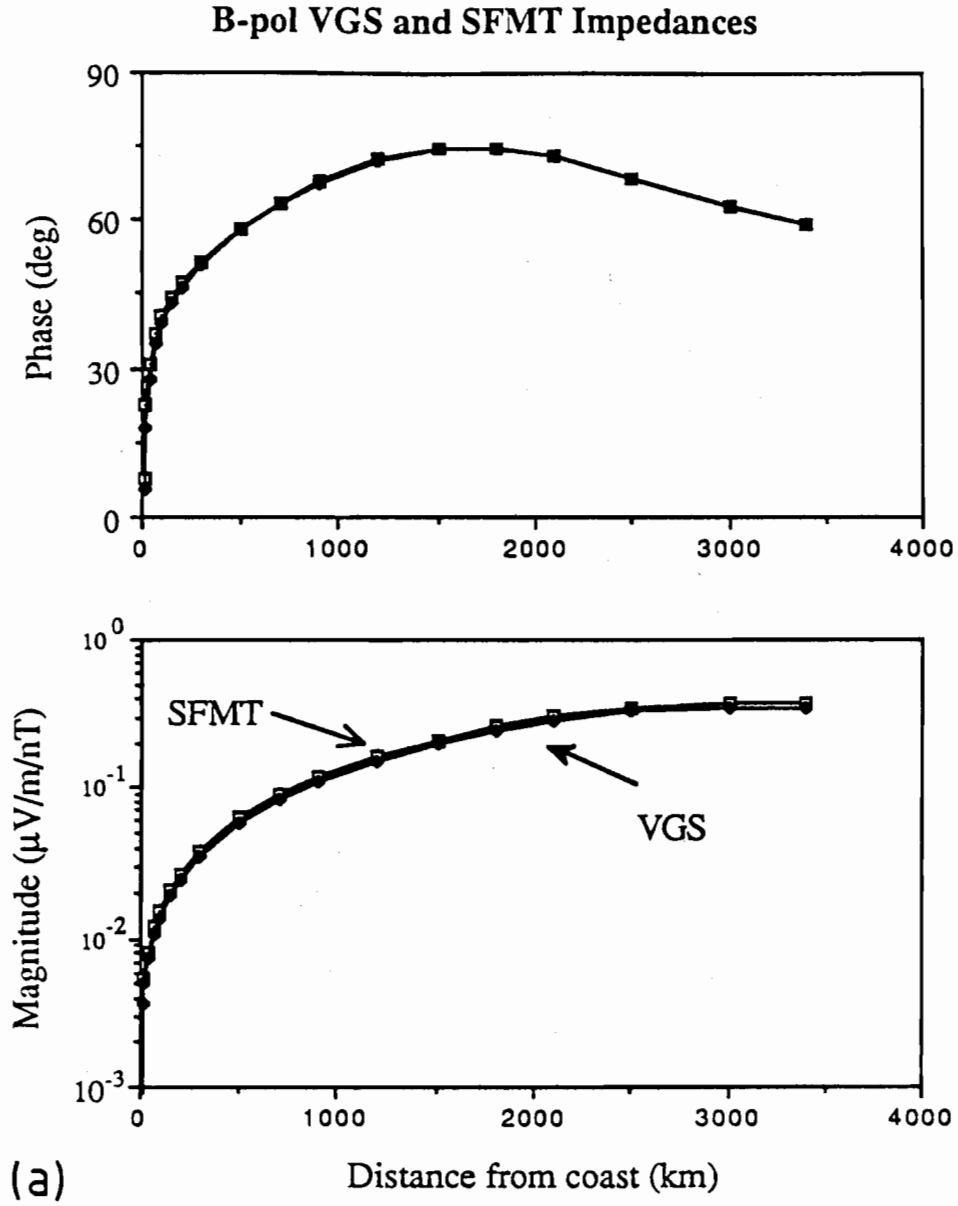

Figure 7.19: SFMT and VGS impedance estimates from 2D data. The diagrams show the two estimates for the seafloor impedance as a function of distance from the model coast. The horizontal electric and magnetic fields are from the conductivity structure shown in Figure 7.11 for the period of 1h.

(a) B-pol impedance component. For this mode there is close agreement between the VGS and SFMT estimates even where the results are strongly distorted from the 1D result (shown by the impedance at large distance from the coastline).

(b) E-pol impedance component. For this mode the VGS impedance magnitude is smaller than the SFMT magnitude. This difference decreases slowly with distance from the coast. The VGS and SFMT phase estimates are very similar. Note the strong distortion of the E-pol impedance phase at small distances from the coast.

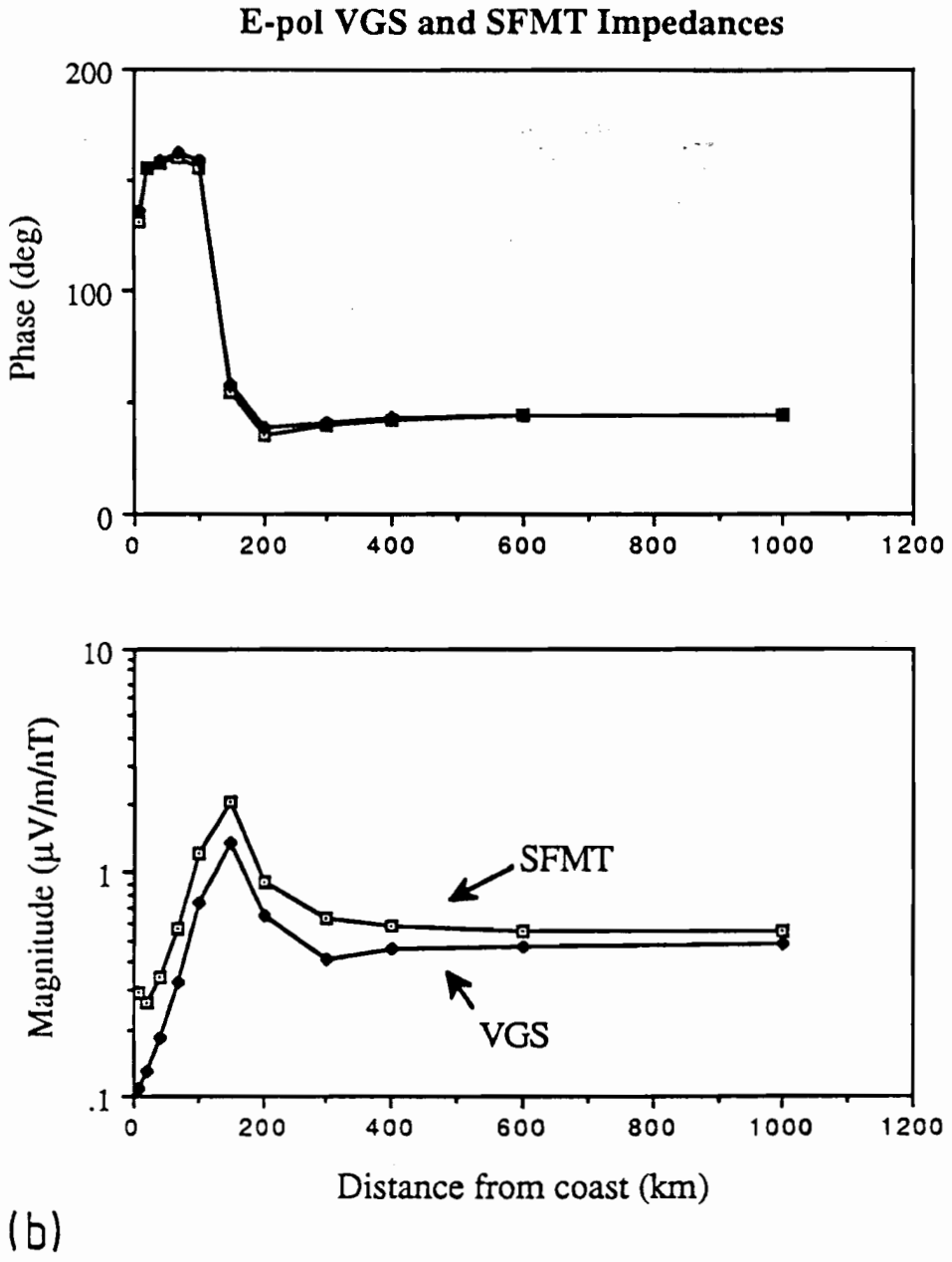

Figure 7.19 cont.

Table 7.10: Comparison of SFMT and VGS impedance estimates.

Period	Impedance ($\mu V.m^{-1}.nT^{-1}$, degrees)						VGS
(h)	SFMT		VGS		1D		SFMT
B-POL model 2, 50 km from coast							
16.67	.0291	76.3	.0273	76.3	.0417	74.3	0.94
1.0	.2638	61.5	.2470	61.3	.3389	54.5	0.92
E-POL model 1, 50 km from coast							
16.67	.0454	77.1	.0262	59.9	.0417	74.3	0.58
2.0	.2356	108.1	.1299	104.6	.2083	60.2	0.55
0.5	.4037	158.9	.2191	160.8	.5194	43.8	0.55
0.25	.4663	-178.7	.2615	-173.6	.6911	30.9	0.56

Table shows the effect of 2D influence on different estimates of the seafloor impedance. The electric and magnetic fields used to estimate the impedance are derived from 2D conductivity models described in the text. Impedances are estimated using the SFMT method (with seafloor E and B fields) and the VGS method (with the seafloor B field and remote surface B field). The 1D solution is for the ocean conductivity profile.

flow in the northern Tasman Sea caused by the merging of the Lord Howe Rise and Australian continental margin. Longitudinal currents induced in the Tasman Sea will cause a charge build-up on the boundary of the Lord Howe Rise. From the seafloor adjustment-distance determined in chapter 6 it is known that the B-pol effects of this charge will extend over a distance of 500 to 1000 km. Longitudinal currents flowing in this region will be affected by the B-pol type anomaly and funnelled towards the centre of the Tasman Sea; the increased current in the central Tasman will be associated with an E-pol type anomaly. A similar deflection will occur for east-west flowing currents, but because the anisotropy caused by the Australian coastline these currents (and associated 3D effects) will be smaller. It is again stressed that these processes are part of the geomagnetic induction and not an ohmic conduction, or static distortion, processes (since a simple ohmic deviation of currents would create a recognizable magnetic field response).

The proposed model for 3D induction in the Tasman Sea is supported by the observed MT impedance skew angles, the observed 3D terms in the distortion elements, and the difference between the VGS and SFMT impedance estimates. It is also consistent with the

3D effects noted in the induction arrow results in chapter 6. As stated above, verification of the proposed pattern of electromagnetic induction in the Tasman Sea, should be possible using 3D modelling techniques such as thin-sheet modelling.

A final question to be answered is how the observed distorted impedances relate to the 'local' 1D impedances. An important feature to note from Figure 7.19 and Table 7.10 is that although the SFMT and VGS estimates may have impedance magnitude functions which differ by a frequency-independent constant, the impedances are not necessarily related to the true 1D impedance by such a constant. Thus the co-incidence of the Tasman sea VGS and SFMT impedances does not directly establish either estimate as the true 'local' impedance. In order to proceed with the MT analysis it is necessary to assume that the undistorted impedance is similar to either the SFMT or VGS E-pol estimate.

This assumption is supported by two arguments. Firstly, the form of the observed MT phase curve at sites TP3, TP4 and TP5 is consistent with a 1D impedance. As shown by the 2D forward modelling (eg. Figures 7.13, 7.19) the phase response is a sensitive indicator of 2D effects and therefore the absence of anomalous phase values in the E-pol impedances at these sites suggests a 1D response. Similarly the smooth frequency-variations of phase at these sites suggests a 1D response (Figure 7.12). The second argument supporting the assumption (that the E-pol impedances are closely related to the undistorted 1D impedance) is that when the Tasman Sea is viewed as a large-scale feature, its form is relatively 2D. Effects caused by the Lord Howe Rise and the finite length of the Tasman Sea are of lesser significance. Although these 3D features will introduce perturbations to the MT response, the E-pol impedance should be dominantly related to underlying conductivity structure. Mathematically, this argument is supported by the large size of the Z_{HD} or Z_{12} impedance tensor element relative to the other impedance tensor elements. Corrections for 3D effects (eg. deskewing) do not greatly change the E-pol impedance element.

7.5 Error and Noise Estimates

Remote Reference Error Estimates

Error estimates for the final remote-reference impedances were calculated using the equations presented in section 4.2 and are listed with the impedances in appendix 6. The statistical measure used for the remote-reference error estimates is the standard deviation (67% confidence limit) which is a smaller statistical measure than the 95% confidence limit used for the LS impedance errors. For the F-distributed random errors characteristic of a transfer function (Bendat & Piersol 1971), the standard deviation errors should be about 0.6 times the 95% confidence limit magnitude. The remote-reference error estimates however depend on more factors than the LS impedance error estimates, for example on the coherence between the remote-reference and SFMT data. For a given statistical measure,

the remote-reference error estimate is expected to be larger, since the remote-reference calculations involve two additional time series and therefore have additional sources for random errors.

Table 7.11 lists the LS and remote-reference error estimates for the E-pol impedance at site TP5. The data do not reveal a consistent relationship between the remote-reference and LS errors. Over most of the period range the remote-reference errors are smaller than the LS errors by a factor of about two however at the shortest periods the remote-reference errors larger than the LS errors. For the other SFMT sites, the E-pol remote-reference errors are larger than the LS errors at TP7, comparably sized at TP6 and TP1, and smaller at TP5, TP4 and TP3. These results suggest the remote-reference errors are more sensitive to high noise levels (as present at sites TP7 and TP6) than are the LS error estimates. For the B-pol impedance component, the remote-reference errors are smaller than the least squares errors at all sites.

Table 7.11 also lists various other parameters which may be used to indicate error levels. The partial coherence of E_1 with B_2 is only slightly less than the multiple coherence of E_1 with B_1 and B_2 reflecting the small E_1-B_1 coherence after the deskewing of the data. For the shortest period bands the coherence becomes very small, and as can be seen from the table, the level of noise is much higher than the level of signal in these bands. The relative confidence limits are still small for these bands because the results are based on large numbers of degrees of freedom. (As has been mentioned above, results from such bands are often anomalous, suggesting the possibility of accumulated bias errors.) The re-calculated multiple coherences are shown in Table 7.10 and indicate a much improved coherence level after correction for the magnetic field noise (also see section 4.2). It is inappropriate to re-calculate confidence limits based on the re-calculated multiple coherences, since the the remote-reference method does not decrease the random errors on which the confidence limits are based.

Table 7.12 lists the standard deviation for the E-pol (Z_{12}) impedance at each of the SFMT sites. Of particular note are the errors on the TP3, TP4 and TP5 impedance since these errors will be used as error estimates for 1D inversions. The largest errors occur at sites TP6, TP7 and TP1 and the smallest errors at TP3. The errors at TP4 and TP5 are slightly larger than expected from an examination of errors at the adjacent sites, reflecting the smaller number of time series segments used in the derivation of the TP4 and TP5 impedances.

The smallest errors occur in the period range of one to two hours with the error magnitude increasing at longer and shorter periods. Within the period range of 1 to 16 h error magnitudes are less than 10 % (of impedance magnitudes) at all sites and except for sites TP7 and TP1, the errors are also less than 10 % in the short-period range between 1.(and 0.36 h. For the period range of 16.7 to 0.36 h, the main band range used in the MT inversions, the average errors at sites TP5, TP4 and TP3 are; 6 %, 4 % and 3 %.

Table 7.11: Error Estimates for TP5 E-pol Impedance.

Period	Mul. coh	Par. Coh	Noise/Signal		95% cl	σ	Recal.
(h)	$\gamma^2_{E1.B1B2}$	$\gamma^2_{E1B1.B2}$	S_{E1E1}	S_{B2B2}	$\lvert Z_{12} \rvert$	$\lvert Z_{12} \rvert$	Mul.Coh
49.951	.1330	.0506	5.71	.041	2.322	.6658	.1518
32.508	.5943	.4881	.69	.057	1.076	.2693	.5938
16.650	.7528	.7521	.24	.076	.2189	.0868	.8087
9.615	.8055	.7945	.12	.109	.1729	.0781	.8992
6.849	.8402	.8219	.073	.098	.1573	.0769	.9351
4.443	.6874	.6750	.039	.36	.0998	.0605	.9764
2.999	.6552	.6027	.045	.53	.1081	.0541	.9708
2.079	.5819	.5502	.14	.52	.0888	.0462	.8886
1.442	.6715	.6390	.15	.29	.0783	.0358	.8708
1.000	.5127	.5073	.41	.38	.0778	.0347	.7159
0.693	.3597	.3596	.90	.47	.0995	.0435	.5337
0.481	.1329	.1153	3.00	1.05	.1190	.0614	.2522
0.357	.0513	.0405	6.25	2.29	.1427	.0982	.1384
0.267	.0256	.0206	9.08	3.00	.1065	.1059	.1013
0.190	.0018	.0002	11.8	83.8	.0761	.1238	.0164

The table gives various measures of the random error estimates for the TP5 E-pol impedance component. The partial, multiple and re-calculated multiple coherence are defined in chapter 4. The noise/signal ratio is given for the E_1 and B_2 and is the inverse of the standard SNR. Note that the confidence limit and the standard deviation have been divided by the impedance magnitude.

Table 7.12 : Standard Deviations for E-pol (Z_{12}) Impedances

Period	Relative Error					
(h)	TP7	TP6	TP5	TP4	TP3	TP1
49.951	.3808	2.5692	.6658	.4384	.1368	.2991
32.508	.2450	.3342	.2693	.1635	.1036	.1211
16.650	.0677	.0632	.0868	.0947	.0579	.0741
9.615	.0605	.0571	.0781	.0291	.0508	.0754
6.849	.0615	.0610	.0769	.0456	.0428	.0523
4.443	.0527	.0601	.0605	.0614	.0419	.0512
2.999	.0486	.0552	.0541	.0432	.0360	.0500
2.079	.0433	.0523	.0462	.0317	.0291	.0397
1.442	.0436	.0651	.0358	.0280	.0209	.0369
1.000	.0462	.0700	.0347	.0229	.0167	.0478
0.693	.0731	.0678	.0437	.0265	.0217	.2030
0.481	.3347	.0397	.0614	.0298	.0248	.1805
0.357	.2223	.0522	.0982	.0449	.0298	.0817
0.267	.1792	.0509	.1060	.0469	.0334	.0315
0.190	.1084	.0584	.1238	.0666	.0480	.0217

The table gives the magnitude of the standard deviation divided by the magnitude of the corresponding impedance term.

Signal / Noise Separation

Using the methods described in chapter 4 and with CMO as the remote-reference, signal / noise separations were performed for the power spectra at the SFMT sites. The full results may be found in appendix 6 however some of the important features of the separation will be now illustrated. Figure 7.20 illustrates the signal and noise spectra at sites TP6 and TP3. The figure shows that the noise levels are similar for B_1 and B_2 and for E_1 and E_2 suggesting that the noise is isotropic in the horizontal directions. As stated above, the noise is attributed mainly to induction of electromagnetic fields by the moving ocean water. The changes in slope of the horizontal electric field and magnetic field spectra (eg. the flatter slope of the electric field spectra at periods shorter than 10 h) are associated with the different types of water motion (eg. eddies, internal waves) and the different modes of electromagnetic induction the different types of water motions cause.

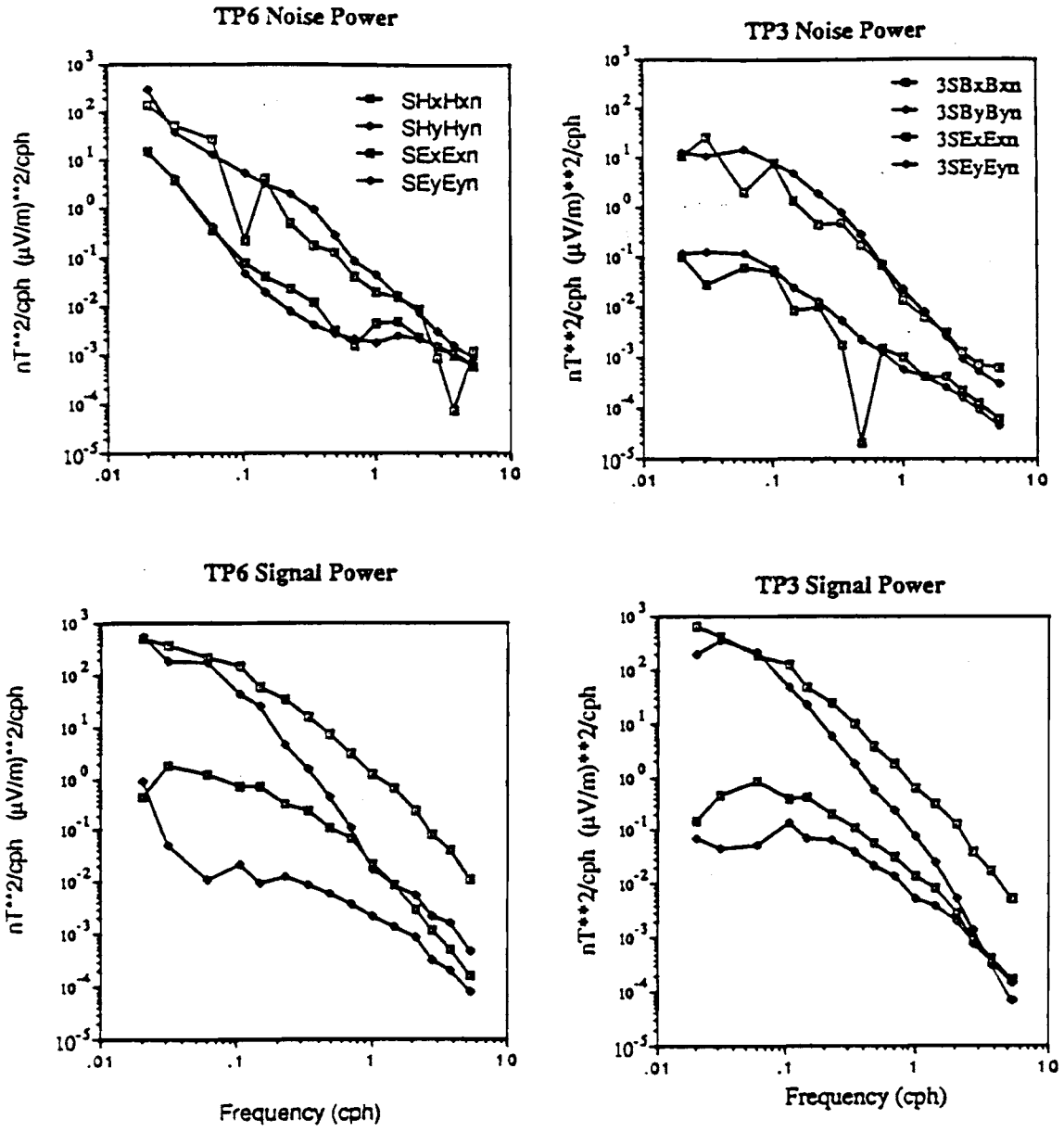

Figure 7.20: Separated signal and noise spectra for sites TP6 and TP3. Note the similar levels of noise B_1 and B_2 and also on E_1 and E_2, suggesting that at each site the noise is relatively isotropic in the horizontal directions. In contrast there are large differences between the longitudinal and perpendicular components of the signal spectra. The occasional erratic points in the spectra are attributed to numerical instability of the data, probably resulting from the subtraction of two quantities which both contain random errors. In this figure the traces labelled with suffixes x and y actually refer to the (similar) directions 1 (parallel to Tasman) and 2 (perpendicular to Tasman).

Figure 7.21 shows the noise spectra for the electric and magnetic fields at each of the SFMT sites. The smoother form of the B_2 and E_2 spectra suggests these components are more accurately estimated using the signal / noise separation method. For frequencies between 1 cph and 0.1cph the magnetic field noise levels are similar at all sites suggesting a uniformity of the oceanic processes inducing the noise at these periods. At higher frequencies, the B_2 component at site TP3 contains less noise than at the other sites and at low frequencies, site TP6 has significantly more noise than the other sites. The higher level of the noise in the TP4 B_1 component at frequencies above 1 cph follows a 1/frequency slope and is attributed to an instrumental source (see chapter 3). For the electric field data there is a relatively similar noise level at all sites in the decade between 0.1 cph and 1 cph, but at higher frequencies the effect of 1/frequency distributed noise becomes significant for a number of components (see chapter 3). At longer periods the TP6 electric field components have the highest level of noise, reflecting the strong eddy activity at this site. Site TP3 has the smalles level of low-frequency noise.

Figure 7.22 compares the signal and noise spectra for the "quietest" and "noisiest" sites: TP3 and TP6. Although the noise level is similar for the two magnetic field components and for the two electric field components, differences in the signal levels cause the SNR to vary widely between the parallel and perpendicular field components. Smaller B_2 and E_2 signal levels are associated with low SNRs for these components.

At site TP6 the SNR for S_{B1B1} lies between 10 and 30. In contrast the SNR for S_{B2B2} close to 1 for much of the frequency range, indicating comparable levels of signal and noise in the B_2 time series. The B_2 magnetic field component is used in the E-pol impedance estimate on which the 1D MT inversions described in chapter 8 are based. The high noise level on the B_2 component confirms that the application of a noise-reduction technique to the Tasman Project data was essential in order to obtain unbiased impedance estimates. Figure 7.22 show the existence of a 'window' in the oceanic noise spectrum where a level of SNR suitable for MT analysis occurs. At frequencies less than 0.5 cph and greater than 2 to 5 cph the oceanic noise overwhelms the available ionospheric signal and excludes effective SFMT studies.

At site TP3 the SNRs are much higher than at TP6, partly because of reduced noise level and partly because of increased signal levels relative to TP6. For the horizontal electric field at TP3, the signal level exceeds or is comparable to the noise level for all the frequency range (Figure 7.22). For much of this range the signal power is a decade higher than the noise power. For the B_2 component used in the E-pol impedances, the SNR decreases to small values at high frequencies, but drops below 2.0 only at frequencies above 2 cph. The data at site TP3 will therefore permit a much wider band SFMT analysis than will the data from TP6.

It is valuable to consider an estimate of the amplitude of the noise in the time domain. Using equation 3.3 one can obtain the amplitude (standard deviation) of time-domain Gaussia

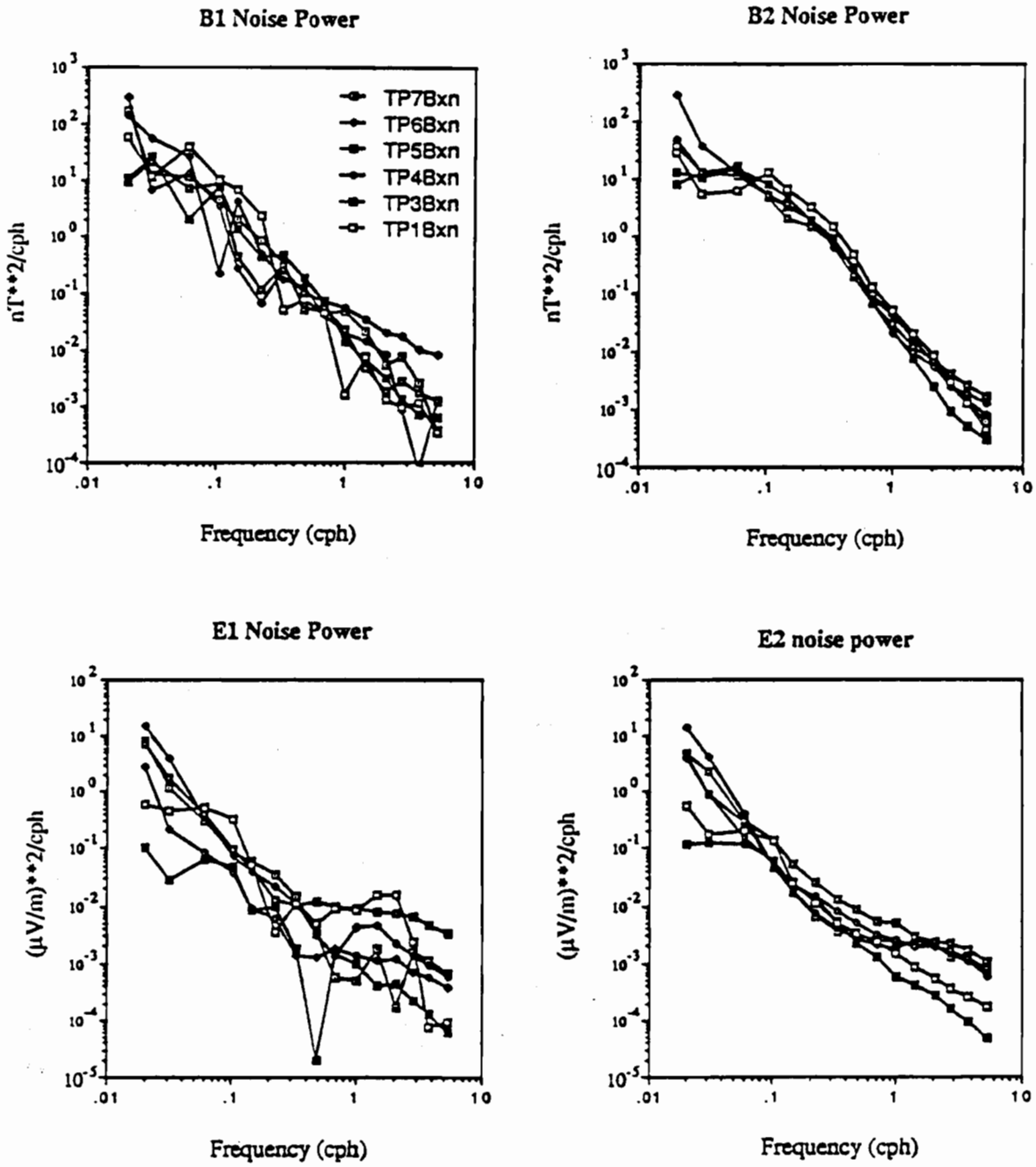

Figure 7.21: Noise spectra for the horizontal magnetic and electric field components at the seafloor sites. The symbols denoting the seafloor sites are the same in each panel; the key is given in the upper left panel.

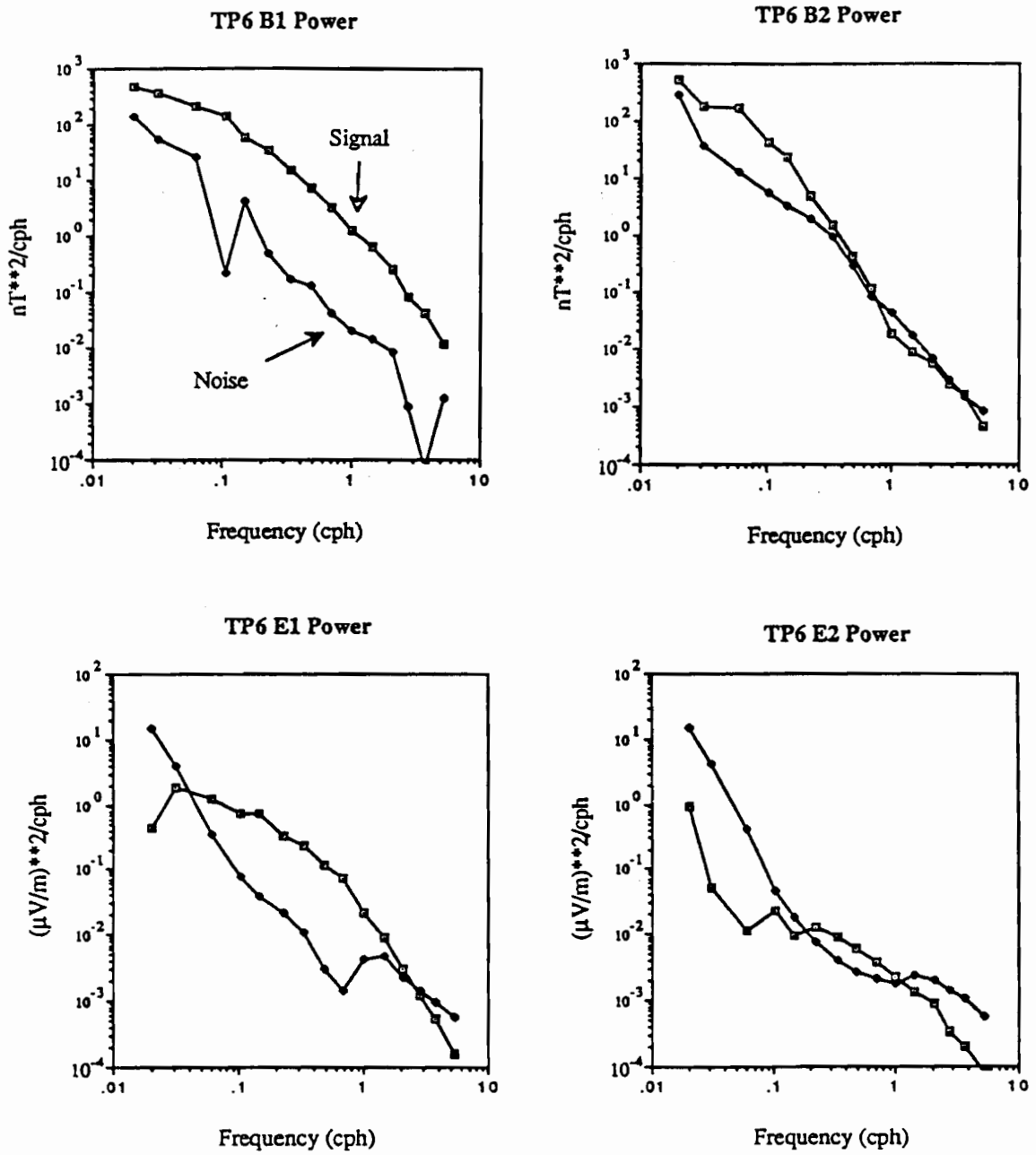

Figure 7.22: Signal and noise spectra for the individual components at site TP6 (a "noisy" site) and site TP3 (a "quiet" site). The MT inversions in this thesis are based on the E_1 and B_2 components. Note the narrow window available for satisfactory SFMT results at site TP6.

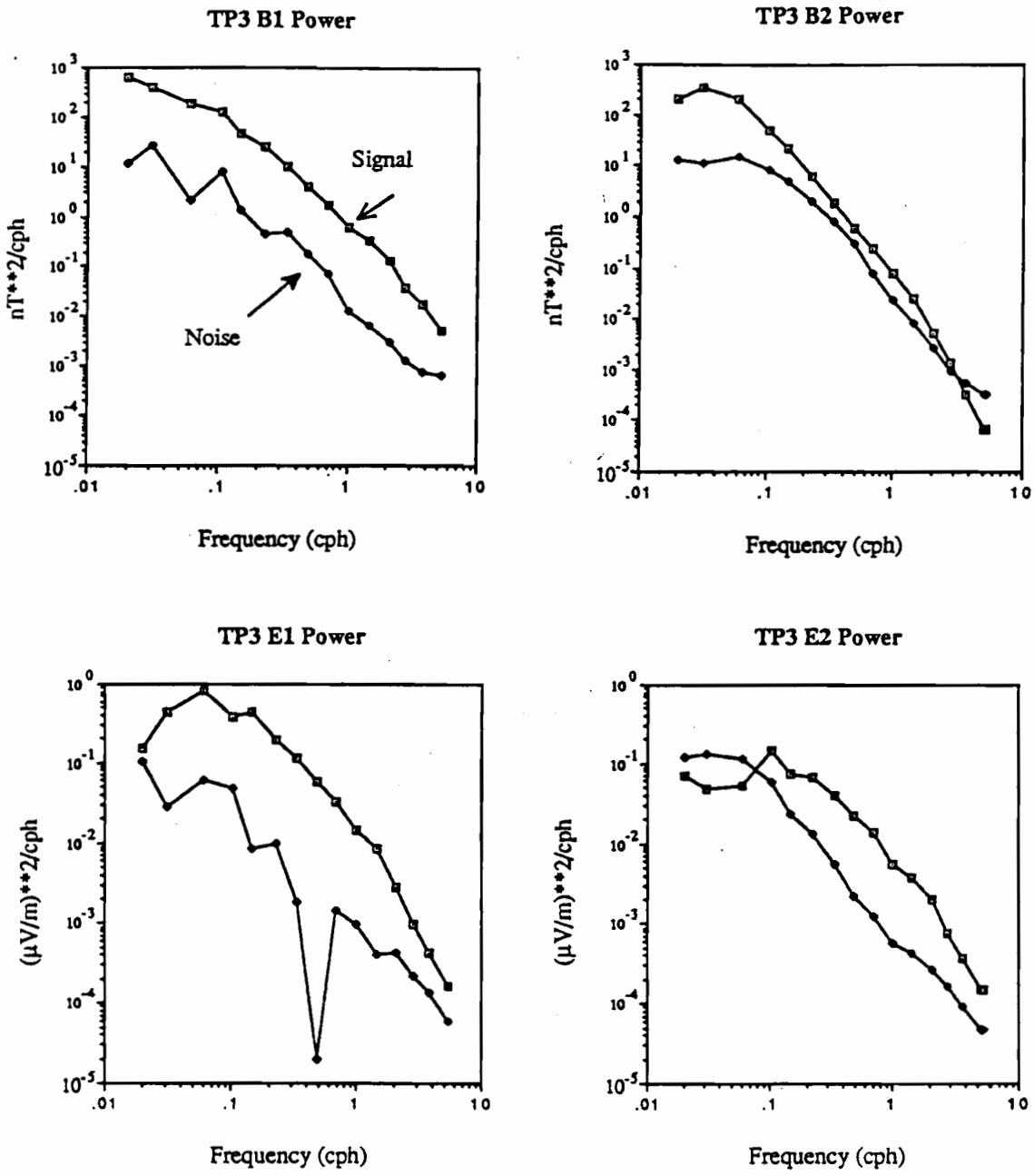

Figure 7.22 continued

noise which would produce the same power as observed in the noise spectra. (The actual time-domain noise structure is clearly not Gaussian though, since such noise would have a white spectrum.) For site TP3, at the period of 1 h, the standard deviation of equivalent Gaussian noise is 0.3 nT for B_1, 0.5 nT for B_2, and 0.07 $\mu V.m^{-1}$ for E_1 and E_2. These values are consistent with the observed SNR and the observed magnitude of signal fluctuation in the time series.

The signal / noise separation method could possibly be used to assess the noise levels at the remote reference (CMO and EYR) sites. Any correlated noise between the magnetic and electric field components at the SFMT site will however bias this separation. Results from such an analysis are therefore not presented here.

Correlated Noise Between Seafloor Sites

As described above, preliminary remote-reference calculations reveal the presence of correlated noise between the different seafloor sites. An examination of the magnitude of this correlated noise will now be made. Because of the probability that the noise is also correlated between the magnetic and electric components, absolute results will not be attainable without more detailed calculations than those described here.

Effects observed when using seafloor electric or magnetic field recordings as the remote-reference are as follows. When a seafloor MAG recording is used, the signal / noise separation indicates a large decrease occurs in the B_1 noise level and a smaller decrease in the B_2 noise level. When a seafloor HEF recording is used, a decrease occurs in the E_1 and E_2 noise levels. The decreased noise levels occur because correlated noise between the remote-reference and SFMT components is interpreted as signal rather than noise. This process also causes the impedances to be biased and affects the signal / noise separation for the field (magnetic or electric) not used as the remote reference. For example, the use of a seafloor magnetic field as the remote reference also causes a large increase in the E_1 noise level and the use of a seafloor electric field as the remote reference causes an increase in the B_1 noise level.

If it is assumed that the correlated noise between the remote reference and the SFMT data occurs only on individual pairs of components (for example H_1,R_1 or E_1,R_1) then the noise level obtained from the remote-reference calculations, are the levels of uncorrelated noise between the remote-reference and SFMT sites. In this case the difference between the total noise level (obtained when CMO or EYR is used as the remote reference) and the reduced noise level (obtained when a seafloor site is the remote reference) gives the level of correlated noise between the seafloor remote reference and SFMT sites. For example if site TP6 is the SFMT site, the total levels of magnetic-field and electric-field noise are the levels determined when CMO is used as the remote reference. If the TP7 HEF is used as the remote reference, the smaller electric-field noise level obtained corresponds to the uncorrelated electric-field noise

at TP6. The difference between the two levels of noise gives the correlated electric field nois between TP6 and TP7. Similarly the use of TP5 MAG as the remote reference will allow separation of the uncorrelated magnetic-field noise at TP6 from the correlated magnetic-field noise between TP6 and TP5.

Figure 7.23 plots the correlated and uncorrelated noise at TP6 obtained using this method. The curves are quite erratic as the final results are based on calculations involving a number of subtractions of terms including random errors. Nevertheless the curves show significant differences between the correlated and uncorrelated noise spectra, indicating different sources of noise. At longer periods the correlated and uncorrelated noise have similar magnitude however at shorter periods the uncorrelated spectra flatten while the correlated spectra descend steeply. The uncorrelated spectra for the horizontal electric field approach a 1/frequency slope. Thus uncorrelated (instrumental) noise has been successfully separated from the correlated noise spectra.

It is possible to assess the validity of the correlated-noise separation using a synthetic dat set similar to that used in section 4.2. Using this method, the levels of correlated electric and magnetic noise determined for site TP6 (for the 1 h period), were added to a synthetic data set possessing a similar impedance to TP6. The correlated noise was also added to the remote-reference component. Remote-reference calculations and signal / noise separations were performed on the synthetic data set and it was found that the results reproduced the

1. reduced noise levels on the components containing correlated noise
2. changed noise levels on the components not containing the correlated noise and
3. bias of the impedances

observed in the actual Tasman Project results. It is therefore concluded that correlated noise between the remote-reference and SFMT sites is very likely to explain the observed variations in impedance results when different sites are chosen as the remote reference.

It is unlikely that correlated noise will occur between a remote-reference and only one SFMT component. For example any correlated noise between a remote-reference and a magnetic-field component is also likely to correlate with noise on the orthogonal electric-field component. The Tasman Project results show there is large-scale correlation of noise on both magnetic and electric fields; unless two independent processes cause this noise (an improbable physical situation) the spatially-correlated noise components of the electric and magnetic fields will also be correlated. In addition the noise on the two systems (R_1,B_1,E_2) and (R_2,B_2,E_1) may also be correlated (where R is assumed to be a MAG recording).

As discussed in chapter 4, the non-Hermitean component of the electric and magnetic field signal matrices (estimated using the remote-reference method) may provide an indication of the level of correlated noise. An examination was made of the non-Hermitean to Hermitear ratios for signal matrices of the synthetic data set. The ratio is significant when correlated noise is present on two components, but decreases when the correlated noise occurs on three or more components. An examination was also made of the non-Hermitean / Hermitean ratio for site TP6 when CMO, TP5 MAG and TP7 HEF are used as the remote reference reveals

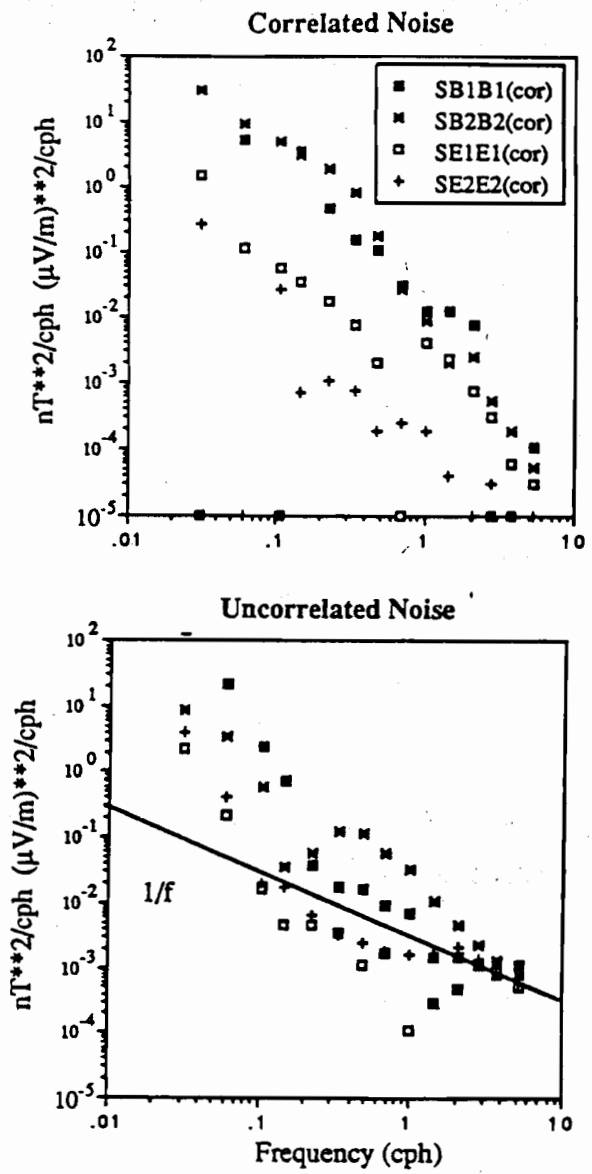

Figure 7.23: Correlated and uncorrelated noise spectra for site TP6. The total noise levels are defined using a signal/noise separation with CMO as the remote reference. For the magnetic field components, the uncorrelated noise levels are obtained when the TP5 MAG recordings are used as the remote reference. For the electric field components, the uncorrelated noise levels are obtained when the TP7 HEF recordings are used as the remote reference. The difference between the total noise and the uncorrelated noise for each component gives the level of correlated noise. Although these results (incorrectly) assume that noise is not multipl correlated on more than two components they should be approximately correct. Note the partitioning of the 1/frequency noise in the electric field data (at frequencies less than 1 cph) into the uncorrelated noise spectra.

that the ratios are highest when CMO is used as the remote reference. This observation suggests that when a seafloor site is used as the remote reference, correlated noise is present on at least three of the magnetic and electric field components. The results confirm that the spatially-correlated noise in the electric and magnetic fields in the Tasman Sea is correlated between the electric and magnetic fields.

Because the correlated noise is present on more than two components it is difficult to calculate the precise magnitude of the noise on each component and to predict the bias the nc will cause in the remote-reference impedances. In order to isolate the noise it is recommend that a multiple-site analysis be performed, involving decomposition of a combined spectral matrix for all of the sites. Such an approach should isolate eigenvalues corresponding to the source-field signal and to the correlated noise (eg. Egbert & Booker 1985). Although the results obtained above using the synthetic data set (Figure 7.23) neglect multiply correlated noise, they should be approximately correct. The overall noise levels for the electric and magnetic fields are probably reasonable estimates, while more detailed results such as the relative noise level between the different orthogonal directions, may not be well resolved.

The final question to be addressed concerns the source of the correlated noise. Any proposed source must provide a signal which occurs over the frequency range of 0.1 to 1.0 cph (Figure 7.2) and is coherent over distance scales of order a thousand kilometres. The signal must also be coherent over time scales of at least tens of days in order to be visible in tl long time-series analysis method used in the analysis. Two possible sources for the coheren noises are electromagnetic induction by large-scale oceanic processes, and current channelling of out-of-phase (relative to the local Tasman Sea electric fields) electric currents through the Tasman Sea . The main argument against an oceanic source is the difficulty of generating a coherent signal over such a large region. Possible sources, such as trains of storm-induced waves travelling from a consistent source region, may not have the required frequency characteristics or persist over long enough time segments. Large-scale oscillations of the Tasman Sea are also unlikely to provide a signal which is continuous over the required frequency range.

It is concluded that channelled out-of-phase electric currents are a more probable source of the correlated noise. As discussed above, such currents could be driven by non-uniform source-field components. For Sq harmonics with periods as low as 8 h, the source-fields drive large-scale electric current systems in the oceans (Bullard & Parker 1970). It is therefore plausible that the non-uniform component of storm fields (see chapter 4.3) should also induce large-scale current systems, at least at periods of 5 to 10 h. Providing the oceanic crust is sufficiently resistive and source-field wavelengths are appropriate, this effect could extend to shorter periods. An argument against this proposed source for the coherent noise is the observation that there is no significant channelling of in-phase currents (from outside the induction region) through the Tasman Sea.

There are many interesting aspects of the noise signal in the Tasman Sea that require further clarification and research. The results will be useful for both oceanography and

electromagnetic induction studies. In thesis however time limitations have restricted the analysis of the noise to a preliminary examination and often qualitative interpretation of th results.

Chapter 8 Magnetotelluric Inversions

This chapter provides an introduction to inverse problems and particularly the 1D MT inverse problem. Examples are presented of two important methods of MT inversion, determination of best-fitting D^+ conductivity models (Parker 1980) and determination of minimum-structure (Occam) models (Constable et al. 1987). These methods are then applied to the Tasman Project impedances in order to obtain 1D conductivity profiles. Finally the important features of these Tasman Project conductivity models are investigated in order to assess the resolution of the results.

8.1 One-dimensional Magnetotelluric Inversion

The geophysical inverse problem involves finding a model $\mathbf{m} = m_1, m_2 ... m_p$ with the same response (within certain limits) as a geophysical measurement $\mathbf{d} = d_1, d_2, .. d_n$. The response of the model, $\mathbf{r} = r_1, r_2, .. r_n$ is defined by an associated forward problem eg. the 1D MT problem defined by equations 4.73 and 4.74. Each observed datum $\mathbf{d}$ has an measure of random error $\mathbf{s} = s_1, s_2 .. s_n$ and the inverse problem involves matching the model and observed response to a level of misfit appropriate to this random error.

The 1D MT inverse problem involves finding the 1D conductivity model, or range of conductivity models, with the same response as an observed MT response. The most common MT inverse problem is: given an observed MT response as a function of frequency, find the model parameters of a layered conductivity profile with the same response. Alternative inverse problems may use a different parameterization of the 1D conductivity profile and a further inverse problem consists of inverting the impedance defined as a function of wavenumber (eg. Hooshyer & Razavy 1982). For the MT inverse problem, the geophysical measurement may be either the observed complex impedance or the apparent resistivity and phase; $\mathbf{d} = Z(\omega_1), Z(\omega_2), .. Z(\omega_m)$ or $\mathbf{d} = (\rho_1, \phi_1), (\rho_2, \phi_2) ... (\rho_m, \phi_m)$ where $m = n / 2$. Other forms of the response may also be used, for example the c response function or a $(\log[\rho_a]_m, \phi_m)$ representation. In general there are two observed data at each frequency.

In order to assess the goodness-of-fit of a model it is necessary to sum the misfit between the response and the data. It is also useful to weight the misfit on each datum by its standard deviation so that points with large error estimates contribute relatively less to the misfit. An important measure of misfit is the chi-squared criterion which is defined as

$$\chi^2 = \sum_{i=1}^{n} \frac{(d_i - r_i)^2}{\sigma_i^2} \qquad 8.2$$

This quantity is closely related to the standardized root-mean-square misfit or **tolerance**

$$t = \sqrt{\frac{1}{n}\sum_{i=1}^{n}\frac{(d_i - r_i)^2}{\sigma_i^2}} \qquad 8.3$$

by

$$\chi^2 = n\,t^2 \qquad 8.4$$

When fitting a response to a set of data it is important that the misfit lies between certain upper and lower bounds. A lower bound exists because it is desirable not to overfit a set of data which contain random errors. Exactly, or too closely, fitting such data will mean that the model is fitting the noise as well as the underlying data. This is usually an undesirable situation. The upper bound on the misfit corresponds to fitting the data to a satisfactorily high level compared with the size of the random errors. If the minimum misfit for a particular type of model exceeds this bound it may be concluded that the data will not be fully explained by that type of model.

If the error distribution on each datum is Gaussian, the χ^2 misfit for a model will possess the standard χ^2 distribution (Parker & Whaler 1981). Bentley (1973) examined random error distributions on apparent resistivity / phase terms and found that while the distribution of phase errors is approximately Gaussian, the distribution of apparent resistivity errors is approximately log-normal. In order to compare an observed apparent resistivity misfit (eg. between a model and a response) with standard χ^2 values, the misfit should therefore be calculated using the difference of the logarithm of the apparent resistivity values.

For a misfit with the standard χ^2 distribution, the appropriate lower bound for χ^2 is given by the expected (or expectation) value of χ^2. This value is equal to n, the number of data. The upper bound for the misfit is taken to be the level of χ^2 which is two standard deviations above the expectation value. This upper bound, approximately equal to the 95% confidence limit, is given by

$$\chi^2 < n + 2\sqrt{2n} \qquad 8.5$$

(Parker & Whaler 1981). For MT inversions in which there exist data at m frequencies (a total of 2m data), the acceptable range of χ^2 for the fit of a model to the data is

$$2m < \chi^2 < 2m + 4\sqrt{m} \qquad 8.6$$

If a model **m** can be found which acceptably fits a set of data **d** then the **existence** of a solution to the inverse problem is established. The model may however not be **unique** and other models may fit the data with the same (or at least a satisfactory) level of misfit. Once the existence of solution is established it is necessary to construct further models to

investigate the range of possible solutions. The problem of investigating the range of models which fits a given set of data is called the **inference** problem.

In the construction of models the problem of over-fitting the data may be encountered. If the model is parameterized too finely, for example a conductivity profile contains too many layers, then the number of independent parameters in the model will exceed the number of data. In this case it will not be possible to independently determine all the model parameters. As the level of errors on the data increases, this situation becomes more extreme as the data effectively contain less information. The avoidance of over-fitting the data is termed **regularization.**

A common method of regularization is to simply limit the number of model parameters being fitted. For the MT case this procedure may involve determining the conductivity of a small number of thick layers with specified thicknesses. The number of layers is adjusted according to the number of data and to the error levels such that the fit to the data produces a value of χ^2 close to its expectation value. Other methods of regularization use a larger numbers of model parameters but constrain the parameters so that they are not completely independent. This procedure may involve limiting the 'roughness' of the final model.

As mentioned in chapter 4, if a perfect set of 1D MT data exists (ie. at all frequencies and with zero errors) an inversion of the data will return the correct conductivity structure. It has been shown by Parker (1980) that for incomplete MT data, ie. data at discrete frequencies and with non-zero errors, the best-fitting model consists of a set of delta-functions located at varying depths. Each delta-function has infinite conductivity but is associated with a finite conductance. Since observed MT data is always incomplete, the delta-function inversion provides a straightforward test for the existence of a 1D conductivity profile. If an inversion shows the best-fitting model has a value of χ^2 which is greater than some tolerance (eg. the expectation value of χ^2) then it follows that no 1D model will satisfactorily fit the data.

A delta-function inversion will usually over-fit a 1D MT data set, producing a value of χ^2 much less than the expectation value. In this case there will be a range of alternate models which also fit the data ie. the inverse problem for 1D MT with incomplete data has non-unique solutions. The inference problem for 1D MT inversion has not been fully solved (Parker 1983).

Alternate 1D MT Inversion Schemes

Parker (1980) and Parker & Whaler (1981) describe the inversion method for constructing delta-function conductivity models or D^+ models. The methods are not described here, but are based on solving 'a least squares problem linear in the spectral function of the electric field differential equation' (ie. equation 4. 24). The authors also

provide methods for constructing two further classes of models. Their H^+ models consist of stacks of layers of uniform conductors, each with a constant value of

$$d^2 = \mu \sigma h^2 \qquad 8.7$$

As the value of d is increased, these models change from a delta-function type solution to a stack of thicker layers with more uniform conductivity. The final value of d is chosen such that an appropriate value of χ^2 misfit is obtained. The third class of models of Parker & Whaler (1981) produces smooth conductivity profiles.

Many inversions of MT data have been based on determining the conductivity of a small number of uniform layers (eg. Jupp & Vozoff 1975, Filloux 1982a, Pedersen & Hermance 1986). These inversions are based on determining the partial derivatives of the response terms with respect to the model parameters. The inversion is performed by minimizing the misfit (usually a sum-of-squares misfit), by changing the model in the direction dictated by the partial derivatives. This procedure is performed in an iterative fashion since the partial derivatives change as the model changes; various numerical techniques are use to stabilize the iteration. A number of slightly different forms of this type of inversion are performed. Some inversions involve fixing the layer thicknesses and determining only the conductivity of each layer (eg. Filloux 1982a). Larsen (1981) sets the layers to a uniform value of d (as defined above) and inverts for the logarithm of the conductivity contrast between adjacent layers. Other inversions determine both the conductivity and the thickness of layers but this method doubles the number of model parameters needed to be defined.

Oldenburg (1979) and Hobbs (1982) describe inversion schemes which generate continuous 1D conductivity profiles. The two methods use different schemes to produce stable iteration towards a reasonable final conductivity model; Oldenburg (1979) uses various smoothing functions at each iterative stage, while Hobbs (1982) determines the conductivity model which lies close as possible to a uniform conductor. Whittal & Oldenburg (1986) and Whittal (1986) describe methods for determining a variety of model classes and for introducing external geophysical constraints into an inversion. The latter may include forcing the conductivity to lie between certain bounds over a particular depth range or forcing the conductivity to increase monotonically with depth. These constraints are forms of regularization.

Another method sometimes used for 1D MT inversion is Monte-Carlo inversion (eg. Jones & Hutton 1979). Lilley et al. (1981) used a similar scheme for inverting SGS results from central and south-eastern Australia. The Monte-Carlo inversion technique has the advantage of partially investigating the range of all possible models which can fit the data. A number of MT inversions have also employed advanced forms of the direct inversion techniques described in chapter 4, for example Nabetani & Rankin (1969), Fischer et al. (1981) and Coen et al. (1983).

An important development in 1D MT inversions has been the development of

minimum-structure inversions (Marchisio & Parker 1984, Constable et al. 1987). Because the physical parameters of the Earth may not possess 'minimum-structure' some of the structures determined in minimum-structure inversions may not be geophysically realistic. For example, in inversions of SFMT data, the sharp layer of conductance associated with the upper sediments may be smoothed out over a depth range of tens of kilometres (see section 8.3). The importance of minimum-structure inversions is that they show the minimum structure (ie. roughness) necessary to explain the data. Thus if a particular feature appears in a minimum-structure model it can be concluded that the structure is a necessary feature of the solution. Such information is not obtained from other inversion techniques which (because of the non-unique nature of the MT problem) may include a wide range of structures not required by the data.

Constable et al. (1987) argue that because the "diffusive nature of energy propagation 'smears out' the real Earth structure" it is inappropriate for electromagnetic inversion models to include unresolvable sharp boundaries or thin layers. This argument must however be moderated if a priori information indicates the presence of sharp features in the conductivity profile, for example a distinct high-conducting sediment layer.

The **Occam inversion** method of Constable et al. (1987) obtains the conductivity model which has the minimum roughness at a specified level of misfit. Roughness is defined in terms of the discrete equivalent of the integral of either the first derivative

$$R_1 = \int \left(\frac{dm}{dz} \right)^2 dz \qquad 8.8a$$

or the second derivative

$$R_2 = \int \left(\frac{d^2m}{dz^2} \right)^2 dz \qquad 8.8b$$

of the model m(z) with depth z. For MT inversions the model is usually parameterized in terms of the logarithm of the resistivity. In the Occam inversion the standard least-squares inversion problem is re-formulated into a Lagrange multiplier form. This form allows minimization of the roughness functional with the necessary constraint that the model must also fit the data to within defined bounds. Details of the full solution and iterative method are explained in Constable et al. (1987). The Occam inversion algorithm is in general an efficient, stable and rapidly convergent method.

8.2 Investigation of the Forward Problem

Before undertaking inversions it is wise to investigate the corresponding forward problem. This research will provide information on the sensitivity of the response to various model parameters and therefore indicate the appropriate parameterization for the inversions. For example for 1D MT inversions, if some broad ranges are predicted for the

conductivity structure, forward modelling can show how deep it is necessary to extend the inversion model. Investigation of the forward problem may indicate how finely it is necessary to parameterize the inversion models (eg. what layer thicknesses to choose) especially at shallow depths where SFMT results provide limited resolution. Forward modelling can also provide some information on the inference problem. Evaluation of the MT response for judiciously varied conductivity models (cf. performing full-scale Monte-Carlo inversions) can quickly show the minimum range of the model parameters for a specified level of errors.

A trial 1D conductivity profile and the calculated 'seafloor' apparent resistivity and phase responses are shown in Figure 8.1. The first forward-modelling test performed using this model involved varying the conductivity of each layer and examining the change in the seafloor MT response. Specifically it was examined by how much the conductivity of each layer could be varied before the response in the period range 0.1 - 100 h changed by more than a fixed level. The level of response variation chosen was ± 10% for the apparent resistivity and ± 2.9° for the phase, with both of these values corresponding to a relative standard deviation of 7% on each complex impedance term (see section 4.2).

Table 8.1 lists the range of allowable conductivity values for each layer and the frequency (or frequencies) at which the response of the extreme conductivity models reached the 7 % limits. Figure 8.1c illustrates the range of allowable conductivities. There is no constaint placed on the conductivity of the overlying ocean by the SFMT data. For the underlying structure, the conductivity of the sediment layer is closely resolved, that of the resistive region is very poorly resolved and that of the deep conductive regions is relatively well resolved.

The sensitivity of the MT response to a layer in the model depends upon the degree to which the layer attenuates the electromagnetic fields. This level of attenuation by each layer is related to the ratio r_s, of the total thickness of the layer to the skin depth. This quantity is closely related to the parameter d

$$r_s^2 = h^2 \left(\frac{2}{\omega \mu \sigma} \right)^{-1} = d^2 \frac{\omega}{2} \qquad 8.9$$

and thus inversions based on layers with constant values of d were developed so that all layers possessed the same attenuation (Nabetani & Rankin 1969, Lowenthal 1975). The sensitivity of the MT response also depends upon the depth of the layer in the conductivity profile. For deeper levels, to which less electromagnetic energy penetrates, the response is less sensitive to the conductivity structure. Larsen (1975) corrects for this effect in his inversion scheme.

Returning to the conductivity model of Figure 8.1 it can be seen that if the sediment (upper layer) thickness is known accurately then the sediment conductivity is accurately defined. If the layer thickness is poorly known, the integrated conductance will still be

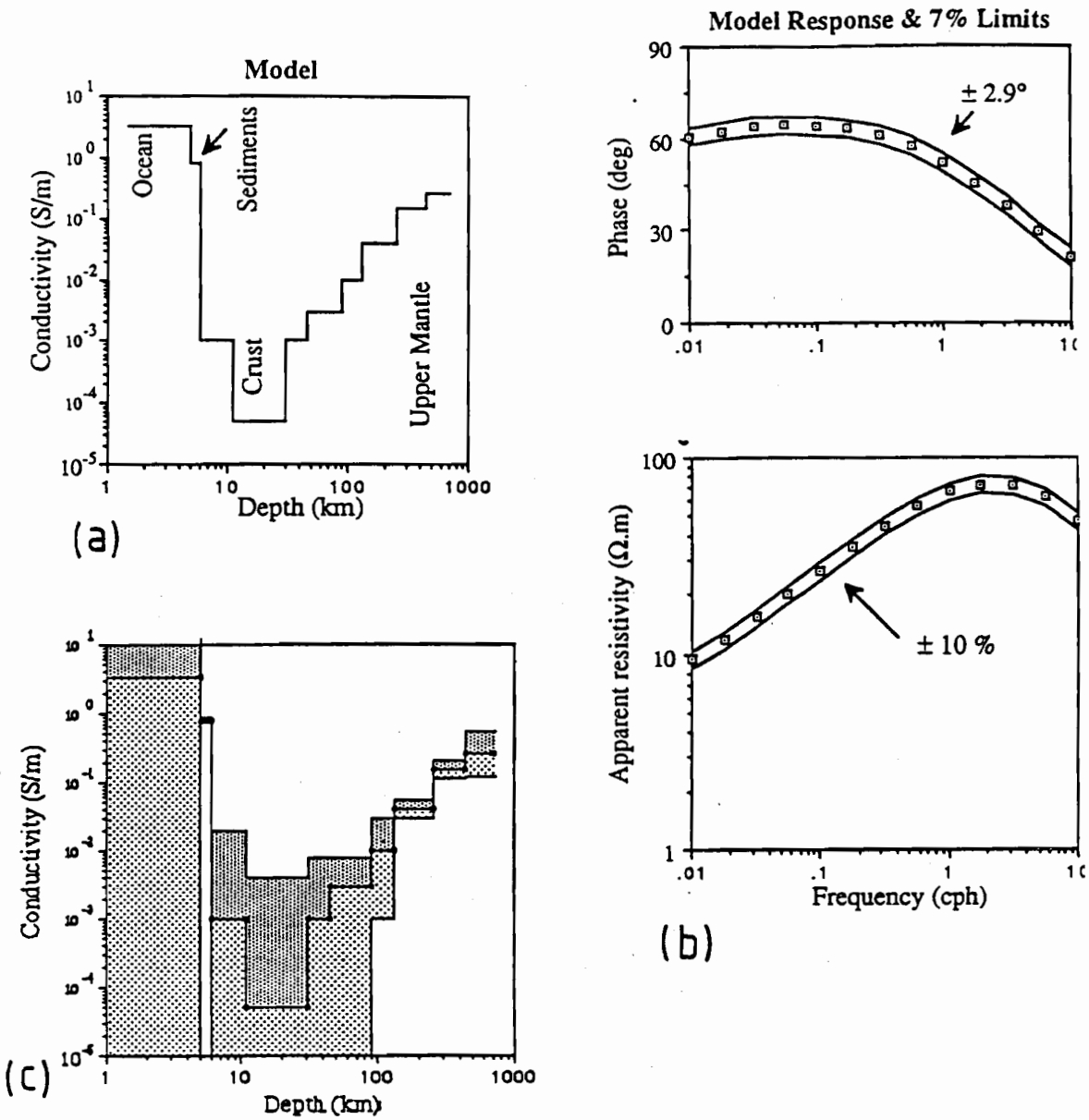

Figure 8.1: Examination of the resolution of 1D MT data using forward modelling.
(a) The trial 1D conductivity structure. The model is based on previous seafloor conductivity determinations (see section 4.1 for the derivation of a similar model).
(b) The apparent resistivity and phase response of the trial model (squares). In the tests described in the text the response is always evaluated at these frequencies. The lines on either side of the response correspond to 7 % errors on the complex response terms equating to the errors shown on the apparent resistivity and phase.
(c) Range of conductivity models with the same layer thicknesses as the trial model with responses inside the limits shown in b. The conductivity has been varied one layer at a time and the range of models shown is thus a minimum range for all possible models which will fit the data.

Table 8.1: Resolution of MT data; from forward modelling

Layer	Thick (km)	Depth (km)	Model σ ($S.m^{-1}$)	Min σ ($S.m^{-1}$)	Limiting Resp. (h)	Max σ ($S.m^{-1}$)	Limiting Resp. (h)
1	5.0	5.0	3.3	No constraint from SFMT data			
2	1.0	6.0	0.8	0.75	0.1 ρ	0.86	0.1 ρ
				0.73	0.2 ρ *	0.88	0.2 ρ *
3	5.0	11.0	1.0×10^{-3}	$< 10^{-7}$	-	0.02	0.1 - 0.2 ρ
4	20.0	31.0	5.0×10^{-5}	$< 10^{-7}$	-	0.004	0.1 ρ
5	15.0	46.0	1.0×10^{-3}	$< 10^{-7}$	-	0.008	0.1 ρ
6	45.0	91.0	3.0×10^{-3}	$< 10^{-7}$	-	0.008	0.1 - 0.3 ρ
7	40.0	131.0	0.01	0.001	.6 ρ	0.03	0.3 - 1.8 ρ
8	125.0	256.0	0.04	0.029	1.0 - 3.2 ρ	0.054	1.8 ρ
9	180.0	436.0	0.15	0.11	18 ρ	0.21	18 - 56 ρ
10	h.s.	-	0.26	0.18	100 ρ ϕ	0.38	100 ρ
				0.12	18 ϕ *	0.55	18 ϕ *

Notes: The table shows the trial conductivity profile (thickness, model σ) and the amounts by which the conductivity of each layer can be varied without the change in apparent resistivity response exceeding 10 % and the change in the phase response exceeding 2.9°. The response term(s) at which these limits are first exceeded are also shown. The symbols ρ and ϕ indicate whether the apparent-resistivity response or the phase response, or both, fall outside the limits. Figure 8.1 illustrates the model and the response limits. For the lowest layer in the model "h.s." denotes half-space.

Note that for most of the results in the table the response was constrained using periods lying between 0.1 and 100 h. The results with asterisks were obtained with the response constrained by the more narrow period range of 0.2 to 17 h, typical of the period range of the Tasman data.

well-defined since the value of d for the layer is relatively high. For the resistive regions from 1 to 90 km beneath the seafloor, the value of d for each layer is very small, and the only constraint which can be placed on the conductivity is to give it an upper bound. From 90 to 500 km deep the conductivity is reasonably well-defined, from 125 - 400 km it is defined to within a factor of two. At depth greater than 500 km the conductivity is defined less accurately because the moderately conductive region around 100 - 500 km attenuates much of the penetrating electromagnetic energy.

The conductivity bounds defined above are minimum ranges for the conductivity of each layer. Parameterization into thinner layers allows increased conductivity ranges. For example division of the bottom half-space of the model into layers lying above and below 700 km shows that there is very little constraint on the conductivity below 700 km depth. Division of the sediment layer into sub-layers allows the total conductance to be arranged in various distributions without significantly changing the response. This effect is illustrated in Figure 8.2 in which the MT response is calculated for different values and distributions of conductance of the upper layers in the model. The MT method responds to the integrated conductance in the different parts of the conductivity profile and is insensitive to the 'internal' distribution of this conductance. The possibility of covariance between the conductivities in different layers also means that Figure 8.1 shows only the minimum range of acceptable conductivity models. An increased conductivity in one layer may be compensated by a decreased conductivity in an adjacent layer, without significantly changing the response.

The ranges of conductivity obtained from the forward modelling give important information for the parameterization for the final inversions. They show that for observations with similar apparent resistivity to the trial forward model, the inversion models should extent to a depth of order 1000 km. For the MT responses of the Tasman Project with apparent resistivities which are larger than those of the trial forward model an increased depth range is advisable since the attenuation depth-scales will be larger. The results of the forward modelling show that detailed parameterization in the upper sediment depths is unnecessary. SFMT data sets with a typical minimum period of 0.1 h and typical errors at higher frequencies of 1-5 % are not capable of differentiating between slightly different distributions of conductance at these depths.

For the intermediate depth range of 20 - 600 km the number of layers used in an inversion should depend on the inversion method. The layering should however reflect the decreasing information available as the depth into the Earth is increased. For minimum-structure inversions in which increasing the number of layers does not result in over-fitting of the data, a choice of around 10 layers per decade of depth seems appropriate. This number of layers will allow the inversion to reproduce features in the conductivity structure at the level of smoothness appropriate to the electromagnetic diffusion process. The use of fewer layers may introduce artificial roughness into the inversion model, a result antagonistic to the philosophy of minimum-structure inversion. For the Occam inversions

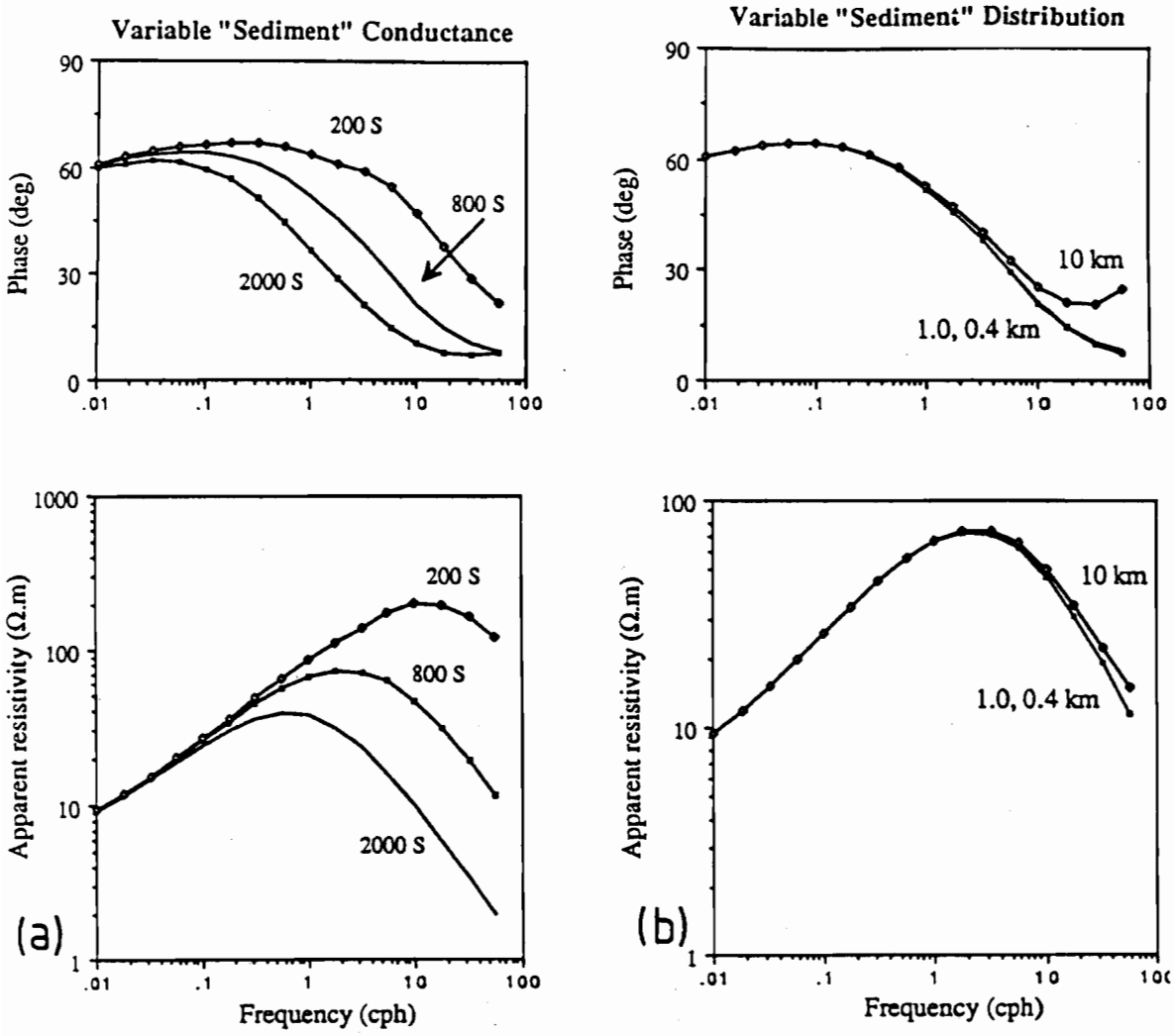

Figure 8.2: Effect of the conductance of the upper conducting, "sediment" layer on the 1D SFMT response. The basic conductivity model and different upper level structures are listed in Table 8.2

(a). SFMT response when the conductance in the upper layer is varied from 200 to 2000 S. Changing the sediment conductance changes the apparent resistivity and phase response over a wide frequency range. This result suggests SFMT data should resolve the conductance at the top of the conductivity profile accurately.

(b). SFMT response when the distribution of conductance in the upper layer is varied. In all models the total conductance of the upper layers is 800 S. The response curves for models in which the conductance is confined to the upper 0.4 km and upper 1.0 km overlie each other in the frequency range shown. Some variation in the response curves occurs when the conductance is spread over 10 km. Such variation will however not be resolved in typical SFMT data in which the highest frequency of resolved data is around 10 cph and relative errors are typically 1-5%.

Table 8.2: Variations to distribution of conductance in "sediment" layer.

	1.0 km model			0.4 km model			10.0 km model		
Layer	Thick (km)	Base (km)	σ ($S.m^{-1}$)	Thick (km)	Base (km)	σ ($S.m^{-1}$)	Thick (km)	Base (km)	σ ($S.m^{-1}$)
1	5.0	5.0	3.3	5.0	5.0	3.3	5.0	5.0	3.3
2	1.0	6.0	0.8	0.4	5.4	2.0	10.0	15.0	0.08
3	5.0	11.0	1.0×10^{-3}	5.6	11.0	1.0×10^{-3}	3.0	18.0	1.0×10^{-3}
4	20.0	31.0	5.0×10^{-5}	20.0	31.0	5.0×10^{-5}	13.0	31.0	5.0×10^{-5}
5	15.0	46.0	1.0×10^{-3}	15.0	46.0	1.0×10^{-3}	15.0	46.0	1.0×10^{-3}
Remaining layers same as for model in Table 8.1									

The table shows the conductivity models used to generate the MT responses in Figure 8.2. The models above give the 'variable sediment distribution' responses. All three models are identical below 31 km depth and all have an integrated conductance in the upper layer of 800 S. The 'variable sediment conductance' responses were obtained using the 1.0 km model and varying the conductivity of layer 2 from 0.2 to 0.8 to 2.0 $S.m^{-1}$. This variation gives sediment layer conductances of 200, 800 and 2000 S.

performed on trial and on Tasman data below, the layering was set to 10 layers per decade with a total of 35 layers extending from 1 to 2000 km depth.

It is instructive to examine the frequencies at which particular model variations most strongly affect the MT response, ie. the frequencies which will most strongly constrain the different parts of the model in an inversion. Variations to the sediment layer or to the resistive layers above 90 km depth, cause the response to be most strongly affected at the 0.1 h period (Table 8.1). For depths between 150 and 300 km the conductivity is most tightly constrained by the response in the period range 0.5 - 3.2 h. For the layer between 256 to 436 km depth, the conductivity is constrained by the response at 18 h, and at greater depths, the conductivity is constrained by the longest period response terms. If the available period range is decreased so that it extends from 0.2 to 18 h (typical of the available range for the Tasman Project) the model resolution is decreased only slightly.

The apparent resistivity response is more sensitive than the phase response to variations in the conductivity structure. This result suggests that for most of depth range, inversion models will be more tightly constrained by the apparent resistivity response than by the phase response. For the deepest layer however the conductivity is constrained by both the long-period apparent resistivity and phase values. For the realistic period range 0.2 - 18 h, the apparent resistivity response is in fact insensitive to large variations in the conductivity of the deepest layer.

Extending these observations to the Tasman Project MT data it follows that for the important depth range from 150 - 400 km the conductivity profile will be constrained by periods from 0.5 - 10.0 h. This is a very useful result because it is over this period range that the experimental data have the smallest random errors (see chapter 7). At longer periods, which tend to constrain the model at greater depths, errors are larger and resolution will be lower. A method based on the D^+ inversions (Parker 1982) can be used to assess the depth of resolution of MT data; its application to the Tasman Project MT data is described below. For periods shorter than 0.5 h, errors in the Tasman Project data again become more significant and little structure at depths more shallow than 50 km will be resolved in the Tasman Sea conductivity profiles. As shown by the forward modelling in Figure 8.2 a reasonable estimate should still be obtained for the integrated conductance of the sediment layer.

A final exercise in forward modelling involves examining the effect of a deep high conducting layer (HCL) on the MT response. Since the search for such a layer is an important part of the Tasman Project it is useful to examine with what strength and over what frequency range a HCL changes the MT response function. Figure 8.3 shows the response for models with and without a HCL located at 100 km depth. The differences between the two responses exceed the level of errors on the Tasman Project data, suggesting that the Tasman data should be able to resolve the presence of such a layer. The HCL significantly changes the apparent resistivity response over a frequency range of

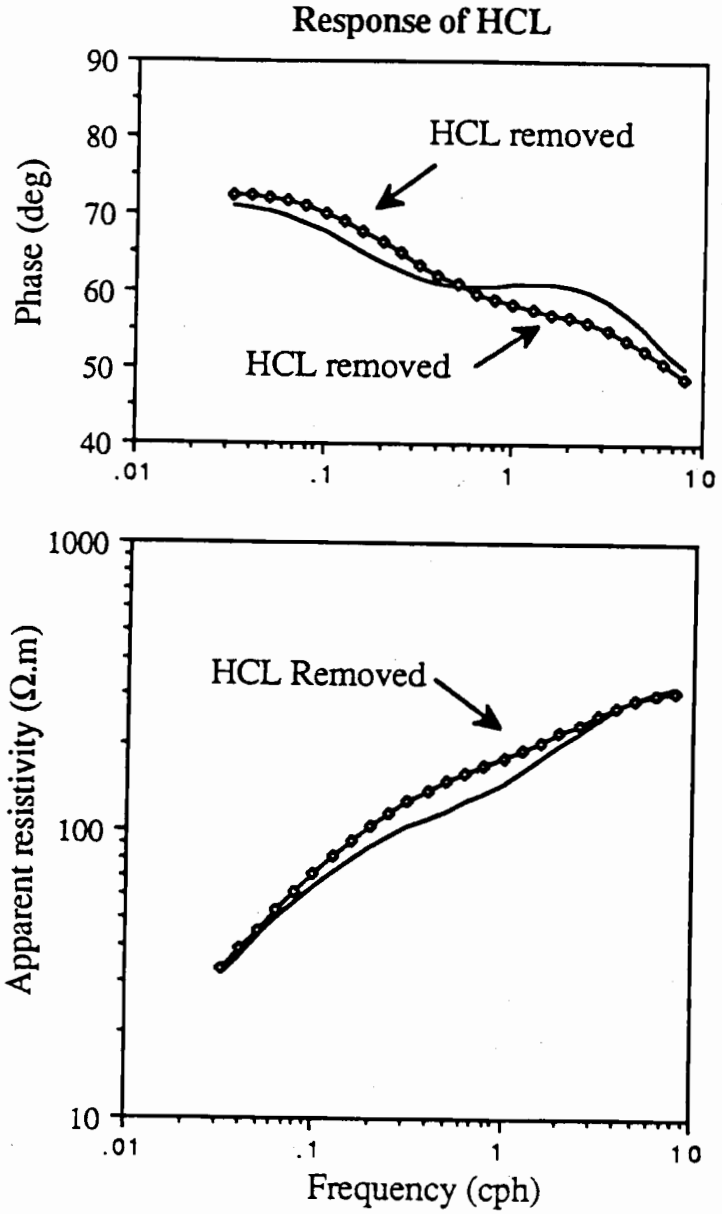

Figure 8.3: Forward modelling showing the effect on the MT response of an HCL deep in the conductivity profile. Note that the HCL changes the response over a wide range of frequencies. The conductivity model with and without the HCL is shown in Figure 8.20.

more than a decade ie. in the final inversions the resolution of an HCL will rely on a data from a wide frequency range. The presence of an HCL changes the phase response over a wider frequency range than it changes the apparent resistivity response (although interestingly, the phase change passes through a minimum at the frequency where the apparent resistivity change is largest).

8.3 Testing of Inversion Methods

This section summarises some inversions performed on test data using D^+ and Occam inversions. These tests provide information on the performance of the inversions, for example on the resolution and accuracy of the resulting conductivity models. The tests also serve to confirm the correct operation of inversion programs on the ANU computers. The D^+ program was kindly provided by R.L. Parker from the Institute Geophysics and Planetary Physics, San Diego and the Occam Inversion program by S.C. Constable from Scripps Institution of Oceanography, San Diego.

D^+ Inversions

In order to investigate the D^+ inversion method a trial conductivity model (which includes a HCL) was chosen and the MT response calculated. Random (Gaussian) noise of a specified level was added to the calculated response, error estimates were assigned to each term, and the data set inverted using the D^+ inversion program. Examination of the results, and comparison of them with the original conductivity model, confirms the correct program operation and reveals a number of useful features of delta-function inversions.

The D^+ program parameterizes the data in terms of the MT c response function and is based on the assumption that the errors on Re(c) and Im(c) are identical and independent Gaussian variables. The error estimate used on the input data is the one standard deviation estimate. For the trial inversions, noise was generated with a frequency-independent relative standard deviation, s_r ie.

$$\frac{\sigma(\omega)}{|\, c\,(\omega)\,|} = s_r \qquad 8.10$$

Noise values were generated by selecting random reals, ξ from a Gaussian distribution with zero mean and unit standard deviation. For each frequency, the value of ξ was converted to an absolute noise level ν by

$$\nu = \xi\, |c|\, s_r \qquad 8.11$$

Independent noise terms were then added to Re(c) and Im(c). In chapter 4 it was shown for the impedance Z that if there is an equal distribution of noise on real and imaginary

components, the standard deviation of noise on the impedance magnitude, |Z|, is equal to standard deviation on Re(Z) or Im(Z). Since this result is true for any complex quantity, the addition of the noise terms to Re(c) and Im(c) produces noise on |c| with a standard deviation equal to s_r |c|. The noise thus has the desired property given by equation 8.10. For the test inversions, noise with relative standard deviations of 0.1, 1.0 and 5.0 % was added to Re(c) and Im(c). These values correspond to relative standard deviations of 0.0014, 0.014 and 0.07 on the complex c values.

The data for the D^+ inversions of the test data comprised values at 17 frequencies (equally spaced in the log frequency domain) between 0.01 cph and 100 cph. Figure 8.4 illustrates the input data for the 5 % noise inversions using equivalent c and (ρ_a, ϕ) representations. The D^+ models from the inversions are shown in Figure 8.5. (Before the application of the D^+ computer program it was checked using an internal data set provided with the program and analysed in Parker & Whaler (1981) and found to produce correct and accurate solutions.)

The number of delta functions included in the inverted models decreases as the level of noise increases and therefore the data resolution decreases. For each of the examples shown, the delta-function models strongly over-fit the data. The observed values of χ^2 for the 0.1, 1.0 and 5.0 % cases were respectively 9.5, 4.2 and 13.0 which are all much smaller than the expectation value of χ^2 for 34 data, viz. 50.5. The over-fit of the data is illustrated by the response of the 5 % model shown in Figure 8.4. On only four data points does the response curve not pass through the error bar. However with the error bar corresponding to one standard deviation, a correct fit to the data should involve the response curve missing the error bar on approximately 0.33 x 34 or 11 of the data. It may therefore be concluded that the delta-function models are to some extent fitting the random noise in the data.

The depths of the delta functions are closely correlated with regions of high conductivity in the model; delta functions appear at the depths of the sediment layer, the HCL and the deeper rise in conductivity. The conductance of the most shallow delta function, located at the depth of the sediment layer, is respectively 811, 822 and 833 S in the 0.1, 1.0 and 5.0 % inversions . If this value is compared with the integrated conductance in the upper 41 km beneath the seafloor in the original model, ie. 821 S, it is evident that the upper delta function closely resolves the integrated conductance of the upper layers of the conductivity profile.

Although the main value of delta-function inversions is their information on the minimum value of χ^2 attainable with 1D conductivity models, the above results also show that the D^+ models contain some useful information on the actual conductivity structure.

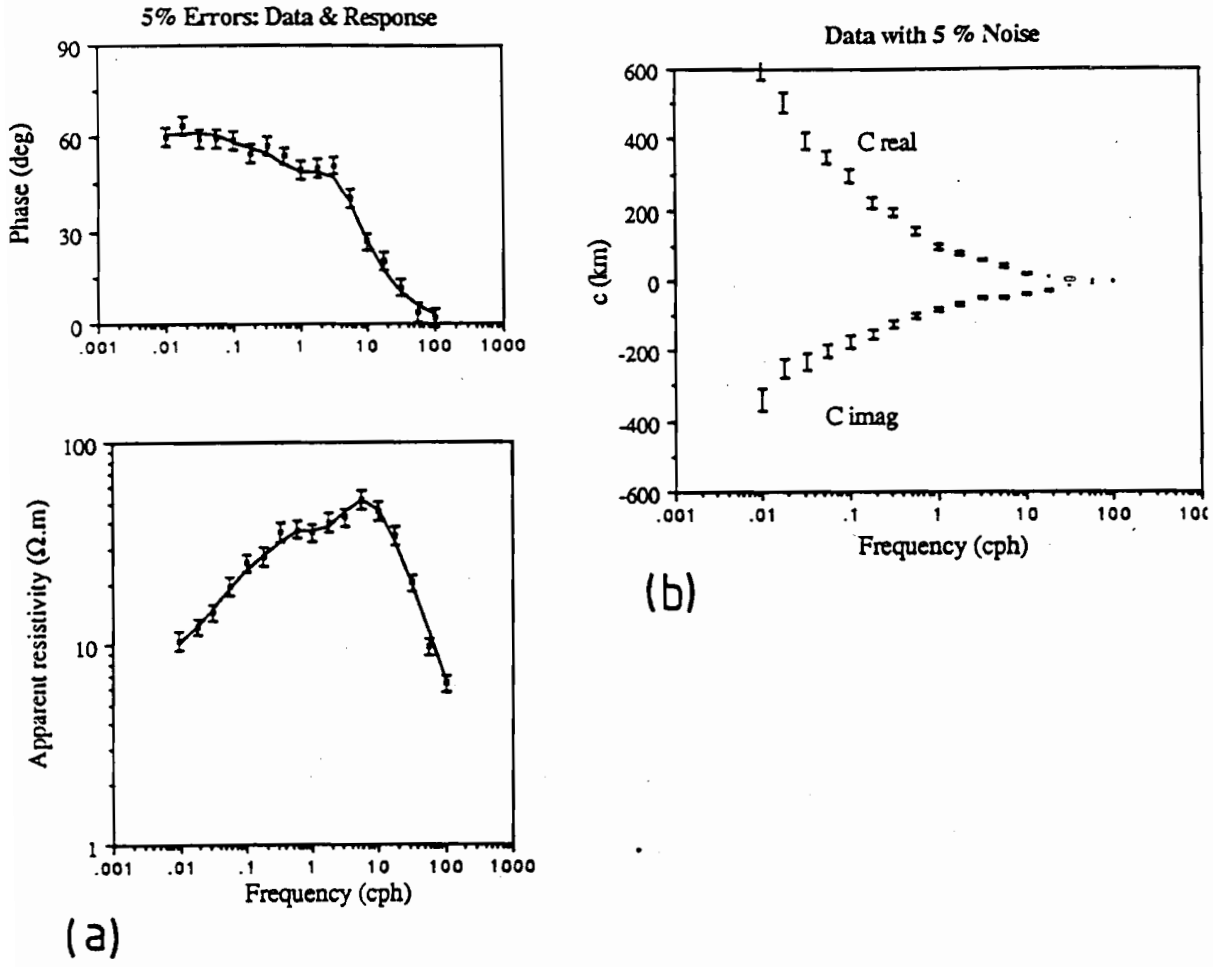

Figure 8.4: MT data used in D^+ inversion tests. The data were derived from the MT response of the 1D conductivity profile (shown in Figure 8.5). Noise with a relative standard deviation of 5 % was then added to the real and imaginary parts of each response term (equivalent to a relative standard deviation on the complex response of 0.07).

(a) The data in the ρ_a, ϕ parameterization. The 5 % relative error on the magnitude of c is doubled to 10% in the conversion to apparent resistivity and is equivalent to a $\pm 2.9°$ error on the phase. Also shown is the response of the D^+ inversion. Note that the response curve lies outside only 4 of the (standard deviation) error bars indicating the inversion over-fits of the data.

(b) The data in the c parameterization as used by the D^+ inversion program. Note that the large dynamic range of c (and the linear scale) makes it difficult to discern small features such as the added noise.

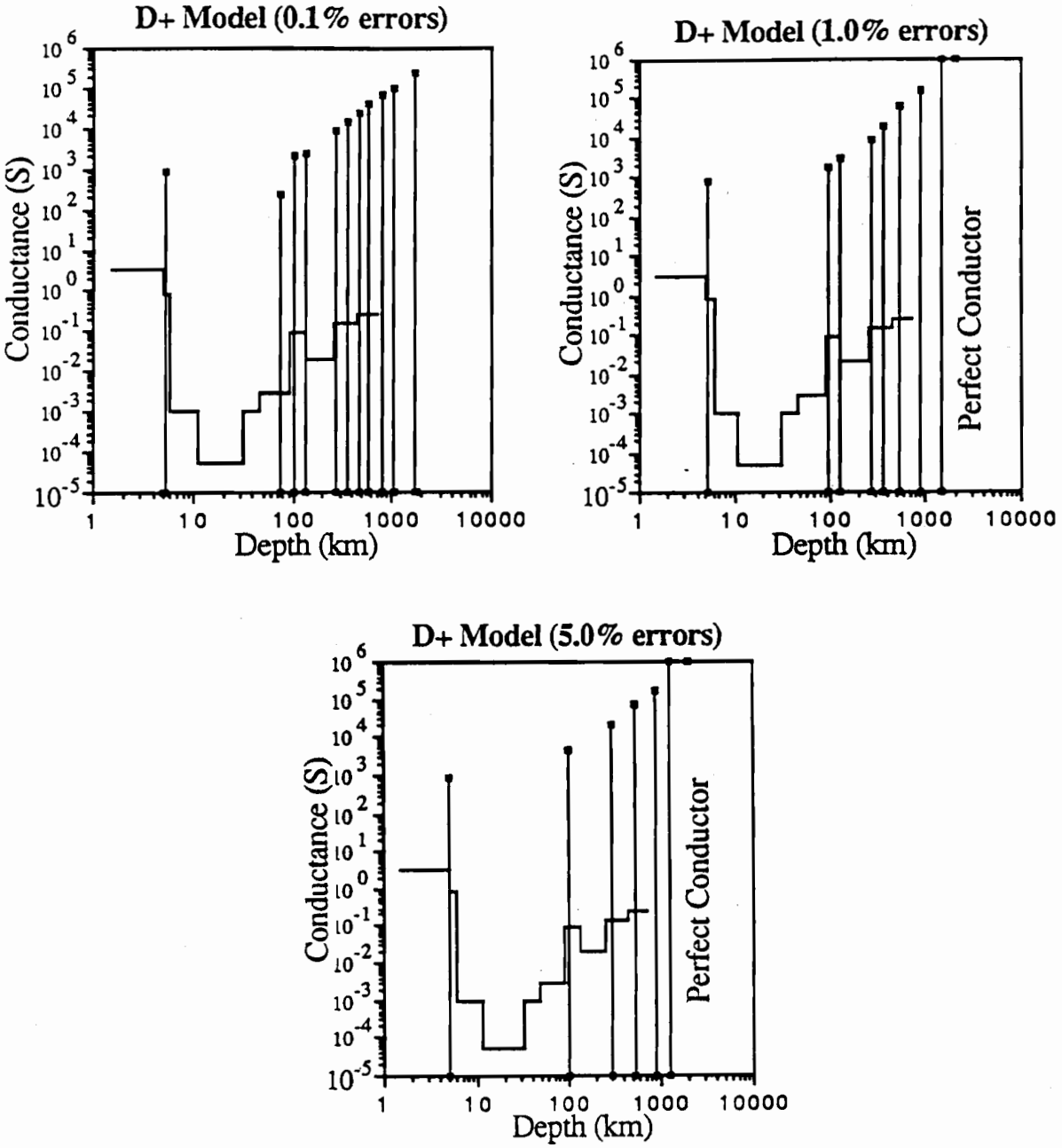

Figure 8.5: Delta-function models from D^+ inversions of trial data sets. The original conductivity model is shown superimposed on each panel (the conductivity shares the same numerical scale as the conductance). Note the decrease in the number of delta functions as the noise level increases. Also note the correspondence of the depth of the delta functions with layers of higher conductivity. The model for 0.1 % errors terminates in a resistive half-space, those for 1.0 % and 5.0 % errors terminate in an infinite conductor.

Penetration Depth Studies

The deepest limit of resolution of MT data ie. the effective depth of penetration of the electromagnetic energy may be obtained using the D^+ program. The method involves inserting a perfect conductor at increasingly large depths at the base of the conductivity profile (the depth of this layer is equivalent to the value of Re(c) at zero frequency). When it is inserted at shallow depths the conductor causes a large value of χ^2 since the data are not compatible with a 1D model in which there is a perfect conductor at shallow depth. As the perfect conductor is moved deeper it has less effect on the response, as the resolution of the MT sounding decreases. The depth at which the conductor ceases to cause a statistically significant misfit may then be taken to be the depth below which no information can be obtained from the MT method. Physically, this depth is that at which the level of penetrating electromagnetic energy is insufficient to cause the surface MT response to be significantly affected by a change in the conductivity.

Applying this method to the 0.1, 1.0 and 5.0 % data sets described above one obtains depths of penetration of 1460, 1000 and 700 km respectively. The depth decreases significantly as the noise level increases and the data place less constraints on the conductivity profile. If a more realistic period range of 0.2 -32 h is used for the data in the calculations, depths of penetration equal to 950, 700 and 500 km are obtained. These results show that the change in depth of penetration of electromagnetic energy is not directly proportional to the change in period. Moving from a maximum period of 30 h to one of 100 h produces only a 40 % increase in the depth of resolution.

It is of note that the lowest delta function or the terminating infinite conductor for each of the 0.1, 1.0 and 5.0 % inversion models in Figure 8.5 occurs at a greater depth than the penetration depth for the corresponding data set. This result shows that the estimate of the depth of penetration is a statistically conservative estimate compared with the D+ models which over-fit the data. Because it is based on the 95 % confidence limit rather than the expectation value of χ^2 it may be argued that the penetration depth estimate will in general be a minimum estimate for the depth. Situations may occur in which a fit to the data at the expectation χ^2 level gives a model with conductivity variations located beneath the penetration depth. In these cases, for which the deep conductivity variations will usually be a conductivity increase, the results are perhaps best interpreted as indicating only the necessity for a deep increase in conductivity, without revealing the exact detail of the structure.

Occam Inversions

The same basic data sets used for assessing the D^+ inversion method were also used for studying the Occam inversions. For the Occam inversion the data were parameterized into a log apparent resistivity, phase form. Noise (as described for the D^+ inversions) was added to the Re(Z) and Im(Z) terms and $\log(\rho_a)$ and ϕ calculated from these data. For log-domain data, the absolute error is given approximately by 0.434 times the relative error in the linear domain. Thus the absolute error on $\log(\rho_a)$ equals 0.868 times the relative standard deviation of |Z|. Unless otherwise specified the Occam inversions involved minimization of the first derivative of the model with depth. The correct operation of the Occam program was verified by running a sample set of data provided with the program.

Figure 8.6 shows the Occam inversion for the case of 0.1 % errors and based on data in the period range 0.01 - 100 cph. This model was calculated in order to examine how the inversion program performs with almost perfect data. The inversion model reproduces the conductive regions of the model, at depths of greater than 70 km, very well. The HCL is accurately defined, as is the deeper conductivity rise. At depths greater than 2000 km the resolution decreases as expected from the penetration-depth result for this data set. In the resistive regions of the conductivity profile the resolution is poor even though the data set contains only very small errors. As found from the forward modelling, the inverted model provides only an approximate upper limit for the conductivity of the resistive region.

As shown above in the forward modelling, the MT response is not very sensitive to the distribution of conductance in the upper layers. The minimization of the roughness in the Occam inversion smooths out the upper layer conductance into a broad zone extending to tens of kilometres depth (Figure 8.6). The integrated conductance in the upper part of the Occam model (823 S above 32 km depth) however closely matches that of the original conductivity model (821 S).

The Occam model characteristics described are close to the best possible resolution of the original conductivity structure. It will now be examined how the inversion method performs as the level of noise increases and the period range decreases. Figure 8.7 shows the Occam models for the 0.1, 1.0 and 5.0 % noise data sets and for the 100 to 0.01 and 32 to 0.2 h data sets. The models show the expected decreasing resolution with increasing noise and decreasing period range. The HCL in the models shows this effect particularly well, ranging from being accurately defined in the low noise inversions to being absent from the 5 % noise, narrow period-range inversion. The estimated maximum conductivity of the resistive region above 70 km, becomes larger as the noise increases and as the period range decreases, ie. the conductivity becomes less accurately defined.

An important question is: to which of the cases in Figure 8.7 will the Tasman Project models correspond ? For the Tasman Project data the relative standard deviation varies with frequency (see chapter 7) but for the period range 4.4 to 0.7 h it averages 4 % at TP4

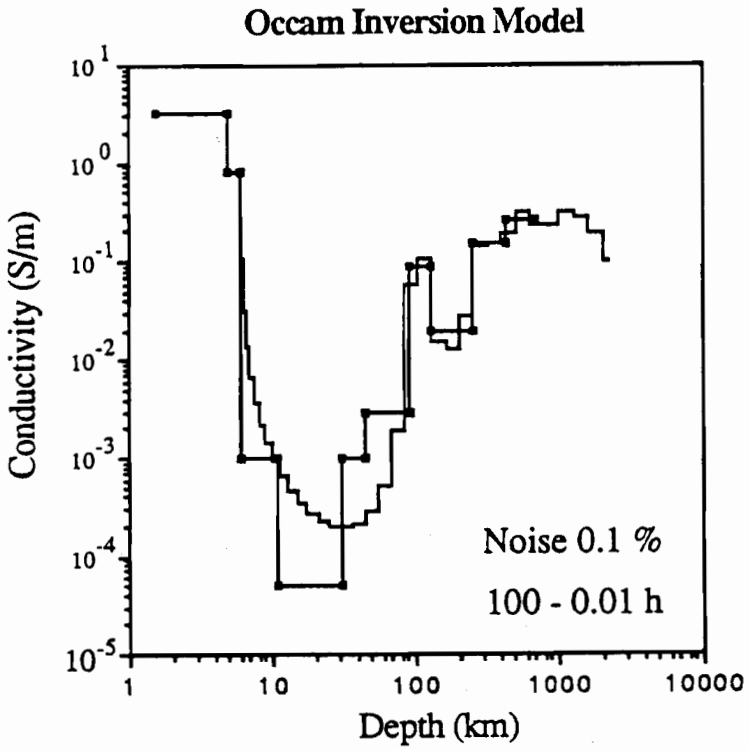

Figure 8.6: Occam inversion model for test data set containing 0.1 % noise and extending over a period range of 100 - 0.01 h. The original conductivity model is also shown (with solid squares at the edges of layers). Note that the inversion reproduces the HCL and deeper increase in conductivity accurately. Resolution is however poor in the resistive regions of the profile and below 2000 km depth.

and 5 % at TP3 and TP5. The errors increase at longer periods for sites TP3, TP4 and TP5 and also, for TP5, at shorter periods. As indicated by the forward modelling above, the conductivity structure in the important part of the profile between 80 and 400 km will be largely constrained by the 0.7 - 4.4 h period range where the errors are lowest.

The Tasman Project errors given above are for standard deviations on the complex impedance terms and must be reduced by a factor of $\sqrt{2}$ in order to be compared with the standard deviations on impedance magnitudes given in Figure 8.7. Also the Tasman

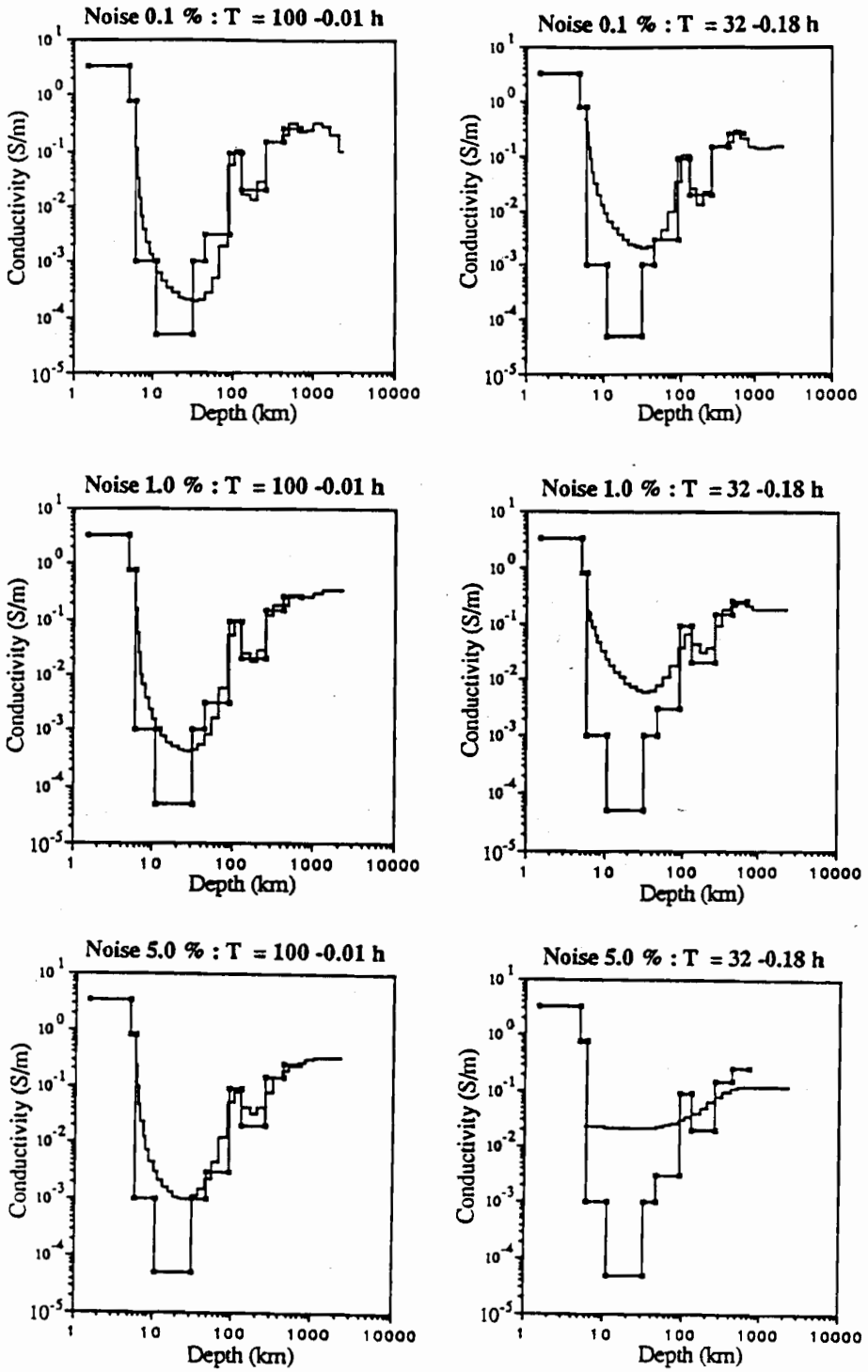

Figure 8.7: Occam inversion models for a range of noise levels and for two period ranges. Note the decrease in the resolution of the HCL with increasing noise and decreasing period range. The resolution of the resistive part of the profile also decreases with increasing noise level.

data are sampled at approximately 7 periods per decade compared with 4 periods per decade for the trial inversion data and therefore the Tasman error estimates should be reduced when they are compared with the trial inversion results. For the central part of the available period range the Tasman Project results will have 'effective' relative standard deviations (cf. the trial inversions) of around 2 %. For depths between 150 and 400 km the Tasman data will therefore have a slightly lower resolution than that in the middle right-hand panel of Figure 8.7.

It is concluded that inversion of the Tasman Project data should reveal the presence of an HCL, if such a feature exists beneath the Tasman Sea. If such a feature appears in a model it also seems probable its true conductivity contrast may be under-estimated. Deep conductivity structure (say > 400 km) will be less well resolved by the Tasman data because the errors are larger at longer periods. The omission of the 32 h data from the inversions for TP3 and TP4 (see chapter 7) will exacerbate this situation. Forward modelling and inversions of accurate data have shown that for the depths of the sediment and resistive parts of the conductivity profile, the MT method is not able to provide a great deal of resolution. The errors on the Tasman data however suggest the results should provide a reasonable estimate of the upper layer conductance (as did the D^+ inversion for the 5 % noise case) and a moderately well-defined upper limit for the conductance of the resistive region.

For all of the Occam inversions described above, except for the 0.1% noise and wide period-range case, the misfit was set to a tolerance of t = 1, ie. χ^2 equal to its expectation value. For the model in Figure 8.6 the iteration would not converge to t < 1.28, probably because at the 0.1 % error level, the layering in the inversion model was not sufficiently fine to reproduce that in the original conductivity model. Figure 8.8 shows the response of the Occam inversion model for the 5 % noise data set. The response lies outside the error bars on approximately one third of the data, indicating an appropriate level of fit. The figure should be compared with Figure 8.4 showing the overfit of the D^+ model to the same data.

In Occam inversions it is important not to over-estimate the errors. If error estimates are too large the inversion method will 'build-up' the required level of misfit (t = 1) by excluding real features from the conductivity profile and fitting unrealistically smooth conductivity profiles. For example in a conductivity model consisting of a conductive-resistive-conductive layering, as error estimates are increasingly overestimated, the inversion will produce a model lying increasing close to a half-space (with the average conductivity of the original profile). The resulting distribution of misfit will vary systematically with frequency, with the model apparent-resistivity being too high at short and long periods and too low at intermediate periods. There is no strong evidence for such a systematic distribution of misfit in Figure 8.8. In an earlier inversion test, in which error bars were assigned to data without any actual errors being added (ie. the error estimates were too large), a systematic distribution of the misfit was clearly evident.

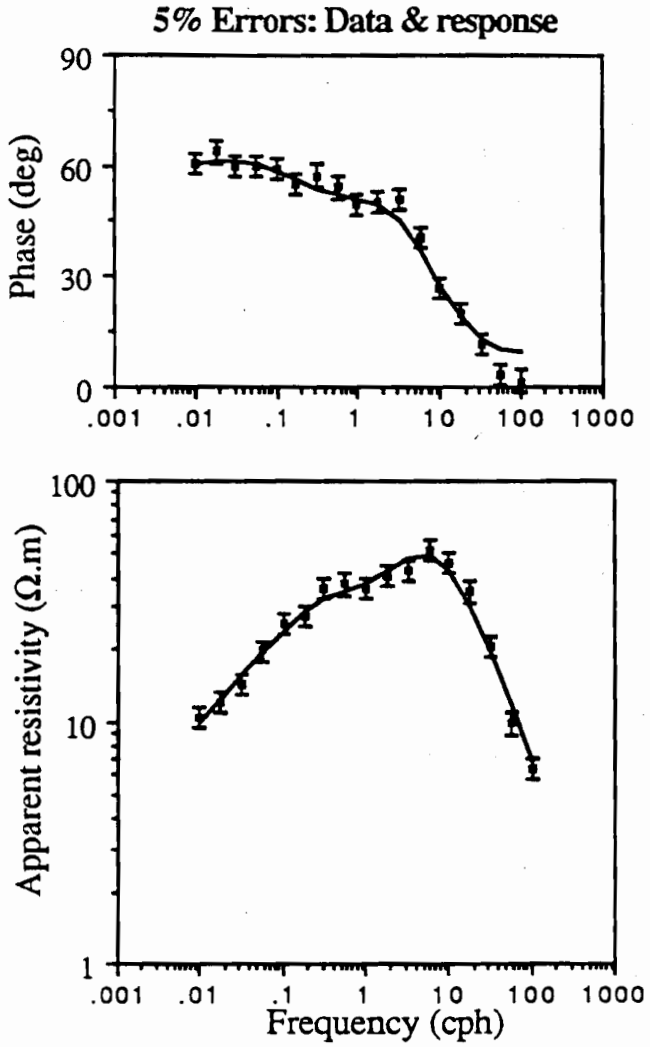

Figure 8.8: MT response of the Occam inversion model for the 5 % noise and wide period-range case. The response lies outside the error bar for approximately 10 data indicating an appropriate fit to the data.

All of the inversion models shown above have been based on minimization of the first derivative of the model with depth. Figure 8.9 shows the conductivity model for the 2nd-derivative inversion of the 5% noise wide period-range data. For depths between 80 and 700 km the 1st and 2nd-derivative inversions agree closely. The HCL for the 2nd derivative inversion however has a slightly reduced conductivity contrast. This result is expected since the HCL is a '2nd-derivative' feature (involving two changes of slope of the conductivity versus depth function) and will thus be minimized in a 2nd-derivative inversion. A 2nd-derivative inversion is therefore a suitable method for assessing if any satisfactory conductivity models without an HCL exist.

Regions in which the 1st and 2nd-derivative inversion models differ significantly correspond to regions of poor resolution. The calculation of the two models thus provides a measure of resolution of the models. For example, at the base of the conductivity profile the 1st and 2nd-derivative models diverge at a depth of about 700 km. This value is in agreement with the 700 km penetration depth obtained using the D^+ inversion method. Where the 1st and 2nd-derivative models diverge, the 2nd-derivative results tend to have the more extreme conductivity values (Figure 8.9). For this reason the more conservative 1st-derivative inversion results will in general be used for the Tasman Project. Although the 2nd-derivative conductivities are closer to the true conductivities in Figure 8.9 (in the resistive region of the model), other inversions with different period ranges and errors have shown that the second derivative results generally include far more extreme conductivity values.

8.4 Inversion of Tasman Project Data

This section describes the D^+ and Occam inversion of the (E-pol) impedances from Tasman Project sites TP3, TP4 and TP5. Although most of the inversions are performed on the SFMT rather than the VGS impedance estimates, final results are presented for both sets of impedance estimates.

D^+ Inversions

The Tasman Project SFMT impedances were inverted using the D^+ program and the resulting χ^2 values are summarised in Table 8.3. For all sites the observed value of χ^2 exceeds the 95 % confidence limit indicating that no 1D model can satisfactorily fit the data. The site TP5 data is the closest to an acceptable 1D response, with a χ^2 value of 46.4 compared with the 95 % confidence value of 32.6.

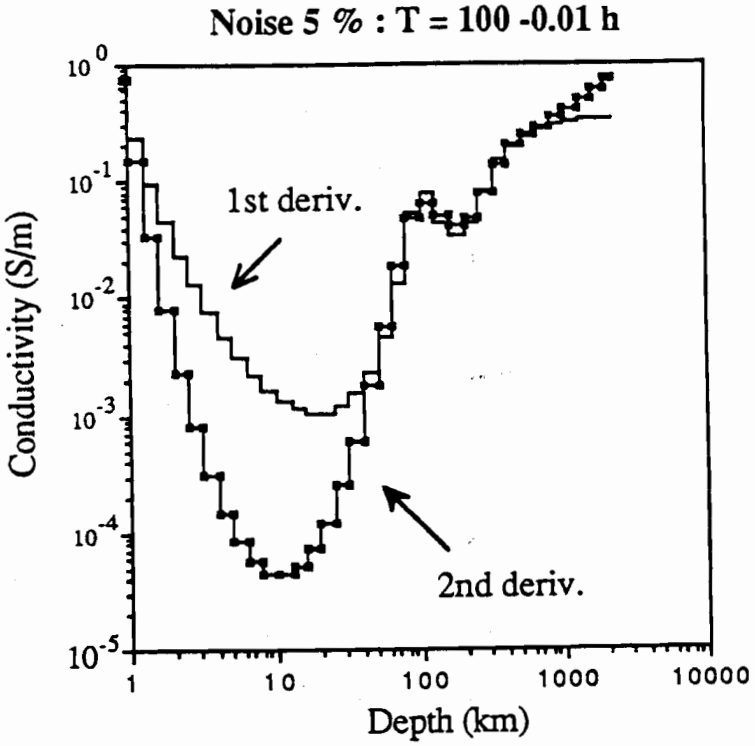

Figure 8.9: Occam inversion models in which the (a) 1st and (b) 2nd-derivative of the model with depth have been minimized. The data used in the inversion was the 5 % noise and wide period-range data set. The HCL is resolved in both inversions but is weaker in the 2nd-derivative model. In regions of poor resolution the 1st and 2nd-derivative models show large differences, with the 2nd-derivative model tending to include the more extreme conductivity values.

Table 8.3: Statistics for D^+ inversions of Tasman Project SFMT Impedances

Site	Number of Frequencies	Number of Data	Expectation χ^2	95 % conf. χ^2	Observed χ^2
TP3	14	28	28	43.0	271.3
TP4	12	24	24	37.9	143.3
TP5	10	20	20	32.6	46.4

Figure 8.10 shows the D^+ or best-fitting response for each of the sites. The high observed χ^2 values are confirmed by the number of data for which the response lies outside the error bars. It should be noted that in many geomagnetic induction studies, and in fact in other geophysical studies, fits to the data such as shown in Figure 8.10 would be regarded as satisfactory. This observation is especially true if it is noted that the error bars shown in Figure 8.10 are the relatively small, one standard deviation error bars. If 95 % confidence limits were plotted, the response would pass through a larger number of error bars. On this basis the analysis here will proceed with careful interpretation of the 1D results based on the data. The approach taken will not be as brazen as that advocated by Hobbs (1982) who states 'MT analysists are notoriously optimistic in believing the significance of the errors...A simple remedy is to adjust the errors , admitting that they do not adequately represent the situation' and in this thesis careful assessment will be made of important features in the final 1D conductivity structures.

Figure 8.11 shows the D^+ models for sites TP3, TP4 and TP5 and Table 8.4 tabulates this information. The models consist of only two (TP5) or three (TP3 & TP4) delta functions and a terminating perfect conductor, reflecting the low resolution of the SFMT data. The TP3 and TP4 models are very similar, with a delta function in the upper part of the profile, one at around 250 km depth and one around 600 km depth. In the Occam inversions performed below it will seen that the delta function at 250 km corresponds to an HCL which is present at TP3 and TP4 but is absent from TP5. The shallow delta function at TP4 has a higher conductance than that at TP3, 1253 S compared with 475 S, suggesting that the upper part of the conductivity profile is more conductive at TP4 than at TP3. The TP5 model is significantly different from that at TP3 and TP4; the 250 km deep delta function is absent and the lower delta functions occur at greater depth than at TP3 and TP4 suggesting that the conductivity profile at TP5 is more resistive.

There are four possible sources for the large misfit of the 1D models to the Tasman data: local 2D or 3D effects in the conductivity structure at each site; large-scale effects associated with the 3D induction in the Tasman Sea as a whole; bias in the data; or an under-estimation of the errors. By examining the frequency and spatial dependence of the misfit it is possible to attribute much of the misfit to large-scale induction effects.

Figure 8.12 shows the misfit between the data and the best-fitting 1D model at each site plotted as a function of frequency. The first feature to note is that there is contribution to the misfit from over a considerable frequency range. Examination of the contribution to the χ^2 total from each frequency term (Table 8.5) shows that there is no particular period range which contributes the majority of the misfit at all of the sites. The largest contribution to the total χ^2 is from the period range 2.08 - 4.44 h. (This result is not seen as readily in Figure 8.11 because of the inverse weighting of the misfit by error bar size in the contribution to χ^2). Separate inversions performed with just the longer period or

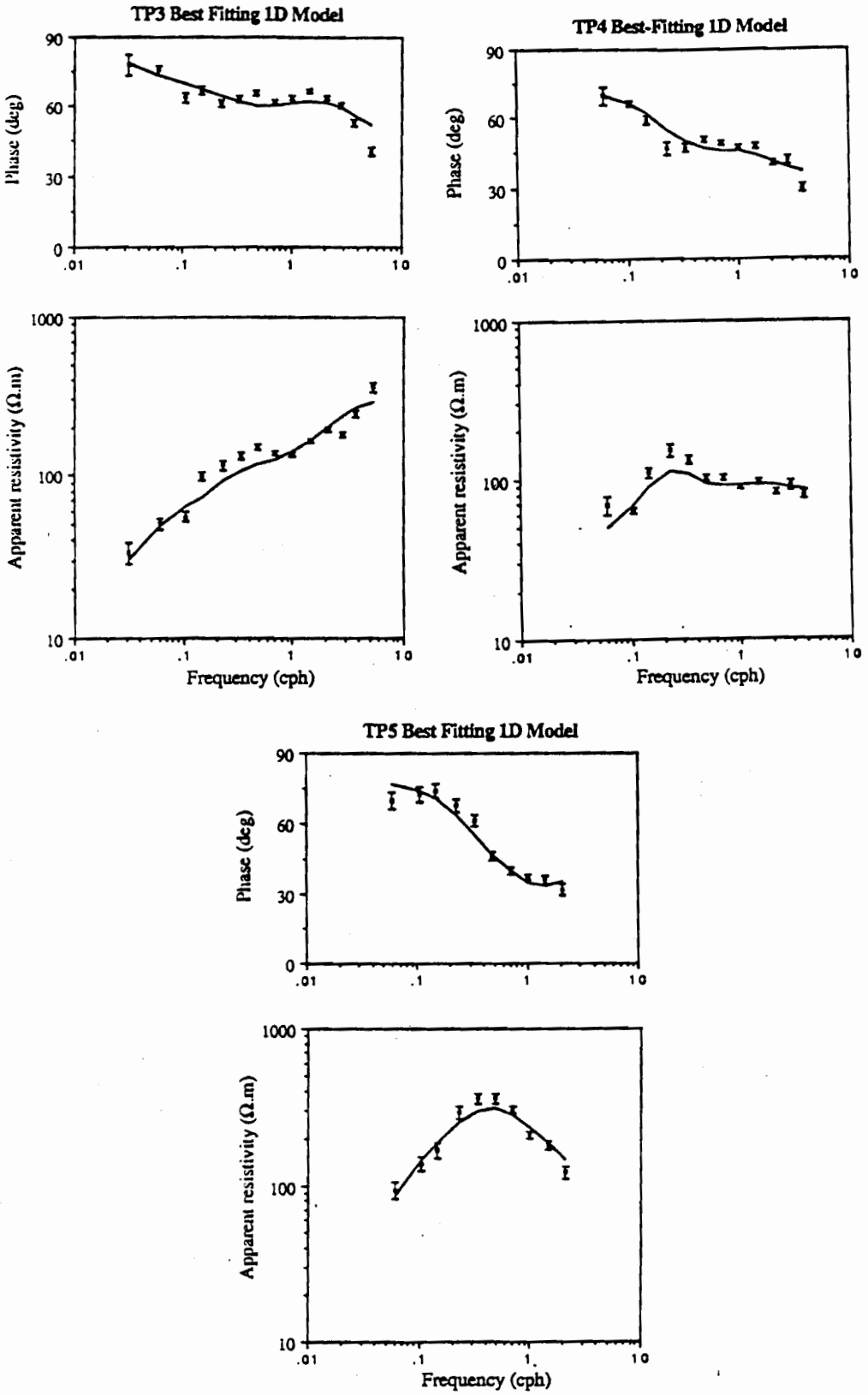

Figure 8.10: Response of the best-fitting 1D model (D^+ model) at the Tasman Project sites. Also shown are the data for each site and the one standard deviation error bars.

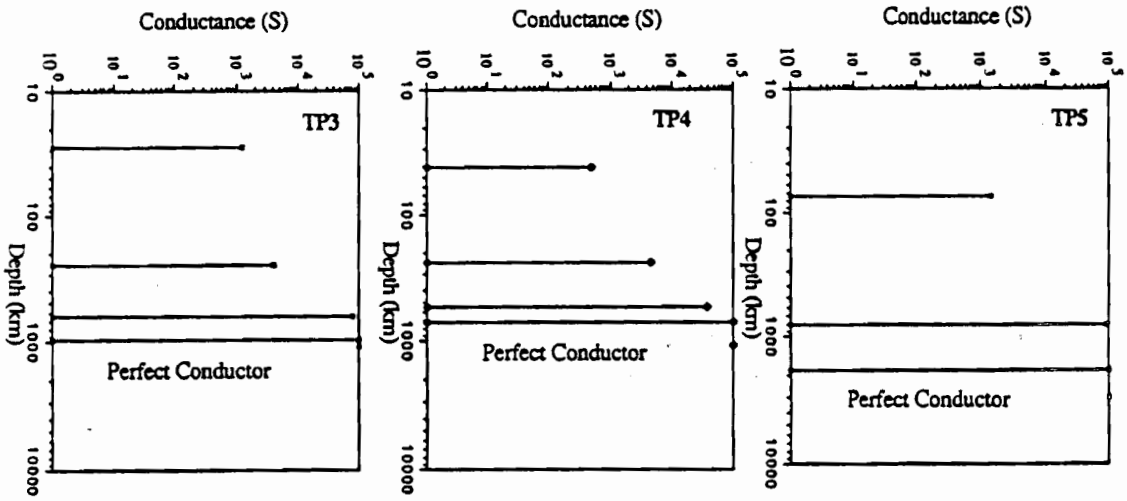

Figure 8.11: D^+ conductivity models for Tasman Project sites. Each of the models terminates in an infinite conductor at the depth shown.

Table 8.4: Details of D^+ models for TP3, TP4 and TP5

TP3		TP4		TP5	
Depth (km)	Conductance (kS)	Depth (km)	Conductance (kS)	Depth (km)	Conductance (kS)
41.6	0.475	28.4	1.253	74.6	1.44
238.0	4.46	251.3	4.114	-	-
546.3	37.3	633.1	78.2	817.7	88.9
713.2	∞	962.5	∞	1866.0	∞

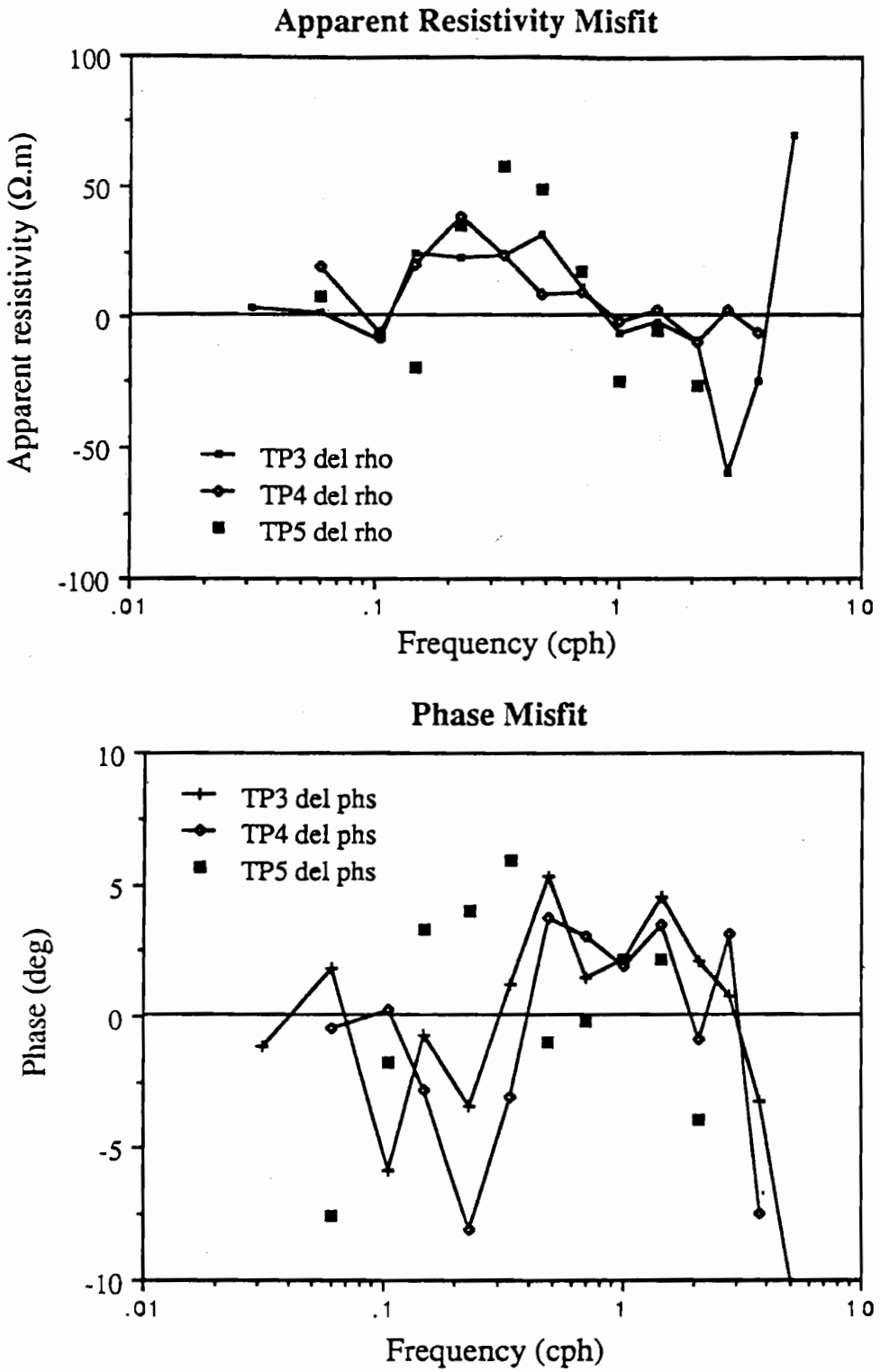

Figure 8.12: Misfit between Tasman SFMT response and best-fitting 1D (ie. D^+) response. The similarity of the misfit between the different sites strongly suggests that the misfit is caused by large-scale 3D induction effects in the Tasman Sea.

Table 8.5: Misfit between SFMT response and best-fitting 1D (ie. D^+) response

Band	Period (h)	χ^2 contribution TP3	TP4	TP5
1	32.51	0.61	n.i.	n.i.
2	16.65	1.29	5.71	2.76
3	9.62	12.52	8.00	0.42
4	6.85	14.55	11.66	2.09
5	4.44	13.59	29.25	5.25
6	3.00	13.88	19.08	11.73
7	2.08	50.64	9.32	4.79
8	1.44	10.95	10.96	1.55
9	1.00	14.25	5.42	7.75
10	0.693	28.49	9.48	1.76
11	0.481	6.19	15.36	8.29
12	0.357	54.02	2.82	n.i.
13	0.267	10.38	16.23	n.i.
14	0.190	39.95	n.i.	n.i

The table gives the contribution of the response at each frequency to the total value of χ^2

$$\chi^2(\omega) = \frac{\Delta^2 c_{re}(\omega) + \Delta^2 c_{im}(\omega)}{\sigma^2(\omega)} \qquad 8.12$$

where

$$\Delta^2 c_{re} = [\, c_{re}(\text{data}) - c_{re}(\text{model response}) \,]^2 \qquad 8.13$$

and $\sigma(\omega)$ is one standard deviation for the c_{re} and c_{im} terms for frequency ω. Note that "n.i." denotes frequency bands not included in the D^+ inversions.

shorter period half of the data from TP3 or TP4 also fail to produce a satisfactory 1D fit to the data. These results all suggest that bias of the data values is unlikely to contribute significantly to the misfit. Most sources of bias, such as source-field variations or residual effects from oceanic noise (after remote-referencing), will be frequency-dependent and strongest in the shorter or longer period bands.

Figure 8.12 shows that the 1D misfit is very similar at TP3 and TP4 in both the phase and apparent resistivity components. Also, for the apparent resistivity, the misfit at TP5 has a similar form to that at the other sites. These similarities strongly suggest that the misfit from a 1D response is due to a large-scale effect in the Tasman Sea. It is unlikely that local 2D and 3D effects, or random misfits exaggerated by under-estimated error size, could be so similar at each of the sites. One is thus left with the conclusion that large-scale 3D induction effects in the Tasman Sea are the major source of misfit. Large-scale frequency-independent 3D effects have previously been noted in the data, for instance the non-zero skew angles and the differences between VGS and SFMT impedance estimates, and it is therefore feasible that large-scale frequency-dependent 3D effects are also present.

Having established that the non-1D effects observed in the data are probably due to large-scale effects (probably related to the Tasman Sea morphology) it is likely that the conductivity structure beneath each recording site is 1D. (This observation is especially true for TP3 and TP4 for which the 1D misfit is very similar.) This result support the decision made above to proceed with further 1D inversions and to accept the results (with appropriate caution) as representative of the true conductivity structure.

Occam Inversions

Because of the large values of χ^2 associated with the Tasman data it is not possible to produced Occam models with the desired level of 1D misfit. It is therefore necessary to decide on some higher level of misfit for the inverted models. As the chosen level of misfit approaches its minimum value the roughness of the models will increase. The first set of Occam inversions performed on the SFMT data were used to produce relatively 'rough' conductivity models while a second set of inversions produced 'smooth' models with a level of roughness commensurate with the level of errors on the data.

The level of tolerance for the rough models was chosen in an empirical manner and was based on obtaining both an acceptable level of misfit and an acceptable level of roughness. With 1D data, the iteration procedure of the Occam inversion program is terminated automatically when the specified level of tolerance is reached. For data in which the misfit cannot be reduced to the required tolerance, the program will stop iterating at a larger level of misfit and correctly issue a 'failure to converge' message. After observing the behaviour of the smoothness and misfit measures at progessive iterations of such an inversion, it is evident that in the early stages of iteration the misfit decreases rapidly and the roughness increases at a moderate rate. As the inversion approaches a minimum value of misfit the changes in misfit between successive iterations become very

small and the increases in roughness very large (Figure 8.13). The level of misfit chosen for the 'rough' Occam models was a level occurring just after the start of this accelerationin the model roughness.

In order to produce the 'rough' Occam models the inversions were firstly run to determine the minimum level of misfit. The inversions were then re-run with the specified tolerance level set slightly above the minimum level achievable by the first run. The tolerance levels set for TP3, TP4 and TP5 correspond respectively to χ^2 values of 281, 165 and 58 which may be compared with the best-fitting D^+ χ^2 values of 271, 143 and 46. The Occam models are much smoother than the D^+ models and it is surprising that the χ^2 values for the models are so close to those of the best-fitting models. Figure 8.14 shows the 'rough' Occam models and Table 8.6 list their statistical parameters. Because of the subjectivity of the choice of the specified tolerances, the relative roughness of the models between the different sites is not a well-determined estimate. Small decreases in the specified tolerance at each site would produce large increases in roughness.

The 'rough' Occam models for TP3 and TP4 are quite similar, but are significantly different from the TP5 model. At TP3 and TP4 the models show a shallow conductivity maximum at 25 km depth and then a decrease in conductivity to a minimum value at 100 km depth. The models show a HCL between 200 and 320 km depth and a deeper rise at 500 km. For site TP5, the rough Occam model has a 'shallow' conductivity maximum at 70 km depth, the conductivity decreases to a minimum around 250 km depth and the deep rise in conductivity occurs around 800 km. These results closely reflect the earlier delta-function models determined for each of the sites.

A preliminary consideration of the 'rough' conductivity profiles suggests they may not be geophysically reasonable profiles. For example a shallow conductivity maximum would be expected to be located at sediment layer and upper crustal depths, rather than at 25 km or 70 km depth (see chapter 5). Fitting models close to the minimum misfit may have caused the models to include spurious features which fit the noise and non-1D response. The next step in the modelling process is therefore to obtain models with a level of roughness appropriate to the size of the error bars. This operation will ensure that the models do not fit the noise in the data.

With 1D data, an Occam inversion with the tolerance set to t =1 will give the model with minimum roughness, which is also the best-fit (without over-fitting) to the data. The procedure matches the level of roughness to the number of data and level of errors ie. the 'data quality'. For data which is not 1D it is also desired to invert to a level of roughness appropriate to the data quality but this can no longer be done by inverting to the t=1 tolerance level (since for non-1D data the inversion is unable to attain this level).

For the non-1D data, the appropriate level of smoothness will therefore be determined by inverting a very similar, but 1D, data set to a tolerance of t = 1. The obvious data set to

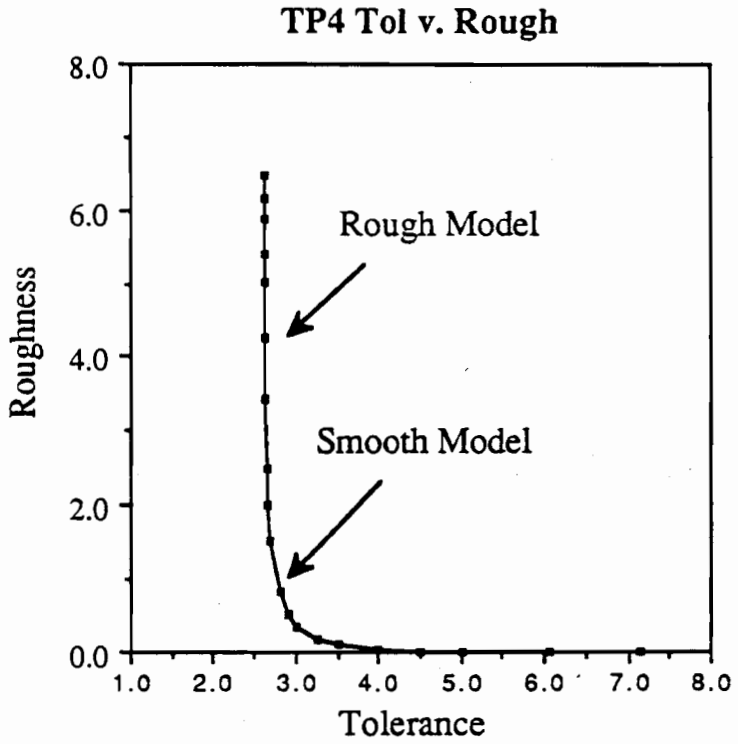

Figure 8.13: Example of the relationship between the tolerance (or misfit) of an inverted model and the roughness of the model The example shown corresponds to a (1st-deriv.) Occam inversion of data from site TP4. Each point on the above curve actually represents the final model from a separate inversion. The relationship of roughness and misfit at successive iterations from a single inversion has a very similar form.

The end members for the left and right ends of the misfit-roughness curve are respectively the D^+ model (minimum tolerance) and a half-space (minimum 1st-derivative roughness). The positions of the 'rough' and 'smooth' Occam models for TP4, shown in Figures 8.14 and 8.15 are shown on the figure. The roughness and tolerance are dimensionless quantities.

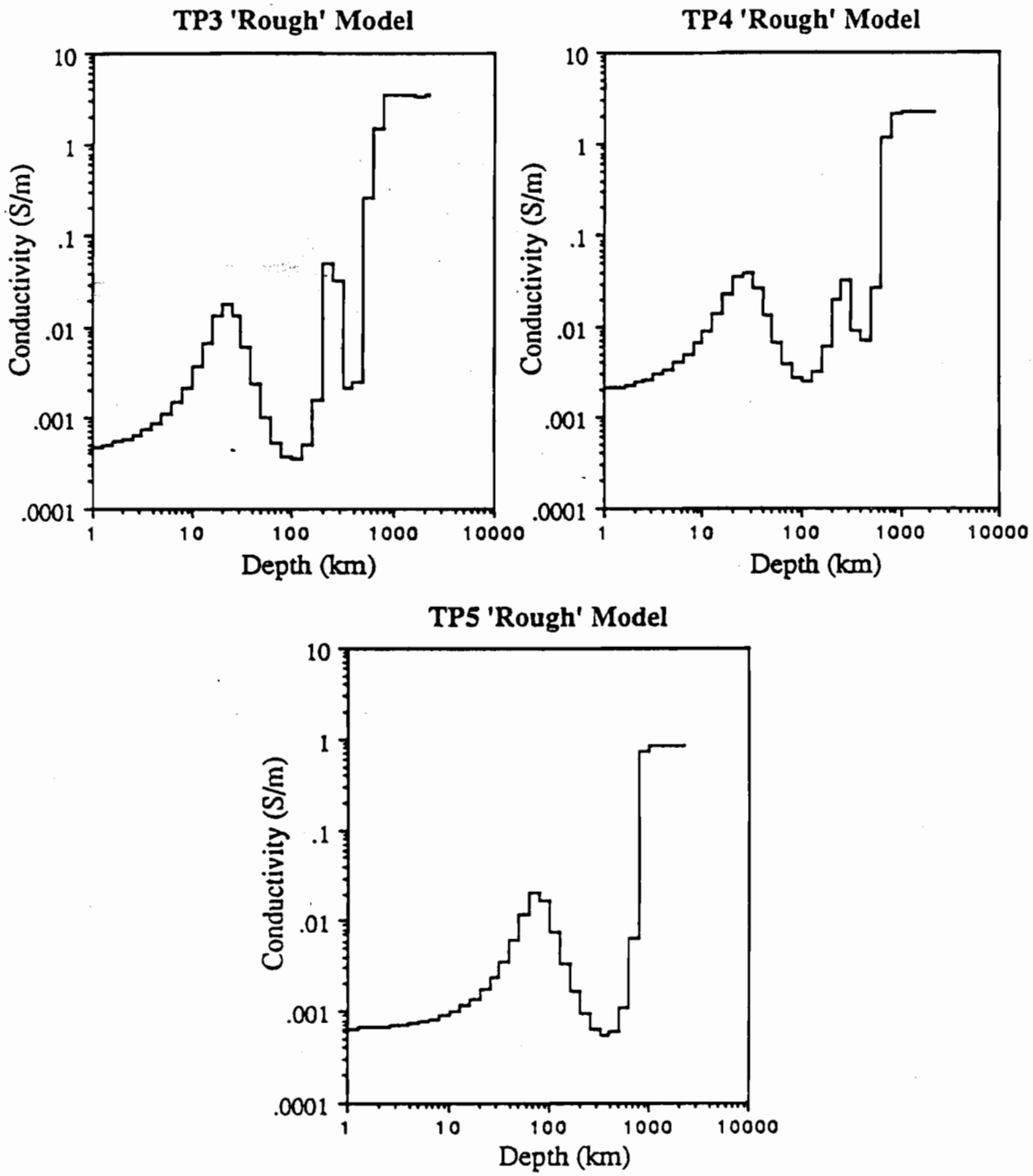

Figure 8.14: 'Rough' Occam models for Tasman Project sites. Note the similar form of the TP3 and TP4 conductivity profiles. The models lie close to the minimum levels of misfit and are therefore over-fitting the data.

use for this purpose is the response of the D^+ model fitted to the original data. This 'test' data set consists of the D^+ response at each of the frequencies of the original data with the error estimates from the original data. The 'test' data set is inverted to t = 1 and the level of smoothness noted. The original data set is then inverted (using trial values for the tolerance) until the same level of smoothness is obtained.

Strictly, the 'test' data set should have artificial noise added at the level of the assigned errors. As discussed above, if noise is not added the inversions will give models which are too smooth and with a non-random misfit. Because the 'test' data set is being used only to determine an appropriately levels of smoothness, such effects are of minor importance. (The final model is obtained from the original data and is not related to the model obtained from the 'test' data set.) Also a small under-estimation of the smoothness level does not contradict the minimum-structure philosophy of Occam inversions. The validity of using of a second data set to estimate smoothness levels is a more critical question, however it should be noted that the process is being used only to distinguish between a number of inversions of the original data.

Table 8.6 lists the levels of appropriate roughness determined from the 'test' data sets for TP3, TP4 and TP5. The level of roughness is largest for site TP5, reflecting the greater amount of 'structure' in the MT response at this site compared with that at sites TP3 and TP4. Returning to the original Tasman Project data sets, inversions were performed with the tolerance being adjusted until the desired smoothness was obtained. This procedure did not require a large number of trial iterations: it involves moving along simple curves such as that shown in Figure 8.13 for TP4. Figure 8.15 shows the resulting 'smooth' conductivity models for the Tasman Project sites.

The smooth models for sites TP3 and TP4 still resolve an HCL between 200 and 320 km depth and a deeper rise in conductivity at 500 to 600 km depth. However the shallow conductivity maximum appearing in the 'rough' models at TP3 and TP4 does not appear in the 'smooth' models. In the smooth models the conductivity decreases monotonically from the surface to a minimum at around 80 km depth in a similar pattern to that observed in the synthetic-data inversions in Figure 8.7. The smooth model for TP5 has retained the same features as the rough model but the magnitude of the conductivity contrasts of these features is reduced.

As was shown in section 8.2 the response of conducting layers at shallow depths beneath the seafloor affects the MT response over a range of frequencies. It is therefore unlikely that the changes at shallow depth in the TP3 and TP4 conductivity profiles (between the rough and smooth models) are simply due to the model ceasing to fit random errors in the data. It is more probable that the larger misfit associated with the smooth model inversions allows the model to less-closely fit 3D or bias effects in the MT data (ie. systematic errors in the 1D response). This conclusion is supported by an examination of the response of the smooth Occam models shown in Figure 8.16. Comparison of these responses with the D^+ model responses (in Figure 8.11) shows systematic differences

Table 8.6: Details of Occam inversions of Tasman Project data

Parameter	Site		
	TP3	TP4	TP5
'Rough' Occam models 1st derivative			
Tolerance	3.17	2.62	1.86
Observed χ^2	281	165	58
Roughness	9.57	4.281	5.54
D^+ 1D Response with Tasman Errors 1st derivative			
Tolerance	1.0	1.0	1.0
Roughness	0.99	0.896	1.858
'Smooth' Occam models 1st derivative			
Tolerance	3.35	2.78	2.115
Observed χ^2	314	185	69
Roughness	0.99	0.903	1.855
D^+ 1D Response with Tasman Errors 2nd derivative			
Tolerance	1.0	1.0	1.0
Roughness	0.189	0.194	*
'Smooth' Occam models 2nd derivative			
Tolerance	3.4	2.81	2.115*
Observed χ^2	324	190	69
Roughness	0.193	0.189	0.298

* For site TP5 the 2nd-derivative inversion using the D^+ response with the observed error estimates failed to converge. The smooth 2nd-derivative model for TP5 was therefore obtained by fitting to the tolerance indicated by the 1st-derivative results.

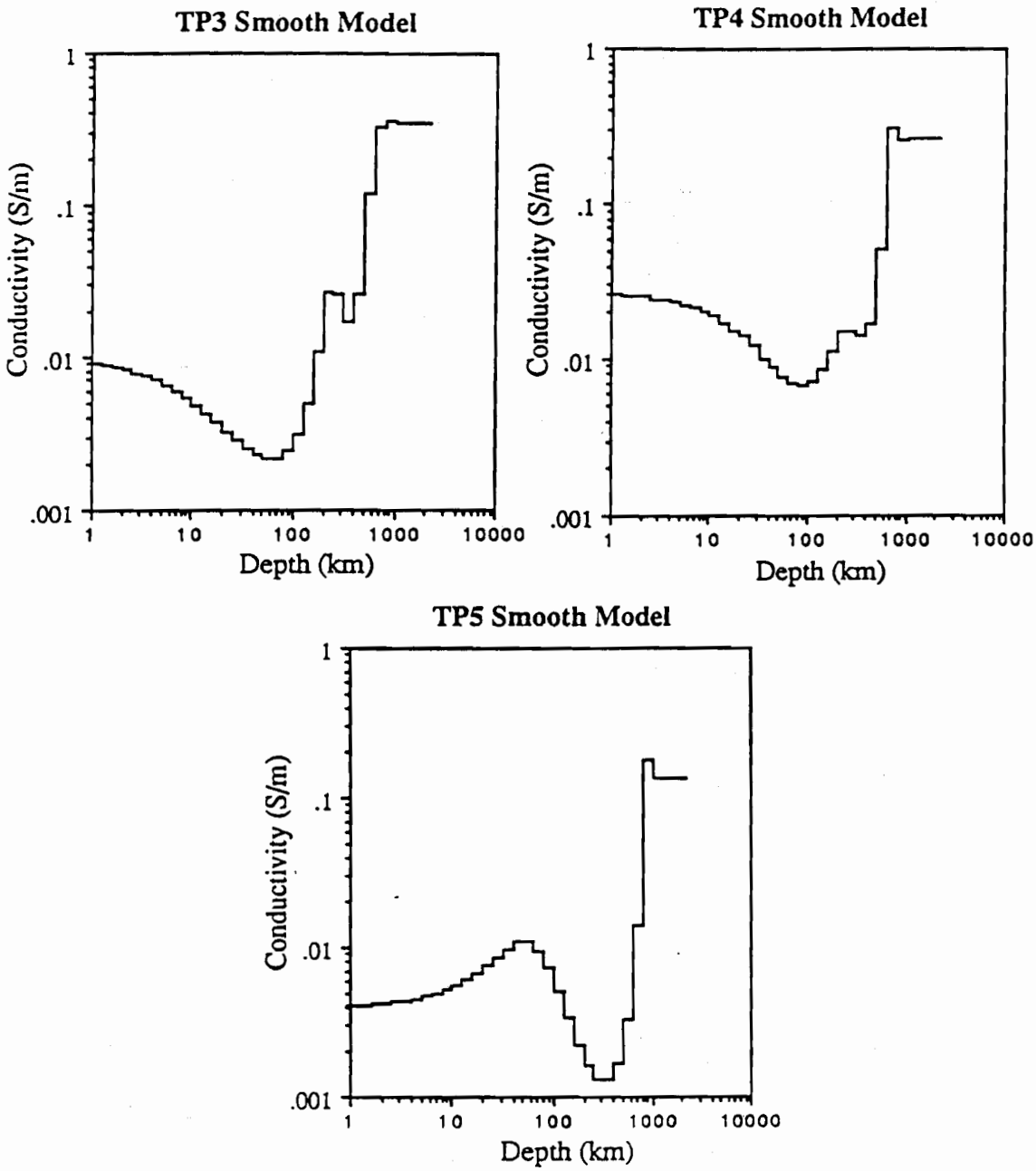

Figure 8.15: 'Smooth' Occam models for the Tasman Project sites. The roughness for these models has been matched to the level of the random error estimates on the data.

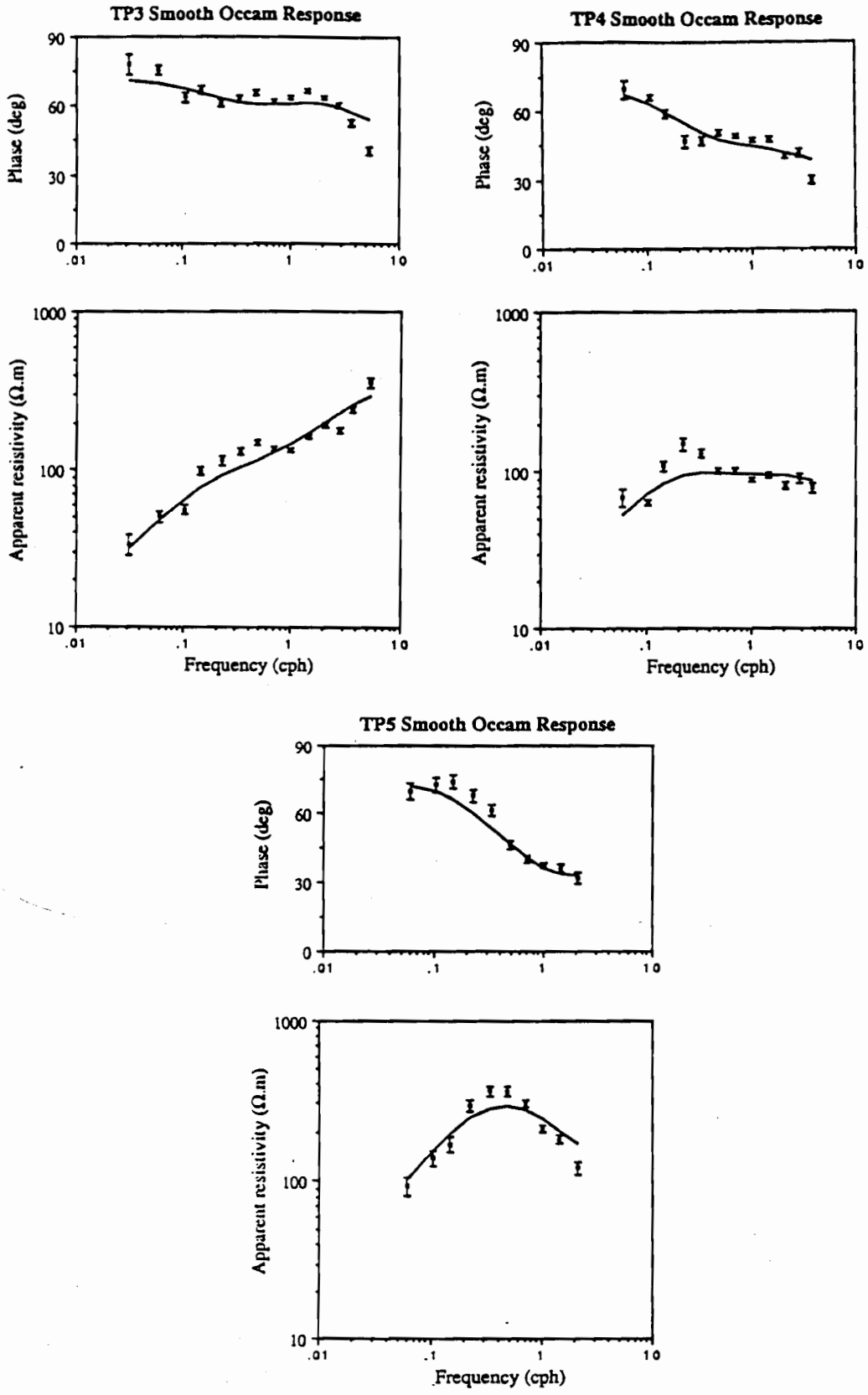

Figure 8.16: Response of smooth Occam models in apparent resistivity / phase form. Also shown is the original data with one standard deviation error bars.

(as a function of frequency) exist between the responses, with the smooth Occam models having smoother response functions but larger levels of misfit.

It is evident is that the shallow conductor at 25 km depth is a less essential feature of the 1D model fitted to the response than are other structures, such as the HCL at 200 km or the conductivity increase at 500 to 600 km depth. An assessment of the reliability of the shallow and deep features of the Occam models will be made below.

Depth of Penetration and Joint Inversions

The use of D^+ inversions for the determination of the depth of penetration requires data to be 1D. It is therefore not possible to obtain these depths directly from the Tasman Project MT data. Once again though, it is possible to use the 'test' (best-fitting D^+ model response) data sets, in order to estimate the depth of penetration.

Using these data, depths of penetration of 560, 580 and 725 km are obtained for sites TP3, TP4 and TP5 respectively . These depths will be slightly too shallow because there is no contribution to the limiting χ^2 value from random errors in the 'test' data set. Figure 8.17 shows the relationship of the χ^2- misfit to the depth of insertion of a perfect conductor in the model, for site TP4. It is evident that the depth of penetration is not too strongly dependent on the exact χ^2 measure used and therefore to the absence of an random error contribution to χ^2. The penetration depths calculated for the Tasman sites should represent reasonable minimum estimates for the depths of MT resolution at the Tasman sites.

At each of the sites the penetration depth corresponds closely to the depth of the deepest increase in conductivity shown in the Occam models. This result suggests that the data resolves the presence of an increase in conductivity, but the increased conductivity prevents the deeper penetration of the electromagnetic energy at the periods considered. The meaning of the terminating perfect conductor in the D^+ models, which occurs at a depth greater than the penetration depth, is unclear.

The D^+ inversion method provides a formal method for testing whether two (or more) 1D MT responses are significantly different (eg. Oldenburg et al. 1984). The method involves performing an inversion using the data from both MT responses. If a model can be found which fits the combined data set to within a specified confidence level (say 95 %) then it can be concluded that the two data sets are not significantly different at this level of confidence. For the Tasman data it is only possible to test whether there are significant differences between the best-fitting D^+ responses at each of the sites, because the use of the original (non-1D) MT responses would immediately cause the misfit to exceed the allowable range.

Combining the TP3 and TP4 data sets gives 26 frequencies, or 52 data, corresponding

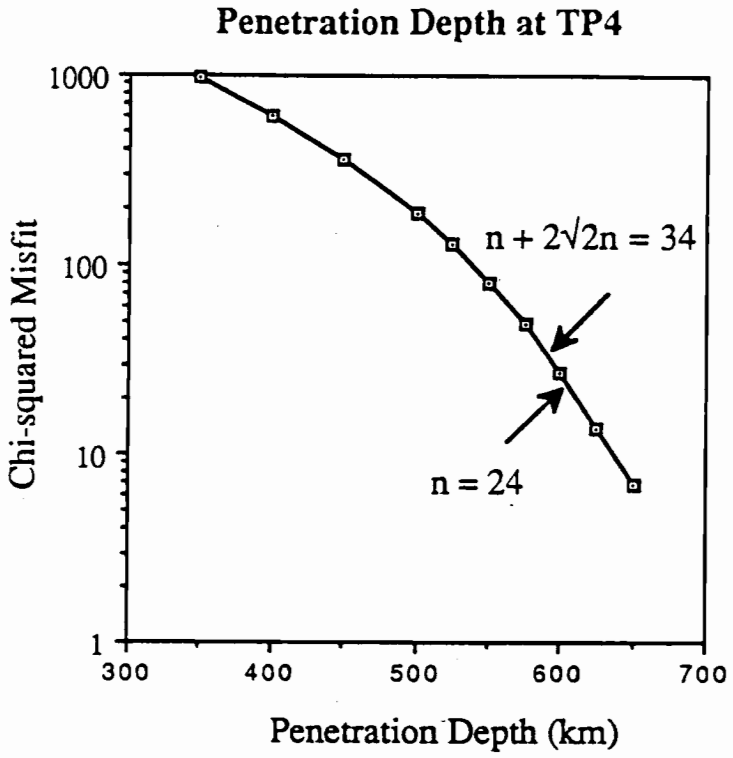

Figure 8.17: Penetration depth for TP4 based on the D^+ 1D response with the observed TP4 errors. The figure shows the variation in χ^2-misfit as a perfect conductor is inserted at different depths in the model. The misfit is plotted at a logarithmic scale with large variations in misfit corresponding to only small changes in depth. The penetration depth is taken at the 95 % confidence limit of χ^2 (= 34) and is approximately 580 km. The use of a smaller statistical measure, such as the expectation value of χ^2 (=24) would give a slightly deeper penetration depth.

to a 95 % confidence limit on χ^2 of 72.4. Inversion of the data showed the D^+, or best-fitting, 1D model has an observed misfit of 1966.2. This result is interpreted as showing the existence of significant differences between the TP3 and TP4 conductivity profiles. If the combined TP3 and TP4 data set is restricted to periods of longer than 3.0 h the different data sets are much more similar. In this case, the 95 % confidence limit on χ^2 equals 35.3 (for the 11 frequencies) while the observed χ^2 equals 36.0. Although the models are still formally different at the 95 % confidence limit, they will not be at a slightly higher confidence limit. It is probably safe to conclude that for longer periods the response at TP3 and TP4 is not significantly different.

This result means that the MT data provides no evidence that the deeper part of the conductivity profile (say deeper than 100 km) is different between TP3 and TP4. The result does not prove that the deep structure is the same at the two sites but merely the structure at the two sites has a similar MT response and must therefore be similar in certain properties. It should also be remembered that the result is also based on the best-fitting 1D model for each site rather than on the original data. A full solution of the inference problem is needed to assess the possible differences between sites TP3 and TP4. The forward modelling performed in section 8.2 however suggests that the structure at the two sites must be quite similar in the depth range of 150 to 500 km.

Joint inversion of the combined best-fitting 1D responses from TP4 and TP5 data sets reveals that there is little similarity between the conductivity profiles at these sites. For the complete data set, involving 22 frequencies, the observed value of χ^2 is 959 which compares with the 95 % confidence limit of 62.8. There are no parts of the period range over which the two data sets are not significantly different; the greatest differences occur around the period of 1.0 h.

8.5 Assessment of Features in the Tasman Sea Conductivity Models

High Conducting Layer at TP3 and TP4

The existence of an HCL beneath sites TP3 and TP4 is an important result and therefore it is important to check that the structure is a valid and necessary feature of the 1D models at these sites. The forward modelling described above, which showed that SFMT data similar to that from the Tasman Project could resolve an HCL, provides some initial support for the HCL being a valid feature. Further support comes from the smooth Occam models which include the HCL and thereby show that less tightly constrained fits to the data still require an HCL. Since it is known that there are non-1D effects present in the data it is however important to verify that the HCL is not a spurious feature caused by 3D effects.

Once a 1D MT response function is perturbed by external effects (not associated with the underlying conductivity structure) it is possible that the 1D models fitted to the data do not represent the true 1D conductivity structure. In order to assess whether a spurious HCL could be caused in this manner it is necessary to compare the perturbation of the response function needed to produce the HCL, with the external effects in the data. The change in a response function required to produce a HCL is simply the difference between the response of models with and without an HCL. Figure 8.3 illustrates this change in response for TP3. The change in response extends over a wide frequency range and involves changes to both apparent resistivity and phase components.

It is much more difficult to assess the exact form of external effects in the data. For the Tasman Project data the external effects are interpreted as large-scale 3D effects

associated with the morphology of the Tasman Sea and therefore the ultimate availability of thin-sheet modelling should indicate their exact form. For the present analysis one is restricted to estimating the general character ie. the frequency-dependent form, of the external effects. It is here assumed that the character of the external effects is closely represented by the form of the frequency-dependent misfit between the observed data and the best-fitting 1D model.

This assumption is illustrated schematically in Figure 8.18. Consider the true response of the conductivity structure, **T** which is perturbed by external effects to give the observed response **O**. A 1D inversion may fit part of the perturbation (as well as the true response) and will have a response **R** lying between **T** and **O** at a point depending on the amount of perturbation fitted. The parameter we wish to estimate is the character of the perturbation incorporated into the 1D model ie. the frequency-dependent **R-T** . The assumption made is that the general character of **R-T** is the same as that of **O-R** ie. the measurable difference between the observed response and that of the inverted 1D model.

The validity of this assumption relies on the form of the perturbation being relatively simple so as to allow the 1D models to incorporate a 'representative sample' of the total external perturbation. The relatively simple form of the 1D misfit functions (as shown in Figure 8.12) suggests the external effects will have such a relatively simple form. The assumption (that the misfit between the observed data and the D^+ model response has the same general form as any external effects incorporatedinto the D^+ model) should therefore be acceptable.

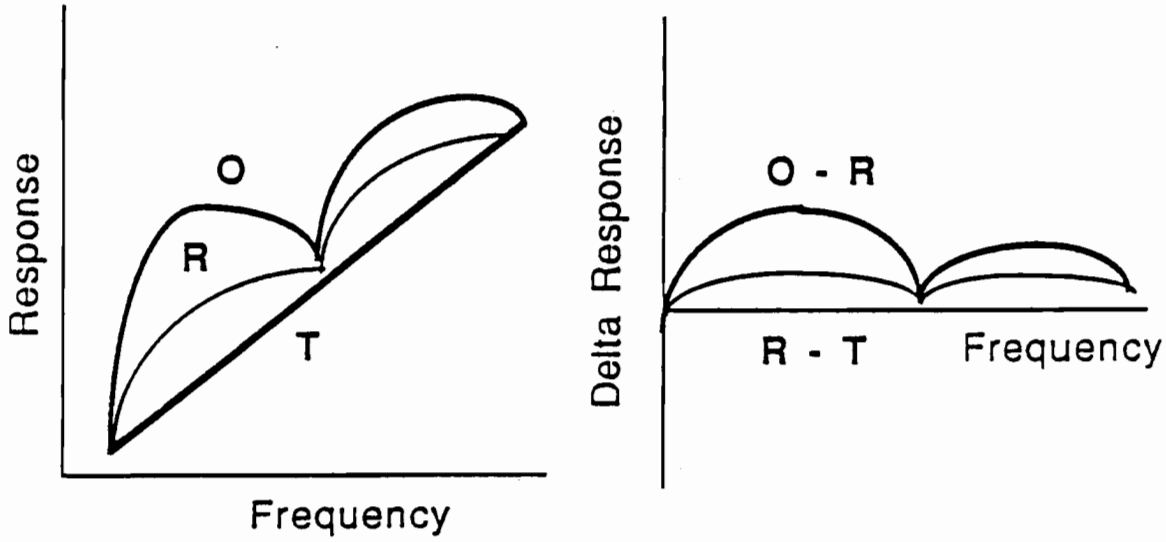

Figure 8.18: Schematic illustration of the relationship between the true response **T**, the observed response **O** which is perturbed by external non-1D effects, and the best-fitting 1D response **R**. In order to assess the features in the 1D model it is necessary to know the form of any perturbation in the 1D model response (**R-T**). The assumption is made that the general form of (**R-T**) is the same as the form of the measurable difference between the observed response and that of the best-fitting 1D model (**O-R**).

Figure 8.19 compares the change in response needed to produce an HCL with the estimate of the external effects in the MT response. The results are for site TP3. It is evident that for the apparent resistivity, the external effects have almost the opposite form from that required to cause an HCL to appear in a 1D model. Although the external phase effects in the data have approximately the correct form to cause a HCL it is unlikely that they would do so, considering the misfit that would be caused in the apparent resistivity. As shown by the forward modelling summarised in Table 8.1, the layering at intermediate depths in the conductivity profile tends to be constrained more strongly by the apparent resistivity than by the phase.

As shown by Figure 8.20 the presence of an HCL in the conductivity profile could be caused by either the HCL itself, or by the presence of the underlying decrease in conductivity ie. a low conducting layer (LCL). Figure 8.19 examines whether the external effects in the data have the same form as the change in response necessary to cause an LCL to appear in the profile. The estimated external effects in the apparent resistivity do have the correct form to cause the appearance of a spurious LCL. The inclusion of an LCL into the profile does however produce a significant phase response and this phase response is inconsistent with the estimated external effects in the phase response. It is concluded that although a spurious LCL is more likely than a spurious HCL, the phase results, which do constrain the layering to some extent, would tend to prevent a spurious LCL appearing in the conductivity models.

It has been shown that the HCL occurring at site TP3 is unlikely to be caused by external effects in the data. The same procedure may be followed to derive this conclusion for the TP4 data. It therefore appears extremely likely that the HCL is a true feature of the conductivity profile at sites TP3 and TP4. As will be shown below, 2nd-derivative Occam inversions also confirm the necessity of the feature in the models. Because the HCL is resolved in the minimum-structure Occam inversions of the data it is possible that the HCL in the actual conductivity profile involves a larger conductivity contrast than that in the inverted model. Indeed, from the trial Occam inversions performed on noisy data (Figure 8.7) it would seem probable that this is so. If the HCL were as small as that suggested for TP4 in the smooth Occam models (Figure 8.15) it would not be resolved in the Tasman Project data with its significant noise levels.

Shallow Structure at TP3 and TP4

As shown by the forward modelling and trial Occam inversions in sections 8.2 and 8.3, the main constraints SFMT impedances place on the upper part of the conductivity structure is the integrated conductance of the upper part of the profile and the maximum conductivity of the resistive parts of the profile. Figure 8.21 compares the 'rough' Occam models at TP3 and TP4. The integrated conductance in the upper part of the conductivity profile (above 100 km) for TP3 and TP4 is respectively 300 S and 1250 S which compares

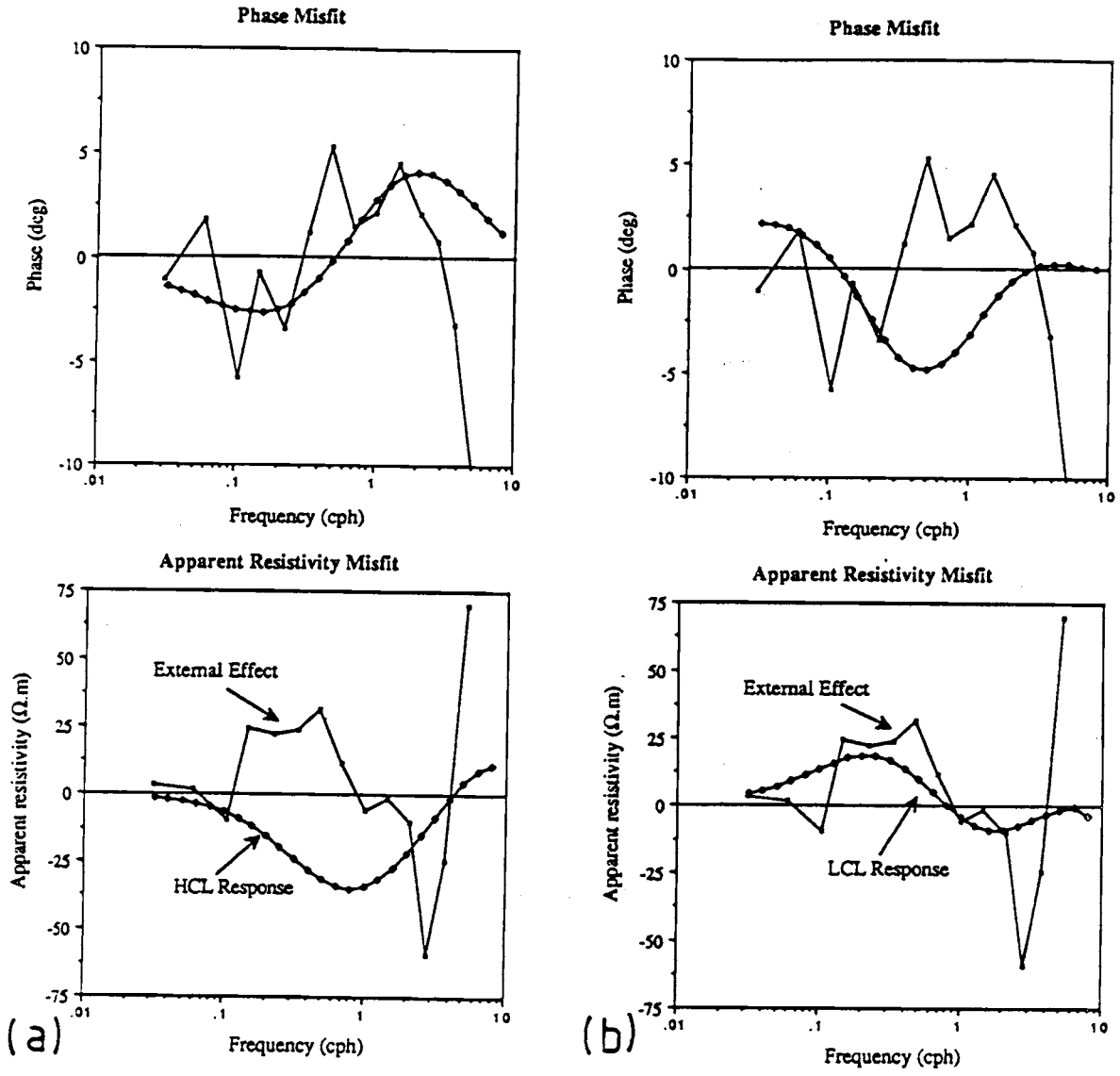

Figure 8.19: Comparison of the form of external effects in the 1D model with the change in response necessary to produce (a) a high conducting layer (HCL) or (b) a low conducting layer (LCL). It is important to look for similarity in the shape of the curves rather than exact matching of magnitudes, since the estimate of external effects only gives the shape or frequency-dependence of the external effect. The figure suggests that the external effects do not provide both the necessary apparent resistivity and phase response to produce either a spurious HCL or a spurious LCL in the 1D conductivity model.

The HCL (LCL) response is given by the difference in the TP3 response between a model including the HCL (LCL) and a model without it. The conductivity models are shown in Figure 8.20. The external effect is estimated from the difference between the observed MT response at TP3 and the response of the corresponding D^+ model.

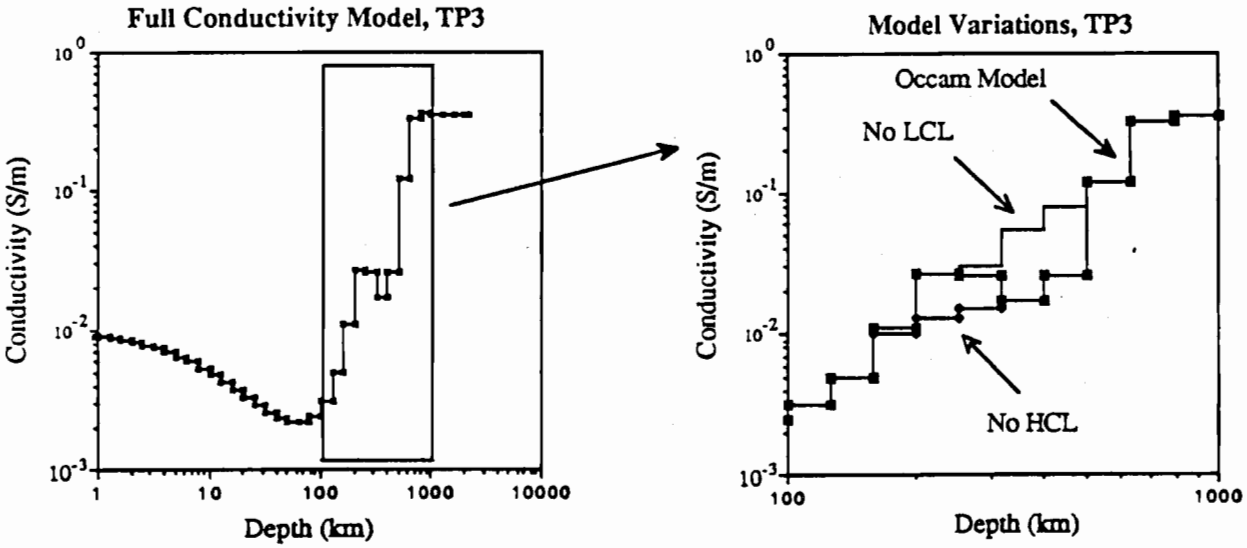

Figure 8.20: Variations in the TP3 conductivity model. The basic profile is the smooth Occam model for the site and the variations both involve removal of the high conducting layer. The variations are removal of the HCL itself and removal of the underlying LCL.

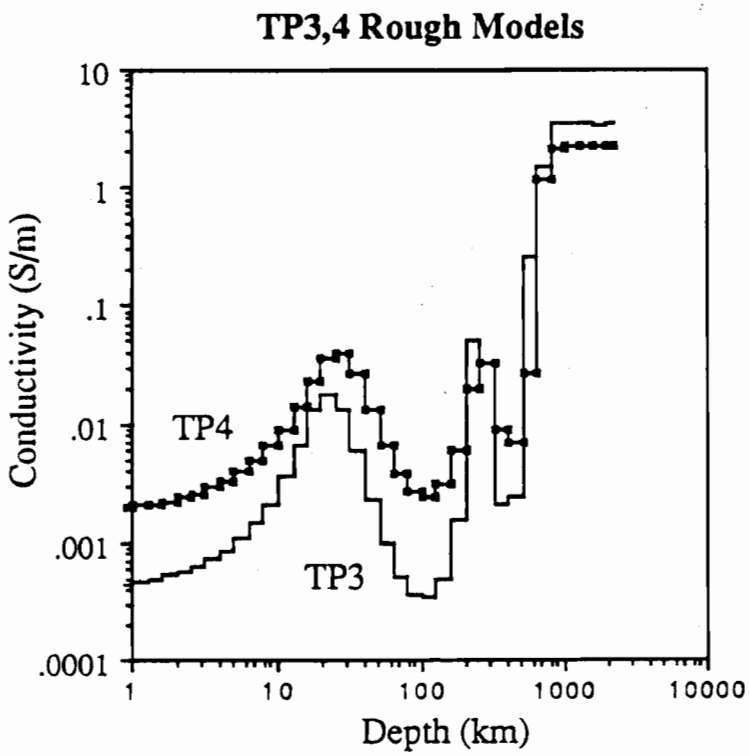

Figure 8.21: Comparison of the 'rough' Occam models for TP3 and TP4. Note the higher conductance in the upper 110 km at site TP4.

well with the delta-function estimates of 475 S and 1253 S.

The gradual decrease in conductivity between 20 and 100 km depth at TP3 and TP4 most probably represents the 'smearing-out' of the upper-layer conductance as observed in the trial Occam inversions. The results suggest that the maximum conductivity of the resistive region is less than 2×10^{-3} S.m^{-1} at TP4 and less than 3×10^{-4} S.m^{-1} at TP3. These results are in agreement with the 10^{-2} S.m^{-1} maximum estimate obtained from the B-pol impedances in chapter 7. The disappearance of the 20 km-deep conductivity maximum from the smooth Occam models at TP3 and TP4 suggests that it is not a real feature of the underlying conductivity structure. The conductivity maximum may be a spurious feature caused by external 3D induction effects or by bias in the short period MT response estimates.

The difference in the conductance of the upper part of the profile between TP3 and TP4 is more likely to be a real feature. Extreme influence by external or bias effects would be necessary to produce the observed differences in the apparent resistivity and the phase response between TP3 and TP4 (see Figure 8.11). Assuming the estimates of upper level conductance at TP3 and TP4 are correct, and that only the structure is perturbed by the non-1D effects an examination will now be made of alternative models for the upper layers.

Figure 8.22 compares the response of the rough Occam model at TP3 with a similar model in which all of the upper layer conductance is confined to a 1 km thick 'sediment' layer of conductivity 0.3 S.m^{-1}. The response of the 'sediment' model reproduces the apparent resistivity of the rough Occam model very closely. The phase of the 'sediment' model is significantly different from that of the rough Occam model at high frequencies, but is in fact closer to the phase observed in the actual data. It is concluded that the 'sediment' model probably lies quite close to the true conductivity structure at TP3, with a minor distortion of the response, caused by external effects or bias, producing the spurious 20 km deep conductivity-maximum in the rough Occam model.

In the rough Occam models, the additional conductance at TP4 (compared with TP3) is spread evenly over the upper 110 km of the conductivity profile. Figure 8.23 shows two alternative models for TP4, in which the upper layer conductance is firstly confined to a 4 km thick layer and secondly, spread over the upper 50 km of the profile. Neither model reproduces the rough Occam model response acceptably, with the main discrepancy being short-period phase values which are in the alternate models. The response of the second model however is a much better fit than the first, and is favourably close to the observed MT response. Investigation of further models, confirms that a significant proportion of the upper layer conductance at TP4 must be located below 20 km depth.

It is concluded that the upper layer conductance at TP4 is significantly higher than at TP3 and that a significant proportion of the additional conductance must be located deeper than 20 km. To confirm that the upper layer conductance is the only necessary difference between sites TP3 and TP4, the response was calculated for a model consisting of the shallow conductivity profile from site TP4 and the deeper structure from site TP3. The

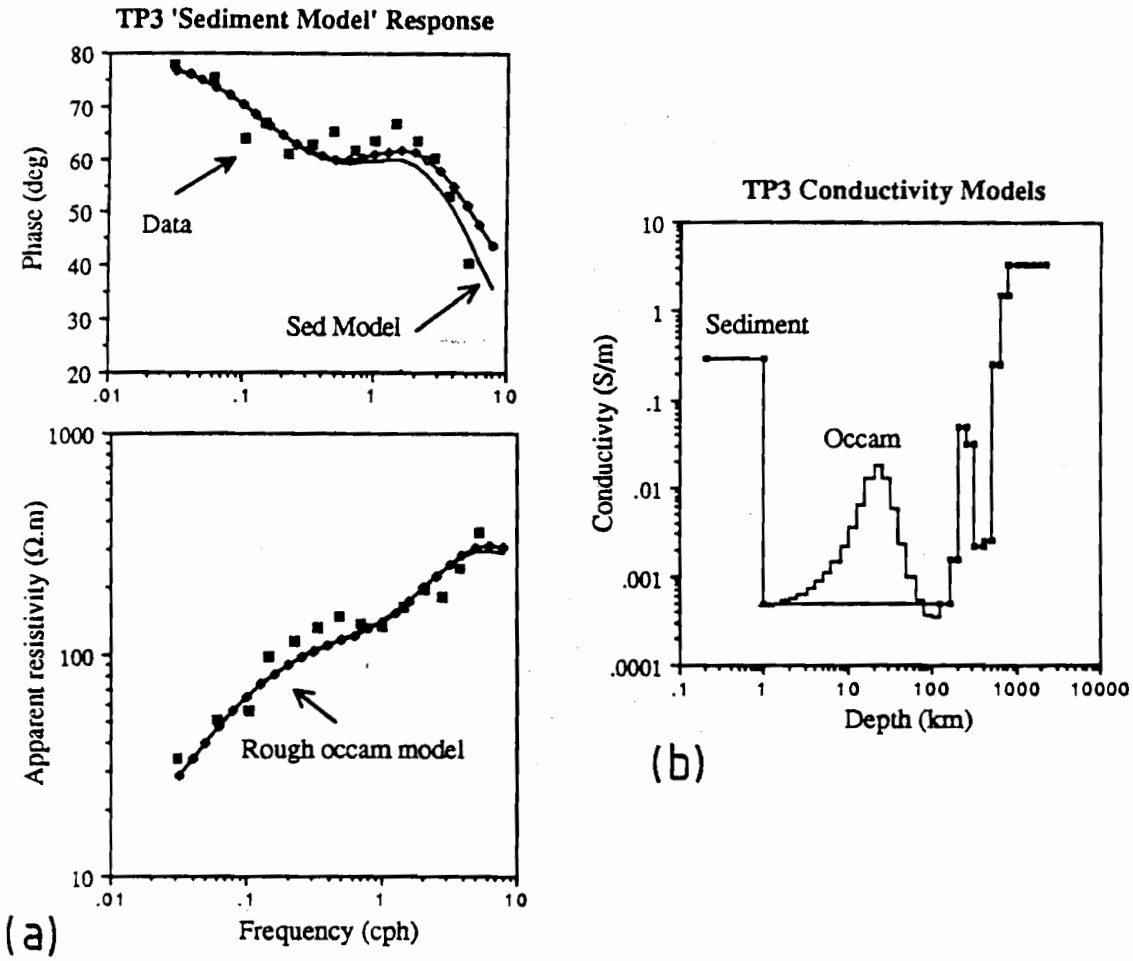

Figure 8.22: Simplified conductivity model for TP3. (a) The MT response of the original TP3 data (large squares), the rough Occam model (open diamonds), and the modified, 'sediment' conductivity model (plain line). (b) The rough Occam conductivity model and the 'sediment' conductivity model in which all of the conductance in the upper 100 km of the Occam model is replaced by a 1 km thick layer of conductivity 0.3 $S.m^{-1}$.
Note that the 'sediment' model fits the original data reasonably closely.

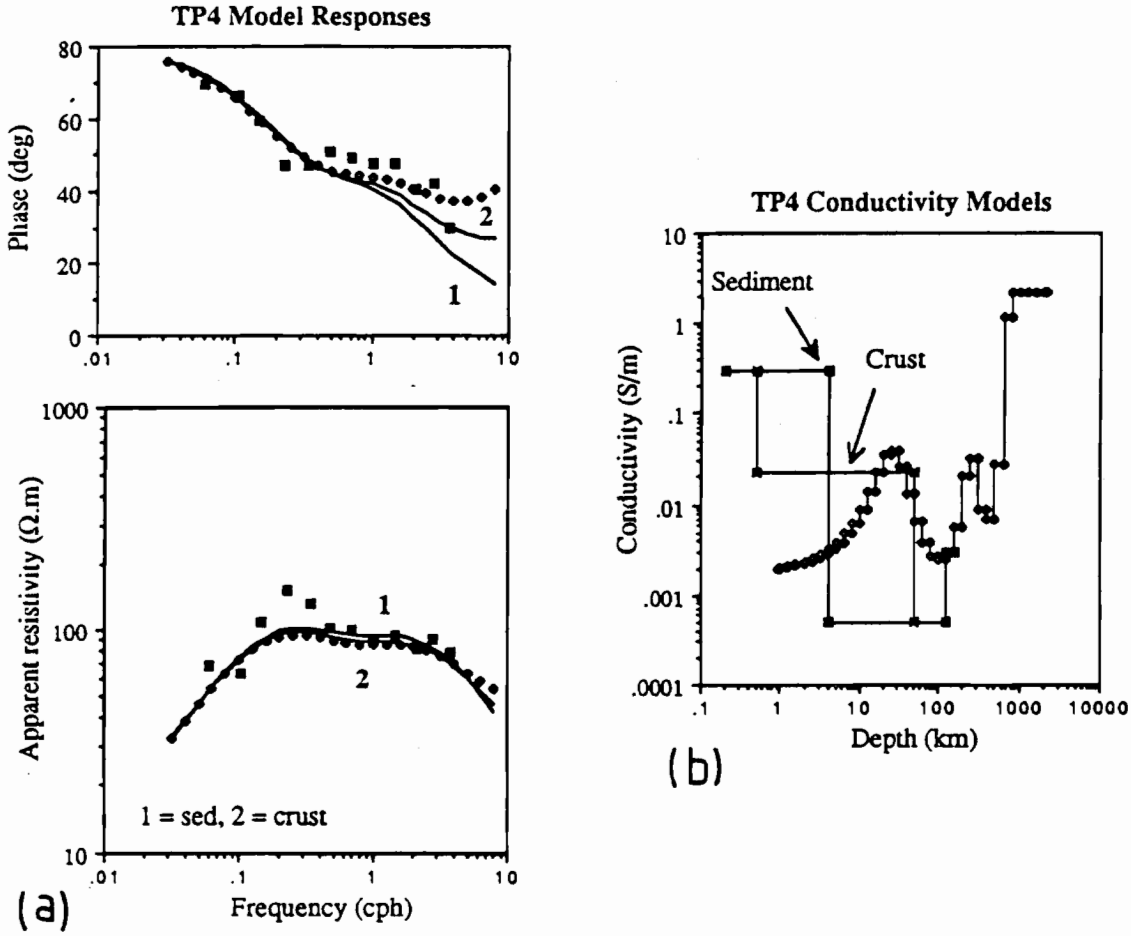

Figure 8.23: Simplified conductivity models for TP4. (a) The MT response of the original TP3 data (large squares), the rough Occam model (open diamonds), and the modified, 'sediment' conductivity model (plain line 1) and 'crust' conductivity model (plain line 2). (b) The rough Occam conductivity model and the two modified conductivity models. For the 'sediment' model all of the conductance from the upper 100 km of the Occam model is placed in 4 km thick layer of conductivity 0.3 $S.m^{-1}$. For the 'crust' model the upper conductance is divided between a 150 S sediment layer and an underlying 50 km thick region with conductance 1110 S. Note that the 'crust' model fits the original data reasonably closely.

response, shown in Figure 8.24 is very similar to the observed TP4 response. It is therefore concluded that the only major difference between the TP3 and TP4 conductivity profiles (which is resolvable by the MT method) occurs in the upper part (say above 100 km) of the conductivity profile.

TP5 Conductivity Structure

The large difference between the TP5 and the TP4 / TP3 conductivity profiles is quite surprising considering the similarities of the TP4 and TP3 profiles. The validity of these differences will now be assessed. The 2D modelling performed in chapter 7 shows E-pol anomalies can extend several hundred kilometres from a coastline and therefore there exists a possibility that the data at TP5 contain some 2D effects. The moderately rapid change of phase at intermediate periods in the TP5 data (as also observed at TP6 and in 2D model results) suggests the presence of some 2D effects in the TP5 data.

Two-dimensional effects should not effect the h-line part of the MT response and thus should not affect the deep structure determined for site TP5. In order to examine whether 2D effects could influence the shallow features in the TP5 profile, approximate 2D effects (predicted from the forward modelling) were subtracted from the TP5 MT response and the residual response re-inverted (Figure 8.25). The resulting conductivity model does not become significantly more similar to the TP4 / TP3 models. It therefore appears that 2D effects are not responsible for the differences between the TP4 and TP5 conductivity profiles.

There are two further possible sources of perturbations to the measured MT response at site TP5. At shorter periods bias may occur in the data. Returning to the initial examination of data quality (chapter 3, appendix 2) it is noted that the TP5 HEF instrument had a timing loss of 156 s at the end of the recording period. Given the additional fact that the TP5 instrument stopped recording for several weeks during the middle of the recording period, some doubt must exist regarding the accuracy of the timing and hence the shorter period phase values. A second source of perturbation to a 1D response at site TP5 is the presence of external 3D effects in the data. Figure 8.12 shows that the 1D misfit at TP5 involves some differences from that at TP3 and TP4 and from chapter 7 it is noted that the distortion elements and skew angle at TP5 differ from those at TP3. Thus 3D effects could produce some differences between the TP5 and the TP4 / TP3 conductivity models.

Figure 8.11 shows the difference in response between TP5 and TP4/TP3 is large and systematic. It therefore seems unlikely that the effects noted above can explain the complete form of the TP5 response. It is concluded that the conductivity structure at TP5 is significantly different from sites further east in the Tasman. The TP5 profile is more resistive and possesses a deeper conductivity rise. The possibility of 2D, 3D and bias effects in the measured response however reduces confidence in specific details shown in the model.

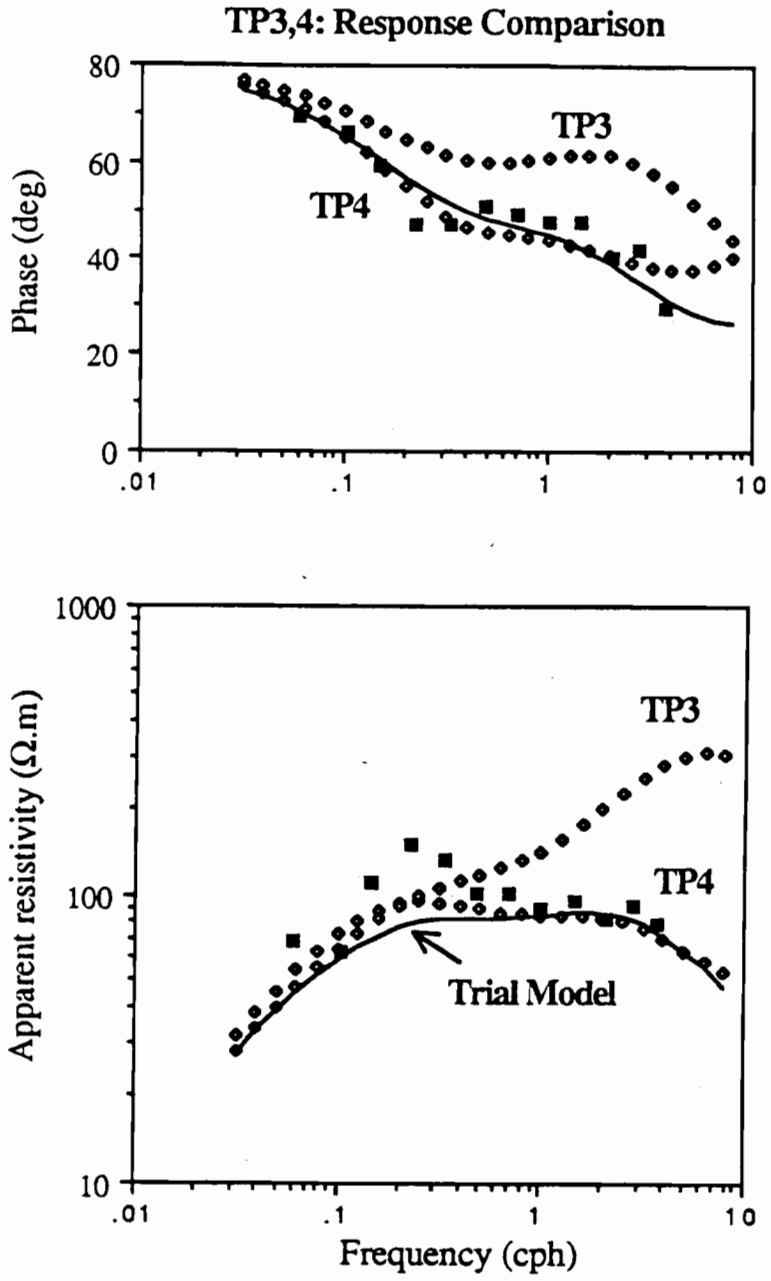

Figure 8.24: Examination of the similarity of the TP3 and TP4 conductivity profiles. The diagram shows the response of a trial conductivity structure (plain line) which is composed of the deep structure at TP3 (> 120 km deep) and the shallow structure (< 120 km deep) at TP4. The response of the trial data fits both the Occam model response for TP4 (diamonds) and the actual TP4 data (squares) reasonably closely. The diagram also shows the Occam response for TP3 (diamonds).

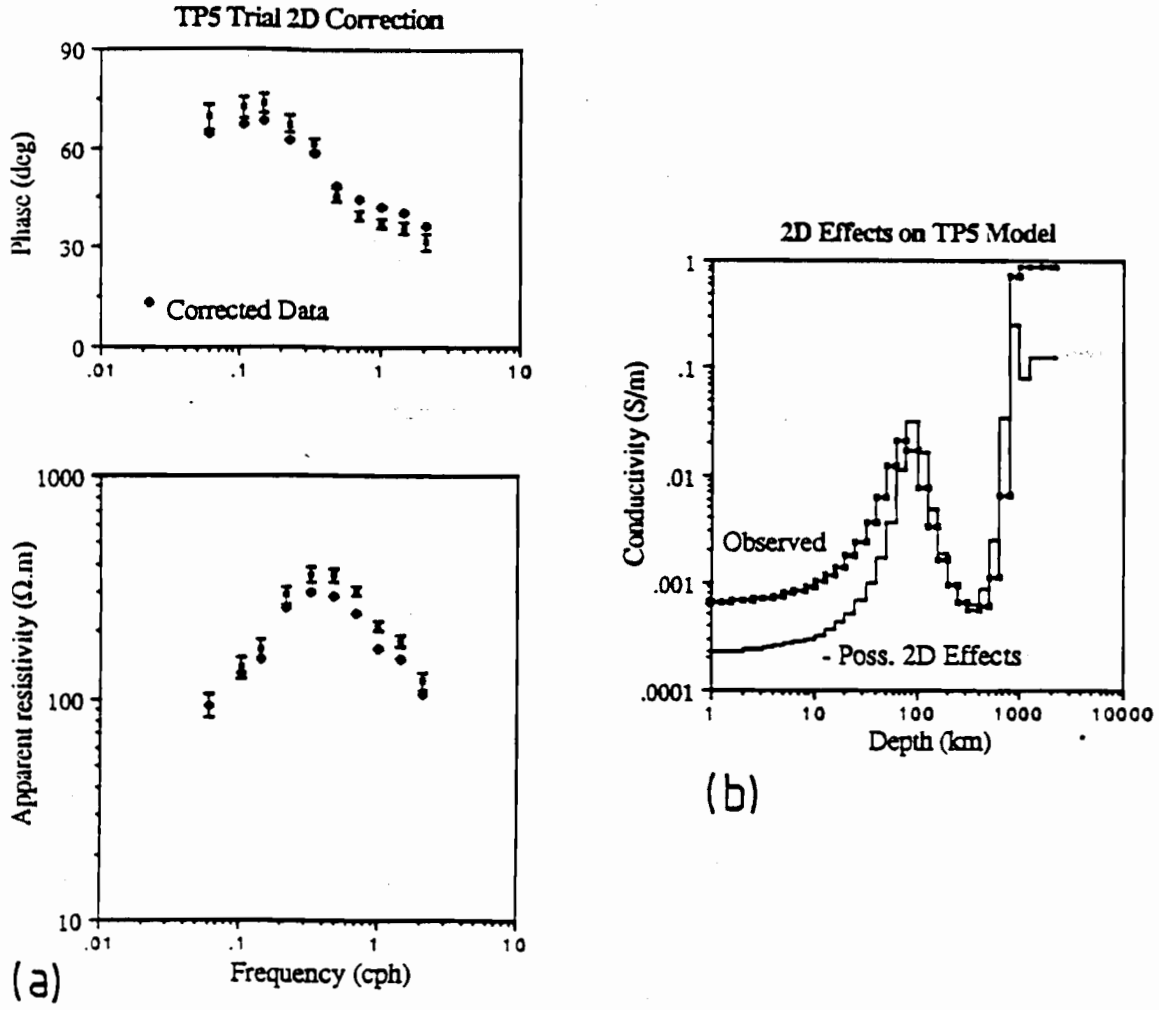

Figure 8.25: Investigation of possible 2D effects in the TP5 response. (a) The observed TP5 MT response (squares) and corrections for possible 2D effects (diamonds) based on the 2D forward modelling illustrated in Figure 7.13. (b) The inverted model for the observed and corrected response. The correction for the 2D effects does not significantly alter the shape of the conductivity model, leading to the conclusion that E-pol effects from the Australian coastline do not explain the differences between the TP5 and the TP4 / TP3 conductivity profiles.

Second-Derivative Occam Inversions

A final check on features in the conductivity models is provided by 2nd-derivative Occam inversions, which as discussed above, will minimize conductivity contrasts such as those associated with a HCL. Figure 8.26 compares 1st and 2nd-derivative smooth Occam inversions for sites TP3, TP4 and TP5.

The appropriate smoothness for each 2nd-derivative model model (listed in Table 8.6) was obtained in the same manner as for the 1st-derivative inversions. A corresponding 'test' data set consisting of the D^+ response with the observed errors estimates, was inverted with a 2nd-derivative Occam inversion to a specified tolerance of 1.0, and the resulting smoothness noted. Returning to the original data, inversions were performed with varied specified tolerances until the same smoothness was obtained. Unfortunately this method fails for site TP5, for which the Occam inversion on the 'test' data set (which is by definition 1D data) fails to converge. From site TP3 and TP4 results it is noted that the final 2nd-derivative tolerances for the smooth models are very similar to the final 1st-derivative tolerances for the smooth models (Table 8.6). The final tolerance for the 2nd-derivative smooth model at TP5 was therefore assigned to be the same as the final 1st-derivative tolerance.

The 1st and 2nd-derivative inversions show good agreement in the depth range of the HCL and the deeper rise in conductivity. Although the 2nd-derivative models do not show a definite HCL at TP3 and TP4 they show a bulge in the conductivity structure, at the same depth as the HCL occurs in the 1st-derivative inversions, indicating the definite existence of a region of increased conductivity at this depth. The site TP5 2nd-derivative smooth model reproduces the 70 km deep conductivity maximum noted in the 1st-derivative models. This result shows the feature is essential for generating the observed TP5 MT response, although as discussed above, it may be caused by bias or by non-1D effects.

The 1st and 2nd-derivative inversion models diverge at a depth of about 800 km at TP3 and TP4, and 1000 km at TP5. These depths are slightly greater than the depths of penetration determined from the D^+ results. The 1st and 2nd-derivative models also diverge at shallow depths confirming the absence of resolution in the resistive and sediment part of the conductivity profiles.

Inversion of the VGS Impedance Estimates

As shown in chapter 7 there exists an ambiguity in the seafloor impedances with the VGS and SFMT estimates differing by a factor of two. Assuming the VGS and SFMT impedances define the range of possible impedance estimates, an indication of the corresponding range of conductivity models will be given comparing the conductivity models corresponding to both sets of impedances. Figure 8.27 shows the rough Occam

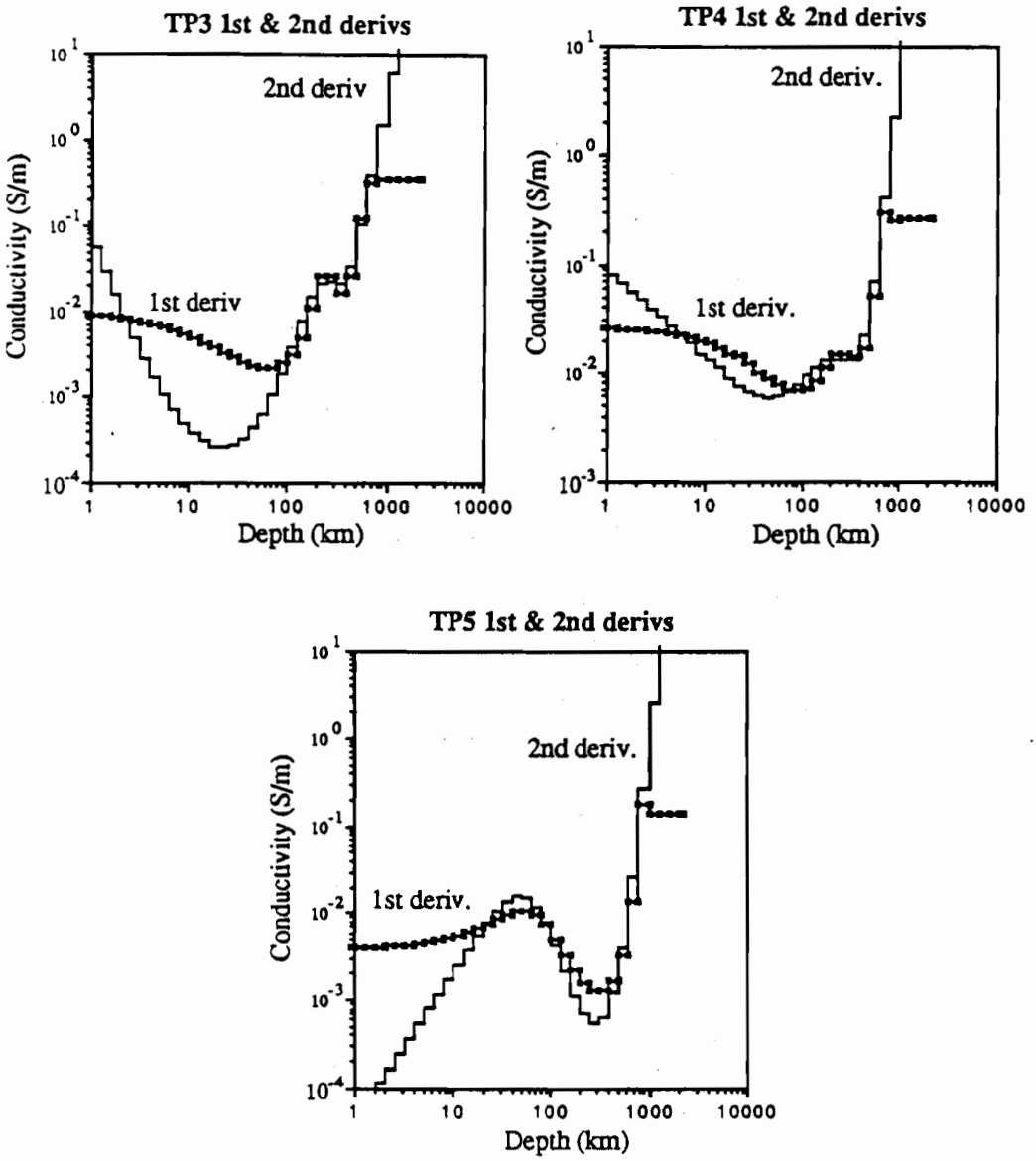

Figure 8.26: Second-derivative Occam inversions of the Tasman Project data. The models are smooth models with the level of roughness set to match the errors on the data. Also shown are the 1st-derivative smooth Occam models.

models corresponding to the VGS estimates. Rather than inverting the actual VGS estimates, the VGS models are derived from a set of SFMT estimates in which the apparent resistivity values have been decreased by a factor of four (ie. the impedance values have been halved). This method was used to avoid the erratic phase estimates obtained in the VGS results (eg. Figure 7.17).

The error magnitudes for the VGS impedances were not calculated directly and are assumed to be identical to the SFMT errors. Because the VGS impedance magnitudes are smaller than the SFMT magnitudes, this assumption results in an increase in the level of the relative error. A corresponding decrease occurs in the minimum value of χ^2 (by a factor of approximately 4) and also in the tolerance achievable in the inversions of the VGS data. The TP4 and TP3 VGS data were inverted to tolerances of t = 1.59 and t = 1.35 respectively which are close to the minimum tolerance levels possible for each data set. The TP3 and TP4 VGS models have roughness values of 4.01 and 1.65 respectively, and are smoother than the corresponding SFMT models. For site TP5, the VGS data set is satisfactorily 1D and the VGS model has a tolerance of t = 1.0.

In the VGS models, well-resolved features such as the HCL and the deeper conductivity rise, occur at more shallow depths and have higher conductivity values than in the SFMT models. The depth to these features is approximately halved, so that in the VGS models for TP3 and TP4, the HCL is between 100 and 158 km depth, and the deeper rise in conductivity occurs at 250 km depth. At site TP5 the deep rise in conductivity occurs at 300 km depth. The penetration-depth estimates will be similarly decreased for the VGS data sets. In the VGS models, the conductivity of resolved features is higher by a factor of two to four compared with the SFMT models. This relationship does not persist in parts of the conductivity profile which are poorly resolved.

If the impedance corresponding to the true structure beneath the Tasman Seafloor lies outside the range of values defined by the SFMT and VGS estimates, then the position of features in the true model will lie outside the range shown by the SFMT and VGS models. As long as the 'true' impedance is however related to the SFMT and VGS values by a real constant, the position of features such as the maximum conductance of the HCL will lie close to the diagonal line defined by these features on the VGS and SFMT models (eg. Larsen 1977).

Summary of Tasman Project Inversion Results

The important features of the above 1D inversions of the Tasman Project data are summarised as follows:

1. The SFMT data sets for TP3, TP4 and TP5 lie outside the 95 % confidence limit for satisfactory 1D models.

2. The misfit from one-dimensionality is consistent between sites and interpreted as being due to large-scale

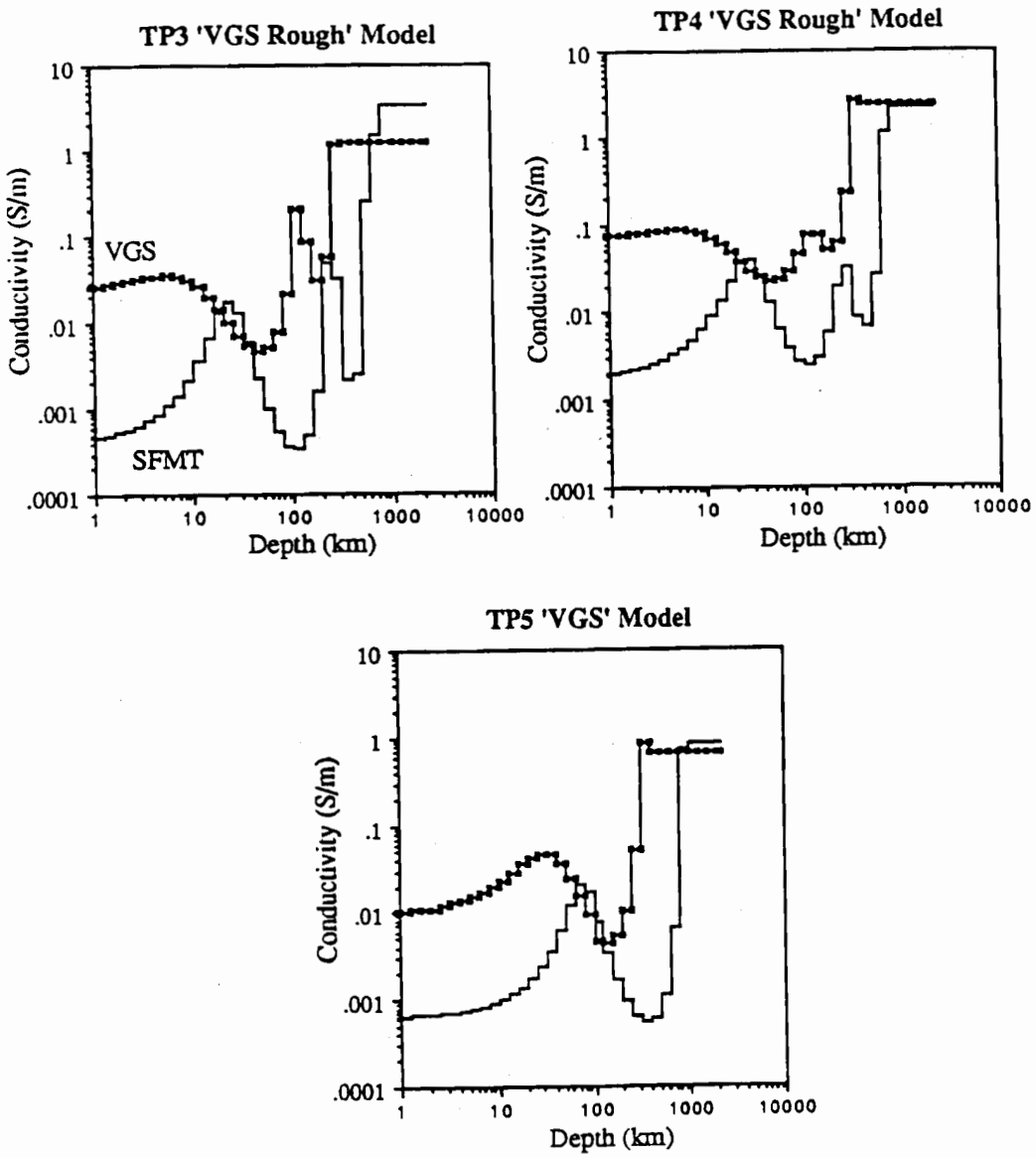

Figure 8.27: Conductivity models derived from VGS (squares) and SFMT (plain line) impedance estimates. The VGS results are actually based on the SFMT data, scaled to give the same impedance magnitude as the VGS estimates. Resolved features in the VGS models occur at more shallow depths and with higher conductivity than the corresponding SFMT models.

3D induction effects.

3. It is assumed that these external effects do not totally dominate the response of the local conductivity structure (which is assumed to be 1D) and further inversions are performed.

4. The SFMT Occam models for TP3 and TP4 are similar at depth (>100 km) and show a HCL between 200 and 350 km. The HCL does not appear to represent a spurious feature caused by external 3D effects in the response. A deep conductivity rise occurs at 500 km at these sites.

5. At shallow depths the conductivity profile at TP4 is more conductive than at TP3. The additional 700-900 S of conductance in the upper part of the profile at site TP4 must be spread over at least the upper 20 to 50 km.

6. Site TP5 is more resistive than site TP4 and TP3 with a deep conductivity rise at 800 km in the SFMT model and no resolved HCL. The shallow structure at site TP5 does not appear geophysically reasonable, for example it possesses no response associated with the sediment layer at the site. The response may be affected by bias or by 3D effects.

7. Inverted models based on the VGS impedance estimates include features at about half the depth and with 2 to 4 times the conductivity of the same features in the SFMT models.

Conductivity models of various kinds including D^+ models, rough and smooth Occam models and modified Occam models have been used to represent the conductivity structure for each site. These models comprise some of the non-unique solutions to the MT problem. Different features of the models, for example the deep layering of the Occam models and the shallow layering of the modified-occam models, may occur in the true conductivity structure. The geophysical significance of the models is discussed in chapter 9.

Chapter 9 Geophysical Interpretation

In this chapter the geophysical significance of the Tasman Sea electrical conductivity results is discussed. The chapter starts with a broader consideration of the interpretation of electrical conductivity structure: the laboratory measurements of conductivity and the relationship of conductivity to tectonic structure at a global scale. The varying tectonic features of the Tasman Sea are then described and the relationship of the observed conductivity results to these tectonic features examined. Since the conductivity structure determined for the Tasman Sea is a first estimate based mainly on 1D analysis, the tectonic interpretation is relatively brief. Explanations are provided for the observed features in the conductivity profiles and conclusions are drawn regarding their tectonic and petrological implications.

9.1 Sub-oceanic Electrical Conductivity Structure

Mantle Structure

Most of the conductivity information obtained from the Tasman Project pertains to the upper mantle. It is therefore useful to consider the information available on the structure of the mantle from other geophysical and geochemical sources before considering the electrical conductivity structure.

Figure 9.1 shows a schematic illustration of the oceanic and continental crust and mantle from Ringwood (1975). This model is included because it plausibly explains much of the geochemical and geophysical information on the mantle, and therefore provides an indication of the possible compositional variations which might influence the electrical conductivity in these regions. In the model the bulk of the upper mantle is composed of pyrolite - a pyroxene-olivine rock with a composition which yields basaltic magmas on partial melting and leaves refractory material of a peridotite composition. It is noted that alternative models exist for the composition and the evolution of the upper mantle, for example models in which the mantle is composed dominantly of eclogite or lherzolite.

The major element composition of the mantle varies considerably in the upper 150 km and between sub-oceanic and sub-continental locations and within this depth range there is also likely to be significant variation in the minor constituents including the trace elements and volatiles such as H_2O, CO_2, SO_2 (Ringwood 1975). The differentiation of the oceanic crust from the upper mantle occurs at mid-ocean ridges where it is proposed that partial melting of the pyrolite is occurring at the depths of the LVZ ie. between about 70 and 150 km depth. Partially molten material rises towards the surface where it is forms the mafic gabbros of crustal layer 3 and is also extruded through feeder dykes to form crustal layer 2 (chapter 5). Ultramafic (peridotitic) material carried by the partial melt, sinks back to the mantle creating a sharp, chemical, crust / mantle transition which is recognized

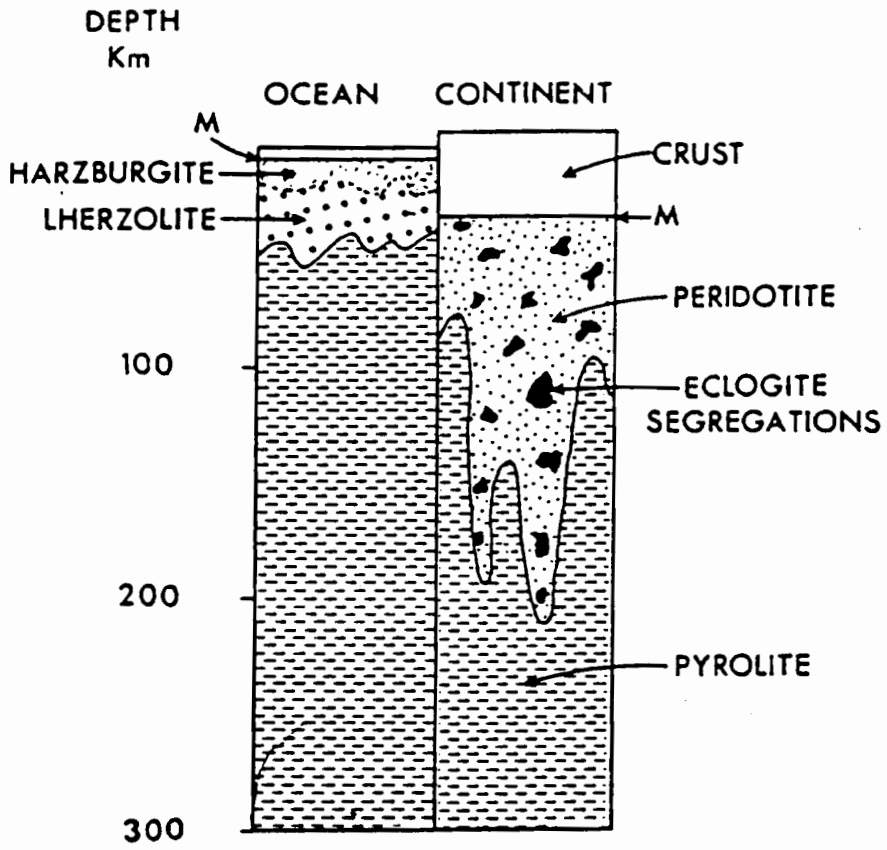

Figure 9.1: Schematic illustration of the 'pyrolite' model for the upper mantle in oceanic and continental settings. 'M' denotes the Mohorovicic seismic discontinuity at the base of the crust. (From Ringwood 1975).

seismically as the Mohorovicic discontinuity. The peridotite forms the oceanic sub-crustal lithosphere and is internally layered into harzburgite and lherzolite, or slightly depleted pyrolite, layers. These layers are associated with a decreasing degree of basalt depletion.

The continental lithosphere is thicker than its oceanic counterpart and is relatively heterogeneous. It builds up through accretionary processes at subduction zones and may contain: magmas derived from the subducting slab; entrapped sediments; and bodies of eclogite derived from subducted basalt (Figure 9.1). Generation of secondary granitic magmas leads to differentiation of lower continental crust (Ringwood 1975).

As well as compositional variations, mineralogical phase changes form important layers in the upper mantle. The phase changes cause changes in the physical properties of the rock, such as the density and the elasticity, and are therefore generally able to be

recognized by seismic discontinuities. Figure 9.2 shows the effect of phase transitions on the density of a pyrolite mantle; Liu (1979) reviews the results.

The mineral assemblage between 150 to 350 km depth, ie. the region below the LVZ, is proposed to be relatively uniform and composed of olivine (57 %), orthopyroxene (17%), clinopyroxene (12 %) and pyrope garnet (14 %) (Ringwood 1975). Two phase transitions occur near 400 km depth. Firstly, olivine is transformed into the β-Mg_2SiO_4 (spinel-like) structure which increases its density by 8 %. This change is probably responsible for the 420 km seismic discontinuity. The second transition involves pyroxene entering a solid solution with the garnet phase. The combined effect of the two transitions is a 4.6% increase in the (zero-pressure) density of the mantle rock (Liu 1979).

Between 420 and 600 km the mantle is composed of β-phase $[Mg,Fe]_2SiO_4$ (~57%) and the garnet solid-solution (~43%). Around 550 km the $[Mg,Fe]_2SiO_4$ transforms into the γ-phase spinel structure (Ringwood 1979). The major 670 km seismic discontinuity is attributed to transformation of the spinel phase $[Mg,Fe]_2SiO_4$ into perovskite $[MgFe]SiO_3$ plus rocksalt [MgFe]O, and of the garnet phase into an ilmenite phase. These changes produce a large, 9.1 %, increase in the (zero-pressure) density of the rock. A further transformation of the ilmenite phase into an orthorhombic perovskite phase is expected at 800 km depth (Liu 1979).

The above information indicates that many physical and compositional parameters will vary in the upper mantle and perhaps cause changes in electrical conductivity. As well as the compositional, melting and density changes already noted, other physical and chemical properties such as the stress field and the oxygen fugacity may also vary throughout the mantle and therefore influence electrical conductivity.

The mantle temperature is one of the most critical factors controlling its electrical conductivity. The temperature will increase with depth through the crust and lithosphere, reaching temperatures of 850° to 1150°C at 100 km depth (Ringwood 1975). This increase will vary between different tectonic settings, for example the geotherm in oceanic areas will be steeper than for Precambrian shields. The temperature distribution at greater depth in the mantle is not fully known and depends upon whether convection extends over the whole mantle or occurs in two separate cells in the upper (> 670 km) and lower mantle (eg. Davies 1983, Jeanloz & Richter 1979).

Certain constraints can however be placed upon the temperature distribution. In the lower mantle the temperature gradient is known from seismic observations to lie close to the adiabatic gradient (Dziewonski et al. 1975). For the case of two-layer convection it is assumed that the temperature gradient within the upper convecting cell is also adiabatic (eg. Schubert & Spohn 1981) although phase transitions will allow some local steepening of the gradient. The 420 km and 550 km $[MgFe]SiO_4$ phase transitions constrain the temperature

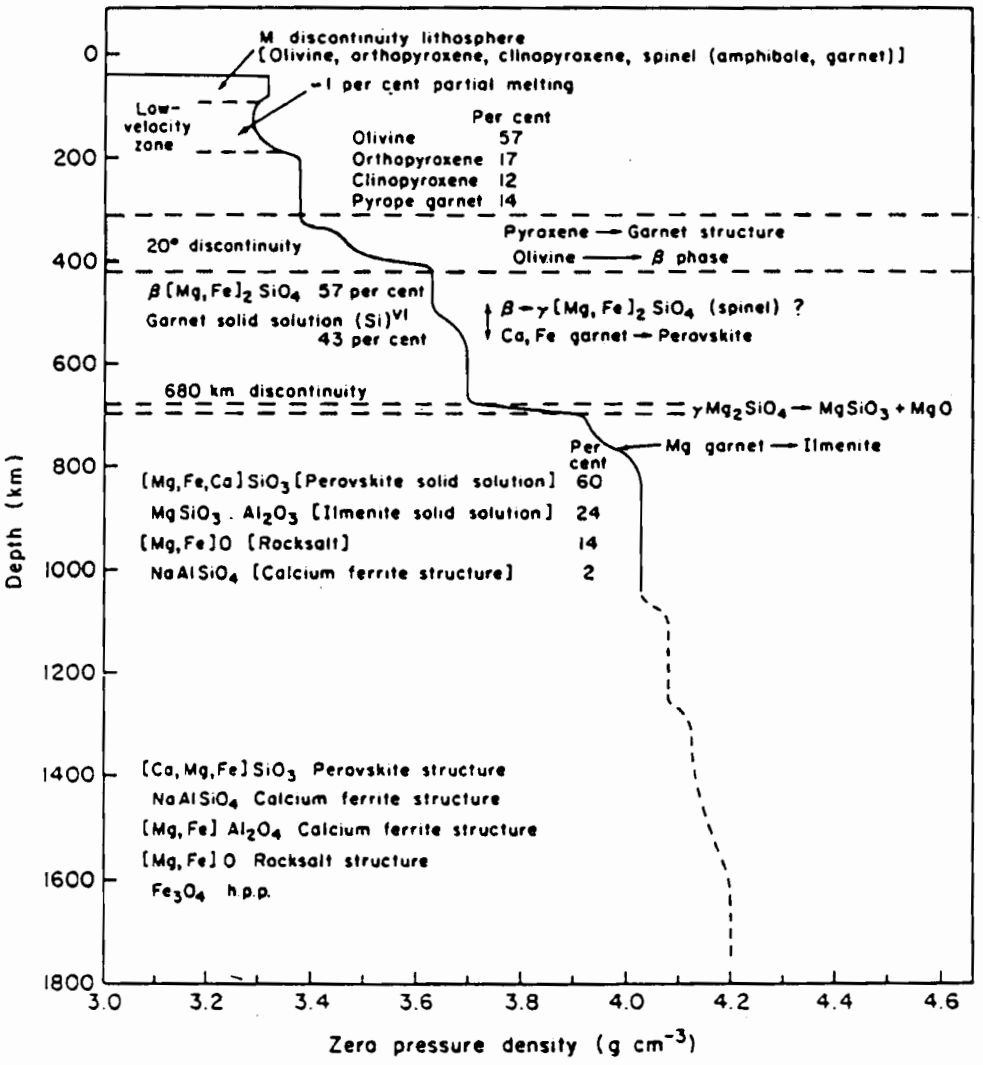

Figure 9.2: Mineral assemblages and phase changes in a model mantle of pyrolite composition. The horizontal axis shows the (zero-pressure) density; note the major density increases around 420 and 670 km depth. (From Ringwood 1979).

at 670 km depth to be around 1900 to 2000° C (Jeanloz & Richter 1979). A significant difference between the one and two-layer convection systems is that the two-layer convection would involve a large temperature increase in the vicinity of 670 km.

For both mantle convection models there will be a decrease in temperature across the top of the convecting layer ie. between the spreading ridge and the subduction zone (eg. McKenzie et al. 1974). The effects of this temperature decrease will include an increase in the depth of the ocean, and a decrease in seafloor heat flow, with both effects being related to the square root of lithospheric age (Parsons & Sclater 1977). Parker & Oldenburg (1973) also predict a thickening of the lithosphere at a rate proportional to the square root of lithospheric age.

Laboratory Measurements of Electrical Conductivity

There have been numerous laboratory measurements of the electrical conductivity of mantle minerals, particularly olivine and pyroxene, and of whole-rocks likely to exist in the upper mantle. Recent reviews are given by Shankland (1979, 1981) and Lastovickova (1983). Results have shown that the electrical conductivity of rocks and minerals depends upon many parameters including the composition, temperature (T), pressure (P), oxygen fugacity (fO_2), point-defect concentration, chemical activities of constituent binary oxides, grain-shape, degree of melting and content of the volatiles H_2O (pH_2O), CO_2 and SO_2 (eg. Hinze 1982, Lastovickova 1983).

The laboratory measurement of conductivity has divided into two approaches. The first approach involves simplifying the system as much as possible and studying the intrinsic conduction mechanisms eg. measuring the conductivity of single minerals under tightly constrained laboratory conditions (P, T, fO_2, pH_2O etc.) with one physical parameter only varying (Hinze 1982) . The second approach involves measuring, under approximate mantle conditions (T, P, fO_2), the conductivity of rocks expected to occur in the mantle (eg. Rai & Manghnani 1978). Both approaches are important, the first for extrapolating from known thermodynamic systems to systems unattainable in the laboratory, the second for revealing more complicated conduction mechanisms such as those involving polymineralic assemblages and those involving grain boundary effects.

The most important results of the laboratory measurements will now be noted. Many studies have shown the increase of the conductivity of minerals and rocks on temperature. Examples of conductivity temperature-dependence for pyrolite constituents, olivine, orthopyroxene, and garnet are shown in Figure 9.3. There is a great deal of scatter in the results, largely due to the conductivity-dependences other than temperature. It is of note that olivine is not significantly more conductive than the other mantle minerals. This result means that definition of the mantle conductivity on the basis of olivine observations alone is an inadequate procedure (eg. Tozer 1979).

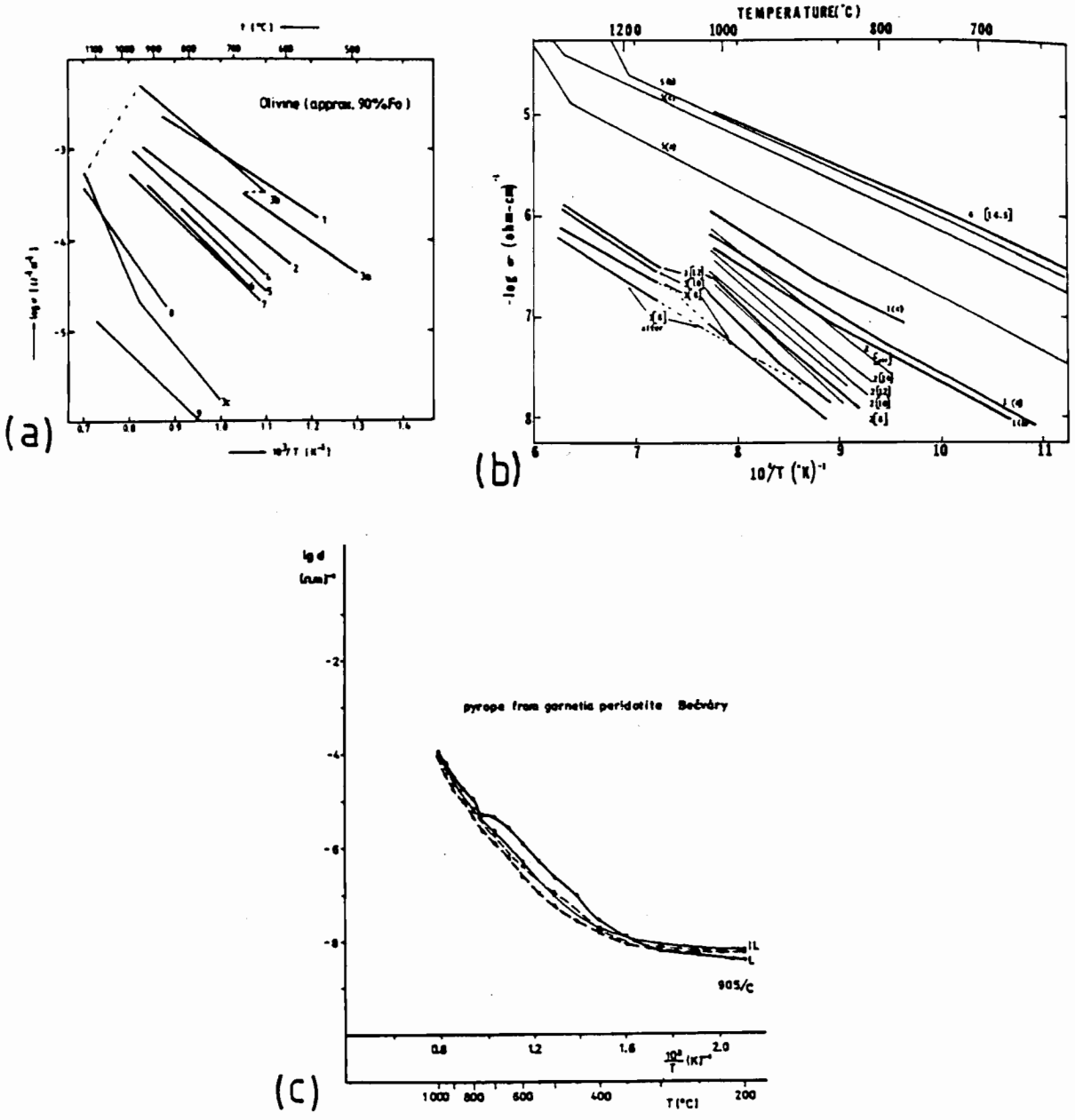

Figure 9.3: Conductivity versus temperature results for important upper mantle minerals.
(a) Olivine, with close to the expected mantle composition (from Hinze 1982)
(b) Orthopyroxene; relevant lines are numbered 1-3. The variation in line 2 is due to variation in oxygen fugacity (from Duba et al. 1973).
(c) Pyrope garnet (from Lastovickova 1983).
In each of the diagrams log conductivity ($S.m^{-1}$) is plotted against the inverse of the temperature times a constant.

Electrical conductivities have been determined for minerals under mantle conditions corresponding to depths of up to 200 km (Schock et al. 1977 produce P = 5 GPa T = 1000° C). Although the thermodynamic conditions at the important phase boundaries h not yet been duplicated, measurements on the olivine-spinel phase change for fayalite (Fe_2SiO_4) indicate an increase in conductivity by two orders of magnitude (Akimoto & Fujitso 1965). The phase change occurs at much lower pressures for fayalite than for olivine of mantle composition, $[Fe_{0.1}Mg_{0.9}]_2SiO_4$ (eg. Ringwood 1975). The result for fayalite however suggests a conductivity increase should occur across the corresponding transition in the mantle.

Figure 9.4 shows measurements of conductivity versus temperature in mantle-type rocks from Rai & Manghnani (1978) and Lastovickova (1983). Although the results range quite widely, the conductivity of the rocks tends to exceed that of the pure constituent minerals at a given temperature. Results of Rai & Manghnani (1978) and Waff & Weill (1975) show that rocks in their molten form are approximately 2 orders of magnitude more conductive than in solid form. For rocks with significant partial melt, the conductivity will therefore depend critically on the melt conductivity and on the interconnection of the melt-phase and to a lesser extent on the conductivity of the solid rock. Many studies have examined the relationship between electrical conductivity and the geometry of partially molten rocks (eg. Schmeling 1986, Toramaru & Naoyuki 1986).

The electrical conductivity of solid olivine and some pyroxenes has been shown to depend on the oxygen fugacity (Duba et al. 1973, Duba 1976, Figure 9.3) suggesting that the conductivity in the mantle will also do so. The iron content of the mantle minerals will strongly influence the conductivity, with the conductivity of fayalite exceeding that of forsterite (Mg_2SiO_4) by at least several orders of magnitude (Hinze 1982). In contrast some parameters have been found to be of lesser importance to the the conductivity of upper mantle rocks. These parameters include the pressure (Shankland 1981) and the stress field (Hirsch & Wang 1986).

Interpretation of Mantle Conductivity Variations

Having examined the structure of the mantle and the dependence of electrical conductivity on the parameters which vary in this structure (such as composition) it is of interest to examine the observed electrical conductivity structure.

The exact conductivity structure in the electrically resistive regions of the lower crust and uppermost mantle cannot be resolved using MT methods (see chapter 8). For normal oceanic lithosphere it is however possible to predict some of the features of the conductivity profile using laboratory results and other measurements. From measurements in DSDP holes the electrical conductivity of the crustal layer 2C is around 10^{-3} $S.m^{-1}$. The conductivity of layer 3 is probably lower than this value because gabbros are generally

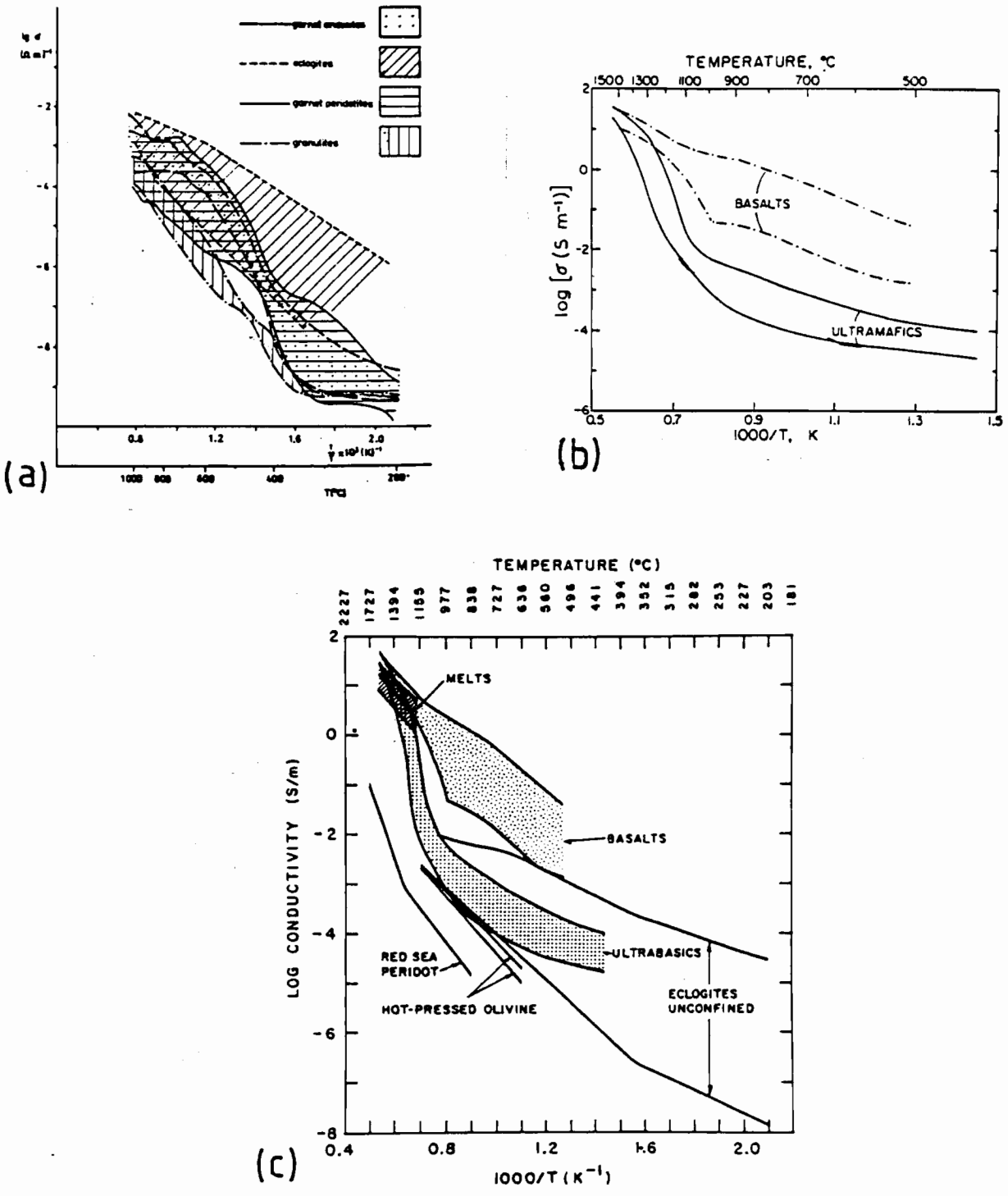

Figure 9.4: Electrical conductivity of possible mantle rocks.

(a) Results from Lastovickova (1982)

(b) Results from Rai & Manghnani (1978).

(c) A compilation of results from Shankland (1979). Note that rocks become partially molten at around 1000° C resulting in a conductivity increase of several orders of magnitude. The ultrabasics and basalts are more conductive than mono-mineralic olivine.

more resistive than basalts (eg. Cermak & Lastovickova 1987) and the sheeted dykes of layer 2C are likely to have undergone some fracturing during hydrothermal alteration (Alt et al. 1987).

A sharp conductivity decrease caused by the transition from gabbros to ultramafic rocks is expected at the base of the crust. Cermak & Lastovickova (1987) determined the conductivity of ultrabasite rocks to be one-half to one order of magnitude less than those of gabbros. This result is also supported by the low conductivities indicated by the control-source experiments of Cox et al. (1986). Within the uppermost oceanic mantle there may also be conductivity variations associated with the varying degree of basalt depletion as proposed in the pyrolite model. The increasing temperature between the seafloor and the base of the lithosphere (of order 1000°) will also influence the electrical conductivity of the rocks occurring in the oceanic crust and upper mantle.

Observations of the conductivity in the upper 300 km of the oceanic mantle were reviewed in chapter 5 and demonstrated a wide range of structures depending upon the particular tectonic setting. The same result is also true of the upper 300 km of the mantle beneath continents, with the conductivity varying between stable shields, fold belts, rift zones and other tectonic settings. Reviews of conductivity structures observed at these depths may be found in Garland (1981), Gregori & Lanzerotti (1982), Roberts (1983) and Campbell (1987). The large variation in conductivity structure is in accord with the mantle models which predict considerable compositional variation in the upper mantle.

The presence of an HCL in the upper mantle is a unifying feature of many sub-oceanic conductivity profiles. Figure 9.5 shows a compilation plot of the depth to the top of the mantle HCL versus the lithospheric age for several of the Pacific Ocean conductivity profiles. The data lie relatively close to a linear, depth versus square-root of lithospheric age, relationship. This result reflects the decreasing temperature across the top of the convecting mantle cell and in the overlying lithosphere. The result supports the relationship predicted for lithospheric thickness by Parker & Oldenburg (1973).

A number of petrological interpretations of the mantle HCL have been made (eg. Shankland & Waff 1977, Oldenburg 1981, Tarits 1986, Tozer 1979). Oldenburg (1981) interpreted inverted conductivity models from the Juan de Fuca Ridge (JDF), SF Revisited (CAL) and AGGY III (NCP) (see chapter 5) in terms of partial melting of a pyrolite composition mantle. He specified: the mantle composition (incorporating 0.1 % water); the relationship of the volume fraction of partial melt to the temperature and pressure; and the conductivity of the melt and solid phase as a function of temperature and pressure. Using a model for the partial melting involving high connectivity of the melt phase, Oldenburg then obtained an estimate for the minimum melt fraction required to explain the observed conductivity. The method also provided an estimate for the temperature at depth.

Results of the analysis are shown in Figure 9.6 and suggest that partial melting is

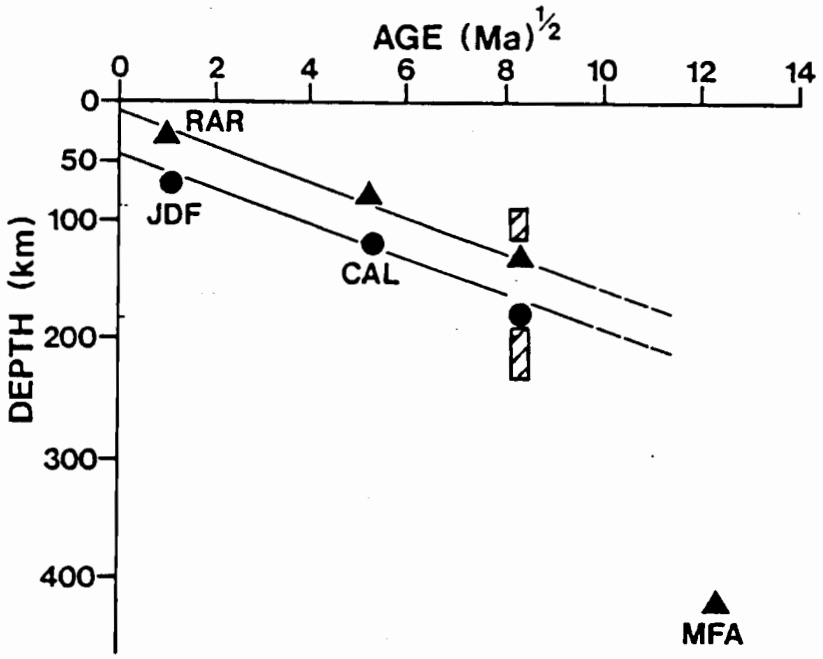

Figure 9.5: Depth to conductive layer as a function of lithospheric age. The triangles denote the results and inversions of Dr J. Filloux and the circles the inversions of Dr D. Oldenburg (after Law 1983). The shaded regions are the estimates obtained for the Tasman Sea; the upper region is the estimate derived from the VGS results and the lower region from the SFMT results.

occurring in the upper 150 km beneath each site. The maximum percentage of partial melt decreases from around 8 % on the 1 Ma lithosphere at JDF to 1 % on the 72 Ma lithosphere at NCP and the distribution of melt with depth becomes more even with increasing lithospheric age. This age dependence reflects the decreasing temperature with distance from the spreading ridge. The temperatures determined by Oldenburg (1981) show the zone of maximum partial melt is associated with a relatively rapid increase in the mantle temperature to above 1300°C. Using the improved inversions of Oldenburg et al. (1984) for the same sites, the partial melt and temperature distributions change slightly, but the results noted above are still applicable.

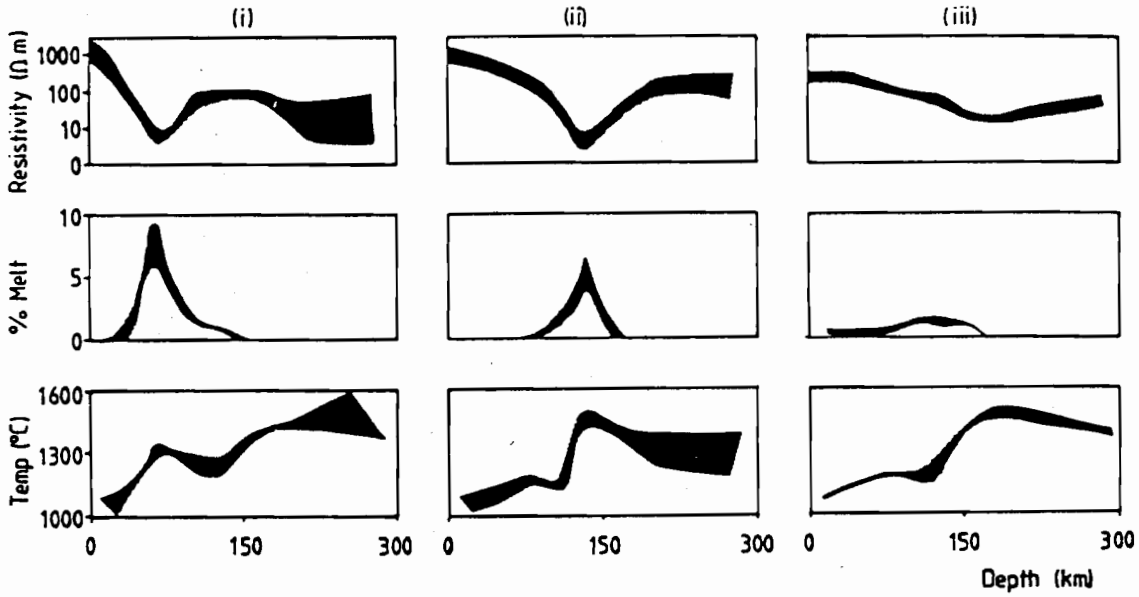

Figure 9.6: Fractions of partial melt and temperature versus depth curves determined from Pacific Ocean conductivity profiles. The results were obtained by Oldenburg (1981) for (i) 1 Ma lithosphere (JDF), (ii) 30 Ma lithosphere (CAL = SF Revisited), (iii) 72 Ma lithosphere (NCP = AGGY III). (Figure is from Roberts 1983).

An important argument used against the hypothesis of partial melting in the HCL is based on the gravitational instability of the melt phase. Walker et al. (1978) showed that an HCL could be maintained only with a melt fraction of order 0.1 % or less, and that larger melt fractions led to melt segregation and subsequent vertical melt migration. Two mechanisms have been proposed which would stabilize melt at greater melt fractions. Waff (1980) suggested that melt fractions of up to 5-22 % could occur in horizontal stratified form. Such a configuration would still produce high electrical conductivity values in MT measurements because the MT method resolves the horizontal conductivity. Stolper et al. (1981) found that if melt compressibility is considered, then an HCL containing 1 % melt could be stable at 100 km depth.

Tarits (1986) re-examined the 'Oldenburg data set' using extreme anhydrous and 'hydrous' estimates of mantle composition. The anhydrous model comprised peridotite (cf. pyrolite) with 0.1 % H_2O and indicated partial melt fractions of 8 to 14 % at JDF and 3 to 6 % at NCP. These partial melt fractions correspond to temperatures ranging from 1300

to 1350° at HCL depths which Tarits (1986) concludes represent maximum temperature estimates for this depth in the mantle. Using estimates for the conductivity of H_2O-rich fluids, Tarits (1986) found a fluid fraction of 0.5 to 7 % (depending on connectivity) is necessary to explain the observed conductivity in the HCL. Noting the fluid fraction limitations of Walker et al. (1978) he accepted a combination of approximately 1 % H_2O-rich fluid and 1 % partial melt as the likely explanation for the HCL beneath the older lithosphere at CAL and NCP. For JDF, near the spreading ridge, 1 % H_2O rich fluids and 10 % melt are required. These compositions lead to an estimate of minimum temperatures at the HCL depth in the mantle of 1050 to 1150°C (Tarits 1986).

Tozer (1979, 1981) proposes a mantle model with temperatures considerably less than those stated above. The model involves horizontally averaged temperatures, at 100 to 300 km depth beneath oceans, which are as low as 500°C. In this model the HCL is attributed to the presence of water derived from dehydration of amphiboles. A final mechanism suggested for the HCL is that it is caused by a sub-solidus increase in electrical conductivity. It has been shown that sub-solidus effects can account for the low seismic velocities and high seismic attenuation in the LVZ (Shankland 1981). Although sub-solidus conductivity increases have been noted in albite, the major mantle minerals have not been observed to exhibit such effects (Shankland 1981).

The conductivity structure in the depth range of 300 to 1000 km tends to be more uniform than at more shallow depths but significant variation between different regions is still observed (see chapter 5). Information on the conductivity in this region comes from global and regional analyses of observatory data as well as from local soundings; reviews of major studies may be found in Filloux (1982b), Roberts (1986), Campbell (1987) and Pecova et al. (1987).

Figure 9.7 illustrates some of the deep conductivity models obtained in localized studies and shows the variation which exists in conductivity between these locations. Although some of the variation between the models can be attributed to differences between analysis and inversion techniques, much of the variation must represent true conductivity variation. Schultz & Larsen (1987) present uninverted MT response functions (derived from data for a number of world observatories) which show significant variation and confirm the existence of lateral heterogeneity in the mid-mantle. Further support for the heterogeneity is given by Roberts (1986) who inverted data from different regions with consistent inversion schemes and found significant differences in conductivity at depths of hundreds of kilometres exist between different locations.

It is of interest to examine the deep conductivity models for any indication of conductivity changes associated with the major mineralogical phase changes. Most of the deep conductivity models show a relative rapid rise in conductivity between a depth of 400 and 800 km (Roberts 1986, Campbell 1987) however there is no clear correlation of the conductivity rises with the 420 km and 670 km seismic discontinuities (Roberts 1986).

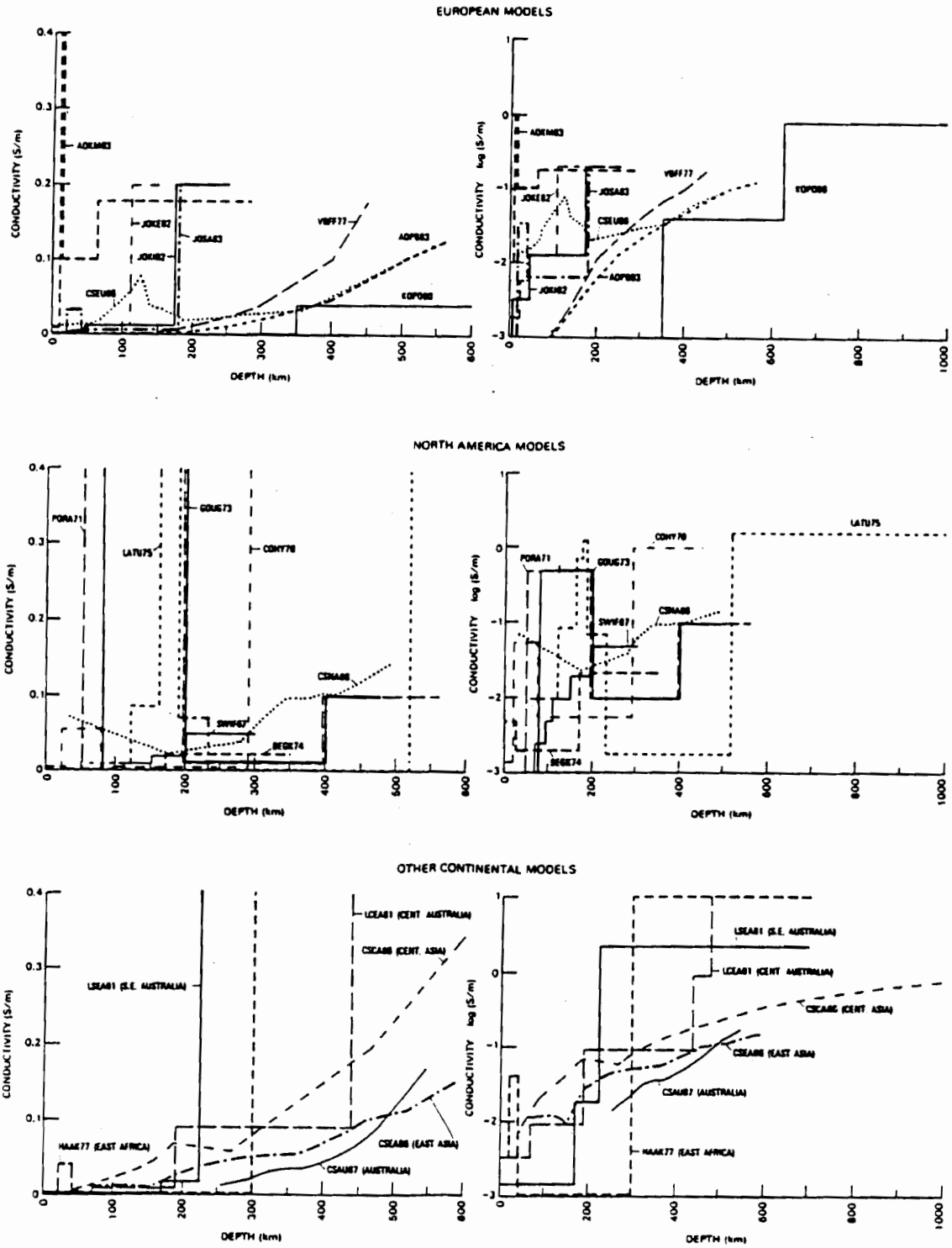

Figure 9.7: Compilation of conductivity results from different continental regions (from Campbell 1987). The diagrams show both linear and logarithmic conductivity scales. Note the variation in the depth of the deep electrical conductivity increase.

Figure 9.8 shows a compilation of the conductivity models derived for the Pacific Ocean. These results and those in Figure 9.6 illustrate the range of depths observed for the deep conductivity rise.

Given the relatively poor depth resolution of MT sounding results it would be valuable to use forward modelling to determine how well the method could resolve different conductivity increases occurring at 420 , 550 and 670 km; the depths of the $[Mg,Fe]_2SiO_4$ α to β phase transition, the β to γ phase transition, and the spinel to perovskite + rocksalt transition. Theoretical predictions of the electrical conductivity changes at these phase transitions and of the slope of the geothermal gradient across the transitions could also be of great value. Such results would provide theoretical conductivity profiles for different mantle models and perhaps allow conductivity sounding results to differentiate between the models.

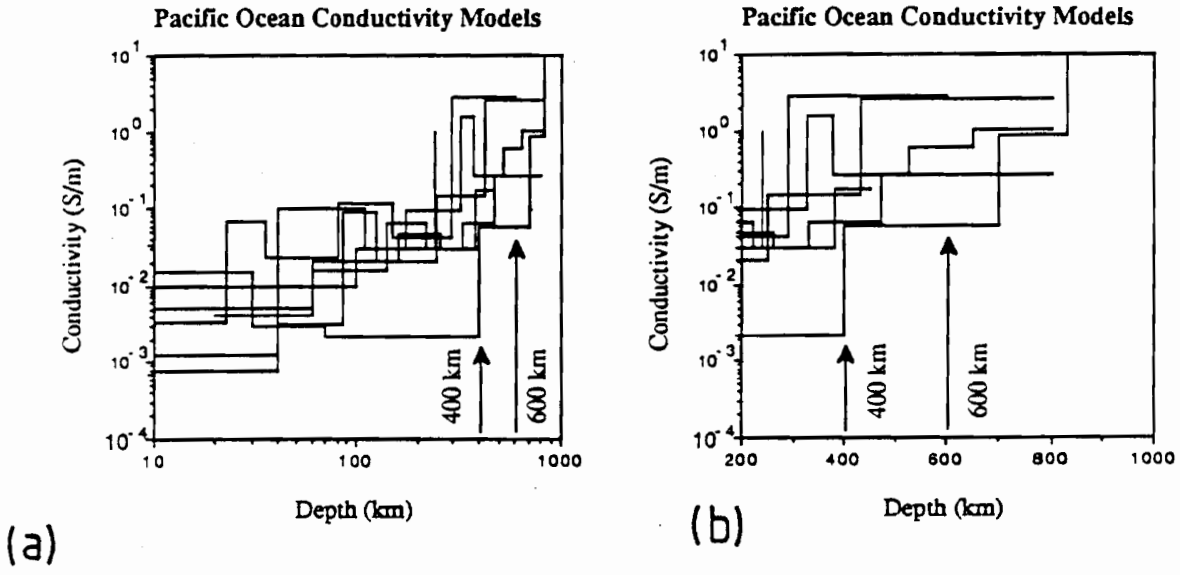

Figure 9.8: Compilation of Pacific Ocean electrical conductivity profiles. Results are for PR12°, JDF, SF Revisited, AGGY III, Hawaii and the Mariana Forearc (see chapter 5 for references). Note the variation in the depth to the good conductor. Except for the Mariana Forearc profile, the conductivity in the depth range 100 to 300 km is tightly grouped between 10^{-2} and 10^{-1} $S.m^{-1}$. (a) Log depth scale. (b) Linear depth scale.

Figure 9.9 shows compilations of recent global models of conductivity. Because the derivation of such models assumes spherical symmetry of the mantle conductivity structure one may question the interpretation of such models. Assuming however that the profiles form correct global-averages of the electrical conductivity they support the possibility of major conductivity rises at 420 and 670 km (Figure 9.8a) or at 550 km (Figure 9.8b). The models also suggest that the average conductivity between 200 km and 400 km depth is close to 10^{-2} S.m^{-1} and between 700 km and 1000 km it is close to 10^{0} S.m^{-1}. These results will be used in a composite global conductivity model below.

Correlation of conductivity results with seismic results

The electrical conductivity of rock will be affected by changes in physical properties such as the temperature, pressure and fraction of melt, which also affect other physical parameters such as the seismic velocity. As a result, correlation will occur between the electrical conductivity structure and other geophysical properties.

The correlation of the electrical HCL and the seismic LVZ has already been noted. In global models, the LVZ comprises a decrease in shear-wave (v_s) velocity between depths of 80 and 300 km and a smaller decrease in compressional wave (v_p) velocity (Dziewonski et al. 1975, Dziewonski & Anderson 1981). This depth correlates closely with the depth of the HCL noted in many oceanic studies (eg. the 30 Ma and 72 Ma lithosphere results for the Pacific Ocean). Oldenburg (1981) examined the correlation between the LVZ and HCL in more detail, comparing the age-dependent depth to the LVZ with the age-dependent depth to the HCL in the Pacific Ocean. He found a 'remarkable' correlation, with the lid of the LVZ corresponding to the depth estimated for the onset of partial melting and the base of the LVZ corresponding to the cessation of melting. In other tectonic settings there is also a correlation between seismic and conductivity mantle anomalies. The HCL correlates well with both seismic velocity anomalies and zones of strong seismic attenuation (Shankland et al. 1981).

The causes postulated for the HCL, partial melting and/or the presence of aqueous fluids, would produce both a seismic velocity anomaly and seismic attenuation anomaly in addition to the conductivity anomaly. The presence of such a liquid phase in the mantle could also change the long-period rheological properties. This possibility has led to the definition of the HCL as the 'electrical asthenosphere' (and the LVZ as the seismic equivalent). The observation of the HCL (or the LVZ) does not however prove that true model for plate tectonics and mantle convection involves a zone of mechanical decoupling between the 'rigid plates' and the fluid mantle (eg. Maxwell 1984). All that should be concluded from the conductivity results is that there is some process, probably involving the presence of fluids and/or elevated temperatures, causing an increase in conductivity. The ability of such a process to produce long-period mechanical decoupling of overlying

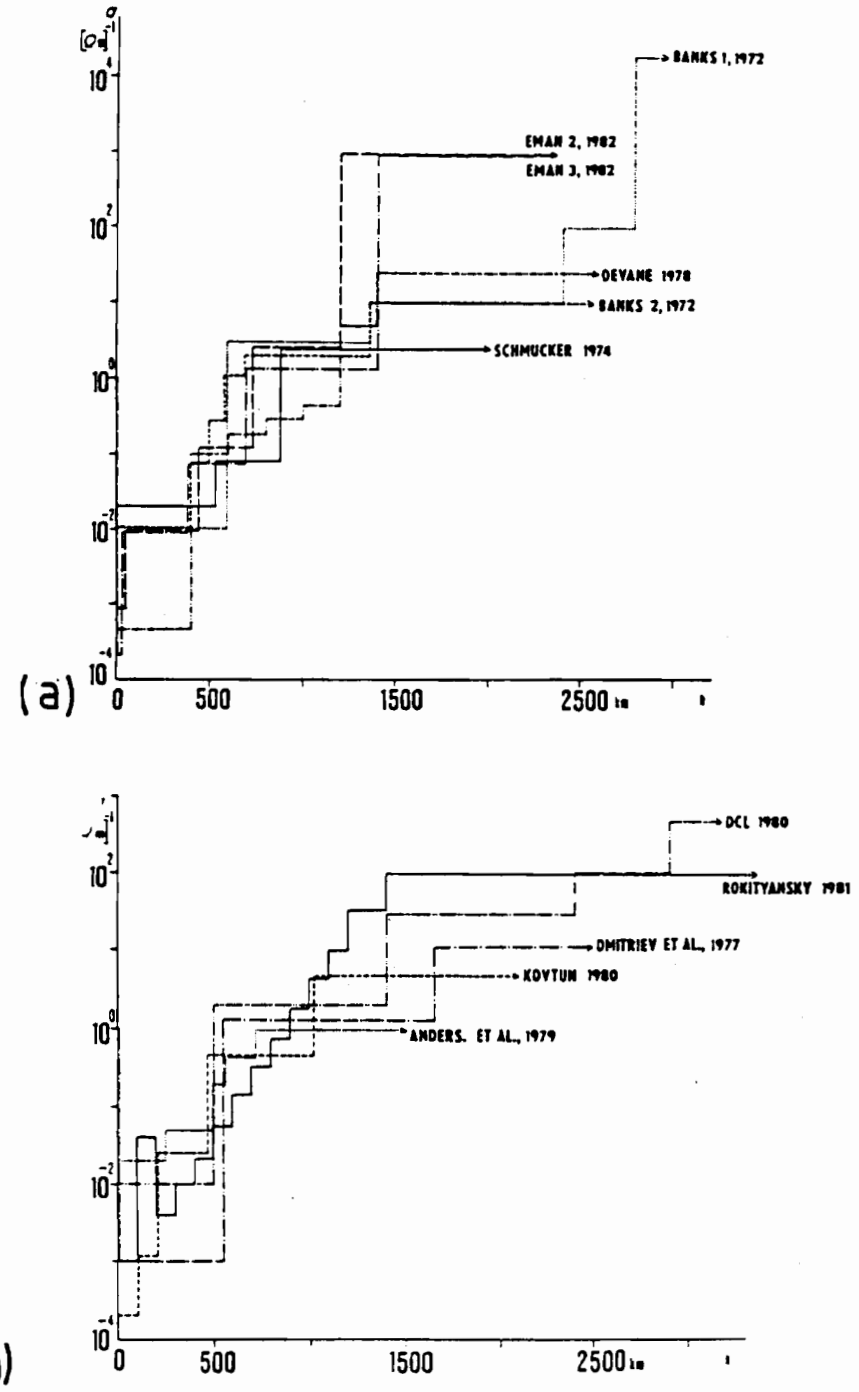

Figure 9.9: Compilations of global electrical conductivity models (from Pecova et al. 1987). Most of the profiles in (a) have conductivity increases between 400 and 500 km and between 600 and 700 km and in (b) have a conductivity increase between 500 and 600 km.

and underlying regions, and the relationship of any decoupling to plate-tectonic motions are important, but separate, fields of study.

At depths greater than the HCL there is also a correlation between the heterogeneity in the conductivity structure and in that in the seismic structure. Figure 9.10 compares the differences between the observed and global-average electrical conductivity with the differences between the observed and the global-average seismic velocity. The global-average conductivity is a composite of the global models presented in Pecova et al. (1987) and the seismic data are from the tomographic analyses of Woodhouse & Dziewonski (1984) and Dziewonski (1984). Although it is not perfect, there is a definite correlation between geographical regions with relatively high conductivity and regions with relatively slow seismic velocity. The Pacific Rise results are generally more conductive and have slower seismic velocity than the global-average while the results from the Mariana Forearc tend to be more resistive and have faster velocity than the global-average.

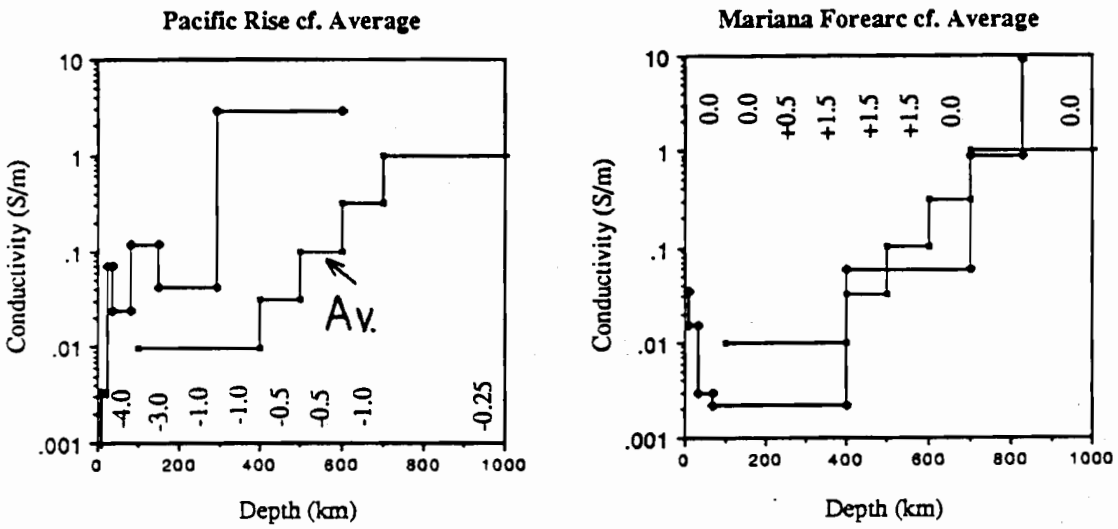

Figure 9.10: Comparison of electrical conductivity heterogeneity with seismic heterogeneity. The curves show the conductivity profile for the Mariana Forearc and for the Pacific Rise compared with a global-average profile. The numbers on each diagram indicate the percentage difference between the observed seismic velocity and globally averaged seismic velocity as a function of depth. The seismic results are scaled from maps presented by Dziewonski (1984) and Woodhouse & Dziewonski (1984) and are for v_s above 550 km and v_p below 670 km.

9.2 Interpretation of Tasman Sea conductivity results

Tectonics of the Tasman Sea Region

The Tasman Sea is bounded by passive continental margins at the Australian continent and the (probably) continental Lord Howe Rise and formed by seafloor spreading between 82 and 60 Ma.

Development of the present tectonic structure in the Tasman started around 95 Ma when slow spreading began between the Australian continent and the Lord Howe Rise, at the same time as slow spreading occurred between Australia and Antarctica (Duncan & McDougall 1987). The spreading accelerated around 80 Ma and ceased at 60 Ma (Weissel & Hayes 1977). Seafloor magnetic lineations indicate the Tasman Sea opened from a ridge trending NNW through the Tasman, oblique to the Australian continent (Figure 9.11). The ridge is offset by a number of fracture zones and is now characterized by a shallowing of the seafloor and a basement ridge (eg. Hayes & Ringis 1973).

Earlier interpretations of the oblique spreading relative to the Australian continent included a period of subduction beneath the Australian continent (eg. Hayes & Ringis 1973). More recent analyses have suggested that considerable strike-slip motion occurred in the northern Tasman Sea during its opening (Shaw 1978, Mutter & Jongsma 1978). There is also evidence that in the northern Tasman, the spreading centre jumped to the west between 75 and 69 Ma, isolating the Dampier Rise and the Lord Howe and Middleton Basins (Weissel & Hayes 1977).

Geophysical measurements suggest the Lord Howe Rise comprises continental crust and that the eastern margin of the Rise once formed the margin of the Australian-Antarctic continent (Willcox et al. 1980). The magnetic anomaly of the Rise however suggests that the lower crust must now consist of a rock of high susceptibility, possibly basalt or high-susceptibility plutons (Frey 1985). This suggestion is compatible with the hypothesis that the onset of seafloor spreading occurred at the western edge of an existing rift valley (eg. Willcox et al. 1980) leaving a relative simple continental margin at the present east coast of Australia (Mutter & Jongsma 1978). The high susceptibility material beneath the Lord Howe Rise could represent altered lower crust, replaced during crustal thinning and magmatic processes at the time of rifting (Frey 1985). Using the detachment-fault model of passive margin evolution of Lister et al. (1986) the Lord Howe Rise would comprise the lower-plate margin and the present Australian continental margin, the upper-plate margin.

The two meridionally-trending seamount chains in the Tasman Sea are much younger features than the spreading ridge and are therefore probably of more importance to electrical conductivity results. Evidence indicates that both the Tasmantid Seamount Chain and the Lord Howe Seamount Chain (Figure 2.1) become younger towards the south (Vogt & Conolly 1971, Duncan & McDougall 1987). This age distribution parallels a similar southwards younging of central volcano provinces along the east of the Australian

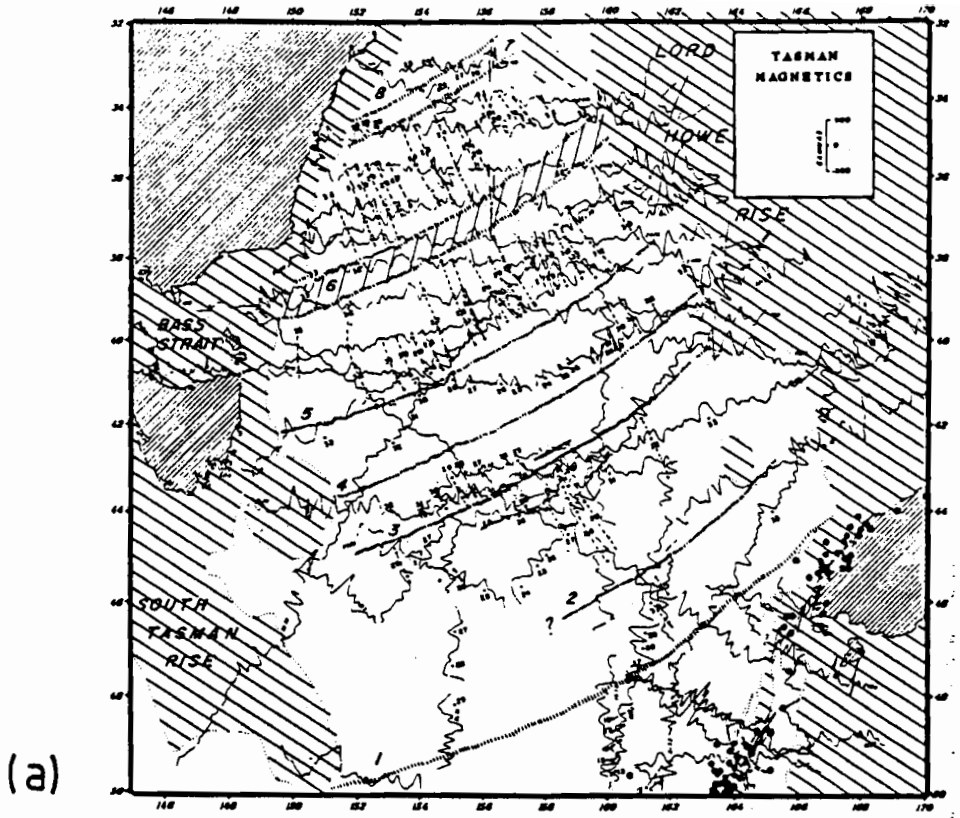

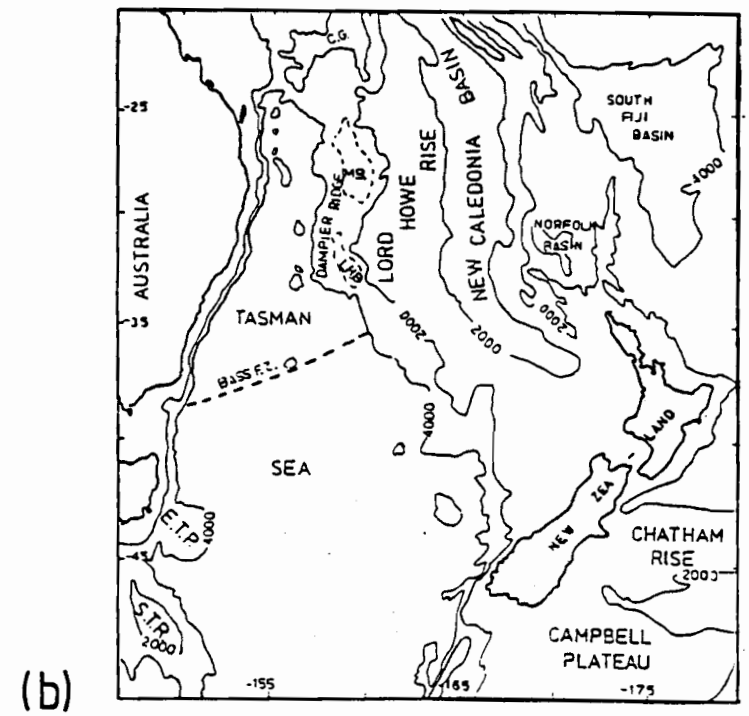

Figure 9.11: Maps of the Tasman Sea and adjacent region.

(a) Seafloor spreading magnetic anomalies (from Weissel & Hayes 1977). The open circles are (in west to east direction) Tasman Project sites TP5 to TP1.

(b) Major physiographic features of the Tasman Sea (from Shaw 1978). Abbreviations for features referred to in text are M.B.- Middleton Basin and L.H.B. - Lord Howe Basin.

continent and also corresponds closely to the rate of northwards movement of the Australian plate over a fixed point in the mantle (Duncan & McDougall 1987). Preliminary dating of rocks dredged from the Tasmantid Seamount Chain indicates an age progression of the seamounts of 7.0 ± .34 mm.yr^{-1} which is close to the plate velocity of 6.0 mm.yr^{-1}. The age for the Gascoyne Seamount, the most southern seamount in the Tasmantid chain, is approximately 5 Ma (McDougall 1986).

Three mechanisms have been proposed for the source of seamount chains. Duncan & McDougall (1987) attribute the chains to the passage of the Australian plate over two stationary hot spots in the mantle. Sutherland (1983) attributes the seamounts to the passage of the plate over a 'hotline' located at the position of earlier seafloor spreading in the Coral Sea. Pilger (1982) attributes the seamount chains to changing intraplate stress in the Australian plate. Each of these models would be associated with a different electrical conductivity structure in the mantle. The hotspot mechanism would involve localized deep mantle conductivity anomalies associated with rising plumes, whereas the hotline mechanism would involve a broader-scale anomaly. In the stress model, Pilger (1982) attributes the volcanism to melting at the base of the lithosphere, and therefore the model involves no deep mantle conductivity anomaly.

The Tasman Sea High Conducting Layer

As discussed in chapter 8 there is firm evidence for the presence of a HCL in the mantle beneath the central Tasman Sea. It is present beneath sites TP3 and TP4 but not beneath site TP5. Because of 3D induction effects in the Tasman there is some ambiguity regarding the depth of the HCL; SFMT impedance estimates suggest the HCL lies between 200 and 300 km depth and the VGS impedances suggest it is located at a depth of 100 to 160 km. No difference is resolved between the depth of the HCL at sites TP3 and TP4 although the conductivity contrast of the HCL is strongest at TP3.

Figure 9.5 shows the HCL-depth / lithospheric-age relationship in the Tasman Sea compared with corresponding results from the Pacific Ocean. The lithospheric ages for sites TP3 and TP4 are approximately 65 and 70 Ma respectively (Weissel & Hayes 1977, Figure 1) and the VGS 100 km HCL-depth for these sites is only slightly more shallow than for the corresponding depth in the Pacific Ocean (Figures 9.5, 9.12). The SFMT and VGS HCL-depth estimates for the Tasman data in fact bracket the Pacific Ocean HCL curve. The results strongly suggest that the HCL beneath the Tasman Sea may have the same age-dependence as observed in the Pacific Ocean

This is a significant result. It provides an indication that the conductivity structure observed beneath the Pacific Ocean may be characteristic of most undisturbed oceanic lithosphere. The soundings performed in the Arctic Ocean have not been analysed with sufficient resolution to be diagnostic regarding this point. The results from the Atlantic suggest a more conductive profile than for the Pacific Ocean but should be duplicated in a

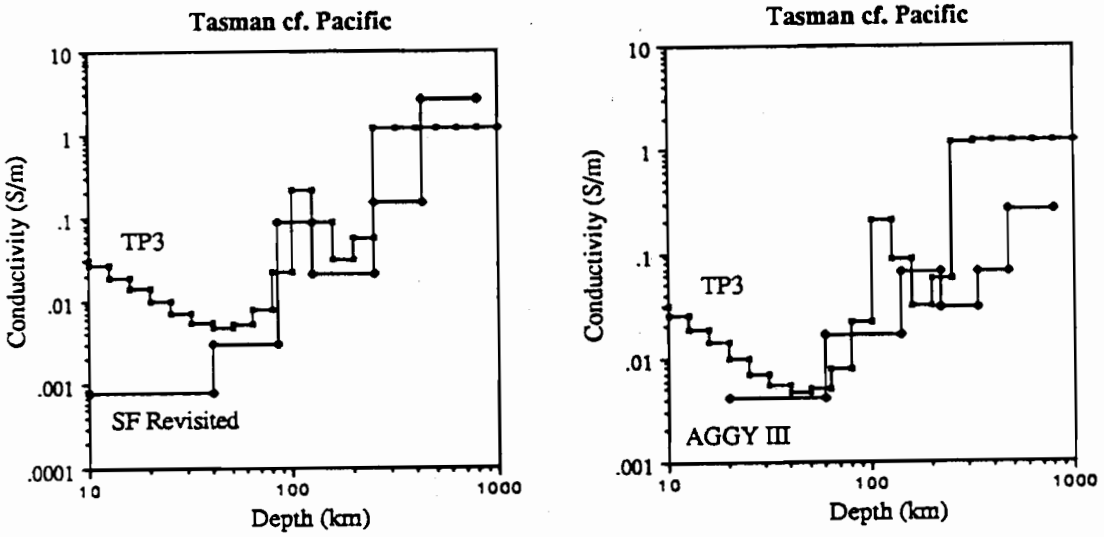

Figure 9.12: Comparison of TP3 (VGS) conductivity structure with the AGGY III (72 Ma) and SF Revisited (30 Ma) conductivity structure. Note that the depth of the HCL at TP3 falls between the HCL depth for SF Revisited and AGGY III. The (VGS) HCL depth for the ~70 Ma Tasman Sea lithosphere is therefore slightly more shallow than the corresponding depth in the Pacific Ocean. Also note that in the depth range 40 to 200 km the magnitude of the conductivity value is similar for TP3 and for the Pacific Ocean sites.

second geographical location before this result is finally accepted. The Tasman Sea results provide independent confirmation of the Pacific Ocean results. A similar form for the Tasman Sea HCL was obtained at sites TP3 and TP4 which are located 370 km apart. This observation suggests that the observed deep structure of the Tasman Sea is relatively uniform over this distance scale and that the form of the HCL structure obtained at TP3 and TP4 is a characteristic of much of the Tasman Sea. (The differing profile at TP5 will be discussed below.)

A second important implication of the agreement between the Tasman and Pacific results is that at depths of around 100 to 200 km the tectonic structure of the Tasman Sea is not anomalous ie. the tectonic processes influencing the HCL are similar in the Pacific Ocean and the Tasman Sea. The process causing the HCL in the Pacific, partial melting or aqueous fluids, is also likely to be causing the HCL in the Tasman Sea.

It is of interest to examine other geophysical evidence on the deep structure of the Tasman Sea. Sundaralingam & Denham (1985) used Rayleigh waves arriving at eastern Australian stations to determine the depth to the seismic LVZ. Fixing the v_s structure below 220 km to the global PREM model (Dziewonski & Anderson 1981) they determined the depth and v_s velocity for a LVZ lying above 220 km. For the Tasman Basin they obtained a velocity of about 4.25 $km.s^{-1}$ and a depth to the LVZ of 65 ± 10 km. This depth is more shallow than the depth determined for the electrical HCL in the Tasman but it is compatible with Pacific Ocean LVZ results for lithosphere of ~ 60 Ma (Oldenburg 1981).

There are several possible sources for the difference between the depth estimate for the LVZ and the HCL in the Tasman Sea. The difference could be due to systematic errors in the seismic study (eg. due to local heterogeneity) or to systematic errors in the electromagnetic results associated with 3D induction effects. The difference may also be due to the inversion technique used for the SFMT data. An Occam inversion will place an HCL at the depth at which it minimizes the structure in the model, but this is not necessarily the only possible (or correct) depth. Examination of minimum-structure and alternate inversion results for data from site SF Revisited (CAL), shows depths for the HCL ranging from 75 km (Oldenburg et al. 1984) to 85 km (Filloux 1980c) to ~ 120 km Oldenburg (1981). Finally the difference between the Tasman Sea HCL and LVZ depths could be a real result, with the seismic velocity responding to slightly different rock properties than the conductivity (for example, the seismic velocity responding to sub-solidus effects or the velocity and conductivity responding differently to the pattern of connectivity of a liquid phase).

Further verification of both the seismic derivation of the LVZ depth and the MT result for the HCL are necessary before petrologic conclusions can be drawn on the LVZ / HCL in the Tasman Sea. The LVZ results certainly suggest that the VGS impedance estimates for the Tasman are closer to the true local impedances (those of the local underlying conducting structure) than are the SFMT estimates.

Except for localized features such as seamounts, the bathymetry of the Tasman Sea is close to that expected for 'normal' oceanic lithosphere. From models of seafloor depth versus lithospheric age (eg. Parsons & Sclater 1977) a seafloor basement of 5200 m depth is predicted for regions near the spreading-ridge crest and a basement depth of 5500 m is predicted for the oldest Tasman seafloor. These values compare well with observed ridge-crest depths of 4500 to 5200 m, and basement depths for the oldest seafloor of 6000 m near the Australian continent and 5500 m near the base of the Lord Howe Rise (Hayes & Ringis 1973). The deeper basement near the Australian margin may be attributed in part to sediment loading (Hayes & Ringis 1973).

There are limited heatflow data available for the Tasman Sea. Grim (1969) determined heat flow along a line crossing the northern Tasman Sea at 32° S and observed values ranging from 45.0 to 64.2 $mW.m^{-2}$. These results agree well with the heat flow

values predicted for 60 and 80 Ma oceanic lithosphere using the empirical relationship of Parsons & Sclater (1977) viz. 53 to 61 $mW.m^{-2}$. Grim also determined two values on the Lord Howe Rise of around 100 $mW.m^{-2}$ however these results are not likely to be as reliable as the lower values of 57.8 $mW.m^{-2}$ determined in the New Caledonia Basin to the east (Von Herzen 1972) and 56.9 $mW.m^{-2}$ determined in a DSDP hole in the northern Lord Howe Rise (Morin & Von Herzen 1986).

In contrast to the above results, observations of the seismic Sn phase suggest that the lithosphere of the Tasman Sea is anomalous (Molnar & Oliver 1969). The Sn phase travels in the lithosphere and its absence at a particular site is interpreted as indicating strong seismic attenuation in the lithosphere comprising the travel path. Most travel paths crossing the Tasman Sea, for example those from earthquakes originating on the Macquarie Rise and New Zealand and being recorded in Sydney, indicate strong attenuation of the Sn phase leading to the interpretation of the Tasman Sea as being anomalous. Examination of other travel paths across the Coral Sea and Southern Ocean however also reveals strong Sn attenuation (Molnar & Oliver 1969). Since all of these travel paths are unlikely to cross anomalous lithosphere there is some doubt regarding the Tasman Sea results. Bennett (1972) assesses the Sn results in more detail.

The seafloor spreading magnetic lineations, the depth to the LVZ, the bathymetry and the available heatflow data all suggest that much of the Tasman Sea represents undisturbed oceanic lithosphere. The depth to the electrical HCL observed in the Tasman Sea also agrees with observations of the depth to the HCL in undisturbed lithosphere in the Pacific Ocean.

Tasman Sea deep conductivity structure

Figure 9.12 compares the TP3 conductivity profile with results from the Pacific Ocean and shows that between the depths of about 40 and 300 km the magnitude of the electrical conductivity is relatively similar at TP3 and at the Pacific Ocean sites. Considering the variability that exists in the conductivity of near-surface rocks this is an important result. The magnitude of the TP3 conductivity adds statistical significance to the conductivity levels obtained in the Pacific and suggests that, apart from the lateral variations associated with the HCL and other obvious features such as subduction zones, lateral variations in the composition and physical properties of the oceanic mantle are relatively small. This result contrasts with the large variations observed at crustal depths and in the more heterogeneous sub-continental lithosphere (eg Figure 9.7).

In the conductivity profile determined from the VGS impedances the deep conductivity rise at sites TP3 and TP4 is located at about 300 km depth and for the SFMT results it is located at 500-600 km depth. This VGS depth is more shallow than the deep conductivity rise observed in global models and other Pacific studies (Figures 9.9 and 9.7) however such a result has also been observed in the Atlantic Ocean and in a number of continental

studies (Figure 9.7 and 5.5). The observed results suggest the true local impedances (free of 3D induction effects) for the Tasman Sea lie between the VGS and SFMT estimates. Such impedances would place the deep conductivity rise at around 400 km depth and give an HCL depth very close to the Pacific Ocean trend.

Table 7.7 listed for each of the SFMT sites, the depth h, to the deep conductor determined using the asymptotic method and the SFMT impedance estimates. (The depths obtained for sites TP3 to TP5 agree well with the depths indicated by Occam inversion results in chapter 8.) From equation 4.96b it follows that the equivalent VGS estimates will be half the SFMT estimate. For sites TP7, 6, 5, 4, 3 and 1 the VGS estimates for h are thus 322, 384, 394, 291, 274 and 492 km respectively. Although these results may be influenced by 3D-induction effects they show a consistent spatial pattern across the Tasman Sea. Further modelling of the 3D effects in the Tasman Project impedances will allow verification of these results.

If the estimates for h are assumed to be reasonable measures of the deep conductivity structure, the results for TP6 and TP7 add confirmation to the deep structure determined for site TP5 (discussed below). The results also show a deepening of the conducting layer over the Lord Howe Rise. This result seems geophysically reasonable considering the continental origin of the Lord Howe Rise.

Validity of site TP5 conductivity profile

As stated in chapter 8 there are possible reasons, based on geomagnetic induction considerations, why the determined TP5 conductivity profile may not be as valid as those at TP4 and TP3. The reasons relate to the possible influence of 2D and 3D and bias effects in the data. The profile also seems to be geophysically unreasonable. It does not include a layer corresponding to the sediment layer which has a estimated conductance of 640 S predicted from seismic observations (Table 5.2). The profile also differs significantly from the similar profiles at TP3 and TP4 despite being located only 230 km from site TP4, and there is no other geophysical evidence in the gravity, magnetics (Haxby et al. 1983), or heat flow (Grim 1969) for such a rapid change in the deep structure. It is therefore concluded that the conductivity structure determined for TP5 may be significantly perturbed from the true structure.

The part of the TP5 profile which is likely to be the most valid is the deep structure, corresponding to the h-line of the apparent resistivity curve. These results will be free of 2D perturbations (see chapter 4) and from any errors in the higher-frequency phase values. The deep part of the TP5 VGS model shows a rise in conductivity between 200 and 400 km. This model falls inside the field of possible models defined for southeastern Australia by Lilley et al. (1981) using Monte Carlo modelling of spatial gradient data (see Figure 9.13). The deep TP5 data could therefore be interpreted as being transitional between the oceanic and the continental structure. The decrease in the magnitude of the HCL between

TP3 and TP4 also adds some support to the possibility of a gradual transition in the deep structure between the Australian continent and the eastern Tasman Sea.

Any mechanism for such a gradual transition would however require a contribution from the sub-lithospheric mantle. The time elapsed since spreading ceased (60 Ma) is too short to have allowed thermal equilibration through the lithosphere over the 320 km distance between TP5 and the Australian continent. Further verification of the TP5 conductivity profile by 3D modelling is however necessary before a more precise tectonic interpretation of the conductivity structure at the site is justified.

Shallow Conductivity Structure in the Tasman Sea

The conductivity models presented in chapter 8 indicate that the conductance in the shallow part of the conductivity model at site TP4 is considerably higher than at site TP3. The VGS models suggest a conductance of 2200 S in the upper part of the profile at TP4 and 700 S at TP3 and the corresponding SFMT models suggest conductances of 1250 S at TP4 and 300 S at TP3. These values compare with estimates of sediment conductance by P.J. Mulhearn (see Table 5.2) of 740 S at TP4 and 504 S at TP3.

The contribution of the basaltic crust to the total shallow conductance at site TP3 is estimated to be small. Seismic results (Shor et al. 1971) indicate a thickness for the crust in the Tasman Sea of around 10 km. The conductance of the crust is estimated to be less than

$$S_{crust} = 500m \times 0.1\ S.m^{-1} + 9500m \times 0.001\ S.m^{-1} \sim 60\ S$$

with the first term corresponding to crustal layers 2A and 2B, and the second term to the rest of the crust. Adding this value to Mulhearn's estimate of sediment conductance, a total shallow conductance of 560 S is obtained. Considering that the estimated sediment conductance is probably accurate only to within ± 20 % this value is in close agreement with the VGS estimate of 700 S. (Once again the results suggest that the true impedance should lie between the SFMT and VGS values.) Therefore both the forward modelling performed in chapter 8, and the estimated shallow conductance indicate that the sediment layer contributes most of the conductance at shallow depths (ie. above 50 km) at site TP3.

At TP4 the estimated crustal plus sediment conductance is 60 + 740 S or 800 S which is much less than the VGS estimate of 2200 S and also the SFMT estimate of 1250 S. This result along with the forward modelling in chapter 8 indicates that the conductivity profile at TP4 must include moderately high conductivities at upper mantle depths. The absence of a corresponding result at TP3 suggests the source of the higher conductivity at TP4 is a tectonic feature which is present at TP4 but not at TP3. The possible sources for the conductivity are therefore; the fossil spreading ridge located near TP4, the Tasmantid Seamount Chain which passes close to TP4, or a fracture zone near the site. If the additional 1400 S conductance at TP4 (using the VGS estimate) was spread evenly over the

upper 50 km of the conductivity profile, then a conductivity of 0.03 $S.m^{-1}$ would be required at these depths. Examination of the range of conductivity observed in the upper 100 km in various continental locations (Figure 9.7) indicates that this is not an unreasonably high conductivity value.

The fossil spreading ridge is unlikely to explain the higher conductivity at TP4. Since seafloor spreading ceased 60 Ma there is unlikely to be any localized thermal anomaly near the site, leaving only compositional anomalies to explain the higher conductivity. If basalt was solidified in the 'plumbing-system' at the spreading ridge at the cessation of spreading it may provide a conductive anomaly against the surrounding gabbros and residual harzburgite. Such an anomaly however would be mainly in the vertical conductivity rather than in the horizontal conductivity measured by the MT method. The integrated crustal resistivity obtained from the MT anisotropy method indicates that no strong conductivity path exists between the ocean and the conductive mantle. The effect of any connected conductivity anomaly parallel to the spreading ridge is unlikely to be significant except at the actual ridge (Filloux 1982a).

Fracture zones are also unlikely to explain the higher conductance at TP4. The magnitude of the integrated crustal resistivity of the seafloor means the MT impedance obtained at each seafloor site is a spatially-averaged impedance over a relatively large adjustment distance, say 400 km. (The impedance will however be weighted towards the response of the local area.) The fracture zones are aligned in a dominantly ENE-WSW direction (Figure 9.11) and are normal to the E-pol electric field used to derive the conductivity structure. It is unlikely the fracture zones could contribute significantly to the E-pol conductivity over the required spatial scale of a few hundred kilometres. Also the results suggest a strong mantle contribution is required for the additional conductance at site TP4.

Effects associated with the Tasmantid seamount chain are perhaps the most plausible explanation of the additional conductance at TP4. The Gascoyne Seamount is located only 120 km to the north of TP4 and as stated above contains rocks possibly as young as 5 Ma. With the adjustment distance of around 400 km, the impedance recorded at site TP4 could be affected by an increase in conductivity in the vicinity the seamount. Such an increase could be associated with compositional changes or thermal effects of the seamount. There could also be local effects in the lithospheric conductivity structure beneath TP4.

At the rate of movement of the Australian plate (~ 6 $cm.yr^{-1}$, Duncan & McDougall 1987) the 5 Ma age for the Gascoyne Seamount suggests the effects of the seamount source may be present at 300 km south of the seamount. A region of enhanced seismicity occurs approximately 200 km south of this point (Denham 1985) and approximately 400 km south of site TP4. This observation suggests the effects of the seamount source may extend over a significant north-south distance and therefore that there could be local anomalies (thermal or compositional) in the deep conductivity structure beneath TP4. Sleep (1987) also shows that heating of the lower lithosphere can occur downstream of a hotspot. For the

Tasman Sea however there is no evidence of a hotspot swell associated with such heating and it is unclear whether a less intense hotspot could produce the required conductivity increase in the lithophere without causing observable seafloor effects.

The Tasman Project was largely an exploratory examination of the Tasman Seafloor. It has therefore achieved its aim in locating a variation in the conductivity structure between sites TP3 and TP4. As in any geophysical survey of this scale, further measurements would be required to map and interpret the increased conductivity in greater detail. Such additional research may allow discrimination of the three models proposed for the formation of the seamounts. The existing results suggest that the additional conductance at TP4 is spread over a considerable depth range and considering the adjustment distance of the seafloor MT data the effect is likely to be of a regional rather than local scale. The results therefore point towards a thermal source for the higher conductance rather than a magmatic source which would be expected to be more localized. Further verification of the TP4 conductivity profile eg. by thin sheet modelling, should be performed before stronger petrologic conclusions are drawn regarding the structure.

Comparison of the Tasman Sea and the Australian continental conductivity structures

The conductivity profile for the central Tasman Sea is more conductive than that for southeastern Australia which is in turn more conductive than the profile for the Australian shield to the west. Figure 9.13 shows the conductivity profile for site TP3 superimposed upon SGS results for the Australian continent from Woods (1979) and Lilley et al. (1981). Over much of the resolved depth range, the conductivity profile for TP3 lies inside the range of allowable models for southeast Australia. The conductivity of the TP3 HCL however exceeds the conductivity of the southeastern Australian models. The conductivity of the TP3 profile is significantly higher than the conductivity in central Australia.

Figure 9.13 also compares the conductivity profile for TP5 with the southeastern Australia results. The TP5 VGS profile falls almost within the range of possible southeastern Australian models. Although the TP5 is slightly more resistive around 300 km, the depth resolution (on a linear depth scale) is relatively poor and rearrangement of the depth parameterization in the Occam inversions could well result in the TP5 model lying completely inside the range of southeast Australia results.

The increased conductivity of the Tasman Sea relative to the Australian continent may be partially due to direct compositional differences in the lithosphere, however a larger contribution to the difference is probably attributable to the steeper geotherms in the oceanic environment. Seismic results also show large-scale differences between the Tasman Sea, eastern and shield Australia. Frohlich & Barazangi (1980) examined travel time residuals from deep Tongan earthquakes at stations on the Australian shield, the mobile continental region of eastern Australia, and in the Tasman Sea and southwest Pacific Ocean. Consistent (S-P) and (ScS-ScP) residuals exists between the ocean, eastern Australian and

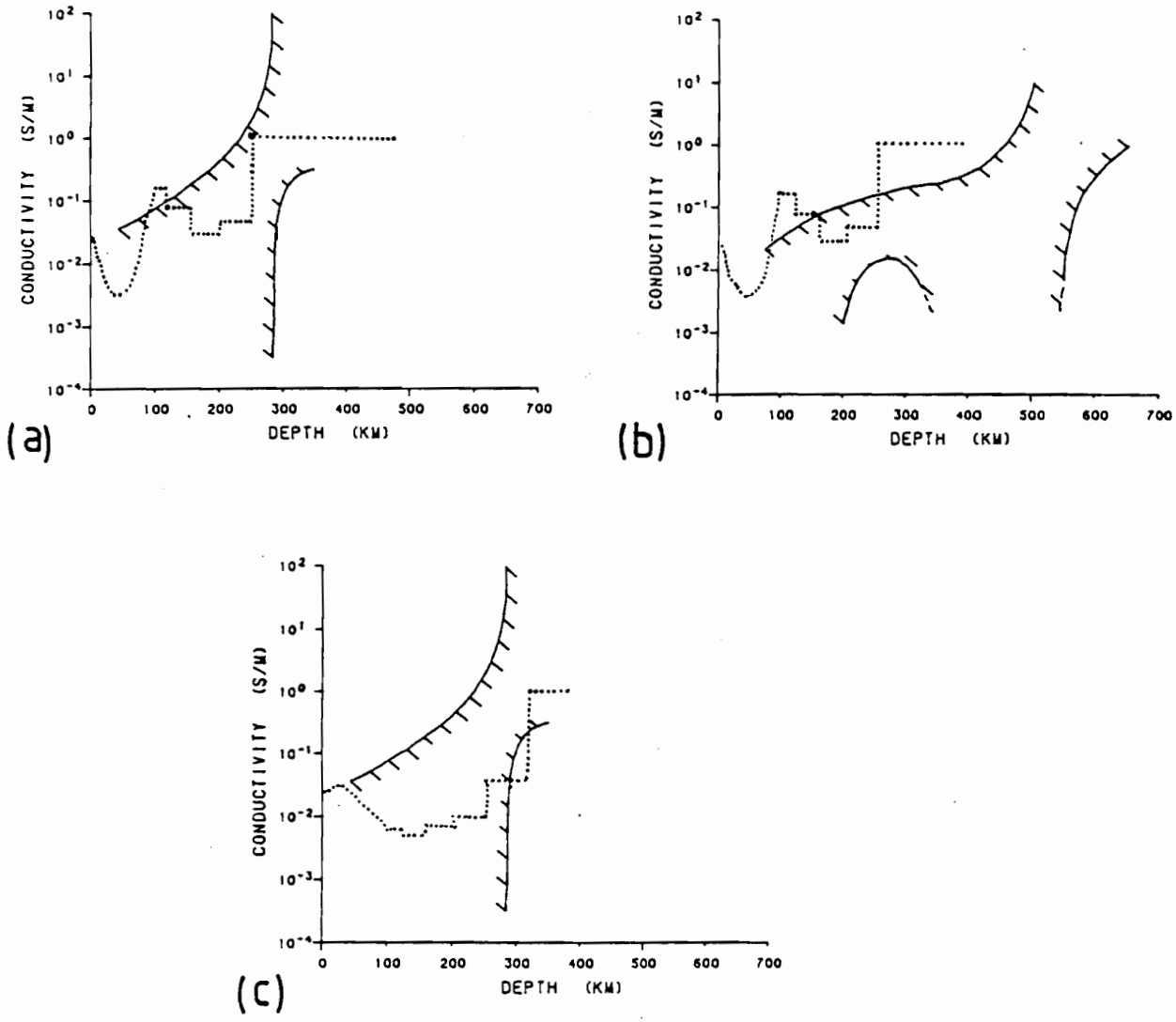

Figure 9.13: Comparison of Tasman Sea and Australian conductivity profiles. The outlined area shows the range of models which fit the southeast Australian and central Australian spatial gradient data, the dotted line is the Tasman Project (VGS) conductivity profile.

(a) Comparison of profiles from TP3 and southeast Australia

(b) Comparison of profiles from TP3 and central Australia

(c) Comparison of profiles from TP5 and southeast Australia

central Australian sites and are interpreted as being due to variations in v_s in the upper mantle. The depth of the v_s variations is not resolved, however if the variations are assumed to extend to 400 km depth, a 4 % difference in velocity is required between the shield and ocean regions. The residuals show the slowest v_s occurs in the oceanic region indicating a correlation with the higher electrical conductivity of the region. Both effects are therefore probably due to relatively higher temperatures in the oceanic upper mantle.

The seismic tomography results of Woodhouse & Dziewonski (1984) and Dziewonski (1984) support the earlier seismic observations. The tomography results show systematic differences between across the Tasman Sea, eastern Australia and Central Australia. Table 9.1 lists the velocity anomalies as a function of depth for these regions. Because the tomography results cannot resolve anomalies with a scale smaller than about 2000 km, the only meaningful velocity differences are those between Central Australia and the Tasman Sea with the western Tasman and Eastern Australian results constrained to lie between these extremes.

Table 9.1: Seismic velocity anomalies in the Australian and Tasman Sea Region.

Depth	Percentage Anomaly			
(km)	Central Tasman	Western Tasman	SE Australia	Central Australia
50	-1.5	-0.5	+1.5	+3.0
150	-2.0	-1.5	-1.0	+2.0
250	-2.0	-2.0	-1.0	0.0 (+2.0)
350	-1.0	-1.0	-0.5	-0.5 (+1.0)
450	-0.5	0.0	+0.5	0.0 (+1.5)
550	+0.5	+1.0	+1.5	+1.0
670	-0.3	-0.2	-0.2	+1.0
1000	+0.1	0.0	+0.1	0.0

Anomalies are scaled from colour plates in Woodhouse & Dziewonski (1984) and Dziewonski (1984) with an estimated accuracy of ±50%. Results above 550 km are for v_s and deeper results are for v_p. The bracketed results for Central Australia are for a model in which different velocities were set for oceanic and continental crust.

The v_s velocity is consistently higher beneath the Australian shield than the Tasman Sea; the differences are greatest at shallow depths but appear to extend to at least 400 km depth. The magnitude of the velocity difference between the shield and ocean is around 2 to 4 % which is similar to the results of Frohlich & Barazangi (1980). These seismic results correlate with the electrical conductivity results, which also show that differences between the Tasman Sea and central Australian profiles must extend to at least 450 km depth. At the 670 km depth the v_p velocity is higher beneath the Australian shield than the Tasman Sea suggesting physical differences between the two regions extend to at least this depth.

It is interesting to compare the Tasman Sea and Australian conductivity profiles with the global average, in order to produce results which correspond to the tomography results. Figure 9.14 shows the results of such a comparison. In the depth range 100 to 300 km the Tasman Sea conductivity profile is more conductive than the global average by about an order of magnitude and the v_s velocity is 2 % below the global average. The combined results suggest that the region is warmer than the global average temperature at the same depths.

The eastern Australian conductivity structure is not as well constrained as that for the Tasman Sea. At shallow depths it is based on a compilation of MT soundings from non-Precambrian eastern Australia (eg. Lilley 1987) and at greater depth by the SGS results of Lilley et al. (1981). The eastern Australian profile appears to be more conductive than the global average at depths of 100 to 300 km and corresponds to shear wave velocities which are slower than the global average. The possibility that temperatures in the lithosphere beneath eastern Australia are higher than the global average is supported by heat flow data which indicates that eastern Australia is characterized by a high heat flow of 60 to 80 $mW.m^{-2}$ (Cull 1982).

Summary

The Tasman Project comprised an exploratory investigation of the conductivity structure of the Tasman Sea. The results obtained from 1D analyses found that the deep conductivity structure in the Central Tasman is similar to the structure beneath lithosphere of a corresponding age in the Pacific Ocean. Local variation observed across the Tasman Sea includes a deepening of the deep increase in conductivity near the Australian continent and over the Lord Howe Rise. The shallow conductivity at site TP4 is higher than at site TP3, a result probably attributable to thermal effects associated with the nearby active end of a seamount chain.

Comparison of the Tasman Sea results with other MT and geophysical results provides some insight into the ambiguity of the two different impedance estimates for the Tasman Sea. Sediment conductance, the depth to the HCL and the depth to the deeper

conductivity rise all indicate that the true local impedance values should lie between the VGS and SFMT estimates. The results, along with information on the LVZ beneath the Tasman, suggest that between these extremes the impedance should lie closer to the VGS estimate. For sites TP3 and TP4 a depth to the HCL of 120 to 150 km is suggested.

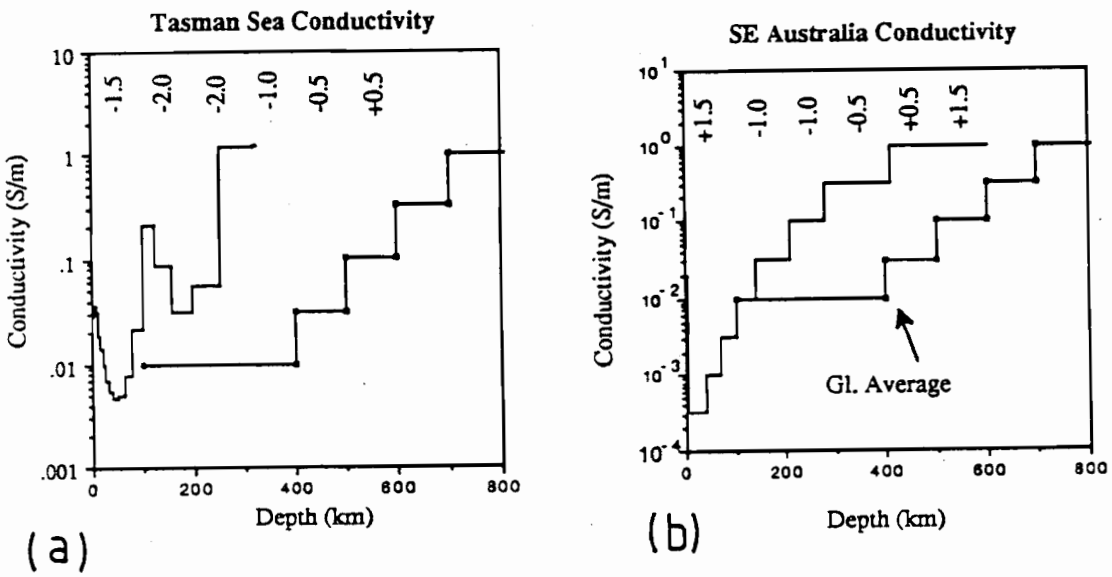

Figure 9.14: Comparison of conductivity profiles with a global-average profile. The numbers on each graph are the corresponding seismic tomography anomalies as a function of depth.

(a) Tasman Sea. The profile is the TP3 (VGS) profile.

(b) Eastern Australia. The profile is a composite result derived from all available MT soundings in eastern Australia and also the spatial gradient results of Lilley et al. (1981).

Chapter 10 Conclusions

The Tasman Project of Seafloor Magnetotelluric Exploration was carried out between December 1983 and April 1984 with the aim of investigating the conductivity structure of the Tasman Sea and the Australian continental margin and also aspects of the physical oceanography of the Tasman Sea. The experiment comprised MT and oceanographic instruments (from Scripps Institution of Oceanography) at nine seafloor sites in the Tasman and magnetic field recordings at nine sites on the Australian continent. The data return from both sets of instruments was nearly complete and the data quality was high.

Reduction of the recorded land and marine data into final MT and oceanographic time series involved a considerable amount of effort but was completed within two years of the end of the experiment. The time series are now stored on magnetic tape in formats which allow easy and accurate access to different components and to selected parts of the time series. A number of analyses have already been performed on the data; published results are listed in chapter 1. This thesis describes the analysis of the SFMT data using mainly 1D modelling and inversion techniques. The aim of this research is to determine the conductivity structure beneath the Tasman Sea. Future research using more complex, 2D, 3D and thin-sheet modelling techniques will refine the existing information on the sub-oceanic conductivity structure.

The conclusions of the research described in this thesis will now be noted. They may be divided into four categories which relate to; the geomagnetic source-field, seafloor geomagnetic induction studies, the electrical conductivity structure beneath the Tasman Seafloor, and tectonic / petrological implications of the electrical conductivity structure.

The geomagnetic source-field

The geomagnetic storms and substorms occurring during the Tasman Project recording period were used as the source for investigating the seafloor electrical conductivity. The time series were investigated to determine the average spatial uniformity of the these geomagnetic source-fields. Ordinary and multiple coherence functions show that the source-field is reasonably coherent over distance scales of 2000 km, for periods between 10 min. and 1 day. These results apply for spatial variations in a magnetic east-west direction and at the 42°- 44° S geomagnetic latitude of the Tasman Project sites Strictly, the results apply only for the ensemble of storms and substorms occurring during the analysis period. Assuming approximate stationarity of the magnetic field fluctuations (between different 10 and 42 day time-intervals) the results will also be applicable at other times.

A numerical examination of the average spatial-coherence scale found that the B_H and B_D crosspower between two sites decreases approximately exponentially with increasing

inter-site distance. For B_H the average (for the period range) distance-scale of of the exponential decrease is approximately 5900 km and for B_D the average distance-scale is 3900 km. The distance-scale for both components increases with increasing period.

Seafloor Geomagnetic Induction Studies

The Tasman Project was performed in active oceanic environment and the recorded data therefore contain a relatively high proportion of oceanically induced noise. The horizontal electric-field signal induced by an oceanographic eddy is particularly conspicuous and dominates the signal induced by ionospheric / magnetospheric sources.

The presence of the oceanic noise at higher frequencies in the magnetic and electric fields necessitates the use of a noise-reduction technique in the data analysis; for the Tasman Project the remote-reference technique of Gamble et al. (1979a) has been used. Experimentation using different sites as the remote reference indicates that land observatory sites are the most suitable remote references. The seafloor electric and magnetic fields all contain a component of correlated noise which; occurs at periods of 1 to 10 h, is correlated over a distance scale of at least 1000 km, and must be coherent for periods of at least 10 days. The noise is interpreted as being either the signal of a large-scale oceanographic process, or more probably as being due to channelling of electric currents induced by non-uniform source-field components. Hand-digitization of the analogue recordings from the Gough-Reitzel land sites causes minor degradation of the signal, and makes these sites less suitable for use as remote-reference sites.

The remote-reference impedances exhibit significant 2D and 3D components. The impedances are dominantly 2D, showing strong anisotropy which decreases systematically towards the centre of the Tasman Sea. The 3D effects, include non-zero impedance skew angles, also vary systematically across the Tasman Sea. The spatially-systematic form of the non-1D effects leads to their interpretation in terms of large-scale 3D geomagnetic induction in the Tasman Sea. The pattern of the non-1D effects is dependent upon the overall morphology of the Tasman Sea (ie. its shape and bathymetry) and not upon local variations in the underlying conductivity structure.

Support for the hypothesis of large-scale 3D geomagnetic induction comes from both the E-pol impedances (parallel to the Australian coast) and B-pol impedances. The B-pol impedances increase smoothly with distance from the coast. The distance-scale of this increase is around 400 km and is used to show minimum integrated crustal resistivity of the Tasman Seafloor is $10^7\ \Omega.m^2$. At this distance-scale it is conceivable that for most sites in the Tasman Sea, geomagnetic induction will be influenced by the (non-parallel) conductivity boundaries of the Australian continent and the Lord Howe Rise. This situation will cause 3D induction.

The E-pol impedances at sites TP3, TP4 and TP5 in the central Tasman Sea have been

estimated using both the SFMT and VGS methods and the resulting impedance magnitudes exhibit a frequency-independent difference of a factor of two. The sites involved in these calculations lie more than 300 km from either the Australian coast and the Lord Howe Rise and any 2D E-pol effects from these conductivity boundaries will therefore be weak. The VGS / SFMT differences are therefore interpreted as further evidence for 3D induction effects. The larger values of the SFMT impedances may be due to the funnelling of north-south electric currents into the central Tasman, caused by the shape of the sea. The impedance skew angles support this model.

The 3D geomagnetic induction effects in the central Tasman Sea (eg. the skew) are largely independent of frequency. Formally, the impedances should be examined using a more advanced modelling technique such as thin-sheet modelling, in order to obtain the correct relationship between the observed impedances and the 'local 1D' response at each recording site. The procedure followed in this thesis assumes the local impedance results are closely related to the SFMT and VGS impedance estimates. In order to proceed with the analysis the impedances were 'deskewed', rotated to the principal axes, and 1D MT inversions then performed on the E-pol impedance terms. This approach was considered justified because of the simple relationship of the SFMT and VGS impedance estimates, the dominantly 2D form of the impedance tensors (deskewing causes only minor changes to the E-pol impedance term) and the well-behaved form of the E-pol impedance magnitude and phase.

One-dimensional inversions were performed on the E-pol impedances from only sites TP3, TP4, and TP5 since the impedances at other sites are influenced by 2D effects from the Australian continent and the Lord Howe Rise. The inversion results show the E-pol impedances contain frequency-dependent non-1D effects which are again attributed to the large-scale 3D induction process. The conductivity models obtained from the inversions for TP3 and TP4 however appear to be geophysically reasonable. Forward modelling indicates that important features of these models are unlikely to be caused by the non-1D effects in the data, and the models are therefore cautiously accepted as being indications of the true Tasman Sea conductivity structure. The model for TP5 is more likely to contain 2D and 3D effects and is interpreted with greater caution.

The analysis described in this thesis also contains a determination of induction arrows at the seafloor and land sites. It is concluded that when dealing with seafloor data, it is preferable to use a reference horizontal magnetic-field (cf. the seafloor horizontal magnetic-field) to calculate the induction arrows. The attenuation of the horizontal magnetic field through the ocean means that 'local' seafloor arrows are very sensitive to changes in the ocean depth and 2D and 3D effects. The spatial variation of the 'local' induction arrows associated with variations in both the horizontal and the vertical magnetic field makes the interpretation of the arrows difficult.

The transverse component of the Tasman Project induction arrows, calculated using the horizontal magnetic field at CMO as a reference, shows a systematic coast effect across

the Australian continental margin. Qualitative interpretation of the results suggests the coast effect contains a contribution from crustal/mantle sources in addition to the ocean/ land conductivity contrast. A weak coast effect is also observed over the Lord Howe Rise. The data resolution is too low to allow discrimination of any contribution to this coast effect from the transition between oceanic and continental lithosphere. Induction arrows at sites near the southeast Australian coast contain a significant longitudinal component. This component is interpreted as a 3D effect associated with the deviation of perpendicular electric currents by the Australian coast.

Conductivity Structure Beneath the Tasman Sea

A variety of MT inversions have been performed in order to investigate the conductivity structure beneath the Tasman Sea. The inversion methods used have included Parker D^+ inversions, Occam inversions minimizing the 1st and 2nd derivative of the conductivity model, and 'smooth' Occam inversions adjusted to give models with a smoothness corresponding to the level of random errors. Inversions have been performed on both the SFMT and VGS impedance estimates. Before their application to the Tasman data, the inversion techniques were applied to synthetic data sets in order to test their resolution.

All of the inversion techniques give conductivity models for sites TP3 and TP4 which include an HCL. The HCL occurs at the same depth at both sites; joint inversion of the MT data in fact suggests that the deep (> 100 km) conductivity profile is not significantly different between the two sites. The SFMT impedances suggest the HCL is located between 200 and 300 km depth and the VGS estimates suggest 100 to 160 km depth. A deeper conductivity rise at the sites is found to occur at 300 km (VGS estimate) or 600 km (SFMT estimate) depth. At shallow depths, the electrical conductivity at site TP4 is higher than at TP3. The impedance results show that in the upper, conductive, part of the conductivity profile, the TP4 profile contains approximately three times the conductance present at TP3. Forward modelling indicates that this additional conductance at TP4 must be distributed over at least the upper 20-50 km.

The conductivity profile determined for TP5 appears to be geophysically unreasonable at depths more shallow than 200 km. For example, the profile does not show any evidence of the sediment layer at the site (which has an estimated conductance of 600 S). The profile may however be more accurate at greater depth, where it shows the absence of an HCL. The inversion results indicate that the deep conductivity rise at this site occurs at a greater depth than at sites TP3 and TP4. Application of the MT asymptotic method to the impedances determined at sites TP6 and TP7 suggests a similar deep structure to that at TP5. The asymptotic method also shows that the depth to the deep conductor increases beneath the Lord Howe Rise.

Tectonic and Petrological Results for the Tasman Sea

Comparison of the VGS and SFMT conductivity models with results for lithosphere of a similar age in the Pacific Ocean, and comparison of the conductivity profiles with other geophysical evidence, suggests the undistorted Tasman Sea impedance values must lie between the SFMT and VGS estimates, and probably closer to the VGS results. For sites TP3 and TP4 the depth to the top of the HCL is therefore estimated to be around 120 to 150 km, and the depth to the deep conductivity rise 400 to 450 km. Even with the ambiguity between the VGS and SFMT conductivity profiles, the depth to the HCL in the Tasman Sea is very similar to the corresponding depth observed in the Pacific Ocean. This result adds support to the existence of a characteristic conductivity model for undisturbed oceanic lithosphere/mantle and also to the classification of the Tasman Sea as possessing a normal lithospheric profile.

It is difficult to adequately interpret the increased conductance observed at shallow depth in the TP4 conductivity profile using the results from only one recording site. The results however suggest a reasonably broad distribution of the higher conductance at the site, an effect tentatively interpreted as being due a thermal anomaly associated with the source of a nearby seamount chain. Further modelling of the Tasman Sea results is necessary to investigate the possible distortion of the SFMT impedances by the large-scale 3D induction effects, and until this analysis has been performed it is unwise to draw stronger conclusions on the tectonic and petrologic implications of the conductivity profiles.

Objectives Achieved and Further Research

During the last four years many of the objectives of the Tasman Project (listed in chapter 1) have been achieved. Information has been obtained on the sub-oceanic conductivity structure beneath the Tasman Sea, physical oceanography of the Tasman Sea, and research is currently in progress on the conductivity structure of the Australian continental margin. Results applicable to other seafloor geomagnetic studies have also been obtained. For example, results from the Tasman Project provide a measure of the adjustment-distance MT anisotropy can extend from a coastline, and also a measure of the east-west uniformity of geomagnetic source-fields at the latitude of the Tasman Sea.

The data set obtained from the Tasman Project is of great value, and has the potential to yield further important results. Suggestions for future research, which have been made throughout this thesis, will now be summarised.

With the inclusion of data from the EYR site in New Zealand, the Tasman Project data set contains magnetic-field recordings from a 2000 km line of almost constant geomagnetic latitude. As such the data has great potential for the study of the zonal uniformity of geomagnetic source-fields. The recordings contain a variety of storms and substorms and

could be used to examine the source-field uniformity as a function of disturbance intensity. Another important point to examine is whether the motion of these source-fields can be legitimately neglected in geomagnetic induction studies. Methods which could be used advantageously in this research include robust statistical analyses and multiple-site spectral analyses.

The correlated noise between the seafloor sites, noted during the remote-reference calculations, warrants further investigation. Such effects could be important in future seafloor geomagnetic induction studies in which a second seafloor site is to be used as the remote-reference. Correlation of the noise with magnetic recordings from a site in the auroral region (eg. the Macquarie Island Geophysical Observatory) could reveal whether the noise is due to current channelling associated with spatially non-uniform components of the source-field.

Much of the suggested future research concerning the refined determination and modelling of the induction arrows is currently being pursued by R.L. Kellett. In this research, the data from the Tasman Project have been supplemented by data from the Australian Continental Shelf. Oceanographic analyses of the Tasman Project data, particularly of tidal signals, are being performed by N.L. Bindoff. The Tasman Project data however contain considerable oceanographic information yet to be investigated. Such aspects include; separation of the higher-frequency oceanic signal from the geomagnetic signal in the horizontal and magnetic field data at each of the sites, examination of the correlation of such oceanic signal between the different sites, and examination of the magnetic field signal from the oceanographic eddy.

In terms of the analysis described in this thesis, the main area of future research is more detailed modelling and study of the SFMT impedance results. The (~) 4 yr time available for this Ph.D. study was sufficient to allow participation in the experimental part of the Tasman Project, the data reduction of the seafloor MT recordings, the determination of induction arrows and seafloor impedances, and a preliminary 1D-based analysis of the seafloor MT impedances. The need for more advanced modelling, and the probability that such modelling will reveal important information on geomagnetic induction in the Tasman Sea and on the underlying conductivity structure is however clearly recognized.

It is believed that thin-sheet modelling (eg. Vasseur & Weidelt 1977) would be a suitable form of modelling to pursue. The pattern of geomagnetic induction in the Tasman Sea is three-dimensional however much of the three-dimensionality appears to be directly attributable to the shape of the Tasman Sea. (This result will be true if the conductivity contrast between the ocean and the surrounding rocks is much larger than any conductivity contrasts within the rocks.) If this hypothesis is correct, thin-sheet modelling of a region of approximately 3000 x 3000 km centred on the Tasman Sea should be able to reproduce, to first order, the observed 3D and 2D effects such as the impedance anisotropy and skew, the longitudinal components of induction arrows, and the difference between the VGS and SFMT impedance estimates.

An important result of such modelling would be the determination of the form of distortion of the impedance by 3D effects. Modelling should reveal which impedance axis or combination of axes should be inverted to retrieve the underlying conductivity structure. This modelling may allow the MT data from all of the seafloor sites to be used for deriving conductivity information. In the analysis in this thesis, the E-pol component of the deskewed impedance tensors was used for MT inversions; 3D modelling should reveal the accuracy of this procedure. A possible alternative to thin-sheet modelling of the Tasman Sea region would be analogue modelling (eg. Dosso et al. 1985) if an opportunity for such research ever arose.

On a more general note, it is concluded that the performance of further SFMT studies throughout the world would be of great value. SFMT studies have been shown to provide useful information on the structure of the upper mantle and the results of such studies confirm results from other geophysical measurements such as heat flow and seismic tomography. SFMT arrays can in fact provide greater lateral resolution (with scales of several hundred kilometres) than land-based seismic tomography studies.

Seafloor electromagnetic measurements may be combined with traditional oceanographic measurements to enhance the separation of oceanic and ionospheric signals and therefore to provide both solid-Earth and oceanographic results (as in the recent BEMPEX Project, Luther et al. 1987). SFMT measurements also may be combined with control-source measurements in order to produce more complete conductivity profiles. As experimental and analytical techniques advance, and more projects are completed, the results of previous SFMT experiments should not be neglected. These results contribute to defining general conductivity profiles for different tectonic settings, and the older results may often be refined by using more advanced analysis techniques.

References

Akasofu, S.-I., 1985: Explosive magnetic reconnection: puzzle to be solved as the energy supply process for magnetospheric substorms. *EOS* **66**, 2, 9-10.

Akimoto, S.I. & H. Fujisawa, 1965: Demonstration of the electrical conductivity jump produced by the olivine-spinel transition. *J. Geophys. Res.* **70**, 443-449.

Alldredge, L.R. & J.C. Fitz, 1964: Submerged stabilized platform. *Deep-Sea Res.* **11**, 935-942.

Alt, J.C., J. Honnorez, C. Laverne & R. Emmermann, 1986: Hydrothermal alteration of a 1 km section through the upper oceanic crust, Deep Sea Drilling Project hole 504B: mineralogy, chemistry, and evolution of sea-water basalt interactions. *J. Geophys. Res.* **91**, 10309-10335.

Bailey R.C., 1970: Inversion of the geomagnetic induction problem. *Proc. Roy. Soc. London* **315**, 185-194.

Bannister, J.R. & D.I. Gough, 1978: A study of two polar magnetic substorms with a two-dimensional array. *Geophys. J. R. astr. Soc.* **53**, 1-26.

Beamish, D., 1986: Deep crustal geoelectric structure beneath the Northumberland Basin. *Geophys. J. R. astr. Soc.* **84**, 619-640.

Beamish, D. & D.K. Smythe, 1986: Geophysical images of the deep crust: the Iapetus suture. *J. Geol. Soc., London* **143**, 489-497.

Beblo, M., A. Bjornsson, K. Arnason, B. Stein & P. Wolfgram, 1983: Electrical conductivity beneath Iceland - constraints imposed by magnetotelluric results on temperature, partial melting, crustal and mantle structure. *J. Geophys.* **53**, 16-23.

Becker, K., R.P. Von Herzen, T.J.G. Francis, R.N. Anderson, J. Honorez, A.C. Adamson, J.D. Alt, R. Emermann, P.D. Kempton, H. Kinoshita, C. Laverne, M.J. Mottl & R.L. Newmark, 1982: *In situ* electrical resistivity and bulk porosity of the oceanic crust Costa Rica Rift. *Nature* **300**, 594-598.

Bendat, J.S. & A.G. Piersol, 1971: *Random Data: Analysis and Measurement Procedures*. Wiley-Interscience, New York, 407 pp.

Bennett, D.J., 1972: Geomagnetic depth sounding studies in south-eastern Australia, Ph.D. thesis, Aust. Nat. Univ., Canberra.

Bennett, D.J. & F.E.M. Lilley, 1971: The effect of the south-east coast of Australia on transient magnetic variations. *Earth Planet. Sci. Lett.* **12**, 392-398.

Bennett, D.J. & F.E.M. Lilley, 1973: An array study of daily magnetic variations in southeast Australia. *J. Geomag. Geoelectr.* **25**, 39-62.

Bennett, D.J. & F.E.M. Lilley, 1974: Electrical conductivity structure in the South-east Australian Region. *Geophys. J. R. astr. Soc.* **37**, 191-206.

Bentley, C.R., 1973: Error estimation in two-dimensional magnetotelluric analyses. *Phys. Earth Planet. Int.* **7**, 423-430.

Berdichevsky, M.N. & V.I. Dmitriev, 1976a: Basic principles of interpretation of

magnetotelluric sounding curves, in *Geoelectric and Geothermal Studies*, edited by A.Adam, 165-221, KAPG Geophys. Monogr., Budapest.

Berdichevsky, M.N. & V.I. Dmitriev, 1976b: Distortion of magnetic and electric fields by near-surface lateral inhomogeneities. *Acta Geod., Geophys. Mont. Hung.* **11**, 447-483.

Berdichevsky, M.N. & M.S. Zhdanov, 1984: *Advanced Theory of Deep Geomagnetic Sounding*. Elsevier, Amsterdam, 408pp.

Bindoff, N.L., 1988: Electromagnetic induction by oceanic sources in the Tasman Sea. Ph.D. thesis, Aust. Nat. Univ., Canberra.

Bindoff, N.L., J.H. Filloux, P.J. Mulhearn, F.E.M. Lilley & I.J. Ferguson, 1986: Vertical elctrical field fluctuations at the floor of the Tasman Abyssal Plain. *Deep-Sea Res.* 33, 587-600.

Booker, J.R., D.I. Gough & J.H. Filloux (and others), 1988: The EMSLAB electromagnetic sounding experiment. *EOS* (in press).

Boteler, D.H., A.B. Kaiser & M.R. Ingham, 1987: Direct observation of channelling of induced currents. *Geophys. J. R. astr. Soc.* **88**, 529-534.

Boyce, W.E. & R.C. DiPrima, 1969: *Elementary differential equations and boundary value problems*. 2nd edn, Wiley, New York, 533 pp.

Brewitt-Taylor, C.R. & J.T. Weaver, 1976: On the finite-difference solution of two-dimensional induction problems. *Geophys. J. R. astr. Soc.* **47**, 375-396.

Bullard, E.C. & R.L. Parker, 1970: Electromagnetic induction in the oceans, in *The Sea*, Vol 4, edited by A. Maxwell, Ch. 18, 695-730, Wiley-Interscience, New York.

Bureau of Mineral Resources, Geology & Geophysics, 1984: *Geophysical Observatory Report, Magnetic Observatories* **31** (12) - **32** (4), Commonwealth of Australia.

Cagniard, L., 1953: Basic theory of the magneto-telluric method of geophysical prospecting. *Geophys.* **18**, 605-635.

Campbell, W.H., 1987: Introduction to *ElectricalProperties of the Earth's mantle. Pure Appl. Geophys.* **125**, 193-204.

Cermak, V. & M. Lastovickova, 1987: Temperature profiles in the Earth of importance to deep electrical conductivity models. *Pure Appl. Geophys.* **125**, 255-284.

Chave, A.D. & C.S. Cox, 1983: Electromagnetic induction by ocean currents and the conductivity of the oceanic lithosphere. *J. Geomag. Geoelectr.* **35**, 491-499.

Chave, A.D. & J.H. Filloux, 1984: Electromagnetic induction fields in the deep ocean off California: oceanic and ionospheric sources. *Geophys. J. R. astr. Soc.* **77**, 143-171.

Chave, A.D. & J.H. Filloux, 1985: Observation and interpretation of of the seafloor vertical electric field in the eastern North Pacific. *Geophys. Res. Lett.* **12**, 793-796.

Chave, A.D., J.H. Filloux & D.S. Luther, 1987: Electromagnetic induction by ocean currents: BEMPEX. *Phys. Earth Planet. Int.* (submitted).

Chave, A.D., D.J. Thompson & M.E. Ander, 1987: On the robust estimation of power spectra, coherences and transfer functions. *J. Geophys. Res.* **92**, 633-648.

Chave, A.D., R.P. Von Herzen, K.A. Poehls & C.S. Cox, 1981: Electromagnetic induction fields in the deep ocean north-east of Hawaii: implications for mantle conductivity and source fields. *Geophys. J. R. astr. Soc.* **66**, 379-406.

Chen, P.F. & P.C.W. Fung, 1985: Significance of the sign changing of the imaginary arrows in geomagnetic induction investigation. *Geophys. J. R. astr. Soc.* **80**, 257-263.

Cheesman, S.J., R.N. Edwards & A.D. Chave, 1987: On the theory of sea-floor conductivity mapping using transient electromagnetic systems. *Geophys.* **52**, 209-217.

Clarke, A.J. & R.O.R.Y Thompson, 1984: Large scale wind-driven response in the Australian Coastal Experiment region. *J. Phys. Oceanog.* **14**, 338-352.

Coen, S., F. Quercia & M. Mackiewicz, 1983: Direct inversion of one-dimensional magnetotelluric data. *J. Geophys. Res.* **88**, 2407-2412.

Constable, S.C., R.L. Parker & C.G. Constable, 1987: Occam's inversion: a practical algorithm for generating smooth models from electromagnetic sounding data. *Geophys.* **52**, 289-300.

Counil, J.L., J.L. Le Mouel & M. Menvielle, 1986: Associate and conjugate directions concepts in magnetotellurics. *Ann. Geophys.* **4**, 115-130.

Cox, C.S., 1980: Electromagnetic induction in the oceans and inferences on the constitution of the Earth. *Geophys. Surv.* **4**, 137-156.

Cox, C.S., S.C. Constable, A.D. Chave & S.C. Webb, 1986: Controlled-source electromagnetic sounding of the oceanic lithosphere. *Nature* **320**, 52-54.

Cox, C.S., J.H. Filloux, D.I. Gough, J.C. Larsen, K.A. Poehls, R.P. Von Herzen & R. Winter, 1980: Atlantic lithosphere sounding. *J. Geomag. Geoelectr.* **32**, *Suppl I*, SI 13-SI 32.

Cox, C.S., J.H. Filloux & J.C. Larsen, 1971: Electromagnetic studies of ocean currents and electrical conductivity below the seafloor, in *The Sea*, Vol 4, Part I, edited by A. Maxwell, 637-693, Wiley-Interscience, New York.

Cull, J.P., 1982: An appraisal of Australian heat-flow data. *BMR J. Aust. Geol. Geophys.* **7**, 11-21.

Creager, K.C. & T.H. Jordan, 1986: Slab penetration into the lower mantle beneath the Mariana and other island arcs of the Northwest Pacific. *J. Geophys. Res.* **91**, 3573-3589.

Davies, G.F., 1983: Viscosity structure of a layered convecting mantle. *Nature* **301**, 592-594.

Davies, G.F., 1984: Geophysical and isotopic constraints on mantle convection: an interim synthesis. *J. Geophys. Res.* **89**, 6017-6040.

Dawson, T.W. & J.T. Weaver, 1979: Three-dimensional induction in a non-uniform thin sheet at the surface of a uniformly conducting Earth. *Geophys. J. R. astr. Soc.* **59**, 445-462.

Demenitskaya R.M. & A.M. Karasik, 1969: The active rift system of the Arctic Ocean. *Tectonophys.* **8**, 345-351.

Denham, D., 1985: The Tasman Sea earthquake of 25 November 1983 and stress in the Australian plate. *Tectonophys.* **111**, 329-338.

d'Erceville, I. & G. Kunetz, 1962: The effect of a fault on the Earth's natural electromagnetic field. *Geophys.* **27**, 651-665.

Dinger, R.J., J. Davis, J. Goldstein, W. Meyers, S.A. Wolf & M. Cates, 1977: Techniques for ocean bottom measurements of magnetic field with a superconducting magnetometer. *IEEE Trans. Geosc. El. GE* **15**, 228-231 (original not seen).

Dosso, H.W. & W. Nienaber, 1986: A laboratory electromagnetic model study of the Juan de Fuca plate region. *Phys. Earth Planet. Int.* **43**, 34-46.

Dosso, H.W., W. Nienaber & W.D. Parkinson, 1985: An analogue model study of electromagnetic induction in the Tasmania region. *Phys. Earth Planet. Int.* **39**, 118-133.

Duba, A., 1976: Are laboratory electrical conductivity data relevant to the Earth ? *Acta Geod., Geophys. Mont. Hung.* **11**, 485-495.

Duba, A., J.N. Boland & A.E. Ringwood, 1973: The electrical conductivity of pyroxene. *J. Geol.* **81**, 727-735.

Duba, A., A.J. Piwinskii, M.Santor & H.C. Weed, 1978: The electrical conductivity of sandstone, limestone and granite. *Geophys. J. R. astr. Soc.* **53**, 583-597.

Duncan, R.A. & I. McDougall, 1987: Time-space relationships for cainozoic intraplate volcanism in Eastern Australia, the Tasman Sea, and New Zealand, in *Intra-plate Volcanism in Eastern Australia and New Zealand.* ed. by Johnson, R.W. & S.R. Taylor, Australian Academy of Science, Canberra, (in press).

Dziewonski, A.M., 1984: Mapping the lower mantle: determination of lateral heterogeneity in P velocity up to degree and order 6. *J. Geophys. Res.* **89**, 5929-5952.

Dziewonski, A.M. & D.L. Anderson, 1981: Preliminary reference Earth model. *Phys. Earth Planet. Int.* **25**, 297-356.

Dziewonski, A.M., A.L. Hales & E.R. Lapwood, 1975: Parametrically simple Earth models consistent with geophysical data. *Phys. Earth Planet. Int.* **10**, 12-48.

Edwards, R.N., L.K. Law & J.M. DeLaurier, 1981: On measuring the electrical conductivity of the ocean crust by a modified magnetometric resistivity method. *J. Geophys. Res.* **86**, 11609-11615.

Edwards, R.N., L.K. Law, P.A. Wolfgram, D.C. Nobes, M.N. Bone, D.F. Trigg & J.M. DeLaurier, 1985: First results of the MOSES experiment, Bute Inlet, British Columbia, by magnetometric offshore electrical sounding. *Geophys.* **50**, 153-161.

Egbert, G.D. & J.R. Booker, 1985: A preliminary multiple site analysis of long period MT data from EMSLAB. *EOS* **66**, 871 (abstract).

Egbert, G.D. & J.R. Booker, 1986: Robust estimation of geomagnetic transfer functions. *Geophys. J. R. astr. Soc.* **87**, 173-194.

Egeland, A., Ø. Holter & A. Omholt (eds), 1973: *Cosmical Geophysics*. Universitetsforlaget, Oslo, 360 pp.

Elsasser, W.M., 1971: Sea-floor spreading as thermal convection. *J. Geophys. Res.* **76**, 1101-1112.

Falvey, D.A. & J.C. Mutter, 1981: Regional plate tectonics and the evolution of Australia's passive continental margins. *BMR J. Aust. Geol. Geophys.* **6**, 1-29.

Ferguson, I.J., 1985: Reduction of TPSME magnetotelluric data to final time series. Unpublished report, Research School of Earth Sciences, Australian National University, 69p.

Ferguson, I.J., J.H. Filloux, F.E.M. Lilley, N.L. Bindoff & P.J. Mulhearn, 1985: A seafloor magnetotelluric sounding in the Tasman Sea. *Geophys. Res. Lett.* **12**, 545-548.

Filloux, J.H., 1967: Oceanic electric currents, geomagnetic variations and the deep electrical conductivity structure of the ocean-continent transition of central California. Ph.D. Thesis, University of California, San Diego, California.

Filloux, J.H., 1971: Deep-sea tide observations from the northeastern Pacific. *Deep-Sea Res.* **18**, 275-284.

Filloux, J.H., 1973: Techniques and instrumentation for study of natural electromagnetic induction at sea. *Phys. Earth Planet. Int.* **7**, 328-338.

Filloux, J.H., 1974: Electric field recording on the sea floor with short span instruments. *J. Geomag. Geoelectr.* **26**, 269-279.

Filloux, J.H., 1977: Ocean-floor magnetotelluric sounding over North Central Pacific. *Nature* **269**, 297-301.

Filloux, J.H., 1980a: Observation of very low frequency electromagnetic signals in the ocean. *J. Geomag. Geoelectr.* **32**, *Suppl I*, SI 1-SI 12.

Filloux, J.H., 1980b: North Pacific magnetotelluric experiments. *J. Geomag. Geoelectr.* **32**, *Suppl I*, SI 33-SI 43.

Filloux, J.H., 1980c: Magnetotelluric soundings over the Northeast Pacific may reveal spatial dependence of depth and conductance of the asthenosphere. *Earth Planet. Sci. Lett.* **46**, 244-252.

Filloux, J.H. 1980d: Pressure fluctuations on the open ocean floor over abroad frequency range: new program and early results. *J. Phys. Oceanog.* **10**, 1959-1971.

Filloux, J.H., 1981: Magnetotelluric exploration of the North Pacific: progress report and preliminary soundings near a spreading ridge. *Phys. Earth Planet. Int.*. **25**, 187-195.

Filloux, J.H., 1982a: Magnetotelluric experiment over the ROSE Area. *J. Geophys. Res.* **87**, 8364-8378.

Filloux, J.H. 1982b: Seafloor magnetotelluric soundings in the Mariana Island Arc Area, in *A.G.U Geophysical Monograph Series*, Vol. 27 *The Tectonic Evolution of Southeast Asian Seas and Islands*, Part 2., 225-265.

Filloux, J.H., 1982c: Electrical conductivity structure of the seafloor beneath the North

Pacific. Trans. Earthquake Res. Inst., Conductivity Anomaly Conf., 41-48.

Filloux, J.H., 1987: Instrumentation and experimental methods for oceanic studies, in *Geomagnetism Vol 1* , 3 edited by J.A. Jacobs, 143-247, Academic Press (in press).

Filloux, J.H., L.K. Law, T. Yukutake,, J. Segawa, Y. Hamano, H. Utada, A.White, A.D. Chave, P.Tarits & A.W. Green, 1988: Offshore EMSLAB: objectives, experimental phase and early results. *Phys. Earth Planet. Int.* (in press)

Filloux, J.H., F.E.M. Lilley, I.J. Ferguson, N.L. Bindoff & P.J. Mulhearn, 1985: The Tasman Project of Seafloor Magnetotelluric Exploration. *Explor. Geophys.* **16**, 221-224 (extended abstract).

Filloux, J.H. & T. Yukutake, 1982: Preliminary report on the investigation of the electrical conductivity of the Pacific Plate near the Japan Trench. Trans. Earthquake Res. Inst., Conductivity Anomaly Conf., 77-82.

Finlayson, D.M., 1973: Isomagnetic maps of the Australian Region for epoch 1970.0. *Bur. Mineral Res. Aust. Rep.* **159**, 15 pp.

Finlayson, D.M., C.D.N. Collins & D.Denham, 1980: Crustal structure under the Lachlan Fold Belt, southeastern Australia. *Phys. Earth Planet. Int.* **21**, 321-342.

Fischer, G., P.-A. Schnegg, M. Peguiron & B.V. Le Quang, 1981: An analytic one-dimensional magnetotelluric inversion scheme. *Geophys. J. R. astr. Soc.* **67**, 257-278.

Fischer, G. & J.T. Weaver, 1986: Theoretical investigations of the ocean-coast effect at a passive continental margin. *Phys. Earth & Planet. Int.* **42**, 246-254.

Fonarev G.A., 1982: Electromagnetic research in the ocean. *Geophys. Surv.* **4**, 501-508.

Frey, H., 1985: Magsat and POGO magnetic anomalies over the Lord Howe Rise: evidence against a simple continental crustal structure. *J. Geophys. Res.* **90**, 2631-2639.

Frohlich, C. & M. Barazangi, 1980: A regional study of mantle velocity variations beneath eastern Australia and the southwestern Pacific using short period recordings of P, S, PcP, ScP and ScS waves produced by Tongan deep earthquakes. *Phys. Earth Planet. Int.* **21**, 1-14.

Fukushima, N. & Y. Kamide, 1973: Partial ring current models for worldwide geomagnetic disturbances. *Rev. Geophys. Space Phys.* **11**, 795-853.

Gamble, T.D., W.M. Goubou & J. Clarke, 1979a: Magnetotellurics with a remote reference. *Geophys.* **44**, 53-68.

Gamble, T.D., W.M. Goubou & J. Clarke, 1979b: Error analysis for remote reference magnetotellurics. *Geophys.* **44**, 959-968.

Garland, G.D., 1981: The significance of terrestrial electrical conductivity variations. *Ann. Rev. Earth Planet. Sci.* **9**, 147-174.

Godfrey, J.S., G.R. Cresswell, T.J. Golding & A.F. Pearce, 1980: The separation of the East Australian Current. *J. Phys. Oceanog.* **10**, 430-440.

Goubou, W.M., T.D. Gamble & J. Clarke, 1978: Magnetotelluric data analysis: removal

of bias. *Geophys.* **43**, 1157-1166.

Gregori, G.P. & L.J. Lanzerotti, 1980: Geomagnetic depth sounding by induction arrow representation: a review. *Rev. Geophys. Space Phys.* **18**, 203-209.

Gregori, G.P. & L.J. Lanzerotti, 1982: Electrical conductivity structure in the lower crust. *Geophys. Surv.* **4**, 467-499.

Grim, P.J., 1969: Heat flow measurements in the Tasman Sea. *J. Geophys. Res.* **74**, 3933-3934.

Gundel, A., 1977: Estimation of transfer functions with reduced bias in geomagnetic induction studies. *Acta Geodaet. Geophys. Mont. Hung.* **12**, 345-352.

Hamilton, E.L., 1976: Variations of density and porosity with depth in deep-sea sediments. *Jour. Sed. Petrology* **46**, 280-300.

Hamilton, E.L., 1985: Sound velocity as a function of depth in marine sediments. *J. Acoustic Soc. Amer.* **78**, 1348-1355.

Haxby, W.F., G.D. Karner, J.L. LaBrecque & J.K. Weissel, 1983: Digital images of combined oceanic and continental data sets and their use in tectonic studies. *EOS* **64**, 995-1004.

Hayes, D.E. & J. Ringis, 1973: Seafloor spreading in the Tasman Sea. *Nature* **243**, 454-458.

Hermance, J.F. & J. Pedersen, 1980: Deep structure of the Rio Grande Rift: a magnetotelluric interpretation. *J. Geophys. Res.* **85**, 3899-3912.

Hermanto, M.R., 1985: Underground Conductivity Structure in Tasmania. M.Sc. thesis, Univ. of Tasmania, Hobart.

Hinze, E., 1982: Laboratory electrical conductivity measurements on mantle relevant minerals. *Geophys. Surv.* **4**, 337-352.

Hirsch, L.M. & C. -Y. Wang, 1986: Electrical conductivity of olivine during high-temperature creep. *J. Geophys. Res.* **91**, 10429-10441.

Hobbs, B.A., 1982: Automatic model for finding the one-dimensional magnetotelluric problem. *Geophys. J. R. astr. Soc.* **168**, 253-266.

Hooshyar, M.A. & M. Razavy, 1982: The inverse problem of geomagnetic induction at a fixed frequency. *Geophys. J. R. astr. Soc.* **71**, 139-150.

Hyndman R.D. & M.H. Salisbury, 1984: The physical nature of young upper oceanic crust on the mid-Atlantic Ridge, DSDP Hole 395A, in Hyndman, R.D., M.H. Salisbury et al., *Init. Repts. DSDP* **78B**, 839-848. Washington (U.S. Govt. Printing Office).

Ingham, M.R., 1985: Magnetovariational measurements in the Cook Strait region of New Zealand. *Phys. Earth Planet. Int.* **39**, 182-193.

Ingham, M.R., D.I. Gough & W.D. Parkinson, 1987: Models of conductive structure under the Canadian Cordillera. *Geophys. J. R. astr. Soc.* **88**, 477-485.

Irish, J.D. & M.D. Levine, 1977: Digitizing error from period and frequency counting techniques. *Deep-Sea Res.* **25**, 211-219.

Isacks, B., J. Oliver & L.R. Sykes, 1968: Seismology and the new global tectonics. *J. Geophys. Res.* **73**, 5855-5899.

Jacoby, W.R., 1970: Instability in the upper mantle and global plate movements. *J. Geophys. Res.* **75**, 5671-5680.

Jarrard, R.D. & D.A. Clague, 1977: Implications of Pacific island and seamount ages for the origin of volcanic chains. *Rev. Geophys. Space Phys.* **15**, 57-76.

Jeanloz, R. & F.M. Richter, 1979: Convection, composition and the thermal state of the lower mantle. *J. Geophys. Res.* **84**, 5499-5504.

Jiracek, G.R., 1984: *The Magnetotelluric Method.* Lecture notes, San Diego State University, San Diego.

Johnson, I.M. & D.E. Smylie, 1971: An inverse theory for the calculation of the electrical conductivity of the lower mantle. *Geophys.* **22**, 41-53.

Jones, A.G., 1983: The problem of current channelling: a critical review. *Geophys. Surv.* **6**, 79-122.

Jones, A.G., 1986: Parkinson's pointers' potential perfidy. *Geophys. J. R. astr. Soc.* **87**, 1215-1224.

Jones, A.G., 1987: MT and reflection: an essential combination. *Geophys. J. R. astr. Soc.* **89**, 7-18.

Jones, A.G. & R. Hutton, 1979: A multi-station magnetotelluric study in southern Scotland - II. Monte-Carlo inversion of the data and its geophysical and tectonic implications. *Geophys. J. R. astr. Soc.* **56**, 351-368.

Jupp, D.L. & K. Vozoff, 1975: Stable iterative methods for the inversion of geophysical data. *Geophys. J. R. astr. Soc.* **42**, 957-976.

Jupp, D.L. & K. Vozoff, 1977: Two-dimensional magnetotelluric inversion. *Geophys. J. R. astr. Soc.* **50**, 333-352.

Kao, D.W. & D. Rankin, 1977: Enhancement of signal-to-noise ratio in magnetotelluric data. *Geophys.* **42**, 103-110.

Kamide, Y. & A.D. Richmond, 1986: Recent advances in studies of magnetosphere-ionosphere coupling. *J. Geomag. Geoelectr.* **38**, 653-714.

Kanasewich, E.R., 1975: *Time Sequence Analysis in Geophysics*. 2nd ed., University of Alberta Press, Edmonton, 364 pp.

Kaufman, A.A. & G.V. Keller, 1981: *The Magnetotelluric Sounding Method.* Elsevier, Amsterdam, 583 pp.

Kellett, R.L., I.J. Ferguson & F.E.M. Lilley, 1988: Magnetic field fluctuations at the Eyrewell Observatory, Christchurch, New Zealand. *NZ J. Geol. Geophys.* (in press).

Kisabeth, J.L., 1975: Substorm fields in and near the auroral zone. *Phys. Earth Planet. Int.* **10**, 241-249.

Kisabeth, J.L. & G. Rostoker, 1971: Development of the polar electrojet during polar magnetic substorms. *J. Geophys. Res.* **76**, 6815-6828.

Klein, D.P. & J.C. Larsen, 1978: Magnetic induction fields (2-30 cpd) on Hawaii Island and their implications regarding electrical conductivity in the oceanic mantle. *Geophys. J. R. astr. Soc.* **53**, 61-77.

Korotayev, S.M., S.V. Shabelyanskiy, I.L. Trofimov, Yu. M. Abramov, V.V. Kutkin, S.P. Gaydash & L.M. Abramova, 1984: Electromagnetic field of currents and its use in evaluating total conductivity of sedimentary deposits in the western Black Sea. *Izvestiya, Earth Physics* **20**, 466-472 (English translation).

Kovtun, A.A. & N.D. Chichera, 1976: Deep magnetotelluric surveys in the north-western part of the Russian Platform, in *Geoelectric and Geothermal Studies*, edited by A.Adam, 620-628, KAPG Geophys. Monogr., Budapest.

Kunetz, G., 1972: Processing and interpretation of magnetotelluric soundings. *Geophys.* **37**, 1005-1021.

Lahiri, B.N. & A.T. Price, 1939: Electromagnetic induction in non-uniform conductors, and the determination of the conductivity of the Earth from terrestrial magnetic variations. *Phil. Trans. R. Soc. London* **237**, 509-540.

Larsen, J.C., 1968: Electric and magnetic fields induced by deep sea tides. *Geophys. J. R. astr. Soc.* **16**, 47-70.

Larsen, J.C., 1975: Low frequency (0.1-6.0 cpd) electromagnetic study of the deep mantle electrical conductivity beneath the Hawaiian Islands. *Geophys. J. R. astr. Soc.* **43**, 17-46.

Larsen, J.C., 1977: Removal of local surface conductivity effects from low frequency mantle response curves. *Acta Geod., Geophys. Mont. Hung.* **11**, 183-186.

Larsen, J.C., 1981: A new technique for layered earth magnetotelluric inversion. *Geophys.* **46**, 1247-1257.

Lastovickova, M., 1983: Laboratory measurements of the electrical properties of rocks and minerals. *Geophys. Surv.* **6**, 201-213.

Law, L.K., 1981: Ocean bottom magnetometer results across the continental slope of southern Vancouver Island: coast effect and an oceanographic wave. *EOS* **62**, 846 (abstract).

Law, L.K., 1983: Marine electromagnetic research. *Geophys. Surv.* **6**, 123-135.

Law, L.K. & J.P. Greenhouse, 1981: Geomagnetic variation sounding of the asthenosphere beneath the Juan de Fuca Ridge. *J. Geophys. Res.* **86**, 967-978.

Le Mouel J.L. & M. Menvielle, 1982: Geomagnetic variation anomalies and deflection of telluric currents. *Geophys. J. R. astr. Soc.* **68**, 575-587.

Lilley, F.E.M., 1975: Running waves and standing waves in geomagnetic depth sounding. *J. Geomag Geoelectr.* **27**, 491-504.

Lilley, F.E.M., 1984: On the spatial pattern of magnetic fluctuations in the Cobar area, NSW. *Explor. Geophys.* **15**, 79-83.

Lilley, F.E.M., 1987: Contribution on ELAS in Australia and surrounding oceans, in *The Composition, Structure and Dynamics of the Lithosphere-Asthenosphere System*. ed.

K.Fuchs & C. Froidevaux, 229-231, Vol. 16 Geodynamic Series, American Geophysical Union, Washington, 340 pp.

Lilley, F.E.M. & B.R. Arora, 1982: The sign convention for quadrature Parkinson arrows in geomagnetic induction studies. *Rev. Geophys. Space Phys.* **20**, 513-518.

Lilley, F.E.M., F.R. Burden, G.W. Boyd & M.N. Sloane, 1975: Performance tests of a set of Gough-Reitzel magnetic variometers. *J. Geomag. Geoelectr.* **27**, 75-83.

Lilley, F.E.M., J.H. Filloux, N.L. Bindoff, I.J. Ferguson & P.J. Mulhearn, 1986a: Barotropic flow of a warm-core ring from seafloor electric measurements. *J. Geophys. Res.* **91**, 12979-12984.

Lilley, F.E.M., J.H. Filloux, I.J. Ferguson, N.L. Bindoff & P.J. Mulhearn, 1988: The Tasman Project of Seafloor Magnetotelluric Exploration: experiment and observations. *Phys. Earth Planet Int.* (in press).

Lilley, F.E.M., P.J. Mulhearn, J.H. Filloux, N.L. Bindoff & I.J. Ferguson, 1986b: Pressure fluctuations on the open ocean floor: mid Tasman Sea at 38° 30' S, 162° 38' E, near the Lord Howe Rise. *Aust. J. Mar. & Freshwater Res.* **37**, 27-37.

Lilley, F.E.M., D.V. Woods & M.N. Sloane, 1981: Electrical conductivity from Australian magnetometer arrays using spatial gradient data. *Phys. Earth Planet. Int.* **25**, 202-209.

Lister, G.S., M.A. Etheridge & P.A. Symonds, 1986: Detachment faulting and the evolution of passive continental margins. *Geology* **14**, 246-250.

Liu, L.-g., 1979: Phase transformations and the constitution of the deep mantle, in *The Earth: Its Origin, Structure & Evolution*, ed. by M.W. McElhinny, chap 6, 177-202, Academic Press, London.

Lorrain P. & D.R. Corson, 1970: *Electromagnetic Fields and Waves*. 2nd edn, Freeman, San Francisco, 706 pp.

Lowenthal, D., 1975: Theoretical uniqueness of the magnetotelluric inverse problem for equal penetration discretizable models. *Geophys. J. R. astr. Soc.* **43**, 897-907.

Luther, D.S., A.D. Chave & J.H. Filloux, 1987: BEMPEX: A study of barotropic ocean currents and lithospheric electrical conductivity. *EOS* **68**, 618-619,628-629.

Mareschal, M., 1976: On the problem of simulating the Earth's induction effects in modelling polar magnetic substorms. *Rev. Geophys. Space Phys.* **14**, 403-409.

Mareschal, M., 1981: Source effects and the interpretation of geomagnetic sounding data at sub-auroral latitudes. *Geophys. J. R. astr. Soc.* **67**, 125-136.

Mareschal, M., 1986: Modelling of natural sources of magnetospheric origin in the interpretation of regional induction studies: a review. *Surv. Geophys.* **8**, 261-300.

Marchisio, G.B. & R.L. Parker, 1984: Exact non-linear inversion of electromagnetic induction soundings. *EOS* **64**, 692 (abstract).

Maxwell, J.C., 1984: What is lithosphere? *EOS* **65**, 321-325.

McDougall, I., 1986: Samoan Island Chain - a hotspot trace ? Seminar, Research School Earth Sciences, Australian National University, 13 March 1986.

McKenzie, D.J., J.M. Roberts & N.O. Weiss, 1974: Convection in the Earth's mantle: towards a numerical solution. *J. Fluid Mech.* **62**, 465-538.

Melchior, P., 1983: *The Tides of the Planet Earth.* 2nd Edn. Pergamon Press, Oxford, 641pp.

Menvielle, M., J.C. Rossignol & P.Tarits, 1982: The coast effect in terms of deviated electric currents: a numerical study. *Phys. Earth Planet. Int.* **28**, 118-128.

Molnar, P. & J. Oliver, 1969: Lateral variations of attenuation in the upper mantle and discontinuities in the lithosphere. *J. Geophys. Res.* **74**, 2648-2682.

Morelli, A. & A.M. Dziewonski, 1987: Topography of the core-mantle boundary and lateral homogeneity of the liquid core. *Nature* **325**, 678-683.

Morin, R.H. & R.P. Von Herzen, 1986: Geothermal measurements at Deep Sea Drilling Project site 587, in Kennett, J.P. & C.C. von der Borch et al., *Init. Repts DSDP* **90**, 1317-1324, Washington (U.S. Govt. Printing Office).

Mosnier, J., 1982: Induction in the Earth's crust: observational methods on land and sea. *Geophys. Surv.* **4**, 353-371.

Mosnier, J., 1985: A study of the physics of telluric current flow at very low frequencies in the Earth's crust. *Geophys. J. R. astr. Soc.* **82**, 479-496.

Muirhead, K.J., 1985: The base of the lithosphere under Australia, in *Rheology of the Lithosphere and Australian Earthquakes* ed. by B.J. Drummond, M.O. Michael-Leiba, D. Denham & C.D.N. Collins, Bur. Min. Resour. Record 1985/31, 1 (abstract).

Mulhearn, P.J., J.H. Filloux, F.E.M. Lilley, N.L. Bindoff & I.J. Ferguson, 1986: Abyssal currents during the formation and passage of a warm-core ring in the East Australian Current. *Deep-Sea Res.* **33**, 1563-1576 and 13109.

Mulhearn, P.J., J.H. Filloux, F.E.M. Lilley, N.L. Bindoff & I.J. Ferguson, 1988: Comparisons between surface, barotropic and abyssal flows during the passage of a warm-core ring. *Aust. J. Mar. Freshwater Res.* (submitted).

Mutter, J.C. & D. Jongsma, 1978: The pattern of the pre-Tasman Sea rift system and the geometry of breakup. *Bull. Aust. Soc. Explor. Geophys.* **9**, 70-75.

Nabetani, S. & D. Rankin, 1969: An inverse method of magnetotelluric analysis for a multilayered Earth. *Geophys.* **34**, 75-86.

Niblett, E.R., R.D. Kurtz & C. Michaud, 1987: Magnetotelluric measurements over the Alpha Ridge. *Phys. Earth Planet. Int.* **45**, 101-118.

Nobes, D.C., L.K. Law & R.N. Edwards, 1986a: The determination of resistivity and porosity of the sediment and fractured basalt layers near the Juan de Fuca Ridge. *Geophys. J. R. astr. Soc.* **86**, 289-318.

Nobes, D.C., H. Villinger, E.R. Davis & L.K. Law, 1986b: Estimation of sediment bulk physical physical properties at depth from sea floor geophysical measurements. *J. Geophys. Res.* **91**, 14033-14043.

Oldenburg, D.W., 1979: One-dimensional inversion of natural source magnetotelluric

observations. *Geophys.* **44**, 1218-1244.

Oldenburg, D.W., 1981: Conductivity structure of oceanic upper mantle beneath the Pacific Plate. *Geophys. J. R. astr. Soc.* **65**, 359-394.

Oldenburg, D.W., K.P. Whittal & R.L. Parker, 1984: Inversion of ocean bottom magnetometer data revisited. *J. Geophys. Res.* **89**, 1829-1833.

Oni, E. & O. Agunloye, 1974: A predominant parameter ν_p of the inducing source field for induction studies in low-latitudes. *Pure Appl. Geophys.* **112**, 967-975.

O'Nions, R.K., N.M. Evensen & P.J. Hamilton, 1979: Geochemical modelling of mantle differentiation and crustal growth. *J. Geophys. Res.* **84**, 6091-6101.

Park, J. & A.D. Chave, 1984: On the estimation of magnetotelluric response functions using the singular value decomposition. *Geophys. J. R. astr. Soc.* **77**, 683-709.

Parker, R.L., 1980: The inverse problem of electromagnetic induction: existence and construction of solutions based on incomplete data. *J. Geophys. Res.* **85**, 4421-4428.

Parker, R.L., 1982: The existence of a region inaccessible to magnetotelluric sounding. *geophys. J. R. astr. Soc.* **68**, 165-170.

Parker, R.L., 1983: The magnetotelluric inverse problem. *Geophys. Surv.* **6**, 5-25.

Parker, R.L. & D.W. Oldenburg, 1973: Thermal model of ocean ridges. *Nature Phys. Sci.* **242**, 137-139.

Parker, R.L. & K.A. Whaler, 1981: Numerical methods for establishing solutions to the inverse problem of electromagnetic induction. *J. Geophys. Res.* **86**, 9574-9584.

Parkinson, W.D., 1959: Directions of rapid geomagnetic fluctuations. *Geophys. J. R. astr. Soc.* **2**, 1-14.

Parkinson, W.D., 1962 : The influence of continents and oceans on geomagnetic variations. *Geophys. J. R. astr. Soc.* **6**, 441-449.

Parkinson, W.D., 1983 : *Introduction to Geomagnetism.* Scottish Academic Press, Edinburgh, 433pp.

Parkinson, W.D. & F.W. Jones, 1979: The geomagnetic coast effect. *Rev. Geophys. Space Phys.* **17**, 1999-2015.

Parsons, B. & J.G. Sclater, 1977: An analysis of the variation of ocean floor bathymetry and heat flow with age. *J. Geophys. Res.* **82**, 803-827.

Pecova, J., Z. Martinec & K. Pec., 1987: Appreciation of spherically symmetric models of electrical conductivity. *Pure Appl. Geophys.* **125**, 291-318.

Patra, H.P. & K. Mallick, 1980: *Geosounding Principles, 2 Time-Varying Geoelectric Soundings.* Elsevier, Amsterdam, 419 pp.

Pedersen, J. & J.F. Hermance, 1986: Least-squares inversion of one-dimensional magnetotelluric data: an assessment of procedures employed at Brown University. *Surv. in Geophys.* **8**, 187-231.

Pilger, R.H. Jr, 1982: The origin of hotspot traces: evidence from eastern Australia. *J.*

Geophys. Res. **87**, 1825-1834.

Poehls K.A. & R.P. Von Herzen, 1976: Electrical resistivity structure beneath the North-west Atlantic Ocean. *Geophys. J. R. astr. Soc.* **47**, 331-346.

Porath, H., D.W. Oldenburg & D.I. Gough, 1970: Separation of magnetic variation fields and conductive structures in the western United States. *Geophys. J. R. astr. Soc.* **19**, 237-260.

Price, A.T., 1950: Electromagnetic induction in a semi-infinite conductor with a plane boundary. *Quart. J. Mech. and Appl. Math.* **3**, 385-410.

Price, A.T., 1962: The theory of magnetotelluric methods when the source field is considered. *J. Geophys. Res.* **67**, 1907-1918.

Rai, C.S. & M.H. Manghnani, 1978: Electrical conductivity of ultramafic rocks to 1812 Kelvin. *Phys. Earth Planet. Int.* **17**, 6-13.

Ranganayaki, R.P. & T.R. Madden, 1980: Generalized thin sheet analysis in magnetotellurics: an extension of Price's analysis. *Geophys. J. R. astr. Soc.* **60**, 445-457.

Ringwood, A.E., 1975: *Composition and Petrology of the the Earth's Mantle.* McGraw-Hill, New York, 618 pp.

Ringwood, A.E., 1979: Composition and origin of the Earth, in *The Earth: Its Origin, Structure & Evolution*, ed. by M.W. McElhinny, chap 1, 1-58, Academic Press, London.

Roberts, R.G., 1983: Electromagnetic evidence for lateral imhomogeneities within the Earth's upper mantle. *Phys. Earth Planet. Int.* **33**, 198-212.

Roberts, R.G., 1986: The deep electrical structure of the Earth. *Geophys. J. R. astr. Soc.* **85**, 583-600.

Rokityansky, I.I., 1975: The interpretation of anomalous fields by using their frequency characteristics. *Phys. Earth Planet. Int.* **10**, 271-281.

Rokityansky, I.I., 1982: *Geoelectromagnetic Investigation of the Earth's Crust and Mantle.* Springer-Verlag, Berlin.

Salisbury, M.H., R. Stephen, N.I. Christensen, J. Francheteau, Y. Hamano, M. Hobart & D. Johnson, 1980: The physical state of the upper levels of cretaceous oceanic crust from the results of logging, laboratory studies, and the oblique seismic experiment at deep sea drilling project sites 417 and 418. *Init. Repts. DSDP* **51-53**, 2, 237-244. Washington (U.S. Govt. Printing Office).

Sanford, T.B., 1971: Motionally induced electric and magnetic fields in the sea. *J Geophys. Res.* **76**, 3476-3492.

Sanford, T.B., R.G. Drever & J.H. Dunlop, 1978: A velocity profiler based on the principles of geomagnetic induction. *Deep-Sea Res.* **25**, 183-210.

Schmeling, H., 1986: Numerical models on the influence of partial melt on elastic, anelastic and electrical properties of rocks. Part II: electrical conductivity. *Phys. Earth Planet. Int.* **43**, 123-136.

Schock, R.N., A.G. Duba, H.C. Heard & D.H. Stromberg, 1977: The electrical conductivity of polycrystalline olivine and pyroxene under pressure, in *High-Pressure Research Application in Geophysics*, ed. by M. Manghnani & S. Akimoto, 39-51, Academic, New York.

Schmucker, U. 1970: Anomalies of geomagnetic variations in the southwestern United States. *Bull. Scripps Inst. Oceanog.* **13**, 165 pp.

Schmucker, U. 1973: Regional induction studies: a review of methods and results. *Phys. Earth Planet. Int.* **7**, 365-378.

Schmucker, U. 1987: Substitute conductors for electromagnetic response estimates. *Pure & Appl. Geophys.* **125**, 341-368.

Schmucker, U. & J. Jankowsky, 1972: Geomagnetic induction studies and the electrical state of the upper mantle. *Tectonophys.* **13**, 233-256.

Schubert, G. & T. Spohn, 1981: Two-layer mantle convection and the depletion of radioactive elements in the lower mantle. *Geophys. Res. Lett.* **8**, 951-954.

Schubert, G. & D.L. Turcotte, 1972: One-dimensional model of shallow-mantle convection. *J. Geophys. Res.* **77**, 945-951.

Schultz, A. & J.C. Larsen, 1987: On the electrical conductivity of the mid-mantle - I. Calculation of equivalent scalar magnetotelluric response functions. *Geophys. J. R. astr. Soc.* **88**, 733-761.

Segawa, J., 1986: Review of the development of ocean bottom magnetometers. Trans. 8th Workshop on Electromagnetic Induction in the Earth and Moon, Neuchatel, Switzerland.

Shankland, T.J., 1979: Physical properties of minerals and melts. *Rev. Geophys. Space Phys.* **17**, 792-802.

Shankland, T.J., 1981: Electrical conduction in mantle materials, in *Evolution of the Earth, Geodynamics Ser.*, vol. 5, edited by R.J. O'Connell & W.S. Fyfe, 256-263, AGU, Washington D.C. & Geol. Soc. America, Boulder, Colo.

Shankland, T.J. & H.S. Waff, 1977: Partial melting and conductivity anomalies in the upper mantle. *J. Geophys. Res.* **82**, 5409-5417.

Shaw, R.D., 1978: Sea floor spreading in the Tasman Sea: a Lord Howe Rise - Eastern Australian reconstruction. *Bull. Aust. Soc. Explor. Geophys.* **9**, 75-81.

Shor, G.G. Jr, H.K. Kirk & H.W. Menard, 1971: Crustal structure of the Melanesian Area. *J. Geophys. Res.* **76**, 2562-2586.

Silsbee, H.C. & E.H. Vestine, 1942: Geomagnetic bays, their frequency and current system. *Terr. Magn. Atmos. Elec.* **47**, 195-208 (original not seen).

Sims, W.E., F.X. Bostick Jr & H.W. Smith, 1971: The estimation of magnetotelluric impedance tensor elements from measured data. *Geophys.* **36**, 938-942.

Sleep, N.H., 1987: Lithospheric heating by mantle plumes. *Geophys. J. R. astr. Soc.* **91**, 1-11.

Srivastava, S.P., 1966: Theory of the magneto-telluric method for a spherical conductor.

Geophys. J. R. astr. Soc. **11**, 373-387.

Srivastava, S.P., 1985: Evolution of the Eurasian Basin and its implications to the motion of Greenland along Nares Strait. *Tectonophys.* **114**, 29-53.

Stolper, E.M., D. Walker, B.H. Hager & J.F. Hays, 1981: Melt segregation from partially molten source regions: the importance of melt density and source region size. *J. Geophys. Res.* **86**, 6261-6271.

Sundaralingam, K. & D.Denham, 1985: Structure of the upper mantle beneath the Coral and Tasman Seas, as obtained from group and phase velocities of Rayleigh waves, in *Rheology of the Lithosphere and Australian Earthquakes* ed. by B.J. Drummond, M.O. Michael-Leiba, D. Denham & C.D.N. Collins, Bur. Min. Resour. Record 1985/31, 27 (abstract).

Sutherland, F.L., 1983: Timing, trace and origin of basaltic migration in eastern Australia. *Nature* **305**, 123126.

Sweeney, J.F., 1985: Comments on the age of the Canadian Basin. *Tectonophys.* **114**, 1-10.

Tammemagi, H.Y., 1972: A magnetotelluric study in southeastern Australia. Ph.D. thesis, Aust. Nat. Univ., Canberra.

Tammemagi, H.Y. & F.E.M. Lilley, 1971: Magnetotelluric studies across the Tasman Geosyncline, Australia. *Geophys. J. R. astr. Soc.* **22**, 505-516.

Tarits, P., 1986: Conductivity and fluids in the oceanic upper mantle. *Phys. Earth Planet. Int.* **42**, 215-226.

Tarits, P., J.H. Filloux, J.C. Larsen & D.P Klein, 1986: Seafloor electromagnetic sounding near Hawaiian Islands. Trans. 8th Workshop on Electromagnetic Induction in the Earth and Moon, Neuchatel, Switzerland (abstract).

Teramoto, T., 1971: Estimation of sea-bed conductivity and its influence upon velocity measurements with towed electrodes. *J. Oceanograph. Soc. Japan* **27**, 7-18.

Tikhonov, A.N., 1950: On investigation of electrical characteristics of deep strata of the Earth's crust. *Dokl. Akad. Nauk SSSR* **73** 295-297 (In Russian, original not seen).

Ting, S.C. & G.W. Hohmann, 1981: Integral equation modelling of three-dimensional magnetotelluric response. *Geophys.* **46**, 182-197.

Toramaru, A. & F. Naoyuki, 1986: Connectivity of melt phase in a partially molten peridotite. *J. Geophys. Res.* **91**, 9239-9252.

Tozer, D.C., 1979: The interpretation of upper-mantle electrical conductivities. *Tectonophys.* **56**, 147-163.

Tozer, D.C., 1981: The mechanical and electrical properties of Earth's asthenosphere. *Phys. Earth Planet. Int.* **25**, 280-296.

Trofimov I.L., 1973: Interpretation of deep magnetotelluric sounding curves, taking into account the finiteness of the specific electrical resistivity of the mantle. *Geomagn. and Aeron.* **13**, 959-961 (English Translation).

Trofimov I.L., 1979: Magnetotelluric sounding in the Canadian Basin. *Geomagn and*

Aeron. **19**, 602-604 (English translation).

Trofimov, I.L. & G.A. Fonarev, 1976: Deep magnetotelluric surveys in the Arctic Ocean, in *Geoelectric and Geothermal Studies*, edited by A.Adam, 712-715, KAPG Geophys. Monogr., Budapest.

Vasseur, G. & P. Weidelt, 1977: Bimodal electromagnetic induction in non-uniform thin sheets with an application to the northern Pyrenan induction anomaly. *Geophys. J. R. astr. Soc.* **51**, 669-690.

Vogt, P.R. & J.R. Conolly, 1971: Tasmantid guyots, the age of the Tasman Basin, and motion between the Australian plate and the mantle. *Bull. Geol. Soc. Amer.* **82**, 2577-2584.

Volkomirskaya, L.B. & G.A. Fonarev, 1978: Experiment in local magnetic variation sounding in the Arctic Ocean Region. *Geomagn. and Aeron.* **18**, 773-774 (English translation).

Volland, H., 1984: *Atmospheric Electrodynamics* Springer-Verlag, Berlin, 205 pp.

Von Arx, W.S., 1950: An electromagnetic method for measuring the velocities of ocean currents from a ship under way. *Pap. Phys. Oceanogr. Meteor.* **11**, 1-62 (original not seen).

Von Herzen, R.P., 1972: Geothermal measurements, Leg 21, in Burns, R.E., J.E. Andrews et al., *Init. Repts DSDP* **21**, 443-457. Washington (U.S. Govt. Printing Office).

Von Herzen, R.P., T.J.G. Francis & K. Becker, 1983: *In situ* large-scale electrical resistivity of ocean crust, hole 504B, in Cann, J.R., M.G. Langseth, J. Honnorez, R.P. Von Herzen, S.M. White et al. *Init. Repts. DSDP* **69**, 237-244. Washington (U.S. Govt. Printing Office).

Vozoff, K., 1972: The magnetotelluric method in the exploration of sedimentary basins. *Geophys.* **37**, 98-141.

Waff, H.S., 1980: Effects of the gravitational field on liquid distribution in partial melts within the upper mantle. *J. Geophys. Res.* **85**, 1815-1825.

Waff, H.S. & D.F. Weill, 1975: Electrical conductivity of magmatic liquids; effects of temperature, oxygen fugacity and composition. *Earth Planet. Sci. Lett.* **28**, 254-260.

Wait, J.R., 1954: On the relation between telluric currents and the Earth's magnetic field. *Geophys.* **19**, 281-289.

Walker, D., E.M. Stoplar & J.F. Hays, 1978: A numerical treatment of melt/solid segregation: size of the eucrite parent body and stability of the terrestrial low-velocity zone. *J. Geophys. Res.* **83**, 6005-6013.

Wannamaker, P.E., G.W. Hohmann & S.H. Ward, 1984: Magnetotelluric responses of three-dimensional bodies in layered earths. *Geophys.* **49**, 1517-1533.

Weaver, J.T., 1970: The general theory of geomagnetic induction in a conducting half space. *Geophys. J. R. astr. Soc.* **22**, 83-100.

Webb, S.C., S.C. Constable, C.S. Cox & T.K. Deaton, 1985: A seafloor electric field

instrument. *J. Geomag. Geoelectr.* **37**, 1115-1129.

Weaver, J.T. & C.R. Brewitt-Taylor, 1978: Improved boundary conditions for the numerical solution of *E* -polarization problems in geomagnetic induction. *Geophys. J. R. astr. Soc.* **54**, 309-317.

Weissel J.K. & D.E. Hayes, 1977: Evolution of the Tasman Sea reappraised. *Earth Planet. Sci. Lett.* **36**, 77-84.

Weidelt, P., 1972: The inverse problem of geomagnetic induction. *Z. Geophys.* **38**, 257-289.

Weidelt, P., 1977: Numerical study of a conductive channelling effect. *Acta Geod., Geophys. Mont. Hung.* **11**, 195-205.

White, A., 1979: A seafloor magnetometer for the continental shelf. *Mar. Geophys. Res.* **4**, 105-114.

White, A. & O.W. Polatajko, 1978: The coast effect in geomagnetic variations in South Australia. *J. Geomag. Geoelectr.* **30**, 109-120.

Whittal, K.P., 1986: Inversion of magnetotelluric data using localized conductivity constraints. *Geophys.* **51**, 1603-1607.

Whittal, K.P. & D.W. Oldenburg, 1986: Inversion of magnetotelluric data using a practical inverse scattering formulation. *Geophys.* **51**, 383-395.

Wiese, H., 1962: Geomagnetisches tiefentellurik. *Geophys. Pure Appl.* **52**, 83-103 (In German, original not seen).

Willcox, J.B., P.A. Symonds, K. Hinz & D. Bennett, 1980: Lord Howe Rise, Tasman Sea-preliminary geophysical results and petroleum prospects. *BMR J. Aust. Geol. Geophys.* **5**, 225-236.

Woodhouse, J.H. & A.M. Dziewonsky, 1984: Mapping the upper mantle: three dimensional modelling of Earth structure by inversion of seismic waveforms. *J. Geophys. Res.* **89**, 5953-5986.

Woods, D.V., 1979: Geomagnetic depth sounding studies in central Australia, Ph.D. thesis, Aust. Nat. Univ., Canberra.

Young, P.D. & C.S. Cox, 1981: Electromagnetic active source sounding near the East Pacific Rise. *Geophys. Res. Lett.* **8**, 1043-1046.

Yukutake, T., J.H. Filloux, J. Segawa, Y. Hamano & H. Utada, 1983: Preliminary report on a magnetotelluric array study in the Northwest Pacific. *J. Geomag. Geoelectr.* **35**, 575-587.

ADDENDUM OF 20 AUGUST 1988

A. CALIBRATION OF SEAFLOOR MAGNETIC FIELD RECORDINGS

After completion of this thesis the author was advised of a small error in the calibration factors for the seafloor magnetic field (SIO MAG) recordings. To obtain the correct value for magnetic field results, the fields should be multiplied by the factor

$$K = 1.215 \quad .$$

This correction does not alter any of the qualitative conclusions made in the thesis. The following changes must be made however to obtain exact quantitative results.

1. TIME SERIES - Multiply SIO MAG by K to obtain correct values.

2. POWER SPECTRA - For power spectra involving two SIO MAG components (eg. SIO MAG autopowers) multiply by K^2 and for power spectra involving one SIO MAG component multiply by K.

3. COHERENCE - All coherence results are unchanged by the calibration correction.

4. STANDARDIZED CROSSPOWERS - The standardized crosspowers (section 6.4.3) are unchanged.

5. SEAFLOOR INDUCTION ARROWS - The length of seafloor induction arrows calculated using the magnetic field from CMO as the horizontal reference field should be multiplied by K. Arrows based on local horizontal magnetic fileds are unchanged.

6. SFMT IMPEDANCES - The magnitude of SFMT impedances should be multiplied by K^{-1}. The impedance phase, distortion elements, rotation angles, Hermitean to non-Hermitean ratio and SNR are unchanged. Absolute signal, noise, Hermitean and non-Hermitean power estimates for SIO MAG components should be multiplied by K^2.

7. ERRORS ON 1-6 ABOVE - Relative errors are unchanged. Absolute standard deviation and confidence limit errors are scaled with the same correction factor as the parameter they relate to. Absolute variance errors scale with the square of this factor.

8. VGS IMPEDANCES - The attenuation of the horizontal magnetic field through the ocean, R, should be multiplied by K. This correction changes the VGS impedance magnitude by approximately K^{-1} and has minor effect on the VGS impedance phase. The VGS/SFMT impedance ratio is therefore NOT significantly altered by the calibration change.

9. INVERSION RESULTS - The effect of the calibration correction is to decrease the depth of features in 1D conductvity models by a factor of K, ie. the depth is multiplied by K^{-1}, and to increase the conductivity of features by K^2. Conductances (eg. of D^+ layers or of the near-surface part of the conductivity profile) are multiplied by $K^2 \times K^{-1} = K$. Because of the finite depth-discretization used in the Occam inversions, models based on corrected impedances will exhibit slight differences from models which have been scaled directly, to correct for the calibration change.

10. EARLIER SFMT RESULTS - The calibration correction noted above also applies to SFMT studies performed by the SIO group between 1976 and 1987. Previous SFMT results (eg. in Figures 5.4, 9.5 and 9.12) therefore also require a small correction.

B. EQUATION 4.114

Equation 4.114 (p. 92) contains a typographical error. As stated in the text R is correctly defined as the ratio of the SEAFLOOR over the SEA-SURFACE horizontal magnetic field. This correct form of the equation was used in all calculations.

C. ACKNOWLEDGEMENTS

This addendum provides an opportunity to add to my acknowledgements Dr H. Petersens, of the ANU, whose Applied Mathematics course in Geomagnetism provided an introduction to and an understanding of a variety of geomagnetic phenomena. Finally I would like to include in my acknowledgements my two High School Mathematics teachers, Mr H. Grgus and Mr F. Hurley, who developed my initial interest and education in mathematics and physics.